Thermal structure, composition, atmospheric dynamics and long-terme evolution of irradiated exoplanets

Vivien Parmentier

Université de Nice Sophia Antipolis – Observatoire de la Côte d'Azur
École Doctorale des Sciences Fondamentales et Appliquées

Thèse de Doctorat – PhD Thesis
spécialité Sciences de l'Univers

Vivien Parmentier

Structure thermique, composition, dynamique de l'atmosphère et évolution à long-terme des exoplanètes irradiées

---

Thermal structure, composition, atmospheric dynamics, and long-term evolution of irradiated exoplanets

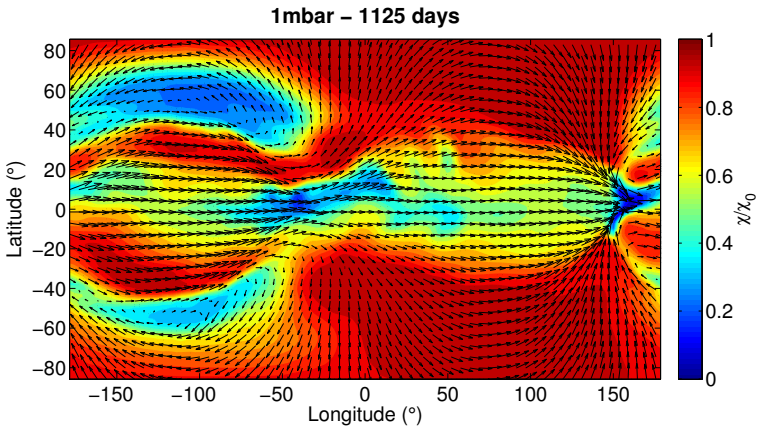

Soutenue le 17 Juin 2014 à l'Observatoire de la Côte d'Azur devant le jury composé de :
Defended June 17^{th} 2014 at the Observatoire de la Côte d'Azur in front of the committee:

Isabelle Baraffe	University of Exeter	Rapporteur/Reviewer
François Forget	Université Pierre et Marie Curie	Rapporteur/Reviewer
David Charbonneau	University of Harvard	Examinateur/Examinator
Olivier Grasset	Université de Nantes	Examinateur/Examinator
Marianne Faurobert	Observatoire de la Côte d'Azur	Examinatrice/Examinator
Thierry Lanz	Observatoire de la Côte d'Azur	Examinateur/Examinator
Tristan Guillot	Observatoire de la Côte d'Azur	Directeur de thèse/PhD advisor

Cover picture: 2D map from a simulated hot Jupiter's atmosphere. The planet is in synchronous rotation and have a permanent dayside and a permanent nightside. The substellar point is at longitude zero. The winds are represented by arrows. The colors represent the total abundance (in condensed or gaseous phase) of a chemical species condensing in the nightside of the planet (such as iron, silicates or titanium oxide). At the equator, the winds blow principally from west to east, a situation known as *superrotation* and caused by the large day/night temperature contrast. In the mid-latitudes and at the poles, the winds blow principally from the substellar point to the antistellar point. Although our chemical compound condenses and rains in the nightside of the planet, it remains present in the atmosphere: vertical mixing by the atmospheric circulation lifts it back to the upper atmosphere. The abundances are linked to the circulation: the spatial variations of the abundance reflect the different circulation regimes between the equator and the pole.

Illustration de couverture: Planisphère issu d'une simulation numérique de l'atmosphère d'un Jupiter-Chaud. La planète est en rotation synchrone et présente toujours la même face à son étoile. Le point sub-stellaire (où le soleil est toujours au zénith) est situé à la longitude zéro. Les flèches représentent les vents dominants. Les couleurs représentent l'abondance totale dans l'atmosphère (en forme condensée ou en forme gazeuse) d'un composé qui condense du côté nuit de la planète mais devient gazeux du côté jour. C'est le cas par exemple du fer, des silicates ou de l'oxyde de titane. A l'équateur les vents soufflent principalement d'ouest en est, une structure due à la grande différence de température entre le jour et la nuit. Aux pôles, le même contraste de température provoque une circulation allant directement du point sub-stellaire au point anti-stellaire. Bien que notre composé condense et pleuve côté nuit, il ne disparaît pas complètement de l'atmosphère: le mélange vertical causé par la circulation permet de le ramener dans la haute atmosphère. L'abondance de notre composé suit les vents dominants: circulation atmosphérique et composition chimique sont reliées.

Abstract

More than a thousand exoplanets have been discovered over the last decade. Perhaps more excitingly, probing their atmospheres has become possible. We now have spectra of hot Jupiters like HD 189733b and HD 209458b, of Neptune-like planets like GJ1214b and even smaller planets are within reach. Most exoplanet atmospheric observations are averaged spatially, often over a hemisphere (during secondary eclipse) or over the limb of the planet (during transit). For favorable targets, longitudinal and latitudinal resolution can also be obtained with phase curve and secondary eclipse mapping techniques respectively. The closer the planet orbits to its star, the easier it is to observe. These hot planets strongly differ from the examples we have in our solar-system. Proper models of their atmospheres are challenging yet necessary to understand current and future observations.

In this thesis, I use a hierarchy of atmospheric models to understand the interactions between the thermal structure, the composition, the atmospheric circulation and the long-term evolution of irradiated planets. In these planets, the strong stellar irradiation dominates the energy budget of the atmosphere. It powers a strong atmospheric circulation that transports heat and material around the planet, driving the atmosphere out of thermal and chemical equilibrium and affecting its long-term evolution. Future instruments (Gaia, SPIRou, MASCARA, CHEOPS, TESS, PLATO etc) will discover many more planets that the next generation of ground-based (GMT, TMT or E-ELT) and space-based (JWST) telescopes will characterize with an unprecedented accuracy. Models will be tested on a large sample of planets, extending the study of climates to exoplanets.

Résumé

Plus d'un millier d'exoplanètes ont été découvertes depuis une dizaine d'années. Plus incroyable encore, nous pouvons maintenant caractériser les atmosphères de ces mondes lointains. Des spectres de Jupiter-chauds tels que HD 189733b et HD 209458b et de planètes similaires à Neptune telles que GJ1214b sont déjà disponibles et ceux de planètes plus petites le seront bientôt. La plupart des observations caractérisent l'état moyen de l'atmosphère : les éclipses secondaires permettent de déterminer le spectre moyen de l'hémisphère jour et les transits permettent d'observer celui du limbe. Pour les cas les plus favorables, l'observation des courbes de phase et la technique de cartographie par éclipse secondaire permettent d'obtenir une résolution en longitude et en latitude. Les planètes les plus proches de leurs étoiles sont aussi les plus faciles à observer. Ces mondes chauds sont radicalement différents des exemples que nous avons dans le système-solaire. Modéliser correctement leurs atmosphères est un défi à relever pour comprendre les observations présentes et à venir.

Durant cette thèse, j'ai utilisé des modèles de différente complexité pour comprendre les interactions entre la structure thermique, la composition, la circulation atmosphérique et l'évolution à long terme des exoplanètes irradiées. La forte luminosité de leur étoile hôte détermine le climat de ces planètes. Elle engendre une circulation atmosphérique qui maintient l'atmosphère dans un état de déséquilibre thermique et chimique, affectant son évolution. Avec l'arrivée de nouveaux instruments (Gaia, SPIRou, MASCARA, CHEOPS, TESS, PLATO etc) de nombreuses autres planètes vont être découvertes. Elles seront caractérisées par les futurs télescopes tels que le GMT, le TMT, l'E-ELT ou bien le télescope spatial James Web. Nos modèles seront testés sur une large diversité de planètes, ouvrant les portes de la climatologie aux exoplanètes.

Remerciements

Je suis un de ces petits garçons qui a toujours voulu être astronome et qui a eu la chance de pouvoir en devenir un. Par une belle nuit d'été, en haut du Pic de Château-Renard, un astronome amateur venu avec son télescope m'a fait découvrir la beauté du ciel: ce soir-là, Saturne et ses anneaux ont décidé de ma vocation. Si j'ai pu entretenir ma passion, c'est d'abord grâce à ma famille, pour qui la curiosité n'a jamais été un vilain défaut. C'est aussi grâce à mes professeurs: de la primaire au master ils m'ont montré que le monde était certes complexe mais compréhensible ou du moins explicable.

Les années de thèses sont charnières. C'est le moment où on passe du monde confortable, dans lequel on sait que les problèmes posés ont déjà des solutions, au monde ardu où le premier défi est de trouver le problème à résoudre. S'engager sans guide c'est se perdre assurément. Merci Tristan d'avoir été là, présent à chaque étape, encourageant lorsque c'était difficile, pressant lorsque cela devenait nécessaire. Tu m'as ouvert les portes de la recherche, celles académiques ô combien nécessaires, mais aussi, plus fondamentalement, les portes intellectuelles. Dans un cas comme dans l'autre tu m'as laissé en franchir le seuil par moi-même. Sans cela, cette thèse n'aurait pas été aussi riche, ni en idées ni en rencontres.

L'observatoire de Nice est un endroit merveilleux pour la recherche tant pour sa situation exceptionnelle (merci Raphaël Bischoffsheim), pour l'exigence intellectuelle de ses chercheurs que pour les amis qu'on peut y trouver. Merci à tous de contribuer à la magie de ce lieu.

Merci à Olivier Grasset de m'avoir accueilli à Nantes à plusieurs reprises. La thèse a rapidement bifurqué du projet initial, laissant ouvert le champs des possibles. J'espère que nous aurons l'occasion de l'explorer plus en détail dans les années qui viennent.

J'ai eu la chance de participer au programme ISIMA créé par Pascale Garaud. La recette est simple: enfermez une dizaine d'étudiants et autant de professeurs pendant six semaines, si les cerveaux chauffent trop arrosez les de píjiŭ et de báijiŭ et emmenez les s'aérer sur la grande muraille. Après six semaines les idées sont semées. Attendez encore quelques mois et vous pouvez récolter les papiers (11 articles ont été publiés suite à la session 2012 !). C'est grâce à ISIMA que j'ai rencontré Adam Showman. Pendant six semaines à Pékin, puis un mois à Tucson, Arizona il est devenu à la fois un *advisor* exigeant mais aussi un compagnon sur lequel compter.

Je me dois de remercier le programme de bourses Franco-Américaines Fullbright. Grâce à lui j'ai pu découvrir pendant six mois le monde de la recherche aux Etats-unis. C'est à Santa-Cruz que j'ai rencontré Jonathan Fortney. Sans son accueil chaleureux et sa disponibilité le monde du transfert radiatif me serait demeuré inaccessible.

Il y a dans une vie certaines personnes qui reviennent de manière discrète mais récurrente. Je dois beaucoup à Douglas Lin: il fût mon directeur de stage à Pékin, organisa ISIMA avec Pascale Garaud et, finalement, nous reçu Tristan et moi à Santa-Cruz. Je n'ai encore jamais vu plus d'idées foisonnant dans la tête d'une seule personne, il faut s'accrocher pour suivre !

Enfin merci à Coline. Ton rôle dans ce travail est indéniable. Ton esprit critique et exigeant a beaucoup contribué à ce manuscrit et aux travaux qui le composent. Mais surtout, sans ta présence à mes côtés, rien ne serait pareil:

El amor constituye una fuerza motriz impresionante, la única capaz de inclinar las palancas de la conducta individual hacia lo mejor del hombre mismo: su plenitud.

Cuitláhuac Arroyo Parra

Pour Acté,
quand tu seras en âge de comprendre
tout ceci sera probablement dépassé.

Contents

"This space we declare to be infinite... In it are an infinity of worlds of the same kind as our own."

Giordano Bruno - On the Infinite Universe and Worlds (1584)

Thousands of new worlds to explore

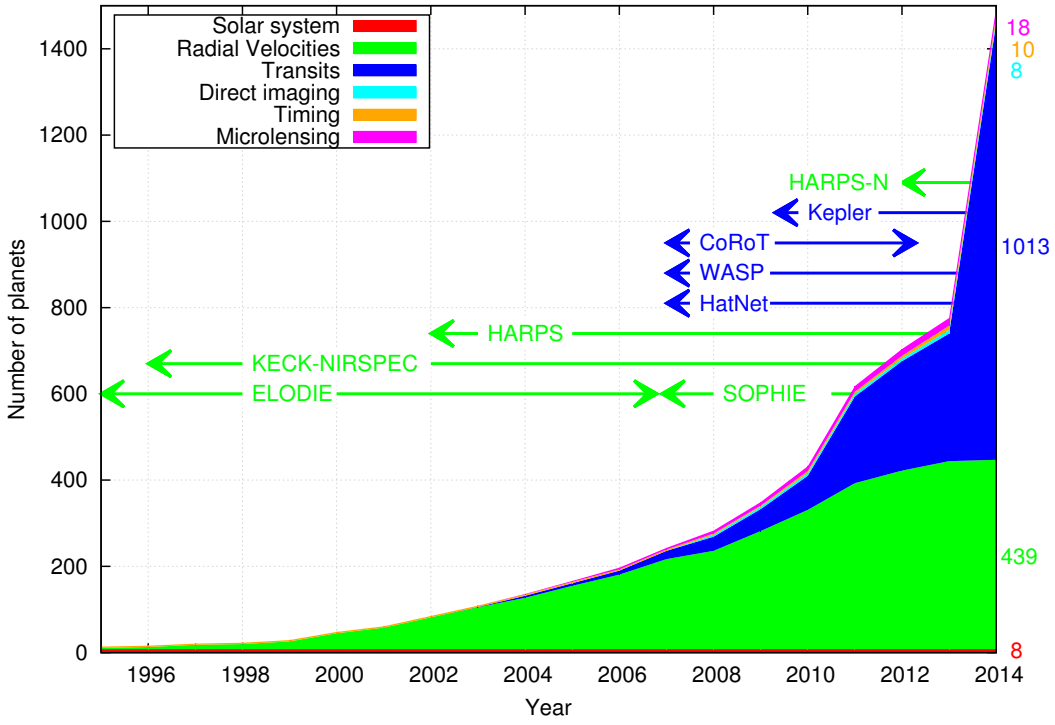

Figure 1. Number of known planets as a function of time listed by detection technique. The different colors represent planets discovered by different detection techniques. The main instruments used for their discoveries are listed above (the ones that detected less than ≈ 10 planets are not listed). Note that part of the 3700 unconfirmed Kepler candidates could increase drastically the number of planets in this list.

So many planets around so many stars ! In the last twenty years, the total number of planets went from 8 (the ones of the solar system) to more than 1500 and an equivalent number of planet candidates observed by the Kepler Space Telescope are waiting for confirmation of their status. This large increase was triggered by a conceptual and technological revolution. With the Copernican revolution in the 16^{th} century, the old ideas of the Greek atomists philosophers were brought back to light by astronomers such as Giordano Bruno: if the sun is just a star among others, planetary systems should be common too. For centuries the technology was not available to detect those far-away planets. In the 1990s, the first exoplanets were detected. They had,

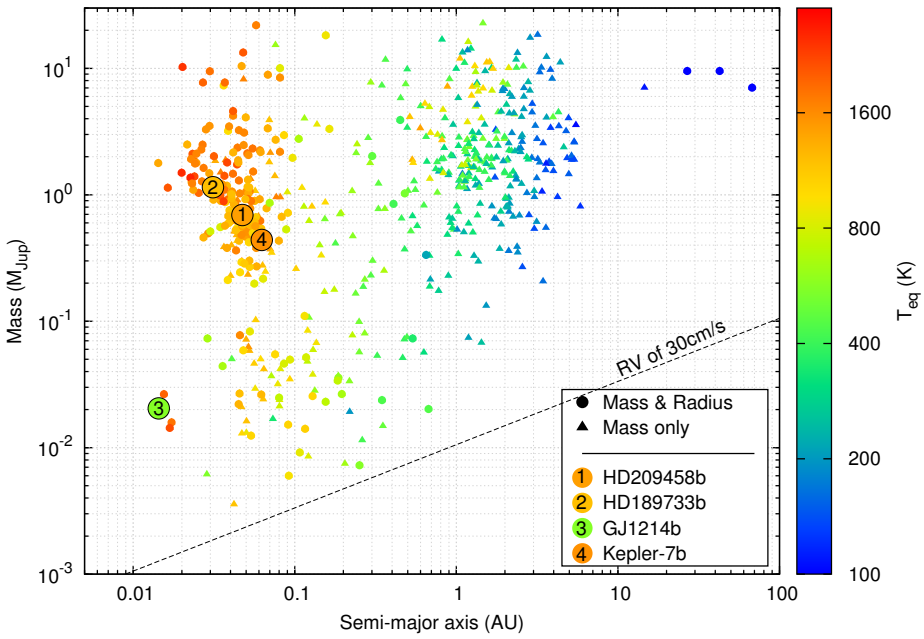

Figure 2. Known planets in the mass/semi-major axis plane. The color represents the equilibrium temperature of the planet assuming zero albedo. Planets for which both mass and radius are known (circles) are a small sample of the total number of known planets (triangles). Listed are specific planets that will be studied more carefully in this manuscript. The dotted line shows the actual limitation of the HARPS instrument.

however, little in common with their solar-system sisters. The first ones were two planets orbiting a pulsar that either survived the supernova explosion, or formed after from the remaining gas and dust. The third planet discovered was the first one orbiting a main sequence star. Although closer to what we used to call planets than the previous ones, this planet seemed very exotic at the time of its discovery: 51 Peg b is an object of roughly half the mass of Jupiter orbiting 10 times closer to its star than Mercury from the Sun. This was unexpected from most planet formation models. Astronomers rapidly realized, however, that 51 Peg b was not an exception, but the first planet of a whole family soon to be discovered: hot Jupiters. In the following two decades, instruments of higher quality, dedicated to the search for new worlds were planned and constructed. Discovering smaller planets, down to Earth-size, orbiting further away from their stars became possible.

The majority of exoplanets have been discovered either via the radial velocity or the transit method (see Figure 1). The first method is based on high spectral resolution observations of the host star. As the planet and the star orbit their common barycenter of mass, the star periodically moves back and forth with respect to us. The spectral lines of the star are therefore Doppler shifted periodically with time, what can be measured with a high resolution spectrograph. The semi-amplitude of the radial velocity shift is directly proportional to the mass of the planet and inversely proportional to the square root of its semi-major axis. The method therefore provides a measurement of the mass of the planet. The sensitivity of the radial-velocity method is directly related to the contrast of the spectral lines and thus the luminosity of the star and the stability of the spectrograph. The radial velocity technique is therefore used with ground-based spectrographs mounted on large telescopes, such as SOPHIE at the Observatoire de Haute Provence, NIRSPEC at the Keck telescope, HARPS at La Silla and HARPS-N at La Palma. With the radial velocity technique, massive planets on tight and wide orbits have been discovered. Smaller planet, down to Earth-size have also been discovered, but only in tight orbits (see Figure 2).

The method of transit is based on the periodic dim of light that can be observed when a planet passes between its host star and the Earth. The shadow cast by the planet on its host star is proportional to the square of the ratio of the planet radius to the stellar one. The transit

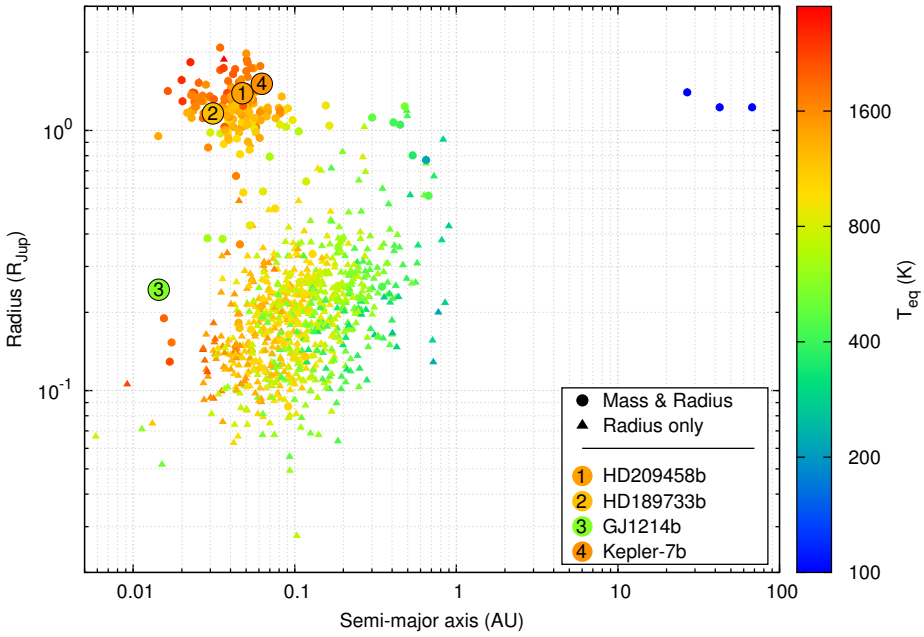

Figure 3. Known planets in the radius/semi-major axis plane. The color represents the equilibrium temperature of the planet assuming zero albedo. Planets for which both mass and radius are known (circles) are a small sample of the total number of known planets (triangles). Listed are the specific planets that will be studied more carefully in this manuscript.

method thus provides a way to measure the radius of the planet. Planets in a wide orbit are much more difficult to discover by transit spectrophotometry. First, as their period is long, observers need to wait a long time to detect a large number of transits. Second, the probability that the orbital plane of the planet is aligned with the star-Earth direction is inversely proportional to the semi-major axis of the planet. Ground based surveys such as SuperWASP and HatNet can probe a large portion of the sky and efficiently discover hot Jupiters. They are nonetheless limited in precision by the atmospheric turbulence and in observation time by the day/night alternation. Space telescopes such as CoRoT and Kepler have a much better photometric precision and can stare at the same target for month or years. They are the main instruments used to discover smaller, down to Earth-size, planets (see Figure 3). The PLATO mission, selected by the ESA cosmic vision program will combine both qualities: it will observe wide portions of the sky for month to years with an outstanding photometric precision.

Among all discovered exoplanets, only $\approx$ 20% have measurements of both their mass and radius. Most of them are hot Jupiters: those large planets with tight orbits are accessible to both transits and radial velocity measurements. Smaller planets and planets on wider orbits discovered by transit by the Kepler Space Telescope usually orbit stars too dim to be observed with the radial velocity technique. Future instruments such as CHEOPS and PLATO will be able to observe planetary transits with a good photometric precision around all the bright stars in the sky. They will therefore increase the number of planets for which both transits and radial velocity measurements are available.

As incredible as it may seem, detecting and characterizing exoplanets atmospheres has become possible. Although this is a challenging task, already $\approx$ 1% of all known exoplanets have been probed. High precision spectrally resolved observations of the planet-star system are necessary to probe the planet's atmosphere. Hot Jupiters, with their large radius and short rotation period are the best targets for atmospheric characterization. Up to date, most observations of exoplanets' atmospheres concern hot Jupiters

Observations can determine the thermal structure, the chemical composition and the atmo-

spheric dynamics of exoplanets atmospheres. Those three fundamental properties of planetary atmospheres affect each other via the different mechanisms described in Figure 4. The thermal structure sets the chemical equilibrium whereas the composition determines the atmospheric opacities, which in turn controls the radiative transfer and thus the temperature. The atmospheric circulation is driven by the temperature contrasts. It transports heat and material, shaping the three-dimensional distribution of the temperature and the composition. Finally, the presence of ionized material directly affects the circulation via the Lorentz forces whereas the bulk composition of the planet sets the mean molecular weight.

In this thesis, I first review the different constraints about the thermal structure, the chemical composition and the atmospheric dynamics of exoplanets that have been gathered from the observations. How does the atmospheric composition influence the thermal structure of the planet is the subject of Chapter 2. The dominant role of the atmospheric dynamics in shaping the chemical composition and the thermal structure of the planet is studied in Chapter 3. Finally, Chapter 4 focuses on the interactions between the atmosphere, the internal structure and the evolution of gas giants planets and super-Earths.

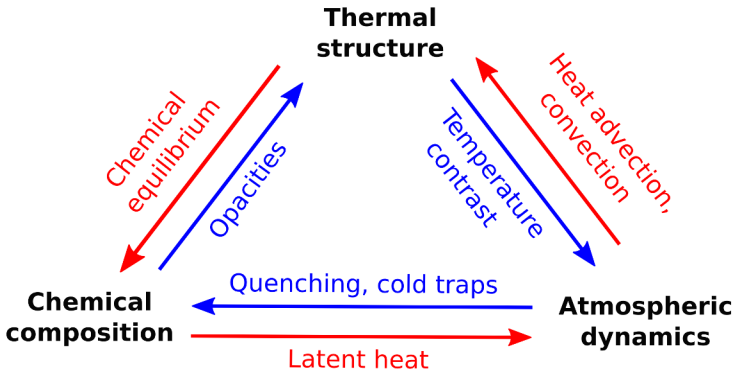

Figure 4. Main physical characteristics of planets atmospheres and their relationships.

"Without atmosphere a painting is nothing"

Attributed to Rembrandt (1606-1669)

Chapter 1

Characterization of exoplanets atmospheres

Contents

Introduction

Astronomy has always been a field driven by observations. Exoplanets exist, they are observed and their atmospheres can be probed, that is why we study them. Several techniques based on simple physical phenomena allow the determination of the composition, the thermal structure, and the dynamics of exoplanets' atmospheres. Those observations are primordial to test theories and calibrate models. Up to now, we retrieved some atmospheric properties of short period planets orbiting bright stars. Those planets can be observed repeatedly with a high signal-to-noise ratio and are thus more amenable to atmospheric characterization. Current observations, however, are limited by the technical characteristics of instruments. Although great work has been done to push the limits of current instruments, observations remain affected by error bars of the order of the searched signal. Most recent discoveries about exoplanets' atmospheres are therefore more hints than unambiguous detections. The first generation of instruments that were built with exoplanets characterization in mind will arrive before the end of the decade. They should lead to a revolution in our comprehension of exoplanets' atmospheres.

To characterize exoplanets' atmospheres, current instruments observe photons that are emitted by the planet, reflected by the upper atmosphere or filtered through the atmospheric limb. This chapter thus begin with some basic definitions concerning the radiative transfer in planetary atmospheres (see Section 1.1). Then, I review the different methods used to characterize exoplanets' atmospheres and their current results. Transit spectrophotometry and high resolution spectroscopy are the two techniques that led to the strongest claims about exoplanets' atmospheres (see Section 1.2). Secondary eclipses can, in principle, characterize the planet's dayside composition and thermal structure. Many claims have been based on secondary eclipses data. However, due the difficulty to interpret the observations and the underestimation of the error bars of some instruments, most of those claims have now been revised (see Section 1.3). Horizontal resolution can be obtained from phase curve observations and secondary eclipse mapping. Those techniques necessitate either high signal-to-noise ratio (secondary eclipse mapping) or long observation time (phase curve). Although they seem promising, they have been used to characterize only a handful of planets (see Section 1.4.1). Today's observations barely lead to unambiguous results and many questions are still unanswered. I end this Chapter by describing how a dedicated space-based mission such as EChO is needed to really open the field of climate research to exoplanets (see Section 1.5.3).

1.1 Basic notions of radiative transfer

A beam of light can be described accurately by its energy, direction, color and polarization. We hereafter neglect the polarization[1]. We define the specific intensity I_λ as the amount of energy that crosses a surface $\mathrm{d}S$ with a direction $\theta = \cos^{-1}\mu$ in a solid angle $\mathrm{d}\Omega = \mathrm{d}\mu\mathrm{d}\phi$ with frequencies $\mathrm{d}\lambda$ around λ during a time $\mathrm{d}t$:

$$I_\lambda(\mu,\phi) = \frac{\mathrm{d}E}{\mu\,\mathrm{d}\mu\,\mathrm{d}\lambda\,\mathrm{d}S\,\mathrm{d}\phi\,\mathrm{d}t} \tag{1.1}$$

[1]Polarization can carry important information, in particular about the presence of clouds. Up to date, only two measurements of polarized light coming from an exoplanet have been claimed (Berdyugina et al. 2008, 2011) but remain unconfirmed by other authors.

In vacuum, I_λ is conserved. When propagating a distance ds through a medium of density ρ the radiation can be either absorbed (i.e. it is transferred to another source of energy) or scattered (i.e. its direction of propagation is modified). Moreover, in local thermodynamic equilibrium, the matter itself emits radiation with a power spectrum given by the Planck function:

$$B_\lambda(T) = \frac{2hc^2}{\lambda^5}\frac{1}{e^{hc/\lambda k_\mathrm{B}T} - 1}\,. \tag{1.2}$$

Then, the specific intensity I_λ along a path s follows the radiative transfer equation (Chandrasekhar 1960):

$$\frac{\mathrm{d}I_\lambda(\mu,\phi)}{\mathrm{d}s} = -\rho(\kappa_\lambda + \sigma_\lambda)I_\lambda(\mu,\phi) + \rho\kappa_\lambda B_\lambda + \rho\frac{\sigma_\lambda}{4\pi}\int_\mu\int_\phi p(\mu,\phi,\mu',\phi')I_\lambda(\mu',\phi')\,\mathrm{d}\mu'\,\mathrm{d}\phi'\,. \tag{1.3}$$

We define κ_λ the *absorption opacity* of the medium, σ_λ the *scattering opacity* and $p(\mu,\phi,\mu',\phi')$ the *scattering function*. This last one is the probability for a scattered photon propagating with an angle (μ',ϕ') to be deflected toward and angle (μ,ϕ) by the ambient medium. Note that we must have $\frac{1}{4\pi}\int_\mu\int_\phi p(\mu,\phi,\mu',\phi')\,\mathrm{d}\mu'\,\mathrm{d}\phi' = 1$. We define ω_ν, the scattering albedo, as the fraction of photons that are scattered:

$$\omega_\lambda = \frac{\sigma_\lambda}{\kappa_\lambda + \sigma_\lambda} \tag{1.4}$$

For a purely absorbing atmosphere, $\omega = 0$ whereas for a purely scattering atmosphere $\omega = 1$. The first term of equation (1.3) describes the apparent absorption of the irradiation due to both the true absorption and the scattering. The second term is the emission of the medium itself. The last term describes the fraction of the light coming from all the possible directions is deflected toward an angle (μ',ϕ') and thus appears in our pencil of light. We can already foresee the difficulties to solve the radiative transfer equation. The opacities κ_λ and σ_λ both depend on the wavelength and on the local conditions of the medium (temperature, pressure and composition). The Planck function B_λ is very sensitive to the temperature and the frequency. Lastly, the scattering term $\frac{\sigma_\lambda}{4\pi}\int_\mu\int_\phi p(\mu,\phi,\mu',\phi')I_\nu(\mu',\phi')\,\mathrm{d}\mu'\,\mathrm{d}\phi'$ couples the intensity propagating in different directions.

Absorbers and scatterers can be any type of particles: electrons, atoms, ions, molecules, water droplets, snow flakes or any kind of condensates. Absorption and scattering opacities are characteristics of the medium. They can be derived from the absorption and scattering *cross-sections*, a physical characteristics of a single particle. For a homogeneous mixture, the relationship is:

$$m\kappa_\lambda = S_\lambda \tag{1.5}$$

where m is the mass of a single particle and S_λ is the absorption cross-section of the particle. For an inhomogeneous medium the total opacity can be derived from the cross-section of the different elements:

$$\kappa_\lambda = \frac{1}{\mu}\sum_i \xi_i S_{i,\lambda}\,. \tag{1.6}$$

ξ_i is the number abundance of species i, $\xi_i = N_i/\sum_i N_i$ and μ is the mean molecular weight of the atmosphere. Cross-sections of different molecules can differ by several orders of magnitudes. At a given wavelength a single particle type usually dominates the opacities and equation (1.6) can be approximated by:

$$\kappa_\lambda \approx \frac{\xi_i}{\mu}S_{i,\lambda}\,. \tag{1.7}$$

The relationships between the scattering opacities and the scattering cross-sections are exactly the same.

1.2 Characterizing exoplanets' atmospheres with transit spectrophotometry and high resolution spectroscopy

1.2.1 Constraints from transit spectrophotometry

Transit spectrophotometry offers the possibility to probe the atmospheric limb of the planet. During a transit, the planet casts a shadow on its host star. The dim of light observed from Earth is directly proportional to the ratio of the planetary and the stellar projected areas:

$$\frac{F_{\rm out} - F_{\rm in}}{F_{\rm out}} = \left(\frac{R_{\rm p}(\lambda)}{R_*(\lambda)}\right)^2 . \tag{1.8}$$

In this equation, $F_{\rm in}$ is the flux observed during transit and $F_{\rm out}$ is the flux observed out of the transit. $R_{\rm p}$ is the apparent planetary radius and R_* is the apparent radius of the star[2]. A Jupiter-like planet orbiting a Sun-like star produces a flux variation of the order of 1%, whereas an Earth-like planet around a Sun-like star produces a flux variation of the order of 0.01%. Both the star and the planet can have a spectral variation of their radius. The variations of the stellar radius are usually much smaller than the variations of the plane radius. They are taken into account via the spectral dependence of the stellar limb-darkening coefficients (see Sing et al. 2008a). The variation of the apparent radius of the planet is due to the differential absorption of the grazing rays during the transit: a planet with an atmosphere that absorbs strongly at wavelength λ_1 but that is almost transparent at a wavelength λ_2 casts a larger shadow at λ_1 than at λ_2.

We now derive an order of magnitude estimate of the expected variation of the apparent planetary radius during transit. The geometry of the problem is described in Figure 1.1: a ray of light (blue line) originating from the star is observed form the Earth after propagating through the planet atmosphere. z is the altitude of a point above a reference radius $R_{\rm p0}$, chosen arbitrarily. A ray of light at wavelength λ of intensity I_λ that propagates a distance $\mathrm{d}s$ along the path s is absorbed and scattered by the atmospheric gas. We now consider that the planetary emission is much smaller than the incoming stellar light and that forward scattering of the stellar light by the atmosphere is negligible (see de Kok & Stam 2012, for a discussion on forward-scattering). Thus, we drop the emission term and the integral term in equation (1.3) and write:

$$\frac{\mathrm{d}I_\lambda}{\mathrm{d}s} = -\rho\chi_\lambda I_\lambda \,, \tag{1.9}$$

where $\chi_\lambda = \kappa_\lambda + \sigma_\lambda$ is the extinction opacity. The ratio of the outgoing intensity I_λ to the incoming stellar intensity I^0_λ of a ray of light crossing the atmospheric limb during the transit of an exoplanet is obtained by integrating equation (1.9) over the path s of Figure 1.1:

$$\log \frac{I_\lambda}{I^0_\lambda} = -\int_{-\infty}^{+\infty} \chi_\lambda(s)\rho(s)\,\mathrm{d}s \,. \tag{1.10}$$

We define the *chord optical depth* by $\mathrm{d}\tau_{\rm chord} = \chi_\lambda\rho\mathrm{d}s$ where $\mathrm{d}s$ is taken along the line of sight. Equation (1.10) then becomes:

$$I_\lambda(z) = I^0_\lambda e^{-\tau_{\rm chord}} \,. \tag{1.11}$$

[2]In the case where the planet or the star are not circular, $R_{\rm p}$ and R_* are the radius of a spherical object with the same projected area.

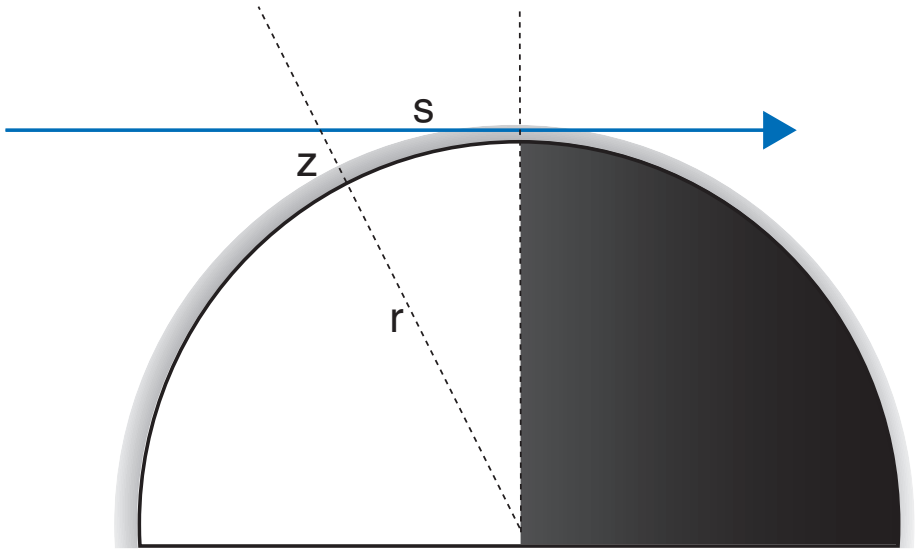

Figure 1.1. Geometry of the transit. The star is at the left and the Earth at the right. The ray of light observed from Earth goes through the path s. Figure from Guillot (2010).

The apparent radius of the planet $R_\mathrm{p}(\lambda)$ is determined by the smallest altitude $z_\mathrm{p}(\lambda)$ that can be reached by a ray of light of frequency λ : $R_\mathrm{p}(\lambda) = R_\mathrm{p0} + z_\mathrm{p}(\lambda)$. Lecavelier Des Etangs et al. (2008a) show that the apparent planetary radius corresponds to a radius where $\tau_\mathrm{chord} = \tau_\mathrm{eq} \approx 0.56$. Thus, our goal is now to solve for z_p in the equation $\tau_\mathrm{chord}(z_\mathrm{p}(\lambda)) = \tau_\mathrm{eq}$. During the transit of an exoplanet, the distance between a given location in the line of sight and the limb of the planet is given by (see Fig. 1.1) :

$$s^2 = (R_\mathrm{p0} + z)^2 - (R_\mathrm{p0} + z_p(\lambda))^2 \,. \tag{1.12}$$

We now look for a solution of eq. (1.10) in a simplified case. We first assume that the atmosphere is in hydrostatic equilibrium (i.e. $\mathrm{d}P/\mathrm{d}z = -\rho g$) and that the gravity does not vary along the line of sight. We furthermore suppose that $z << R_\mathrm{p0}$. Those hypothesis are reasonable close to the planet but are obviously violated infinitely far from the planet, when $s \to \pm\infty$. At visible and infrared wavelengths, most of the absorption takes place at the closest points of the planet, at pressures larger than 1 μbar and those two hypothesis are valid[3]. We also suppose that the atmosphere behaves like a perfect gas, thus ρ can be related to the local pressure and temperature:

$$\rho = \frac{\mu P}{k_\mathrm{B} T} \,. \tag{1.13}$$

As shown later, most of the absorption happens at pressures smaller than a few bars and this assumption should remain valid. We now make a more restrictive assumption: we assume that the atmosphere is isothermal so that the density can be approximated by the exponential law:

$$\rho = \rho_0 e^{-z/H} \,, \tag{1.14}$$

where $H = k_\mathrm{B}T/\mu g$ is the atmospheric scale height. Although not always true, this assumption simplifies the equations enough to get a first picture of the physical problem. We refer the reader to Guillot (2010) for the case of a non-isothermal atmosphere. Given those assumptions, we can

[3]More energetic photons, such as X-rays, can be absorbed up to one planetary radius above the planet (Poppenhaeger et al. 2013). Even there, hydrostatic equilibrium holds (Murray-Clay et al. 2009) and most of the light is absorbed in a region where the gravity can be considered constant and $z << R_\mathrm{p0}$ given a wise choice of R_p0.

write equation (1.10) as:

$$\tau_{\rm chord}(\lambda) = e^{-z_p(\lambda)/H} \int_{-\infty}^{+\infty} \chi_\lambda \rho_0 e^{-\frac{s^2}{2R_{\rm p0}H}} \, {\rm d}s \, . \tag{1.15}$$

To solve this integral, we further need to assume that χ_λ is independent of s. This is clearly false in the general case, as χ_λ depends on the the composition, temperature and pressure and should therefore vary along the line of sight (see the supplementary material of de Wit & Seager 2013, for a detailed review). However, given the strong dependence of the density with height, the atmospheric levels that contribute most to the absorption are concentrated on a vertical range of a few scale heights. Thus, to a first order, we may assume that χ_λ is independent of s. Removing χ_λ from the integral we get the final expression for $\tau_{\rm chord}$:

$$\tau_{\rm chord}(\lambda) = \chi_\lambda \rho_0 e^{-z_p(\lambda)/H} \sqrt{2\pi R_{\rm p0} H} \, . \tag{1.16}$$

The variations of the apparent planet radius between two different wavelengths is therefore given by:

$$R_{\rm p}(\lambda_1) - R_{\rm p}(\lambda_2) = \log\left(\frac{\kappa_{\lambda_1}}{\kappa_{\lambda_1}}\right) H \, . \tag{1.17}$$

At pressures probed by transit spectrophotometry (typically $\approx$ 1bar to 1 µbar, the opacities can vary by several orders of magnitude with wavelength (see Fig. 1 of Parmentier et al. 2014a, described in Sec. 2.2). The radius variation between two wavelengths is thus of the order of several times the atmospheric scale height. Hot planets with a small molecular weight and a weak gravity have large vertical scale heights and are thus good targets for atmospheric characterization by transmission spectroscopy. This is the case of hot Jupiters for which the atmospheric scale height is of order of $100 - 500$km. The relative radius variation of the planet with wavelength is therefore $\Delta R_{\rm p}/R_{\rm p} \approx 1\%$. Figure 1.2 summarizes the radius measurements of HD 189733b obtained by different instruments at different wavelengths. The observed radius of the planet varies from $\approx 0.1575 R_*$ and $\approx 0.1555 R_*$ between 400 and 800nm. This leads to $\Delta R_{\rm p}/R_{\rm p} \approx 1.2\%$. At those short wavelengths, the opacities are dominated by Rayleigh scattering and vary as $\chi_\lambda \propto \lambda^{-4}$. HD 189733b has a scale height of the order of $H \approx 200$km and a radius of $R_{\rm p} \approx 1.38 R_{\rm J}$. Thus, using equation (1.17) we expect a relative radius variation of $\Delta R_{\rm p}/R_{\rm p} \approx 0.7\%$. This is slightly smaller than the observed variation between those two wavelengths. The difference is likely due to a strong temperature gradient in the atmosphere, not included in this estimate: a larger temperature at low pressure increases the scale height and consequently increases the slope of the spectrum at small wavelengths (Pont et al. 2013).

Molecular abundances

The transit spectrum is also used to determine the abundances of the different species contributing to the extinction opacities. From equation (1.17) we see that the first order variation in the transit spectrum are due to the variations of the extinction with wavelength. The extinction is due to both scattering and absorption. Thus the strength of the extinction is proportional to the quantity of absorbers/scatterers. In particular, if the opacity at wavelength λ_1 is due to a species a and the opacity at wavelength λ_2 is due to a species b, we can write (1.17) as a function of the extinction cross-sections $S_{\rm a}$ and $S_{\rm b}$ and the abundances ξ_a and ξ_b of species a and b:

$$R_{\rm p}(\lambda_1) - R_{\rm p}(\lambda_2) = \log\left(\frac{\xi_a}{\xi_b}\frac{S_{\rm a}(\lambda_1)}{S_{\rm b}(\lambda_2)}\right) H \tag{1.18}$$

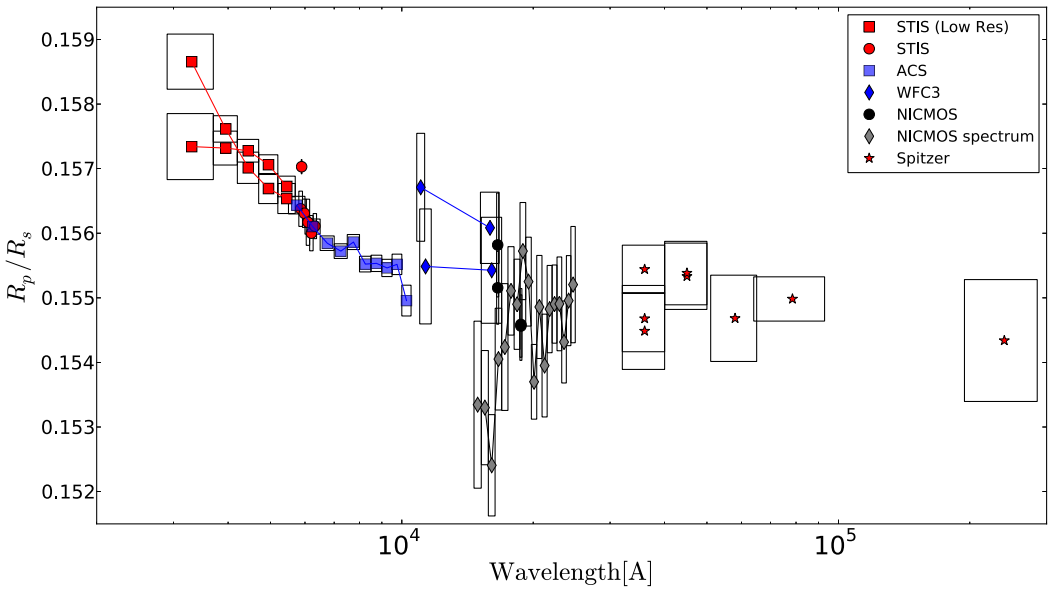

Figure 1.2. Summary of current transit observations of HD 189733b. The planet-to-star radius ratio is plotted as a function of wavelength. Points of different sizes and colors correspond to different instruments used to observe the system. The boxes represent the error on the measurement and the bandwidth of the observations. Observations done simultaneously are connected by a line. Figure from Pont et al. (2013).

$S_a(\lambda_1)$ and $S_b(\lambda_2)$ are physical characteristics of the elements a and b. They can be calculated or measured on the laboratory. The relative abundances of species a and b can therefore be retrieved from the transit spectrum. Importantly, only the abundance ratio can be determine. If the abundance of one species is known by another way, the absolute abundances of all the detected species can be retrieved. For cloudless hot Jupiters, Rayleigh scattering by H_2 dominates the spectrum at short wavelengths. The abundance of H_2 can be estimated *a-priori* (*e.g.* assuming a solar abundance). The signature of the Rayleigh scattering by H_2 can therefore be used as a calibrator, allowing the retrieval of the absolute abundances of other species. Using this technique Sing et al. (2008b) determined the absolute abundance of sodium in HD 209458b.

Temperature

The temperature and the mean molecular weight of the atmosphere can be derived from the transmission spectrum of an exoplanet. With current data, only their values averaged over the whole atmospheric limb are obtained. In the future, high signal-to-noise ratio of the transit ingress and egress could, in principle, probe the differences between different latitudes along the atmospheric limb. For now, we can model the atmospheric limb of the planet with a single, one-dimensional temperature profile $T(P)$.

It is apparent from equation (1.17) that the temperature and the mean molecular weight of the atmosphere will influence the transit spectrum via the atmospheric scale height. We now take the limit $\lambda_1 \to \lambda_2 \to \lambda$ of equation (1.17). Assuming that a single particle type dominates the opacity

at this wavelength, we can re-write equation (1.17) as a function of cross-sections only and obtain:

$$\frac{\mathrm{d}R_\mathrm{p}(\lambda)}{\mathrm{d}\log(S(\lambda))} = \frac{k_\mathrm{B}T}{\mu g} \tag{1.19}$$

If the mean molecular weight is known *a-priori*, as is the case for gas giant atmospheres dominated by hydrogen and helium, a *mean* temperature of the atmosphere can be retrieved from the slope of the transit spectrum.

Which levels are probed ?

The mean temperature retrieved from the transit spectrum is determined by the atmospheric layers where most of the absorption occurs. The vertical extent of the atmospheric slice that contributes to the absorption is estimated by measuring the contribution to the chord optical depth of a length $2\Delta s$ taken along the line of sight and centered around $s = 0$:

$$\frac{\Delta\tau_\mathrm{chord}}{\tau_\mathrm{chord}} = \frac{\int_{-\Delta s}^{+\Delta s} e^{-\frac{x^2}{2R_\mathrm{p0}H}}\,\mathrm{d}x}{\int_{-\infty}^{+\infty} e^{-\frac{x^2}{2R_\mathrm{p0}H}}\,\mathrm{d}x} = \mathrm{erf}\left(\frac{\Delta s}{\sqrt{2R_\mathrm{p0}H}}\right) . \tag{1.20}$$

Using the plane parallel approximation, we can relate Δs to the corresponding atmospheric height Δz and we obtain:

$$\frac{\Delta\tau_\mathrm{chord}}{\tau_\mathrm{chord}} = \mathrm{erf}\left(\sqrt{\frac{\Delta z}{H}}\right) . \tag{1.21}$$

This equation shows that $\approx 90\%$ of the light is absorbed in a slice of atmosphere of $\Delta z \approx 1.3H$ whereas 99% is absorbed in $\Delta z \approx 3.3H$. The temperature derived from equation (1.19) is therefore the atmospheric temperature averaged over $\approx 1-2$ scale heights. This corresponds roughly to a factor $3-6$ in pressure.

The actual levels probed during transit at a given wavelength were measured numerically by Barstow et al. (2013). They perturbed the temperature profile of a reference model by $\Delta T = 1\mathrm{K}$ at a given pressure and quantified the relative changes in the planet radius. As shown in Figure 1.3, transit spectrophotometry can probe the temperature for a large range of pressures: from $P = 10^{-6}$ bar to $P = 1$ bar. The thickness of the atmospheric layer probed are of the order of one magnitude in pressure, which confirms our estimate of $1-2$ atmospheric scale heights. Given the large variation of the pressure probed with wavelength, a spectral resolution of approximately $\lambda/\Delta\lambda \approx 10-100$ is needed to obtain a good vertical resolution in the retrieved temperature profile.

Calibrating the pressure scale

Equation (1.19) provides a relation between the temperature and the radius of the planet. To determine the temperature/pressure profile, we need to determine the pressure at a given radius. If we call $z_\mathrm{p} = 0$ our reference radius, corresponding to the radius at a wavelength λ_0, equation (1.16) becomes:

$$\rho_0 = \frac{\tau_\mathrm{chord}(\lambda_0)}{\kappa_{\lambda_0}\sqrt{2\pi R_\mathrm{p0}H}} . \tag{1.22}$$

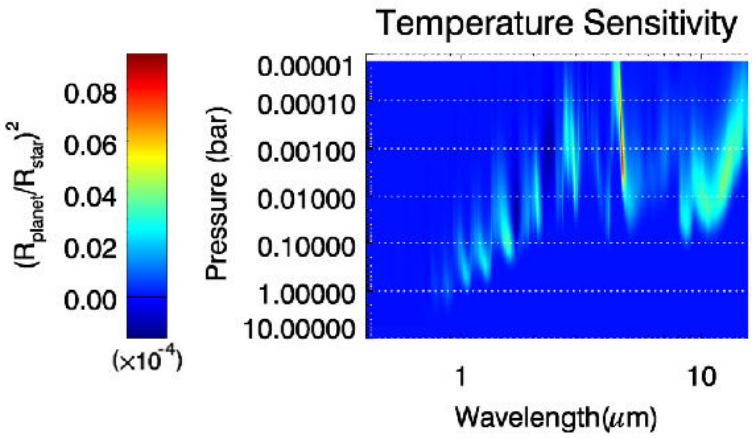

Figure 1.3. Atmospheric pressures probed with transit spectrophotometry as a function of wavelength for a typical hot Jupiter. The variation of the transit depth at a given wavelength due to a temperature increase of 1 K is color-coded. Figure adapted from Barstow et al. (2013).

We now write this expression as a function of the cross-section S_i and of the number abundance ξ_i of the species dominating the extinction opacity at λ_0:

$$\frac{\rho_0}{\mu} = \frac{\tau_{\mathrm{chord}}(\lambda_0)}{\xi_i S_i(\lambda_0)\sqrt{2\pi R_{\mathrm{p0}} H}} \tag{1.23}$$

The apparent radius is the radius of a hard sphere that projects the same shadow as the planet. The emergent intensity from the atmospheric limb is a continuous function of the height. The apparent radius can therefore be calculated by integrating the emergent intensity as a function height. Numerical integration carried by (Lecavelier Des Etangs et al. 2008a) and confirmed by de Wit & Seager (2013) showed that in most cases $\tau_{\mathrm{chord}} \approx 0.56$ is a good approximation. Using the ideal gas law and $\tau_{\mathrm{chord}}(\lambda_0) = 0.56$, we obtain an expression for the pressure P_0 corresponding to the observed radius R_{p0}:

$$\xi_i P_0 = \frac{0.56}{\sigma_i(\lambda)} \frac{\sqrt{k_\mathrm{B} T \mu g}}{\sqrt{2\pi R_{\mathrm{p0}}}} \tag{1.24}$$

This equation links the observed radius of the planet R_{p0} at $\lambda = \lambda_0$ to the *partial* pressure of the molecule dominating the extinction at a given wavelength. If we choose a wavelength λ_0 where the dominant absorber has a known abundance, this expression gives the atmospheric pressure corresponding to the measured planetary radius R_{p0} at λ_0. Combined with the temperature/radius relationship derived in equation (1.19), it allows us to obtain the temperature/pressure profile averaged over the atmospheric limb of the planet. For cloudless hot Jupiters, the extinction at short wavelengths is due to the Rayleigh scattering by H_2. As the abundance of molecular hydrogen can be estimated *a-priori* (*e.g.* taken to be the solar abundance), the observation of the Rayleigh scattering at short wavelengths allows the calibration of the pressure/radius relationship and thus the derivation of the temperature/pressure profile. This technique was used to derive the low resolution temperature profile of HD 209458b (Sing et al. 2008b; Vidal-Madjar et al. 2011b,a, see right panel of Figure 1.4). For HD 189733b, clouds are hiding the signature of the Rayleigh scattering by H_2 and the retrieved temperature profile needs an ad-hoc assumption to calibrate the relationship between the pressure and the observed planetary radius (see Huitson et al. 2012, and left panel of Figure 1.4).

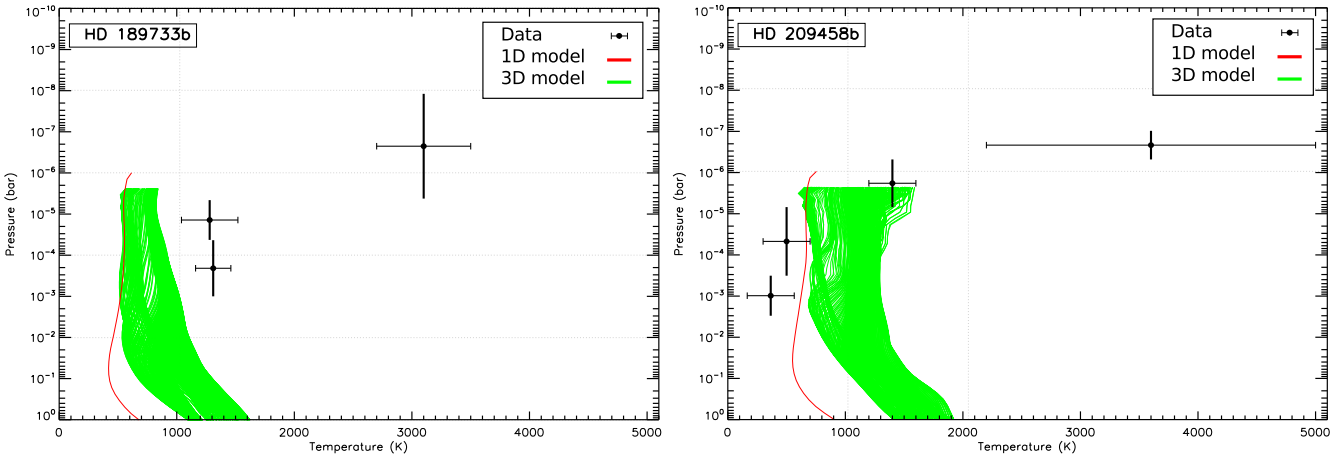

Figure 1.4. Pressure-temperature profile at the terminator of the hot Jupiter HD 189733b (left) and HD 209458b (right). Data are retrieved from the sodium absorption line of the planet observed during transit by Vidal-Madjar et al. (2011b) and Huitson et al. (2012). For HD 209458b, the pressure scale is based on the detection of the Rayleigh scattering by H_2. For HD 189733b, the pressure scale is model dependent: it is determined assuming that top of the cloud deck is at 10^{-4}bar‘". The red line is obtained using the 1D numerical model described in Chapter 2 whereas the green lines are all the limb temperature profiles predicted by the 3D model described in Chapter 3. The difference between the 1D and the 3D temperature profiles is mainly due to the advection of heat by the atmospheric circulation. At pressures lower than 10^{-5}bar, non-LTE effects, not taken into account in our models, become important Barman et al. (2002). Figure adapted from Huitson et al. (2012).

Mean molecular weight

The mean molecular weight of the atmosphere depends on its chemical composition. Gas giant planets are mostly composed of hydrogen and helium. Small planets, conversely, can have a large diversity of atmospheric bulk composition. Equation (1.19) can constrain the mean molecular weight, which is usually unknown. If the temperature is known to a precision δT (*e.g.* , assuming that the temperature is close to the equilibrium temperature of the planet), the mean molecular weight is given by the formula:

$$\mu = \frac{k_\mathrm{B}}{g} \frac{\mathrm{d}R_\mathrm{p}(\lambda)}{\mathrm{d}\sigma(\lambda)} (T \pm \delta T) \tag{1.25}$$

Using this relation, even if the temperature is known with a 50% uncertainty, one can differentiate between an atmosphere dominated by H_2 ($\mu \approx 2.3\,\mathrm{m_H}$), by water ($\mu \approx 18\,\mathrm{m_H}$), by nitrogen ($\mu \approx 28\,\mathrm{m_H}$ – as on Earth or Titan), or carbon dioxide ($\mu \approx 44\,\mathrm{m_H}$ – as on Venus and Mars).

Global retrieval

With spectrally resolved high signal-to-noise observations, second-order effects can appear in the transmission spectrum of a planet. In particular, the temperature, the pressure, the chemical abundances and the gravity affect the absorption and scattering cross-sections in a unique way. As shown by de Wit & Seager (2013), all these quantities, including the mass of the planet, can be retrieved from a high quality transit spectrum alone.

1.2.2 High resolution spectroscopy

An unambiguous method to detect a given molecule in an exoplanet atmosphere is to detect the absorption (during transit) or emission (along the orbit) by a large number of spectral lines of a specific molecule. This can be achieved from the ground using large mirror telescopes and high resolution spectrometers. A resolution of $\approx 100,000$ is necessary to resolve the spectral lines. As the planet orbits its star, the frequency at which a given molecule absorbs and emits radiation is Doppler-shifted (see Figure 1.5). By cross-correlating a laboratory spectrum of a given molecule with the observed planetary signal, the signature of the molecule and its velocity with respect to us can be retrieved. The cross-correlation usually involves ~ 50 distinct spectral lines, leading to a small number of false-positive. Moreover, the orbital motion of the planet can be detected from the Doppler-shift of the lines. For transiting planets, it can be compared with the known orbit of the planet and is used as a confirmation. For non-transiting planets, it can be used to determine the orbital inclination. Because the lines are Doppler-shifted, their location is different from the spectral lines present in Earth atmospheres. They can therefore be observed from ground-based telescopes. Molecules such as CO Brogi et al. (2012); Rodler et al. (2012); de Kok et al. (2013); Rodler et al. (2013) and even water Brogi et al. (2013) can thus be detected via high-resolution spectroscopy[4]. High resolution spectroscopy can also be used to probe the dynamics of the planet.

The observed shift of the spectral lines is due to the combined motion of the planet and its atmosphere. Once the contribution of the planet orbit is removed, any remaining Doppler-shift can be interpreted as being due to the atmospheric motions. For HD 209458b Snellen et al. (2010) detected a Doppler-shift of the carbon monoxide lines that is $\approx 2\,\mathrm{km/s}$ higher than expected from the planet orbit alone. At the low pressures probed by high-resolution spectroscopy, atmospheric

[4] CO_2 and CH_4 were unfruitfully searched by de Kok et al. (2013) in HD 189733b.

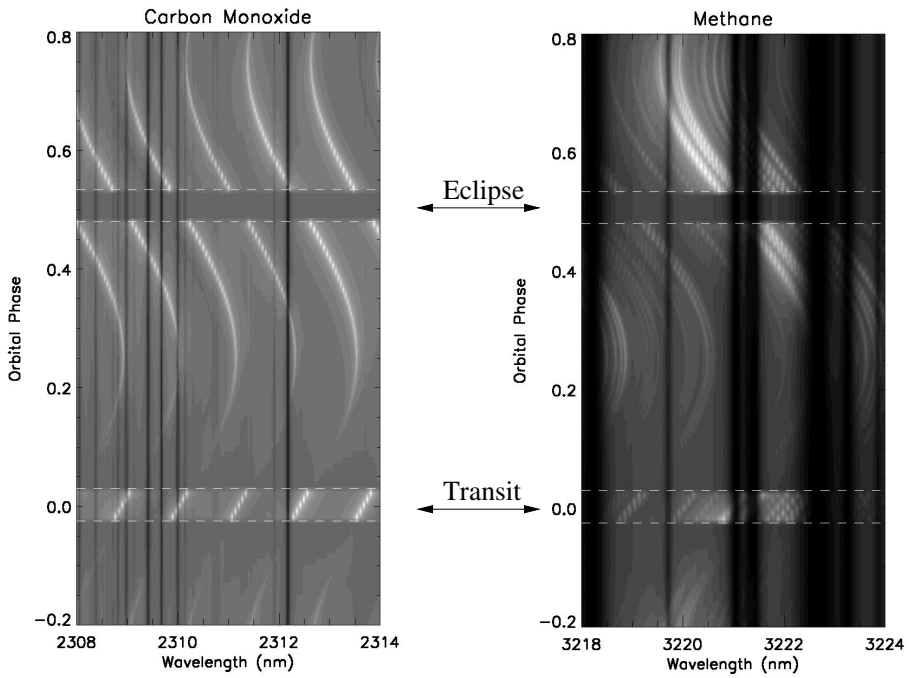

Figure 1.5. Toy model simulations of ground-based spectra of hot Jupiters as a function of planet orbital phase, targeting carbon monoxide (left) and methane (right). The vertical bands are telluric absorption whereas the planet signal appears in emission. The signal during the transit is also shown in emission, for clarity assuming uniform emission from the planet dayside, producing a planet signal equally strong as in transmission. Most of the methane transmission features are blocked by Earth atmosphere, but can be observed around phases ≈ 0.4 and ≈ 0.6. Figure from (Snellen et al. 2011).

models of hot Jupiters predict kilometer per second winds flowing straight from the substellar point to the anti-stellar point (see Chapter 3). Such a large-scale wind pattern could explain this $\approx 2\,\mathrm{km/s}$ Doppler-shift (Showman et al. 2013a, see).

1.2.3 Main instruments and their limits

Up to date, no dedicated instrument were built to characterize exoplanets' atmospheres. To obtain the transmission spectrum of a hot Jupiter, spectral variations of the order of $\approx 1\%$ on the transit depth must be spotted. Observations obtained at different times with different instruments need to be compared. Although great efforts have been made by many authors to push the limitations of current instruments, the reachable precision remains of the order of the signatures that are searched for. Planets in tight orbits around bright stars can be observed repeatedly with a good signal-to-noise ratio. They have therefore the best characterized atmospheres (see Figure 1.6)

Broadband photometry

The InfraRed Array Camera (IRAC) on board the Spitzer Space Telescope has been widely used to observe exoplanets' transits and secondary eclipses. It can observe in four different broadband channels centered at 3.6, 4.5, 5.6 and $8\,\mu\mathrm{m}$. In may 2012, Spitzer ran out of the liquid helium necessary to cool down the 5.6 and $8\,\mu\mathrm{m}$ detectors, although the first two channels remained unaffected. During the warm Spitzer mission, a large amount of telescope time were allocated

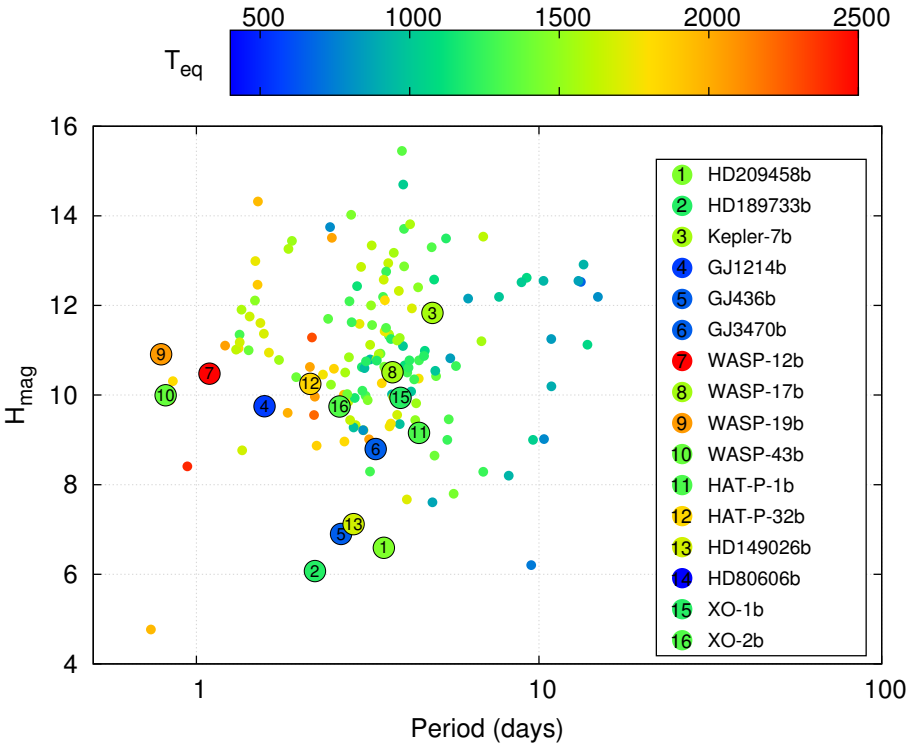

Figure 1.6. H magnitude (magnitude at 1.65 µm) of transiting planets as a function of their revolution period. The color indicates the equilibrium temperature of the planet, assuming no albedo. Planets for which atomic/molecular/cloud detections have been claimed are numbered. Most observations concern planet orbiting bright stars with a small revolution period.

to exoplanets' observations. The IRAC instrument can theoretically search for the signature of water in the transit and in the secondary eclipse spectrum of an exoplanet. During transit, an increased absorption in the 5.8 and 8 µm channels compared to the 3.6 and 4.5 µm ones is a hint for the presence of water. In a planet emission spectrum, water can be detected in absorption or in emission, depending on the temperature profile of the planet. However, broadband photometry with Spitzer/IRAC is not well suited for the detection of molecules. First, as the feature remains unresolved, an increased absorption in one channel compared to another can lead to multiple interpretations on the nature of the active molecule at this wavelength. For example the presence of clouds or CO can mitigate claims of water detection using IRAC. Moreover, IRAC is subject to instrumental systematics that are of the order of the signal. Although great efforts have been made by several authors to correct these systematics, they did not converge toward a reliable method. As an example Désert et al. (2009) and Beaulieu et al. (2008) reached conflicting conclusions concerning the presence of water in the atmosphere of HD 189733b by applying distinct instrumental corrections on the same dataset. As shown by Beaulieu et al. (2010) all these instrumental corrections are valid (see Fig. 1.7), making Spitzer/IRAC an unreliable instrument concerning molecular detections in exoplanets (see also Hansen et al. 2014).

The MIPS instruments on board the Spitzer Space Telescope have been shut down in may 2012 for the Spitzer Warm Mission. It allowed the characterization of the thermal emission of several hot Jupiters at 24 µm and the measurement of the transit radius for the planets HD 189733b and HD 209458b. Given the small number of measurements made with this instrument, extensive study of the instrumental noise has not been performed (at least not as much as for the IRAC measurements), thus it is unclear how reliable are these observations.

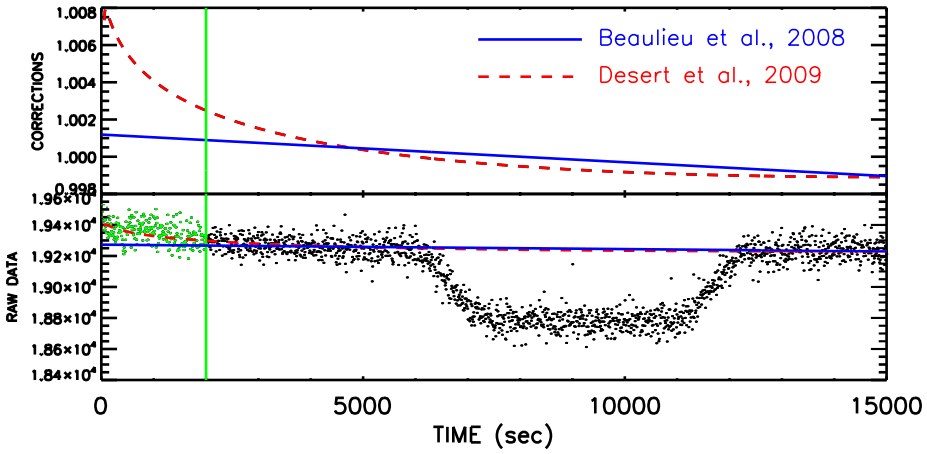

Figure 1.7. Illustration of the difficulty to analyze Spitzer/IRAC transit spectrophotometry measurements. The data is the 5.8 µm Spitzer/IRAC observation of the transit of HD 189733b from Ehrenreich et al. (2007) reprocessed by Beaulieu et al. (2010). The red dotted curve is the final correction applied to the data by Désert et al. (2009) whereas the blue curve is the correction applied by Beaulieu et al. (2008). The two corrections are indistinguishable before and after the transit but are slightly different during the transit, affecting the transit depth differently. The difference between the blue and the red curve is at the origin of the discrepancy about the water detection in HD 189733b between Tinetti et al. (2007) (who claim a detection) and Désert et al. (2009) (who claim no detection). Figure from Beaulieu et al. (2010)

Low resolution spectroscopy

The Space Telescope Imaging Spectrograph (STIS) on board the Hubble Space Telescope covers a large range of wavelengths from the far ultra-violet (FUV) to the near infra-red (NIR), although each observation has to be done in one of the four spectral bands at a time. Distinct spectral resolutions are available: low ($\approx 500 - 1000$), medium ($\approx 5000 - 10000$), high ($20000 - 50000$), and very-high ($\approx 10^5$) (Woodgate et al. 1998). Given this large flexibility, HST/STIS has been used to detect both atmospheric features covering a large spectral range such as the signature of the Rayleigh scattering and thinner features like the absorption by the core of the sodium D line.

The Near Infrared Camera and Multi-Object Spectrometer (NICMOS) on board HST has been used as a spectrograph of resolution ≈ 35 in the $1.5 - 1.8\,\mu$m band to detect methane in the planet HD 189733b (Swain et al. 2008b) and in the $1.2 - 1.8\,\mu$m band to detect water in the planet XO-1b (Tinetti et al. 2010). Sing et al. (2009) used the camera to perform broadband spectrophotometry of HD 189733b at 1.66 and $1.8\,\mu$m. Their results show that the Rayleigh scattering signature observed in the visible and NUV spectra of HD 189733b extends at infrared wavelengths, washing out every molecular feature at those wavelengths. Those results were in strong discrepancy with the methane detection of Swain et al. (2008b). As shown later by Crouzet et al. (2012), Gibson et al. (2012) and Deming et al. (2013), large instrumental systematics polluted the NICMOS signal when used as a spectrograph, invalidating the previous claims of water and methane detection (see Fig. 1.8). As the NICMOS camera is not available for science anymore since July 2010 and has been superseded by the WFC3 camera, no further studies were carried out to properly correct for instrumental systematics.

The WFC3 camera was installed on board the HST in may 2009. Since then, it has been mainly used in transmission spectrophotometry to detect the water absorption feature with a resolution of $\lambda/\Delta\lambda = 300$ between 1.1 and $1.7\,\mu$m. Although Swain et al. (2013) showed that WFC3 was much more reliable than NICMOS, Mandell et al. (2013) discovered that the water signature observed by Huitson et al. (2012) is affected by the spectral binning of the data. Although it seems a promising instrument for the study of exoplanets' atmospheres, WFC3 still has to prove its reliability.

The IRS instruments on board the Spitzer Space Telescope has been shut down in may 2012 for the Spitzer Warm Mission. It was a spectrograph that has been used to observe the emission spectrum of HD 209458 b (Richardson et al. 2007) and HD 189733 b (Grillmair et al. 2008) between 5 and $14\,\mu$m. Given the small number of measurements made with this instrument, extensive study of the instrumental noise have not been performed (at least not as much as for the other instruments), thus it is unclear how reliable those observations are.

Ground based instruments

Ground base observations have increased in sensitivity in the past years. They are less limited in terms of observing time and the instruments systematics can be carefully characterized. Moreover they can observe in spectral bands unavailable for space-based observatories. Broad band, low resolution and high resolution spectroscopy are all achievable from ground based telescopes, sometimes with a unique instrument. Ground-based telescopes are therefore complementary to space-based observatories. They can look for molecules whose spectral signatures are out of the range observed by other instruments. Given the increasing quality of ground-based observations, they might soon become as important as current space-based observatories in the characterization of exoplanets' atmospheres.

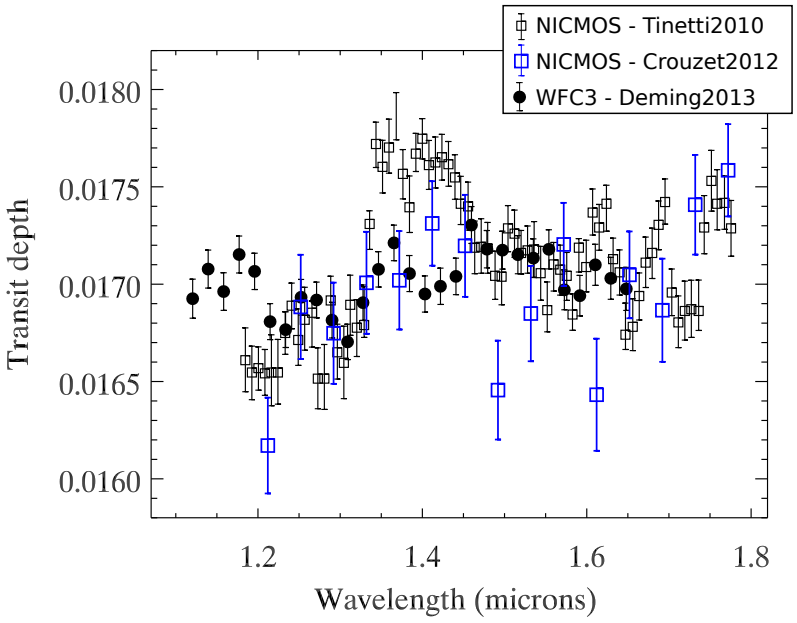

Figure 1.8. Water feature in the absorption spectrum of HD 189733 b. The empty black squared are the observations from the NICMOS instrument analyzed by Tinetti et al. (2010), the blue squares are the same data analyzed by Crouzet et al. (2012) whereas the black points are the observations from WFC3 analyzed by Deming et al. (2013). The water feature seen by Tinetti et al. (2010) is not visible in the analyzes of Crouzet et al. (2012), showing the difficulty to analyze observations with large instrumental noise. The WFC3 observations should be more reliable. They are in strong disagreement with Tinetti et al. (2010) but are still compatible with Crouzet et al. (2012). Figure from Deming et al. (2013)

High resolution spectroscopy, in particular, cannot be obtained from space-based observatories. Large telescopes are needed to obtain a good signal-to-noise ratio with a spectral resolution of the order of $\lambda/\Delta\lambda \approx 100,000$, necessary to resolve the spectra lines of molecules such as carbon monoxide, water or methane. The NIRSPEC instrument at the Keck telescope or the CRIRES at the VLT are the two main instruments performing high resolution spectroscopy for exoplanets.

1.2.4 Possible molecular detections in the atmosphere of exoplanets.

We now focus on the detection of molecules and clouds in exoplanets' atmospheres from transit spectrophotometry and high resolution spectroscopy. Results from other methods such as secondary eclipses spectroscopy lead to more ambiguous results and are therefore discussed later on. The detections are classified by molecules. Table 1.1 summarizes the different notations.

Table 1.1. Notations used in the following tables.

Notation	Meaning
BB	Broad-band
LR	Low resolution
HR	High resolution
TS	Transit spectrophotometry
ES	Emission spectroscopy

Sodium

Sodium was predicted to be the most prominent feature in the transit spectrum of clear-sky gas giant exoplanets. Since the first detection by Charbonneau et al. (2002), sodium have been observed in a handful of planets (see Table 1.2). The smaller than expected signature is currently interpreted as a depletion due to either its ionization or its condensation in the lower atmosphere. In most planets, only the core of the line have been observed whereas the wings of the line are missing, probably hidden below a cloud deck that lay in the $\approx$ mbar levels.

Table 1.2. Claimed detections of sodium in exoplanets' atmospheres from transit spectrophotometry.

Planet	Instrument	Technique	Reference	Comments
HD209458b	HST/STIS	LR TS	Charbonneau et al. (2002)	First detection, low abundance may be due to clouds.
	SUBARU/HDS	LR TS	Narita et al. (2005); Snellen et al. (2008)	Ground-based detection.
	HST/STIS	LR TS	Sing et al. (2008a,b); Vidal-Madjar et al. (2011b,a)	Abundance 2× solar int the deep atm. and < 0.2× solar upper atm. due to condensation ?
	HST/STIS	LR TS	Knutson et al. (2007a); Barman (2007)	Photoionization explains the small abundance ?
	HET/HRS	LR TS	Jensen et al. (2011)	Ground-based.
HD189733b	HET/HRS	LR TS	Redfield et al. (2008)	First ground-based detection. 3× larger than HD 209458b absorption.
	HET/HRS	LR TS	Jensen et al. (2011)	Ground-based.
	HST/STIS	LR TS	Huitson et al. (2012)	$\xi_{Na}/\xi_{H_20} \approx 100 \times$ solar[a]
	Subaru/HDS	LR TS	Astudillo-Defru & Rojo (2013)	Ground-based.
XO-2b	GTC/OSIRIS	LR TS	Sing et al. (2012)	Only line's core, the wings are missing.
WASP-17 b	VLT/GIRAFFE	LR TS	Wood et al. (2011)	Only line's core, the wings are missing. Condensation/ Ionization + masked by clouds.
	Magellan/MIKE	LR TS	Zhou & Bayliss (2012)	-
Hat-P-1 b	HST/STIS	LR TS	Nikolov et al. (2014)	$\xi_{Na}/\xi_{H_20} \approx 1000 \times$ solar[b].
HD 149026 b	HET/HRS	LR TS	Jensen et al. (2011)	Ambiguous because too noisy.
WASP-43 b	GTC/OSIRIS	LR TS	Murgas et al. (2014)	Detection of a small signature of sodium. Hidden by TiO ?

[a] This estimate assumes that water is the source of the 8 µm feature and thus must be handle carefully (Désert et al. 2008)

[b] This estimate assumes that water is the source of the $1.2 - 1.6$ µm feature and that it remains unaffected by the presence of clouds contrary to the HD209458b case (Deming et al. 2013). Thus it must be handle carefully

Potassium

Together with sodium, potassium was predicted to be the most prominent feature in the transit spectrum of clear-sky exoplanets' atmospheres. Contrary to the sodium line, no space-based instrument was able to probe the spectral range covered by the potassium I line. The only unambiguous detection of potassium was done during the transit of XO-2b by Sing et al. (2011a). Its abundance is consistent with solar metallicity, whereas similar observations show a depletion of sodium in the same planet Sing et al. (2012) (see Table 1.3).

Table 1.3. Claimed detections of potassium in exoplanets' atmospheres from transit spectrophotometry.

Planet	Instrument	Technique	Reference	Comments
XO-2b	GTC/OSIRIS	T. S.	Sing et al. (2011a, 2012)	Compatible with solar metallicity.
HD 80606b	GTC/OSIRIS	T. S.	Colón et al. (2012)	Ambiguous.[a]

[a]The detected signal has an unexpected amplitude and spectral location.

Water

Water, if present in solar abundances in clear-sky atmospheres, should create large spectral signatures in the infrared part of the transit spectrum. The first claims of water detection (Barman 2007; Tinetti et al. 2007; Beaulieu et al. 2010) were based on broad band observations with Spitzer/IRAC. Subsequent studies, however, invalidate the use of IRAC for probing the water signature during the transit of an exoplanet Désert et al. (2009); Beaulieu et al. (2010). The second claim of water detection was done using the NICMOS instrument on board the Hubble Space Telescope Tinetti et al. (2010) at shorter wavelength ($1.2 - 1.8\mu$m). Again, subsequent studies (Crouzet et al. 2012; Gibson et al. 2012; Deming et al. 2013) invalidated the use of HST/NICMOS to characterize the absorption feature of water during transit. Later, the NICMOS instrument was replaced by the WFC3 camera and has been proven to be much more reliable (Swain et al. 2013). First results indicate a water signature much smaller than first expected, probably due to the presence of a cloud deck (Deming et al. 2013). Water absorption in the dayside emission spectrum of the planet have also been unambiguously detected using high resolution spectroscopy (Birkby et al. 2013; Brogi et al. 2013). Claims of detection during secondary eclipses were also made (Swain et al. 2010), however, as shown by Hansen et al. (2014), secondary eclipses spectra are, for now, highly unreliable (see section 1.3). Claims of water detections from transit spectrophotometry and high-resolution spectroscopy are reviewed in Table 1.4

Table 1.4. Claimed detections of water in exoplanets' atmospheres from transit spectrophotometry and high-resolution spectroscopy.

Planet	Instrument	Technique	Reference	Comments
HD209458b	HST/STIS	LR TS	Knutson et al. (2007b); Barman (2007)	Compatible with solar metallicity. Ambiguous interpretation due to large spectral bins.
	Spitzer/IRAC	BB TS	Beaulieu et al. (2010)	Detection compatible with a mixing ratio of 4.5×10^4.
	HST/WFC3	LR TS	Deming et al. (2013)	Small amplitude can be explained by the presence of clouds. No constraints on the abundance can be given.
HD189733b	Spitzer/IRAC	BB TS	Tinetti et al. (2007); Beaulieu et al. (2008)	Compatible with solar metallicity. Challenged by Désert et al. (2009)
	Spitzer/IRAC	BB TS	Désert et al. (2009, 2011)	No conclusive evidence for water.
	VLT/CRIRES @3.6µm	HR ES	Birkby et al. (2013)	Detection of water absorption in the dayside spectrum.
XO-1b	HST/NICMOS	LR TS	Tinetti et al. (2010)	Compatible with solar abundances. Challenged by Crouzet et al. (2012); Deming et al. (2013)
	HST/WFC3	LR TS	Deming et al. (2013)	Detection but no quantification (clouds or low abundance). Incompatible with Tinetti et al. (2010).
XO-2b	HST/NICMOS	LR TS	Crouzet et al. (2012)	Compatible with no detection.
WASP-19b	HST/WFC3	LR TS	Huitson et al. (2013)	Detection of water with solar abundance or no detection at all Mandell et al. (2013).
WASP-17b	HST/WFC3	LR TS	Mandell et al. (2013)	Water detected with a low abundance or clouds.
WASP-12b	HST/WFC3	LR TS	Swain et al. (2013)	No conclusive evidence for water.
51 Peg b	VLT/CRIRES	HR ES	Brogi et al. (2013)	Detected during 2 observation nights over 3.
τ Bootis b	Keck/NIRSPEC	HR ES	Lockwood et al. (2014)	Detection of water in emission at 3.3µm.
HD 179949b	VLT/CRIRES	HR ES	Brogi et al. (2014)	Emission in the dayside spectrum.

Carbon monoxide and methane

In hydrogen dominated atmospheres, carbon monoxide should be in equilibrium with methane via the chemical reaction: $CO + 3H_2 \rightleftarrows CH_4 + H_2O$. In chemical equilibrium, CO is the dominant species at high temperatures, whereas CH_4 should dominate at low temperatures. In planetary atmospheres, this picture would lead to a dominance of CH_4 in the upper, cooler atmosphere whereas CO should dominate at deep pressure. However, the reaction rate of this chemical reaction strongly decreases when the pressure and temperature decrease. As a result, the composition of a parcel gas that is advected upward from the deep layers of the planet can keep its high CO abundance in the colder upper atmosphere because the chemical reaction is not fast enough to convert CO into CH_4. This phenomenon, known as *quenching* is predicted to lead to strong disequilibrium chemistry in the atmosphere of hot Jupiters, with atmospheres dominated by CO rather than CH_4 (Cooper & Showman 2006; Visscher & Moses 2011, and also Chapter 3). Carbon monoxide was first detected in absorption during transit by Désert et al. (2009), however only high resolution spectroscopy provided the first non-ambiguous detection (Snellen et al. 2010) (see Table 1.5).

Methane has been searched for in the atmosphere of HD 189733b using multiple instruments. A first detection by (Swain et al. 2008a) in the transmission spectrum of the planet was followed by the detection of CH_4 fluorescence in the emission spectrum of the planet (Swain et al. 2010). Both detections were later challenged. Although Waldmann (2012) confirmed the data analyses of (Swain et al. 2008a), Gibson et al. (2012) showed that the instrumental systematics of the HST/NICMOS instrument were too important to draw any conclusion from this dataset. Using HST/NICMOS in broadband photometry, Sing et al. (2009) found a transit spectrum dominated by hazes, in contradiction with the methane detection of (Swain et al. 2008a). The detection of (Swain et al. 2010) in the dayside spectrum was later challenged by Birkby et al. (2013) who did not detect the non-LTE emission using high resolution spectroscopy[5]. Thus, up to now, there is no strong evidence for methane in exoplanets' atmospheres.

[5]Secondary eclipses measurements are described in Section 1.3.

Table 1.5. Claimed detections of carbon monoxide in exoplanets' atmospheres from transit spectrophotometry and high-resolution spectroscopy.

Planet	Instrument	Technique	Reference	Comments
HD 189733b	Spitzer/IRAC	BB TS	Désert et al. (2009)	Absorption feature at 4.5μm. Not conclusive.
	Spitzer/IRAC	BB TS	Knutson et al. (2012)	Confirmed 4.5 μm feature in TS. Possible higher than equilibrium abundance of CO from the nightside emission.
	VLT/CRIRES	HR ES	de Kok et al. (2013)	Detection of CO absorption in the dayside. Haze is optically thin or is located at high pressure.
	Keck/NIRSPEC	HR ES	Rodler et al. (2013)	Detection of CO absorption in the dayside.
HD 209458b	VLT/CRIRES	HR TS	Snellen et al. (2010)	Volume mixing ratio $1 - 3 \times 10^{-3}$, C/H ratio 2-6 times greater than the stellar one.
τ **Bootis b**	VLT/CRIRES	HR ES.	Brogi et al. (2012)	Absorption in the dayside spectrum.
	VLT/CRIRES	HR ES	Rodler et al. (2012)	Absorption in the dayside spectrum.
51 Peg b	VLT/CRIRES	HR ES	Brogi et al. (2013)	Absorption in the dayside spectrum seen in two of three observations.
HD 179949b	VLT/CRIRES	HR ES	Brogi et al. (2014)	Emission in the dayside spectrum.

Titanium oxide

Titanium oxide is the most volatile of the metal oxides that can be found in exoplanets' atmospheres. Its signature has been observed in brown dwarfs with the same atmospheric temperature as in the dayside of numerous hot Jupiters. Moreover, if present in solar abundances in those atmospheres, absorption of the stellar light by the broadband absorption bands of titanium oxide should lead to a temperature inversion (i.e. a region where the temperature increases with altitude) around $\approx 100-1$mbar (see Fortney et al. 2008, and Chapter 2). Such temperature inversions are possibly detected from the secondary eclipses of several exoplanets, although no unambiguous conclusion has yet been drawn from the datasets. In the other hand, the condensation of TiO in the deep layers of the planet (Spiegel et al. 2009), in the nightside (Parmentier et al. 2013) or its destruction in the upper atmosphere by the stellar X and UV radiations (Knutson et al. 2010) could severely deplete this molecule from the atmosphere of giant exoplanets. Up to now, two planets show hints of titanium oxide absorption. Other observations confirmed the lack of TiO in planets where it was not expected to be present from secondary eclipses data (see Table 1.6).

Table 1.6. Claimed detections of titanium oxide in exoplanets' atmospheres from transit spectrophotometry.

Planet	Instrument	Technique	Reference	Comments
HD 209458b	HST/STIS	SR TS	Désert et al. (2008)	Absorption feature at 0.6 – 0.8μm. Low abundance (10-1000 below solar). Ambiguous detection.
Wasp-19 b	HST/STIS	SR TS	Huitson et al. (2013)	Detection of a lack of TiO.
Wasp-12 b	HST/STIS	SR TS	Sing et al. (2013)	Detection of a lack of TiO.
WASP-43 b	GTC/OSIRIS	BB TS	Murgas et al. (2014)	Possible hint for TiO.

Hydrogen

Although hydrogen is believed to be the main constituent of gas giant atmosphere, it has only been detected in one of the numerous transiting planets. The Rayleigh scattering of H_2 has been observed in HD 209458b by Lecavelier Des Etangs et al. (2008a) (see Table 1.7). In other planets, it might be hidden by clouds.

Table 1.7. Claimed detections of hydrogen in exoplanets' atmospheres from transit spectrophotometry.

Planet	Instrument	Technique	Reference	Comments
HD 209458b	HST/ACS	LR TS	Lecavelier Des Etangs et al. (2008b)	Rayleigh scattering in absorption.
	HST/STIS	LR TS	Ballester et al. (2007)	Detection of hot (excited) hydrogen at high altitude, consistent with $\approx 5000K$ layer.

Calcium

Recently, the detection of calcium in the atmosphere of HD 209458 b have been claimed by Astudillo-Defru & Rojo (2013) (see Table 1.8). Calcium is an important element as it may condense with TiO forming $CaTiO_3$ condensates.

Table 1.8. Claimed detections of calcium in exoplanets' atmospheres from transit spectrophotometry.

Planet	Instrument	Technique	Reference	Comments
HD 209458b	Subaru/HDS	SR TS	Astudillo-Defru & Rojo (2013)	Also a possible detection of Scandium.

Clouds

The planet HD 189733b shows the best evidence for clouds, with a transit spectroscopy dominated by Rayleigh scattering from UV to infrared wavelengths (Lecavelier Des Etangs et al. 2008a; Sing et al. 2009, 2011b; Gibson et al. 2013; Pont et al. 2013). The presence of a large, wavelength-dependent albedo observed by Berdyugina et al. (2011) and later confirmed by Evans et al. (2013) provided more evidence for the presence of aerosols in this planet (see Section 1.3.2). Recently, using the WFC3 camera on-board the Hubble Space Telescope, several authors realized that clouds were weakening the absorption signature of water in numerous hot Jupiters (Sing et al. 2013; Deming et al. 2013). Clouds also seem to dominate the the transit spectrum of mini-Neptune and Super-Earth such as GJ1214b (Kreidberg et al. 2014), GJ436b(Knutson et al. 2014) and GJ3470b (Crossfield et al. 2013). The high-precision, long-term photometry of the Kepler spacecraft's observations provided evidences for the presence of clouds in a dozen of planets (Heng & Demory 2013). In the case of Kepler-7b, constraints on the horizontal distribution of clouds have been derived by Demory et al. (see 2013, presented in Chapter 3). Hints for cloudy atmospheres from transit spectrophotometry are reviewed in Table 1.9.

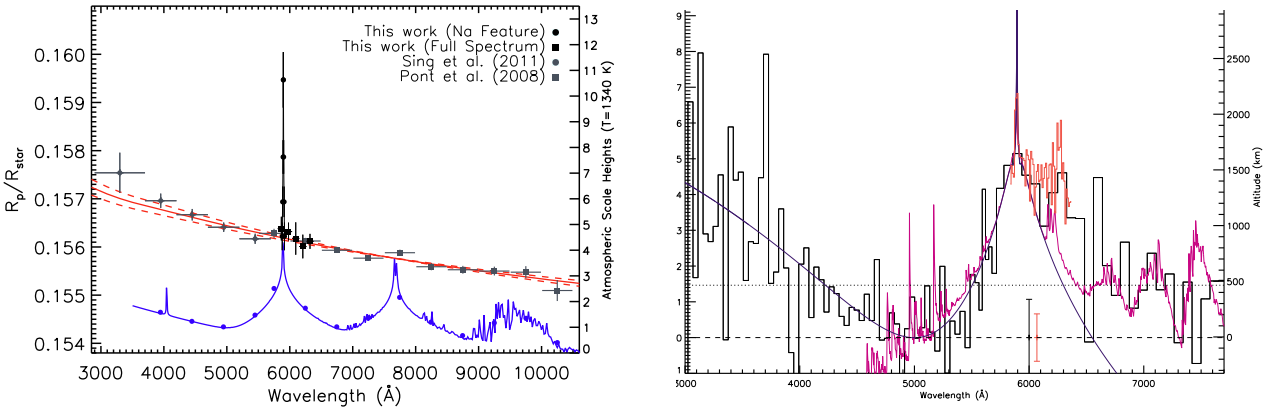

Figure 1.9. Cloudy vs. cloudless transmission spectra of hot Jupiters.
Left panel : transmission spectrum of HD 189733b obtained with HST/STIS and HST/ACS. The blue line is a modeled transmission spectrum for a clear-sky, solar-composition atmosphere from (Fortney et al. 2010) whereas the red line is the transmission expected from Rayleigh scattering by sub-micron size particles (Lecavelier Des Etangs et al. 2008a). Clearly, absorption by clouds hide most of the molecular features predicted by the model and the core of the sodium line peaks above the clouds.
Right panel : transmission spectrum of HD 209458b obtained with HST/STIS at low (black line) and high resolution (red line) from Sing et al. (2008b) (the y-axis is the planetary absorption percentage compared to the minimum absorption level referenced at 5,000Å (1.440%)). The dark blue line is a model including Rayleigh scattering by molecular hydrogen and absorption by atomic sodium. The purple line show the absorption due to sodium, TiO and VO. Rayleigh scattering by molecular hydrogen dominates the spectrum at small wavelengths, whereas the sodium line is clearly visible at larger wavelengths. Right of the sodium line, the excess absorption was interpreted as the signature of titanium oxide by Désert et al. (2009).

Table 1.9. Claimed detections of haze in exoplanets' atmospheres from transit spectrophotometry.

Planet	Instrument	Technique	Reference	Comments
HD 189733b	HST/ACS	LR TS	Lecavelier Des Etangs et al. (2008a)	Rayleigh scattering, particle size $< 0.1\,\mu$m.
	HST/NICMOS (photometry) 1.66 and 1.8 µm	T. S.	Sing et al. (2009)	Consistent with Lecavelier Des Etangs et al. (2008a).
	HST/STIS $0.3 - 0.6\,\mu$m	LR TS	Sing et al. (2011b)	Rayleigh scattering.
	HST/WFC3 $0.3 - 0.6\,\mu$m	LR TS	Gibson et al. (2013)	Rayleigh scattering.
	HST/STIS $0.3 - 0.6\mu$m	LR TS	Pont et al. (2013)	Dust shapes the whole transit spectrum.
	NOT/TurPol polarimeter	BB ES	Berdyugina et al. (2011)	Detection of high, wavelength-dependent, polarized albedo. Interpreted as Rayleigh scattering by clouds.
	HST/STIS	BB ES	Evans et al. (2013)	Confirmation of Berdyugina et al. (2011).
Wasp-12 b	HST/STIS,WFC3 and Spitzer/IRAC	LR TS	Sing et al. (2013)	Rayleigh scattering by sub-micron size particles explains the lack of molecular features.
Hat-P-12 b	HST/WFC3	LR TS	Line et al. (2013)	Flat spectrum, lack of water feature.
Hat-P-32 b	Gemini-North/GMOS	LR TS	Gibson et al. (2013)	Flat spectrum
HD 209458b	HST/WFC3	LR TS	Deming et al. (2013)	Small amplitude of the water feature.
GJ3470 b	Keck/MOSFIRE, Spitzer/IRAC, MITSuME	LR TS	Crossfield et al. (2013), Fukui et al. (2013),Demory et al. (2013)	Flat transmission spectrum. Either a metal rich, a cloudy or a methane depleted atmosphere.
	LBC	BB TS	Nascimbeni et al. (2013)	Rayleigh scattering at small wavelengths.
GJ436 b	HST/WFC3	LR TS	Knutson et al. (2014)	Flat spectrum explained by a cloudy or a metal-rich atmosphere.
GJ1214 b	HST/WFC3	LR TS	Kreidberg et al. (2014)	Clouds *needed* to explain the flat spectrum.
Kepler-7 b	Kepler	BB ES	Demory et al. (2011)	High albedo ($A_g = 0.32 \pm 0.02$) explained by the presence of clouds.
	Kepler	Phase curve	Demory et al. (2013)	Shift of the phase curve interpreted as a western dayside cloudier than eastern dayside.

Probing the extended atmosphere

Near and far ultra-violet (NUV and FUV) observations of transiting exoplanets allow to probe their extended atmosphere because resonant lines of atomic species are very strong in this wavelength range. The presence of an extended atmosphere of hydrogen overfilling the Roche lobe of HD 209458b was first observed by Vidal-Madjar et al. (2003). They measured the Doppler shift of the absorption lines and proposed that the planet was loosing its hydrogen via atmospheric escape. Subsequent observations of heavier atoms such as silicon, carbon and magnesium overfilling the Roche lobe of the planet confirmed the "blow off" escape of HD 209458b's atmosphere. Atmospheric escape has been detected around two other planets (Wasp-12 b and HD 189733b) and seems to be a common characteristics of hot Jupiter. The mass loss rates derived for hot Jupiters should not affect their long-term evolution. Smaller planets, however, might be stripped-out from their atmosphere (Lecavelier Des Etangs 2007). Such an atmospheric mass loss depends strongly on the mass of the planet and is believed to sculpt the population of close-in planets with a mass smaller than Jupiter (*e.g.* Lopez et al. 2012; Lopez & Fortney 2013; Kurokawa & Nakamoto 2014). For smaller, rocky planets, silicates can also evaporate. This lead to a large cloud of material around the planet, analogous to a cometary tail, allowing to spot very small (down to Moon-size) objects (Perez-Becker & Chiang 2013). Observations of extended atmospheres from transit spectrophotometry are reviewed in Table 1.10.

Table 1.10. Claimed detections of upper atmospheric constituents in exoplanets' atmospheres from transit spectrophotometry.

Planet	Instrument	Technique	Reference	Comments
HD 209458b	HST/STIS (FUV)	TS	(Vidal-Madjar et al. 2003)	Hydrogen (Lyman-α) escaping at high velocity. Interpretation challenged by Ben-Jaffel (2007).
	HST/STIS (FUV)	TS	Vidal-Madjar et al. (2004)	Carbon (C II[6]) and oxygen (O I) atoms filling the Roche lobe.
	HST/ACS (FUV)	TS	Ehrenreich et al. (2008)	Confirmation of Lyman-α absorption.
	HST/COS (FUV)	TS	Linsky et al. (2010)	Ionized silicon (Si III) and carbon (C II) escaping the atmosphere.
	HST/STIS (NUV)	TS	Vidal-Madjar et al. (2013)	Magnesium atoms (Mg I) escaping the atmosphere. Velocity measured.
	HET	TS	Jensen et al. (2012)	Hα absorption, ground-based.
HD 189733b	HST/ACS	TS	Lecavelier Des Etangs et al. (2010)	Atmospheric escape of hydrogen from Lyman-α observations.
	HST/STIS	TS	Lecavelier Des Etangs et al. (2010)	Atmospheric escape enhanced after a stellar flare.
	HST/COS	TS	Ben-Jaffel & Ballester (2013)	Neutral oxygen detected. Early ingress in the absorption of C II caused by magnetosphere ?
	Chandra (X-Ray)	TS	Poppenhaeger et al. (2013)	Planet radius of $\approx 1.75 R_{\rm p}$. Absorption due to ionized metals.
	HET	TS	Jensen et al. (2012)	Hα absorption, ground-based.
Wasp-12 b	HST/COS (NUV)	TS	Fossati et al. (2010)	Ionized magnesium (Mg II) filling the Roche lobe. Hints for other metals : neutral sodium, tin, and manganese, and singly ionized ytterbium, scandium, manganese, aluminum, vanadium, and magnesium. Unexpected early ingress.
	HST/COS (NUV)	TS	Haswell et al. (2012)	Ionized magnesium (Mg II) and iron (Fe II) overfilling the Roche lobe of the planet.
KIC 12557548b	Kepler	TS	Rappaport et al. (2012)	Large variability in the transit, comet-like shape are evidence for a disintegrating body.
	Kepler	TS	Budaj (2013)	Particle size of $\approx 0.1 - 1\,\mu$m derived from forward-scattering. Smaller particles after than before the mid-transit. Unexplained quasi-periodicity of the tail of 1.5 years.
	Kepler, WFC3, NIRC2	TS	Croll et al. (2014)	Particle size greater than $\approx 0.5\,\mu$m derived from the flat spectrum.
	Kepler	TS	Van Werkhoven et al. (2014)	Confirmed the previous analyses.
KOI-2700b	Kepler	TS	Rappaport et al. (2012)	Similar properties than KIC 12557548b

1.3 Constraints from secondary eclipses

Half an orbital period after the transit, the star eclipses the planet. When comparing the total flux received by an observer before and during the secondary eclipse, the emission spectra of the planet can be observed. With F_p the planetary flux and F_* the stellar flux, we can write:

$$\frac{F_\mathrm{p}(\lambda)}{F_*(\lambda)} = \frac{F_*(\lambda) + F_\mathrm{p}(\lambda)}{F_*(\lambda)} - 1\,, \tag{1.26}$$

where $F_*(\lambda)+F_\mathrm{p}(\lambda)$ is observed before and after the secondary eclipse and $F_*(\lambda)$ is observed during the eclipse.

We now want to estimate the expected spectral variations in the measured planetary flux during secondary eclipse. For this purpose, we separate the flux coming from the planet into two contributions: the planetary thermal emission and the light reflected from the star.

1.3.1 The planetary emission

The atmospheres of irradiated planets absorb the stellar irradiation, convert it into heat, and then radiate their thermal energy back to space. We now consider a planet as seen just before and just after the secondary eclipse. The point of the planet that is directly below the star is called the substellar point and is facing us. Any point on the dayside can be described by two angles: θ is the angle between the point of study, the center of the planet and the substellar point whereas ϕ is the angle between the point of study, the center of the planet and the eastern part of the equatorial line. We define $\mu = \cos\theta$. μ goes from 0 to 1; $\mu = 1$ corresponds to the substellar point and $\mu = 0$ to the terminator. ϕ goes from 0 to 2π, $\phi = 0$ pointing east, $\phi = \pi/2$ pointing north etc.. to the stellar emission flux. The star is much hotter and much larger than the planet, its flux is therefore larger and peaks at smaller wavelengths than the planetary emission. Even for the hottest planets, at visible wavelengths, the detection of thermal emission from the planet is difficult, because the stellar flux is much larger than the planetary emission and because the light scattered by the planet also contributes to the observed flux. Thus, we focus on the thermal emission at infrared wavelengths, where the scattering of the light becomes inefficient and can be neglected.

We now consider the light escaping from an atmospheric column situated at a location (μ, ϕ) in the planet's dayside. The ray of light that propagates in our direction makes an angle $\theta = \cos^{-1}\mu$ with the local vertical, described by the z coordinate. We define the *normal optical depth* as the optical depth in the vertical direction $\mathrm{d}\tau_\lambda = \rho\kappa_\lambda \mathrm{d}z$. The radiative transfer equation writes:

$$\mu\frac{\mathrm{d}I_{\lambda_\mu}}{\mathrm{d}\tau_\lambda} = -I_\lambda + B_\lambda(\tau_\lambda) \tag{1.27}$$

The intensity escaping from the atmosphere is given by Chandrasekhar (1960):

$$I_\lambda = I_{\lambda,\mathrm{deep}} e^{-\tau_{\lambda,\mathrm{deep}}/\mu} + \frac{1}{\mu}\int_0^{\tau_{\lambda,\mathrm{deep}}} B_\lambda(\tau') e^{-\tau'/\mu}\,\mathrm{d}\tau'\,, \tag{1.28}$$

where $\tau_{\nu,\mathrm{deep}}$ is the optical depth of an arbitrary level in the atmosphere and $I_{\lambda,\mathrm{deep}}$ the intensity emitted by this level. For terrestrial planets it corresponds to the optical depth of the solid surface.

For giant planets with no surface it is set to infinity and the equation becomes simply:

$$I_\lambda = \frac{1}{\mu}\int_0^\infty B_\lambda(\tau')e^{-\tau'/\mu}\,\mathrm{d}\tau'\,, \tag{1.29}$$

This integral depends on the source function B_λ and thus on the exact temperature profile in the atmosphere $T(P)$. The exponential weights ensure that the deep atmosphere does not contribute to the outgoing flux,i.e. the deep atmosphere is unobservable. Therefore, only the source function in the observable, low optical depth regions contributes to the thermal emission. For small values of τ the Planck function can be approximated by a linear trend:

$$B_\lambda = a_\lambda + b_\lambda\tau_\lambda\,. \tag{1.30}$$

The solution simplifies to:

$$I_\lambda = a_\lambda + b_\lambda\mu\,, \tag{1.31}$$

which can be written:

$$I_\lambda = B_\lambda(\tau_\lambda/\mu = 1)\,. \tag{1.32}$$

From this last equation we see that the thermal flux emerging from an atmospheric column of gas corresponds to the blackbody emission of the $\tau_\lambda/\mu = 1$, called the photosphere. The observed flux of the planet is obtained by integrating 1.32 over the whole dayside:

$$\left\langle F_{\mathrm{p}(\lambda)}\right\rangle_{\mathrm{d}} = R_{\mathrm{p}}^2\int_{\phi=0}^{\phi=2\pi}\int_{\mu=0}^{\mu=1} I_\lambda\mu\,\mathrm{d}\mu\mathrm{d}\phi. \tag{1.33}$$

If we assume that the atmosphere is homogeneous in latitude and longitude, we obtain:

$$\left\langle F_{\mathrm{p}}(\lambda)\right\rangle_{\mathrm{d}} = 2\pi R_{\mathrm{p}}^2\int_{\mu=0}^{\mu=1}\mu\left(a_\lambda + b_\lambda\mu\right)\,\mathrm{d}\mu\,. \tag{1.34}$$

This gives:

$$\left\langle F_{\mathrm{p}}(\lambda)\right\rangle_{\mathrm{d}} = 2\pi R_{\mathrm{p}}^2\left(\frac{a_\lambda}{2} + \frac{b_\lambda}{3}\right)\,, \tag{1.35}$$

that can be written:

$$\left\langle F_\lambda\right\rangle_{\mathrm{d}} = \pi R_{\mathrm{p}}^2 B_\lambda\left(\tau_\lambda = 2/3\right)\,. \tag{1.36}$$

The outgoing flux from the atmosphere at a given frequency is determined by the thermal emission of the level where the optical depth *at this particular frequency* reaches 2/3. The expected contrast between different spectral bands is therefore given by the combined variations of the temperature and of τ_λ with λ. Thus, information about the composition and the temperature profile are embedded in the secondary eclipse data. The flux contrast between a wavelength λ_1 and λ_2 is given by:

$$\frac{\left\langle F_{\mathrm{p}}(\lambda_2\right\rangle_{\mathrm{d}}}{\left\langle F_{\mathrm{p}}(\lambda_1\right\rangle_{\mathrm{d}}} = \frac{B_{\lambda_2}(T_{\lambda_2})}{B_{\lambda_1}(T_{\lambda_1})}\,. \tag{1.37}$$

T_{λ_1} and T_{λ_2} are the temperatures where optical depth is equal to 2/3 for wavelengths λ_1 and λ_2 respectively. We define $\Delta T = T_{\lambda_1} - T_{\lambda_2}$ the temperature contrast between the levels where $\tau_1 = 2/3$ and $\tau_2 = 2/3$. Equation (1.37) becomes:

$$\frac{\left\langle F_{\mathrm{p}}(\lambda_1\right\rangle_{\mathrm{d}}}{\left\langle F_{\mathrm{p}}(\lambda_2\right\rangle_{\mathrm{d}}} \approx \left(1 + \frac{\mathrm{d}\log B_\lambda}{\mathrm{d}T}\Delta T\right)\frac{B_{\lambda_2}(T_1)}{B_{\lambda_1}(T_1)}\,. \tag{1.38}$$

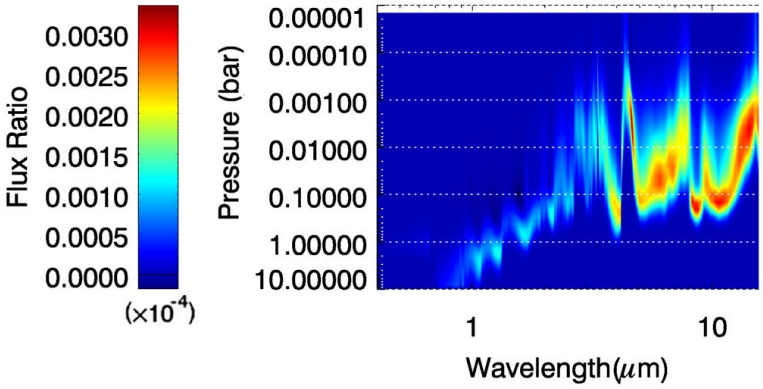

Figure 1.10. Atmospheric pressures probed during secondary eclipse as a function of wavelength for a typical hot Jupiter. The variation of the planetary flux at a given wavelength due to a temperature increase of 1 K is color-coded. Figure adapted from Barstow et al. (2013).

Hot exoplanets such has HD209458b have temperatures of $\approx 1500K$ and are observed in the thermal infrared $\lambda \approx 1 - 100\,\mu$m. Therefore, $hc/\lambda k_B T > 1$ and the exponential term dominates the Planck function. Thus, we can approximate the Planck function by $B_\lambda \propto 2hc^2/\lambda^5 e^{hc/k_B T\lambda}$ and the flux ratio becomes:

$$\frac{\langle F_p(\lambda_1\rangle_d}{\langle F_p(\lambda_2\rangle_d} \approx \left(1 + \frac{hc}{\lambda k_B T^2}\Delta T\right)\frac{B_{\lambda_2}(T_1)}{B_{\lambda_1}(T_1)}\,. \tag{1.39}$$

Thus, for an isothermal atmosphere ($\Delta T = 0$), the emission spectrum of the planet is a blackbody. Any departure from a blackbody emission is due to temperature contrasts in the atmosphere of the planet. In hot Jupiters, the vertical temperature contrast can reach $\Delta T \approx 500$K. From equation 1.39, we expect departures of 50% from a blackbody emission around 5μm. Unfortunately, this corresponds roughly to the current error in the data, as shown by Hansen et al. (2014). Thus, in most cases, no departures from a blackbody emission have been clearly observed.

Figure 1.10 shows the levels probed by the secondary eclipse spectrum. At a given wavelength, the emitted flux is sensitive to the temperature structure over 1 to 2 orders of magnitude in pressure. By observing at different wavelengths, information about the temperature structure from ≈ 10 bar to $\approx 10\,\mu$bar can, in principle, be retrieved. A spectral resolution of $\approx \lambda/\Delta\lambda \approx 10 - 100$ is clearly necessary to obtain a good vertical resolution.

Retrieval models

Planetary emission spectra are shaped by the combined variations of the atmospheric composition and the vertical temperature structure. For brown dwarfs and directly observed planets (*e.g.* HR 8799b Lee et al. 2013), the spectra can be observed with a good spectral resolution. The spectrum of exoplanets observed during secondary eclipse, however, is generally under-resolved. It often consists of a few broadband observations obtained with Spitzer, a low-resolution spectrum obtained by HST/WFC3 and a few points obtained from ground-based telescopes. Thus, many combinations of temperature structure and composition can reproduce the data. Several techniques have therefore be developed to analyze secondary eclipse observations. Based on our knowledge of physics and on our expectations, we can find a set of atmospheric characteristics that provides a reasonable explanation of the observations. A second possibility is to blindly produce millions of atmospheric models varying all the possible characteristics of the atmosphere and derive a range of parameters that is allowed by the data. Whereas the first set of models allows a useful physical insight in the relationships between spectrum, temperature and abundances, it cannot be used efficiently with current data. The second set of models opens possibilities that can be missed by

the first type of models and gives a more robust estimate of the error bars associated with each retrieved parameters.

The resulting numerical spectra are compared to the observed ones. The match between the two is usually measured by χ^2, the root-mean square of their difference. Although the χ^2 allows a fair comparison between two spectra, it does not give insights in the validity of the model used. Scientists exploring new worlds should always be careful to not over-interpret the data they have in hand. Given a set of data points, it is always possible to produce a model that fits the data with very small value of χ^2 or even $\chi^2 = 0$. As an example, a model with more free parameters than the number of data points to fit can easily provide low values of χ^2. However, in science the simplest explanation always prevails, a principle called *parsimony*. Adding a new parameter to fit a model needs to increase *significantly* the goodness of the fit to be considered relevant. The main idea is to add a *penalty* to the χ^2 value when a new parameter is added to the model. The most common criterion (after the χ^2) used in the study of exoplanets' atmospheres is the *Bayesian Information Criterion* (hereafter BIC) defined as:

$$BIC = \chi^2 + k \log N \,. \tag{1.40}$$

Here k is the number of parameters of the model and N the number of data points. A new parameter can be added to the model only if it increases the goodness of the fit by $\log N$. The dependence on $\log N$ is directly related to the mean information brought by the introduction of a new parameter (this is related to the Shannon entropy, the Fisher information and the Bayesian statistics that we will not review here). Choosing to minimize either χ^2 or the BIC influences the conclusions from a given data set. As an example, the claimed detection of a high carbon to oxygen ratio in the planet WASP-12b from secondary eclipse measurements was done based on minimum χ^2 values of 10 for a set of 10 free parameters fitting 10 data points (Madhusudhan et al. 2011b). This corresponds to a BIC of 36. For comparison, an isothermal model (i.e. a model where the secondary eclipse spectrum is a black-body) produces a worst fit $\chi^2 = 15$ but decreases the BIC to 19 (Crossfield et al. 2012a) and should therefore be preferred.

An example of temperature retrieval analyses performed by Line et al. (2013) for a typical hot Jupiter is shown in Figure 1.11. The profiles retrieved using only the Spitzer observations have large uncertainties. This is expected since the four IRAC channels of Spitzer have a band-pass of the order of 1µm leading to a resolving power of $\lambda/\Delta\lambda \approx 2-5$, which is smaller than the required minimum resolving power of 10 described in the previous section. The profiles retrieved using most of today's available instruments (Spitzer/IRAC, HST/WFC3 and ground-based H and K_s band photometry) give better constraints on the profile, reducing the uncertainty to $\approx$ 500K at $P \approx$ 1bar. However, they cannot give good constraints on the upper and deep atmospheric temperatures. Future instruments, such as JWST or EChO will reduce the uncertainties on the temperature to $\Delta T \approx 100-300$K around $P =$ 1bar and will constrain also the upper and deep temperature structure. The first raw of Figure 1.11 assumes a semi-grey temperature profile based on the analytical expression of Guillot (2010). If the temperature is used as a free parameter at each atmospheric levels, the temperature profile becomes much less constrained. As shown in Parmentier et al. (2014b), the semi-grey model is too constrained and cannot explore all the physically plausible temperature profiles. The level-by-level retrieval overestimates the uncertainty on the temperature by considering nonphysical models whereas the parametric temperature profile approach underestimates the uncertainties by considering only part of the possible profiles. Ideally, one should run a full radiative transfer code for each of the models probed that links the composition and the temperature structure of the atmosphere. Given the large number of models needed to use

those retrieval methods, running a full radiative transfer code becomes computationally limiting. In Chapter 2 we provide a non-grey analytical temperature/pressure profile that allows to probe a wider range of temperatures. Such a model could be used to improve the results of the retrieval methods.

1.3.2 The reflection of the stellar light

Planets not only emit their thermal radiation, they can also reflect the light coming from their parent star. The total flux we receive from the planet is thus the sum of the thermal and the reflected components. Because the planet is cooler than the star, the emitted and reflected flux are shifted in wavelengths. The reflected component usually peaks in the visible spectral range whereas the planet's emission is in the infrared. For hotter planets, the thermal contribution can leak in the visible wavelengths and extensive observations are necessary to separate the two contributions. Reflection by a planetary atmosphere is due to scattering either due to the gas itself or to the clouds that can form if the temperatures are cool enough. The spherical albedo, A_s is the portion of the flux received by the planet that is reflected away in all directions at a given wavelength[7]. The geometrical albedo, A_g is the portion of the stellar flux that is reflected in one direction only at a given wavelength. The geometrical albedo can be measured during the secondary eclipse of the planet:

$$A_g = \frac{F_p}{F_*} \left(\frac{2a}{R_p} \right)^2 , \tag{1.41}$$

where $\frac{F_p}{F_*}$ is directly observed, a is the semi-major axis of the orbit and R_p is the planetary radius. The relationship between the geometrical and the spherical albedo depends on the exact scattering mechanism. Both strongly depend of the single-scattering albedo ω_λ and of the phase function. They both vanish when $\omega_\lambda = 0$ and the spherical albedo reaches 1 in a purely scattering atmosphere.

The variations of the geometrical albedo with wavelength contain information about the physical properties of the scattering species. These variations have been first observed in the atmosphere of HD 189733b by Berdyugina et al. (2011) and confirmed by Evans et al. (2013). As shown in Figure 1.12, the albedo is large at small wavelengths where Rayleigh scattering is dominant (either due to clouds or to H_2) and becomes smaller at larger wavelengths, when atomic and molecular absorption become important.

1.3.3 Current questions raised from the secondary eclipses observations

Albedos

The geometrical albedo of a dozen of exoplanets, mainly hot Jupiters, have been measured from secondary eclipses. Whereas the gas giants of our solar-system planets have bond albedos between 0.3 and 0.4, most of the measured albedos of gas giant extrasolar planets are between 0 and 0.2 (Heng & Demory 2013), with the exception of $Kepler-7b$ where a bond albedo higher than 0.4 was reported (Demory et al. 2011).

[7]Another albedo, the Bond albedo is the spherical albedo integrated over all wavelengths. It is useful to determine the radiative balance of the whole atmosphere.

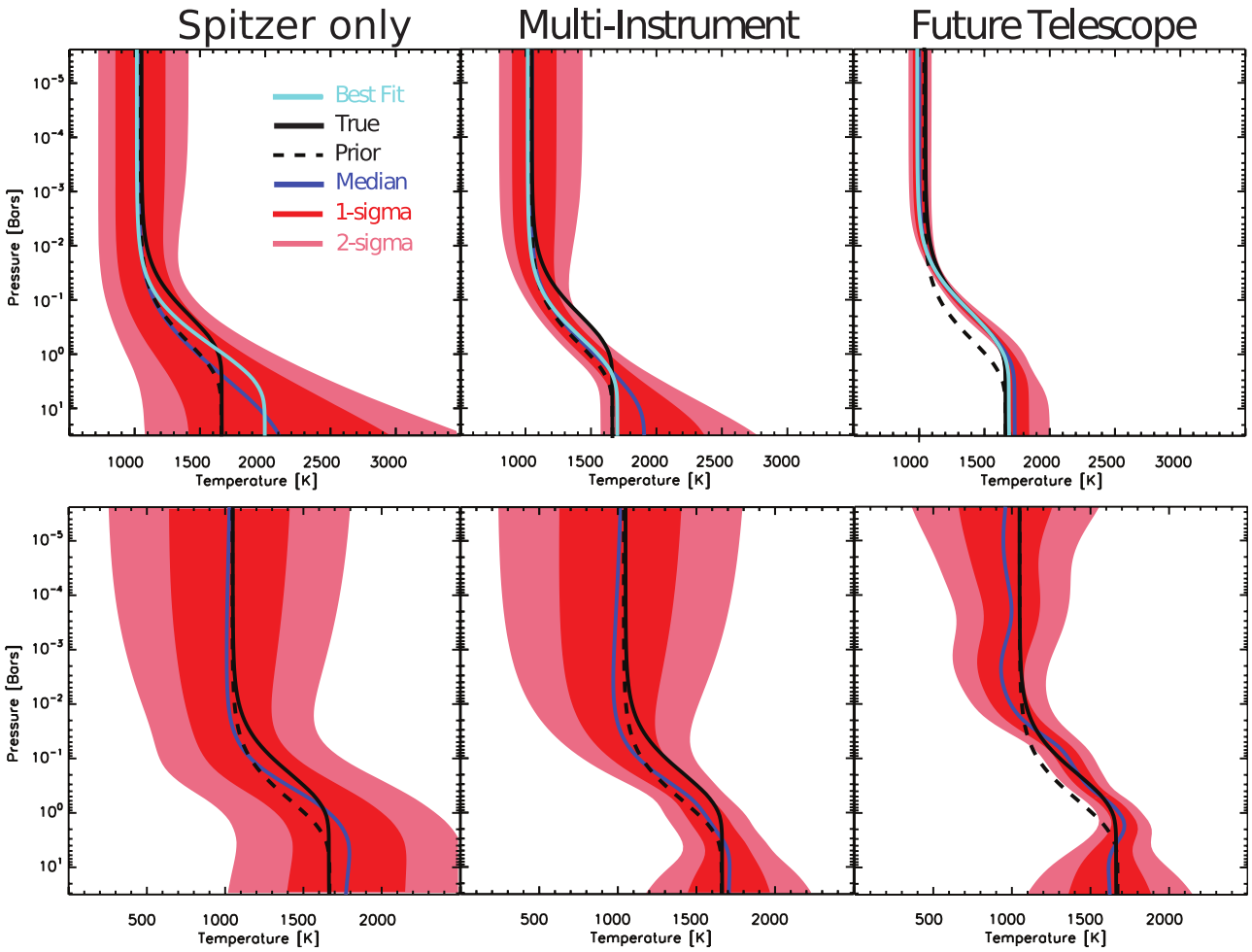

Figure 1.11. Temperature retrieval for a typical hot Jupiter using simulated observations with the four IRAC channels of the Spitzer Space Telescope (left panel), all the telescopes used to characterize the dayside emission spectrum of hot Jupiters (middle panel) and the possible future space based observatory, such as EChO (right panel). The top row uses a semi-grey analytical model based on Guillot (2010) for the temperature profile whereas in the second row the temperature at each atmospheric level is retrieved independently from the others. Figure adapted from Line et al. (2013)

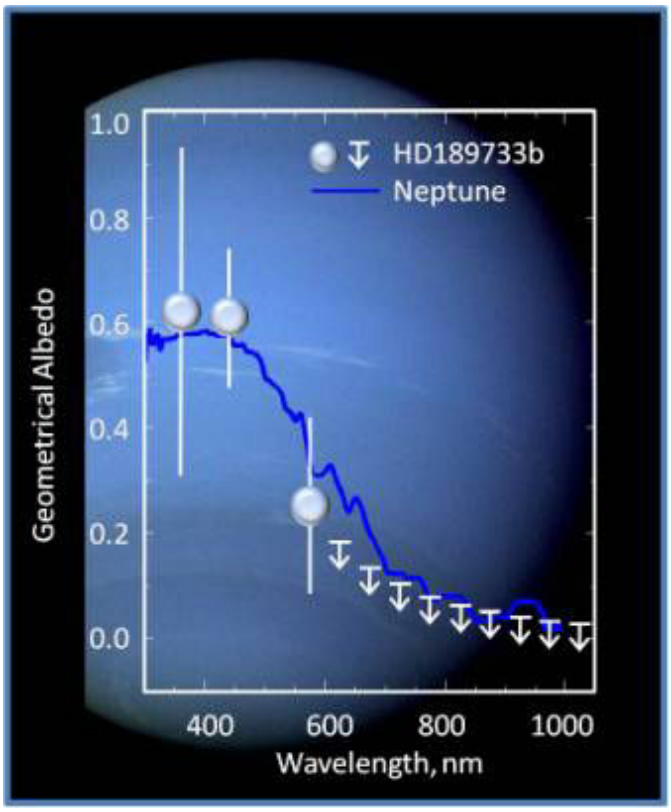

Figure 1.12. Geometrical albedo of HD 189733b as a function of wavelength (points) compared to the geometrical albedo of Neptune (line). The albedo decreases with wavelength. It indicates a transition from an atmosphere dominated by Rayleigh scattering to an atmosphere dominated by molecular absorption (methane, water and, for HD 189733b, alkali metals). Figure based on Berdyugina et al. (2011).

The albedo of close-in giant planets can be due either to the scattering by the gas (mainly H_2 and H_e in giant planets) or by clouds. As shown by (Sudarsky et al. 2000), a cloudless atmosphere can have a bond albedo up to $A_B = 0.1$. Thus, the higher than 0.1 Bond albedo measured in numerous hot Jupiters confirms that clouds play an important role in exoplanets' atmospheres.

Dayside brightness temperatures

Secondary eclipses were measured for more than thirty planet. From each observations, a brightness temperature at a given wavelength can be derived. The brightness temperature is the temperature of a blackbody emitting the same flux as the planet at this particular wavelength. It roughly corresponds to the temperature at the $\tau_\lambda \approx 2/3$ level in the atmosphere. In Figure 1.13 we show the observed brightness temperature as a function of the equilibrium temperature of the planet for planets that have been observed during secondary eclipse. For each planet, measurements at different wavelengths are shown. For a planet that absorbs all the stellar irradiation, homogenizes and re-emits it, the points should be spread around the equilibrium temperature of the planet, (i.e. if, at some wavelengths the emitted flux per unit wavelength is larger than $\sigma T_{\rm eq}^4$, then, at other wavelengths, it should be smaller). As seen in Figure 1.13, the brightness temperature is always higher than the equilibrium temperature. Although the total energy escaping the planet must correspond to its brightness temperature, the one escaping from the dayside can correspond to higher brightness temperatures as long as a reduced nightside emission compensates for it. The dayside equilibrium temperature can be written :

$$T_{\rm day}^4 = \frac{T_{\rm eq}^4}{F} \tag{1.42}$$

where the factor F is equal to 1 when the energy is emitted homogeneously over the whole planet, to 1/2 when the dayside emits homogeneously but nothing is emitted from the nightside and 3/8 when each parcel of atmosphere instantaneously re-emits its radiation. Thus, a dayside temperature higher than the equilibrium temperature denotes an inefficient redistribution of energy from the dayside to the nightside of the planet. Planets with an equilibrium temperature smaller than ≈ 2000 K in Figure 1.13 seem to have brightness temperatures that lay along the full redistribution case whereas hotter planets are closer to the no redistribution case.

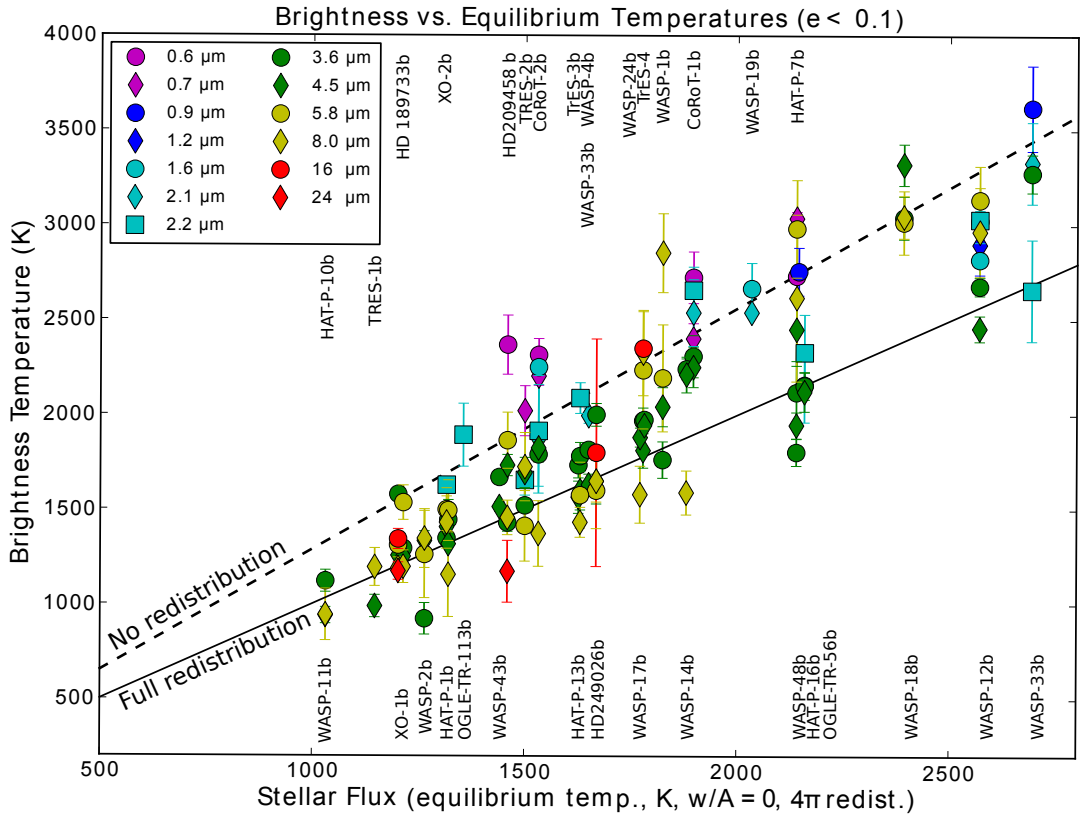

Figure 1.13. Dayside brightness temperature observed at different wavelengths as a function of the equilibrium temperature of the planet for all planets with an observed secondary eclipse. The brightness temperature expected for an efficient redistribution and no redistribution of the incoming stellar energy are shown by lines. Courtesy of J. Harrington, based on a figure first published in Harrington et al. (2007).

Several theoretical explanations could explain this trend :

- The presence of clouds : cloudy atmospheres below 2000K would have higher albedos and thus lower dayside temperatures than planets without clouds.

- A breakdown in the circulation : because the radiative timescale decreases with the temperature, the hotter the planet, the smaller the heat redistribution and the higher the dayside temperature (Perez-Becker & Showman 2013).

- Ohmic dissipation : hot planets can have ionized sodium and potassium in their atmospheres. The interactions between the ionized atmosphere and the magnetic field of the planet can slow down the winds by Ohmic dissipation, heating the dayside atmosphere and reducing the heat redistribution (Menou 2012; Rauscher & Menou 2013; Batygin et al. 2013; Rogers & Showman 2014).

- Presence of TiO : hot planets might have gaseous TiO in their atmosphere whereas it should condense in cooler atmospheres (Hubeny et al. 2003; Fortney et al. 2005). The presence of TiO would lead to a strong absorption of the stellar flux in the upper atmosphere, where radiative timescales are short, leading to a less efficient energy redistribution and thus larger dayside temperatures.

Presence of a temperature inversion in some hot Jupiters

Thermal inversions are a natural consequence of visible/UV absorption of the incident star light high in the atmosphere. For an isolated planetary atmosphere, the atmospheric temperature decreases with pressure. In planetary atmospheres irradiated by their host star, strong optical/UV absorbers in the upper layers can intercept part of the incident star light. With such a local heating, a zone where the temperature increases with decreasing pressure can form, named a *temperature inversion*. Most solar system planets have temperature inversions in their atmospheres. In Earth's atmosphere, for example, a thermal inversion is caused by ozone (O3), which is a strong absorber in the UV (Chamberlain & Hunten 1987). In Jupiter's atmosphere, a thermal inversion is caused by the strong absorption in the visible of hazes resulting from methane photochemistry.

The compounds producing thermal inversions in solar system atmospheres do not survive the high temperatures of hottest hot Jupiters. Nevertheless, it has been proposed that thermal inversions could form in the atmosphere of very hot Jupiters due to strong absorption of incident stellar radiation in the visible by gaseous titanium oxide (Hubeny et al. 2003). The so-called TiO-hypothesis differentiate between planets hot enough to have gaseous TiO and thus a thermal inversion (pL class) and planets too cold to have gaseous TiO and thus without thermal inversion (Fortney et al. 2008). Evidences for the presence of a thermal inversion have been claimed for several planets. Most of these claims where based on the ratio between the 3.6 µm and the 4.5 µm thermal fluxes observed by the Spitzer space telescope (Knutson et al. 2010). Assuming that the water is the main absorber at those wavelengths, a higher flux at 4.5 µm can be interpreted as an emission band, created by an inverted temperature profile. Conversely a smaller flux at 4.5 µm than at 3.6 µm can be interpreted as an absorption feature, resulting from a non-inverted temperature profile. Up to now, most of the claims did not survive a more exhaustive analysis that included a large range of possible atmospheric chemical composition and temperature profiles (Madhusudhan & Seager 2010). In current data there is no strong evidence for a thermal inversion but it is not ruled out either (Hansen et al. 2014).

Several authors challenged the TiO hypothesis. Spiegel et al. (2009) noted that in moderately irradiated planets, condensation of TiO in the deep atmosphere ($1 - 100$bar) should deplete the upper atmosphere of TiO. The presence of a strong vertical mixing would be necessary to overcome this cold trap and maintain a large enough concentration of TiO in the upper atmosphere

to create an inversion. Knutson et al. (2010) noted that TiO could be destroyed by the strong stellar FUV flux. Temperature inversions could therefore exist only in low activity stars. Madhusudhan et al. (2011b) showed that in atmospheres with a carbon to oxygen ratio higher than one, the abundance of TiO was reduced by several orders of magnitudes, preventing it to create a thermal inversion. Pont et al. (2013) proposed that absorption by hazes instead of TiO could be responsible for the thermal inversions. More recently, we showed in Parmentier et al. (2013) that the condensation and rainout of TiO in the cold nightside of the planet could reduce significantly the abundance of TiO if it condenses in particles larger than a few microns (see Chapter 3).

As a conclusion, with better secondary eclipses observations, the existence of thermal inversions in the dayside atmosphere of irradiated exoplanets will be determined with a higher confidence. Quantifying their occurrence and strength will allow comparisons with theoretical models and will teach us about the interactions between thermal structure, chemical composition and atmospheric dynamics of irradiated planets.

Presence of disequilibrium chemistry

Although chemical equilibrium is a useful tool to understand the composition of planetary atmospheres, the actual chemical composition of a parcel of gas depends on its history. When strong temperature gradients, advection and photochemistry comes into play, chemical equilibrium might not hold anymore. Because the reaction rate of a chemical reaction strongly depends on temperature and pressure, a parcel of gas that is advected upward in an atmosphere can have its chemical abundances quenched to the equilibrium state that holds in the deep, hot regions of the atmosphere. This explanation was proposed for the higher than equilibrium CO abundances observed in Jupiter (Prinn & Barshay 1977).

Chemical disequilibrium is expected in irradiated giant planets atmospheres. Cooper & Showman (2006) and Agúndez et al. (2012) show that the large-scale circulation in hot Jupiter should lead to an enhanced CO abundance and a depletion in CH_4 compared to equilibrium. CO and CH_4 abundances have been retrieved from a dozen of planets. However, the large error bars on those mixing ratios (usually several orders of magnitudes) prevented (Line & Yung 2013) from building a strong conclusion. The planet GJ436b is now the best candidate for the presence of disequilibrium carbon chemistry (Madhusudhan & Seager 2011) however, the evidences are based on Spitzer observations that are now considered unreliable (Hansen et al. 2014).

Evidence for disequilibrium chemistry have been found in brown dwarfs and directly imaged planets (*e.g.* HR 8799b Lee et al. 2013), mainly because much higher quality spectrum are available for those objects. With observation of better quality and with higher spectral resolution, the presence of disequilibrium processes in irradiated exoplanets should be revealed in the next decade.

Planets with a high C/O ratio.

The lack of water absorption in the dayside spectrum of the planet WASP-12b raised the possibility that the atmosphere of some planets may have a carbon to oxygen ratio greater than one (Madhusudhan et al. 2011a). This led several authors to study the chemistry (Moses et al. 2013) or the formation (Madhusudhan et al. 2011b) of such planets. Madhusudhan (2012) proposed that carbon-rich atmospheres should be depleted in TiO, explaining the lack of observed temperature inversions in numerous planets. The possibility of a carbon-rich composition was raised for the super-earth 55 Cancri *e* assuming that carbon-rich stars should harbor carbon-rich planets (Mad-

husudhan et al. 2012). Mousis et al. (2012) furthermore argued that carbon-rich planets could even form in oxygen-rich environment, which could explain the low abundance of water observed by the Gallileo probe in Jupiter[8].

Although a carbon-rich atmosphere for WASP-12b has now been ruled out by Crossfield et al. (2012b) and Stevenson et al. (2013)[9], carbon-rich planets may still exist. Better quality observations are needed to determine with enough precision the C/O ratio of known planets.

1.4 Horizontal resolution

We saw previously how spectrally resolved transit and secondary eclipses spectra can provide vertical insights on the physical characteristics of planetary atmospheres. Those observations, however, only provide horizontally averaged quantities, over the dayside for secondary eclipses spectrum and over the limb for transit spectrum. We now describe two methods than can also provide longitudinal and latitudinal constraints on exoplanets' atmospheres. Combined with secondary eclipses and transit spectrophotometry, those methods can lead to a three-dimensional vision of exoplanets' atmospheres.

1.4.1 Phase curves

When observing a star/planet system, we observe the sum of the stellar and planetary brightnesses. As the planet orbits the star, different hemispheres are facing us. We represent the position of the planet within its orbit by the phase angle α. During the secondary eclipse, the dayside of the planet faces us and $\alpha = 0$ whereas during transit we can observe the nightside of the planet and $\alpha = \pi$. The variations of the luminosity of the star/planet system with the phase angle is called the *phase curve* of the system. The measured phase curve is given by:

$$\frac{F_{\rm p}(\lambda,\alpha)}{F_*(\lambda,0)} = \frac{F_*(\lambda,\alpha)+F_{\rm p}(\lambda,\alpha)}{F_*(\lambda,0)} - 1\,, \tag{1.43}$$

where the sum of the stellar and planetary brightnesses are normalized by the stellar brightness measured during the secondary eclipse. Note that both the planetary and stellar brightnesses can vary with the phase angle.

As for the secondary eclipse, the phase curve can be observed in both infrared and optical wavelengths. The phase curved obtained through infrared observations probe the variations in the thermal emission of the planet. The phase curve obtained at optical wavelengths usually measure the light reflected by the planet.

Thermal phase curves

As seen in the previous section, the thermal emission of the planet at a given wavelength is directly related to the Planck function, and hence to the temperature at pressure levels where the optical depth is equal to 2/3 at this specific wavelength. During the orbit of the planet, we see different

[8]The Juno mission, arriving at Jupiter in 2016 should measure correctly the global water abundance of Jupiter and settle this question for Jupiter.

[9]The presence of a M dwarf in the field of view was diluting the signal and the data points coming from Spitzer/IRAC had underestimated error-bars.

hemispheres. Thus, the brightness temperature observed at any given time is representative of the mean temperature of a given hemisphere. Phase curve variations with time can therefore be related to the longitudinal thermal structure of the planet.

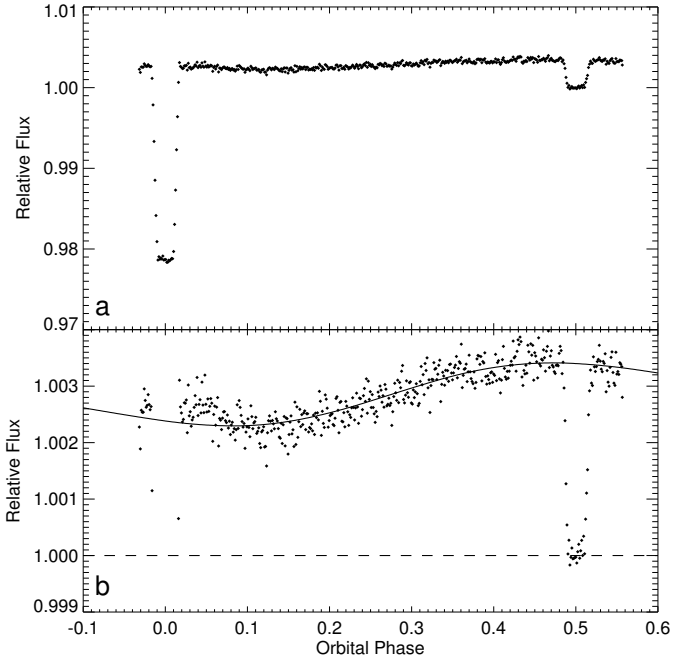

Figure 1.14. 8 µm thermal lightcurve of the hot Jupiter HD189733b obtained with the Spitzer Space Telescope by Knutson et al. (2008). Transit happens at orbital phase 0 whereas secondary eclipse happens at orbital phase 0.5. In the zoomed view of panel b the flux increase between the transit and the secondary eclipse is interpreted as a variation of the thermal flux emitted by the planet. After the transit we see the cold and dim night-side whereas before the secondary eclipse we see the warm and bright dayside. Figure from Knutson et al. (2008).

Knutson et al. (2008) observed the first phase curves variations with Spitzer/IRAC (see Fig. 1.14). They derived a brightness temperature difference between the nightside and the dayside of the planet HD 189733b of $\Delta T \approx 240\,\mathrm{K}$ at $6.44 - 9.34\mu\mathrm{m}$. It means that a certain atmospheric layer of pressure P_{Day} in the day side atmosphere is 240 K hotter than at another atmospheric layer of pressure P_{Night} located in the nightside. The ratio $P_{\mathrm{Day}}/P_{\mathrm{Night}}$ is directly related to the opacity differences between the day and the night. These opacity differences are probably not caused by differences in the chemical composition (see Chapter 3) but are more certainly set by a difference in cloud coverage between the dayside and the nightside of the planet. Several subsequent studies used the Spitzer Space Telescope to obtain the thermal phase curves of HD189733b at other wavelengths (Knutson et al. 2010) and of other transiting planets such as HD209458b, Hat-P-2b (Lewis et al. 2013), WASP-12b (Cowan et al. 2012) or even of non-transiting planets such as HD 179949, 51Pegb (Cowan et al. 2007) or υ-Andromedae b (Crossfield et al. 2010) (see Table 1.11 for a review).

The second feature observed in most phase curves is the phase of the flux maximum. For planets in circular orbit, if the dayside were the hottest hemisphere of the planet, the phase curve should peak during the secondary eclipse. Any shift of the maximum away from the secondary eclipse can be interpreted as a shift of the hottest point of the planet. Up to date, all hot Jupiters in circular orbit have a phase curve corresponding to an eastward shift of the hottest point of the planet. This shift can be explained by the eastward advection of heat by a circulation dominated by an equatorial superrotating jet (see Chapter 3).

Optical phase curves

The Kepler Space Telescope is a unique spacecraft to obtain phase curves of exoplanets in the visible wavelength range. As the contrast needed to observe exoplanets' light curves in the visible

is much larger than in the infrared (due to the increased stellar emission in the visible wavelength range), it is necessary to sum up hundreds of single orbit light curves to obtain the desired precision. For a hot Jupiter such as Kepler-7b with an orbital period of ≈ 5 days, the four and half years of the Kepler mission provided more than 300 single orbit phase curves.

As for the secondary eclipse case, the optical phase curves usually probe the reflected light by the planet. However, as explained in Esteves et al. (2013), two mechanisms can alter the visible phase curve for close-in planets: the ellipsoidal variations and the Doppler beaming effect.

The ellipsoidal variations are due to the tides risen by the planet on the star. Due to the proximity of the planet, the stellar disk becomes an ellipsoid elongated in the planet-star direction. The stellar area projected on the sky changes with the orbital phase of the planet. When the planet is close to transit or eclipse, the star appears smaller and hence dimmer whereas at quadrature the star appears bigger hence brighter. The relative flux variations expected from the ellipsoidal effect are of the order of (Esteves et al. 2013):

$$\left.\frac{\Delta F}{F}\right|_e = \alpha_2 \frac{M_\mathrm{p}}{M_*}\left(\frac{R_*}{a}\right)^3 \sin^2 i\,, \tag{1.44}$$

where α_2 is a order of unity coefficient that can be calculated from the gravity and limb-darkening coefficient (Claret & Bloemen 2011).

Along its orbit, the planet pulls the star. The star periodically goes toward and away from us. The stellar light is therefore periodically blue-shifted and red-shifted. Given the bell shape of spectral dependence of the stellar flux (comparable to a Planck function), the flux integrated over the spacecraft band-pass increases and decreases periodically (*e.g.* Mazeh & Faigler 2010). The expected amplitude of the beaming effect is given by (Barclay et al. 2012):

$$\left.\frac{\Delta F}{F}\right|_D = \alpha_\mathrm{D}\left(\frac{G}{M_*}\right)^{1/2}\frac{\sin i}{c}\frac{M_\mathrm{p}}{a^{1/2}} \tag{1.45}$$

Where α_2 is a order of unity coefficient that can be calculated from the gravity and limb-darkening coefficient.

Finally there is a variation with phase that is due to the reflected light from the planet. Before the transit, we see the nightside of the planet and thus no light is reflected whereas just before secondary eclipse, the full disk of the planet reflects the stellar light. The expected amplitude of the phase curve due to the reflection by the planet atmosphere is thus:

$$\left.\frac{\Delta F}{F}\right|_A = A_\mathrm{g}\left(\frac{R_\mathrm{p}}{a}\right)^2 \tag{1.46}$$

The optical phase curve can be used to determine the variations with longitude of the planetary albedos. This is discussed in more details in section 3.5.2.

The ellipsoidal variations and the Doppler beaming are proportional to the mass of the planet. They can therefore be used to measure the mass of the planet (Barclay et al. 2012). They are of primary importance to study the lightcurve of close-in binaries where they often dominate the modulation due to the reflection (*e.g.* Bloemen et al. 2011). For close-in, massive planets, such as TrES-2b they can be of the same order of magnitude as the contribution from the reflected light (see Figure 1.15). However, they provide no information on the atmosphere and they need to be modeled and removed from the lightcurve in order to obtain the contribution from the reflected light. Planets for which the optical phase curve due to the reflection of the stellar light have been observed are listed in Table 1.11.

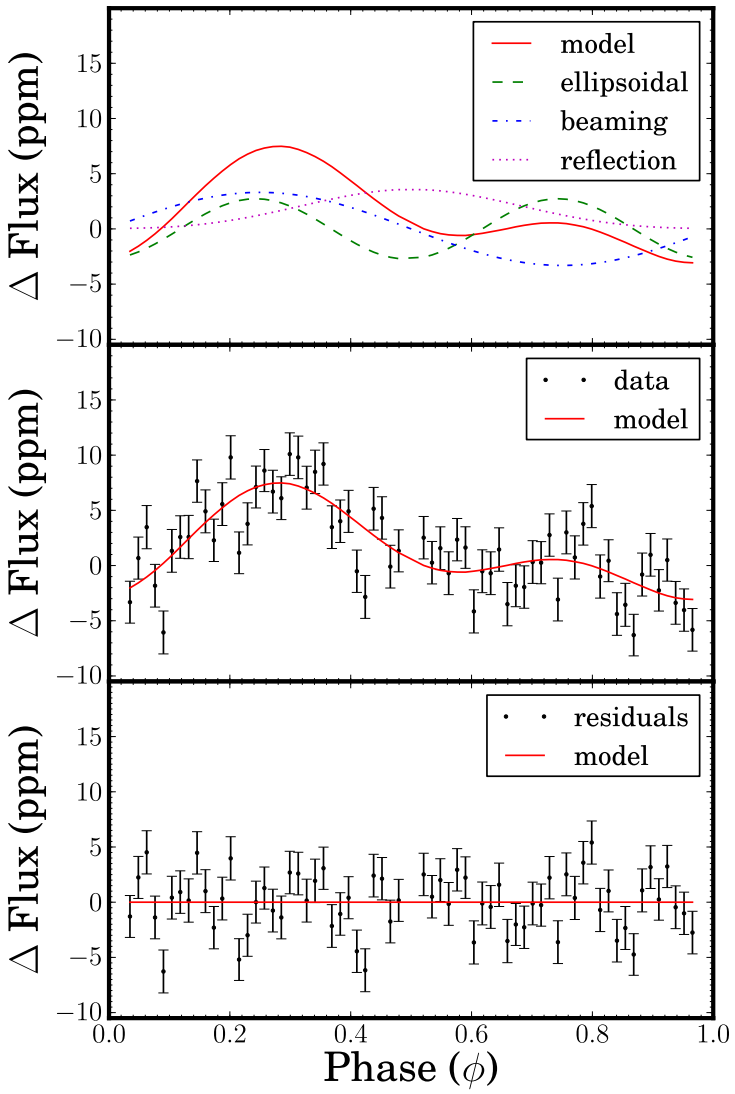

Figure 1.15. *Top panel:* The optical lightcurve of TrES-2b modeled as the sum of three contributions : the ellipsoidal variations (dashed curve), the Doppler beaming (dot-dashed curve) and the reflection by the planet (dotted curve).*Middle panel:* The optical lightcurve of TrES-2b observed by the Kepler Space Telescope together with the best fit model.*Bottom panel:* Residual lightcurve once the model have been subtracted. Figure from Barclay et al. (2012)

Table 1.11. Planets for which phase curve modulation due to the atmosphere has been observed.

Planet	Instrument	Wavelength	Reference	ϕ_{max}	$\Delta T(K)$	Comments
HD189733b	Spitzer/IRAC	3.6µm	Knutson et al. (2012)	0.40 ± 0.011	503 ± 21	Disequilibrium chemistry ?
	Spitzer/IRAC	4.5µm	Knutson et al. (2012)	0.44 ± 0.015	264 ± 24	–
	Spitzer/IRAC	8µm	Knutson et al. (2007a)	0.46 ± 0.017	239 ± 44	–
	Spitzer/MIPS	24µm	Knutson et al. (2009b)	0.396 ± 0.022	236 ± 67	–
ν And b	Spitzer/MIPS	24µm	Harrington et al. (2006); Crossfield et al. (2010)	0.27 ± 0.006	$\gtrsim 900$	$i \gtrsim 28°$
HD149026 b	Spitzer/IRAC	8µm	Knutson et al. (2009a)	$--$	480 ± 140	–
HD8606 b	Spitzer/IRAC	8µm	Laughlin et al. (2009)	–	–	$e = 0.93$.
HAT-P-7 b	Kepler	Optical	Borucki et al. (2009); Welsh et al. (2010)	–	–	Ellipsoidal variations.
CoRoT-1b	CoRoT	Optical	Snellen et al. (2009)	–	–	$A < 0.2$.
WASP-12 b	Spitzer/IRAC	3.6, 4.5µm	Cowan et al. (2012)	–	–	Ellipsoidal variations/Instrumental noise.
Kepler-7b	Kepler	Visible	Demory et al. (2013)	0.61 ± 0.03	–	West of the dayside is cloudy.
HD 46375b	CoRoT	Visible	Gaulme et al. (2010)	–	–	Non-transiting. $0.16 < A < 0.33$.
HD 179949 b	Spitzer/IRAC	8 µm	Cowan et al. (2007)	–	–	No detection at 3.6 µm

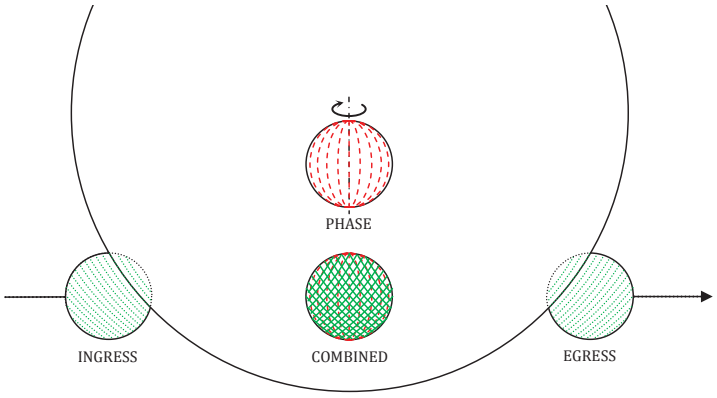

Figure 1.16. Schematic view of the secondary eclipse mapping technique. The large circle represents the star and the small circle is the planet. During the ingress and egress of the secondary eclipse the planet disappears and reappears by slices tilted with respect to the equator (green doted lines). This observation can be combined with the phase curve observation that gives the longitudinal dependency of the planets' brightness (red doted lines). Figure from (de Wit et al. 2012).

1.4.2 Latitudinal resolution with eclipse mapping

During the secondary eclipse of a planet, the planet disappears behind its host star. Whenever the impact parameter is not zero, i.e. whenever the planet does not disappear at the equator of the star, the planet disappears by slices that are tilted with respect to the equator of the planet (see Figure 1.16). When combined with the full phase-curve observations, the secondary eclipse can constrain the latitudinal variation of the planets brightness. This technique has been applied to observations of HD189733b with the Spitzer Space Telescope (Majeau et al. 2012; de Wit et al. 2012). However, greater signal-to-noise observations are needed to unambiguously constrain the brightness distribution of the planets dayside.

1.5 What will we learn from a future space mission ?

Our understanding of exoplanets' atmospheres is currently limited by the precision of instruments. Most spectral observations have error bars close to the expected signal of molecular signatures. Future space missions will collect observations of higher quality will lead to unambiguous answers to today's scientific questions. Two main type of missions have been proposed in the last years. Photometric missions, such as CoRoT and Kepler observe numerous transit in a given spectral band. They can discover numerous planets and measure with a good precision their radii. Spectroscopic observatories, such as the Hubble Spitzer, observe the emission and transiting spectrum as well as the full light curve of exoplanets. They can provide a wealth of information about exoplanets atmospheres but they need to know in advance where to look. In an ideal world, photometric missions find the planets that spectroscopic missions characterize.

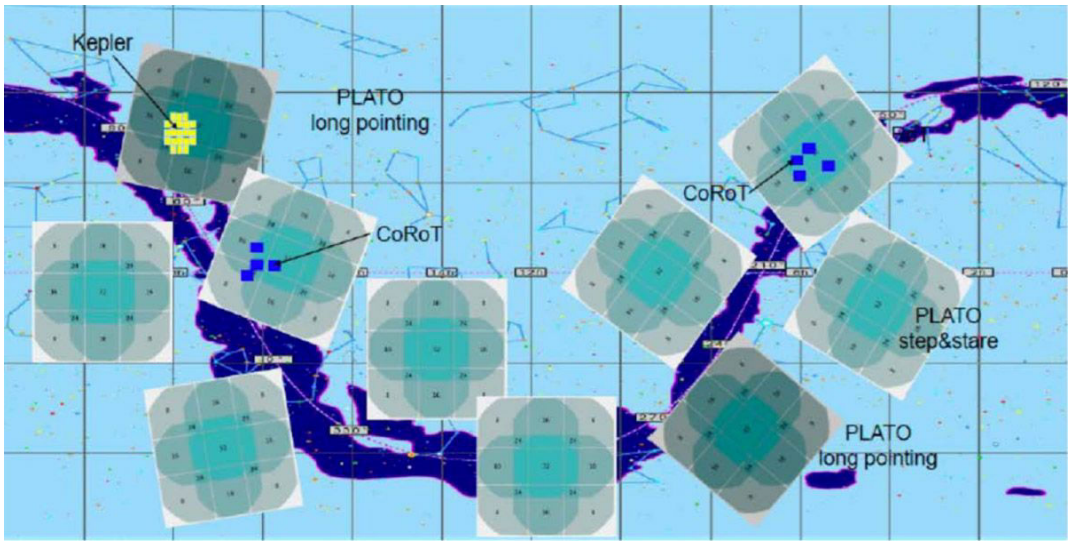

Figure 1.17. Field of view that will be observed by PLATO. The light grey zones will be observed repeatedly for periods of 2-5 months whereas the dark grey zones will be observed for a continuous period of three years. The fields of view observed by Kepler and CoRoT are shown in yellow and blue respectively for comparison. Figure from Rauer et al. (2013).

1.5.1 Photometric missions

Three space-based photometers working in the optical spectral range are currently planned. CHEOPS and PLATO for the European Space Agency (ESA) and TESS for the National Aeronautics and Space Administration (NASA). The primary goal of these missions is to detect or confirm the presence of exoplanets around bright stars. They plan to overcome the main limitations of the CoRoT and Kepler missions. Kepler discovered numerous planets but most of them orbit dim stars and are therefore difficult to characterize. CoRoT observed numerous planets around bright stars, but was limited by its photometric precision and its relatively small field of view.

CHEOPS (CHaracterizing ExOPlanets Satellite) will be launched in 2017. The aim of the mission is to detect transiting planets among the planets that have already been discovered by radial velocities. This will highlight good candidates for future atmospheric characterization. For planets that are already known to transit, CHEOPS' observations will increase the precision of the transit lightcurve and provide a better estimate of the radius of the planet.

TESS (Transiting Exoplanet Survey Satellite) is scheduled for launch in 2017, at the same time as CHEOPS. TESS will perform a survey of the whole sky with a minimal staring time of 27 days and a maximal one of 6 months. It should detect the majority of planets that orbit bright stars in less than 10 days, at least the big ones and down to Earth-size. Planets with a period up to 2 months will also be discovered.

The PLATO mission (Planetary Transits and Oscillations of stars) was selected in 2014 by ESA and will be launched in 2024. PLATO is a space-based photometer that will detect planets around bright stars. It will stare at numerous field of views for a continuous duration of 2-5 months, covering 42% of the sky. For two specific fields of view, PLATO will point continuously for three years (see Figure 1.17). As for TESS, PLATO will detect planets orbiting bright stars for which atmospheric characterization is possible.

Those surveys will provide good targets for atmospheric characterization. They will also provide high precision optical lightcurves that will be used to have a broad census of planetary albedos and their variations with longitude (see Sections 1.3.2 and 1.4.1)

1.5.2 Spectroscopic missions

Spectral resolution is essential to the characterization of exoplanets' atmospheres. The James Web Space Telescope (JWST) will hopefully be launched in 2018. It has a 6.5 meter mirror and can observe a wide spectral range (from 0.6 to 28.8 µm) with a good spectral resolution ($\lambda/\Delta\lambda = 700 - 3000$).

EChO (Exoplanet Characterization Observatory) and FINESSE (Fast Infrared Exoplanet Spectroscopy Survey Explorer) missions are two space-based spectrographs dedicated to the characterization of exoplanets atmospheres. Unfortunately neither missions have been selected for funding. Their main advantages compared to JWST are their dedication to exoplanets characterizations (JWST time will have to be shared with the entire astrophysics community) and their possibility to observe the whole spectra of a planet in one shot (whereas JWST needs three different observations). The next section details the scientific questions that could be investigated with such an EChO-class mission.

1.5.3 Characterizing gas giant atmospheres with an EChO-class mission

EChO is a space mission dedicated to the spectroscopic characterization of exoplanets that was proposed to the ESA in 2014. As part of the scientific team of EChO, I wrote the following note about EChO's potentialities concerning the dynamics and the thermal structure of giant exoplanets' atmospheres. The note was submitted together with the EChO proposal in early 2014. Unfortunately, the mission was not selected by the science advisory committee. The note, however, applies to any future EChO-class mission. It was submitted to the journal *Experimental Astronomy* and received a positive response from the editor.

Characterizing gas giant exoplanets with an EChO-class mission.

Vivien Parmentier[1], Adam P. Showman[2], Julien de Wit[3]

[1] Université de Nice-Sophia Antipolis, Observatoire de la Côte d'Azur, CNRS UMR 6202, Nice, France [vivien.parmentier@oca.eu]
[2] Department of Planetary Sciences, Lunar and Planetary Laboratory,University of Arizona, Tucson AZ, USA
[3] Department of Earth, Atmospheric and Planetary Sciences, MIT, 77 Massachusetts Avenue, Cambridge, MA 02139, USA.

Accepted to the Experimental Journal of Astronomy April 8, 2014

Abstract . More than a thousand exoplanets have been discovered over the last decade. Perhaps more excitingly, probing their atmospheres has become possible. With current data we have glimpsed the diversity of exoplanet atmospheres that will be revealed over the coming decade. However, numerous questions concerning their chemical composition, thermal structure, and atmospheric dynamics remain to be answered. More observations of higher quality are needed. In the next years, the selection of a space-based mission dedicated to the spectroscopic characterization of exoplanets would revolutionize our understanding of the physics of planetary atmospheres. Such a mission was proposed to the ESA cosmic vision program in 2014. Our paper is therefore based on the planned capabilities of the Exoplanet Characterization Observatory (EChO), but it should equally apply to any future mission with similar characteristics. With its large spectral coverage (4 − 16 μm), high spectral resolution ($\Delta\lambda/\lambda > 300$ below 5 μm and $\Delta\lambda/\lambda > 30$ above 5 μm) and 1.5m mirror, a future mission such as EChO will provide spectrally resolved transit lightcurves, secondary eclipses lightcurves, and full phase curves of numerous exoplanets with an unprecedented signal-to-noise ratio. In this paper, we review some of today's main scientific questions about gas giant exoplanets atmospheres, for which a future mission such as EChO will bring a decisive contribution.

Introduction

Characterizing exoplanets atmospheres has recently become within reach. Nowadays, a significant number of atmospheric measurements have been acquired on a dozen of exoplanets. Unfortunately, none of those measurements were done with a dedicated instrument. Although researchers have made the best use of available telescopes, the observations still suffer from large error bars, from possible instrumental noise (Hansen et al. 2014), are averaged over large bins of frequency, and measurements at different wavelength are usually made at different times. The construction of a reliable spectrum is therefore a difficult task. Few unambiguous molecular detections have been claimed and most of the physical characterizations are qualitative rather than quantitative. Better data are needed. The future of exoplanet characterization should be based on high signal-to-noise, spectrally resolved observations with a large spectral coverage accessible in a single observation.

A mission with those capabilities was proposed to the ESA Cosmic Vision program in 2014. With its large spectral coverage (4 – 16 μm), high spectral resolution ($\lambda/\Delta\lambda > 300$ below 5 μm and $\lambda/\Delta\lambda > 30$ above 5 μm), and 1.5 m mirror, EChO (the Exoplanet Characterization Observatory) is an ideal instrument to characterize exoplanets atmospheres (see Tinetti et al. 2012, for more technical details about the mission). Although it was not selected in 2014, it should serve as a baseline for future missions with similar goals. The following review is based on the expected capabilities of EChO but is also relevant for any future mission with similar characteristics. In the following, the term *EChO* should therefore be understood as *an EChO-class mission*.

We will now review why a mission such as EChO will be a decisive step toward understanding exoplanets atmospheres and atmospheric physics in general.

On the large diversity of observable exoplanets atmospheres

Most EChO targets – and the ones for which the best observations will be available – are planets orbiting close to their host star. Tidal interactions should force them toward a tidally locked state (Lubow et al. 1997; Guillot & Showman 2002) where their rotation period is the same as their revolution period (see Fig. 1). A whole range of atmospheric constraints is obtainable for those close-in, tidally locked planets because *we know which hemisphere is facing us at any orbital phase*. Monitoring the star-planet system during its whole orbit, one can obtain longitudinal information on the planet's brightness distribution (Knutson et al. 2008). During the ingress and egress of the secondary eclipse, the technique of eclipse mapping (Majeau et al. 2012; de Wit et al. 2012) can constrain the horizontal (both longitudinal and latitudinal) brightness distribution of the planet's dayside. Finally, the frequency dependence of the thermal flux emitted by the planet and of the stellar flux filtered through the planet atmosphere during transit depends principally on the temperature profile, the atmospheric composition and their variations with depth (Barstow et al. 2013; de Wit & Seager 2013).Thus, with a high enough signal-to-noise ratio and a large enough spectral coverage, the spectral resolution of transmission and emission spectra can translate into vertical resolution of the temperature and composition of the atmosphere. Combining those techniques, EChO will provide a three dimensional vision of numerous close-in planets.

Hundreds of close-in transiting planets with very different gravities and orbital periods are already known and more will be discovered and confirmed before the launch of the mission. Although, for a given star, the irradiation is only function of the distance to the star, the large diversity in exoplanets stellar hosts ensure a good coverage of the rotation period / equilibrium temperature parameter space. As seen in Fig. 2, the irradiation temperature can vary by a factor 4 (corresponding to a factor 256 for the irradiation flux) between planets with similar rotation period but orbiting different stellar types. Planet gravity, for its part, varies

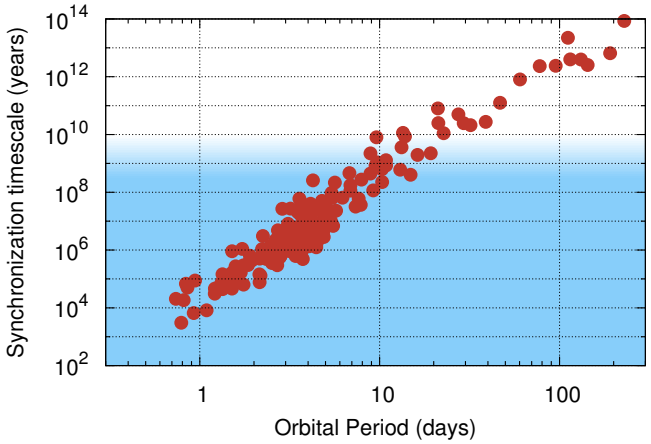

Fig. 1: Tidal synchronization timescale based on Guillot et al. (1996) for all known exoplanets with a measured mass and radius in function of their orbital period for a dissipation factor $Q = 6\times10^5$, typical for hot Jupiters (Ferraz-Mello 2013) and an initial rotation rate equal to Jupiter's one. Planets in the shaded area are likely to be tidally locked.

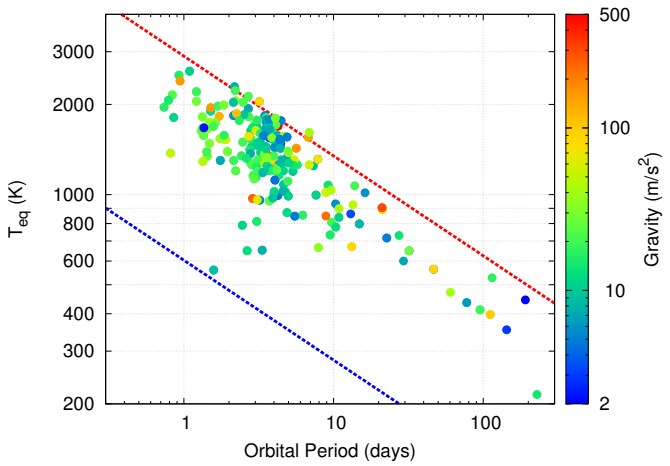

Fig. 2: Equilibrium temperature (assuming zero albedo) of exoplanets with a measured mass and radius. Planets are color-coded by their gravity. The blue (red) line is the equilibrium temperature for a planet orbiting a M5 (A5) type star. Planets with an orbital period smaller than ≈ 10 days are likely to have a rotation period equal to their orbital period (see Fig. 1).

by more than two orders of magnitude among known planets, ranging from ≈ 2.5 to ≈ 500m/s^2. The sample of planets EChO will observe thus covers a large area in the irradiation / rotation / planet gravity parameter space, three of the main parameters shaping the atmospheric circulation.

Thermal structure, composition and atmospheric circulation are essential characteristics of planetary atmospheres. They affect each other via the different mechanisms described in Fig. 3. The thermal structure sets the chemical equilibrium whereas the composition determines the atmospheric opacities, controlling the radiative transfer and thus the temperature. The atmospheric circulation is driven by the temperature contrasts. It transports heat and material, which shapes the temperature and composition both horizontally and vertically. Finally, the presence of ionized material directly affects the circulation via the Lorentz forces. The spatial variation of the temperature and composition, together with their departure from equilibrium are thus signatures of the atmospheric circulation.

EChO can observe hundreds of exoplanets atmospheres with a high spectral resolution and an exquisite photometric precision. It can obtain a full exoplanet spectrum in one observation and will be able to observe periodically a given target. Such a mission is essential to determine the spatio-temporal variability of exoplanets atmospheres and understand their diversity in terms of composition, thermal structure and dynamics. Hereafter we list several key scientific questions concerning the thermal structure and atmospheric dynamics of gas giant atmospheres that EChO's observations will help to solve. Questions related to atmospheric chemical composition are treated in a separate article.

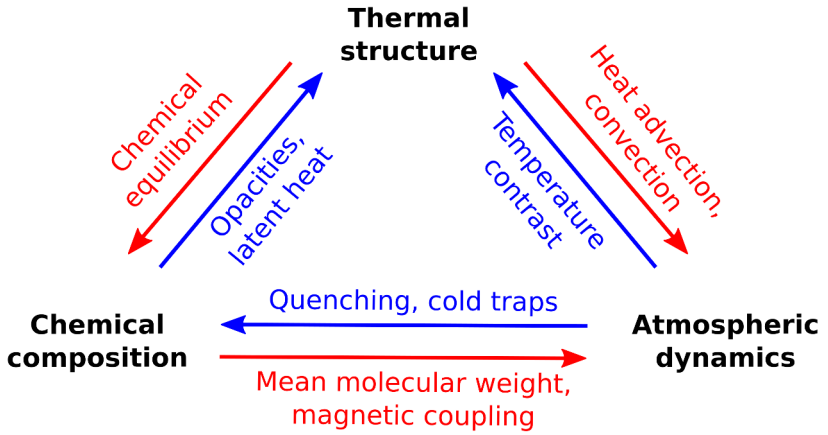

Fig. 3: Schematic view of the main atmospheric characteristics and how they affect each other.

Key questions in atmospheric structure and dynamics to be addressed by an EChO-class mission

1. What is the longitudinal structure of the temperature in hot Jupiter atmospheres, and how does it depend on depth?

High-quality lightcurves—as obtainable from EChO for a wide range of close-in planets—will allow longitudinal maps of brightness temperature to be derived. This will allow the longitudinal locations of hot and cold spots, among other features, to be identified; observations at many wavelengths will allow the depth-dependence to be determined in the range ~0.001–10 bar. Spitzer observations of several hot Jupiters, including HD 189733b (Knutson et al. 2007, 2009, 2012), Ups And b (Crossfield et al. 2010), and WASP-43b (Stevenson 2014) indicate that the hottest regions are displaced eastward of the substellar point by tens of degrees of longitude or more (see Figs. 4 and 5). This phenomenon was predicted and has now been reproduced in a wide range of three-dimensional circulation models under conditions appropriate to benchmark hot Jupiters such as HD 189733b and HD 209458b (Showman & Guillot 2002; Cooper & Showman 2005; Showman et al. 2008, 2009; Menou & Rauscher 2009; Dobbs-Dixon & Lin 2008; Dobbs-Dixon et al. 2010; Rauscher & Menou 2010, 2012a; Heng et al. 2011a,b; Perna et al. 2012). In these models, the eastward displacement results from advection by an eastward "superrotating" jet stream at the equator. Theory shows that, on tidally locked planets, such superrotation is the natural result of the day-night heating pattern, which leads to planetary-scale waves that pump angular momentum to low latitudes (Showman & Polvani 2011). Nevertheless, current predictions—yet to be tested—suggest that the longitudinal offset of the hotspot should scale inversely with incident stellar flux (Showman & Polvani 2011; Perna et al. 2012; Showman et al. 2013). The extent to which such longitudinal offsets are prevalent on hot Jupiters—and their dependence on incident stellar flux, planetary rotation rate, atmospheric composition, and other factors—remains unknown. Recent magnetohydrodynamic calculations that properly represent the full coupling of the dynamics to the magnetic field furthermore suggest that, under particularly hot conditions, a westward equatorial jet can sometimes emerge (Rogers & Showman 2014; Rogers & Komacek 2014), potentially leading to a *westward* hot spot offset in these cases. EChO can address this question with a broad census, determining the amplitude and sign of the offset under a broad range of conditions, and map the depth dependence of these features.

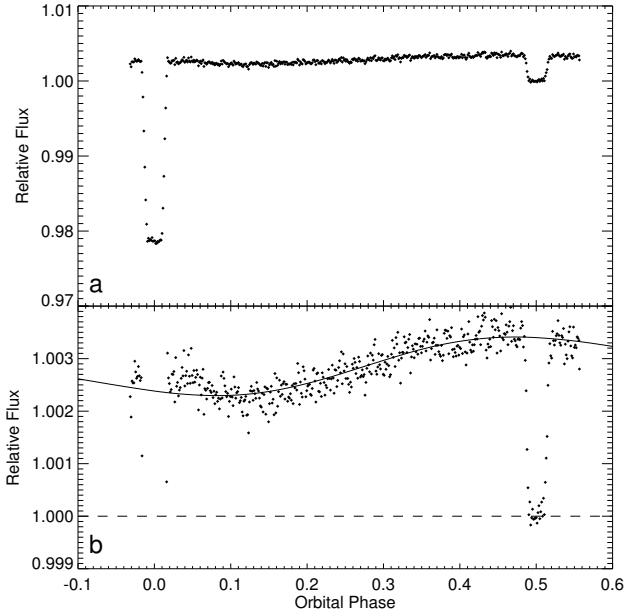

Fig. 4: Thermal phase curve of HD189733 observed with the IRAC instrument on the Spitzer Space Telescope at 8 microns by Knutson et al. (2007). In the top panel, the transit (orbital phase 0) and secondary eclipse of the planet orbital phase 0.5) are visible. In the bottom panel, the increase of flux between the transit and the secondary eclipse is due to the planet phase: before and after the transit the planet shows its cold and thus dark nightside whereas before and after the secondary eclipse it shows its warm, and thus luminous, dayside.*Reprinted by permission from Macmillan Publishers Ltd. Nature Copyright 2007.*

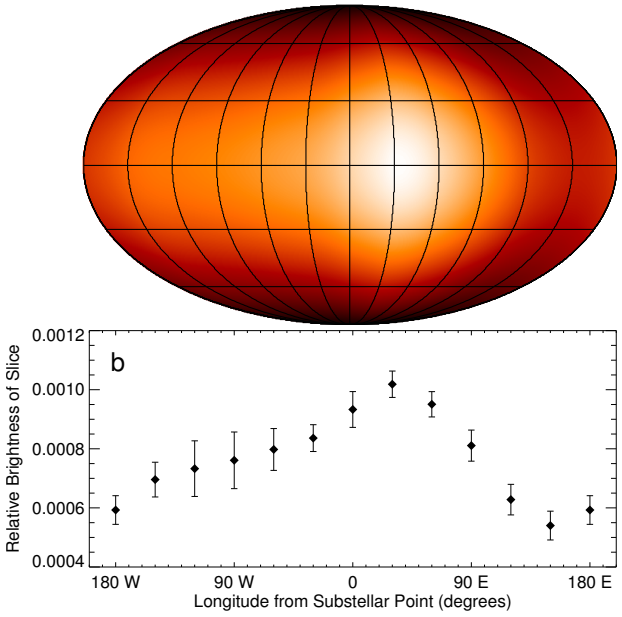

Fig. 5: Longitudinal temperature map of the planet HD189733b retrieved from the phase curve observation depicted in the previous figure (Knutson et al. 2007, from). The shift of the hottest point of the planet east of the substellar point is attributed to fast eastward equatorial winds (Showman et al. 2009).*Reprinted by permission from Macmillan Publishers Ltd. Nature Copyright 2007.*

2. What sets the day-night temperature contrast? How does it vary with depth (wavelength) and among different planets? What is the mechanism that controls the day-night temperature contrast on tidally locked planets?

Current lightcurve observations have allowed the day-night brightness temperature contrast to be determined for over a dozen hot Jupiters. These observations suggest a trend wherein cooler planets exhibit modest fractional day-night temperature contrasts whereas hotter planets exhibit near-unity fractional day-night temperature variations (Cowan & Agol 2011; Perna et al. 2012; Perez-Becker & Showman 2013). As emphasized by Perez-Becker & Showman 2013, the details of this trend place strong constraints on the mechanisms that maintain the day-night temperature differences on hot Jupiters (e.g., on the relative roles of horizontal advection, vertical advection, wave propagation, and radiative cooling) and on the conditions under which frictional drag and ohmic drag become important (Li & Goodman 2010; Rauscher & Menou 2012b, 2013; Showman et al. 2013). Current observations exist at only a few broadband wavelengths, and full spectral information as obtainable from EChO would provide significant information on how the transition from small to large fractional day-night flux difference depends on wavelength, and in turn how this transition depends on depth in the atmosphere.

3. What physical mechanisms determine the vertical temperature profile at the terminator of the planet ?

The terminator of close-in, tidally locked planets is extremely interesting but very complex. It is located at the middle of the largest temperature gradients and where the fastest winds are present. Hydrodynamics shocks might be present (Heng 2012). Scattering should become important due to the grazing path of the stellar rays (Fortney 2005). Condensation of numerous species is expected to take place close to the terminator, depositing latent heat and increasing even more the importance of scattering. From the combined effects of the dynamics and the condensation processes, a significant differences in the cloud coverage between the western and the eastern atmospheric limbs is expected (Iro et al. 2005). Whether the ions produced in the hot dayside recombine before or after crossing the terminator will influence the strength of the magnetic forces acting on the fluid. At low pressures, non local thermodynamic equilibrium (LTE) effects should also play a major role (Barman et al. 2002).

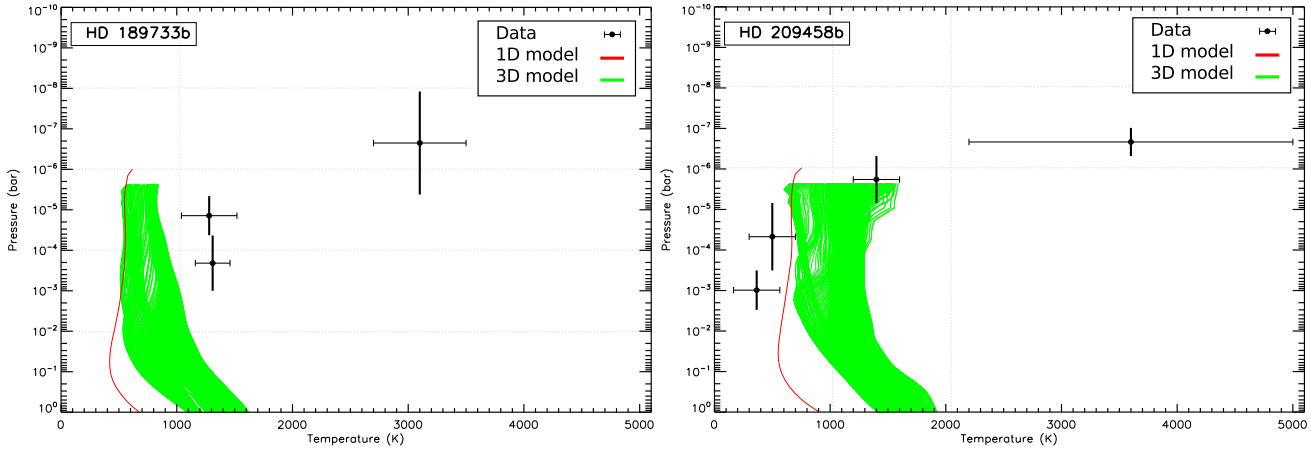

Fig. 6: Pressure-temperature profile at the terminator of the hot Jupiter HD189733b (left) and HD209458b (right). Data are retrieved from the sodium absorption line of the planet observed during transit by Vidal-Madjar et al. (2011) and Huitson et al. (2012). For HD 209458b, the pressure scale is based on the detection of the Rayleigh scattering by H_2. For HD 189733b, the pressure scale is model dependent: it is determined assuming that the top of the cloud deck is at 10^{-4} bar. The red line is obtained from the grid of 1D numerical models used in Parmentier et al. (2014). The green lines are all the limb temperature profiles predicted by the 3D model (SPARC/MIT GCM). The difference between the 1D and the 3D temperature profiles is mainly due to the advection of heat by the atmospheric circulation. At pressures lower than 10^{-5} bar, non-LTE effects, not taken into account in the models become important Barman et al. (2002). Figure adapted from Huitson et al. (2012).

The temperature at the terminator of a planet can be retrieved from the slope of the spectral features apparent in the transit spectrum (Lecavelier Des Etangs et al. 2008). From the absorption feature of the Sodium D line, the temperature profile at the terminator of HD 189733b (Vidal-Madjar et al. 2011) and HD 209458b (Huitson et al. 2012) have been retrieved. As shown in Figure 6, the retrieved temperatures in the upper atmosphere of HD 189733b and HD 209458b are larger than predicted by current LTE models. They are nonetheless consistent with observations of hot hydrogen in the upper atmosphere of HD 209458b by Ballester et al. (2007) and necessary to explain the extended atmosphere observed in both planets (Vidal-Madjar et al. 2003; Lecavelier Des Etangs et al. 2010). At higher pressures, the temperature of HD 209458b is unexpectedly low and cannot be explained by current 1D and 3D models. Those low temperatures are however consistent with the condensation of sodium at low pressures as shown by Sing et al. (2008).

EChO will accurately determine the mean temperature profile at the terminator of a wide range of planets from their transit spectrum. It will disentangle the contributions of the dynamical, chemical and radiative processes shaping the temperature profile at the terminator. For the brightest targets, it will observe the differences between the ingress and the egress of the transit, shedding

light on the differences in temperature, chemical composition and cloud coverage between the western and the eastern atmospheric limbs.

4. What is the latitudinal structure of the temperature in hot Jupiter atmospheres?

The high and low latitudes of a planet differ by the amount of irradiation they receive and by the strength of the Coriolis forces. As a result, in hot Jupiters atmospheric models, the circulation patterns change from a deep super-rotating jet at the equator to a day-to-night circulation at the poles (Showman et al. 2013). Chemical composition and cloud coverage could follow this trend and be significantly different between the poles and the equator (see Parmentier et al. 2013, and Fig. 8 hereafter). The secondary eclipse of an exoplanet yields latitudinal information about the temperature structure of its atmosphere. During a secondary eclipse, the planet disappears behind its host star. For non-zero impact parameter, the disappearance and appearance of the planet happen by slices that are tilted with respect to the north/south direction. The ingress and egress of an exoplanet's secondary eclipse can thus allow the construction of full two-dimensional maps of the dayside hemisphere (Majeau et al. 2012; de Wit et al. 2012), in opposition to phase curves that lead to longitudinal maps only. Furthermore, as each wavelength probes different optical depth of the dayside atmosphere, multi-wavelength observations, as the ones EChO will provide, can allow tri-dimensional maps of the atmosphere. As an example, the eclipse mapping of HD 189733b using Spitzer 8 microns data constrains its hot spot to low latitudes and provides independent confirmation of its eastward shift relative to the substellar point (Majeau et al. 2012; de Wit et al. 2012).

Based on the technique developed by de Wit et al. (2012) we present in Fig. 7 the map retrieval of a synthetic version of the hot Jupiter HD 189733b[1] with a hypothetical hot spot with a temperature contrast of $\Delta T/T \approx 30\%$ located in the northern hemisphere. Such a hot spot in a given spectral bin could be formed by the presence of patchy clouds (see Fig. 8) or chemical differences between the poles and the equator. With one secondary eclipse, EChO will detect the presence of latitudinal asymmetry in the planet's brightness distribution. With ∼10 (resp. ∼100) secondary eclipses, the temperature contrast will be measured with a precision of 300 K (resp. 100 K) and the latitudinal location of the hot-spot will be known with a precision of 10° (resp. 3.5°). This observations will be available in different spectral intervals, with a spectral resolution of ≈ 20, for the most favorable targets.

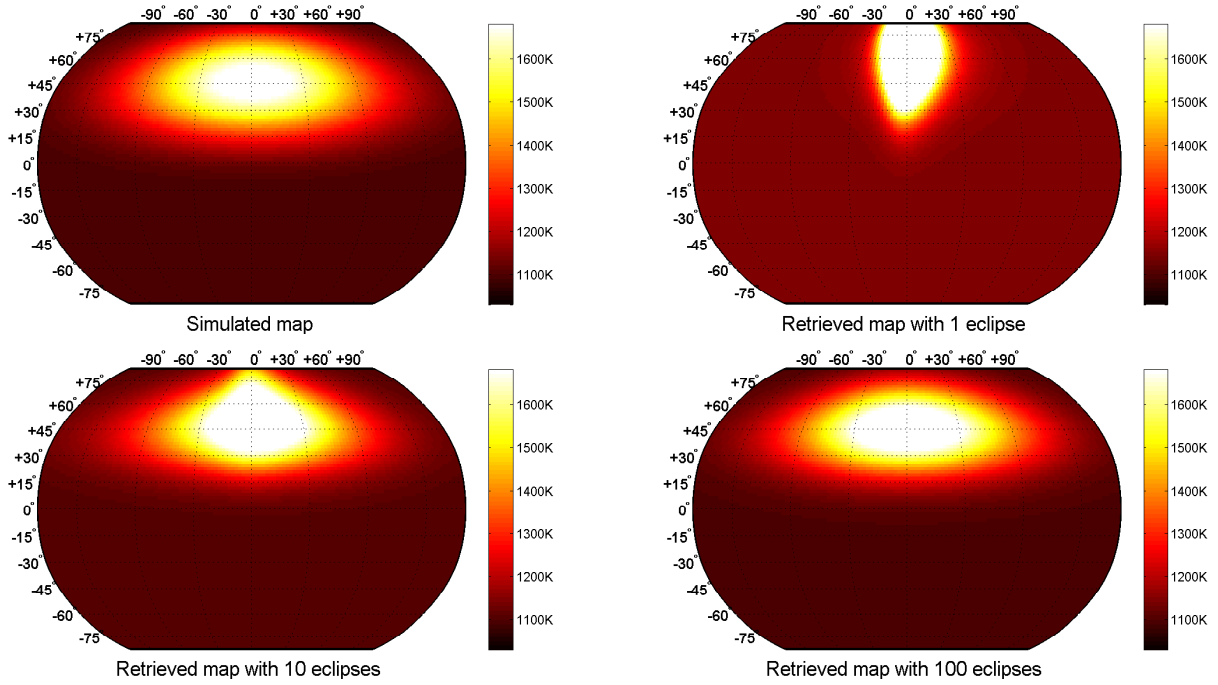

Fig. 7: Simulated retrieval of dayside brightness temperature patterns using ingress/egress mapping for a hypothetical case where a large thermal hotspot resides in the high northern latitudes of the dayside. Planetary and stellar parameters of HD 189733b are adopted. The top left map depicts the synthetic data. The top right, bottom left, and bottom right shows the ability of ingress/egress mapping to recover the temperature structure of the synthetic data with 1, 10, and 100 secondary eclipses observed by EChO, respectively, in a spectral bin of resolution 20.

[1] We use EChO's noise model introduced in Barstow et al. (2013). In particular, we use a telescope effective area of 1.13 square meter, a detector quantum efficiency of 0.7, a duty-cycle of 0.8, and an optical throughput of 0.378 from 2.5 to 5 μm, relevant for this simulation showed in Fig. 7

5. How common are clouds, what are they made of, and what is their spatial distribution?

The atmospheres of many hot and warm Jupiters have temperatures that cross the condensation curves for various refractory materials, suggesting that cloud formation may be an important process on some of those planets. Transmission spectra indicate that HD 189733b and perhaps HD 209458b exhibit haze-dominated atmospheres (Pont et al. 2013; Deming et al. 2013). This may also be true for the super-Earth GJ 1214b (e.g. Bean et al. 2011; Berta et al. 2012; Morley et al. 2013) and GJ 3470b (Crossfield et al. 2013; Nascimbeni et al. 2013). Given the cold conditions on the nightsides of typical hot Jupiters, many chemical species should condense on the nightside. Three-dimensional circulation models including condensable tracers (Parmentier et al. 2013) indicate that complex spatial distributions of clouds—on both the dayside and nightside—can result from such nightside condensation (see Fig. 8).

Multi-wavelength lightcurves obtained by EChO will provide major constraints not only on the chemical composition and thermal structure but on the existence and properties of clouds in gas giant's atmospheres. Phase curves in the visible frequency range will provide insight on the longitudinal variation in albedo along the planet, which could be a strong signature of inhomogeneous cloud coverage on the planet atmosphere (Demory et al. 2013; Heng & Demory 2013). By monitoring planets with widely different equilibrium temperatures, EChO is expected to characterize the transition from cloudy to cloudless atmospheres and the change in the dominant condensable species with equilibrium temperature, from silicate clouds at high temperatures to water clouds in temperate planets.

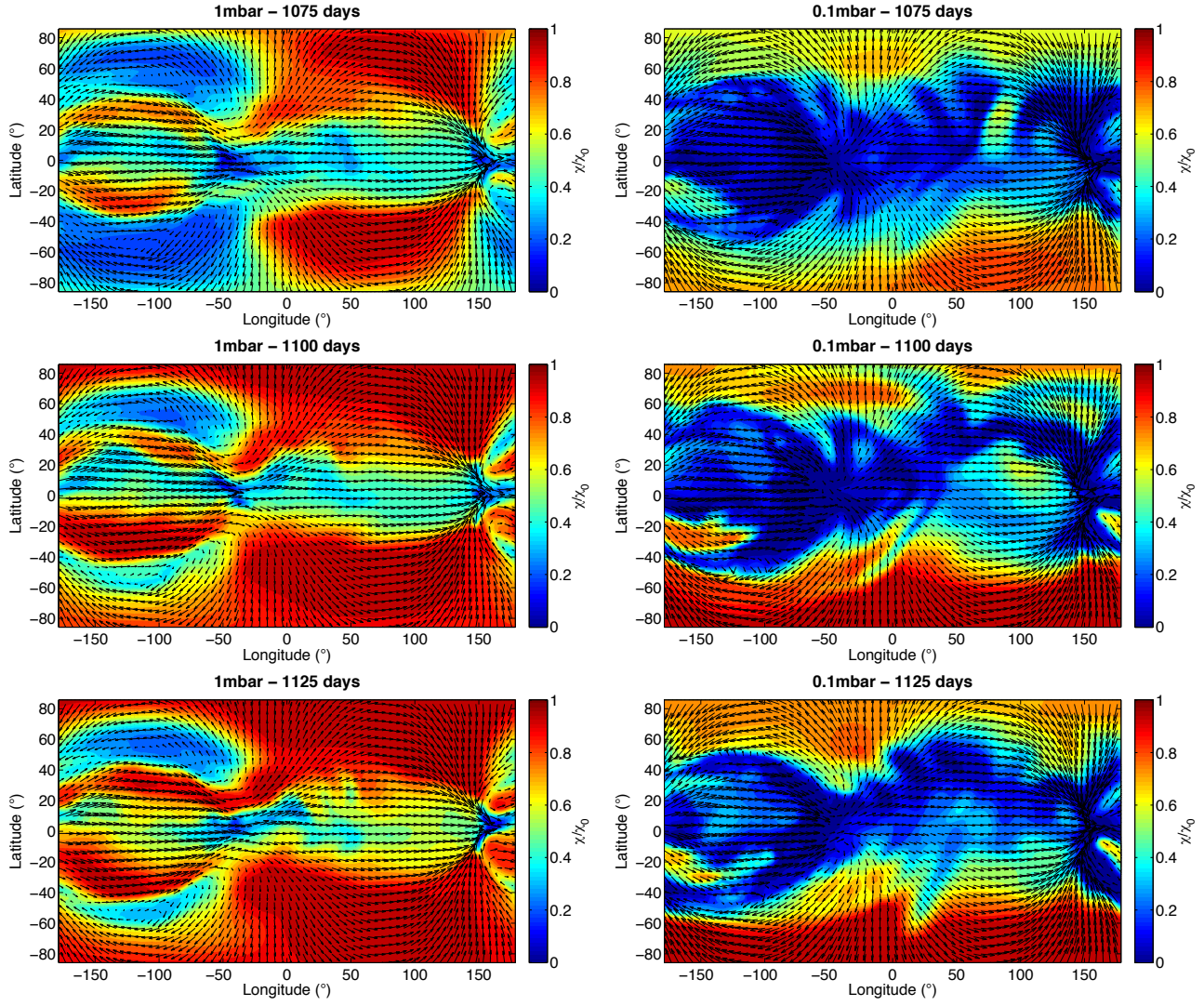

Fig. 8: Spatio-temporal variability of tracer particles (color) and winds (arrows) representing clouds in a hot-Jupiter model of Parmentier et al. (2013). The particles efficiently trace the main circulation patterns of the atmosphere.

6. How common are stratospheres, and what determines their distribution and properties ?

Thermal inversions are a natural consequence of visible/UV absorption of the incident star light high in the atmosphere. For an isolated planetary atmosphere in hydrostatic equilibrium and no local energy sources, the atmospheric temperature decreases with pressure. In planetary atmospheres irradiated by their host star, strong optical/UV absorbers in the upper layers can intercept part of the incident star light. With such a local heating, a zone where the temperature increases with decreasing pressure can form. Most solar system planets have temperature inversions in their atmospheres. In Earth atmosphere it is caused by ozone, which is a strong absorber in the UV (Chamberlain & Hunten 1987). In Jupiter, it is mainly caused by the strong absorption in the visible by hazes resulting from methane photochemistery.

The compounds producing thermal inversions in solar system atmospheres do not survive the high temperatures of hottest hot Jupiters. Nevertheless, it has been proposed that thermal inversions in the $\sim$ 1 mbar $-$ $-$1 bar level could form in the atmosphere of very hot Jupiters due to the strong absorption of the incident stellar radiation in the visible by gaseous titanium oxide (Hubeny et al. 2003), a compound present in brown dwarfs with similar atmospheric temperatures (Kirkpatrick 2005). The so-called TiO-hypothesis differentiates between planets hot enough to have gaseous TiO and thus a thermal inversion and planets too cold to have gaseous TiO and thus without thermal inversion (Fortney et al. 2008). Evidence for the presence of a thermal inversion have been claimed for several planets. Most of these claims were based on the ratio between the 3.6 μm and the 4.5 μm thermal fluxes observed with the Spitzer space telescope (Knutson et al. 2008; Burrows et al. 2008). Assuming that water is the main absorber at those wavelengths, a higher flux at 4.5 μm than at 3.6 μm can be interpreted as an emission band, created by an inverted temperature profile whereas a smaller flux at 4.5 μm than at 3.6 μm can be interpreted as an absorption feature, resulting from a non-inverted temperature profile. Up to now, most of the claims did not survive a more exhaustive analysis that included a large range of possible atmospheric chemical composition and temperature profiles (Madhusudhan & Seager 2010). In current data there is thus no strong evidence for a thermal inversion but it is not ruled out either (Hansen et al. 2014).

Given the apparent lack of large thermal inversions and strong observational signatures of TiO in the transit spectrum of several planets (e.g. Désert et al. 2008; Huitson et al. 2013; Sing et al. 2013), many authors challenged the TiO hypothesis. Condensation in the deep atmosphere Showman et al. (2009); Spiegel et al. (2009) or in the nightside of the planet (Parmentier et al. 2013) could deplete TiO from the dayside atmosphere. Knutson et al. (2010) noted that TiO could be destroyed by the strong stellar FUV flux, implying that only planets orbiting low activity stars could have an inversion. Madhusudhan et al. (2011) showed that atmospheres with a carbon to oxygen ratio higher than one should have a reduced TiO abundance, making them unable to maintain a thermal inversion. Zahnle et al. (2009) and Pont et al. (2013) proposed that absorption by hazes instead of TiO could be responsible for the thermal inversion whereas Menou (2012) showed that ohmic dissipation could also lead to an inverted temperature profile.

EChO will perform a broad census of which hot Jupiters exhibit a thermal inversion and which do not, and will determine to which extent the presence of thermal inversions correlates with incident stellar flux, stellar activity, atmospheric composition, day/night temperature gradients and other parameters. Because EChO will obtain full IR spectra from which absorption and emission features can be well identified, the determination of whether a planet exhibits a stratosphere—and the pressure range of any stratosphere—will be much more robust than possible with existing Spitzer and groundbased data. Moreover, spectral features seen in transit and secondary eclipse will provide strong constraints on the specific chemical absorber that allows for the existence of stratospheres.

7. What are the main dynamical regimes and what determines the shift from one to another?

Hot Neptunes and Jupiters span an enormous range of incident stellar fluxes, orbital parameters, masses, surface gravities, and rotation rates, among other parameters. Not surprisingly, then, theory and numerical simulations suggest that such planets exhibit several fundamentally different circulation regimes depending on these parameters. Most circulation models to date have emphasized the benchmark hot Jupiters HD 189733b and HD 209458b (Showman & Guillot 2002; Cooper & Showman 2005; Showman et al. 2008, 2009; Menou & Rauscher 2009; Dobbs-Dixon & Lin 2008; Dobbs-Dixon et al. 2010; Thrastarson & Cho 2010, 2011; Rauscher & Menou 2010, 2012a; Lewis et al. 2010; Heng et al. 2011b,a; Perna et al. 2012; Miller-Ricci Kempton & Rauscher 2012; Parmentier et al. 2013). These models tend to produce several broad zonal (east-west) jets including a fast superrotating equatorial jet, and day-night temperature differences of hundreds of Kelvin at photospheric levels. Nevertheless, recent theoretical explorations of wider parameter spaces suggest that at extremely large stellar fluxes, the fractional day-night temperature differences increases and the longitudinal offset of hot spots decreases (Perna et al. 2012; Perez-Becker & Showman 2013). This shift is also accompanied by a shift from a circulation dominated by zonal (east-west) jets at moderate stellar flux to a circulation dominated by day-to-night flow at extreme stellar flux (Showman et al. 2013). At orbital separations beyond those typically identified with hot Jupiters ($>$ 0.1 AU), models suggest that the eastward equatorial jet will give way to a circulation exhibiting one or more eastward jets in the midlatitudes of each hemisphere generated by baroclinic instability—a pattern more reminiscent of Earth or Jupiter (Showman et al. 2012). The spatial variation of temperature, clouds, and chemical composition can efficiently trace the atmospheric circulation patterns (Parmentier et al. 2013). By determining those spatial variations for a wide range of planetary conditions, EChO will determine the main circulation regimes of exoplanets atmospheres.

8. What is the role of magnetic coupling in the circulation of hot exoplanets?

Several authors have suggested that, at the extreme temperatures achieved on the most highly irradiated hot Jupiters, thermal ionization may allow a coupling of the atmosphere to the planet's magnetic field, causing the Lorentz force to become dynamically important (Perna et al. 2010a,b; Rauscher & Menou 2013). This could lead to qualitative changes in the day-night temperature difference and the geometry and speed of the global wind pattern relative to an otherwise similar planet without such coupling (Batygin

et al. 2013). Dynamical coupling to the magnetic field could even allow feedbacks that influence the existence and amplitude of a dayside stratosphere (Menou 2012). Moreover, such coupling could lead to Ohmic dissipation, with possible implications for the planet's long-term evolution (Batygin & Stevenson 2010; Perna et al. 2010b; Huang & Cumming 2012; Wu & Lithwick 2013). The sensitivity of the magnetic effects to the ionisation rate – given by the composition and the temperature profile – will allow EChO to identify their role in the hottest planets.

9. Are hot Jupiters temporally variable, and if so, what is the nature and distribution of the variability?

Atmospheres of planets in the solar system are turbulent, leading to temporal fluctuations on a wide range of space and time scales. This question is also a crucial one for hot Jupiters, especially because the temporal behavior of any variability contains telltale clues about the atmospheric state that would be hard to obtain using other techniques. A variety of searches for variability have taken place over the years, so far without any firm detections of variability. Using Spitzer observations of seven secondary-eclipses of HD 189733b, Agol et al. (2010) demonstrated an upper limit of 2.7% of the variability of the secondary-eclipse depth at 8 μm. Most 3D circulation models of typical hot Jupiters exhibit relatively steady circulation patterns; for example, circulation models coupled to radiative transfer predict variability in the secondary-eclipse depth of ~1% in the Spitzer IRAC bandpasses (Showman et al. 2009). Nevertheless, some circulation models predict high-amplitude variability of up to 10% or more at global scales (Cho et al. 2003, 2008; Rauscher et al. 2007). The amplitude and temporal spectrum of variability have much to tell about the basic atmospheric structure. Periods of variability are likely to be linked to the periods for dynamical instabilities in the atmosphere. In turn, these fundamental periods are influenced by the structure of the circulation's basic state including the stratification (e.g., the Brunt-Vaisala frequency), the vertical shear of the horizontal wind, and other parameters. As a dedicated mission, EChO will be able to observe systematically *all* transits and secondary eclipses of a given planet for a given amount of time and shed light on the different timescale and on the amplitude of the variability of a handfull of hot Jupiters. This way, EChO will allow insights into the dynamics not obtainable in any other way.

10. What are the conditions in the deep, usually unobservable atmosphere ?

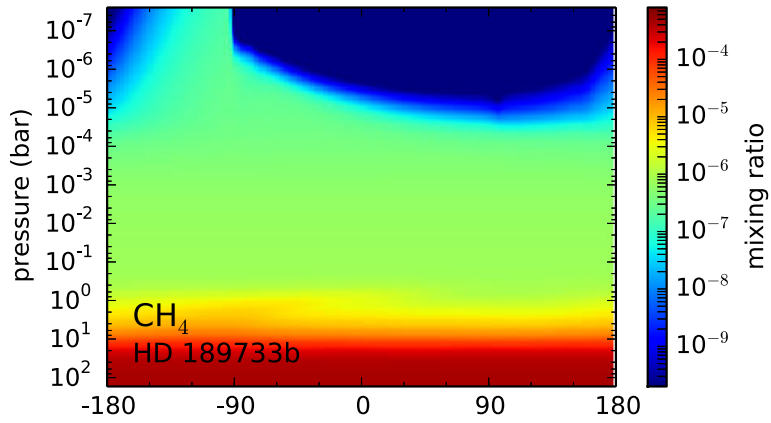

Fig. 9: Abundance of methane in the equatorial plane of HD 189733b predicted by the pseudo-2D chemical model of Agundez et al. (2014). The x-axis represents longitude with respect to the substellar point. In the dayside the abundance in the 10^{-5} – 0.1 bar pressure range is quenched to the abundance at the 0.1 bar level. At lower pressures photochemistery becomes important and the abundance drops. the nightside abundance is quenched to the dayside one due to the horizontal advection by an eastward jet.

EChO observations can be used to detect and infer the atmospheric abundances of major molecules potentially including H_2O, CO, CH_4, CO_2, and various other trace and/or disequilibrium species (see Barstow et al. 2013). To these extent that these species exhibit chemical interactions with short timescales, they may exhibit spatially variable three-dimensional distributions (e.g., differing dayside and nightside abundances). Any detected spatial variations or homogeneity in such chemical species across the planet would thus provide important constraints on the dynamics.

Several species, including CO and CH_4, are predicted to have long interconversion timescales, implying that they will be chemically "quenched" in the observable atmosphere at constant abundances that should vary little from one side of the planet to the other (see Figure 9 and also Cooper & Showman 2006; Moses et al. 2011; Agundez et al. 2014). The quench level—above which the abundances are in disequilibrium and below which they are approximately in equilibrium–is predicted to be at ~0.1–10 bars pressure on typical hot Jupiters (Cooper & Showman 2006; Agundez et al. 2014) and even deeper for cooler planets. Interestingly, this can be deeper than directly probed by thermal emission measurements (which sense pressures less than ~10 bar). Because the quenched abundances depend on the atmospheric vertical mixing rate, this implies that precise measurements of the CO and CH_4 abundances will place constraints on the dynamical mixing rates at pressures deeper than can be directly sensed. These insights on the dynamics via chemistry will thus be highly complementary to insights obtained on the dynamics from light curves and ingress/egress mapping. Moreover, they will give constrains on the deep atmosphere, a fundamental zone for understanding the interior and evolution of gas giant planets (Guillot & Showman 2002). On cooler planets, quenching in the N_2/NH_3 system can provide analogous insights.

11. Why are some hot Jupiters inflated?

Transit observations show that many hot Jupiters have radii larger than can be expected from standard evolution models (see the review by Guillot 2005). The best way of explaining these radii is that some hot Jupiters experience an interior heat source (not accounted for in "classical" evolution models) that maintains a large interior entropy and thereby planetary radius. Several explanations have been put forward for this missing energy source, including tidal dissipation (e.g. Bodenheimer et al. 2001), mechanical energy transported downward into the interior by the atmosphere (Guillot & Showman 2002), suppression of convective heat loss in the interior as a result of compositional layering (Chabrier & Baraffe 2007; Leconte & Chabrier 2012), and Ohmic dissipation associated with ionized atmospheric winds (Batygin & Stevenson 2010; Perna et al. 2010a; Huang & Cumming 2012; Wu & Lithwick 2013). However, the amount of extra-heating needed to keep hot Jupiters inflated is strongly affected by the ability of the atmosphere to transport the energy from the deep interior to the outer space (Guillot & Havel 2011). The efficiency of this transport is tied to the deep atmospheric temperature and it's spatial variations (Rauscher & Showman 2013). The deep temperature is partly determined by the ability of the upper atmosphere to absorb and re-emit the incoming stellar irradiation (Parmentier & Guillot 2014; Parmentier et al. 2014). EChO will determine the chemical composition and the thermal profile of the observable atmosphere. This will restrict the range of possible thermal structures for the deep atmosphere, providing better constraints on the strength of the unknown mechanism inflating hot Jupiters.

12. How does the circulation respond to seasonal and extreme forcing?

Several transiting hot Jupiters, including HD 80606b, HAT-P-2b, and HD 17156 have orbital eccentricities exceeding 0.5, which imply that these planets receive an order of magnitude or more stellar flux at apoapse than at periapse. This extreme time-variable heating may have significant effects on the atmospheric circulation (Kataria et al. 2013). As the planet goes back and forth between apoapse and periapse, EChO will provide a unique opportunity to see the atmosphere heating up and cooling down at different wavelength, measuring its global thermal inertia (Lewis et al. 2013) and how it varies with depth. Then, those heating and cooling rates can be used to better understand the atmospheric dynamics of planets on a circular orbits, where this measurement is not possible.

Conclusion

EChO is a dedicated instrument to observe exoplanets atmospheres proposed to the European Space Agency. Although it was not selected in 2014, its exquisite photometric precision and high spectroscopic resolution over a wide spectral range make it the archetype of a future space-mission dedicated to the spectroscopic characterization of exoplanets in tight orbit. Such a future mission will perform a broad survey of exoplanets atmospheres, exploring a large range of stellar irradiation, rotation period and planetary gravity, three parameters that determine the main dynamical regimes of planetary atmospheres. It will provide a deeper understanding of some benchmark planets, characterizing their three-dimensional thermal, chemical and compositional structure and their variation with time, opening the field of climate study to exoplanets.

References

Agol, E., Cowan, N. B., Knutson, H. A., et al. 2010, ApJ, 721, 1861
Agundez, M., Parmentier, V., Venot, O., Hersant, F., & Selsis, F. 2014, ArXiv e-prints
Ballester, G. E., Sing, D. K., & Herbert, F. 2007, Nature, 445, 511
Barman, T. S., Hauschildt, P. H., Schweitzer, A., et al. 2002, ApJ, 569, L51
Barstow, J. K., Aigrain, S., Irwin, P. G. J., et al. 2013, MNRAS, 430, 1188
Batygin, K., Stanley, S., & Stevenson, D. J. 2013, ApJ, 776, 53
Batygin, K. & Stevenson, D. J. 2010, ApJ, 714, L238
Bean, J. L., Désert, J.-M., Kabath, P., et al. 2011, ApJ, 743, 92
Berta, Z. K., Charbonneau, D., Désert, J.-M., et al. 2012, ApJ, 747, 35
Bodenheimer, P., Lin, D. N. C., & Mardling, R. A. 2001, ApJ, 548, 466
Burrows, A., Budaj, J., & Hubeny, I. 2008, ApJ, 678, 1436
Chabrier, G. & Baraffe, I. 2007, ApJ, 661, L81
Chamberlain, J. W. & Hunten, D. M. 1987, Theory of planetary atmospheres. An introduction to their physics andchemistry.
Cho, J. Y.-K., Menou, K., Hansen, B. M. S., & Seager, S. 2003, ApJ, 587, L117
Cho, J. Y.-K., Menou, K., Hansen, B. M. S., & Seager, S. 2008, ApJ, 675, 817
Cooper, C. S. & Showman, A. P. 2005, ApJ, 629, L45
Cooper, C. S. & Showman, A. P. 2006, ApJ, 649, 1048
Cowan, N. B. & Agol. 2011, ApJ, 729, 54
Crossfield, I. J. M., Barman, T., Hansen, B. M. S., & Howard, A. W. 2013, ArXiv e-prints
Crossfield, I. J. M., Hansen, B. M. S., Harrington, J., et al. 2010, ApJ, 723, 1436
de Wit, J., Gillon, M., Demory, B.-O., & Seager, S. 2012, A&A, 548, A128
de Wit, J. & Seager, S. 2013, Science, 342, 1473
Deming, D., Wilkins, A., McCullough, P., et al. 2013, ApJ, 774, 95
Demory, B.-O., de Wit, J., Lewis, N., et al. 2013, ApJ, 776, L25
Désert, J.-M., Vidal-Madjar, A., Lecavelier Des Etangs, A., et al. 2008, A&A, 492, 585
Dobbs-Dixon, I., Cumming, A., & Lin, D. N. C. 2010, ApJ, 710, 1395
Dobbs-Dixon, I. & Lin, D. N. C. 2008, ApJ, 673, 513
Ferraz-Mello, S. 2013, Celestial Mechanics and Dynamical Astronomy, 116, 109
Fortney, J. J. 2005, MNRAS, 364, 649
Fortney, J. J., Lodders, K., Marley, M. S., & Freedman, R. S. 2008, ApJ, 678, 1419
Guillot, T. 2005, Annual Review of Earth and Planetary Sciences, 33, 493
Guillot, T., Burrows, A., Hubbard, W. B., Lunine, J. I., & Saumon, D. 1996, ApJ, 459, L35
Guillot, T. & Havel, M. 2011, A&A, 527, A20
Guillot, T. & Showman, A. P. 2002, A&A, 385, 156
Hansen, C. J., Schwartz, J. C., & Cowan, N. B. 2014, ArXiv e-prints
Heng, K. 2012, ApJ, 761, L1
Heng, K. & Demory, B.-O. 2013, ApJ, 777, 100
Heng, K., Frierson, D. M. W., & Phillipps, P. J. 2011a, MNRAS, 418, 2669
Heng, K., Menou, K., & Phillipps, P. J. 2011b, MNRAS, 413, 2380
Huang, X. & Cumming, A. 2012, ApJ, 757, 47
Hubeny, I., Burrows, A., & Sudarsky, D. 2003, ApJ, 594, 1011
Huitson, C. M., Sing, D. K., Pont, F., et al. 2013, MNRAS, 434, 3252
Huitson, C. M., Sing, D. K., Vidal-Madjar, A., et al. 2012, MNRAS, 422, 2477
Iro, N., Bézard, B., & Guillot, T. 2005, A&A, 436, 719
Kataria, T., Showman, A. P., Lewis, N. K., et al. 2013, ApJ, 767, 76
Kirkpatrick, J. D. 2005, ARA&A, 43, 195
Knutson, H. A., Charbonneau, D., Allen, L. E., Burrows, A., & Megeath, S. T. 2008, ApJ, 673, 526
Knutson, H. A., Charbonneau, D., Allen, L. E., et al. 2007, Nature, 447, 183
Knutson, H. A., Charbonneau, D., Cowan, N. B., et al. 2009, ApJ, 690, 822
Knutson, H. A., Howard, A. W., & Isaacson, H. 2010, ApJ, 720, 1569
Knutson, H. A., Lewis, N., Fortney, J. J., et al. 2012, ApJ, 754, 22
Lecavelier Des Etangs, A., Ehrenreich, D., Vidal-Madjar, A., et al. 2010, A&A, 514, A72
Lecavelier Des Etangs, A., Pont, F., Vidal-Madjar, A., & Sing, D. 2008, A&A, 481, L83
Leconte, J. & Chabrier, G. 2012, A&A, 540, A20

Lewis, N. K., Knutson, H. A., Showman, A. P., et al. 2013, ArXiv e-prints
Lewis, N. K., Showman, A. P., Fortney, J. J., et al. 2010, ApJ, 720, 344
Li, J. & Goodman, J. 2010, ApJ, 725, 1146
Lubow, S. H., Tout, C. A., & Livio, M. 1997, ApJ, 484, 866
Madhusudhan, N., Mousis, O., Johnson, T. V., & Lunine, J. I. 2011, ApJ, 743, 191
Madhusudhan, N. & Seager, S. 2010, ApJ, 725, 261
Majeau, C., Agol, E., & Cowan, N. B. 2012, ApJ, 747, L20
Menou, K. 2012, ApJ, 754, L9
Menou, K. & Rauscher, E. 2009, ApJ, 700, 887
Miller-Ricci Kempton, E. & Rauscher, E. 2012, ApJ, 751, 117
Morley, C. V., Fortney, J. J., Kempton, E. M.-R., et al. 2013, ApJ, 775, 33
Moses, J. I., Visscher, C., Fortney, J. J., et al. 2011, ApJ, 737, 15
Nascimbeni, V., Piotto, G., Pagano, I., et al. 2013, ArXiv e-prints
Parmentier, V. & Guillot, T. 2014, A&A, 562, A133
Parmentier, V., Guillot, T., Fortney, J. J., & Marley, M. S. 2014, ArXiv:1311.6322
Parmentier, V., Showman, A. P., & Lian, Y. 2013, A&A, 558, A91
Perez-Becker, D. & Showman, A. P. 2013, ArXiv e-prints
Perna, R., Heng, K., & Pont, F. 2012, ApJ, 751, 59
Perna, R., Menou, K., & Rauscher, E. 2010a, ApJ, 719, 1421
Perna, R., Menou, K., & Rauscher, E. 2010b, ApJ, 724, 313
Pont, F., Sing, D. K., Gibson, N. P., et al. 2013, MNRAS
Rauscher, E. & Menou, K. 2010, ApJ, 714, 1334
Rauscher, E. & Menou, K. 2012a, ApJ, 750, 96
Rauscher, E. & Menou, K. 2012b, ApJ, 745, 78
Rauscher, E. & Menou, K. 2013, ApJ, 764, 103
Rauscher, E., Menou, K., Seager, S., et al. 2007, ApJ, 664, 1199
Rauscher, E. & Showman, A. P. 2013, ArXiv e-prints
Rogers, T. M. & Komacek, T. D. 2014, Submitted to ApJ
Rogers, T. M. & Showman, A. P. 2014, ApJ, 782, L4
Showman, A. P., Cooper, C. S., Fortney, J. J., & Marley, M. S. 2008, ApJ, 682, 559
Showman, A. P., Fortney, J. J., Lewis, N. K., & Shabram, M. 2013, ApJ, 762, 24
Showman, A. P., Fortney, J. J., Lian, Y., et al. 2009, ApJ, 699, 564
Showman, A. P. & Guillot, T. 2002, A&A, 385, 166
Showman, A. P. & Polvani, L. M. 2011, ApJ, 738, 71
Showman, A. P., Wordsworth, R. D., & Merlis, T. M. 2012, LPI Contributions, 1675, 8090
Sing, D. K., Lecavelier des Etangs, A., Fortney, J. J., et al. 2013, MNRAS
Sing, D. K., Vidal-Madjar, A., Lecavelier des Etangs, A., et al. 2008, ApJ, 686, 667
Spiegel, D. S., Silverio, K., & Burrows, A. 2009, ApJ, 699, 1487
Stevenson, K. 2014, in Talk at the Exoclimes III conference
Thrastarson, H. T. & Cho, J. Y. 2010, ApJ, 716, 144
Thrastarson, H. T. & Cho, J. Y. 2011, ApJ, 729, 117
Tinetti, G., Beaulieu, J. P., Henning, T., et al. 2012, Experimental Astronomy, 34, 311
Vidal-Madjar, A., Lecavelier des Etangs, A., Désert, J.-M., et al. 2003, Nature, 422, 143
Vidal-Madjar, A., Sing, D. K., Lecavelier Des Etangs, A., et al. 2011, A&A, 527, A110
Wu, Y. & Lithwick, Y. 2013, ApJ, 763, 13
Zahnle, K., Marley, M. S., Freedman, R. S., Lodders, K., & Fortney, J. J. 2009, ApJ, 701, L20

Conclusion

Observing and characterizing exoplanets atmospheres is now within reach. In the hottest planets, sodium, potassium, magnesium, calcium, hydrogen, carbon monoxide, and water have been detected and, in some cases, their mean abundances have been quantified on the dayside and on the atmospheric limb. These signatures become weaker in cooler planets, where clouds unambiguously shape the transit spectra, thermal emission and albedo.

Unambiguous observations and clear molecular signatures should be more common in the near future thanks to the development of ground-based instruments (GMT, TMT, E-ELT etc) and the planned James Web Space Telescope. Observations will determine the thermal structure, atmospheric dynamics, and composition of exoplanets atmospheres. In the following chapters, I describe a modeling effort toward a global understanding of these exotic atmospheres. These models will be of great help to prepare and understand future observations.

"We often search for problems that have a solution rather than solutions of the initial question."

Alessandro Morbidelli, during coffee break.

Chapter 2

Thermal structure of irradiated atmospheres

Contents

Introduction

The thermal structure of planetary atmospheres shapes the emission spectrum, the transit spectrum but also influences the atmospheric dynamics, the chemical equilibrium and, finally, plays a major role in the long-term evolution of planets.

Irradiated planets atmospheres are heated by the incoming stellar irradiation and by the internal flux coming from the deep layers of the planet. The temperature profile at radiative equilibrium is set by the interactions between the gas and the radiation. The opacities, and particularly their spectral variations determine the strength of these interactions. They are therefore determinant to understand the temperature structure of planets atmospheres. Their complex variations with wavelength, however, is a real difficulty in modeling planetary atmospheres. Numerical calculations are often use to properly take into account this complexity. They are, however, time consuming and barely reveal the physical mechanisms shaping the atmospheres. Analytical models, conversely are fast and easy to use but necessarily consider over-simplified opacity functions. What insights analytical models can provide in the mechanisms that shape the temperature profile of irradiated planets ? How accurate can they be ? Can they have a predicting power ?

To answer these questions, we will first derive a new, analytical, non-grey model of irradiated atmospheres. With this model we will show how non-grey thermal opacities fundamentally shape the thermal structure of planetary atmospheres. Then, using a state-of-the-art numerical model we will calibrate our analytical model, leading to a fast and accurate analytical expression for the thermal structure of irradiated planets.

2.1 Opacities for radiative transfer models

Irradiated planets atmospheres absorb part of the incoming energy from their parent star, convert it into heat and radiate it back into space. Atmospheres are globally in radiative equilibrium: they reemit as much energy as they absorb. Locally, the transport of heat by advection and convection can influence the temperature profile and departures from radiative equilibrium are expected. To quantify these departures, however, knowing the temperature profile *at radiative equilibrium* is essential.

The atmospheric thermal structure can be calculated by solving the radiative transfer equation (1.3). In local radiative equilibrium, the total incoming and outgoing energy fluxes at each atmospheric layers must equalize. Thus, the intensities at different wavelengths are coupled. For example, the incoming stellar flux that is absorbed by the atmosphere, mostly in the visible spectral range, must be balanced by the thermal emission of the planet, mostly in the infrared spectral range. The amount of light that is absorbed, scattered or emitted as a function of wavelength depends on the opacities and their spectral variations. Those are determined by complex quantic interactions between atoms and photons. As a result, the opacities can vary by several orders of magnitude on spectral scales close to the picometer. Because the spectral range relevant to understand the radiative transfer in planetary atmospheres goes from $\approx 100\,\mathrm{nm}$ to $\approx 100\,\mu\mathrm{m}$, millions to billions of spectral lines need to be taken into account (see Figure 2.1). Solving the radiative transfer equations with such a high-resolution is clearly challenging, even with today's computational capabilities. When millions of atmospheric models need to be computed, it becomes clearly unpractical.

At the other side of the spectral scale, the Planck function determines the spectral distribution

of the thermal emission of the gas, for both the star and the planet. At 1000 K, relevant for the thermal emission of hot Jupiters atmospheres, the Planck function extends from $\approx$ 1 to 20 µm. The emission from a Sun-like star, for its part, extends from $\approx$ 0.2 to 5 µm. Between the spectral width of the atomic lines and the Planck function, there exists a spectral range containing numerous spectral lines but where the Planck function can be considered constant. In such a spectral interval, the exact location of the spectral lines does not matter and the line opacities can be shuffled and re-organized. This is the basic point of the *correlated-k distribution* method.

The first step is to divide the spectral range of interest in intervals $\Delta\lambda$ small enough such that the Planck function can be considered constant on those intervals but large enough such that a large number of lines are still present. Then, inside each interval, the cumulative distribution function of the line-by-line opacities can be calculated. This cumulative distribution function contains enough information to accurately calculate the thermal structure of the planet[1]. The cumulative distribution function can then be interpolated by a restricted number of points, typically of the order of 10, named the k-coefficients. As shown by Fu & Liou (1992), the correlated-k distribution method can lead to errors of 1 to 2% in the estimation of the thermal fluxes when compared to the line-by-line calculations. In Figure 2.2, we show the 8 k-coefficients inside each of the 196 bins of wavelengths used in our one-dimensional numerical model (see section 2.3 for more details). The radiative transfer equation needs now to be solved at $\approx$ 1500 different k-coefficients. It corresponds to six orders of magnitude less work than using the line-by-line approach. This allows a typical desktop computer to solve for an atmospheric temperature profile in timescales of the order of 1 minute. Reducing the number of bins down to $\approx$ 30 lead to less than 1% error and increases substantially the computational time. This is the choice made by Showman et al. (2009) and Skålid Amundsen et al. (2014) to efficiently couple the radiative scheme to a global circulation model.

Although the correlated-k method is fast, it remains computationally limiting when thousands or millions of atmospheric models need to be computed. This is typically the case for atmospheric retrieval models or when it becomes necessary to compute the long-term (Gyr) temporal evolution of a giant planet.

Analytical solutions of the radiative transfer equation have a negligible computational cost. Moreover, they allow insights into the physical processes that determine the temperature profile and allow a better understanding of the behavior of the numerical models. The simplest model one can imagine is the grey model: a model where there is no spectral variation of the opacities. This model correctly model the deep layers of stars and planets. At very high pressures, when the mean free path of the photons is small compared to the variations of the physical characteristics of the atmosphere, the photons are *thermalized* i.e. the local radiation flux is close to a blackbody radiation. Still, photons that are emitted at wavelengths where the opacity is low can travel a greater distance than photons emitted where the opacity is large. It can be shown that in this so-called *diffusion-limit*, the atmosphere behaves like a grey atmosphere with the Rosseland mean opacity (Mihalas & Mihalas 1984):

$$\frac{1}{\kappa_{\rm R}} \equiv \left(\int_0^\infty \frac{\partial B_\lambda}{\partial T} \, {\rm d}\lambda \right)^{-1} \int_0^\infty \frac{1}{\kappa_\lambda} \frac{\partial B_\lambda}{\partial T} \, {\rm d}\lambda \, . \tag{2.1}$$

[1]Some caveats must be putted here. The main assumption behind this method is that inside each spectral bin the ordering of the opacities remains the same with height, *e.g.* that the highest and lowest opacity values are always at the same frequency throughout the atmosphere. Whereas this is valid for an homogeneous atmosphere, inhomogeneities in composition, such as the presence of an ozone layer or the rainout of a molecule from the upper atmosphere can lead to significant error (Fu & Liou 1992).

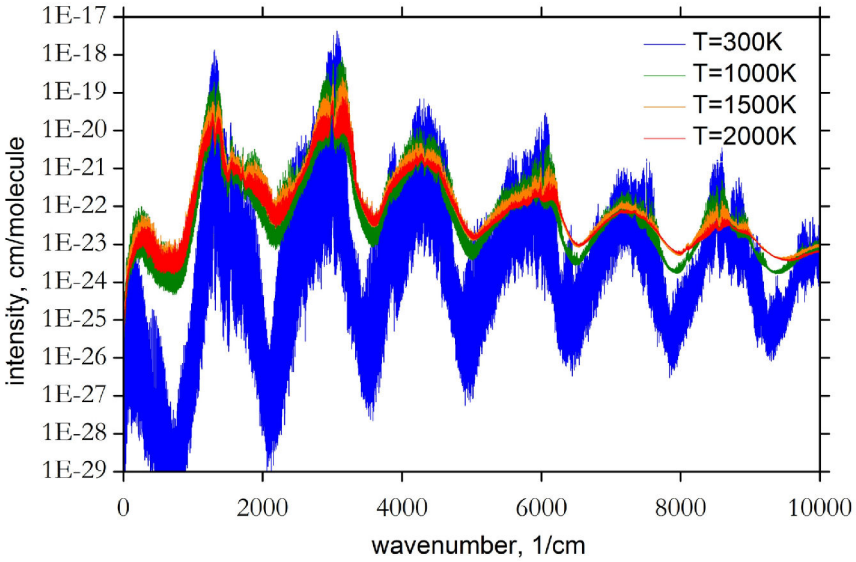

Figure 2.1. Absorption cross-section of methane at different temperatures as a function of wave number calculated by Yurchenko & Tennyson (2014) as part of the ExoMol project (Tennyson & Yurchenko 2012). The intensity of almost ten billion lines were summed up to produce this dataset. Figure from Yurchenko & Tennyson (2014).

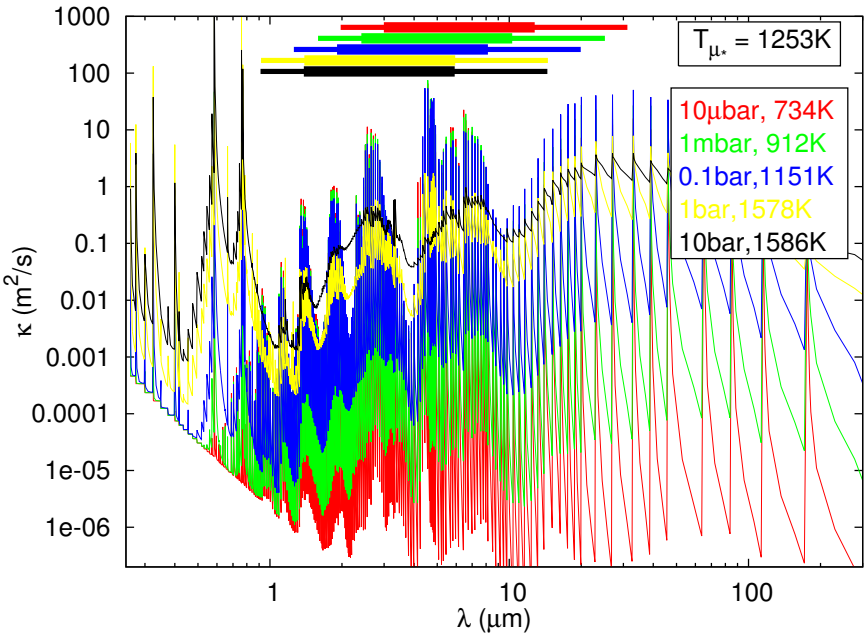

Figure 2.2. Opacities as a function of wavelength for five different conditions corresponding to different points in the dayside average PT profile of a giant planet with $g = 25\,\mathrm{m/s^2}$ orbiting at 0.53 AU from a sun-like star. Inside each of the 196 bins of frequency, we plot the 8 k-coefficients that sample the cumulative distribution function of the opacities.

The Rosseland mean opacity is determined by the lowest values of the opacity function.

When the diffusion limit is no more valid, i.e. when at some wavelengths the mean free path of the photons becomes greater than the atmospheric scale height, the grey approximation is no more accurate. Whereas at some wavelength the atmosphere is still opaque, at others it is already transparent. As an example, if the visible opacities are much smaller than the infrared opacities, the stellar irradiation can penetrate in the deep layers of the planet. There, it is absorbed, converted into heat and re-emitted at infrared wavelengths. Because the infrared opacities are large, the emitted radiation cannot escape immediately. The atmosphere heats up, leading to a *greenhouse effect*. Oppositely, if the visible opacities are large, the stellar energy is deposited in the upper atmosphere where radiative cooling is inefficient due to the small infrared opacities. The upper

atmosphere heats up, leading to a thermal inversion. A model differentiating the visible and the thermal opacities is called *semi-grey*. Semi-grey models such as Guillot (2010) have been proven useful for the study of irradiated exoplanets' atmospheres.

In semi-grey models one opacity corresponds to the absorption of the stellar flux (the *visible* opacity) whereas the other one is used to compute the thermal emission term (the *thermal* or *infrared* opacity).The separation is, however, based on geometry rather than spectral range. For hot planets, the thermal emission flux and the stellar incident flux can cover similar wavelengths but the visible and thermal opacities can still be different (see middle panel of Figure. 2.3).

Differentiating visible and thermal opacities is, however, not such a difficult task. The main reason is that the absorption of the stellar irradiation is mainly independent of the exact temperature profile of the atmosphere. Thus, one can solve for the absorption of the stellar flux and directly use the solution as a source term in the radiative transfer equations. The semi-grey model can therefore easily be extended to any number of visible opacity bands.

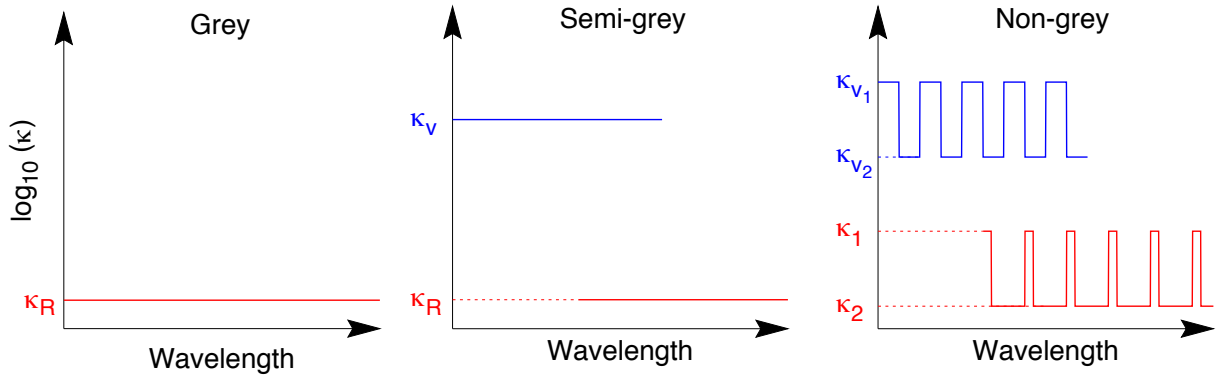

Figure 2.3. Opacities in analytical models of different complexity. In the grey model (left panel), the opacities are constant and equal to the Rosseland mean opacity. In the semi-grey model, the opacity corresponding to the absorption of the stellar flux (blue) and the one corresponding to the thermal emission (red) are different. In the non-grey model both can take two different values. The opacities relevant to the absorption of the stellar irradiation are usually called *visible* opacities whereas the ones corresponding to the thermal emission are called *thermal* or *infrared* opacities. The difference, however, is not linked to the spectral range but to the geometry of the two radiation fields.

2.2 A new, analytical non-grey model of irradiated atmospheres

The discovery of irradiated planets and the characterization of their atmospheres led several authors to develop analytical semi-grey models to calculate their thermal structure (Hansen 2008; Guillot 2010; Robinson & Catling 2012). Although semi-grey models are essential model irradiated planets, they are limited. In particular, they appear to systematically overestimate the temperature profile in the upper atmosphere, a crucial region for the observations. As explained by Pierrehumbert (2010) the radiative cooling of semi-grey models is only efficient around the atmospheric level of

optical depth unity. Non-grey thermal opacities allow the atmosphere to cool from different layers simultaneously, leading to a cooler upper atmosphere.

In the following paper accepted in *Astronomy & Astrophysics* (Parmentier & Guillot 2014) we develop an analytical model where both the thermal and the visible opacities can take two different values (see right panel of Figure 2.3). Such a non-grey analytical model is essential to overcome the limitations of the semi-grey model and explore the diversity of exoplanets' atmospheres.

A&A 562, A133 (2014)
DOI: 10.1051/0004-6361/201322342

Astronomy & Astrophysics

A non-grey analytical model for irradiated atmospheres⋆

I. Derivation

Vivien Parmentier[1,2] and Tristan Guillot[1,2]

[1] Laboratoire Lagrange, UMR7293, Université de Nice Sophia-Antipolis, CNRS, Observatoire de la Côte d'Azur, 06300 Nice, France
e-mail: vivien.parmentier@oca.eu
[2] Department of Astronomy and Astrophysics, University of California, Santa Cruz, CA 95064, USA

Received 22 July 2013 / Accepted 25 November 2013

ABSTRACT

Context. Semi-grey atmospheric models (with one opacity for the visible and one opacity for the infrared) are useful for understanding the global structure of irradiated atmospheres, their dynamics, and the interior structure and evolution of planets, brown dwarfs, and stars. When compared to direct numerical radiative transfer calculations for irradiated exoplanets, however, these models systematically overestimate the temperatures at low optical depths, independently of the opacity parameters.
Aims. We investigate why semi-grey models fail at low optical depths and provide a more accurate approximation to the atmospheric structure by accounting for the variable opacity in the infrared.
Methods. Using the Eddington approximation, we derive an analytical model to account for lines and/or bands in the infrared. Four parameters (instead of two for the semi-grey models) are used: a visible opacity (κ_v), two infrared opacities, (κ_1 and κ_2), and β (the fraction of the energy in the beam with opacities κ_1). We consider that the atmosphere receives an incident irradiation in the visible with an effective temperature $T_{\rm irr}$ and at an angle μ_*, and that it is heated from below with an effective temperature $T_{\rm int}$.
Results. Our non-grey, irradiated line model is found to provide a range of temperatures that is consistent with that obtained by numerical calculations. We find that if the stellar flux is absorbed at optical depth larger than $\tau_{\rm lim} = (\kappa_{\rm R}/\kappa_1\kappa_2)(\kappa_{\rm R}\kappa_{\rm P}/3)^{1/2}$, it is mainly transported by the channel of lowest opacity whereas if it is absorbed at $\tau \gtrsim \tau_{\rm lim}$ it is mainly transported by the channel of highest opacity, independently of the spectral width of those channels. For low values of β (expected when lines are dominant), we find that the non-grey effects significantly cool the upper atmosphere. However, for $\beta \gtrsim 1/2$ (appropriate in the presence of bands with a wavelength-dependence smaller than or comparable to the width of the Planck function), we find that the temperature structure is affected down to infrared optical depths unity and deeper as a result of the so-called blanketing effect.
Conclusions. The expressions that we derive can be used to provide a proper functional form for algorithms that invert the atmospheric properties from spectral information. Because a full atmospheric structure can be calculated directly, these expressions should be useful for simulations of the dynamics of these atmospheres and of the thermal evolution of the planets. Finally, they should be used to test full radiative transfer models and to improve their convergence.

Key words. radiative transfer – planets and satellites: atmospheres – stars: atmospheres – planetary systems

1. Introduction

The discovery of numerous star-planet systems and the possibility of characterizing the planets' atmospheric properties has led to a great many publications using radiative transfer calculations, often taken "off-the-shelf" from numerical models. Given the infinite amount of possible compositions for mostly unknown exoplanetary atmospheres, it is highly valuable to be able to perform very fast calculations and also to understand what determines the thermal structure of an irradiated atmosphere.

Analytical radiative transfer solutions for atmospheres have been calculated with a variety of assumptions and in different contexts (e.g. Eddington 1916; Chandrasekhar 1935, 1960; King 1956; Matsui & Abe 1986; Weaver & Ramanathan 1995; Pujol & North 2003; Chevallier et al. 2007; Shaviv et al. 2011). However, the discovery of super-Earths, giant exoplanets, brown dwarfs, and low-mass stars close to a source of intense radiation has prompted the need for solutions that account for both an outside and an inside radiation field, and properly link low and high optical depths levels. Hubeny et al. (2003), Rutily et al. (2008), Hansen (2008), Guillot (2010), Robinson & Catling (2012), and Heng et al. (2012) provide these solutions in the framework of a semi-grey model, with one opacity for the incoming irradiation (generally mostly at visible wavelengths), and one opacity for the thermal radiation field (generally mostly at infrared wavelengths). These approximations have been used in hydrodynamical models of planetary atmospheres (e.g. Heng et al. 2011; Rauscher & Menou 2013), planetary evolution models (e.g. Miller-Ricci & Fortney 2010; Guillot & Havel 2011; Budaj et al. 2012), planet synthesis models (Mordasini et al. 2012a,b), retrieval methods (Line et al. 2012), and a variety of other applications.

As shown in Fig. 1 for an atmosphere irradiated from above with a flux $\sigma T_{\rm irr}^4$ and heated from below with a flux $\sigma T_{\rm int}^4$, while semi-grey models provide solutions that are well-behaved when compared to full numerical solutions at optical depths larger than about unity, the temperatures at low-optical depths appear to be systematically hotter than in the numerical solutions. Most importantly, this occurs *regardless of the choice of the two parameters of the problem*, i.e. the thermal (infrared) opacity $\kappa_{\rm th}$

⋆ A FORTRAN implementation of the analytical model is available at the CDS via anonymous ftp to cdsarc.u-strasbg.fr (130.79.128.5) or via http://cdsarc.u-strasbg.fr/viz-bin/qcat?J/A+A/562/A133

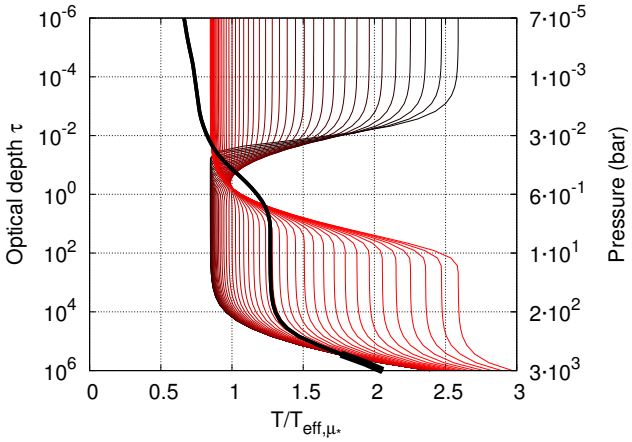

Fig. 1. Optical depth vs. atmospheric temperature in units of the effective temperature. A numerical solution obtained from Fortney et al. (2008) (thick black line) is compared to the semi-grey analytical solutions of Guillot (2010) for values of the greenhouse factor γ_v^{-1} ranging from 0.01 to 100 (black to red lines). Low values of γ_v are redder. We used $\mu_* = 1/\sqrt{3}$, $T_{irr} = 1250$ K corresponding to the dayside average profile of a planet at 0.05 au from a sun-like star, and accounting for the albedo obtained in the numerical model. The internal temperature is $T_{int} = 125$ K and gravity 25 ms^{-2}. The effective temperature of the studied slice of atmosphere[1] is defined by $T^4_{eff,\mu_*} = T^4_{int} + \mu_* T^4_{irr}$. For the numerical solution, the relation between pressure and optical depth was calculated using Rosseland mean opacities; TiO and VO opacities were not included.

and the ratio of the visible to infrared opacity $\gamma_v \equiv \kappa_v/\kappa_{th}$. For hot Jupiters, as in the example in Fig. 1, the real temperature profiles at low optical depths can be several hundreds of Kelvins cooler than predicted by the semi-grey solutions.

The levels probed both by transit spectroscopy and by the observations of secondary eclipses of exoplanets often correspond to low-optical depth levels (e.g. Burrows et al. 2007; Fortney et al. 2008; Showman et al. 2009), i.e. where semi-grey models seem to systematically overestimate the temperatures. Furthermore, because the problem persists regardless of the main parameters, this implies that the functional form of the semi-grey solutions is probably not appropriate for inversion models. Non-grey effects are known to facilitate the cooling of the upper atmosphere (see Pierrehumbert 2010, for a qualitative explanation) so they must be included. This is the purpose of the present paper.

We first describe previous analytical methods used to solve the radiative transfer problem analytically. In Sect. 3, we then derive an analytical non-grey line model and compare it to previous models in Sect. 4. In Sect. 5 we study the role of non-grey effects in shaping the atmospheric thermal structure. Eventually we apply our model to the structure of irradiated giant planets in Sect. 6. We note here that while we focus the discussion on exoplanets, we believe that this model is applicable to a much wider variety of problems, as long as an atmosphere is irradiated both from above and below. Our method can also be used to solve the radiative transfer equations in other geometries, such as the thermal structure of protoplanetary disk. We provide our conclusions in Sect. 7.

2. Assumptions and previous analytical models

2.1. Setting

2.1.1. The equation of radiative transfer

Following Guillot (2010), we will consider the problem of a plane-parallel atmosphere in local thermodynamic equilibrium that receives from above a collimated flux σT^4_{irr} at an angle $\theta_* = \cos^{-1}(\mu_*)$ from the vertical, and from below an isotropic flux σT^4_{int}. The total energy budget of the modelled atmosphere is then set by $T^4_{eff,\mu_*} = T^4_{int} + \mu_* T^4_{irr}$, which defines the effective temperature in this paper[1].The irradiation and intrinsic fluxes are generally characterized by very different wavelengths. Although this is not required in the solution that we propose, it is convenient to think of them as being emitted preferentially in the visible and in the infrared, respectively. Scattering processes can influence both the thermal and visible radiation. As shown by Heng et al. (2012), the solution including symmetrical scattering for the incoming radiation with the Eddington approximation is equivalent to the one obtained without scattering when the irradiation flux is reduced by a factor of $(1 - A)$ and the visible opacity is reduced by a factor $1/\sqrt{\xi}$, where A is the Bond albedo of the planet and ξ is the ratio of the absorption to the extinction opacity (see also Meador & Weaver 1980, for a review of the different two stream methods including scattering). In this paper, the irradiation flux and the visible opacity are treated as parameters, thus we implicitly take into account symmetrical scattering of the incoming radiation (e.g. Rayleigh scattering). Scattering of the thermal radiation, however, is neglected.

In order to solve the radiative transfer problem for a plane parallel atmosphere in local thermodynamic equilibrium, one has to solve the following equation for all frequencies ν and all directions μ (Chandrasekhar 1960),

$$-\mu \frac{\mathrm{d}I_{\mu\nu}}{\mathrm{d}m} = \kappa_\nu I_{\nu\mu} - \kappa_\nu B_\nu(T), \tag{1}$$

where $I_{\mu\nu}$ is the specific intensity at the wavelength ν propagating with an angle $\theta = \cos^{-1}(\mu)$ with the vertical, κ_ν is the opacity at a given wavelength, B_ν is the Planck function, and $\mathrm{d}m = \rho \mathrm{d}z$ is the mass increment along the path of the radiation. As usual, T, ρ, and z are the atmospheric temperature, density and height, respectively. The main difficulty in solving Eq. (1) lies in its triple dependence on μ, ν, and T and its additional dependence on m. An analytical solution requires simplifications of the opacities and of the dependence of the radiation intensity on angle.

2.1.2. Opacities and optical depth

The need for simplification implies that mean opacities must be used. The most common one is the Rosseland mean, defined as

$$\frac{1}{\kappa_R} \equiv \left(\int_0^\infty \frac{\partial B_\nu}{\partial T} \mathrm{d}\nu \right)^{-1} \int_0^\infty \frac{1}{\kappa_\nu} \frac{\partial B_\nu}{\partial T} \mathrm{d}\nu. \tag{2}$$

[1] In stellar physics the effective temperature is usually what we call the internal temperature. In both planetary and stellar fields, the effective temperature aims at representing the total energy budget of the atmosphere. Although in stellar physics most of the flux comes from the deep interior, this is not true in irradiated atmospheres, and $T^4_{eff,\mu_*} = T^4_{int} + \mu_* T^4_{irr}$ is a better representation of the total energy budget of the studied slice of atmosphere. The energy budget of the whole atmosphere is therefore $T^4_{eff} = T^4_{int} + T^4_{irr}/4$.

When at all wavelengths the mean free path of photons is small compared to the scale height of the atmosphere, the radiative gradient obeys its well-defined diffusion limit and (unless convection sets in) the temperature gradient become that obtained from a grey atmosphere in which the opacity is set to the Rosseland mean (Mihalas & Mihalas 1984, p. 350). We hence define the optical depth τ on the basis of the Rosseland mean opacity, such that, along the vertical direction

$$\mathrm{d}\tau \equiv \kappa_{\mathrm{R}} \mathrm{d}m. \tag{3}$$

Assuming hydrostatic equilibrium, the relation between pressure and optical depth can be found by integrating Eq. (3):

$$\tau(P) = \int_0^P \frac{\kappa_{\mathrm{R}}(P', T(P'))}{g} \mathrm{d}P'. \tag{4}$$

The optical depth thus becomes the natural variable to account for the dependence on depth in the radiative transfer problem. For any strictly positive Rosseland mean opacities, Eq. (4) is a bijection relating pressure and optical depth. Thus, solution of the radiative transfer equations in terms of optical depth can be converted to a solution in term of pressure for any functional form of the Rosseland mean opacities.

The second mean opacity that is traditionally used for radiative transfer is the so-called Planck mean:

$$\kappa_{\mathrm{P}} \equiv \left(\int_0^\infty B_\nu \, \mathrm{d}\nu \right)^{-1} \int_0^\infty \kappa_\nu B_\nu \, \mathrm{d}\nu. \tag{5}$$

We use the ratio of the Planck and Rosseland mean opacities to quantify the non-greyness of the atmosphere:

$$\gamma_{\mathrm{P}} \equiv \frac{\kappa_{\mathrm{P}}}{\kappa_{\mathrm{R}}}. \tag{6}$$

While the value of the Rosseland mean opacity is dominated by the lowest values of the opacity function κ_ν, the Planck mean opacity is dominated by its highest values. Thus, it can be shown that $\gamma_{\mathrm{P}} = 1$ for a grey atmosphere and $\gamma_{\mathrm{P}} > 1$ for a non-grey atmosphere (King 1956).

In irradiated atmospheres, a collimated flux coming from the star is absorbed at different atmospheric levels. We name κ_{v} the opacity relevant to the absorption of the stellar flux. As will be shown in Sect. 3.8, the absorption of the visible flux appears linearly in the radiative transfer equations. Thus, a solution can be found using multiple visible opacity bands $\kappa_{\mathrm{v}1}$, $\kappa_{\mathrm{v}2}$, etc.

We further define the ratio of the visible opacity to the mean (Rosseland) thermal opacity:

$$\gamma_{\mathrm{v}} \equiv \kappa_{\mathrm{v}} / \kappa_{\mathrm{R}}. \tag{7}$$

In order to solve the radiative transfer problem analytically, we suppose that γ_{v} is constant with optical depth. Once γ_{v} is chosen, we can solve the equations for the visible radiation independently from the final thermal structure of the atmosphere. Of course, purely grey models are such that $\gamma_{\mathrm{v}} = 1$.

2.1.3. The picket-fence model

It is important to note at this point that two sets of opacities with different wavelength dependences may have the same Rosseland *and* Planck means. We must constrain the problem further, and to this intent, we now consider the simplest possible line model, known as the picket-fence model (Mihalas 1978), where the thermal opacities can take two different values κ_1 and κ_2 (see Fig. 2) such that

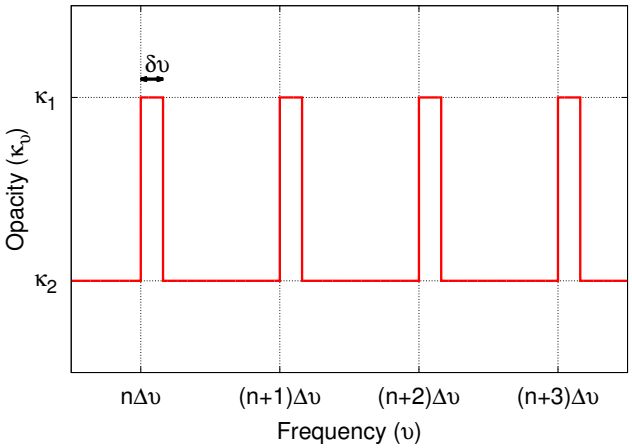

Fig. 2. Simplified thermal opacities for the picket-fence model. $\beta = \delta\nu/\Delta\nu$ is the equivalent bandwidth (see text).

$$\kappa_\nu = \begin{cases} \kappa_1 & \text{for } \nu \in [n\Delta\nu, n\Delta\nu + \delta\nu] \\ \kappa_2 & \text{for } \nu \in [n\Delta\nu + \delta\nu, (n+1)\Delta\nu] \end{cases} \quad n \in [1, N]. \tag{8}$$

We define an equivalent bandwidth by:

$$\beta = \frac{1}{\int_0^\infty B_\nu \, \mathrm{d}\nu} \sum_{n=1}^{N} \int_{n\Delta\nu}^{n\Delta\nu+\delta\nu} B_\nu \, \mathrm{d}\nu. \tag{9}$$

The characteristic width of the Planck function can be defined as $\Delta\nu_P \equiv \left(\frac{1}{B} \frac{\partial B_\nu}{\partial \nu} \right)^{-1}$. When choosing $\Delta\nu \ll \Delta\nu_P$, the Planck function can be considered constant over $\Delta\nu$ and we get $\beta = \delta\nu/\Delta\nu$. The Planck and Rosseland mean opacities then become (see Eqs. (2) and (5))

$$\kappa_{\mathrm{R}} = \frac{\kappa_1 \kappa_2}{\beta\kappa_2 + (1-\beta)\kappa_1} \tag{10}$$

$$\kappa_{\mathrm{P}} = \beta\kappa_1 + (1-\beta)\kappa_2. \tag{11}$$

We also define the following ratios:

$$\gamma_1 \equiv \kappa_1 / \kappa_{\mathrm{R}} \tag{12}$$

$$\gamma_2 \equiv \kappa_2 / \kappa_{\mathrm{R}} \tag{13}$$

$$R \equiv \kappa_1 / \kappa_2 = \gamma_1 / \gamma_2. \tag{14}$$

Following Chandrasekhar (1935), we also define a limit optical depth

$$\tau_{\mathrm{lim}} \equiv \frac{1}{\gamma_1 \gamma_2} \sqrt{\frac{\gamma_{\mathrm{P}}}{3}}. \tag{15}$$

The role of τ_{lim} in shaping the final temperature profile is discussed in Sect. 5 and its variations with R and β is pictured in Fig. 8.

2.2. The method of discrete ordinates for the non-irradiated problem

2.2.1. The grey case

An approximate method to solve Eq. (1) including the angular dependency has been developed by Chandrasekhar (1960) in the

case of a non-irradiated atmosphere ($T_{\rm irr} = 0$). The idea is to replace the integrals over angle in Eq. (1) by a Gaussian sum over μ. It can then be solved to an arbitrary precision by increasing the number of terms in the sum. The boundary condition at the top of the atmosphere is simply given as $I_{\mu<0}(0) = 0$. The expansion to the fourth term yields the temperature profile

$$T(\tau)^4 = \frac{3T_{\rm int}^4}{4}\left(\tau + Q + L_1 {\rm e}^{-k_1\tau} + L_2 {\rm e}^{-k_2\tau} + L_3 {\rm e}^{-k_3\tau}\right), \quad (16)$$

with $Q = 0.706920$, $L_1 = -0.083921$, $L_2 = -0.036187$, $L_3 = -0.009461$, $k_1 = 1.103188$, $k_2 = 1.591778$, and $k_3 = 4.45808$ (Chandrasekhar 1960, Table VIII)[2]. One of the important results from this formalism is that the skin temperature of the planet (defined as the temperature at zero optical depth) is independent of the order of expansion and therefore corresponds to the exact value

$$T_{\rm skin}^4 = \sqrt{3}\frac{T_{\rm int}^4}{4}. \quad (17)$$

This expression is exact only in the limit of a grey, non-irradiated atmosphere.

2.2.2. The non-grey case

Chandrasekhar (1960) also developed a perturbation method in order to include non-grey thermal opacities. This method was improved by Krook (1963). However, these perturbation methods either work for small departures from the grey opacities or involve a fastidious iterative procedure (e.g. Unno & Yamashita 1960; Avrett & Krook 1963) and are no longer fully analytical. However, considering that the variations in the opacities are small compared to the variations of the Planck function, analytical solutions can be found for an arbitrarily large departure from the grey opacities. Noting the similar role of μ and κ_ν in Eq. (1), King (1956), following Münch (1946), used the method of discrete ordinates in order to turn the integrals over frequency into Gaussian sums. For the picket-fence model defined in Sect. 2.1.3 and the second approximation for the angular dependency, King's method leads to the following temperature profile

$$T^4(\tau) = \frac{3}{4}T_{\rm int}^4\left[\frac{1}{\sqrt{3\gamma_{\rm P}}} + \tau + \frac{(\sqrt{\gamma_{\rm P}}-\gamma_1)(\sqrt{\gamma_{\rm P}}-\gamma_2)}{\gamma_1\gamma_2\sqrt{3\gamma_{\rm P}}}({\rm e}^{-\tau/\tau_{\rm lim}} - 1)\right]. \quad (18)$$

As in the grey case, the method of discrete ordinates leads to an exact relation for the skin temperature, whatever the dependency of κ_ν on frequency (but no dependence on pressure or temperature):

$$T_{\rm skin}^4 = \sqrt{\frac{3}{\gamma_{\rm P}}}\frac{T_{\rm int}^4}{4}. \quad (19)$$

In the grey limit, $\gamma_{\rm P} = 1$ and we recover Eq. (17). Otherwise, $\gamma_{\rm P} > 1$, implying that for a non-irradiated atmosphere, non-grey effects always tend to lower the atmospheric skin temperature.

[2] We noticed that the values of L_1 and L_3 in Chandrasekhar's book were inverted and corrected this here.

2.3. Moment equation method

2.3.1. Equations for the momentum of the radiation intensity

A simpler way to solve the radiative transfer equation has been carried out by Eddington (1916). The idea is to solve the equation using the different momentum of the intensity defined as

$$(J_\nu, H_\nu, K_\nu) = \frac{1}{2}\int_{-1}^{1} I_{\mu\nu}(1, \mu, \mu^2)\,{\rm d}\mu. \quad (20)$$

Then, integrating over μ Eq. (1) and μ times Eq. (1) one gets the momentum equations

$$\frac{{\rm d}H_\nu}{{\rm d}\tau_\nu} = J_\nu - B_\nu(T). \quad (21)$$

$$\frac{{\rm d}K_\nu}{{\rm d}\tau_\nu} = H_\nu. \quad (22)$$

Assuming the atmosphere to be in radiative equilibrium, we can write

$$\int_0^\infty (\kappa_\nu J_\nu - \kappa_\nu B_\nu)\,{\rm d}\nu = 0. \quad (23)$$

For a grey atmosphere ($\kappa_\nu = \kappa_{\rm R}\ \forall\nu$), Eqs. (21)–(23) can be integrated over frequency, leading to an equation for J, H, K, and B, the frequency-integrated versions of J_ν, H_ν, K_ν, and B_ν. The radiative equilibrium equation becomes

$$J = B. \quad (24)$$

The frequency integrated versions of Eqs. (21)–(23) are a set of three equations with four unknowns. The system is not closed because by integrating Eq. (1) over all angles we have lost the information on the angular dependency of the irradiation. A closure relationship that contains this angular dependency is therefore needed. A common closure relationship, known as the Eddington approximation is

$$J = 3K. \quad (25)$$

This relationship is exact in two very different cases: when the radiation field is isotropic (I_μ independent of μ), and in the two-stream approximation ($I_{\mu>0} = I_0^+$ and $I_{\mu<0} = I_0^-$). Although this seems to be a very restrictive approximation, it is relevant for the deep layers of the atmosphere because of the quasi-isotropy of the radiation field there. It is also good for the top of the atmosphere, where the flux comes mainly from the $\tau \approx 1$ layer. Indeed, the exact solution gives a ratio J/K that differs by no more than 20% from the 1/3 ratio over the whole atmosphere and leads to a temperature profile that is correct to 4% in the grey case (see the plain blue line in Fig. 4).

2.3.2. Top boundary condition

Although in the method of discrete ordinates the boundary condition at the top of the atmosphere is intuitive, in the momentum equations method it is less obvious and different choices have been made by different authors. Usually, the expression for J is known and some integration constants need to be found. Two equations are needed, one for $J(0)$ and one for $H(0)$. Four possibilities are widely used in the literature from which one has to choose two:

1. The radiative equilibrium equation that relates the emergent flux at the top of the atmosphere to the internal flux from the planet and the incident flux from the star.

2. An ad-hoc relation between $H(0)$ and $J(0)$ at $\tau = 0$: $H(0) = f_{\rm H} J(0)$, where $f_{\rm H}$ is often called the second Eddington coefficient.
3. A calculation of $H(0)$ from the second moment equation (Eq. (22)) and the Eddington approximation.
4. A calculation of $H(0)$ from the integration of the source function through the entire atmosphere, known as the Milne equation (Mihalas & Mihalas 1984, p. 347): $H(0) = \frac{1}{2}\int_0^\infty B(\tau)\, E_2(\tau)\, {\rm d}\tau$.

For grey and semi-grey models, the first condition is natural and so it was used by Hansen (2008) and Guillot (2010). For the other part of the top boundary condition, Guillot (2010) chose to use the second and Hansen (2008) the fourth condition (see Appendix A of Guillot 2010 for a comparison of the two expressions).

In the case of a non-grey model, the first condition cannot be implemented (at least directly) because it is a constraint on the total thermal flux, but it provides no information on how the thermal flux is split between the opacity bands that are considered. Chandrasekhar (1935) therefore uses conditions 2 and 3 in each of the opacity bands for his non-grey, non-irradiated model. He also notes that using condition 4 instead of condition 3 should yield better results, but it leads to more complex expressions. In this work, because an accurate treatment of the flux is needed for the non-grey irradiated model, we will use conditions 2 and 4 in each of the opacity bands. All these models are discussed in the next sections and summarized in Table 1.

2.3.3. Non-irradiated, grey case

In this section we consider the case $T_{\rm irr} = 0$. Under the grey approximation, using the conditions 1 and 4, the temperature profile is given by (Mihalas & Mihalas 1984, p. 357)

$$T^4(\tau) = \frac{3}{4} T_{\rm int}^4 \left(\frac{2}{3} + \tau\right), \tag{26}$$

which leads to the same solution as assuming condition 2 with $f_{\rm H} = 1/2$. The skin temperature is then

$$T_{\rm skin}^4 = 2\frac{T_{\rm int}^4}{4} \tag{27}$$

which differs from the exact solution (Eq. (17)) by a factor of $\sqrt{3}/2$. Assuming $f_{\rm H} = 1/\sqrt{3}$ is thus tempting, as it leads to the correct skin temperature. Unfortunately, it leads to a temperature profile which is less accurate around $\tau \approx 1$.

2.3.4. Non-irradiated non-grey picket-fence model

Chandrasekhar (1935) provides solutions to the moment equations for the picket-fence model presented in Sect. 2.1.3. He assumes that the relation $H(0) = \frac{1}{f_{\rm H}} J(0)$ with $f_{\rm H} = 1/2$, valid in the grey case under the Eddington approximation (see Eq. (27)), holds for the two thermal channels separately. Using this condition together with condition 3, he obtains a temperature profile

$$T^4(\tau) = \frac{3T_{\rm int}^4}{4}\left[\tau + \frac{\frac{2}{3} + \sqrt{\frac{1}{3\gamma_{\rm P}}}}{1 + \frac{1}{2}\sqrt{3\gamma_{\rm P}}}\right] + \frac{3T_{\rm int}^4}{4}\left(\frac{\gamma_{\rm P} - 1}{\sqrt{\gamma_{\rm P}}}\right)\frac{\frac{1}{\sqrt{3}} + \sqrt{\gamma_{\rm P}}\tau_{\rm lim}}{1 + \frac{1}{2}\sqrt{3\gamma_{\rm P}}}\left(1 - {\rm e}^{-\tau/\tau_{\rm lim}}\right) \tag{28}$$

and an equation for the skin temperature

$$T_{\rm skin}^4 = 2\left(\frac{2 + \sqrt{\frac{3}{\gamma_{\rm P}}}}{2 + \sqrt{3\gamma_{\rm P}}}\right)\frac{T_{\rm int}^4}{4}, \tag{29}$$

As expected, this equation reduces to Eq. (27) in the limit $\gamma_{\rm P} = 1$. For high values of $\gamma_{\rm P}$, this relation differs by a factor of 4/3 from the exact one derived with the method of discrete ordinates [19]. As happens for the grey case, using $f_{\rm H} = 1/\sqrt{3}$ would lead to the exact solution for the skin temperature, but at the expense of the accuracy of the profile at deeper levels. Again, we note that, in the non-irradiated case, the temperature at the top of the atmosphere is determined by a single parameter, $\gamma_{\rm P}$, representing the non-greyness of the atmosphere. A comparison of the different expressions for the skin temperature is provided in Sect. 4.

2.3.5. Irradiated semi-grey model

In the case of irradiated atmospheres, the presence of an incoming collimated flux at the top of the atmosphere breaks the angular symmetry of the equations. The radiative transfer problem thus can no longer be solved analytically (at least not in a simple way) through the discrete ordinates technique. The momentum method is thus required.

To solve the problem, the radiation field is split into two parts: the incoming, collimated radiation field on one hand, the thermal radiation field on the other. The radiative equilibrium equation (Eq. (23)) links the two streams, as can be seen in Sect. 3.1 (see also Hansen 2008; Guillot 2010; Robinson & Catling 2012). As mentioned in Sect. 2.1.2, when the incident radiation is at a much shorter wavelength than the thermal emission of the atmosphere, the two streams correspond to different characteristic wavelengths and may often be labelled as *visible* and *infrared*. This is not a requirement, however: the solutions apply if the radiation field corresponds to other wavelengths or if they overlap.

As discussed previously (Sect. 2.3.2), the boundary condition at the top of the model can be chosen in several ways. When using condition 2, Guillot (2010) lets the value of $f_{\rm H}$ be either $1/2$ or $1/\sqrt{3}$. Those values are based on the non-irradiated case: $f_{\rm H} = 1/2$ is the value that arises from the calculation of the angle dependence between $H(0)$ and $J(0)$ in the isotropic case, but $f_{\rm H} = 1/\sqrt{3}$ provides a skin temperature that agrees with the exact value. The two solutions differ by ≈3% at most (see Fig. 5 hereafter), and choosing one over another is not crucial. In any case, for an easier comparison, we provide here the solution of Guillot (2010) for $f_{\rm H} = 1/2$

$$T^4 = \frac{3T_{\rm int}^4}{4}\left[\frac{2}{3} + \tau\right] + \frac{3T_{\rm irr}^4}{4}\mu_*\left[\frac{2}{3} + \frac{\mu_*}{\gamma_{\rm v}} + \left(\frac{\gamma_{\rm v}}{3\mu_*} - \frac{\mu_*}{\gamma_{\rm v}}\right){\rm e}^{-\gamma_{\rm v}\tau/\mu_*}\right], \tag{30}$$

where μ_* is the cosine of the angle of the incident radiation. The skin temperature is

$$T_{\rm skin}^4 = 2\frac{T_{\rm int}^4 + \mu_* T_{\rm irr}^4}{4} + \gamma_{\rm v} T_{\rm irr}^4. \tag{31}$$

For $\gamma_{\rm v} \to 0$, the incident radiation is absorbed in the deep layers of the atmosphere and the skin temperature converges to the

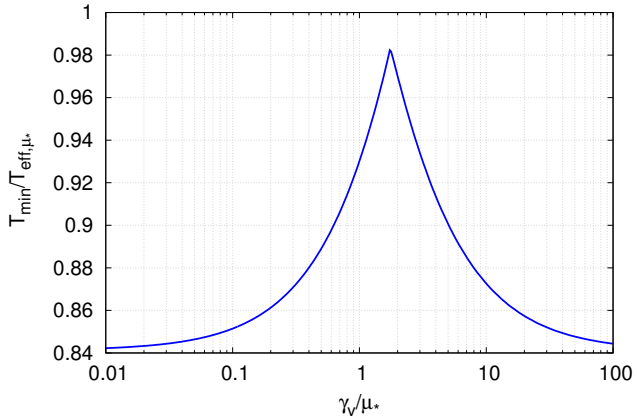

Fig. 3. Minimum temperature of the semi-grey model in terms of the effective temperature as a function of γ_v/μ_*.

skin temperature of a grey model with an effective temperature $T^4_{\rm eff,\mu_*} = T^4_{\rm int} + \mu_* T^4_{\rm irr}$. The semi-grey model depends only on the parameter γ_v.

As discussed in the introduction, the semi-grey model predicts minimum temperatures that are generally higher than the numerical solutions for irradiated exoplanets, independent of the choice of γ_v (see Fig. 1). In fact, similarly to the skin temperature, the minimum temperature of a semi-grey atmosphere, shown in Fig. 3, depends only on the values of $T_{\rm eff,\mu_*}$ and γ_v. It is the lowest and equal to $T_{\rm eff,\mu_*}/2^{1/4}$ both in the $\gamma_v \to 0$ and $\gamma_v \to \infty$ limits. This lower bound for the semi-grey temperature profile is hotter than the one obtained by numerical calculations taking into account the full set of opacities. The discrepancy is much larger than the variations resulting from the approximation of the momentum method. Clearly, non-grey effects must be invoked to explain the low temperatures obtained by numerical models at low optical depths.

3. An analytical irradiated non-grey picket-fence model

3.1. Equations

We now derive the equations for an irradiated atmosphere in local thermodynamic equilibrium with infrared line opacities as described in Sect. 2.1.2. Thus, our model contains three different opacities: κ_1 and κ_2 for the thermal radiation and κ_v for the incoming radiation of the star. As explained before, the difference between the thermal and the visible channel depends on the angular dependency of the radiation and not on the frequency. Although the method of discrete ordinates is shown to lead to more exact results, it is difficult to adapt to the irradiated case. Therefore, following Chandrasekhar (1935) and Guillot (2010), we solve the radiative transfer equations using the momentum equations. Integrating Eqs. (21) and (22) over each thermal band we obtain

$$\frac{{\rm d}H_{(1,2)}}{{\rm d}\tau} = \gamma_{(1,2)} J_{(1,2)} - \gamma_{(1,2)}(\beta, 1-\beta) B(T) \tag{32}$$

$$\frac{{\rm d}K_{(1,2)}}{{\rm d}\tau} = \gamma_{(1,2)} H_{(1,2)}, \tag{33}$$

where the subscript indicates the integrated quantities over the given thermal band. Thus, for a quantity X_ν we have:

$$X_1 = \sum_n \int_{n\Delta\nu}^{n\Delta\nu+\delta\nu} X_\nu \, {\rm d}\nu \tag{34}$$

$$X_2 = \sum_n \int_{n\Delta\nu+\delta_\nu}^{(n+1)\Delta\nu} X_\nu \, {\rm d}\nu. \tag{35}$$

The Planck function is considered constant over each bin of frequency $\Delta\nu$ and therefore $B_1 = \beta B$ and $B_2 = (1-\beta)B$.

We now assume that the Eddington approximation is valid in the two bands separately: $J_{(1,2)} = 3K_{(1,2)}$. Equations (32) and (33) can be combined into

$$\frac{{\rm d}^2 J_1}{{\rm d}\tau^2} = 3\gamma_1^2 (J_1 - \beta B) \tag{36}$$

$$\frac{{\rm d}^2 J_2}{{\rm d}\tau^2} = 3\gamma_2^2 (J_2 - (1-\beta) B) \tag{37}$$

and the radiative equilibrium equation becomes

$$\gamma_1 J_1 + \gamma_2 J_2 + \gamma_{\rm v} J_{\rm v} = \gamma_{\rm P} B, \tag{38}$$

where the quantities with subscript v are the momentum of the incident stellar radiation. Assuming that the incoming stellar radiation arrives as a collimated flux and hit the top of the atmosphere with an angle $\theta_* = \cos^{-1}\mu_*$ they can are given by

$$(J_{\rm v}, H_{\rm v}, K_{\rm v}) = (1, \mu_*, \mu_*^2) I_* \tag{39}$$

with $I_* = \int_0^\infty I_{*\nu} \, {\rm d}\nu$ the total incident intensity.

The absorption of the stellar irradiation can be treated separately from the thermal radiation and $J_{\rm v}$ is given by Eq. (13) of Guillot (2010),

$$J_{\rm v}(\tau) = -\frac{H_{\rm v}(0)}{\mu_*} {\rm e}^{-\gamma_{\rm v}^* \tau}, \tag{40}$$

where we have simplified the notation by introducing the parameter $\gamma_{\rm v}^* \equiv \gamma_{\rm v}/\mu_*$.

Equations (36) to (38) are a set of three coupled equations with three unknowns J_1, J_2, and B. In order to decouple these equations we define two new variables:

$$\begin{cases} J_\gamma \equiv \dfrac{J_1}{\gamma_1} + \dfrac{J_2}{\gamma_2} \\ J_{\gamma^3} \equiv \dfrac{J_1}{\gamma_1^3} + \dfrac{J_2}{\gamma_2^3}. \end{cases} \tag{41}$$

Conversely, we can come back to the original variables:

$$\begin{cases} J_1 = -\dfrac{\gamma_1^3(\gamma_2^2 J_{\gamma^3} - J_\gamma)}{\gamma_1^2 - \gamma_2^2} \\ J_2 = \dfrac{\gamma_2^3(\gamma_1^2 J_{\gamma^3} - J_\gamma)}{\gamma_1^2 - \gamma_2^2}. \end{cases} \tag{42}$$

Using the combination of Eqs. $\frac{1}{\gamma_1}$(36) + $\frac{1}{\gamma_2}$(37) and (38) we get

$$\frac{{\rm d}^2 J_\gamma}{{\rm d}\tau^2} = -3\gamma_{\rm v} J_{\rm v}. \tag{43}$$

Table 1. Summary of the different models compared in this paper.

Model	External irradiation	Eddington approx.	Non-grey thermal opacities	Top boundary condition	Expression
Numerical	√	×	√	$I(0) = I_{\rm star}$ for $\mu < 0$	N/A
King (1955)	×	×	√	$I(0) = 0$ for $\mu < 0$	Eq. (18)
Chandrasekhar (1935)	×	√	√	Eq. (22) & $f_{\rm H} = 1/2$	Eq. (28)
Hansen (2008)	√	√	×	Rad. Eq., & Eq. (50)	–
Guillot (2010), $f_{\rm H} = 1/2$	√	√	×	Rad. Eq., & $f_{\rm H} = 1/2$	Eq. (30)
Guillot (2010), $f_{\rm H} = 1/\sqrt{3}$	√	√	×	Rad. Eq., & $f_{\rm H} = 1/\sqrt{3}$	–
This model	√	√	√	Eq. (50) & $f_{\rm H} = 1/2$	Eq. (76)

The combination of Eqs. $\frac{1}{\gamma_1^3}$(36)+$\frac{1}{\gamma_2^3}$(37) yields

$$\frac{{\rm d}^2 J_{\gamma^3}}{{\rm d}\tau^2} = 3(J_\gamma - B). \tag{44}$$

Noting that $\gamma_1 J_1 + \gamma_2 J_2 = (\gamma_1^2 + \gamma_2^2) J_\gamma - (\gamma_1\gamma_2)^2 J_{\gamma^3}$, Eq. (38) becomes

$$B = \frac{\gamma_1^2 + \gamma_2^2}{\gamma_{\rm P}} J_\gamma - \frac{(\gamma_1\gamma_2)^2}{\gamma_{\rm P}} J_{\gamma^3} + \frac{\gamma_{\rm v}}{\gamma_{\rm P}} J_{\rm v}. \tag{45}$$

Equations (43)–(45) are now a set of two uncoupled differential equations and a linear equation.

3.2. Boundary conditions

To solve the differential equations we need to specify the boundary conditions. When $\tau \rightarrow +\infty$ we want to fulfill the diffusion approximation $J_\nu = B_\nu$ (Mihalas & Mihalas 1984, p. 350). In our case this translates to $J_1 = \beta B$ and $J_2 = (1-\beta)B$. Furthermore, at these levels, the gradient of B should also obey the diffusion approximation (Mihalas & Mihalas 1984)

$$\frac{{\rm d}B}{{\rm d}\tau} \underset{\tau\rightarrow+\infty}{\sim} 3H_\infty, \tag{46}$$

where $4\pi H_\infty = \sigma T_{\rm int}^4$ is the thermal flux coming from the interior of the planet. Using the system of Eqs. (41) and noting that $\frac{\beta}{\gamma_1} + \frac{1-\beta}{\gamma_2} = 1$, we can derive a condition on J_γ and J_{γ^3}:

$$\frac{{\rm d}J_\gamma}{{\rm d}\tau} \underset{\tau\rightarrow+\infty}{\sim} 3H_\infty \tag{47}$$

$$\frac{{\rm d}J_{\gamma^3}}{{\rm d}\tau} \underset{\tau\rightarrow+\infty}{\sim} \left(\frac{\beta}{\gamma_1^3} + \frac{1-\beta}{\gamma_2^3}\right) 3H_\infty\,. \tag{48}$$

For $\tau \rightarrow 0$ we specify the geometry of the intensity by setting:

$$J_{(1,2)}(0) = 2H_{(1,2)}(0). \tag{49}$$

Furthermore, we calculate the flux at the top of the atmosphere in each band using Eq. (79.21) from Mihalas & Mihalas (1984). From the assumption of local thermodynamic equilibrium, the source function in the two bands is $S_1(\tau_1) = \beta B(\tau/\gamma_1)$ and $S_2(\tau_2) = (1-\beta)B(\tau/\gamma_2)$. The upper boundary condition on the flux of the two bands thus becomes

$$H_{(1,2)}(0) = \frac{1}{2}\int_0^\infty (\beta, (1-\beta)) B\left(\frac{\tau}{\gamma_{(1,2)}}\right) E_2(\tau)\,{\rm d}\tau\,. \tag{50}$$

3.3. Solution

The solution of a second-order differential equation with constant coefficient is the sum of the solutions of the homogeneous equation and a particular solution of the complete equation. Thus, solutions of Eq. (43) must be of the form:

$$J_\gamma(\tau) = C_1 + C_2\tau + \frac{3}{\gamma_{\rm v}^*} H_{\rm v}(0) {\rm e}^{-\gamma_{\rm v}^*\tau}. \tag{51}$$

Applying the boundary condition Eq. (47), we get $C_2 = 3H$. For $\tau = 0$ we obtain

$$J_\gamma(0) = C_1 + \frac{3}{\gamma_{\rm v}^*} H_{\rm v}(0). \tag{52}$$

Using Eq. (45) to eliminate B and replacing J_γ by its solution, Eq. (44) becomes:

$$\begin{aligned}\frac{{\rm d}^2 J_{\gamma^3}}{{\rm d}\tau^2} - 3\frac{(\gamma_1\gamma_2)^2}{\gamma_{\rm P}} J_{\gamma^3} = {} & 3\left(1 - \frac{\gamma_1^2+\gamma_2^2}{\gamma_{\rm P}}\right)(C_1 + 3H\tau) \\ & + 3\left(1 - \frac{\gamma_1^2+\gamma_2^2}{\gamma_{\rm P}}\right)\frac{3}{\gamma_{\rm v}^*} H_{\rm v}(0){\rm e}^{-\gamma_{\rm v}^*\tau} \\ & + 3\frac{\gamma_{\rm v}^*}{\gamma_{\rm P}} H_{\rm v}(0){\rm e}^{-\gamma_{\rm v}^*\tau}.\end{aligned} \tag{53}$$

Again, solutions of this differential equation must be the sum of the solutions of the homogeneous equation and one solution of the complete equation. The homogeneous solution must have the form

$$J_{\gamma^3{\rm H}} = C_3 {\rm e}^{-\tau/\tau_{\rm lim}} + C_4 {\rm e}^{+\tau/\tau_{\rm lim}}, \tag{54}$$

where C_3 and C_4 are constants of integration to be determined using the boundary conditions. We look for a particular solution formed by the superposition of an exponential and an affine function. The affine function must then be a solution of Eq. (53) with $H_{\rm v}(0) = 0$

$$J_{\gamma^3{\rm P1}} = -\frac{\gamma_{\rm P}}{(\gamma_1\gamma_2)^2}\left(1 - \frac{\gamma_1^2+\gamma_2^2}{\gamma_{\rm P}}\right)(C_1 + 3H\tau), \tag{55}$$

and the exponential function must be solution of Eq. (53), keeping only the exponential part on the right-hand side

$$J_{\gamma^3{\rm P2}} = \frac{\gamma_{\rm P}}{(\gamma_1\gamma_2)^2}\frac{1}{(\gamma_{\rm v}^*\tau_{\rm lim})^2 - 1}\left[\left(1 - \frac{\gamma_1^2+\gamma_2^2}{\gamma_{\rm P}}\right)\frac{3}{\gamma_{\rm v}^*} + \frac{\gamma_{\rm v}^*}{\gamma_{\rm P}}\right] H_{\rm v}(0){\rm e}^{-\gamma_{\rm v}^*\tau}. \tag{56}$$

Applying the boundary condition defined by Eq. (48) to the full solution $J_{\gamma^3} = J_{\gamma^3\mathrm{P1}} + J_{\gamma^3\mathrm{P2}} + J_{\gamma^3\mathrm{H}}$, we find $C_4 = 0$. The full solution of Eq. (44) is therefore given by

$$J_{\gamma^3}(\tau) = J_{\gamma^3\mathrm{P1}} + J_{\gamma^3\mathrm{P2}} + C_3 \mathrm{e}^{-\tau/\tau_{\mathrm{lim}}}. \tag{57}$$

We can get an expression for the source function by replacing J_γ and J_{γ^3} in the radiative equilibrium equation (Eq. (45)):

$$B = C_1 + 3H\tau - \frac{(\gamma_1\gamma_2)^2}{\gamma_{\mathrm{P}}} C_3 \mathrm{e}^{-\tau/\tau_{\mathrm{lim}}} + \frac{\left[3-(\gamma_{\mathrm{v}}^*/\gamma_1)^2\right]\left[3-(\gamma_{\mathrm{v}}^*/\gamma_2)^2\right]}{3\gamma_{\mathrm{v}}^*(1-\gamma_{\mathrm{v}}^{*2}\tau_{\mathrm{lim}}^2)} H_{\mathrm{v}}(0)\mathrm{e}^{-\gamma_{\mathrm{v}}^*\tau}. \tag{58}$$

To get the complete solution of the problem, we need to determine the two remaining integration constants C_1 and C_3 using the boundary condition (49). For that we need to calculate $J_1(0)$, $J_2(0)$, $H_1(0)$ and $H_2(0)$. The first two quantities can be evaluated by inserting the values of $J_\gamma(0)$ and $J_{\gamma^3}(0)$ from Eqs. (51) and (57) into system (42):

$$\begin{aligned} J_1(0) &= -\frac{\gamma_1(\gamma_2-1)}{\gamma_1-\gamma_2} C_1 \\ &\quad + \frac{\gamma_1\left(3(\gamma_1+\gamma_2)(\gamma_2-1) - \gamma_{\mathrm{v}}^{*2} + 3\gamma_1^2\gamma_{\mathrm{v}}^{*2}\tau_{\mathrm{lim}}^2\right)}{\left(\gamma_1^2-\gamma_2^2\right)\gamma_{\mathrm{v}}^*\left(\gamma_{\mathrm{v}}^{*2}\tau_{\mathrm{lim}}^2-1\right)} H_{\mathrm{v}}(0) \\ &\quad - \frac{\gamma_1^3\gamma_2^2}{\gamma_1^2-\gamma_2^2} C_3 \end{aligned} \tag{59}$$

$$\begin{aligned} J_2(0) &= \frac{\gamma_2(\gamma_1-1)}{\gamma_1-\gamma_2} C_1 \\ &\quad - \frac{\gamma_2\left(3(\gamma_1+\gamma_2)(\gamma_1-1) - \gamma_{\mathrm{v}}^{*2} + 3\gamma_2^2\gamma_{\mathrm{v}}^{*2}\tau_{\mathrm{lim}}^2\right)}{\left(\gamma_1^2-\gamma_2^2\right)\gamma_{\mathrm{v}}^*\left(\gamma_{\mathrm{v}}^{*2}\tau_{\mathrm{lim}}^2-1\right)} H_{\mathrm{v}}(0) \\ &\quad + \frac{\gamma_2^3\gamma_1^2}{\gamma_1^2-\gamma_2^2} C_3 \,. \end{aligned} \tag{60}$$

Noting that

$$\int_0^\infty E_2(\tau)\mathrm{d}\tau = \frac{1}{2} \tag{61}$$

$$\int_0^\infty \tau E_2(\tau)\mathrm{d}\tau = \frac{1}{3} \tag{62}$$

$$\int_0^\infty \mathrm{e}^{-\alpha\tau} E_2(\tau)\,\mathrm{d}\tau = -\frac{1}{2} + \frac{1}{\alpha} - \frac{\ln(1+\alpha)}{\alpha^2}\,, \tag{63}$$

we can evaluate $H_1(0)$ and $H_2(0)$ by inserting Eqs. (58) into (50). Then, Eq. (49) is a linear system of two equations with two unknowns. After some calculations we get the expressions for C_1 and C_3

$$C_1 = (a_0 + a_1 b_0)H + (a_1 b_0 b_1(1+b_2+b_3) + a_2 + a_3)H_{\mathrm{v}}(0) \tag{64}$$

$$C_3 = b_0 H + b_0 b_1(1+b_2+b_3)H_{\mathrm{v}}(0), \tag{65}$$

where we have

$$a_0 = \frac{1}{\gamma_1} + \frac{1}{\gamma_2} \tag{66}$$

$$a_1 = -\frac{1}{3\tau_{\mathrm{lim}}^2}\left[\frac{\gamma_{\mathrm{p}}}{1-\gamma_{\mathrm{p}}}\frac{\gamma_1+\gamma_2-2}{\gamma_1+\gamma_2} + (\gamma_1+\gamma_2)\tau_{\mathrm{lim}} - (A_{\mathrm{t},1}+A_{\mathrm{t},2})\tau_{\mathrm{lim}}^2\right] \tag{67}$$

$$a_2 = \frac{\tau_{\mathrm{lim}}^2}{\gamma_{\mathrm{P}}\gamma_{\mathrm{v}}^{*2}} \times \frac{\left(3\gamma_1^2-\gamma_{\mathrm{v}}^{*2}\right)\left(3\gamma_2^2-\gamma_{\mathrm{v}}^{*2}\right)(\gamma_1+\gamma_2) - 3\gamma_{\mathrm{v}}^*\left(6\gamma_1^2\gamma_2^2 - \gamma_{\mathrm{v}}^{*2}\left(\gamma_1^2+\gamma_2^2\right)\right)}{1-\gamma_{\mathrm{v}}^{*2}\tau_{\mathrm{lim}}^2} \tag{68}$$

$$a_3 = -\frac{\tau_{\mathrm{lim}}^2(3\gamma_1^2-\gamma_{\mathrm{v}}^{*2})(3\gamma_2^2-\gamma_{\mathrm{v}}^{*2})(A_{\mathrm{v},2}+A_{\mathrm{v},1})}{\gamma_{\mathrm{P}}\gamma_{\mathrm{v}}^{*3}(1-\gamma_{\mathrm{v}}^{*2}\tau_{\mathrm{lim}}^2)} \tag{69}$$

$$b_0 = \left(\frac{\gamma_1\gamma_2}{\gamma_1-\gamma_2}\frac{A_{\mathrm{t},1}-A_{\mathrm{t},2}}{3} - \frac{(\gamma_1\gamma_2)^2}{\sqrt{3\gamma_{\mathrm{P}}}} - \frac{(\gamma_1\gamma_2)^3}{(1-\gamma_1)(1-\gamma_2)(\gamma_1+\gamma_2)}\right)^{-1} \tag{70}$$

$$b_1 = \frac{\gamma_1\gamma_2(3\gamma_1^2-\gamma_{\mathrm{v}}^{*2})(3\gamma_2^2-\gamma_{\mathrm{v}}^{*2})\tau_{\mathrm{lim}}^2}{\gamma_{\mathrm{P}}\gamma_{\mathrm{v}}^{*2}(\gamma_{\mathrm{v}}^{*2}\tau_{\mathrm{lim}}^2-1)} \tag{71}$$

$$b_2 = \frac{3(\gamma_1+\gamma_2)\gamma_{\mathrm{v}}^{*3}}{(3\gamma_1^2-\gamma_{\mathrm{v}}^{*2})(3\gamma_2^2-\gamma_{\mathrm{v}}^{*2})} \tag{72}$$

$$b_3 = \frac{A_{\mathrm{v},2}-A_{\mathrm{v},1}}{\gamma_{\mathrm{v}}^*(\gamma_1-\gamma_2)}, \tag{73}$$

where we defined

$$A_{\mathrm{t},i} = \gamma_i^2 \ln\left(1 + \frac{1}{\tau_{\mathrm{lim}}\gamma_i}\right) \tag{74}$$

$$A_{\mathrm{v},i} = \gamma_i^2 \ln\left(1 + \frac{\gamma_{\mathrm{v}}^*}{\gamma_i}\right). \tag{75}$$

3.4. Atmospheric temperature profile

Using the relations $B = \sigma T^4/\pi$, $H = \sigma T_{\mathrm{int}}^4/4\pi$, and $H_{\mathrm{v}}(0) = -\mu_*\sigma T_{\mathrm{irr}}^4/4\pi$ and Eq. (58), we can derive the equation for the temperature at any optical depth

$$T^4 = \frac{3T_{\mathrm{int}}^4}{4}\left(\tau + A + B\mathrm{e}^{-\tau/\tau_{\mathrm{lim}}}\right) + \frac{3T_{\mathrm{irr}}^4}{4}\mu_*\left(C + D\mathrm{e}^{-\tau/\tau_{\mathrm{lim}}} + E\mathrm{e}^{-\gamma_{\mathrm{v}}^*\tau}\right) \tag{76}$$

with

$$A = \frac{1}{3}(a_0 + a_1 b_0) \tag{77}$$

$$B = -\frac{1}{3}\frac{(\gamma_1\gamma_2)^2}{\gamma_{\mathrm{p}}} b_0 \tag{78}$$

$$C = -\frac{1}{3}\left[b_0 b_1(1+b_2+b_3)a_1 + a_2 + a_3\right] \tag{79}$$

$$D = \frac{1}{3}\frac{(\gamma_1\gamma_2)^2}{\gamma_{\mathrm{p}}} b_0 b_1(1+b_2+b_3) \tag{80}$$

$$E = \frac{\left[3-(\gamma_{\mathrm{v}}^*/\gamma_1)^2\right]\left[3-(\gamma_{\mathrm{v}}^*/\gamma_2)^2\right]}{9\gamma_{\mathrm{v}}^*\left[(\gamma_{\mathrm{v}}^*\tau_{\mathrm{lim}})^2-1\right]}. \tag{81}$$

3.5. Grey limit

In the grey limit, $\gamma_P \rightarrow 1$ (as γ_1 and γ_2) and we obtain

$$A \rightarrow 2/3 \tag{82}$$
$$B \rightarrow 0 \tag{83}$$
$$C \rightarrow 2/3 - 2/\gamma_v^{*2} + 2/\gamma_v^{*} + 2\log(1+\gamma_v^{*})\left(1/\gamma_v^{*3} - 1/(3\gamma_v^{*})\right) \tag{84}$$
$$D \rightarrow 0 \tag{85}$$
$$E \rightarrow \gamma_v^{*}/3 - 1/\gamma_v^{*}. \tag{86}$$

If we also assume that $\gamma_v^{*} \rightarrow 0$ we obtain $C \rightarrow 2/3 + 1/\gamma_v^{*}$ and $E \rightarrow -1/\gamma_v^{*}$ and the solution converges towards that of Guillot (2010) (see Eq. (30)). For other values of γ_v^{*} our model differs from the solutions of Guillot (2010, see also Hansen 2008) because of the different boundary conditions used in the two models (see Sect. 2.3.2). However, calculations show that the value of C obtained here differs from the same coefficient extracted from Eq. (30) by at most 12% and that the two solutions also converge for $\gamma_v^{*} \rightarrow \infty$. As seen in Fig. 5, in the semi-grey limit, and when calculating the full temperature profile, our model differs by at most 2% from the Guillot (2010) model. The difference between the various solutions must be attributed to the Eddington approximation.

3.6. Using the model

The temperature vs. optical depth profile for our irradiated picket-fence model is given by Eq. (76). The profile has been derived using the Rosseland optical depth as vertical coordinate. It is therefore valid for any functional form of the Rosseland opacities. Equation (4) allows us to switch from τ to P as the vertical coordinate. Although, for convenience, this expression contains four different variables, $\gamma_1, \gamma_2, \gamma_P$, and τ_{lim}, it must be kept in mind that, besides the Rosseland mean opacity, there are only two independent variables in the problem. The variables β and $R \equiv \gamma_1/\gamma_2 = \kappa_1/\kappa_2$ are the ones to consider to control the shape of the thermal opacities. The variables γ_P and τ_{lim} are the ones to consider to control the profile itself. The variable γ_P is directly related to the skin temperature of the planet (see Sect. 4.3) whereas τ_{lim} is the optical depth at which the irradiated picket-fence model differs from the semi-grey model. The steps to use our model are as follow:

1) choose the pair of variables suitable for the problem: (R, β) or (γ_P, τ_{lim}), for example;
2) using Eqs. (87) to (95), calculate the values of γ_P, γ_1, γ_2, and τ_{lim};
3) using Eqs (77) to (81) and Eqs. (66) to (75), calculate the coefficients A, B, C, D, and E.;
4) using Eq. (76), calculate the temperature/optical depth profile;
5) using Eq. (4), calculate the pressure/optical depth relationship and therefore the pressure/temperature profile.

For Rosseland opacities depending on the temperature, step 5) can be iterated until convergence. Given the apparent complexity of the solution, we provide a ready-to-use code[3] in different languages that gives the temperature/optical depth profile (steps 1 to 4) or the temperature/pressure profile given a Rosseland mean opacity.

[3] https://www.oca.eu/parmentier/nongrey

The relationship between the different variables are listed below:

$$\gamma_P = \beta + R - \beta R + \frac{\beta + R - \beta R}{R} - \frac{(\beta + R - \beta R)^2}{R} \tag{87}$$
$$\tau_{lim} = \frac{\sqrt{R}\sqrt{\beta(R-1)^2 - \beta^2(R-1)^2 + R}}{\sqrt{3}(\beta + R - \beta R)^2} \tag{88}$$
$$R = \frac{\sqrt{3\gamma_P} + 3\gamma_P\tau_{lim} + \sqrt{\Delta}}{\sqrt{3\gamma_P} + 3\gamma_P\tau_{lim} - \sqrt{\Delta}} \tag{89}$$
$$\beta = \frac{\sqrt{\Delta} - \sqrt{3\gamma_P} + 3\gamma_P\tau_{lim}}{2\sqrt{\Delta}} \tag{90}$$
$$\Delta = 3\gamma_P + 3\sqrt{\gamma_P}\tau_{lim}\left(2\sqrt{3}\gamma_P + 3\gamma_P^{3/2}\tau_{lim} - 4\sqrt{3}\right) \tag{91}$$
$$\gamma_1 = \beta + R - \beta R \tag{92}$$
$$\gamma_2 = \frac{\beta + R - \beta R}{R} \tag{93}$$
$$\gamma_1 = \frac{\sqrt{3\gamma_P} + 3\gamma_P\tau_{lim} + \sqrt{\Delta}}{6\tau_{lim}} \tag{94}$$
$$\gamma_2 = \frac{\sqrt{3\gamma_P} + 3\gamma_P\tau_{lim} - \sqrt{\Delta}}{6\tau_{lim}} \tag{95}$$
$$R = 1 + \frac{\gamma_P - 1}{2\beta(1-\beta)} + \sqrt{\left(\frac{\gamma_P - 1}{2\beta(1-\beta)}\right)^2 + \frac{\gamma_P - 1}{2\beta(1-\beta)}}. \tag{96}$$

3.7. About averaging

Equation (76) can thus be considered to depend on κ_R, $\gamma_P \equiv \kappa_P/\kappa_R$, and β. While κ_R can be considered a function of pressure and temperature (e.g. extracted from a known Rosseland opacity table) when deriving the atmospheric temperature profile, it is important to realize that the analytical solution remains valid only if γ_P and β are held constant. This analytical solution therefore cannot accommodate consistent Rosseland *and* Planck opacities as a function of depth. A solution consisting of atmospheric slices with different values of γ_P have been derived by Chandrasekhar (1935) for the non-irradiated case, but it becomes too complex to be handled easily.

Furthermore, the solution is provided only for one fixed direction of the incoming irradiation. When considering the case of a non-resolved planet around a star, any information acquired on its atmosphere will have been averaged over at least a fraction of its surface. Solving this problem for the particular case of Eq. (76) goes beyond the scope of the present work, but it can be approximated relatively well on the basis of the study by Guillot (2010). This work shows that given an irradiation flux at the substellar point $\sigma T_{sub}^4 \equiv \sigma(R_*/D)^2 T_*^4$, where T_* is the star's effective temperature, R_* its radius, and D the star-planet distance, the *average* temperature profile of the planet will be very close to that obtained from the one-dimensional solution with an average angle $\mu^* = 1/\sqrt{3}$ and an average irradiation temperature $T_{irr} = (1-A)^{1/4} f^{1/4} T_{sub}$, where A is the (assumed) Bond albedo of the atmosphere and f is a correction factor, equal to 1/4 when averaging on the entire surface of the planet and equal to 1/2 when averaging on the dayside only. This corresponds to the so-called *isotropic approximation*. In the semi-grey case, it is found to be within 2% of the actual average for a typical hot-Jupiter (see Fig. 2 of Guillot 2010).

For the interpretation of spectroscopic and photometric data of secondary eclipses, the dayside average is often used ($f = 1/2$). For the calculation of evolution models, the global average is the correct physical quantity to be used when the composition and opacity variations in latitude and longitude are not precisely known (see Guillot 2010). In that case, $f = 1/4$ which is equivalent to setting the irradiation temperature equal to the usual equilibrium temperature defined as $T_{\rm eq} \equiv T_*(R_*/2D)^{1/2}$ (Saumon et al. 1996). Obviously detailed interpretations must use an approach mixing three-dimensional dynamical and radiative transfer models (see Guillot 2010; Heng et al. 2012; Showman et al. 2009).

3.8. Adding several bands in the visible

Although, for the simplicity of the derivation, our model used only one spectral band in the visible channel, it can be easily extended to n visible bands. The most important point is that our equations, and in particular Eq. (43), are linear in the visible. Thus, the equations can be solved for any linear combination of visible bands. In that case the first momentum of the visible intensity (see Eq. (40)) writes

$$J_{\rm v}(\tau) = -\frac{H_{\rm v}(0)}{\mu_*}\sum_{i=1}^{n}\beta_{{\rm v}i}{\rm e}^{-\gamma^*_{{\rm v}i}\tau}, \tag{97}$$

where $\beta_{{\rm v}i}$ is the relative spectral extent of the ith band and $\gamma_{{\rm v}i} = \kappa_{{\rm v}i}/\kappa_{\rm R}$ with $\kappa_{{\rm v}i}$ the opacity in the ith visible band. Equation (76) then becomes

$$T^4 = \frac{3T^4_{\rm int}}{4}\left(\tau + A + B{\rm e}^{-\tau/\tau_{\rm lim}}\right) + \sum_{i=1}^{n}\frac{3\beta_{{\rm v}i}T^4_{\rm irr}}{4}\mu_*\left(C_i + D_i{\rm e}^{-\tau/\tau_{\rm lim}} + E_i{\rm e}^{-\gamma^*_{{\rm v}i}\tau}\right) \tag{98}$$

where C_i, D_i, and E_i are the coefficients C, D, and E given by Eqs. (79) to (81) where $\gamma^*_{\rm v}$ have been replaced by $\gamma^*_{{\rm v}i}$.

4. Comparisons

4.1. Comparison of non-irradiated solutions

Figure 4 shows a comparison between our results and the solutions of King (1955) and Chandrasekhar (1935). The solutions are extremely close, the temperatures being always less than a few percentage points of each other. Our solution is almost identical to that of Chandrasekhar (1935), a consequence of using the Eddington approximation and similar boundary conditions. The difference of these with the exact solution from King (1955) can be attributed to the Eddington approximation.

The non-grey effects lead to colder temperatures at small optical depths. When β is close to unity, a blanketing effect leads to a heating of the deeper layers too. All solutions have the correct behaviour (see also Sect. 5).

4.2. Comparison of irradiated solutions

The solutions presented in this work for the irradiated semi-grey case (i.e. $R \equiv \kappa_1/\kappa_2 = 1$) are very similar to those of Guillot (2010). As seen in Fig. 5, the solutions obtained either with $f_{\rm H} = 1/2$, or $f_{\rm H} = 1/\sqrt{3}$ have relative differences of up to 2% with those of this work. These differences are of the same kind as those arising from the use of the Eddington approximation compared to exact solutions discussed previously. They are inherent to the approximation made on the angular dependency of the radiation field and implicitly linked to the choice of the different boundary conditions discussed in Sect. 2.3.2.

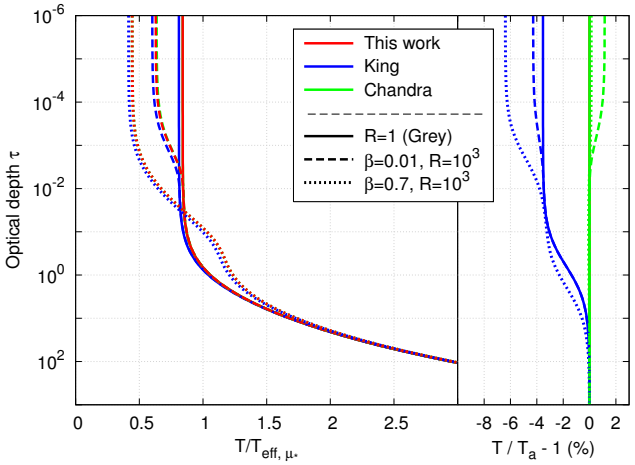

Fig. 4. Comparison of the non-irradiated solutions of the radiative transfer problem within the so-called picket-fence model approximation (see text). The *left panel* shows temperature (in $T_{\rm eff}$ units) vs. optical depth. The right panel shows the relative temperature difference between our model and other works. The models shown correspond to the solutions of King (1955) (blue lines), Chandrasekhar (1935) (green lines), and this work (red lines). Different models correspond to the grey case (plain), i.e. $R = 1$, and 2 non-grey cases: $\beta = 0.01$, $R = 10^3$ (dashed) and $\beta = 0.7$, $R = 10^3$ (dotted) where $R \equiv \kappa_1/\kappa_2$. The red and green lines are so similar that they are almost indistinguishable in the *left panel*.

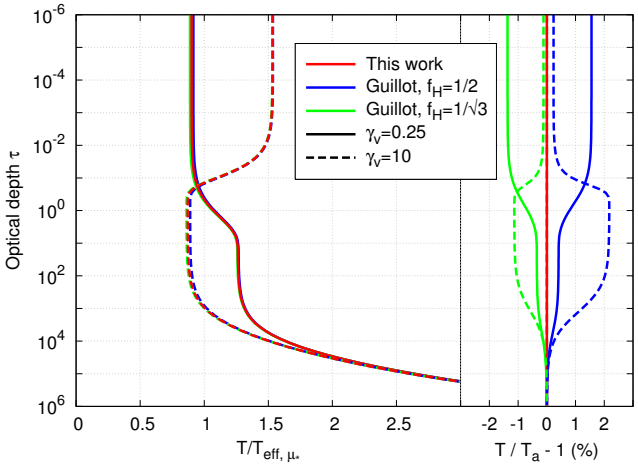

Fig. 5. Comparison between our model in the semi-grey limit and Guillot (2010). We used $\gamma_{\rm v} = 0.25$ (plain line) and $\gamma_{\rm v} = 10$ (dashed line). For the Guillot (2010) model we show the curves for two different boundary conditions: $f_{\rm H} = 1/2$ (blue) and $f_{\rm H} = 1/\sqrt{3}$ (green). We used $\mu_* = 1/\sqrt{3}$.

4.3. Comparison of skin temperatures

As discussed previously, the skin temperature (temperature at the limit of zero optical depth) is an important outcome of radiative transfer and in the case of non-irradiated models, an exact solution is available. We compare our results to other analytical results in Fig. 6. In the limit of a non-irradiated planet and in

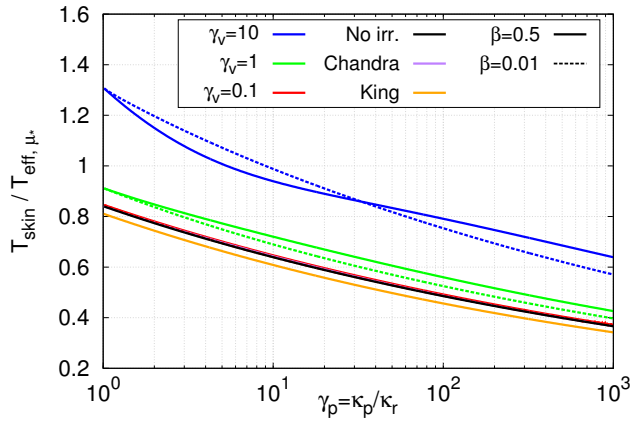

Fig. 6. Skin temperature of the planet given by our irradiated picket-fence model for different values of γ_v and in the non-irradiated case. Curves for $\beta = 0.01$ (plain lines) and $\beta = 0.5$ (dashed lines) are shown. Skin temperature from Chandrasekhar (1935) and King (1956) are also shown. For the irradiated case we used $\mu_* = 1/\sqrt{3}$ and $T_{\rm int} = 0$. The $\gamma_v = 0.1$, the non-irradiated, and the Chandrasekhar (1935) curves are closely packed.

the limit $\gamma_v^* \to 0$, our skin temperature converges to the one derived by Chandrasekhar (1935). This is an important test for the model, as for low values of γ_v, most of the stellar flux is absorbed in the deep layers of the planet and the model is expected to behave as a non-irradiated model with the same effective temperature. Moreover, we note that for low values of γ_v, the skin temperature is affected only by γ_P as was already claimed by King (1956) and Chandrasekhar (1935). This conclusion no longer applies for higher values of γ_v for which the skin temperature also depends on β. This can be seen by comparing the dotted lines and plain lines of the same colour in Fig. 6. At a given value of γ_P, a higher value of β corresponds to a smaller κ_2/κ_1. Depending on the value of β, the stellar irradiation can be absorbed in a region which can be optically thick to the two thermal bands, only one, or none, leading to different behaviour for the skin temperature.

5. Consequences of non-grey effects

In this section we study the physical processes that shape our non-grey temperature profile. To overcome the apparent complexity of our solution, we first derive an approximate expression for the thermal fluxes at the top of the atmosphere. We then obtain a much simpler expression for the skin and the deep temperatures. Comparing these expressions with their semi-grey equivalent, we get physical insights into the processes that shape the temperature profile.

5.1. Estimation of the fluxes in the different bands

In steady state, all the energy that penetrates the atmosphere must be radiated away. Thus, the radiative equilibrium at the top of the atmosphere is of great importance to understand how the non-grey effects shape the temperature profile. In particular, whether the thermal fluxes are transported by the channel of highest opacity (channel 1) or the channel of lowest opacity (channel 2) is of particular importance.

As seen in Eq. (76), the contribution to the final temperature of the internal luminosity and of the external irradiation are independent. Thus, the thermal fluxes can be split into two independent contributions that can be studied separately:

$$H_i = H_{i,\rm int} + H_{i,\rm irr}. \tag{99}$$

Figure 7 shows which thermal band actually carries the thermal flux $H_{\rm irr}(0)$ out of the atmosphere (the flux $F_{\rm irr}(0)$ is equal to $4\pi H_{\rm irr}(0)$). This depends strongly on whether the stellar irradiation is absorbed in the upper or in the deep atmosphere. If it is deposited in the deep layers of the planet (i.e. $\gamma_v \ll 1$), most of the flux is transported by the second thermal channel *whatever the width of the second channel*. Conversely, when the stellar irradiation is deposited in the upper atmosphere, most of the flux is carried by the first thermal channel *whatever the width of the first channel*. The tipping point, i.e. when each channel carries half of the flux, is reached when $\gamma_v = \tau_{\rm lim}^{-1}$. Figure 8 shows the variations of $\tau_{\rm lim}$ with the width and the strength of the two thermal opacity bands; $\tau_{\rm lim}$ increases with β but decreases with $R \equiv \kappa_1/\kappa_2$. It always corresponds to an optical depth where the first channel is optically thick and the second is optically thin.

For high values of γ_P (i.e. $\gamma_P > 2$), we can approximate the ratio of the thermal fluxes related to the irradiation by a much simpler expression:

$$\frac{H_{1,\rm irr}(0)}{H_{2,\rm irr}(0)} \approx \frac{\beta}{\sqrt{\gamma_P}} + \frac{1}{\frac{1-\beta}{\sqrt{\gamma_P}} + \frac{1}{\gamma_v^* \tau_{\rm lim}}}. \tag{100}$$

As shown in Fig. 7 this expression correctly matches the expression of the analytical model. Depending on the value of $\gamma_v^* \tau_{\rm lim}$, the expression reduces to

$$\frac{H_{1,\rm irr}(0)}{H_{2,\rm irr}(0)} \approx \frac{\beta}{\sqrt{\gamma_P}} + \gamma_v^* \tau_{\rm lim}, \text{ when } \gamma_v^* \tau_{\rm lim} < 1 \tag{101a}$$

$$\frac{H_{2,\rm irr}(0)}{H_{1,\rm irr}(0)} \approx \frac{1-\beta}{\sqrt{\gamma_P}} + \frac{1}{\gamma_v^* \tau_{\rm lim}}, \text{ when } \gamma_v^* \tau_{\rm lim} > 1. \tag{101b}$$

We now look for a similar expression for the thermal fluxes resulting from the internal luminosity ($H_{\rm int}$). Because the internal luminosity irradiates the atmosphere from below, the resulting thermal fluxes behave similarly to the irradiated when $\gamma_v \to 0$, thus we have

$$\frac{H_{1,\rm int}(0)}{H_{2,\rm int}(0)} \approx \frac{\beta}{\sqrt{\gamma_P}}. \tag{102}$$

As γ_P is always greater than one and β is always lower than one, the internal luminosity is always transported by channel 2, the channel of lowest opacity.

5.2. The skin temperature

The skin temperature reveals the behaviour of the atmosphere at low optical depths. This is the part of the atmosphere probed during the transit of an exoplanet in front of its host star and is therefore of particular importance to interpret the observations. Figure 9 shows that in the irradiated case non-grey effects always tend to lower the skin temperature compared to the semi-grey case. This upper atmospheric cooling is already significant (>10%) for slightly non-grey opacities (i.e. $\gamma_P \approx 2$). For higher values of γ_P the cooling is stronger, reaching 50% for $\gamma_P \approx 10-1000$. Conversely to the non-irradiated case, the skin temperature is not only a function of γ_P but also depends on β, i.e. not only are the mean opacities relevant, but also their actual shape. For high values of β, when the stellar irradiation is

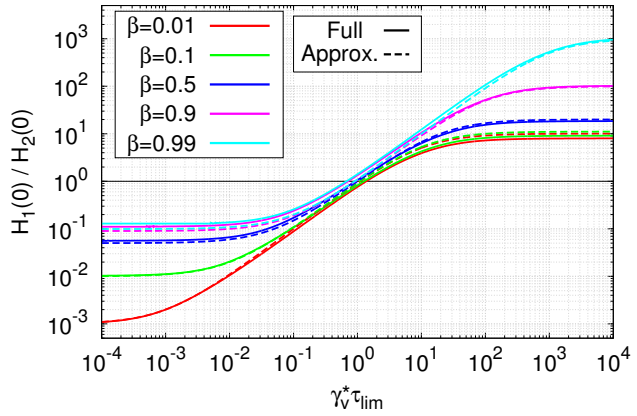

Fig. 7. Ratio of the total flux in the two thermal bands in function of $\gamma_v^* \tau_{\rm lim}$ for different β and for $\gamma_P = 100$ given by our analytical model (plain) and by Eq. (100) (dashed). We used $\mu_* = 1/\sqrt{3}$ and $T_{\rm int} = 0$.

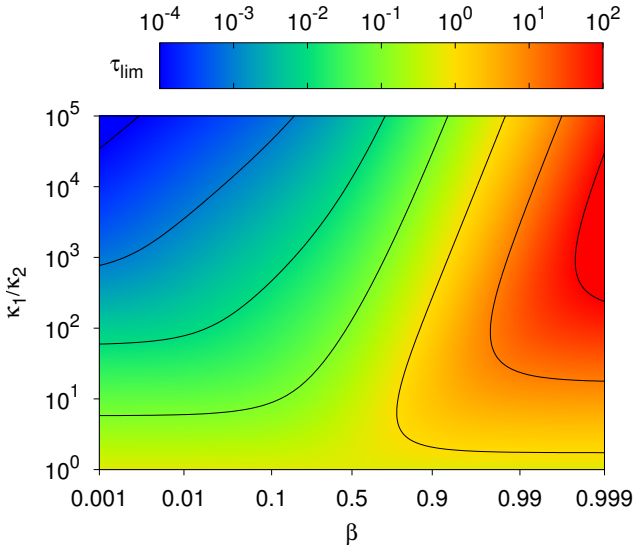

Fig. 8. Value of $\tau_{\rm lim}$ in function of the width of the lines β and their strength κ_1/κ_2. The x-axis is in logit scale, where the function logit is defined as $\mathrm{logit}(x) = \log(x/(1-x))$.

absorbed in the upper layers of the atmosphere (e.g. $\gamma_v = 100$) the cooling is more efficient than when the stellar irradiation is absorbed in the deep layers (e.g. $\gamma_v = 0.01$), whereas for low values of β the cooling is independent of γ_v.

The skin temperature results directly from the radiative equilibrium of the upper atmosphere. Using the boundary condition (49) in the radiative equlibrium Eq. (23) evaluated at $\tau = 0$ we can write

$$2\gamma_1 H_1(0) + 2\gamma_2 H_2(0) - \gamma_v^* H_v(0) = \gamma_P B(0), \quad (103)$$

where the skin temperature is given by $T_{\rm skin}^4 = \pi B(0)/\sigma$. The skin temperature, depends on the values of $H_1(0)$ and $H_2(0)$ and thus on whether the stellar irradiation is absorbed in the deep atmosphere or in the upper atmosphere.

5.2.1. Case of deep absorption of the irradiation flux

When $\gamma_v^* \tau_{\rm lim} < 1$, the stellar irradiation is absorbed in the deep layers of the atmosphere, where the second thermal band, the band of lowest opacity, is optically thick. Thus, most of the flux is transported by the second thermal band and we have $H_2(0) = H_\infty - H_v(0)$. For high values of γ_P, using Eq. (101a) and Eq. (102) we get $\gamma_1 H_1(0)/\gamma_2 H_2(0) > \sqrt{\gamma_P}/(1-\beta)$ which is always larger than one. Thus, although most of the flux is in the second thermal band, it is the first band, the band of highest opacity, that sets the radiative equilibrium. Neglecting the second term in Eq. (103) and calculating $H_1(0)$ with Eqs. (101a) and (102) we obtain:

$$B(0) = \frac{2\gamma_1\beta}{\gamma_P\sqrt{\gamma_P}} H_\infty - \left(\frac{2\gamma_1\beta}{\gamma_P\sqrt{\gamma_P}} + \frac{2\gamma_v^*\tau_{\rm lim}\gamma_1}{\gamma_P} + \frac{\gamma_v^*}{\gamma_P} \right) H_v(0). \quad (104)$$

Noting that for high values of γ_P, $\tau_{\rm lim} \approx \beta(1-\beta)^{-1}\left(\sqrt{3\gamma_P}\right)^{-1}$, and $\gamma_1 \approx \gamma_P/\beta$, the equation becomes

$$B(0) = \frac{2}{\sqrt{\gamma_P}} H_\infty - \left(\frac{2}{\sqrt{\gamma_P}} + \frac{2\gamma_v^*}{(1-\beta)\sqrt{3\gamma_P}} + \frac{\gamma_v^*}{\gamma_P} \right) H_v(0). \quad (105)$$

Replacing the fluxes by their equivalent temperature we get an expression for the skin temperature valid for $\gamma_v^*\tau_{\rm lim} < 1$ and $\gamma_P > 2$:

$$T_{\rm skin}^4 = \frac{2}{\sqrt{\gamma_P}} \frac{T_{\rm int}^4 + \mu_* T_{\rm irr}^4}{4} + \left(\frac{2\gamma_v^*}{(1-\beta)\sqrt{3\gamma_P}} + \frac{\gamma_v^*}{\gamma_P} \right) \frac{\mu_* T_{\rm irr}^4}{4}. \quad (106)$$

When $\gamma_v^*\tau_{\rm lim} < 1$, the first term dominates and the expression differs by a factor of $1/\sqrt{\gamma_P}$ from the semi-grey case (Eq. (31)). Because $\gamma_P > 1$ for non-grey opacities, the skin temperature is always smaller in the non-grey case than in the grey case, as shown in Fig. 9.

Physical interpretation. When $\gamma_v^*\tau_{\rm lim} < 1$ most of the irradiation is absorbed where both thermal channels are optically thick. The flux is mainly transported by the channel of lowest opacity κ_2 but only the residual flux transported by the channel of highest opacity κ_1 contributes to the radiative equilibrium at the top of the atmosphere. Because it represents only a small part of the total flux, the upper atmosphere does not need to radiate a lot of energy and thus the upper atmospheric temperatures are smaller than in the semi-grey case. The larger the departure from the semi-grey opacities, the cooler the skin temperature, without lower bounds.

5.2.2. Case of shallow absorption of the irradiation flux

When $\gamma_v^*\tau_{\rm lim} > 1$, most of the stellar irradiation is absorbed in the upper atmosphere, where only the first thermal band is optically thick. According to Eq. (101a), most of the flux originating from the irradiation $H_{\rm irr}(0)$ is carried by the first thermal band, the band of highest opacity. Conversely, following Eq. (102), the internal luminosity is still transported by the second thermal channel, as in the $\gamma_v\tau_{\rm lim} < 1$ case. As $\gamma_1 > \gamma_2$, the radiative equilibrium of the upper atmosphere is still determined by the channel of highest opacity, channel 1, and the second term of Eq. (103) can be neglected. Conversely to the case $\gamma_v\tau_{\rm lim} < 1$, the top boundary condition now reads $H_1(0) \approx H_{1,\rm int} - H_v(0)$. Using Eq. (102) to calculate $H_{1,\rm int}$ and noting that for high values of γ_P, $\gamma_P \approx \beta\gamma_1$, the radiative equilibrium becomes

$$B(0) = \frac{2}{\sqrt{\gamma_P}} H_\infty - \left(\frac{2}{\beta} + \frac{\gamma_v^*}{\gamma_P} \right) H_v(0). \quad (107)$$

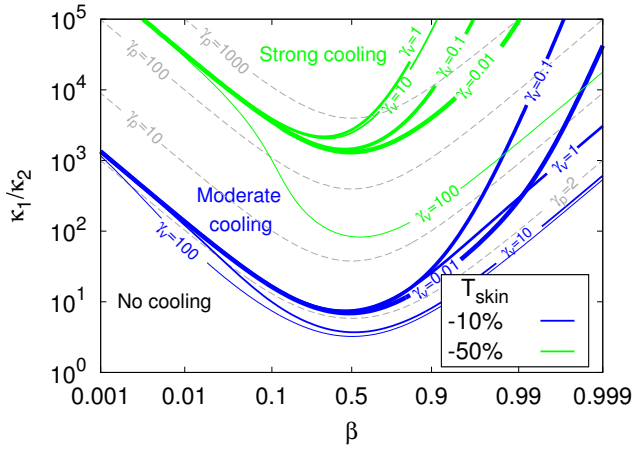

Fig. 9. Contours of the relative difference between the skin temperature in the non-grey model and in the semi-grey model for different values of γ_v in function of the width of the lines and their strength. The non-grey atmosphere is 10% (resp. 50%) cooler than the semi-grey atmosphere above the blue (resp. green) lines. The dashed lines are contours of γ_P. We used $\mu_* = 1/\sqrt{3}$.

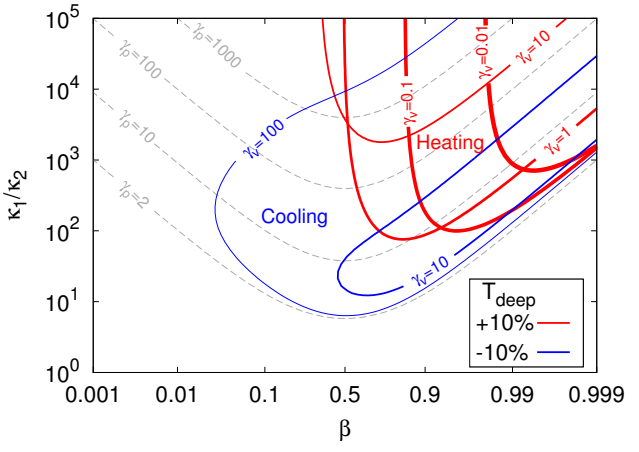

Fig. 10. Contours of the relative difference between the deep temperature in the non-grey model and in the semi-grey model for different values of γ_v in function of the width of the lines and their strength. The non-grey atmosphere is 10% hotter (resp. cooler) than the semi-grey atmosphere inside the red (resp. blue) contours. The dashed lines are contours of γ_P. We used $\mu_* = 1/\sqrt{3}$.

Replacing the fluxes by their equivalent temperatures we get an expression for the skin temperature valid for $\gamma_v^* \tau_{lim} > 1$ and $\gamma_P > 2$

$$T_{skin}^4 = \frac{2}{\sqrt{\gamma_P}} \frac{T_{int}^4}{4} + \left(\frac{2}{\beta} + \frac{\gamma_v^*}{\gamma_P} \right) \frac{\mu_* T_{irr}^4}{4} . \quad (108)$$

This relation differs from the case $\gamma_v^* \tau_{lim} < 1$ as the factor $1/\sqrt{\gamma_P}$ before the irradiation temperatures is replaced by a factor $1/\beta$. Thus, the skin temperature no longer becomes arbitrarily low. However, for high values of γ_v, the second term in the parenthesis dominates and the skin temperature decreases proportionally to $1/\sqrt{\gamma_P}$, which is faster than in the case $\gamma_v^* \tau_{lim} < 1$. As an example, in Fig. 9, for $\gamma_v = 100$, the skin temperature decreases much faster when γ_P increases for large values of β (i.e. when $\gamma_v^* \tau_{lim} > 1$).

Physical interpretation. When $\gamma_v^* \tau_{lim} > 1$, most of the incident irradiation is absorbed in the upper atmosphere, where the second channel is optically thin. Therefore it is mainly transported by the channel of highest opacity: channel 1. Similarly to the case $\gamma_v^* \tau_{lim} < 1$, the radiative equilibrium at the top of the atmosphere is set by the channel of highest opacity, the one that carries most of the thermal flux. Therefore all the flux from the irradiation contributes to the radiative equilibrium of the upper layers and the skin temperature cannot cool as much as in the $\gamma_v^* \tau_{lim} < 1$ case, its lowest value being $\mu^* T_{irr}^4 / 2\beta$. However, for high values of γ_v^* and as long as $\gamma_P < \gamma_v^*$, T_{skin}^4 decreases faster than in the case $\gamma_v^* \tau_{lim} < 1$. This confines the stratosphere due to $\gamma_v^* > 1$ (i.e. the atmospheric levels with a temperature inversion) around the $\tau = \tau_{lim}$ level whereas it extends up to $\tau = 0$ in the semi-grey case (see Figs. 12–14 hereafter).

5.3. The deep temperature

The temperature of the deep atmosphere is a fundamental outcome from radiative transfer models as it reveals the energy exchange between the planet and its surroundings. Therefore, it is often used as a boundary condition of planetary interior models. We define the deep temperature as

$$T_{deep}^4 = \lim_{\tau \to \infty} T(\tau)^4 - 3 T_{int}^4 \tau. \quad (109)$$

Thus, the temperature of the deep atmosphere can be approximated as $T(\tau)^4 = T_{deep}^4 + 3 T_{int}^4 \tau$ between the $\tau \approx 1$ level and the radiative/convective boundary. For irradiated planets, the deep temperature corresponds to the isothermal zone around $\tau \approx 1$ and is close to the temperature at 10 bar often used as a boundary condition for interior models (e.g., Burrows et al. 1997; Guillot & Showman 2002). As seen in Fig. 10, the deep temperature has a complex behaviour. For low values of γ_v, whenever β becomes large enough, the deep temperature increases compared to the semi-grey case, an effect known as the *line blanketing effect* in the stellar literature (e.g. Milne 1921; Chandrasekhar 1935; Hubeny & Lanz 1995). This effect is always maximum when $\gamma_v^* \approx \tau_{lim}^{-1}$ (see Fig. 8). Conversely, for high values of γ_v^* (i.e. $\gamma_v^* > 10$), the deep atmosphere warms up only for high values of γ_P ($\gamma_P > \gamma_v^2$) whereas it becomes cooler than in the semi-grey case for lower values of γ_P, a behaviour that was not spotted in previous analytical models.

The deep atmospheric temperature is directly set by the boundary condition at the top of the atmosphere. From Eq. (58), we see that when $\tau \to \infty$,

$$T_{deep}^4 = \lim_{\tau \to \infty} B(\tau) - 3 H_\infty \tau = C_1, \quad (110)$$

where C_1 is set by the top boundary condition (49) applied on $J_\gamma(0)$ (see Eq. (52)):

$$2 \frac{H_1(0)}{\gamma_1} + 2 \frac{H_2(0)}{\gamma_2} = C_1 + \frac{3}{\gamma_v^*} H_v. \quad (111)$$

Similarly to the skin temperature, the deep temperature depends on $H_1(0)$ and $H_2(0)$, and also depends on whether the thermal flux is transported by the first or by the second thermal channel, i.e. whether $\gamma_v \tau_{lim}$ is larger or smaller than one.

5.3.1. Case of deep absorption of the irradiation flux

In the case $\gamma_{\rm v}^*\tau_{\rm lim} < 1$, most of the thermal flux is transported by the second thermal channel and because $\gamma_1 \gg \gamma_2$ we can write

$$2\frac{H_2(0)}{\gamma_2} \approx C_1 + \frac{3}{\gamma_{\rm v}^*}H_{\rm v}, \tag{112}$$

applying the radiative equilibrium at the top of the atmosphere, and considering that most of the flux is carried by the second thermal channel, we get

$$H_2(0) \approx H_\infty - H_{\rm v}(0). \tag{113}$$

Thus, we can calculate C_1 and obtain

$$B(\tau) - 3H_\infty\tau \underset{\tau\to\infty}{\sim} \frac{2}{\gamma_2}H_\infty - \left(\frac{2}{\gamma_2} + \frac{3}{\gamma_{\rm v}^*}\right)H_{\rm v}(0). \tag{114}$$

For high values of $\gamma_{\rm P}$, $\gamma_2 \approx (1-\beta)$. Replacing the fluxes by their equivalent temperatures we get an expression for $T_{\rm deep}$ valid for $\gamma_{\rm v}^*\tau_{\rm lim} < 1$ and $\gamma_{\rm P} > 2$:

$$T_{\rm deep}^4 \approx \frac{2}{1-\beta}\frac{T_{\rm int}^4 + \mu_* T_{\rm irr}^4}{4} + \frac{3}{\gamma_{\rm v}^*}\frac{\mu_* T_{\rm irr}^4}{4}. \tag{115}$$

This expression differs from the semi-grey value of Guillot (2010) by a factor $1/(1-\beta)$ multiplying the first term. Thus, when $\beta \to 1$, the temperature becomes warmer than in the semi-grey case, as seen for the low values of $\gamma_{\rm v}$ in Fig. 10.

Physical interpretation. When $\gamma_{\rm v}^*\tau_{\rm lim} < 1$, most of the flux from the star is absorbed in the deep atmosphere and is principally transported by the channel of lowest opacity (channel 2), even when the width of this channel is smaller than the width of the first thermal channel. Whenever $\beta \to 1$, the width of the second channel decreases. In order to keep transporting most of the thermal flux, the flux per wavelength in the second channel must increase. This increases the temperature where the second channel is optically thick, i.e. in the deep atmosphere. This is equivalent to the *line blanketing effect* that has been well studied in stars (see Milne 1921; Chandrasekhar 1935; Hubeny & Lanz 1995, for example).

5.3.2. Case of shallow absorption of the irradiation flux

When $\gamma_{\rm v}^*\tau_{\rm lim} > 1$ most of the irradiation flux is absorbed in a region where the second thermal channel is optically thin. Thus the flux is carried by the first thermal channel and we have $H_{1,\rm irr}(0) \gg H_{2,\rm irr}(0)$. However, because $\gamma_2 \ll \gamma_1$, we can use Eq. (101b) to show that $(H_{2,\rm irr}(0)/\gamma_2)/(H_{1,\rm irr}(0)/\gamma_1) > \sqrt{\gamma_{\rm P}}/\beta$, which is larger than 1. Thus Eq. (112) remains valid. However, conversely to the case $\gamma_{\rm v}^*\tau_{\rm lim} < 1$, the top boundary condition now reads

$$\begin{aligned} H_1(0) &\approx -H_{\rm v}(0) + H_{2,\rm int} \\ H_2(0) &\approx H_\infty + H_{2,\rm irr}, \end{aligned} \tag{116}$$

where $H_{2,\rm irr}$ is given by Eq. (101b) and $H_{1,\rm int}$ by Eq. (102). This leads to:

$$C_1 = \frac{2}{\gamma_2}\frac{1-\beta}{\sqrt{\gamma_{\rm P}}}(H_\infty - H_{\rm v}(0)) - \frac{2}{\gamma_2\gamma_{\rm v}^*\tau_{\rm lim}}H_{\rm v}(0) - \frac{3}{\gamma_{\rm v}}H_{\rm v}(0). \tag{117}$$

Again, for large values of $\gamma_{\rm P}$, $\gamma_2 \to 1-\beta$ and replacing the fluxes by their equivalent temperatures we get an expression for $T_{\rm deep}$ valid for $\gamma_{\rm v}^*\tau_{\rm lim} > 1$ and $\gamma_{\rm P} > 2$:

$$T_{\rm deep}^4 = \frac{2}{1-\beta}\frac{T_{\rm int}^4}{4} + \frac{2}{\sqrt{\gamma_{\rm P}}}\frac{\mu^* T_{\rm irr}^4}{4} + \left(\frac{3}{\gamma_{\rm v}} + \frac{2}{1-\beta}\frac{1}{\gamma_{\rm v}^*\tau_{\rm lim}}\right)\frac{\mu^* T_{\rm irr}^4}{4}. \tag{118}$$

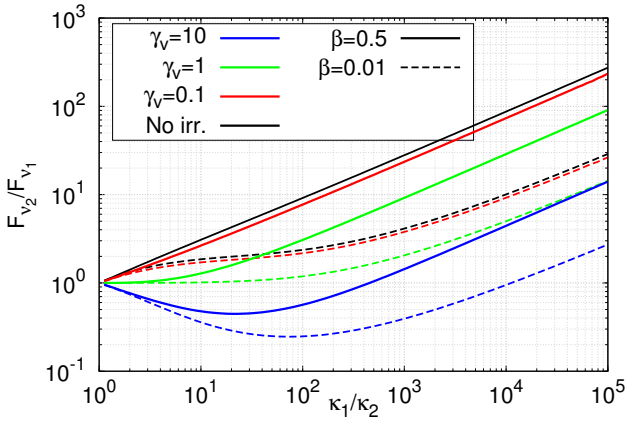

Fig. 11. Ratio of the monochromatic flux in the two bands $F_{\nu_2}/F_{\nu_1} = \beta H_2(0)/(1-\beta)H_1(0)$ in function of the opacity ratio κ_1/κ_2 for different bandwidths β and visible to infrared opacities $\gamma_{\rm v}$. We used $\mu_* = 1/\sqrt{3}$.

When $\gamma_{\rm v}^*\tau_{\rm lim} \gg 1$, the contribution to the deep temperature of the irradiation temperature becomes inversely proportional to $\sqrt{\gamma_{\rm P}}$. As $\gamma_{\rm P} > 1$, the deep temperature is smaller in the non-grey case than in the semi-grey case. This is illustrated by the cases $\gamma_{\rm v} = 10$ and $\gamma_{\rm v} = 100$ in Fig. 10. When $\gamma_{\rm v}^*\tau_{\rm lim} \to 1$, the term in $1/\sqrt{\gamma_{\rm P}}$ becomes very small compared to the term in $1/(1-\beta)$ and the expression converges toward equation Eq. (115), valid for $\gamma_{\rm v}^*\tau_{\rm lim} < 1$.

Physical interpretation. When $\gamma_{\rm v}^*\tau_{\rm lim} \gg 1$, the incident irradiation is absorbed in the upper atmosphere, where only the channel of highest opacity is optically thick. Thus, the channel of highest opacity κ_1 transports all the energy and radiates it directly to space. The incident irradiation is no more transported to the deep atmosphere, leading to a cooler deep atmosphere.

5.4. Outgoing flux

During secondary eclipse observations, the flux emitted by the planet can be observed in different bands (e.g. Seager & Deming 2010). The detection of molecular species in the emission spectrum of an exoplanet depends strongly on the flux contrast between the continuum and the molecular band considered, which in turn depends on the temperature profile. Figure 11 shows the flux per wavelength emitted in the first band ($F_{\nu_1} = 4\pi H_1(0)/\beta$) over the flux per wavelength emitted in the second band ($F_{\nu_2} = 4\pi H_2(0)/(1-\beta)$). This would be the expected contrast in the emission spectrum of the planet between the spectral features and the continuum. For a non-irradiated atmosphere and for low values of $\gamma_{\rm v}$ this is a monotonic function of the opacity ratio κ_1/κ_2. The flux in the band of lowest opacity is always bigger than the flux in the band of highest opacity, i.e. we see absorption bands. For large values of $\gamma_{\rm v}$, whenever a strong temperature inversion happens the absorption bands turn into emission bands. Those different behaviours are captured by the simple expression (100). Note that in all cases, for large values of κ_1/κ_2 we have:

$$\frac{F_{\nu_2}}{F_{\nu_1}} \propto \left(\frac{\kappa_1}{\kappa_2}\right)^{1/2}. \tag{119}$$

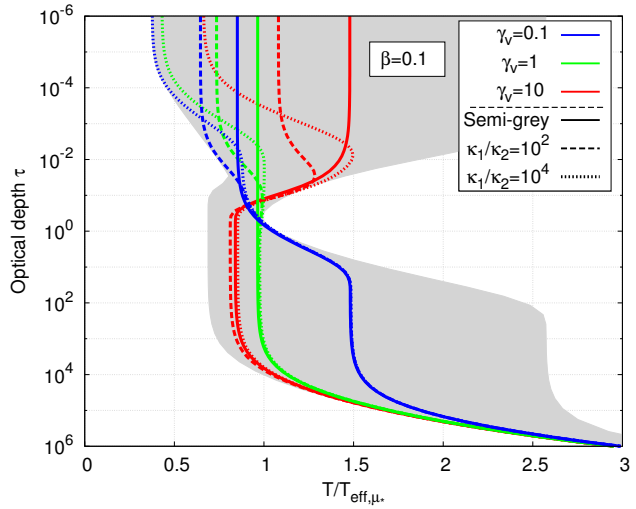

Fig. 12. Pressure/temperature profiles for an irradiated planet ($T_{\rm int} = T_{\rm irr}/10$ and $\mu_* = 1/\sqrt{3}$). The shaded area shows the full range of parameters $10^{-3} < \beta < 10^{-1}$, $1 < R < 10^4$ and $0.01 < \gamma_{\rm v} < 100$. The lines are profiles obtained for $\beta = 0.1$; for $R = 1$ (plain lines), $R = 100$ (dashed lines), and $R = 10^4$ (dotted lines); and for $\gamma_{\rm v} = 0.1$ (blue), $\gamma_{\rm v} = 1$ (green), and $\gamma_{\rm v} = 10$ (red).

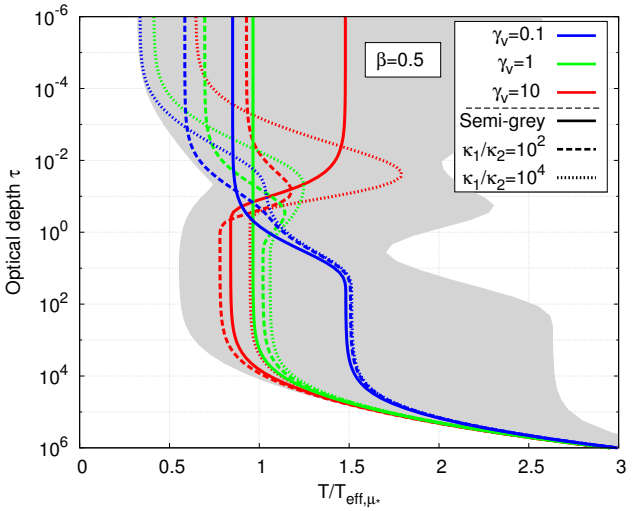

Fig. 13. Pressure/temperature profiles for an irradiated planet ($T_{\rm int} = T_{\rm irr}/10$ and $\mu_* = 1/\sqrt{3}$). The shaded area shows the full range of parameters $0.1 < \beta < 0.9$, $1 < R < 10^4$ and $0.01 < \gamma_{\rm v} < 100$. The lines are profiles obtained for $\beta = 0.5$; for $R = 1$ (plain lines), $R = 100$ (dashed lines), and $R = 10^4$ (dotted lines); and for $\gamma_{\rm v} = 0.1$ (blue), $\gamma_{\rm v} = 1$ (green), and $\gamma_{\rm v} = 10$ (red).

6. Resulting temperature profiles

No matter how strong the non-greyness of the opacities is, there is always a region, at high enough optical depth, where the non-grey solution converges toward the grey solution (see e.g. Fig. 4). The transition between a regime where the grey model is accurate to a regime where the non-grey effects are of prime importance is set by the parameter $\tau_{\rm lim}$. For optical depths lower than $\tau_{\rm lim}$, non-grey effects are always important, whereas for optical depths higher than $\tau_{\rm lim}$, non-grey effects are present only if $\gamma_{\rm v}\tau_{\rm lim} < 1$ and $\beta \rightarrow 1$. Three distinct situations can be observed in Fig. 8. For narrow lines ($\beta < 0.1$), $\tau_{\rm lim}$ is always smaller than one, for larger lines or molecular bands ($0.1 < \beta < 0.9$), $\tau_{\rm lim}$ is close to one, whereas for inverted lines ($0.9 < \beta < 1$), $\tau_{\rm lim}$ can reach much higher values. Thus, when $\gamma_{\rm v} \gg 1$, few non-grey effects are expected in the deep atmosphere, contrary to the cases $\gamma_{\rm v} \approx 1$ and $\gamma_{\rm v} \ll 1$.

In the case of narrow lines ($\beta < 0.1$), only the non-grey cooling of the upper atmosphere is effective. As shown in Fig. 12, the profile remains close to the semi-grey model at large optical depths. However, at low optical depths, for $\tau < \tau_{\rm lim}$, the atmosphere can be much cooler than in the semi-grey case (case $R = 1$). In particular, in the $\gamma_{\rm v} = 10$ case, the non-grey cooling localizes the temperature inversion to a specific layer, contrary to the semi-grey case where it extends to the top of the atmosphere. The envelope of all the profiles (shaded area) is much wider than in the semi-grey case (see Fig. 1).

In the case of large lines or molecular bands ($0.1 < \beta < 0.9$) shown in Fig. 13, both the non-grey cooling of the upper atmosphere and the blanketing effect are important. Whereas the upper atmosphere undergoes an efficient cooling, the lower atmosphere ($\tau > 1$) can experience a significant warming via the blanketing effect. Lowering the ability of the deep atmosphere to cool down efficiently can significantly affect the evolution of the planet (Parmentier & Guillot 2011; Budaj et al. 2012; Spiegel & Burrows 2013; Rauscher & Showman 2013) and could contribute to the radius anomaly of hot-Jupiters (e.g. Guillot & Showman 2002; Laughlin et al. 2011). Whenever $\gamma_{\rm v}^*\tau_{\rm lim} \approx 1$, the stellar irradiation is deposited at a level where non-grey effects lower the ability of the atmosphere to cool down efficiently. This leads to an efficient and localized warming causing a temperature inversion in the profile at $\tau \approx 1/\gamma_{\rm v}^*$, even when none is expected from the semi-grey model (i.e. even when $\gamma_{\rm v}^* < 1$). This happens, for example, when $\beta \approx 0.5$ for $\gamma_{\rm v} = 10$, when $\beta \approx 0.9$ for $\gamma_{\rm v} = 1$, and for $\beta \approx 0.99$ for $\gamma_{\rm v} = 0.1$ (see Fig. 14).

In the case of inverted lines ($\beta > 0.9$), shown in Fig. 14, both the upper temperature and the deep temperature are affected by the non-grey effects. The upper atmosphere cools significantly compared to the semi-grey case. The deep atmosphere can either warm up because of the blanketing effect but, for high values of $\gamma_{\rm v}$ it can also become cooler than in the semi-grey case (see the case $\gamma_{\rm v} = 10$ and $R = 100$ in Fig. 14). Temperatures as cool as $0.5T_{{\rm eff},\mu_*}$ can be reached. This is fundamentally different from the semi-grey case where the deep temperature is always larger than $2^{1/4}T_{{\rm eff},\mu_*}$ (see Fig. 3).

As β increases, $\tau_{\rm lim}$ increases and the blanketing effect disappears. Eventually, when $\beta \rightarrow 1$, the opacities, and thus the profile, become semi-grey again.

In summary, our irradiated picket-fence model can reach the whole temperature range span by the numerical models (see the shaded area in Figs. 12 to 14). Our model should therefore be preferred to classical semi-grey models as an approximate solution for the temperature profile of irradiated atmospheres.

7. Conclusion

We derived an analytic non-grey model to approximate the structure of a plane-parallel irradiated planetary atmosphere. Our model includes both thermal and visible non-grey opacities. The thermal and visible opacities are in the form of a two different picket-fence opacity functions. the thermal opacities are parametrized by the ratio of the visible to the infrared Rosseland mean opacities ($\gamma_{\rm v}$), the ratio of the Planck to the Rosseland mean thermal opacities ($\gamma_{\rm P}$), and the spectral width of the lines (β). The model is valid for any functional form of the

Table 2. Main quantities used in this paper.

Symbol	Quantity	Definition	Units
κ_R	Rosseland mean opacities	Eq. (2)	m^2/kg
κ_P	Planck mean opacities	Eq. (5)	m^2/kg
κ_1	Opacity in the first band	Eq. (8)	m^2/kg
κ_2	Opacity in the second band	Eq. (8)	m^2/kg
β	Relative width of the first band	Eq. (9)	–
κ_v	Opacity in the visible	Eq. (7)	m^2/kg
τ	Rosseland optical depth	Eq. (3)	–
R	Opacity ratio κ_1/κ_2	Sect.3.4	–
γ_1, γ_2, γ_P, γ_v	κ_1/κ_R, κ_2/κ_R, κ_P/κ_R, κ_v/κ_R	Eqs. (12), (13), (6) and (7)	–
τ_{lim}	Limit optical depth	Eq. (15)	Hz
ν	Frequency	–	Hz
μ	cosine of the direction angle θ	–	–
μ_*	cosine of the angle between the vertical and the star	–	–
γ_v^*	γ_v/μ_*	–	–
$I_{\mu\nu}$	Specific intensity at frequency ν and in the direction μ	Chandrasekhar (1960)	$W/m^2/Hz/sr$
J_ν, H_ν, K_ν	First, second, and third momentum of the specific intensity	Eq. (20)	$W/m^2/Hz$
J, H, K	Integrated values of J_ν, H_ν, and K_ν	–	W/m^2
$4\pi H_\infty = \sigma T_{int}^4$	Internal flux from the planet	–	W/m^2
σT_{sub}^4	Stellar flux arriving at the substellar point of the planet	Sect. 3.7	W/m^2
$4\pi H_v(0) = -\sigma\mu_* T_{irr}^4$	Stellar flux that penetrates the modelled atmospheric column	–	W/m^2
$H_{i,irr}$	Contribution of the irradiation to H transported by the ith thermal band	Eq. (99)	W/m^2
$H_{i,int}$	Contribution of the internal luminosity to H transported by the ith thermal band	Eq. (99)	W/m^2
T_{eff}	Effective temperature of the planet	Sect. 2.1	K
T_{eff,μ_*}	Effective temperature of the modelled atmosphere	Sect. 2.1	K
T_{skin}	Temperature at optical depth of zero.	–	K
T_{deep}	Temperature at large optical depth.	Eq. (109)	K
f	Parameter used to calculate dayside and planetary averages	Sect. 3.7	–

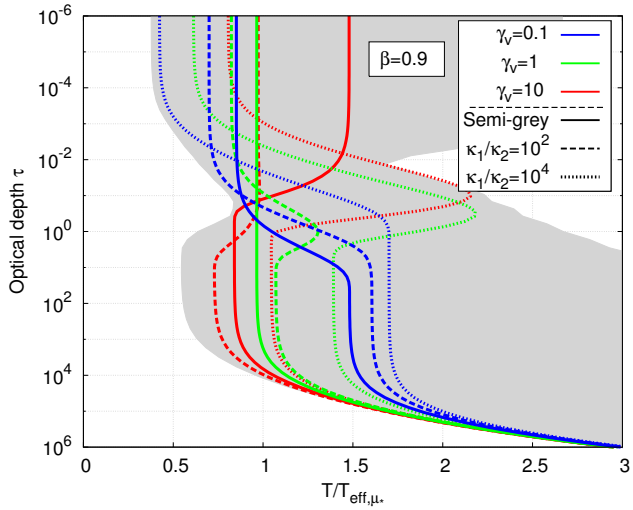

Fig. 14. Pressure/temperature profiles for an irradiated planet ($T_{int} = T_{irr}/10$ and $\mu_* = 1/\sqrt{3}$). The shaded area shows the full range of parameters $10^{-3} < 1-\beta < 10^{-1}$, $1 < R < 10^4$ and $0.01 < \gamma_v < 100$. The lines are profiles obtained for $\beta = 0.9$; for $R = 1$ (plain lines), $R = 100$ (dashed lines), and $R = 10^4$ (dotted lines); and for $\gamma_v = 0.1$ (blue), $\gamma_v = 1$ (green), and $\gamma_v = 10$ (red).

Rosseland mean opacities, the ones obtained from an opacity table for example. However, it cannot account for both realistic Rosseland mean and Planck mean opacities. Their ratio, γ_P and the width of the lines, β, must be held constant through the atmosphere. Although the model is limited to two thermal opacity bands, it can take into account any number of visible opacity bands, each band adding two new parameters, the strength of the band γ_{vi} and its width β_{vi}

Our model solves the inability of previous analytical models to reach temperatures as cold as predicted by the numerical calculations. For opacities dominated by strong and narrow lines ($\beta < 0.1$), non-grey opacities lead to a colder upper atmosphere, but converges toward the grey model at optical depth greater than τ_{lim} (see Fig. 8). For opacities dominated by wide lines, or molecular bands ($\beta \approx 0.5$), non-grey opacities still allow the upper atmosphere to cool down more efficiently, but also inhibit the cooling of the deep atmosphere. In that case, a significant warming of the deep atmosphere can happen, down to optical depths much greater than τ_{lim}. This planetary *blanketing effect* could contribute to the radius anomaly of hot Jupiters.

Temperature inversions that were not predicted by previous analytical models occur whenever $\gamma_v^*\tau_{lim} \approx 1$ because of the interaction between the incoming stellar irradiation and the non-grey thermal opacities. These could have interesting observational consequences.

We show that the internal flux is always transported by the spectral channel of lowest opacity. Conversely, the absorbed irradiation flux is transported by the spectral channel of lowest opacity only when $\gamma_v^*\tau_{lim} < 1$. For values of γ_v^* larger than τ_{lim}^{-1}, it is transported by the spectral channel of highest opacity.We provide simple analytical expressions for the outgoing thermal flux in the different spectral bands.

Finally, our model allows for a much greater range of temperature profiles than other analytical and semi-analytical solutions of the radiative transfer equations for irradiated atmospheres. We encourage the community to use it when fast calculations of atmospheric temperature profiles are needed. Given

the apparent complexity of the solution, a code is available at the CDS or at ww.oca.eu/parmentier/nongrey.

Acknowledgements. This work was performed in part thanks to a joint Fulbright Fellowship to V.P. and T.G. The whole project would not have been possible without the help and support of Douglas Lin. We also acknowledge Jonathan Fortney and Mark Marley for many useful discussions, and the University of California Santa Cruz for hosting us while this work was carried out.

References

Avrett, E. H., & Krook, M. 1963, ApJ, 137, 874
Budaj, J., Hubeny, I., & Burrows, A. 2012, A&A, 537, A115
Burrows, A., Marley, M., Hubbard, W. B., et al. 1997, ApJ, 491, 856
Burrows, A., Hubeny, I., Budaj, J., Knutson, H. A., & Charbonneau, D. 2007, ApJ, 668, L171
Chandrasekhar, S. 1935, MNRAS, 96, 21
Chandrasekhar, S. 1960, Radiative transfer (New york: Dover Publications)
Chevallier, L., Pelkowski, J., & Rutily, B. 2007, J. Quant. Spectr. Radiat. Transf., 104, 357
Eddington, A. S. 1916, MNRAS, 77, 16
Fortney, J. J., Lodders, K., Marley, M. S., & Freedman, R. S. 2008, ApJ, 678, 1419
Guillot, T. 2010, A&A, 520, A27
Guillot, T., & Havel, M. 2011, A&A, 527, A20
Guillot, T., & Showman, A. P. 2002, A&A, 385, 156
Hansen, B. M. S. 2008, ApJS, 179, 484
Heng, K., Menou, K., & Phillipps, P. J. 2011, MNRAS, 413, 2380
Heng, K., Hayek, W., Pont, F., & Sing, D. K. 2012, MNRAS, 420, 20
Hubeny, I., & Lanz, T. 1995, ApJ, 439, 875
Hubeny, I., Burrows, A., & Sudarsky, D. 2003, ApJ, 594, 1011
King, I. J. I. F. 1955, ApJ, 121, 711
King, J. I. F. 1956, ApJ, 124, 272
Krook, M. 1963, ApJ, 137, 863
Laughlin, G., Crismani, M., & Adams, F. C. 2011, ApJ, 729, L7
Line, M. R., Zhang, X., Vasisht, G., et al. 2012, ApJ, 749, 93
Matsui, T., & Abe, Y. 1986, Nature, 322, 526
Meador, W. E., & Weaver, W. R. 1980, Journal of Atmospheric Sciences, 37, 630
Mihalas, D. 1978, Stellar atmospheres, 2nd edn. (W.H. Freeman and Co.)
Mihalas, D., & Mihalas, B. W. 1984, Foundations of radiation hydrodynamics (New york: Oxford University Press)
Miller-Ricci, E., & Fortney, J. J. 2010, ApJ, 716, L74
Milne, E. A. 1921, MNRAS, 81, 510
Mordasini, C., Alibert, Y., Georgy, C., et al. 2012a, A&A, 547, A112
Mordasini, C., Alibert, Y., Klahr, H., & Henning, T. 2012b, A&A, 547, A111
Münch, G. 1946, ApJ, 104, 87
Parmentier, V., & Guillot, T. 2011, in EPSC-DPS Joint Meeting 2011, 1367
Pierrehumbert, R. T. 2010, Principles of Planetary Climate (Cambridge: University Press)
Pujol, T., & North, G. R. 2003, Tellus A, 55, 328
Rauscher, E., & Menou, K. 2013, ApJ, 764, 103
Rauscher, E., & Showman, A. P. 2013, ApJ, submitted [arXiv:1309.7052]
Robinson, T. D., & Catling, D. C. 2012, ApJ, 757, 104
Rutily, B., Chevallier, L., Pelkowski, J., & Bergeat, J. 2008, J. Quant. Spectr. Radiat. Transf., 109, 28
Saumon, D., Hubbard, W. B., Burrows, A., et al. 1996, ApJ, 460, 993
Seager, S., & Deming, D. 2010, ARA&A, 48, 631
Shaviv, N. J., Shaviv, G., & Wehrse, R. 2011, Icarus, 216, 403
Showman, A. P., Fortney, J. J., Lian, Y., et al. 2009, ApJ, 699, 564
Spiegel, D. S., & Burrows, A. 2013, ApJ, 772, 76
Unno, W., & Yamashita, Y. 1960, PASJ, 12, 157
Weaver, C. P., & Ramanathan, V. 1995, J. Geophys. Res., 100, 11585

2.3 Analytical vs. numerical results: building a reliable atmospheric model

More than a thousand exoplanets have been discovered with a large diversity in terms of composition, temperature and gravity. Atmospheric physics can now be applied to atmospheres with a continuum range of gravity and temperatures. Reliable and fast atmospheric models are necessary to investigate this diversity. Semi-grey analytical models of the thermal structure of planetary atmospheres have been used for this purpose, for example to study the chemistry (Miguel & Kaltenegger 2014), the dynamics (Rauscher & Menou 2013) or the thermal evolution (Rauscher & Showman 2014) of irradiated planets. Current analytical models do not provide a reliable method to determine the parameters describing the opacities. A wrong choice of models parameters can, however, have dramatic consequences on the validity of the calculated thermal profile.

In the following paper submitted to *Astronomy & Astrophysics* (Parmentier et al. 2014a) we use a state-of-the-art numerical model to understand what characteristics of the line-by-line opacities affect the thermal structure of the planet. by calibrating the coefficients of our analytical non-grey model we provide a reliable, fast model that can predict the thermal structure of solar-composition atmospheres within a large range of equilibrium temperature and planet gravity.

Astronomy & Astrophysics manuscript no. Parmentier2013c
April 12, 2014

A non-grey analytical model for irradiated atmospheres.

II: Analytical vs. numerical solutions

Vivien Parmentier[1,2], Tristan Guillot[1,2], Jonathan J. Fortney[2], and Mark S. Marley[3]

[1] Laboratoire J.-L. Lagrange, Université de Nice-Sophia Antipolis, CNRS, Observatoire de la Côte d?Azur, BP 4229, 06304 Nice, France e-mail: vivien.parmentier@oca.eu

[2] Department of Astronomy and Astrophysics, University of California, Santa Cruz, CA 95064, USA
[3] NASA Ames Research Center, MS-245-3, Mofett Field, CA 94035

in preparation

ABSTRACT

Context. The recent discovery and characterization of the diversity of the atmospheres of exoplanets and brown dwarfs calls for the development of fast and accurate analytical models.
Aims. We wish to assess the goodness of the different approximations used to solve the radiative transfer problem in irradiated atmospheres analytically and provide a useful tool for a fast computation of analytical temperature profiles that remains correct over a wide range of atmospheric characteristics.
Methods. We quantify the accuracy of the analytical solution derived in paper I for an irradiated, non-grey atmosphere by comparing it to a state-of-the-art radiative transfer model. Then, using a grid of numerical models, we calibrate the different coefficients of our analytical model for irradiated solar-composition atmospheres of giant exoplanets and brown dwarfs.
Results. We show that the so-called Eddington approximation used to solve the angular dependency of the radiation field leads to relative errors of up to $\sim 5\%$ on the temperature profile. For grey or semi-grey atmospheres (i.e. when the visible and thermal opacities respectively can be considered as independent of wavelength), we show that the presence of a convective zone has a limited effect on the radiative atmosphere above it and leads to modifications of the radiative temperature profile of order $\sim 2\%$. However, for realistic non-grey planetary atmospheres, the presence of a convective zone that extends to optical depths smaller than unity can lead to changes in the radiative temperature profile of the order of 20% or more. When the convective zone is located at deeper levels (such as for strongly irradiated "hot Jupiters"), its effect on the radiative atmosphere is again of the same order ($\sim 2\%$) as in the semi-grey case. We show that when a strong absorber in the visible, such as TiO/VO, is present in the upper atmosphere, it decreases significantly the deep atmospheric temperature by lowering the "blanketing effect", an intrinsically non-grey effect. Finally, we provide a functional form for the coefficients of our analytical model for solar-composition giant exoplanets and brown dwarfs. This leads to fully analytical pressure–temperature profiles for the radiative part of the atmospheres with a relative accuracy better than 10% for gravities between 2.5 and 250m s^{-2} and effective temperatures between 100 and 3000 K. This is a great improvement compared to the commonly used "Eddington boundary condition".

Key words. extrasolar giant planets – planet formation

1. Introduction

The large diversity of exoplanets in terms of irradiation temperature, gravity, chemical composition discovered around stars with different properties call for the development of fast, accurate and versatile atmospheric models.

In paper I (Parmentier & Guillot 2013), we derived a new analytical model for irradiated atmospheres. Unlike previous models, our model takes into account non-grey opacities both in the visible and in the thermal frequency ranges. Using two different opacity bands in the thermal frequency range, we highlighted the dual role of thermal non-grey opacities in shaping the thermal structure of the atmosphere. Opacities dominated by lines (i.e. opacities where the lowest of the two values is dominant) enable the upper atmosphere to cool down significantly compared to a grey atmosphere whereas opacities dominated by bands (i.e. opacities where the highest of the two values is dominant) lead both to a significant cooling of the upper atmosphere and a significant heating of the deep atmosphere.

Send offprint requests to: V.Parmentier

The pressure and temperature dependent line-by-line opacities that are used in numerical models to compute accurate temperature profiles are represented in analytical models by only a handful of parameters. Thus, to compute accurate temperature structure from our analytical model for specific planets atmospheres, we need to know how those parameters vary with the physical properties of the planet.

In this study, we apply our model to irradiated, solar-composition, semi-infinite atmospheres e.g., brown dwarfs, giant planets or planets with a surface situated in the optically thick region of the atmosphere. Based on the results from a state-of-the-art numerical model, we assess the goodness of the different approximations inherent in analytical solutions of the radiative transfer equations. Then, using a grid of numerical models, we calibrate the different coefficients of our analytical model and provide a useful tool for a fast computation of analytical temperature profiles for planet atmospheres that remains correct over a wide range of gravity and irradiation temperatures.

As a first step, in Sec. 3 we quantify the accuracy of models derived with the Eddington approximation, a common simplifi-

cation of the radiative transfer equations in analytical model atmospheres. Then in Sec. 4 we build a simple radiative/convective model where the radiative solution of Paper I is replaced by a convective solution whenever the Schwarzschild criterion is verified. We further discuss and quantify the intrinsic error of such a simple model of convective adjustment. Finally, guided by a state-of-the art numerical integration of the radiative transfer equations, we contrain the parameters of the analytical solution of Paper I to develop a fully analytical solution for the atmospheric temperature/pressure profiles of irradiated giant planets. The solution presented in section 5 reproduces with a 10% accuracy the numerical solutions over a wide range of gravity and irradiations.

2. Models

2.1. Setting

We consider the case of a planet with a thick atmosphere (i.e. a planet with no surface or with a surface at very high optical depth) orbiting at a distance a from its host star of radius R_* and effective temperature T_*. At the substellar point, the atmosphere receives a flux $\sigma T_{\rm sub}^4$ where the substellar temperature is defined as:

$$T_{\rm sub}^4 \equiv T_*^4 \left(\frac{R_*}{a}\right)^2 \tag{1}$$

which is the same as the $T_{\rm irr}$ quantity defined in Guillot (2010). In this paper we define $T_{\rm irr}$ by:

$$T_{\rm irr}^4 \equiv (1-A) f T_*^4 \left(\frac{R_*}{a}\right)^2 \tag{2}$$

where A is the Bond albedo of the planet and f is a parameter modulating the flux received by the planet, useful to compute profiles averaged in latitude and longitude. To first order, planets are spherical and the effective irradiation that a column of atmosphere receives depends on its location on the planet. Thus, the flux that penetrates the modeled slice of atmosphere is given by $\sigma T_{\mu_*}^4$ with:

$$T_{\mu_*}^4 \equiv \mu_* T_{\rm irr}^4 = (1-A)\mu_* f T_*^4 \left(\frac{R_*}{a}\right)^2 \tag{3}$$

where $\mu_* = \cos\theta_*$ and θ_* the inclination of the stellar irradiation with respect to the local vertical direction. The combination of μ_* and f can lead to different mean atmospheric profiles. For example, the substellar point profile is obtained by setting $f = 1$ and $\mu_* = 1$ whereas the dayside average profile is obtained for $\mu_* = 1/\sqrt{3}$, $f = 0.5$ and the planet average profile for $\mu_* = 1/\sqrt{3}$ and $f = 0.25$ (see Guillot 2010). Moreover the planet has an internal flux $F_{\rm int} = \sigma T_{\rm int}^4$ which leads to the definition the effective temperature

$$T_{{\rm eff},\mu_*}^4 = T_{\mu_*}^4 + T_{\rm int}^4 \tag{4}$$

2.2. Opacities

The interaction between photons and atmospheric gas is described by opacities which are functions of the wavelength of the irradiation considered and the temperature, pressure and composition of the gas. Although the variety of mixtures and cases to be considered is infinite, we choose to limit the present study to one set of opacities because of its very extensive use both in the context of giant exoplanets and brown dwarfs, i.e. the solar-composition opacities provided by Freedman et al. (2008). These

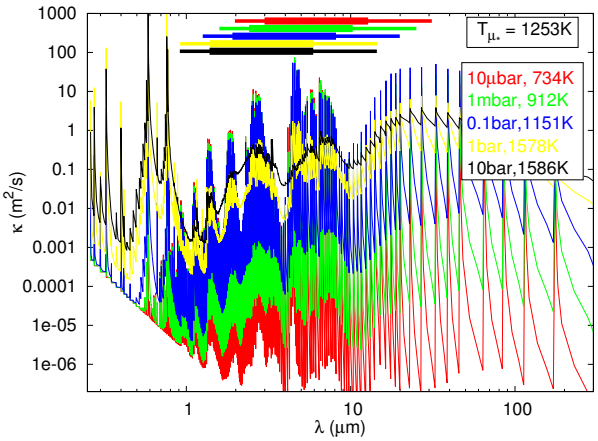

Fig. 1: Line by line opacities in function of wavelength for five different conditions corresponding to different points in the PT profile of a giant planet with $g = 25$ m/s^2, $\mu_* = 1/\sqrt{3}$, $T_{\rm int} = 100$ K and $T_{\mu_*} = 1253$ K, corresponding to the dayside average profile of a planet orbiting at 0.53 AU from a sun-like star. Inside each bin of frequency, we plot the cumulative distribution function of the opacities instead of the line-by-line opacity function.

opacities have been calculated for a solar-composition mixture in chemical equilibrium. They do not account for the presence of clouds, and any chemical species that condenses at a given temperature and pressure is taken out of the mixture. Although clouds are though to exist in planets atmospheres (see Marley et al. 2013, for a review) and should affect the thermal structure of their atmosphere (e.g., Heng et al. 2012), we do not take into account scattering by cloud particles in this study. However, the first order effect of clouds is to reflect part of the incoming stellar light to the space, which is taken into account in the albedo when calculating the irradiation temperature with eq. (2).

While tens of millions of lines have been used for the calculation of these opacities, we choose to show them in fig. 1 in the same form as they are used by the numerical code described hereafter in Section 2.4: In the so-called correlated-k method, the opacities values are sorted from the lowest to the highest values within a limited number of spectral bins (in our case 196). As long as the spectral bins are small compared to the width of the local Planck function, the error made on the wavelength corresponding to a given opacity is expected to be small and the consequences for the computed temperature profile limited (see Goody & Yung 1989).

Figure 1 thus provides the opacities for different pressure and temperature points taken along a selected planetary temperature/pressure profile corresponding approximately to a solar composition 1-Jupiter mass and radius planet at 0.05 AU from a Sun-like star. The wavelength range in which the Planck function has 90% and 99% of the total energy is shown by the thick and thin horizontal bars, respectively, for the different temperatures considered. The contribution of the spectral lines to the opacities shapes the cumulative distribution function inside each bin. As one moves progressively from the top to the bottom of the atmosphere, pressure (always) and temperature (generally) increase which broadens the spectral line profiles. This results in a flattening of the cumulative opacity distribution function within each bin. Opacities in the high atmosphere are characterized by very strong variations with wavelength and a comb-like struc-

ture. Deeper-down, the wavelength dependence is mostly due to the presence of molecular bands and takes place on scales significantly larger than our bin size.

An important feature of these opacities is that most of the variations of the opacity with wavelength take place on scales shorter than the characteristic wavelength range of the Planck function. This is certainly the case at low-pressures when the opacity varies extremely quickly with wavelength, but it remains true (to some extent) at high pressures in the band regime. Another feature of irradiated atmospheres is that the temperature variations remain limited so that there is always a significant overlap between the Planck function from the low to the high optical depth levels. These two features justify the use of the picket-fence approximation, and hence of the analytical model of Paper I.

2.3. Analytical model

Although analytical models of irradiated atmospheres can only be obtained for very restrictive approximations on the opacities, they provide nonetheless a useful tool to understand the physics of the radiative transfer and to compute with a low computational cost temperature profiles for a large variety of atmospheric properties. In the particular model derived in Paper I the line by line opacities are modeled by two different homogeneous set of lines, the full opacity function being described by 6 independent parameters.

The first set of lines, described by three parameters, represents the thermal part of the opacities, i.e.the part of the opacity function in the frequency range covered by the local Planck function of the atmospheric thermal emission. The Rosseland mean opacity $\kappa_R(P,T)$ is the only one of those parameters that can vary with depth in the atmosphere. In particular, it is the relevant opacity to describe accurately the energy transport in the optically thick part of the atmosphere (Mihalas 1984). The other two parameters describe the non-grayness of the opacities, i.e. their variation in frequency. The first one, γ_p is the ratio of the Planck mean opacity to the Rosseland mean opacity, where the Planck mean opacity is dominated by the highest values of the opacities whereas the Rosseland mean is dominated by he lowest values of the opacities. Thus, grey opacities have $\gamma_p = 1$ and any departure from the grey model increases γ_p. The second parameter, β, is the relative width of the opacity lines. Values of β lower than 0.1 represents opacities dominated by atomic lines whereas values of β between 0.1 and 0.9 correspond to opacities dominated by molecular bands. In the following sections, the parameter γ_p will sometimes be replaced by an equivalent parameter : κ_1/κ_2, where κ_1 is the highest of the two opacities and κ_2 the lowest. Value of κ_1/κ_2 between $10^4 - 10^5$ in the upper atmosphere and between $10 - 100$ in the deep atmosphere can be estimated from Fig. 1 for a typical hot-Jupiter. The simple relationship between κ_1/κ_2 and γ_p is described by eq. (87) of Paper I.

The second set of lines, described by three other parameters, represents the visible parts of the opacities, i.e. the part of the opacity function in the frequency range covered by the Planck function of the stellar irradiation. Since the planet's atmosphere is usually cooler than the stellar photosphere, the two set of opacity lines can be considered as independent of each other. The first two parameters, γ_{v1} and γ_{v2} are the ratio of the the highest (resp. lowest) opacity of the line to the thermal Rosseland mean opacity. These ratios set the strength of the greenhouse effect and the presence of a thermal inversion. The last parameter, β_v, describes the relative width of the two visible opacity bands, $\beta_v = 1$ being grey visible opacities described by γ_{v1}. Whereas the model cannot take into account more than two thermal opacity bands, it can model as many visible bands as needed.

In our analytical model, the Rosseland mean opacity can vary with pressure and temperature. Thus, physical processes producing an overall increase of the opacities, such as the increasing importance of the collision induced absorption with pressure can be accurately taken into account. Our model is the first analytical model to take into account non-gray thermal opacities in irradiated atmosphere. However, the variation of the opacity with frequency cannot change through the atmosphere. Thus, all the other coefficients must remain constant in the whole atmosphere and a physical phenomenon such as the variation of the pressure or thermal broadening of the lines through the atmosphere cannot be taken into account.

2.4. Numerical model

Whereas analytical models are confined to model atmospheres with very simplified opacities, the radiative transfer equations can be solved by numerical integration using the full, line-by-line, frequency, pressure-and temperature-dependent opacities described in section 2.2. Moreover, numerical models can integrate the radiative transfer equations by taking into account an arbitrary high number of angular directions, with no need to invoke the Eddington approximation.

Here, we use the EGP (Extrasolar Giant Planet) code initially developed by McKay et al. (1989) for the study of Titan atmosphere. Since then, it has been extensively modified and adapted for the study of giant planets (Marley & McKay 1999), brown dwarfs (Marley et al. 1996, 2002; Burrows et al. 1997), and hot Jupiters (e.g., Fortney et al. 2005, 2008; Showman et al. 2009). The version of the code we employ solves the radiative transfer equations using the the ""delta-discrete ordinates"" method of Toon et al. (1989) for the incident stellar radiation and the ""two-stream source function"" method, also of Toon et al. (1989), for the thermal radiative transfer. In some cases incident stellar and emitted thermal radiation bands may overlap, but the radiative transfer is solved separately for each radiation source. Opacities are treated using the correlated-k method (e.g., Goody & Yung 1989). We consider 196 frequency bins ranging from 0.26 to 300 μm; within each bin, the information of typically 10,000 to 100,000 frequency points is compressed inside a single cumulative distribution function that is then interpolated using 8 k-coefficients. The angular dependency is computed using the Gauss quadrature formula for the fluxes. θ being the angular variable, this formula allows to transform an integral over $\mu = \cos\theta$ into a simple sum over angles:

$$\int_{-1}^{1} \mu I_v(\mu)\, \mathrm{d}\mu = \sum_{i=1}^{n} \omega_i I_v(\mu_i) \tag{5}$$

with the ω_i and the μ_i being tabulated in Abramowitz & Stegun (1965). Here we use 5 Gauss points. The EGP model calculates a self-consistent radiative/convective solution, deriving the adiabatic gradient using the equation of state of Saumon et al. (1995) but can also look for a fully radiative solution.

Although numerical models were built in order to incorporate the full complexity of the opacity function, it can nonetheless solve the radiative transfer equations with the same simplifications than the ones used in the analytical models. In particular, the k-coefficient method can be used to easily implement the simplified opacities of Parmentier et al. (2013) by setting a given number of k-coefficients at κ_1 and the other ones at κ_2 in

each frequency bin. Moreover, the opacities used to compute the absorption of the stellar flux can be independent from the opacities used to compute the thermal fluxes and we can also use the same visible opacities as in the analytical case.

2.5. Comparison to an asymptotically exact solution

In order to test the validity of the radiative solution found by the numerical model, we compare it to the analytical solution obtained by the method of discrete ordinates in the grey case (Chandrasekhar 1960). This method solves the radiative transfer equations with grey opacities for a non-irradiated atmosphere by replacing the integrals over angle by a gaussian sum. By increasing the number of terms in the sum (i.e. the order of the calculation), it converges towards the exact solution. The first order solution being equivalent to the Eddington approximation.

In fig. 2, we compare the numerical model for the grey, non-irradiated case to these analytical solutions up to the 5th order. The first order analytical solution deviates from the others and from the numerical result by about 2% with the maximum deviation occurring near optical depth unity. We can therefore expect the analytical models based on the Eddington approximation to differ from the exact results by about this value at least – we will come back to that in section 3. The higher order analytical solutions appear to smoothly converge towards the exact solution, but the numerical solution is found to be about $\sim 0.5\%$ warmer at low optical depths. This discrepancy arises from a different use of the Gaussian quadrature formula in the two approaches. Whereas the analytical solution uses the gaussian quadrature to compute the integral $\int_{-1}^{1} I_\nu(\mu)\,\mathrm{d}\mu$, the numerical code uses the quadrature formula to compute the flux integral $\int_{-1}^{1} \mu I_\nu(\mu)\,\mathrm{d}\mu$. Therefore, the 5^{th} order analytical solution is formally not the same as the 5 Gauss points numerical model and does not converge toward the same solution. We tested that using 8 Gauss points in the numerical model leads to a solution that is correct to 0.1% when compared to the 8^{th} order analytical solution.

Because a 0.5% error is significantly smaller than the other sources of uncertainties in the model (the first one being due to the use of the Eddington approximation) and because of convergence problems arising in the 8 Gauss points model, we chose to only use the 5 Gauss points numerical model. We note that this kind of test is unfortunately not possible in the irradiated case (even in the grey approximation) for which no exact analytical solution is known.

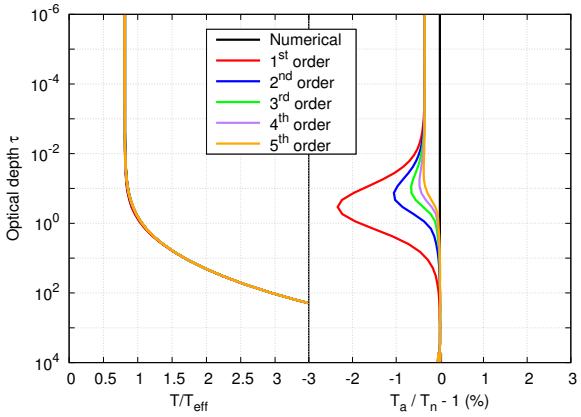

Fig. 2: Radiative numerical temperature profile in units of effective temperature as a function of optical depth compared to the analytical solution from Chandrasekhar (1960) using the discrete ordinate in the first, second, third, fourth and fifth approximation. The left panel shows the profiles whereas the right panel shows their relative difference ($T_\mathrm{a}/T_\mathrm{n} - 1$ where T_a is the analytical solution and T_n is the numerical solution).

3. Consequences of the Eddington approximation

We have seen in section 2.5 that an asymptotically exact solution of the radiative transfer problem can be found in the grey, non-irradiated case. Unfortunately, such a solution does not exist when accounting for external irradiation. The angle dependency of the radiative transfer problem therefore has to be approximated. Analytical models such as that of Paper I use a closure relation between two moments of the intensity field $I_\nu(\mu)$ (with ν the frequency of the radiation):

$$\int_{-1}^{1} I_\nu(\mu)\mu^2\,\mathrm{d}\mu \approx \frac{1}{3}\int_{-1}^{1} I_\nu(\mu)\,\mathrm{d}\mu. \tag{6}$$

This approximation is exact in two specific cases: when the radiation field is isotropic ($I_\nu(\mu) = \mathrm{cte}\ \forall\mu$) and when radiation field is semi-isotropic ($I_\nu(\mu) = I^+ \forall \mu > 0$ and $I_\nu(\mu) = I^- \forall \mu < 0$). In the deep atmosphere, the radiation is quasi-isotropic and this approximation holds. Toward the top of the atmosphere, most of the thermal radiation comes from the deep layers and is therefore close to be semi-isotropic. In-between, the solution is only approximative. In addition, a boundary condition relating two other moments of the intensity field must be adopted :

$$\int_{-1}^{1} I_\nu(\mu)\mu\,\mathrm{d}\mu\Big|_{top} \approx f_\mathrm{H}\int_{-1}^{1} I_\nu(\mu)\,\mathrm{d}\mu\Big|_{top}. \tag{7}$$

These two conditions form what is called the Eddington approximation.

In the grey, non-irradiated case, those two approximations are linked and $f_\mathrm{H} = 1/2$. However using equation 6 and imposing $f_\mathrm{H} = 1/\sqrt{3}$ leads to the exact solution at the top of the atmosphere, even though it lacks of self-consistency. In the irradiated case and in the non-grey case the two approximations are independent and f_H is usually set to either $1/2$ or $1/\sqrt{3}$, following the grey, non-irradiated case (see Paper I, for a complete discussion).

As discussed in section 2.5, the relative uncertainty on the temperature profile resulting from the Eddington approximation is $\sim 2\%$ in the grey, non-irradiated case. In order to estimate its magnitude in the grey and non-grey irradiated cases, we must rely on comparison with numerical models. We hereafter adopt the EGP numerical model with 5 Gauss points shown to be a very good approximation to the exact solution.

Now we compare the radiative solutions from our numerical model and different analytical models using the simplified opacities described in Sec. 2.3. Thus the solution can be expressed in function of the Rosseland optical depth τ only and is independent of the Rosseland mean opacity or of the gravity. Once normalized by the effective temperature, the temperature in function of the optical depth in each model only depends on the values of γ_v,γ_p (or κ_2/κ_1), β and the ratio $T_\mathrm{irr}/T_\mathrm{int}$.

3.1. Irradiated semi-grey solutions

In the grey and semi-grey cases, several analytical models have been developed (Chandrasekhar 1960; Hansen 2008; Guillot 2010; Robinson & Catling 2012). As reviewed in Paper I, those models differ mainly by their choice of $f_{\rm H}$ and their choice of the upper boundary condition. For simplicity, we will compare only three of them: the two different versions of Guillot (2010) (with $f_H = 1/2$ or $f_H = 1/\sqrt{3}$) and the semi-grey limit of the model derived in Paper I with $f_{\rm H} = 1/2$ which uses as upper boundary condition a mix between the model of Guillot (2010) and the one of Hansen (2008). We compare those models for two different values of the main parameter of semi-grey models: the ratio of the visible to the thermal opacities, $\gamma_{\rm v}$.

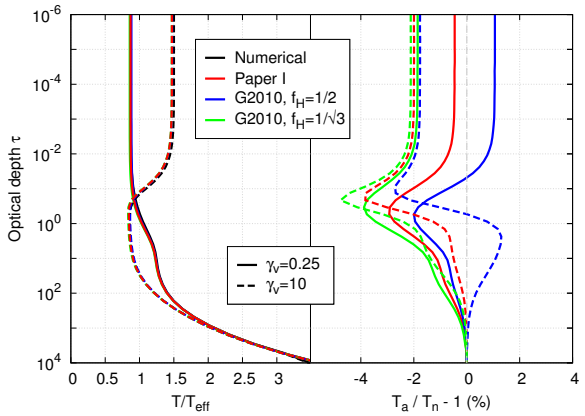

Fig. 3: Comparison between the radiative numerical solution (black line), our work (red line) and Guillot (2010) model for two different values of $f_{\rm H}$ (blue and green lines) for a fully radiative semi-grey atmosphere with $\gamma_{\rm v} = 0.25$ (plain lines) or $\gamma_{\rm v} = 10$ (dashed lines). We set $\mu_* = 1/\sqrt{3}$, $T_{\rm irr} = 1288$ K and $T_{\rm int} = 500$ K.

Figure 3 compares these models for a typical irradiated Jupiter-mass exoplanet close to a solar-type star and shows the magnitude of the error which is due to the Eddington approximation – both the closure relation defined by eq. (6) and the adopted value of $f_{\rm H}$ – and the chosen upper boundary condition, different between Guillot (2010) and Paper I. The left panel shows the temperature profiles as a function of optical depth which mainly depends on the magnitude of the greenhouse effect: when $\gamma_{\rm v}$ is small, most of the incoming irradiation is absorbed deep in the atmosphere, the temperature increases monotonously with increasing depth, and the solution behaves like the non-irradiated solution with the same effective temperature (see the 1^{st} order case of Fig. 2). When $\gamma_{\rm v}$ is large, most of the incoming stellar light is absorbed high up, creating a temperature inversion around visible optical depth unity (and thus thermal optical depth $\tau = 1/\gamma_{\rm v}$).

The right panel of fig. 3 shows that the magnitude of the difference between the numerical solution and the analytical ones strongly depends on the choice of $f_{\rm H}$ and of the top boundary condition, but remains of the same order-of-magnitude as for the non-irradiated grey case of section 2.5. Specifically, the Eddington approximation is found to lead to a $\sim 4\%$ uncertainty on the temperature profile and always converges towards zero at large optical depths. Except for the $f_H = 1/\sqrt{3}$ solution, all other analytical solutions, including the one from Paper I, systematically underestimate the temperature at a given depth.

It is obvious from fig. 3 that, unlike the non-irradiated case, no choice of $f_{\rm H}$ can yield an exact skin temperature $T(\tau = 0)$ (see related discussion in Paper I).

3.2. Irradiated non-grey solutions

We now test the analytical model of Paper I in the non-grey case. In order to do so, we compare the analytical model to the numerical model for different values of the ratio of the thermal opacities κ_2/κ_1 and a single visible channel to the numerical model with the same thermal and visible opacities. We adopt $\beta = 0.86$ and $\gamma_{\rm v} = 0.25$, typical values needed to reproduce detailed models of hot Jupiters (see section 5 hereafter) and the same irradiation and internal temperature as in the previous section.

Figure 4 shows the resulting temperature-optical depth profiles and the relative difference between the numerical and analytical solutions. As κ_2/κ_1 increases, the temperature profile gets cooler in the upper atmosphere and warmer in the deep atmosphere, an effect described in details in Paper I.

The red curve ($\kappa_2/\kappa_1 = 1$) corresponds to the semi-grey solution already seen in section 3.1 and fig. 3. As shown in the right panel, the discrepancy between the analytical and numerical models increases with the "non-greyness" of the opacities. The maximum error (in absolute terms) increases from about $\sim 2\%$ to a little bit less than $\sim 5\%$ when κ_2/κ_1 is increased from 1 to 10^5. Moreover, the optical depth range for which the discrepancy is larger than say 1% increases in the same time from $[0.1 \sim 10]$ to $[10^{-5} \sim 10^3]$.

This increase in the extent of the region in which the temperature profile departs from the numerical solution is a direct consequence of the Eddington approximation in the two thermal channels with opacities κ_1 and κ_2 respectively: At high optical depth, in the diffusion limit, the radiation field is isotropic in each thermal channel and the Eddington approximation is valid. At very low optical depth radiation comes mostly from the levels where the first and the second thermal channels become optically thin, much deeper in the atmosphere. Therefore radiation in the optically thin layers is close to be semi-isotropic which validates the choice of the Eddington approximation. Inbetween, the difference between the analytical and the numerical solutions exhibits two maxima. Those maxima correspond to the levels where the first and the second thermal bands become optically thin. As the ratio κ_1/κ_2 increases, the first channel becomes optically thin at higher Rosseland optical depth and the second channel becomes optically thin at lower Rosseland optical depth, creating the two-peak feature of Fig. 4.

We see however that the error induced by the Eddington approximation remains lower than 5%, with the deep temperatures being colder in the analytical model than in the numerical model. Compared to other sources of uncertainty (in particular our assumptions that β and κ_2/κ_1 are uniform in the atmosphere), this is an acceptable level of uncertainty.

4. Consequences of convection on the overlaying radiative solution

At high-enough optical depth, the deep atmospheres of giant planets and brown dwarfs become convective (e.g., Guillot 2006), a consequence of the increase of the opacity with pressure (see Rauscher & Menou 2012). This increase of the opacity in substellar atmospheres is due both to collision-induced ab-

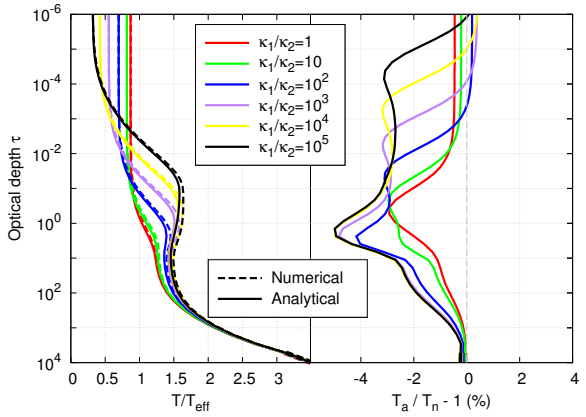

Fig. 4: Comparison between the analytical model (plain lines) and the radiative numerical model (dashed lines) for different values of κ_2/κ_1 (left panel). The right panel shows the relative difference between the analytical and the numerical solution for each case. We used $\mu_* = 1/\sqrt{3}$, $T_{\rm irr} = 1288$ K, $T_{\rm int} = 500$ K, $\gamma_{\rm v} = 0.25$ and $\beta = 0.86$.

sorption by hydrogen molecules increasing with density (above roughly 10^{-3}g cm^{-3}) and eventually to new opacity sources linked to a larger abundance of electrons at temperatures $\sim$ 2000 K and above. Generally, exoplanets and brown dwarfs with low-irradiation levels (i.e. such that $T_{\rm irr} \lesssim T_{\rm int}$) have a convective zone extending all the way from the deep interior to the $\tau \sim 1$ optical depths. This is for example the case of Jupiter, whose atmosphere becomes convective at pressures of order $P \sim 0.3$ bar – but with considerable heterogeneity depending on the latitude and longitude on the planet (e.g. Magalhaes et al. 2002; West et al. 2004). However, in very close-in exoplanets and brown dwarfs, the high stellar irradiation maintains the atmosphere in a very hot state and pushes the radiative/convective transition down to very high optical depths (see Guillot et al. 1996; Guillot 2006).

Numerical models naturally account for these convective zones by imposing a temperature gradient set by convection when a condition such as the Schwarzschild or Ledoux criterion is met. The temperature profile in the radiative part(s) of the atmosphere is recalculated iteratively to fulfill the radiative transfer equations. While it is easy to implement the first condition in analytical atmospheric models, it is generally not possible to implement the second one and modify the radiative solution due to the presence of a convective region. In the specific case of the grey and semi-grey model, Robinson & Catling (2012) recently derived a radiative-convective model that satisfies these two conditions, although it necessitates a small numerical integration. For non-grey thermal opacities, no analytical model solves self-consistently for the convective and the radiative parts of the atmosphere. In the specific case of the model of Paper I, the boundary condition of the radiative atmosphere lays in the optically thick layers and a the solution cannot be modified to account for a change in the temperature gradient at deep levels.

We want to estimate the error made when using the Schwarzschild criterion to include a convective zone at depth without recalculating the temperature of the radiative zone above it. We build our analytical radiative/convective model by switching from our radiative solution to the adiabatic solution whenever the convective gradient becomes lower than the radiative one. We compare the resulting analytical solution to the numerical solution in which both the depth of the radiative/convective boundary and the atmospheric temperature profile are converged iteratively. As the presence and depth of a convective zone depends on the exact value of the opacities, we need to specify the Rosseland mean opacity in our model. In this section, in order to facilitate the comparison, we fix the Rosseland mean opacity in function of pressure to its value in our fiducial model, described in Fig. 1. However, all our results will be relative to the depth of the convective zone and thus independent from the exact Rosseland mean opacity function used.

We only consider the case for which the atmosphere transitions from being radiative at high altitudes to being convective at depth (i.e. we do not include the possibility of alternating radiative and convective zones). In the convective zone, we assume that the temperature gradient is exactly adiabatic (i.e. we do not account for the superadiabatic gradient required to transport the heat flux – see e.g., Guillot (2006)).

4.1. Non-irradiated grey case

We first compare the solutions obtained in the non-irradiated grey case. In order to see how the location of the radiative/convective zone influences the solutions, we artificially modify the adiabatic gradient by a factor that varies from $1/4^{th}$ to 4.

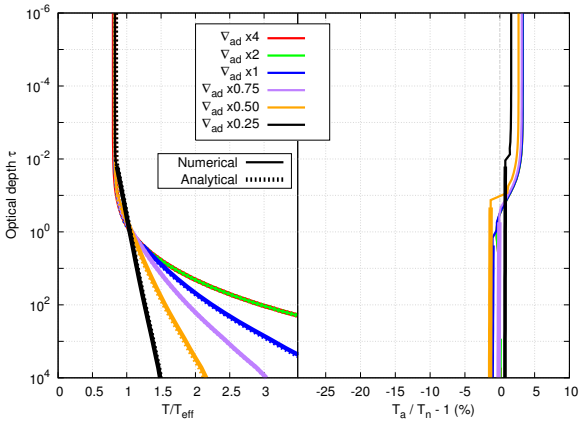

Fig. 5: Comparison of our numerical and analytical radiative-convective models for different adiabatic gradients in the non-irradiated, grey case. The thin line is the radiative zone and the thick one represents the convective zone. We used $T_{\rm int} = 500$ K and $g = 25$ m/s^2. Note that the cases $\nabla_{\rm ad} \times 2$ (green) and $\nabla_{\rm ad} \times 4$ (red) are superimposed.

When the radiative/convective transition occurs below optical depth unity (red, green, blue and purple curves in Fig. 5), the difference between the analytical and numerical solutions is unchanged (the corresponding curves are indistinguishable on the right panel) and entirely due to the Eddington approximation as discussed in the previous section. This error is frozen at the radiative/convective boundary and propagates in the convective zone leading to an estimate of the deep temperature profile that is at most 2% percent off. For a convective zone that crosses the $\tau \approx 1$ limit (orange and black curves of Fig. 5), the lower boundary condition used in the analytical radiative model

– that the deep atmosphere reaches the diffusion limit – is no more valid. The error becomes dependent on the location of the radiative/convective transition (and value of the adiabatic gradient). It however remains of the same order as the one due to the Eddington approximation. This validates models calculating the radiative/convective boundary of the deep convective zone without re-calculating the upper radiative profile. However, the presence of detached convective zones cannot be modeled correctly with this method, and an approach similar to Robinson & Catling (2012) is needed.

4.2. Non-irradiated non-grey case

We now turn, with Fig. 6, to the non-irradiated non-grey case, using the fiducial values $\kappa_2/\kappa_1 = 10^2$ and $\beta = 0.83$. As in the grey case, the errors are dominated by the Eddington approximation as long as the radiative/convective boundary occurs at optical depths larger than unity in the 2 thermal channels that are considered. (The error at low optical depths is larger but this is because the error due the Eddington approximation is increased in the non-grey case). However, as soon as the convective zone extends to levels of optical depth unity or smaller, the discrepancy between the analytical and numerical solutions increases significantly: the upper atmosphere warms up and our analytical solution is no more a good representation of the radiative atmosphere. This is clearly due to a non-grey effect. In a given spectral interval, the thermal flux present a given pressure is set by the integrated thermal emission of all the atmospheric layers below it in this specific spectral interval. At large optical depth, the emission is thermalized and the thermal flux per wavelength emitted in both spectral channels is the same regardless of the temperature gradient. At optical depth close to unity, the thermal flux in each channel depends on the actual temperature gradient. The analytical solution assumes that the temperature gradient is set by radiation transport everywhere and thus calculates inaccurately the flux emitted in the two spectral channels if convection extends to optical depths smaller than unity. The resulting temperature profile can differ by tens of percents from the numerical one. In addition, because the relative error is "frozen" at the one obtained at the radiative/convective transition, it does not tend towards zero at large optical depths as was the case with the purely radiative solutions.

Considerable caution should therefore be exerted when switching from radiative to convective gradient without recalculating the radiative solution in the general (non-grey) case. Specifically, when the atmosphere becomes convective at optical depths smaller than unity, the resulting temperature profile may be inaccurate by several tens of percents.

4.3. Irradiated non-grey case

We now consider the effect of irradiation with our fiducial "hot Jupiter" atmosphere. As already discussed, the strong irradiation tends to push the radiative/convective zone towards deep levels (see Guillot 2006). This is seen in the profiles of fig. 6 which all occur at optical depths $\sim$ 100 or deeper, with only a small dependence on the value of the chosen adiabatic gradient. As expected, this suppresses the changes of the temperature profile in the purely radiative atmosphere. The errors are almost independent of the assumed adiabatic gradient and mostly due to the Eddington approximation. For hot Jupiters, and generally for strongly irradiated atmospheres, the presence of a deep convective zone may be accounted for by adopting a purely radiative solution and switching to the convective one when the Schwarzschild criterion is verified.

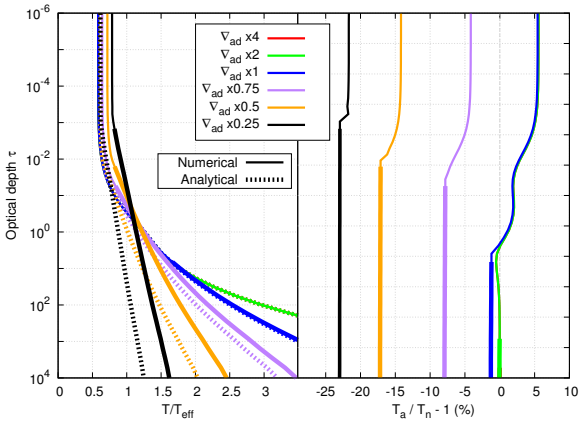

Fig. 6: Comparison of our numerical and analytical radiative-convective solutions for different adiabatic gradients in the non-irradiated, non-grey case. The thin line is the radiative zone and the thick one represents the convective zone. We used $T_{\rm int} = 500$ K, $g = 25$ m/s^2, $\kappa_2/\kappa_1 = 10^2$, and $\beta = 0.83$. The cases $\nabla_{\rm ad} \times 2$ (green) and $\nabla_{\rm ad} \times 4$ (red) are superimposed.

Of course, for a smaller irradiation level and/or larger values of the κ_2/κ_1 ratio, the presence of a convective zone reaching optical depths closer to unity (in one of the thermal channels at least) will lead to an increase on the error of the calculated temperature profile. We expect this error to be approximately bounded by that of the non-grey, non-irradiated case.

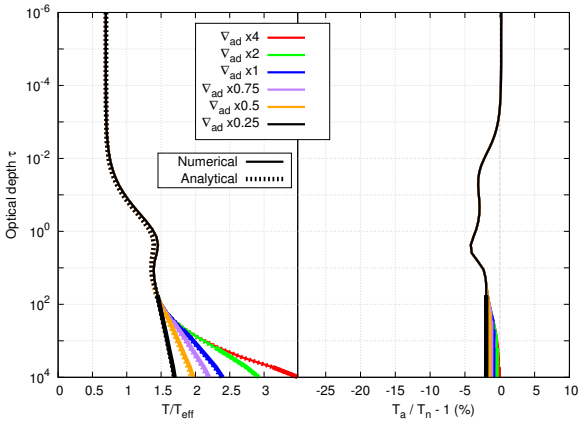

Fig. 7: Comparison of our numerical and analytical radiative/convective solutions for different adiabatic gradients in the non-grey, irradiated case. The thin line is the radiative zone and the thick one represents the convective zone. We used $T_{\rm irr} = 1288$ K, $T_{\rm int} = 500$ K, $\gamma_{\rm v} = 0.25$, $\mu = 1/\sqrt{3}$, $\kappa_2/\kappa_1 = 10^2$ and $\beta = 0.83$.

5. Modeling the non-grey effects

Analytical model atmospheres are useful to understand the key physical processes of the radiative transfer in planetary atmo-

spheres. Unfortunately they cannot take into account the complex variation of the opacities with frequency, temperature and pressure. However, when modeling a specific planet atmosphere with a given chemical composition, the knowledge of the line-by-line opacities should drive the scientist in his choice of parameters when using the analytical models. In this section we wish to understand what characteristics of the opacities shape the temperature/pressure profile of a planet atmosphere and find a method to derive the simplified opacities of our analytical model from the line-by-line opacities. Ideally, the resulting analytical temperature/pressure profile should be a good approximation of the numerical solution computed with the full frequency, temperature and pressure dependent opacities.

A first approach to determine our coefficients is an *a-posteriori* determination i.e. to choose the coefficients such that the analytical and the numerical profiles match correctly. Although this should give the best results in terms of goodness of the fit, the retrieved coefficients might not be physically realistic and it could be difficult to relate them to the real atmospheric opacities. Another approach is to find *a-priori* values, directly from the opacities. This requires a deep understanding of the opacities and how they shape the temperature profile. A last possibility is to combine the two approaches: using an *a-priori* determination when possible and adjusting the remaining coefficients *a-posteriori* to fit the numerical profile.

5.1. A priori determination of the coefficients

5.1.1. Visible coefficients

The visible coefficients control at which depth the stellar flux is absorbed in the atmosphere. When the visible absorption is strong, the stellar flux is absorbed in the upper part of the atmosphere and radiated back to space. At the opposite, when the visible absorption is weak, the incoming irradiation is deposited at depth where the thermal optical depth is large and the deep atmosphere warms up. This is the well-known greenhouse effect.

When taking into account only one visible band (i.e. $\beta_v = 1$, as in Guillot (2010)), a natural choice for the parameter γ_1 is the ratio of the mean Rosseland visible opacity (using the stellar Planck function to weight the line by line opacities) to the mean Rosseland thermal opacity (using the local Planck function to weight the line by line opacities). Unfortunately, this ratio can vary significantly with height. We find that choosing the ratio at $\tau_v = 2/3$ (where τ_v is the Rosseland visible optical depth) leads to a correct representation of the absorbed stellar flux and could be used, together with a correct modeling of thermal non-grey effects, to get a first guess of the deep temperature. The part of the stellar flux that heats up the deep atmosphere is the one that propagates down to the $\tau > 1$ level. Thus, the opacities that determine the relevant strength of the visible absorption are the lowest visible opacities. The Rosseland mean is a good estimate of the weakest opacities over a given frequency range and is thus a suitable estimate.

However, when a significant portion of the stellar radiation is absorbed in the upper atmosphere of the planet, in particular when strong visible absorbers such as titanium oxide or sodium are present in the atmosphere, the stellar flux that reaches the $\tau > 1$ level depends strongly on the amount of absorption in each spectral channels in the upper atmosphere. The knowledge of γ_v at a given level is not sufficient anymore for a correct estimate of the deep temperature. A more sophisticated model of the visible absorption is then needed.

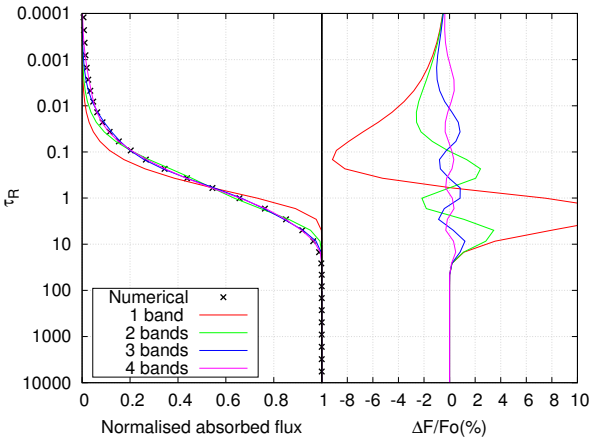

Fig. 8: Absorbed stellar flux from the numerical model (dots) and from the analytical model (lines) considering respectively 1, 2, 3 or 4 absorption bands in the visible for our fiducial hot-Jupiter model (see Fig. 1).

The radiative transfer equations are linear with respect to the absorbed stellar flux. As shown in Paper I, our model can take into account as many spectral bands in the visible as needed with the condition that the different values $\gamma_{vi} = \kappa_{vi}/\kappa_R$ in each visible bands are constant through the atmosphere. If well chosen, constant non-gray visible opacities can relatively well approximate the absorbed stellar flux at all atmospheric levels. We therefore adopt the following method: using the line by line opacities from Freedman et al. (2008) and the actual numerical PT profile, we calculate the total absorbed flux at each layer of the atmosphere. We then adjust the relative contributions of the different visible opacity bands in order to correctly match the absorbed visible flux from the numerical simulation. The stellar flux absorbed by n spectral bands of width β_{vi} is:

$$F(\tau) = F_0 \sum_{i=1}^{n} \beta_{vi} e^{-\gamma_{vi}\tau/\mu_*} \quad (8)$$

where the visible bands are homogeneously distributed in frequency (similar to the thermal bands), F_0 is the total incident stellar flux and the β_{vi} must verify: $\sum_i \beta_{vi} = 1$. We apply this method using one to four opacity bands. As seen in Fig. 8, the absorbed flux can be described with a 2% accuracy with the two bands model and with a 0.5% accuracy for the four bands model. Our analytical model is limited to two spectral bands in the thermal channels. We consider that using two bands in the visible is a good compromise between complexity and accuracy. Fig. 9 compares the numerical model in black, taking into account all the line-by-line opacities and the semi-grey model (blue line) where the visible opacities are adjusted in order to have the same absorbed flux as in the numerical model but where the thermal opacities remain grey. The semi-grey model, *even though it models correctly the absorbed flux in function of depth*, lays far from the numerical solution. Clearly, non-grey thermal opacities are needed.

5.1.2. Thermal coefficients

The thermal coefficients describe how well the atmosphere is able to retain its energy. As explained qualitatively by Pierrehumbert (2010) and quantitatively in Paper I, the pres-

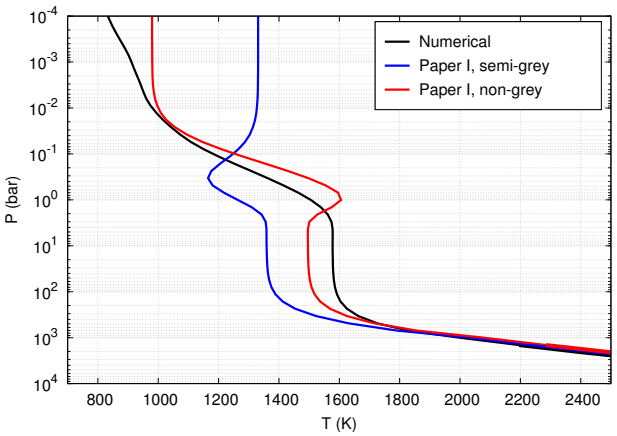

Fig. 9: Pressure-temperature profiles calculated using the numerical model and the full set of opacities (black), the semi-grey (blue) and the non-grey (red) analytical. As un Fig. 1, $g = 25$ m/s^2, $\mu_* = 1/\sqrt{3}$, $T_{\rm int} = 100$ K and $T_{\mu_*} = 1253$ K. The coefficients used for the analytical models are taken from table 1. The non-grey model is a much better match to the numerical profile than the semi-grey one.

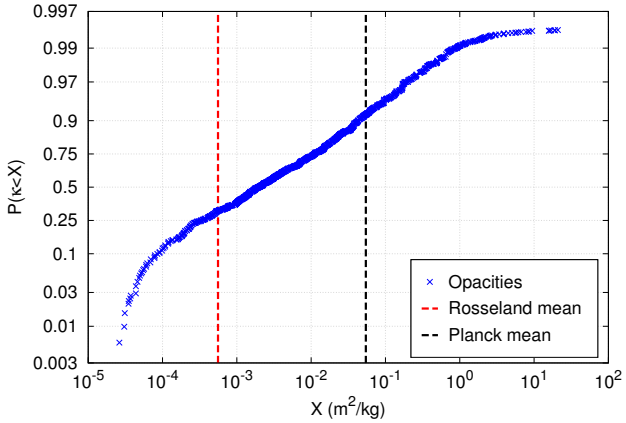

Fig. 10: Cumulative distribution function of the opacities at $P = 0.85$ bar and $T = 1464$ K, corresponding to the $\tau = 2/3$ level of an atmosphere with $T_{\mu_*} = 1253$ K and a gravity $g = 25$ m/s^2. The Y axis represents the fraction of frequency where the monochromatic opacities are lower than the corresponding κ_0 of the X-axis. The red line shows the value of the Rosseland mean opacity and the black line the Planck mean opacity. We can see that 25% of the frequency range have monochromatic opacities smaller than the Rosseland mean opacity whereas 90% have monochromatic opacities smaller than the Planck mean opacity.

ence of non-grey thermal opacities can strongly affect the temperature profile of the planet. Because it is tied to the emission and absorption of the thermal flux, only the opacity variations that have an extent smaller or comparable to the local Planck function can contribute to the non-grey effects. The cumulative distribution function of the opacities in the frequency range covered by the local Planck function should thus contain enough information to constrain the non-grey effects. As a grey atmosphere cools down principally by emission from the $\tau = 2/3$ level, the non-greyness of the opacities at this level should determine the strength of the non-grey effects.

We plot in Fig. 10 the cumulative distribution function of the opacities at this level. It represents the relative spectral width over which the opacities are lower than a given opacity κ_0 as a function of κ_0. The opacities cover a wide range of value (6 orders of magnitude in the specific example shown in Fig. 10). Our analytical model can describe the non-grey thermal opacities with only two parameters: the ratio of the Planck mean opacity to the Rosseland mean opacity, $\gamma_{\rm p}$ and the relative size of the two bands, β. Unlike in the visible case, the thermal effects are local effects that do not depend of the behavior of the rest of the atmosphere. The value of $\gamma_{\rm p}$ can hence be calculated as a function of pressure and temperature from tables available in the community (e.g., Freedman et al. 2008).

The parameter β describes the relative amount of the opacities which are in the first band compared to the second band. The Rosseland mean opacity is determined by the smallest values of the opacities, which is the second band opacity in our model. We decide to use as β the fraction of the opacities in the spectral range covered by the local Planck function that are higher than the Rosseland mean opacity. This can be derived directly from the cumulative distribution function of the opacities plotted in Fig. 10. In the specific example of Fig. 10, 25% of the opacities lay below the Rosseland mean opacity hence $\beta = 0.75$.

5.2. Application/Different models

In order to test the goodness of our analytical model and derive reasonable estimates of the coefficients, we use the EGP numerical code to build a grid of atmospheric radiative/convective models for giant planets with a solar composition atmosphere, three different gravity (2.5, 25, and 250 m/s^2), and an internal temperature of $T_{\rm int} = 100$ K. We consider the case of a planet orbiting a sun-like star at various distances corresponding to irradiation temperatures from 100 K to 3000 K. All the profiles where calculated using $\mu_* = 1/\sqrt{3}$. Figure 11 shows different models obtained for different estimates of our coefficients (top panel) and a comparison between the numerical profiles and the resulting analytical profiles (bottom panel). In all models but model D, we use as Rosseland mean opacity the one calculated by the numerical model directly from the line-by-line opacities. In model D, we use the functional fit of the Rosseland mean opacities of Freedman et al. (2008) provided by Valencia et al. (2013). Model D is therefore a fully analytical model that can be downloaded and implemented by the community. We now describe the different models.

Model A: In this model, we adjust all our coefficients *a-posteriori* in order to have the best match to the numerical profiles. It leads to temperature profiles in agreement within 5% with the numerical ones. Therefore, it shows that our analytical model can represent a large variety of atmospheric temperature profiles and goes beyond the limitation of previous semi-grey models (Parmentier et al. 2013). However, the spread of the retrieved value of the coefficients makes it difficult to derive a trustable functional form and a better approach is needed in order to get a fully analytical model.

Model B: Here we use the methods of Sec. 5.1 to determine *a-priori* the various coefficients. The visible coefficients have four different behaviors in function of T_{μ_*}. Those behaviors reflect changes in chemical composition with the irradiation tem-

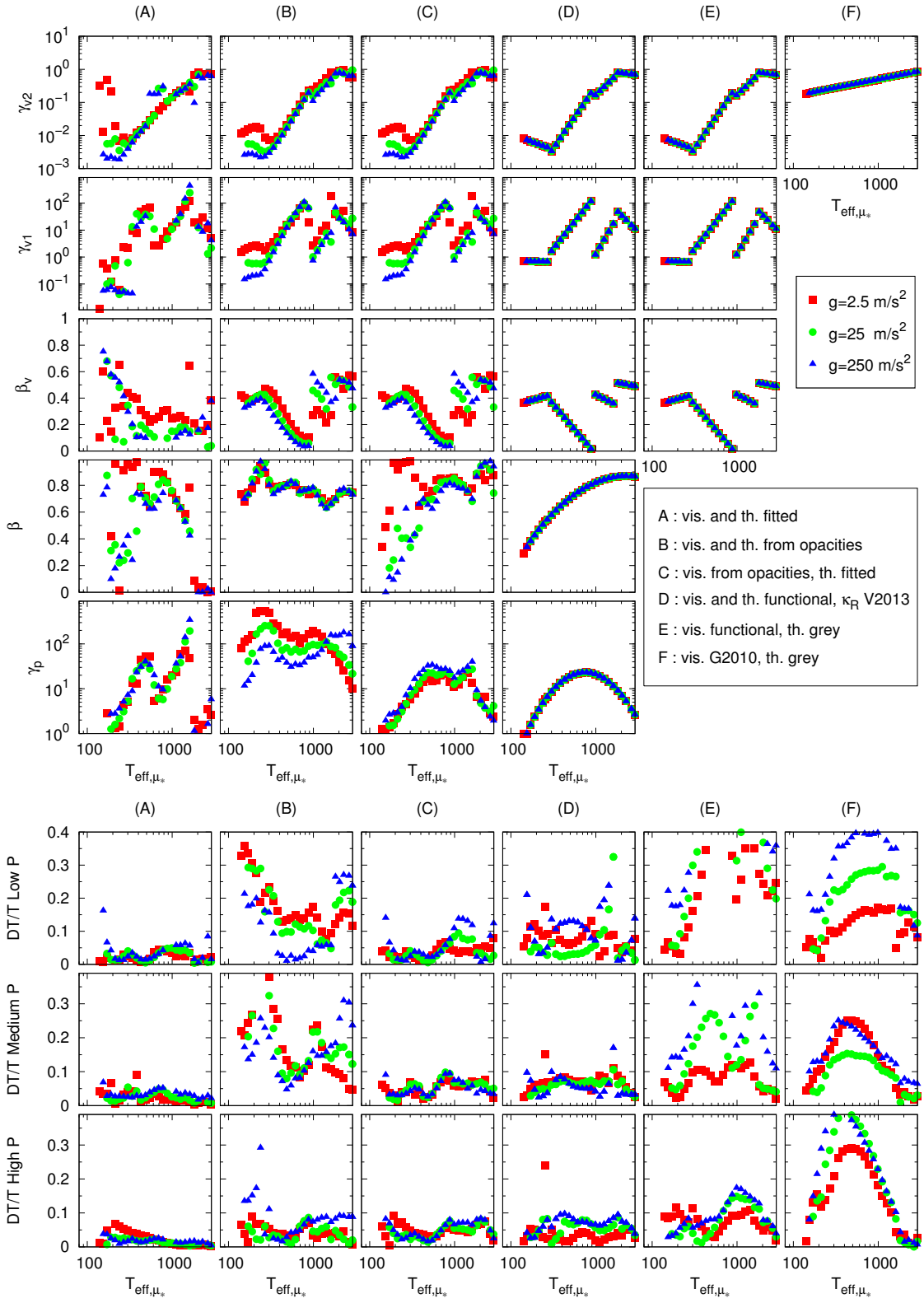

Fig. 11: *Top panel*: coefficients γ_p, β, β_v, γ_{v1}, and γ_{v2} obtained for the six different models described in Sec. 5.2 in function of the irradiation temperature for planets of solar composition with different gravity and an internal temperature of 100K.
Bottom panel: Mean relative difference between the numerical and the analytical model for the six different models described in Sec. 5.2. The first line is the mean difference for 10^{-4} bar $< P < 10^{-2}$ bar, the second one for 10^{-2} bar $< P < 10^{0}$ bar and the third one for 10^{0} bar $< P < 10^{2}$ bar.

Table 1: Functional form of the coefficients of the analytical model of Paper I valid for solar composition atmospheres. We use $X = \log_{10}(T_{\mathrm{eff},\mu_*})$

Coefficient	Expression	$T_{\mathrm{eff},\mu_*} < 300K$	$300K < T_{\mathrm{eff},\mu_*} < 900K$	$900K < T_{\mathrm{eff},\mu_*} < 1600K$	$T_{\mathrm{eff},\mu_*} > 1600K$
$\log_{10}(\gamma_{v2})$	$a + bX$	$a = -0.076$ $b = -0.94$	$a = -11.8$ $b = 3.75$	$a = -8.14$ $b = 2.46$	$a = 0.95$ $b = -0.32$
$\log_{10}(\gamma_{v1})$	$a + bX$	$a = -0.064$ $b = -0.043$	$a = -9.65$ $b = 3.98$	$a = -16.1$ $b = 5.40$	$a = 11.9$ $b = -3.15$
β_v	$a + bX$	$a = -0.039$ $b = 0.19$	$a = 2.23$ $b = -0.75$	$a = 1.37$ $b = -0.32$	$a = 0.90$ $b = -0.12$
β	$a + bX + cX^2$	$a = -3.43, b = 2.60, c = -0.39$			
$\log_{10}(\gamma_p)$	$a + bX + cX^2$	$a = -22.2, b = 16.3, c = -2.83$			

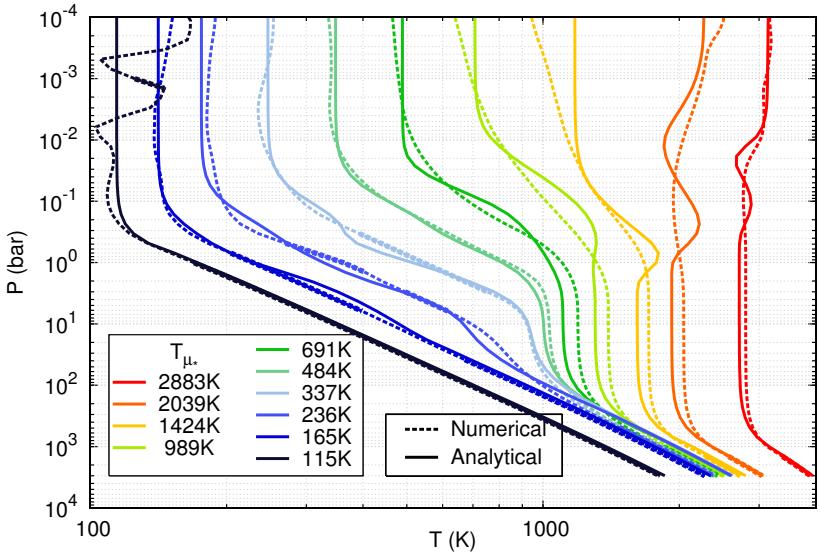

Fig. 12: Comparison between the numerical solutions (dashed lines) and the analytical solutions of model D (using the functional form of the coefficients given in table 1) over a wide range of irradiation temperatures for a giant planet of solar composition orbiting a sun-like star. Here we used $g = 25$ m/s^2, $T_{\mathrm{int}} = 100$ K, and $\mu_* = 1/\sqrt{3}$

perature (a plot of the line-by-line opacities for the four different regimes is shown in appendix):

- For $T_{\mathrm{eff},\mu_*} < 300$ K, the visible coefficients are mostly constant with T_{eff,μ_*}. At those low temperatures, the visible opacities are dominated by Rayleigh scattering and therefore exhibit a slight dependance with the gravity.
- For $300\,\mathrm{K} < T_{\mathrm{eff},\mu_*} < 900$ K, the visible opacities are dominated by the sodium lines at great depth, where the profile is warm enough to have sodium in gaseous state, whereas it is dominated by much smaller lines in the upper atmosphere. As T_{eff,μ_*} increases, the atmospheric Planck function shifts toward smaller wavelength, where the Rosseland mean opacity is smaller. Because the visible opacities stay roughly constant on this temperature range, their ratio to the Rosseland mean opacity, γ_{v1} and γ_{v2} increases with T_{eff,μ_*}
- For $900K < T_{\mathrm{eff},\mu_*} < 1600$ K the sodium and potassium become the main gaseous absorbers in the upper atmosphere, leading to a strong visible absorption and thus a sudden increase in the parameter β_v.
- For $T_{\mathrm{eff},\mu_*} > 1600$ K titanium and vanadium oxides become the main gaseous absorbers in the upper atmosphere, creating again a sudden increase in the parameter β.

The thermal coefficients do not exhibit such discontinuities with T_{eff,μ_*}. β is rather constant and equal to ≈ 0.8. This high value of β can be interpreted as a predominance of the molecular bands (i.e. the water and methane bands) to the atomic lines in the non-grey opacities. Around $T_{\mathrm{eff},\mu_*} = 200$ K, β reaches values even closer to 1. At these temperatures, the Planck function at the atmospheric levels of $\tau \approx 2/3$ overlaps with the 5μm window in the opacities which is consistent with large values of β. In the other hand, γ_p varies significantly with T_{eff,μ_*} with a "saddle-like" shape with two maxima at 200 K and 1000 K. At low temperatures, the Planck function of the atmosphere shifts towards large wavelengths ($> 10\mu$m) for which the opacities are almost constant, leading to small values of γ_p. At very high T_{eff,μ_*}, the Planck function of the atmosphere shifts toward smaller wavelengths ($< 1\,\mu$m) for which the TiO broad-band absorption significantly flattens the opacities, leading to small values of γ_p. In between, when the atmospheric Planck function is between 1 and 10μm, the opacities are dominated by the water and methane bands, which raises the value of γ_p to ≈ 100.

Although this model gives a correct estimate of the profile at high pressure, it leads to errors of $\approx 40\%$ at medium and low pressure. Given that the coefficients were all guessed *a-priori*,

reaching a 40% accuracy can be a fair, first guess of the temperature profile. This method could be extended to planets with very different opacities without going through the whole numerical integration of the radiative transfer equations. However, as proven by model A, a much better accuracy can be obtained by the analytical profile and a mixed method with some coefficients derived *a-priori* and others *a-posteriori* can be a good compromise.

Model C: In this model we use a mixed method to derive the coefficients of the analytical model, with some of them being derived *a-priori* and some of them *a-posteriori*. The method to determine the visible coefficients seems robust, as it can give the correct absorbed flux as a function of optical depth in the atmosphere with a 2% accuracy. The method to determine the thermal coefficients is more subject to caution as it is unclear whether the value of γ_p in our analytical model should correspond to the value of γ_p derived from the real opacities. Moreover, our criteria to choose β (the fraction of the opacities that are higher than the Rosseland mean opacity) is *ad-hoc* and does not rely on strong physical arguments. At last, there is no strong argument to choose the depth at which those coefficients are calculated. We thus decided to obtain the visible coefficients from the a-priori solution and to fit the thermal ones by adjusting the analytical profile to the numerical profile. The resulting analytical solutions lead to an estimate of the temperature profile that always differs by less than 10% from the numerical solution.

Compared to model B, only the thermal coefficients are changed in model C. γ_p keeps the same dependency with T_{eff,μ_*} but is one order of magnitude smaller. This tends to suggest that the relevant opacities to calculate γ_p are at deeper levels than the $\tau = 2/3$ level, as was done in model B. The parameter β has a much higher dependency with T_{eff,μ_*} than in model B. In particular, it decreases significantly at small T_{eff,μ_*}, enhancing the fact that, for small T_{eff,μ_*}, non-grey thermal effects become less important.

Model D: In order to have a fully analytical model we fit a functional form to the coefficients derived in model C as a function of T_{eff,μ_*}. Following the different regimes that we just described, we fit four different affine functions to the visible coefficients. The thermal coefficients having a much smoother variation with the irradiation temperature, we use only a 2^{nd} order polynomial to fit the coefficients over the whole temperature range. The functional form of the coefficients are presented in table 1. The resulting model matches the numerical profiles over a wide range of irradiation temperatures and planet gravity with an accuracy always better than 10% at all pressures (see Fig. 12 and column D of Fig. 11). Whereas for previous models the Rosseland mean opacities used in the analytical solution where calculated by the numerical model directly from the line-by-line opacities, Model D uses the fit of the Freedman et al. (2008) Rosseland mean opacities provided by Valencia et al. (2013). This makes model D a self-consistent fully analytical model.

Model E: Here, the importance of non-grey effects are tested. This model has grey thermal opacities (i.e. $\gamma_p = 1$) but uses the functional form derived in model D for the visible coefficients. Therefore, model E is a good representation of the absorption of the stellar irradiation by the atmosphere but lacks the non-grey effects. As expected, at low T_{eff,μ_*}, where non-grey effects were proven to be negligible, model E gives a reasonable estimate of the temperature profile. Conversely, when T_{eff,μ_*} is higher than 300 K, the analytical profile lays 20 to 50% away from the numerical solution, compared to $\approx$ 10% when including non-grey effects. The non-grey absorption of the stellar irradiation therefore cannot, by itself, explain the temperature structure in planetary atmospheres. Non-grey thermal effects, such as the ones considered in model D, are necessary.

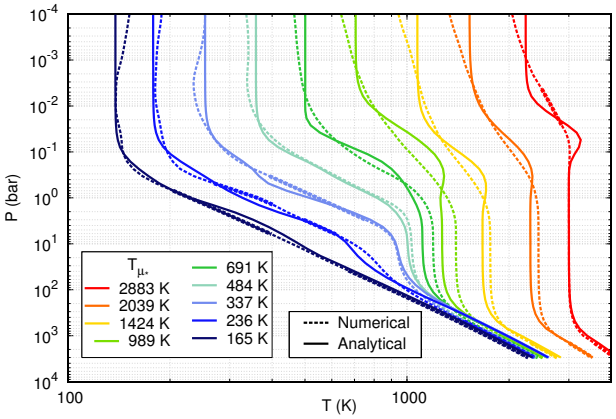

Fig. 13: Comparison between the numerical solutions (dashed lines) and the analytical solutions of model D of Fig. A.2 using the functional form of the coefficients given in table A.1) over a wide range of irradiation temperatures for a planet a giant planet of solar composition orbiting a sun-like star in the case where TiO and VO have been removed from the atmosphere. Here we used $g = 25$ m/s^2, $T_{\mathrm{int}} = 100$ K, and $\mu_* = 1/\sqrt{3}$

Model F: In this model, a comparison with the previous estimate of Guillot (2010) is done. We use grey thermal opacities and the visible coefficients provided by Guillot (2010). Those coefficients were derived in order to match the deep temperature of highly irradiated planets, which it does well. However, for smaller irradiation model F fails to represent the numerical temperature profiles and the relative error between the two models can reach 40% at all atmospheric pressures.

5.3. The role of TiO and VO

The most irradiated planets have dayside atmospheric temperatures high enough such that, for a solar composition atmosphere some metal oxides such as titanium and vanadium oxides (TiO and VO respectively), are chemically stable in gas phase (Lodders 2002). Several studies (e.g., Hubeny et al. 2003; Fortney et al. 2008) show that, if present in solar abundance in the upper atmosphere of irradiated planets, titanium and vanadium oxides could change significantly the temperature structure of those atmospheres, accounting for the strong thermal inversion at high altitude inferred from secondary eclipse measurements (e.g., Knutson et al. 2008; Fortney et al. 2008). Moreover, the presence of TiO/VO changes the deep temperature profiles, the planets with TiO having cooler deep temperatures than planets without TiO, what can affects the cooling rate and thus the long term evolution of gas giant exoplanets (Budaj et al. 2012; Parmentier & Guillot 2011).

To this date, there has been no firm direct detection of TiO in exoplanets atmospheres (see Désert et al. 2008; Huitson et al. 2013; Sing et al. 2013). Several studies show that condensation in a vertical cold trap (Spiegel et al. 2009), in an horizontal cold trap (Parmentier et al. 2013) or dissociation by stellar radiation (Knutson et al. 2010) could significantly deplete the upper atmosphere of irradiated planets in TiO and VO.

We calculated a grid of pressure/temperature profiles and derived the same analytical models as in the previous section in the case where TiO and VO has been removed from the whole atmosphere by any of the aforementioned processes. The resulting coefficients are presented in Fig. A.2 and Table A.1 in appendix. As expected, the absence of TiO /VO changes significantly how the atmosphere absorbs the stellar irradiation. Whereas γ_{v1} and γ_{v2} remain almost unaffected, the parameter β_v vanishes at high temperatures in the case without TiO/VO whereas it converges toward 0.5 in the case with TiO/VO: in the first case ($\beta_v \rightarrow 0$), all the stellar irradiation is absorbed deep in the atmosphere by the second visible band whereas in the second case ($\beta_v \rightarrow 0.5$) half of the stellar irradiation is absorbed at much lower pressures by the large TiO absorption band. This enhanced stellar absorption in the upper atmosphere creates the inversion observed in the profiles at high T_{eff,μ_*} in the case with TiO/VO (e.g., Fig. 12) and not in the case without (see Fig. 13). TiO and VO also affect the thermal coefficients. In particular, γ_p decreases from 20 to 2 when T_{eff,μ_*} goes from $1000K$ to $3000K$ in the case with TiO/VO whereas it remains around ≈ 20 in the case without TiO/VO (see Fig. A.2). TiO has a rather broad band opacity that fills in the gaps due to the water opacities in the $0.4 - 1\,\mu$m wavelength range (see the difference between the two columns of Fig. A.1 at high effective temperatures) whereas absorption by VO is less significant. For large atmospheric temperatures, the local Planck function extends below $1\,\mu$m in wavelength (see Fig. A.1). When TiO is present the opacities are flatter below $1\,\mu$m, therefore non-grey thermal effects are lower in the case with TiO, explaining the trend observed in γ_p.

As a conclusion, the concomitant increase in temperature in the upper atmosphere and decrease in the deep atmosphere created by the presence of TiO/VO is caused not only by the absorption of part of the stellar flux in the upper atmosphere but also by the weakening of the non-grey blanketing effects due to the presence of broad-band TiO opacities in the $0.4 - 1\,\mu$m wavelength range. Both effects contribute equally to the relatively to yield relatively cool temperatures in the deep atmosphere of gas giant planets when TiO and/or VO are present. Conversely, when TiO/VO are absent from the dayside atmosphere the stellar irradiation penetrates deeper and the blanketing is stronger, heating the deep atmosphere.

5.4. Low irradiation planets and brown dwarfs

Gravitational contraction and deuterium burning can be a significant source of internal luminosity in young giant planets and brown dwarfs respectively. This luminosity can overtake the stellar irradiation as the dominant heating source in the atmosphere. We calculated temperature/pressure profiles for planets with an internal temperature of 300K and 1000K and derived the same analytical models as in the case with $T_{\mathrm{int}} = 100$K presented in Sec. 5.2. Figs. 14 and 15 show that, as long as $T_{\mathrm{int}} <\approx T_{\mu_*}$ (i.e.$T_{\mathrm{eff},\mu_*} \approx T_{\mu_*}$), model D of of Sec. 5.2 – derived considering an internal temperature of 100K – correctly matches the numerical temperature/pressure profile for higher internal temperatures. However, when $T_{\mathrm{int}} >> T_{\mu_*}$ (i.e.$T_{\mathrm{eff},\mu_*} \approx T_{\mathrm{int}}$), our analytical model cannot reproduce the temperature/pressure profiles predicted by the numerical model with the same accuracy than in the low internal temperature case (see Fig. A.3 in appendix). In particular, it can be seen from Figs. 14 and 15 that whenever $T_{\mathrm{int}} >> T_{\mu_*}$ our model is systematically hotter than the numerical model at low pressures with a discrepancy up to 40% between the two models. A possible interpretation is that whenever the internal temperature becomes the dominant heating source in the atmosphere, the stellar irradiation cannot balance anymore the non-grey thermal cooling of the upper atmosphere. As a consequence, the temperature gradient in the optically thin part of the atmosphere is larger than in highly irradiated atmospheres with the same T_{eff,μ_*}. Therefore, the local atmospheric Planck function shifts by a frequency range of the order of its own extent along the atmosphere, an effect not taken into account in the model of Paper I where no opacity structures larger than the Planck function are considered. Moreover, when the internal luminosity dominates over the stellar irradiation, the convective zone can reach low optical depths which is another limit of our analytical model (see Sec. 4).

In summary, model D of Sec. 5.2 can be used to model irradiated planets atmospheres as long as the internal temperature is smaller than the irradiation temperature.

5.5. Recommanded model

When modeling gas giant planets of solar composition, we recommend the use of model D of Sec. 5.2. This model uses the solution of the radiative transfer equations given by Paper I where the first five parameters describing the opacities are expressed as a function of the effective temperature (see table 1) whereas the analytical Rosseland mean opacities are given by Valencia et al. (2013). Model D is fully analytical, yet achieves an overall accuracy of 10% in temperature (at a given pressure) for irradiated giant planet atmospheres of solar composition with gravities in the range $2.5 - 250\,\mathrm{m/s^2}$ and effective temperatures from 100 to 3000K assuming a smaller internal temperature. When the internal flux dominates over the external flux, model D becomes less accurate with an error that can reach $\approx 30\%$ in the deep atmosphere and more than 40% at low optical depths.

The model has a proper behavior, but tends to predict temperature inversion absent from the numerical solutions. This is attributed to the simplification of the two thermal opacities when in reality many characteristic values should be used.

This accuracy is to be compared to that of simpler models. For example, models where the temperature is set to the effective temperature at $\tau = 2/3$ and the profile is assumed to follow the diffusion approximation below (i.e. the so-called Eddington boundary condition). We calculated that this commonly used prescription (e.g., Bodenheimer et al. 2003; Batygin et al. 2011, among many others) lead to an error in the temperature profile below the $\tau = 2/3$ level of the order of $\approx 30\%$ except fortuitously for $800K < T_{\mathrm{eff},\mu_*} < 1200K$ where the error is lower than 10%. Such an error on the boundary condition of interior models can strongly affects internal structure and planetary evolution calculations. Even semi-grey model (e.g., Hansen 2008; Guillot 2010) cannot reach an accuracy better than 20%, even with adjusted variable opacity coefficients.

A FORTRAN implementation of model D, including both cases with and without TiO/VO is available for download on the internet[1].

6. Conclusion

Analytical solutions of the radiative transfer equations, although derived using very restrictive (but necessary) approximations, offer a deep insight in the physical processes shaping the temperature profile of planetary atmospheres and can provide fast and roughly accurate solutions to be incorporated in more complex planetary models.

[1] http://www.oca.eu/parmentier/nongrey

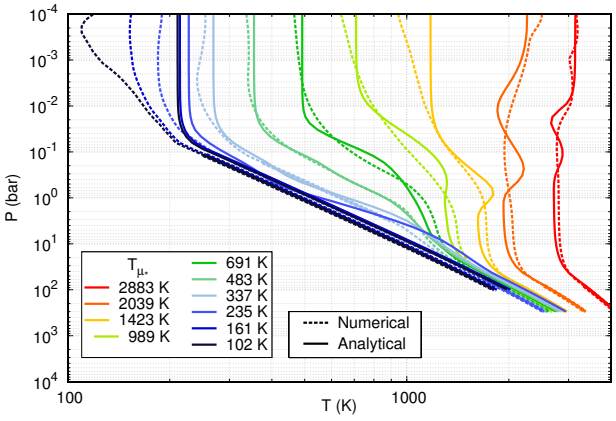

Fig. 14: Comparison between the numerical solutions (dashed lines) and the analytical solutions of model D (using the functional form of the coefficients given in table 1) over a wide range of irradiation temperatures for a giant planet of solar composition orbiting a sun-like star with a significant internal temperature $T_{\rm int}$ = 300K. Here we used g = 25 m/s^2, and $\mu_* = 1/\sqrt{3}$.

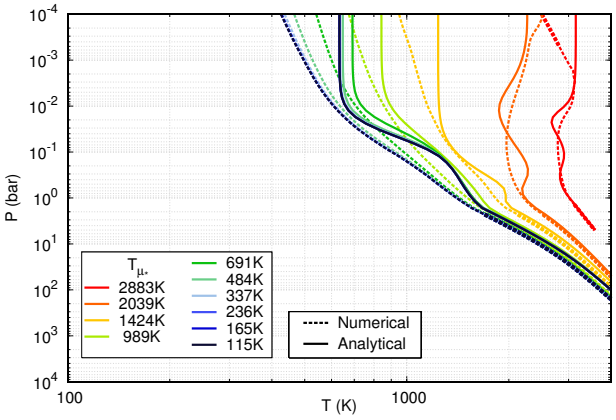

Fig. 15: Comparison between the numerical solutions (dashed lines) and the analytical solutions of model D (using the functional form of the coefficients given in table 1) over a wide range of irradiation temperatures for a giant planet of solar composition orbiting a sun-like star with a high internal temperature $T_{\rm int}$ = 1000K. Here we used g = 25 m/s^2, and $\mu_* = 1/\sqrt{3}$.

In this study we used hand-in-hand the analytical model derived in Paper I, that includes non-grey visible and thermal effects, and a state-of-the-art numerical model that solves the radiative transfer equations considering their full frequency and angular dependency.

We first quantified the validity of the Eddington approximation. We showed that this approximation leads to errors in the temperature profile of at most 2% in the grey case and 4% in the non-grey case.

Planets with a thick atmosphere usually become convective below a certain depth. Thus, a common way to produce a radiative/convective temperature profile is to switch from a radiative solution to a convective solution whenever the Schwarzchild criterion is met, *considering that the radiative solution remains unaffected by the presence of a convective zone below it.* We showed that this approach is always valid in the grey case – the error due to the Eddington approximation being frozen at the radiative/convective boundary and propagated along the convective zone. However, for non-grey atmospheric opacities, we showed that this method is valid only as long as the radiative/convective boundary remains in the optically thick layer of the atmosphere. When the radiative/convective boundary is in the optically thin region of the atmosphere, the radiative solution is very sensitive to the precise location of the radiative/convective boundary and this common approach can lead to relative errors of tens of percents when estimating the upper, radiative, atmospheric temperatures.

We showed that non-grey visible effects are not sufficient to explain the atmospheric temperature profiles that consider the full frequency dependent opacities and that non-grey thermal effects need to be taken into account. We provided a reliable method to obtain the visible coefficients of our analytical model directly from the opacities and explored how the thermal coefficients could also be directly derived from the knowledge of the line-by-line atmospheric opacities.

In particular, we showed that the presence of TiO can warm up the upper atmosphere and cool down the deep atmosphere not only because it absorbs a significant amount of stellar irradiation in the upper atmosphere, but also because its broad band opacity reduces the non-grey thermal "blanketing effect".

Finally, using an *a-priori* determination of the visible coefficients and an *a-posteriori* determination of the thermal coefficients, we provide a fully analytical model for solar composition optically thick atmospheres. This model agrees with the numerical calculations within 10% over a wide range of gravities and effective temperatures. Our model leads to a much better estimate of the deep temperature profile than the previous analytical estimates. Therefore, when modeling the atmospheric structure of giant planets, we recommend the use of Model D described in Sec. 5.5 that uses the analytical expressions derived in Paper I with the first five parameters given in table 1 in the case with TiO and by table A.1 in the case without TiO and the Rosseland mean opacities given by Valencia et al. (2013). For convenience, we provide an implementation in FORTRAN of our model at the adress *http://www.oca.eu/parmentier/nongrey*.

References

Abramowitz, M. & Stegun, I. A. 1965, Handbook of mathematical functions with formulas, graphs, and mathematical tables, ed. Abramowitz, M. & Stegun, I. A.
Batygin, K., Stevenson, D. J., & Bodenheimer, P. H. 2011, ApJ, 738, 1
Bodenheimer, P., Laughlin, G., & Lin, D. N. C. 2003, ApJ, 592, 555
Budaj, J., Hubeny, I., & Burrows, A. 2012, A&A, 537, A115
Burrows, A., Marley, M., Hubbard, W. B., et al. 1997, ApJ, 491, 856
Chandrasekhar, S. 1960, Radiative transfer
Désert, J.-M., Vidal-Madjar, A., Lecavelier Des Etangs, A., et al. 2008, A&A, 492, 585
Fortney, J. J., Lodders, K., Marley, M. S., & Freedman, R. S. 2008, ApJ, 678, 1419
Fortney, J. J., Marley, M. S., Lodders, K., Saumon, D., & Freedman, R. 2005, ApJ, 627, L69
Freedman, R. S., Marley, M. S., & Lodders, K. 2008, ApJS, 174, 504
Goody, R. M. & Yung, Y. L. 1989, Atmospheric radiation : theoretical basis
Guillot, T. 2006, in Saas-Fee Advanced Course 31: Extrasolar planets, ed. D. Queloz, S. Udry, M. Mayor, W. Benz, P. Cassen, T. Guillot, & A. Quirrenbach, 243–368
Guillot, T. 2010, A&A, 520, A27+
Guillot, T., Burrows, A., Hubbard, W. B., Lunine, J. I., & Saumon, D. 1996, ApJ, 459, L35
Hansen, B. M. S. 2008, ApJS, 179, 484
Heng, K., Hayek, W., Pont, F., & Sing, D. K. 2012, MNRAS, 420, 20

Hubeny, I., Burrows, A., & Sudarsky, D. 2003, ApJ, 594, 1011
Huitson, C. M., Sing, D. K., Pont, F., et al. 2013, ArXiv e-prints
Knutson, H. A., Charbonneau, D., Allen, L. E., Burrows, A., & Megeath, S. T. 2008, ApJ, 673, 526
Knutson, H. A., Howard, A. W., & Isaacson, H. 2010, ApJ, 720, 1569
Lodders, K. 2002, ApJ, 577, 974
Magalhaes, J. A., Seiff, A., & Young, R. E. 2002, Icarus, 158, 410
Marley, M. S., Ackerman, A. S., Cuzzi, J. N., & Kitzmann, D. 2013, ArXiv e-prints
Marley, M. S. & McKay, C. P. 1999, Icarus, 138, 268
Marley, M. S., Saumon, D., Guillot, T., et al. 1996, Science, 272, 1919
Marley, M. S., Seager, S., Saumon, D., et al. 2002, ApJ, 568, 335
McKay, C. P., Pollack, J. B., & Courtin, R. 1989, Icarus, 80, 23
Mihalas. 1984, Foundation of Radiation Hydrodynamics (Oxford university press)
Parmentier, V. & Guillot, T. 2011, in EPSC-DPS Joint Meeting 2011, 1367
Parmentier, V. & Guillot, T. 2013, submitted to A&A
Parmentier, V., Showman, A. P., & Lian, Y. 2013, A&A, 558, A91
Pierrehumbert, R. T. 2010, Principles of Planetary Climate
Rauscher, E. & Menou, K. 2012, ApJ, 750, 96
Robinson, T. D. & Catling, D. C. 2012, ApJ, 757, 104
Saumon, D., Chabrier, G., & van Horn, H. M. 1995, ApJS, 99, 713
Showman, A. P., Fortney, J. J., Lian, Y., et al. 2009, ApJ, 699, 564
Sing, D. K., Lecavelier des Etangs, A., Fortney, J. J., et al. 2013, MNRAS
Spiegel, D. S., Silverio, K., & Burrows, A. 2009, ApJ, 699, 1487
Toon, O. B., McKay, C. P., Ackerman, T. P., & Santhanam, K. 1989, J. Geophys. Res., 94, 16287
Valencia, D., Guillot, T., Parmentier, V., & Freedman, R. S. 2013, ApJ, 775, 10
West, R. A., Baines, K. H., Friedson, A. J., et al. 2004, Jovian clouds and haze, ed. F. Bagenal, T. E. Dowling, & W. B. McKinnon, 79–104

Appendix A: Additional material

The opacities in the form of k-coefficients used in the numerical model and discussed in Sec. 5.2 are presented in Fig. A.1 for a solar composition atmosphere and for an atmosphere without TiO/VO.

The analytical model adjusted to match the temperature/pressure profile of an atmosphere without TiO, discussed in Sec. 5.3 is presented in Fig. A.2 and Table A.1.

The effect of a strong internal luminosity on the analytical model, discussed in Sec. 5.4 is presented if Fig. A.3.

Table A.1: Functional form of the coefficients with $X = \log_{10}(T_{\mathrm{eff},\mu_*})$ for atmospheres where TiO has been artificially removed.

Coefficient	Expression	$T_{\mathrm{eff},\mu_*} < 300K$	$300K < T_{\mathrm{eff},\mu_*} < 900K$	$900K < T_{\mathrm{eff},\mu_*} < 1600K$	$T_{\mathrm{eff},\mu_*} > 1600K$
$\log_{10}(\gamma_{\mathrm{v2}})$	$a + bX$	$a = -0.076$ $b = -0.94$	$a = -11.8$ $b = 3.75$	$a = -4.75$ $b = 1.34$	$a = -7.48$ $b = 2.13$
$\log_{10}(\gamma_{\mathrm{v1}})$	$a + bX$	$a = -0.064$ $b = -0.043$	$a = -9.60$ $b = 3.97$	$a = -10.8$ $b = 3.66$	$a = -18.5$ $b = 5.88$
β_{v}	$a + bX$	$a = -0.039$ $b = 0.19$	$a = 2.23$ $b = -0.75$	$a = 1.68$ $b = -0.41$	$a = 4.93$ $b = -1.41$
β	$a + bX + cX^2$	$a = -7.25, b = 5.49, c = -0.93$			
$\log_{10}(\gamma_{\mathrm{p}})$	$a + bX + cX^2$	$a = -11.9, b = 8.46, c = -1.34$			

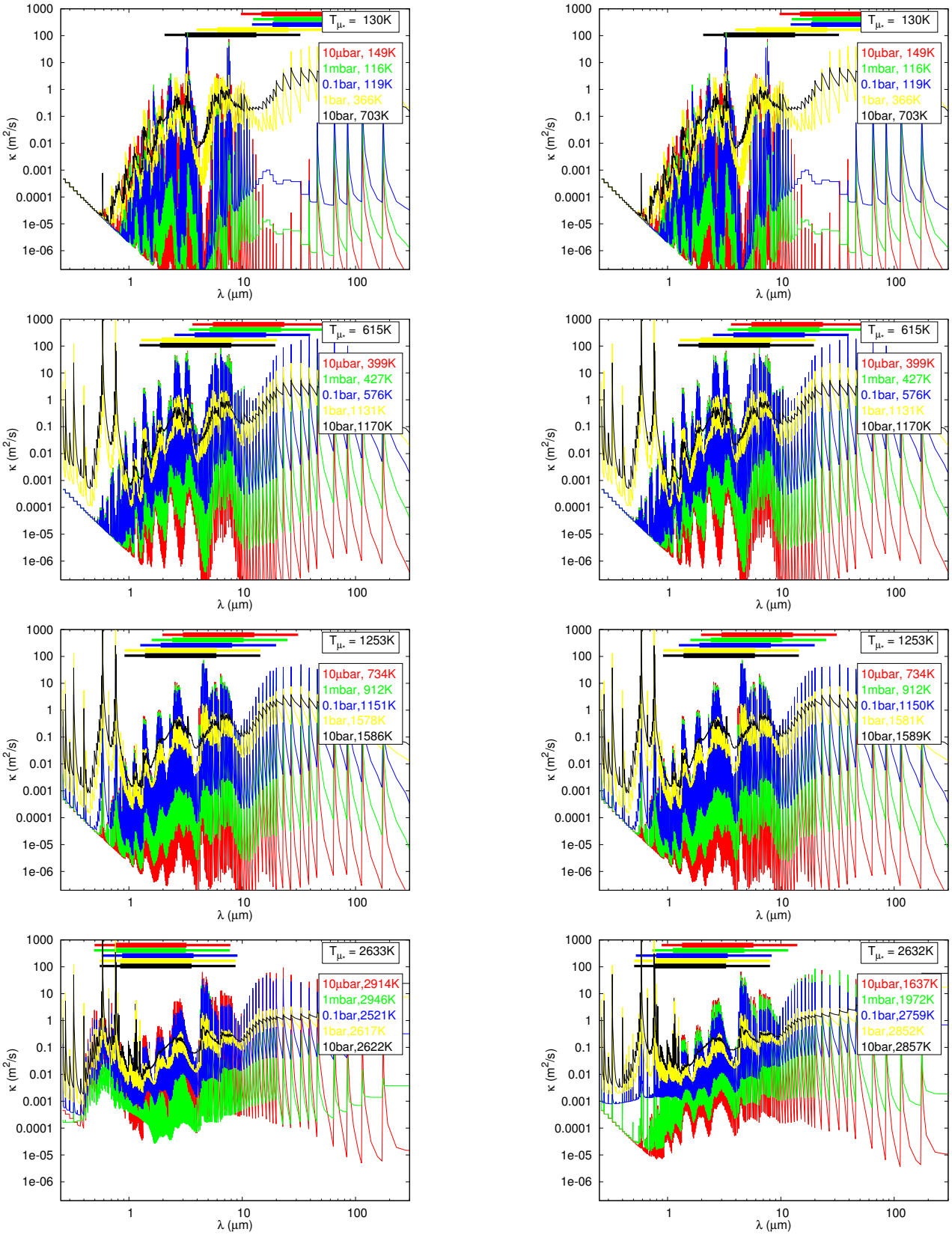

Fig. A.1: Opacities from Freedman et al. (2008) organized as k-coefficient inside each bin of wavelength for a solar composition atmosphere (left column) and an atmosphere without TiO/VO (right column). The different colors are for different temperature and pressure taken along the corresponding numerical P-T profile. The thick bars on top represents the wavelength range where 90% of the thermal flux is emitted, the thin bars where 99% of the thermal flux is emitted. The four lines are for different effective temperature. We used $T_{\rm int}$ = 100 K, $\mu_* = 1/\sqrt{3}$ and g = 25 m/s^2.

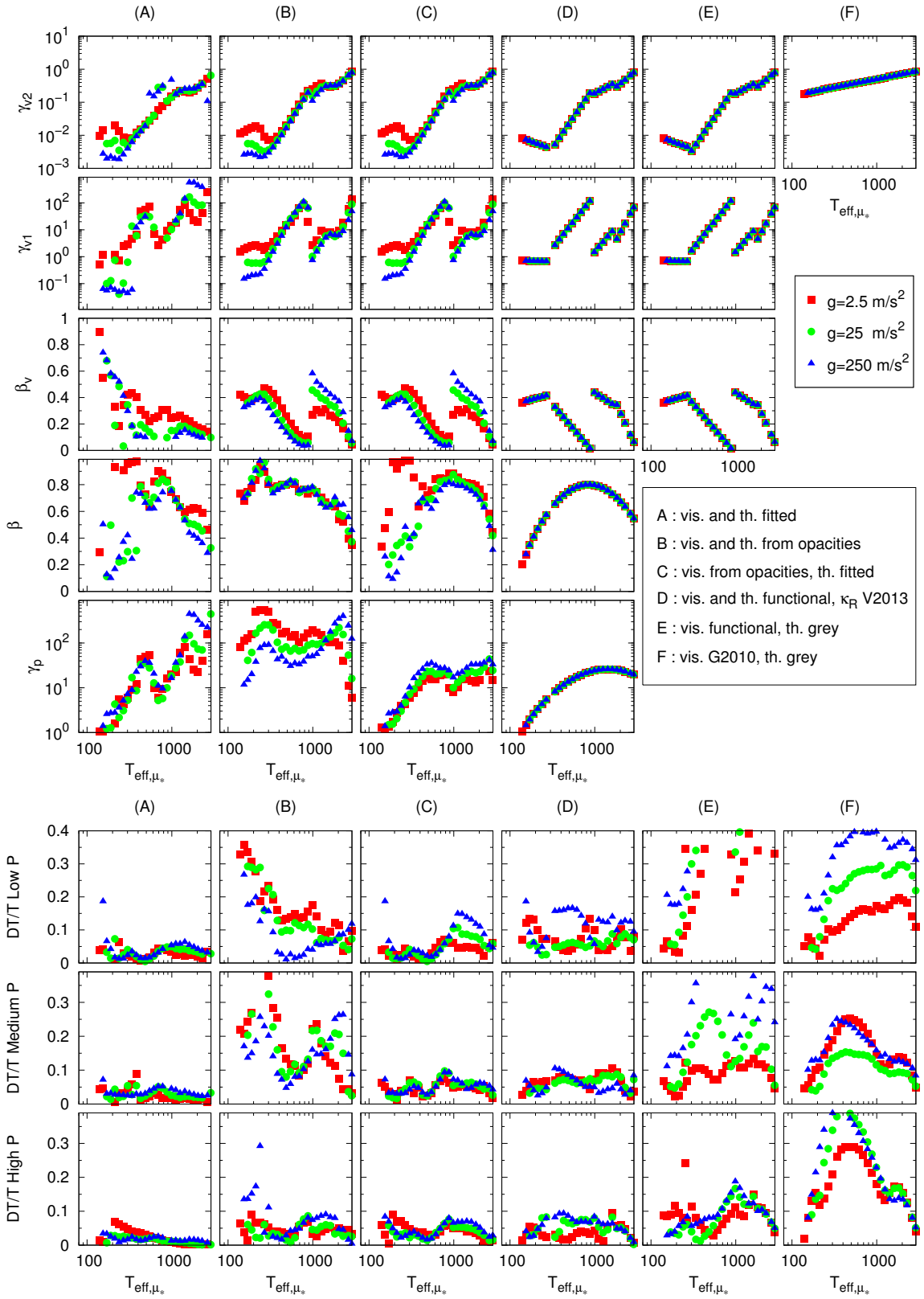

Fig. A.2: *Top panel*: coefficients obtained for the six different models described in Sec. 5.2 in function of the irradiation temperature for planets with different gravities and an internal temperature of 100K, 300K and 1000K. Here, TiO and VO have been artificially removed from the atmosphere. *Bottom panel*: Mean relative difference between the numerical and the analytical model for the six different models described in Sec. 5.2. The first line is the mean difference for 10^{-4} bar $< P < 10^{-2}$ bar, the second line for 10^{-2} bar $< P < 10^{0}$ bar and the third line for 10^{0} bar $< P < 10^{2}$ bar.

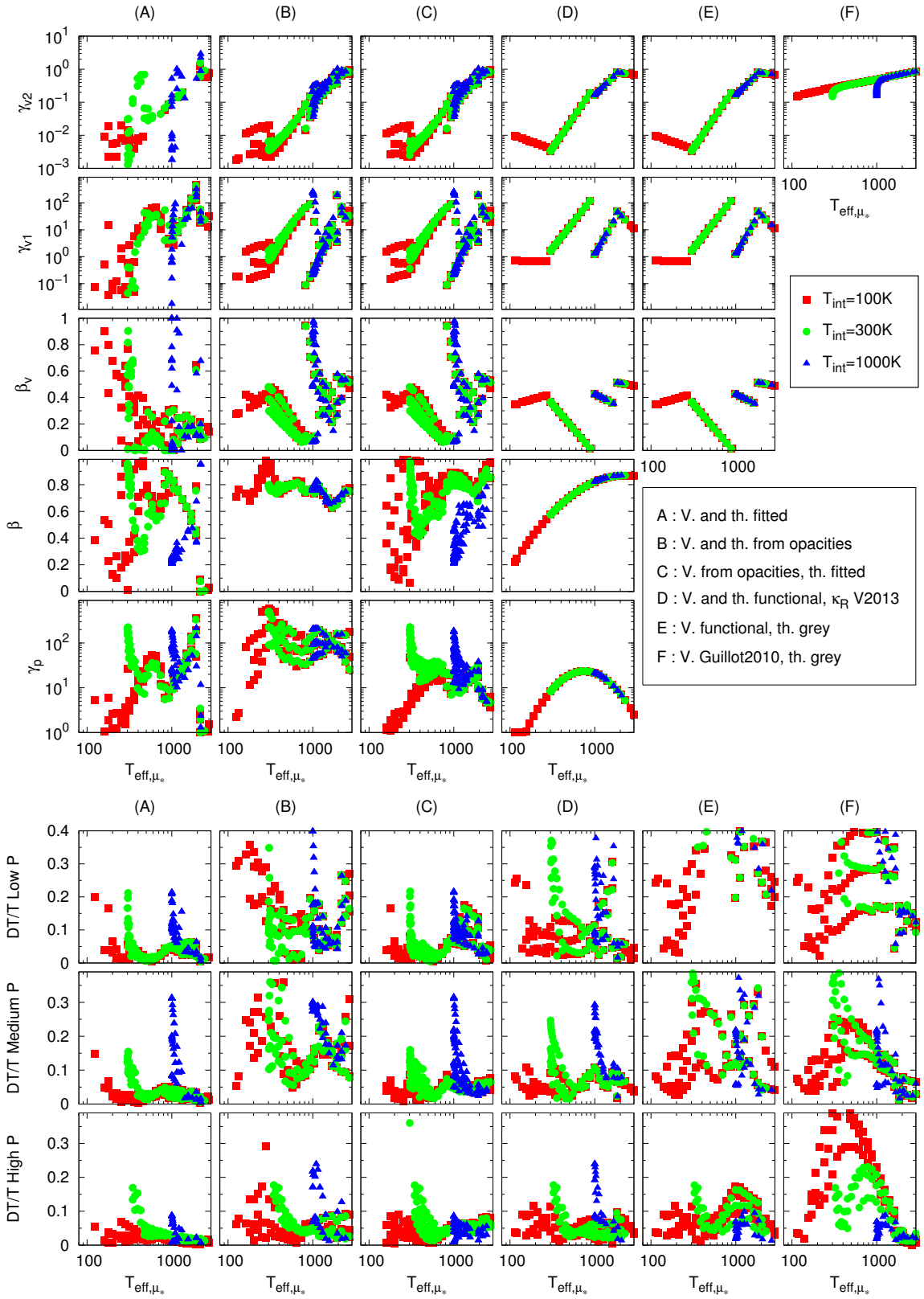

Fig. A.3: *Top panel*: coefficients obtained for the six different models described in Sec. 5.2 in function of the irradiation temperature for planets with a solar composition atmosphere with different gravities and an internal temperature of 100K, 300K and 1000K. The model of column D use the functional form of the coefficients derived in the case $T_{\rm int}$ = 100K only. The outliers at $T_{{\rm eff},\mu_*}$ = 300K and $T_{{\rm eff},\mu_*}$ = 1000K are due to the models with $T_{\rm int}$ = 300K and $T_{\rm int}$ = 1000K respectively. *Bottom panel*: Mean relative difference between the numerical and the analytical model for the six different models described in Sec. 5.2. The first line is the mean difference for 10^{-4} bar $< P < 10^{-2}$ bar, the second line for 10^{-2} bar $< P < 10^{0}$ bar and the third line for 10^{0} bar $< P < 10^{2}$ bar.

Conclusion

With the discovery of exoplanets with a continuum of properties in terms of composition, irradiation and gravity among other parameters, the role of fast and reliable analytical models have been revived. In this chapter, we derived a new, non-grey, analytical model for the thermal structure of irradiated atmospheres. We highlighted the role of the non-grey opacities in shaping the temperature profile. In the upper atmosphere, non-grey radiative cooling can lead to temperatures cooler than predicted by semi-grey models and closer to the outputs of numerical models. The deep atmospheric temperature can significantly increase in the presence of non-grey opacities, an effect known as the *blanketing effect* in stellar physics.

We then used a state-of-the-art numerical model based on the correlated-k distribution method that properly takes into account the line-by-line opacities. The calculated temperature profiles were used to calibrate the coefficients of our analytical model. As a result, we obtained a fast and accurate analytical solution for the thermal structure of irradiated planets that is valid for a wide range of irradiation temperatures and planet gravities. We showed that the condensation of chemical species affects both the optical and the thermal opacities. For example, titanium oxide is a major contributor of the optical opacities of hot, solar-composition atmospheres. We showed that its broad- band opacity flattens the total atmospheric opacities and reduces the non-grey thermal effects. As a consequence, planets without titanium oxide in their dayside atmosphere should have a hotter deep atmosphere than planets with a solar-composition atmosphere.

Pourquoi ces nuages de Jupiter qui répandent l'ombre et la fraîcheur dans ses plaines immenses?

Camille Flammarion - De la pluralité des mondes

Chapter 3

Atmospheric dynamics, clouds and chemical composition of hot Jupiters

Contents

Introduction

Radiative equilibrium sets the mean state of a planets' atmosphere. However, the atmospheric circulation locally redistributes the energy and drives the atmosphere out of equilibrium.

Numerous observations can constrain the atmospheric circulation. Secondary eclipse photometry can determine the mean dayside temperature of the planet and characterize the redistribution of energy (see Section 1.3). Thermal phase curves can determine the longitudinal variations of the temperature (see Section 1.4.1). Optical phase curves can determine the longitudinal variations of the albedo whereas with secondary eclipse mapping, the latitudinal variations of the albedo and the temperature can be retrieved (see Section 1.4.2). Finally, during transit, high resolution spectroscopy can constrain the mean wind speed at the terminator of the planet (see Section 1.2.2).

In this section we focus on the atmospheric dynamics of large planets in tight orbit. They are the planets for which the best observations will be available in the next years. In section 3.1 we show that planets in tight orbit should be tidally locked, with one hemisphere always facing the star. in Section 3.2, we expose the main equations determining the atmospheric circulation. In Section 3.3 we describe the possible circulation regimes for these planets. The consequences of the atmospheric circulation on the distribution and characteristics of condensates and chemical compounds is discussed in Section 3.4. Evidences for these interactions are described in Section 3.5.

3.1 The peculiarities of close-in planets

The best targets for atmospheric characterization are gas giant planets orbiting close to their stars. Close-in planets can have a revolution period of the order of days. Transits, secondary eclipses, and phase curves of the planet can be observed periodically and the signal-to-noise ratio of these observations can be increased by summing numerous observations. Moreover, close-in planets have a large probability to transit. They are therefore more numerous to orbit bright stars and, for this reason, more amenable to atmospheric characterization.

Close-in giant planets have tidal interactions with their stars. For most of the closest ones, no equilibrium is possible and the planet slowly falls toward the star (Levrard et al. 2009). The detection of these planets indicates that the timescale for tidal damping of the semi-major axis is larger than the systems age and thus at least of the order of several gigayears. The angular momentum of the planet can be damped much faster than the orbital momentum. The timescale for dissipating the angular momentum of a planet of mass M_p and radius R_p orbiting at a distance a from a star of mass M_* and radius R_* is given by Guillot et al. (1996)

$$\tau_\mathrm{sync} = Q \left(\frac{R_\mathrm{p}^3}{G M_\mathrm{p}}\right) \omega_\mathrm{p} \left(\frac{M_\mathrm{p}}{M_*}\right)^2 \left(\frac{a}{R_\mathrm{p}}\right)^6 \tag{3.1}$$

where the dissipation factor, Q is of order $2 \times 10^5 - 2 \times 10^6$ for hot Jupiters (Ferraz-Mello 2013) and $\omega = |\omega_\mathrm{rot} - \omega_{orb}|$ is the difference between orbital and rotation rates. Assuming an initial rotation rate equal to Jupiter's one ($\omega_\mathrm{rot} = 1.7 \times 10^{-4}\,\mathrm{s}^{-1}$) we see in Fig. 3.1 that most planets with a revolution period less than ten days should be synchronously rotating, with one side always facing the star and the other side always plunged in the dark.

The timescale for circularizing the orbit can also be calculated from the tide theory (see Gol-

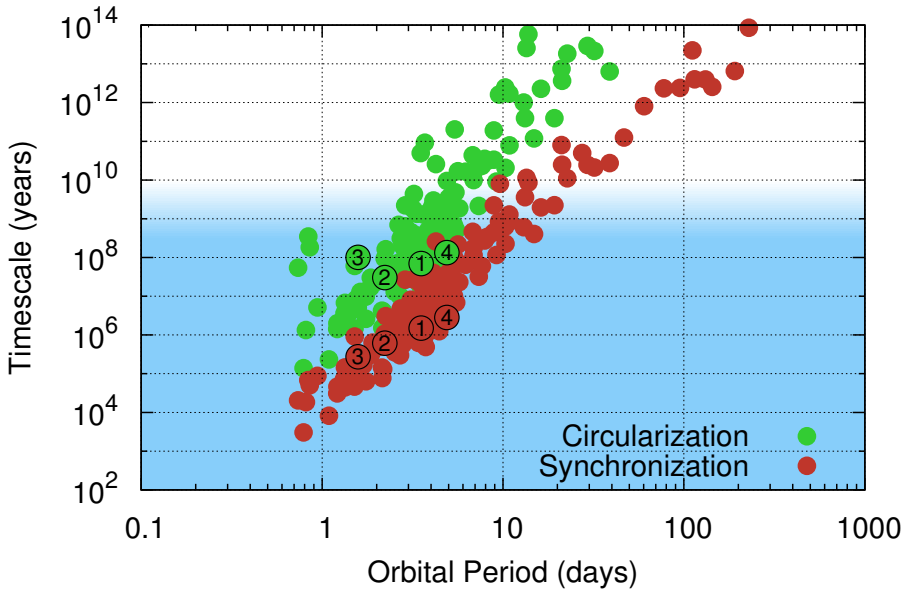

Figure 3.1. Synchronization (red) and circularization (green) timescales of planets with known mass and radius as a function of orbital period calculated for a tidal dissipation factor of $Q = 6 \times 10^5$ following (Ferraz-Mello 2013) and an initial spin rate comparable to Jupiter's. Planets in the blue area are likely to be circularized and/or synchronously rotating. Planets numbered are: 1) HD209458b, 2)HD189733b, 3)Kepler-7b, 4)GJ1214b.

dreich & Soter 1966; Rasio et al. 1996):

$$\tau_{\rm circ} = \frac{4}{63} Q \left(\frac{a^3}{G M_*} \right)^{1/2} \left(\frac{M_{\rm p}}{M_*} \right) \left(\frac{a}{R_{\rm p}} \right)^5 . \tag{3.2}$$

As seen in Fig. 3.1, the circularization timescale is larger than the synchronization timescale. The four planets we will focus on in this study should both synchronous and have their orbit circularized. Other planets can keep a significant eccentricity even if their their rotation period is synchronized. The planet is then in *pseudo-synchronous* state, with a rotation period given by Hut (1981):

$$P_{\rm rot} = \frac{(1 + 3e^2 + \frac{3}{8}e^4)(1 - e^2)^{3/2}}{1 + \frac{15}{2}e^2 + \frac{45}{8}e^4 + \frac{5}{16}e^6} P_{\rm orb} \tag{3.3}$$

This is the case, for example, of the hot Jupiter Hat-P-2b (Lewis et al. 2013).

Numerous exoplanets have been discovered around numerous different stars. For tidally-locked planets, the rotation rate and the irradiation flux at the top of the atmosphere both depend on the distance between the planet and the star. As seen in 3.2, known planets fill a large portion of the rotation rate/equilibrium temperature/gravity plane. Exoplanets in tight orbits therefore provide a unique opportunity to understand how the atmospheric circulation depends on the planet gravity,

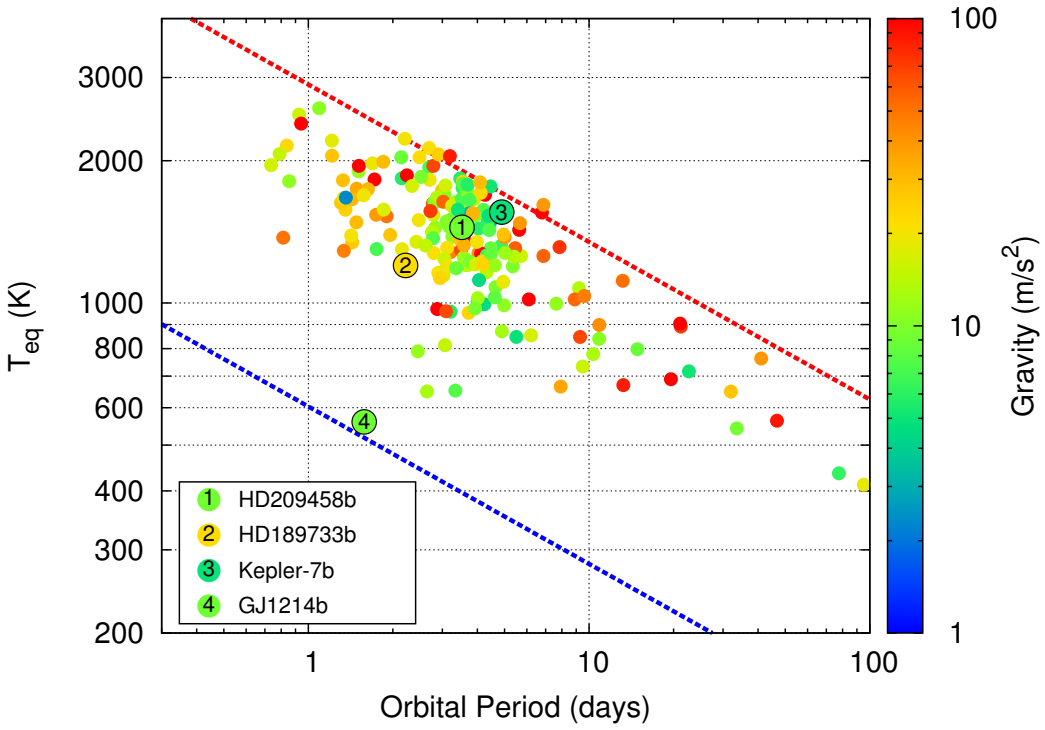

Figure 3.2. Equilibrium temperature assuming zero albedo of all known exoplanets with a mass and radius measured as a function of their rotation period, assuming tidal-locking. The blue (red) line is the equilibrium temperature for a planet around a M5 (A5) type star. Planets are color-coded according to their gravity. Known planets already cover a large portion of the rotation period/equilibrium temperature/gravity parameter space.

its rotation rate of the planet and of the stellar irradiation, three of the main factors governing the climate of a planet.

3.2 Governing equations

3.2.1 Full set of equations

A complete set of six equation with six unknowns governs the evolution of the atmosphere (see page 32 of Kalnay 2003):

- Newton's second law or conservation of momentum (one equation for each of the three velocity components);
- the continuity equation or conservation of mass;
- the equation of state of the gas, usually taken as the ideal gas law;
- the conservation of energy;

n equations must be added when considering n different chemical species that can be subject to chemical and physical reactions (*e.g.* condensation or evaporation). Newton's second law applied to a parcel of fluid in the rotating frame of the planet balances the momentum of a parcel of gas with the pressure gradient, the effective gravity (the gravity plus the centrifugal force) and the Coriolis force:

$$\frac{\mathrm{D}\vec{v}}{\mathrm{D}t} = -\frac{1}{\rho}\vec{\nabla}p - \vec{g} - 2\vec{\Omega} \times \vec{v} + \vec{D}\,. \tag{3.4}$$

In this equation, $\vec{v}$ is the velocity of the fluid parcel, ρ its density, p is the pressure, Ω is the angular velocity of the planet, $\vec{\nabla}$ is the gradient operator and $\vec{D}$ is a diffusion term. The material derivative is given by:

$$\frac{\mathrm{D}}{\mathrm{D}t} = \frac{\partial}{\partial t} + \vec{v} \cdot \vec{\nabla} \tag{3.5}$$

The expression of the gradient $\vec{\nabla}$ depends on the coordinate system. As long as the expression of $\vec{\nabla}$ has not been specified, equation 3.4 is said *vector invariant*. The continuity equation can be written:

$$\frac{\mathrm{D}\rho}{\mathrm{D}t} = -\rho\vec{\nabla} \cdot \vec{v}\,. \tag{3.6}$$

In atmospheres, the equation of state can be well approximated with the ideal gas law:

$$P = \frac{k_\mathrm{B}}{\mu}\rho T\,, \tag{3.7}$$

where k_B is the Boltzmann constant, T the local temperature and μ the mean molecular weight of the atmosphere. The energy equation reads:

$$\frac{\mathrm{D}T}{\mathrm{D}t} = \frac{q}{c_\mathrm{p}} + \frac{1}{\rho c_\mathrm{p}}\frac{\mathrm{D}P}{\mathrm{D}t}\,, \tag{3.8}$$

where c_p is the specific heat at constant pressure and q is the heating rate (in W/kg). The first term is the thermodynamic heating, that usually comes from radiative heating, latent heat or chemical energy. The second term is the diabatic heating: a gas that is compressed increases its temperature.

The expression of the gradient and thus the material derivative depends on the chosen coordinate system. For a planet atmosphere, the natural coordinate are the spherical coordinates (ϕ, λ, r) where ϕ is the longitude, θ is the latitude from equator to the poles, and r is the distance to the center of the planet. The velocities (u, v, w) following the unit vectors $(\vec{e_\phi}, \vec{e_\theta}, \vec{e_r})$ are defined as:

$$\begin{aligned} u &= r\cos\lambda\frac{\mathrm{D}\phi}{\mathrm{D}t}\,, \\ v &= r\frac{\mathrm{D}\lambda}{\mathrm{D}t}\,, \\ w &= \frac{\mathrm{D}r}{\partial t}\,. \end{aligned} \tag{3.9}$$

Then we can express the operator $\vec{\nabla}$:

$$\vec{\nabla} = \frac{1}{r\cos\theta}\frac{\partial}{\partial\phi}\vec{e_\phi} + \frac{1}{r}\frac{\partial}{\partial\theta}\vec{e_\theta} + \frac{\partial}{\partial r}\vec{e_\mathrm{r}} \tag{3.10}$$

and the material derivative:

$$\frac{\mathrm{D}}{\mathrm{D}t} = \frac{\partial}{\partial t} + \frac{u}{r\cos\theta}\frac{\partial}{\partial \phi} + \frac{v}{r}\frac{\partial}{\partial \theta} + w\frac{\partial}{\partial r}\,. \tag{3.11}$$

The momentum and energy equations can now be written in spherical coordinates (Mayne et al. 2014):

$$\frac{Du}{Dt} = \frac{uv\tan\theta}{r} - \frac{uw}{r} + fv - f'w - \frac{1}{\rho\, r\cos\theta}\frac{\partial P}{\partial \phi} + D_\phi, \tag{3.12}$$

$$\frac{Dv}{Dt} = -\frac{u^2\tan\theta}{r} - \frac{vw}{r} - uf - \frac{1}{\rho\, r}\frac{\partial P}{\partial \theta} + D_\theta, \tag{3.13}$$

$$\frac{Dw}{Dt} = \frac{u^2+v^2}{r} + uf' - g(r) - \frac{1}{\rho}\frac{\partial P}{\partial r}, \tag{3.14}$$

$$\frac{D\rho}{Dt} = -\rho\left[\frac{1}{r\cos\theta}\frac{\partial u}{\partial \phi} + \frac{1}{r\cos\theta}\frac{\partial (v\cos\theta)}{\partial \theta} + \frac{1}{r^2}\frac{\partial (r^2 w)}{\partial r}\right], \tag{3.15}$$

$$\tag{3.16}$$

where $g(r)$ is the height dependent gravity:

$$g(r) = g_\mathrm{p}\left(\frac{R_\mathrm{p}}{r}\right)^2, \tag{3.17}$$

with g_p is the gravitational acceleration at $r = R_\mathrm{p}$. f and f' are the Coriolis parameters defined as,

$$f = 2\Omega\sin\theta, \tag{3.18}$$

and

$$f' = 2\Omega\cos\theta, \tag{3.19}$$

3.2.2 Pressure coordinates

In planetary atmospheres, most of the physical processes scale with pressure rather than height. Thus, using the pressure as a vertical coordinate greatly simplifies the governing equations. Moreover, as the pressure depends exponentially with height, the solution of the equations are more easily discretized and solved numerically in pressure coordinates. In pressure coordinate, the material derivative becomes:

$$\frac{\mathrm{D}}{\mathrm{D}t} = \frac{\partial}{\partial t} + \vec{v_h}\cdot\vec{\nabla_p} + \omega\frac{\partial}{\partial p} \tag{3.20}$$

where $\vec{v_h}$ is the horizontal velocity (i.e. the velocity orthogonal to the vertical direction), ∇_p is the gradient in the plane orthogonal to the pressure gradient and $\omega = \frac{\mathrm{D}p}{\mathrm{D}t}$ is the vertical velocity in pressure coordinates. The vertical velocity in pressure and height coordinates are related:

$$\omega = \frac{\partial p}{\partial t} + \vec{v_h}\cdot\vec{\nabla}p + w\frac{\partial p}{\partial z} \tag{3.21}$$

The second term can be written $\vec{\nabla}(p\,\vec{v_h}) - p\vec{\nabla}\cdot\vec{v_h}$. Assuming hydrostatic equilibrium we see that the *average* value of the vertical velocity in pressure coordinate can be easily related to the mean vertical velocity in height coordinate:

$$\langle\omega\rangle = -\rho g\langle w\rangle\,, \tag{3.22}$$

an approximation often used when comparing three average values of three-dimensional models to one-dimensional models.

3.2.3 Primitive equations

The most commonly used set of equations to study the dynamics of an entire planet are the Primitive equations. They can be derived from the full set of equations with four assumptions (see also Table 3.1) :

1. *Constant gravity.* The gravity is supposed constant through the whole atmosphere. This is valid if the vertical extent of the atmosphere is small compared to the radius of the planet.

2. *The shallow-fluid approximation.* We write the position of the gas parcel $r = R_\mathrm{p} + z$ where R_p is the fixed radius of the planet and z is the altitude above this radius. We then re-write the *vector invariant* form of the momentum equation (3.4) assuming that $R_\mathrm{p} >> z$

3. *The traditional approximation.* Whenever the *shallow-fluid approximation* is applied at the spherical coordinates equation and not to the vector invariant equations, the resulting equations lack of self-consistency and, in particular, they do not conserve the angular momentum anymore (Phillips 1966). In that case, the terms proportional to $1/r$ (metric terms) and the Coriolis terms proportional to f' are neglected in the momentum equations. To be valid, this approximation needs $N^2 >> \Omega^2$ (Phillips 1968), however White & Bromley (1995) show that it might break whenever large diabatic processes are at stake, a limitation further confirmed by (Mayne et al. 2014).

4. *The hydrostatic approximation.* In the vertical momentum equation, the gravitational term is assumed to be balanced by the pressure gradient term. This is valid as long as the vertical extent of the atmosphere is small compared to its vertical extent (i.e. $(H/L)^2 << 1$).

The resulting primitive equations in pressure coordinate are (*e.g.* Showman et al. 2008; Kalnay 2003, pp. 60-67):

$$\frac{\partial \vec{v_h}}{\partial t} + \vec{v_h} \cdot \vec{\nabla}_p \vec{v_h} = -\vec{\nabla}_p \Phi - f \vec{k} \times \vec{v_h} + D_{\vec{v_h}} \,, \tag{3.23}$$

$$\frac{\partial \Phi}{\partial p} = -\frac{1}{\rho} \,, \tag{3.24}$$

$$\vec{\nabla} \cdot \vec{v_h} + \frac{\partial \omega}{\partial p} = 0 \,, \tag{3.25}$$

$$\frac{\partial T}{\partial t} + \vec{v_h} \cdot \vec{\nabla}_p T = \frac{q}{c_\mathrm{p}} + \frac{\omega}{\rho c_\mathrm{p}} + D_T \tag{3.26}$$

ϕ is the gravitational potential. D_T and $D_{\vec{v_h}}$ are dissipation terms and are discussed later.

The last equation can be written in a slightly different way:

$$\frac{\partial \Theta}{\partial t} = \frac{\Theta}{T} \frac{q}{c_\mathrm{p}} + D_\Theta \,. \tag{3.27}$$

$\Theta = T \left(P/P_0\right)^{R/c_\mathrm{p}}$ is the potential temperature and P_0 is a reference pressure that does not affect the dynamics and D_Θ is a dissipation term. The potential temperature is conserved in the absence of dissipation or diabatic processes.

Table 3.1. Main approximations of the primitive equations and their validity. N is the Brunt-Väisälä frequency, $N = \sqrt{-\frac{g(r)}{\rho_0}\frac{\partial \rho(r)}{\partial r}}$). SI units are used for the comparisons. Based on a table by Mayne et al. (2014).

Name	Approximation	Formal Condition	HD 209458b
constant gravity	$g(r) = g_\mathrm{p} = \frac{GM_\mathrm{p}}{R_\mathrm{p}^2}$	$z \ll R_\mathrm{p}$	$\left\{ \begin{array}{l} \sim 10^7 < 10^8 \end{array} \right.$
shallow–fluid	$r \to R_\mathrm{p}$ & $\frac{\partial}{\partial r} \to \frac{\partial}{\partial z}$	$z \ll R_\mathrm{p}$	
traditional	$\frac{uw}{r}$, $\frac{vw}{r}$, $\frac{u^2+v^2}{r}$, $2\Omega(u,w)\cos\theta \to 0$	$N^2 \gg \Omega^2$	$\sim 10^{-5} \gg 10^{-10}$
hydrostasy	$\frac{\partial p}{\partial r} = -\rho g$	$H \ll L$	$\sim 10^7 < 10^8$

Even though we assumed hydrostatic equilibrium, the vertical velocity is nonzero as it enters via the mass-continuity equation and the thermodynamic energy equation. This approach provides a reasonable estimate of the vertical velocities as long as the vertical accelerations are negligible. In an atmosphere that is not convective, the vertical motions can only occur as fast as radiation can remove the temperature perturbations caused by the adiabatic ascent/descent. In that case, it is the energy equation (3.26), which *does not* assume hydrostatic equilibrium rather than the momentum equation that determines the vertical velocities (Showman et al. 2008). As shown by Mayne et al. (2014), vertical velocities are rather insensitive to the hydrostatic equilibrium approximation but are indeed affected by the approximation of constant gravity. Relaxing the assumption of constant gravity changes the vertical velocities by a factor of two.

The terms $D_{\vec{v_h}}$ and D_T (or D_Θ) are dissipation terms. They can represent different things. Physically they can parameterize the dissipation of the winds by any kind of drag, such as Ohmic dissipation, Kelvin-Helmoltz instabilities etc. In that case $D_{\vec{v_h}}$ is usually represented by a *Rayleigh drag*:

$$D_{\vec{h}} = -\frac{\vec{v_h}}{\tau_\mathrm{drag}}\,, \tag{3.28}$$

where τ_drag, the *drag* time-scale represents the strength of the drag force. Assuming that the kinetic energy is locally dissipated into heat we obtain

$$D_\mathrm{T} = \frac{\vec{v_h}^2}{2c_\mathrm{p}\tau_\mathrm{drag}}\,. \tag{3.29}$$

Note that *local* dissipation of the kinetic energy is not always true. When magnetic fields are involved, for example, the kinetic energy is transformed into electrical currents that can dissipate at different locations. The dissipation terms are often used as a way to smooth the numerical noise of the simulations. In our simulations, we used a fourth order Shapiro filter (Shapiro 1970) (i.e. a damping proportional to $\vec{v}^4$). This filters the small-scale grid noise whereas the large-scale pattern remain unaffected.

3.2.4 Relevant scales in hot Jupiters atmospheres

To solve the primitive equations on a grid of space and time, we must choose the relevant spatial and temporal grid scales. Although the exact choice is usually done by numerical experiments (i.e.

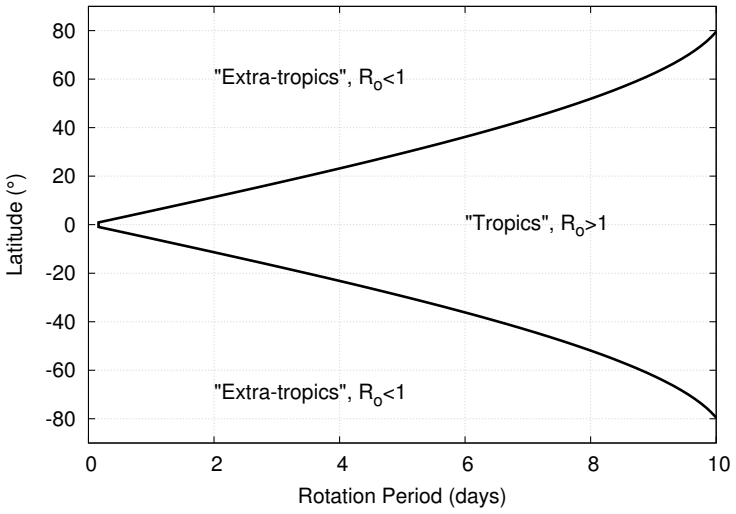

Figure 3.3. Rossby number equal unity line as a function latitude and planet rotation period. The calculation correspond to a Jupiter size planet with fast winds such as the ones predicted in hot Jupiters atmospheres ($U \approx 1\,\mathrm{km/s}$) and a length scale for the flow equal to the planetary radius. When the Rossby number is larger than one, Coriolis forces are negligible. This defines the "Tropical zone". When the Rossby number is smaller than one, Coriolis forces are dominant. This defines the "extra-tropical" zone.

the resolution at which the simulation does not differ significantly if the resolution is doubled and the larger time-step for which the simulation does not crash), simple physical arguments can be made to get an order of magnitude of the scales relevant to study the atmospheric dynamics of hot Jupiters..

Length scale

The momentum equation (3.23) balances the advection, Coriolis, pressure gradient and dissipation forces. Coriolis forces vary strongly with the rotation rate of the planet and, inside one particular planet, with latitude. The Rossby number measures the balance between the advection term and the Coriolis term in the momentum equation:

$$Ro \equiv \frac{U}{fL}\,, \tag{3.30}$$

where U is the typical wind speed, L the typical horizontal scale (typically the deformation radius, see hereafter) and $f = 2\Omega \sin\phi$ is the Coriolis parameter. When the Rossby number is much larger than one, the Coriolis force is negligible and the force balance is between advection, pressure gradient and dissipation. When the Rossby number is much smaller than one, the advection term becomes negligible and the force balance is between pressure gradient and Coriolis forces. A situation known as *geostrophy*. On Earth, the line $Ro = 1$ corresponds roughly to the tropics. Thus, following Showman et al. (2013b), we call *tropics* the zone where $Ro > 1$ and *extra-tropics* the zone where $Ro << 1$. In the tropics local pressure gradients are expected to be small whereas in the extra-tropics, vortices and Rossby waves should dominate the flow. For hot Jupiters, the Rossby number at midlatitudes is of order of $0.01 - 4$ depending on the planet and of the assumed wind speed (see Table **??**). The extent of the tropical and extratropical zones for typical hot Jupiters are described in Figure 3.3. Hot Jupiters with a rotation period between $\approx 2 - 5$ days such as HD 209458b and HD189733b have a tropical zone that extends to $\approx 20°$. Planets that rotate faster are "extra-tropics" planets whereas planets with a smaller rotation rate are "full-tropics" planets.

In planetary atmospheres, pressure gradients tend to be smoothed out by gravity wave adjustment : parcel of gas expand and push their neighbors out of a high pressure zone. However, as the gravity wave expands radially from a maximum of pressure, it is deflected by the Coriolis force.

The distance at which the Coriolis force becomes dominant and stops the gravity wave adjustment is called the Rossby deformation radius:

$$L_D = \frac{ND}{f} \tag{3.31}$$

where N is the Brunt-Väisälä frequency, i.e. the oscillation frequency of gravity waves. For an isothermal atmosphere we have $N = \sqrt{c_\mathrm{p}} k_\mathrm{B} \sqrt{g/H}$ where c_p is the heat capacity at constant pressure per atmospheric particles. For hot Jupiters, $c_\mathrm{p}/k_\mathrm{B}$ can vary from $\approx 3-10$, depending on the pressure and temperature (Showman & Guillot 2002). D is the vertical length scale of the atmosphere, typically of the order of one scale height whereas f is the Coriolis parameter $f = 2\Omega \sin\phi$. The deformation radius gives a good estimate of the size of the eddies in solar-system planets. For hot Jupiters, it predicts atmospheric structures that are of the order of the planetary radius (see table **??**). Thus, the atmospheric circulation of hot Jupiters should be dominated by large scale motions.

Small scale vortices can interact coherently to inject their energy into larger atmospheric structures. At small scales, non-linear advection of vortices makes this inverse cascade possible. At large scales, linear advection of vortices dominates an the cascade becomes inefficient. The transition happens at the Rhines scale :

$$L_\mathrm{Rh} = \pi \sqrt{\frac{U}{\beta}} \tag{3.32}$$

where $\beta = \frac{2\Omega \cos\phi}{R_\mathrm{p}}$ is the meridional gradient of the Coriolis force. This effect, known as the "β-effect" is responsible for the banded appearance of all solar-system atmospheres Cho & Polvani (1996). The Rhines scale is actually a good estimate of the size of the different bands observed in solar-system atmospheres, it is of the order of $\approx 1/10^{th}$ of the planetary radius in Jupiter and Saturn whereas it is comparable to the planetary radius for hot Jupiters (see Table **??**). Thus, hot Jupiters are expected to have a small ($\approx 1-3$) number of zonal jets compared to Jupiter and Saturn. Resolving the Rhines scale in a simulation is fundamental, but the scale at which the energy is injected before cascading up to the Rhines scale should also be resolved. In solar-system atmospheres, the energy at small-scales is contained in turbulence or in the latent heat deposited by thunderstorms (Lian & Showman 2010). Therefore a very high spatial resolution is needed to resolve those scales. Thus, global circulation models of Jupiter and Saturn with zonal jets often assume the presence of an *ad-hoc* small-scale forcing. Global circulation models of hot-Jupiters, however, have produced superrotating jets without the need of an*ad-hoc* forcing. As shown by Showman & Polvani (2011), the large scale day/night forcing, associated with a large deformation radius (a fraction of the planetary radius), ensures that most of the energy that powers the jets is directly injected into large-scale eddies. Thus, global circulation models of hot Jupiters can produce longitudinal jets due to the β-effect without resolving the small turbulent scales. Whether this large scale, day/night forcing is a larger source of energy than the presence of small scale turbulence is still subject of debate (small-scale gravity waves, for example, could participate significantly to the problem).

The large values of the deformation radius and the Rhines scales in hot Jupiters atmospheres, combined with the large-scale day/night forcing ensure that large scales carry most of the energy. A first consequence is that bulk atmospheric properties of these planets can be retrieved from the observations. Observations are often averaged spatially, around the limb of the planet or over one hemisphere of the planet. An atmospheric circulation dominated by large scale patterns produces

signatures that are still observable when averaged spatially. Moreover, this allows global circulation models with only a moderate resolution to provide reasonable insight into the atmospheric circulation of hot Jupiters.

Table 3.2. Planetary parameters, table from Showman et al. (2011)

Planet	$R_{\rm p}^{*}$ (10^3 km)	Rotation period$^{\sharp}$ (Earth days)	Ω (rad sec^{-1})	gravity$^{\aleph}$ (m sec^{-2})	$F_{*}^{\square}$ (W m^{-2})	$T_{\rm e}^{\spadesuit}$ (K)	$H_p^{\dagger}$ (km)	$U^{\ddagger}$ (m sec^{-1})	$Ro^{\P}$	$L_D/R_{\rm p}^{\clubsuit}$	$L_{\rm Rh}/R_{\rm p}^{\diamond}$
Venus	6.05	243	3×10^{-7}	8.9	2610	232	5	~ 20	10	70	7
Earth	6.37	1	7.27×10^{-5}	9.82	1370	255	7	~ 20	0.1	0.3	0.5
Mars	3.396	1.025	7.1×10^{-5}	3.7	590	210	11	~ 20	0.1	0.6	0.6
Titan	2.575	16	4.5×10^{-6}	1.4	15	85	18	~ 20	2	10	3
Jupiter	71.4	0.4	1.7×10^{-4}	23.1	50	124	20	~ 40	0.02	0.03	0.1
Saturn	60.27	0.44	1.65×10^{-4}	8.96	15	95	39	~ 150	0.06	0.03	0.3
Uranus	25.56	0.72	9.7×10^{-5}	8.7	3.7	59	25	~ 100	0.1	0.1	0.4
Neptune	24.76	0.67	1.09×10^{-4}	11.1	1.5	59	20	~ 200	0.1	0.1	0.6
WASP-12b	128	1.09	6.7×10^{-5}	11.5	8.8×10^6	2500	800	-	0.01–0.3	0.1	0.2–1.5
HD 189733b	81	2.2	3.3×10^{-5}	22.7	4.7×10^5	1200	200	-	0.03–1	0.3	0.4–3
HD 149026b	47	2.9	2.5×10^{-5}	21.9	1.8×10^6	1680	280	-	0.06–2	0.8	0.6–4
HD 209458b	94	3.5	2.1×10^{-5}	10.2	1.0×10^6	1450	520	-	0.04–1	0.4	0.5–3
TrES-2	87	2.4	2.9×10^{-5}	21	1.1×10^6	1475	260	-	0.03–1	0.3	0.4–3
TrES-4	120	3.5	2.0×10^{-5}	7.8	2.5×10^6	1825	870	-	0.03–1	0.4	0.4–3
HAT-P-7b	97	2.2	3.3×10^{-5}	25	4.7×10^6	2130	320	-	0.02–1	0.3	0.4–3
GJ 436b	31	2.6	2.8×10^{-5}	9.8	4.3×10^4	660	250	-	0.1–3	0.7	0.8–5
HAT-P-2b	68	5.6	1.3×10^{-5}	248	9.5×10^5	1400	21	-	0.1–3	1	0.8–5
Corot-Exo-4b	85	9.2	7.9×10^{-6}	13.2	3.0×10^5	1080	300	-	0.1–4	1	0.9–5

Note. — *Equatorial planetary radius. $^{\sharp}$Assumes synchronous rotation for exoplanets. $^{\aleph}$ Equatorial gravity at the surface. $^{\square}$Mean incident stellar flux. $^{\spadesuit}$Global-average blackbody emission temperature. †Pressure scale height, evaluated at temperature $T_{\rm e}$. ‡Rough estimates of characteristic horizontal wind speed. Estimates for Venus and Titan are in the high-altitude superrotating jet; both planets have weaker winds (few m sec^{-1}) in the bottom scale height. In all cases, peak winds exceed the listed values by factors of two or more. ¶Rossby number, evaluated in mid-latitudes using wind values listed in Table and $L \sim 2000$ km for Earth, Mars, and Titan, 6000 km for Venus, and 10^4 km for Jupiter, Saturn, Uranus, and Neptune. For exoplanets, we present a range of possible values evaluated with $L = a$ and winds from 100 to 4000 m sec^{-1}. $^{\clubsuit}$Ratio of Rossby deformation radius to planetary radius, evaluated in mid-latitudes with H equal to the pressure scale height and N appropriate for a vertically isothermal temperature profile. $^{\diamond}$Ratio of Rhines length (Eq. 3.32) to planetary radius, calculated using the equatorial value of β and the wind speeds listed in the Table.

Time scales

A fundamental timescale in hot Jupiter atmospheres is the rate at which a parcel of gas looses its energy. Because the blackbody emission is proportional to T^4 hotter atmospheres should cool faster and have smaller radiative timescales. The time to cool is also proportional to the optical depth of the parcel of gas. As the opacities increase rapidly with pressure, the radiative timescale can vary by orders of magnitude between the upper and the deep layers of the atmosphere. For typical hot Jupiters, it goes from thousands of years at pressures of $\approx$ 100bar to hundreds of seconds at $\approx 1\mu$bar (Showman et al. 2009) and tens of seconds at pressures of $\approx 1\mu$bar (see Figure 3.4).

To a first order, the radiative timescale at the photosphere of the planet can be approximated as the ratio between the available thermal energy per unit area within a pressure scale-height and the net radiative flux from that layer (Showman & Guillot 2002):

$$\tau_{\rm rad} \sim \frac{P c_{\rm P}}{4 g \sigma T_{\rm eq}^3} \,. \tag{3.33}$$

Direct measurements of the radiative timescales in exoplanets' atmospheres might become possible with precise, multi-wavelength observations of the thermal phase curves of eccentric planets. As shown by Lewis et al. (2013), planets such as HAT-P-2b ($e \approx 0.5$) provide a unique opportunity to disentangle the thermal and advective processes that shape the thermal phase curves of exoplanets.

3.3 Dynamical regimes of hot Jupiters atmospheres

The dynamics of hot Jupiters atmospheres have now been widely studied with a whole hierarchy of models: order of magnitude considerations, analytical solutions, shallow-water simulations and three-dimensional global circulation models. All those models yield a coherent picture of the atmospheric dynamics of hot Jupiters. The main patterns seem to be a circulation dominated by an equatorial super-rotating jet and a day-to-night flow at higher latitudes, the presence of km/s winds and the presence of a large day/night contrast. I will now describe those different circulation patterns in more details.

3.3.1 Equatorial superrotation

Most global three-dimensional models of hot Jupiters produce an atmospheric circulation dominated by a fast eastward (superrotating) jet at the equator. Such a superrotating equatorial jet exists in Venus, Titan, Jupiter and Saturn, but its origin is not yet completely understood. As the equator lays further away from the rotation axis of the planet than the poles, the momentum per unit mass of a parcel of fluid is higher at the equator than at the poles. Thus, the simple advection of parcel of gas from the high latitudes to the low latitudes cannot produce a superrotating jet: a mechanism to pump angular momentum to the equator is necessary.

Showman & Polvani (2011) proposed a plausible mechanism to generate superrotating equatorial jets in hot Jupiters atmospheres. The main pumping mechanism is due to the presence of tilted eddies in the mid-latitude regions. The flow in the eddies transports angular momentum from the high-latitude regions to the equatorial ones. Such tilted eddies naturally arise from the interaction between two types of planetary-scale waves. The large radiative forcing excites the

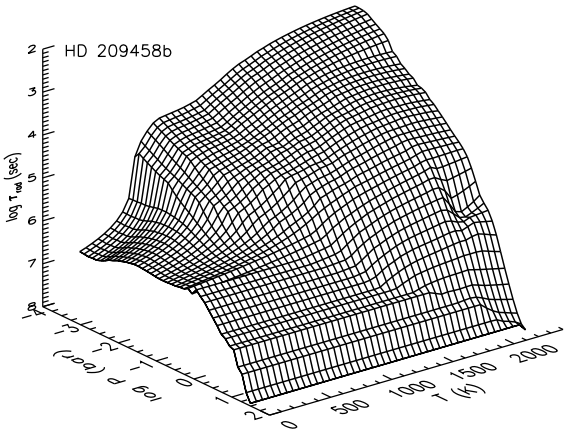

Figure 3.4. Radiative timescale as a function of pressure and temperature for a model of HD 209458b. Figure from Showman et al. (2008).

so-called Kelvin waves (a Kelvin wave is equivalent to a Rossby wave without the meridional component of the wind). At slightly higher latitudes, the forcing excites Rossby waves. Rossby waves arise from the conservation of the total potential vorticity of a parcel of gas. Large scale Rossby waves propagate westward (Durran 1988). The different directions of propagation of these two waves naturally tilt the eddies produced by the Rossby wave in the mid-latitudes. Kelvin and Rossby waves are generated by the strong heating in the dayside. They are trapped around the equator because of the Coriolis forces. They propagate until they are damped, creating steady, planetary-scale, tilted eddies. As the Kelvin and Rossby waves transport energy, the hottest spot in the equator is shifted to the east, whereas the hottest spot in the mid-latitudes is shifted west of the substellar point. The resulting chevron-like structure, as shown in the third panel of Figure 3 of Parmentier et al. (2013) presented in Section 3.4 is a signature of this wave-driven mechanism to produce the superrotation.

This mechanism only works if the Rossby and Kelvin waves can efficiently transport some of the radiative energy. If the atmosphere looses its energy by radiation or if the wave is damped too fast, the tilted eddies cannot form and this mechanism is inhibited. As shown by Showman et al. (2013a), by comparing the radiative timescale, the drag timescale and the time for a wave to propagate over one hemisphere correctly estimate the atmospheric regime. The mechanism for equatorial superrotation is inhibited when :

$$\tau_{\rm rad} \text{ or } \tau_{\rm drag} << \frac{R_{\rm p}}{NH} \tag{3.34}$$

Where N is the Brunt-Väisälä) frequency and H the scale height. For a typical hot Jupiter, $a/NH \approx 10^5$s. This threshold is crossed around $P \approx 0.1$bar in HD 209458b (Iro et al. 2005).

In the presence of drag Showman & Polvani (2011) identified another mechanism to produce tilted eddies in the mid-latitudes. The mechanism is based on an equilibrium between the pressure gradient, the Coriolis and the frictional drag forces. In the northern hemisphere, the Coriolis force points to the right of the direction of the wind (the opposite is true in the southern hemisphere) whereas the drag force usually points opposite to the wind direction. When the radiative timescale is short, the pressure gradient points in the zonal direction and the winds resulting from the three-force balance are tilted toward the equator.

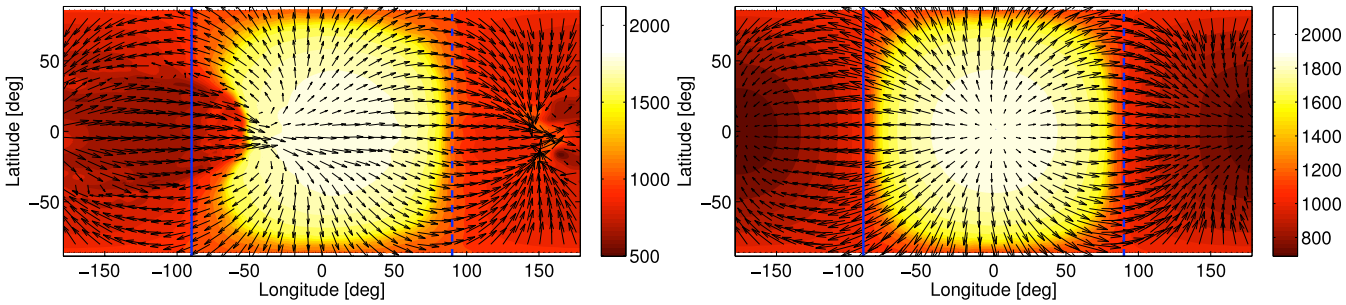

Figure 3.5. Temperature (color) and winds (arrows) at 0.1mbar of three-dimensional models of HD 209458b obtained with the MITgcm without drag (left) and including strong drag (right, $\tau_{\rm drag} = 10^4$s). In the drag-free case, the balance between advection, Coriolis forces, and pressure gradient forces lead to the formation of a superrotating jet. In the strong drag case, the jet is damped and the circulation is dominated by a day-to-night flow. Figure from Showman et al. (2013a).

Drag-free three-dimensional models of HD 209458b produce an equatorial superrotating jet down to pressures of $\approx$ 0.1mbar, as can be seen in the right panel of Figure 3.5. Another mechanism must be present to produce tilted velocities and pump energy into the jet. When the Rossby number is close to unity, the pressure gradient force is balanced by both advection and Coriolis forces. A parcel of gas that is flowing from the substellar to the antistellar point by the poles will be significantly deflected eastward, creating the tilted eddies necessary to pump the superrotating jet. Such a mechanism is valid in the low $\tau_{\rm rad}$ case, when the pressure gradient actually points from the substellar to the antistellar point. This mechanism should only be inhibited by drag. For a typical hot Jupiter Showman et al. (2013a) estimated that a drag time constant of the order of 10^4s at pressure less than $\approx$ 0.1bar to 10^6s at pressures of several bars was necessary to directly damp the jet.

Whenever the mechanism that pumps energy in the superrotating jet is inhibited, due to a strong drag for example, the atmospheric flow becomes symmetrical compared to the substellar-antistellar direction and the circulation is dominated by a day-to-night flow, as shown in the right panel of Figure 3.5. This is particularly true at low pressure, where the radiative timescales are short.

3.3.2 Velocities

Horizontal velocities

Simulations of drag-free hot Jupiters atmospheres lead to horizontal velocities of several kilometers per seconds. Those strong velocities are powered by the large day/night temperature contrast in the atmosphere but the actual strength of the winds results from a balance between forcing and damping. The forcing term depends on how the radiation from the parent star is absorbed in the atmosphere. The chemical composition of the atmosphere sets the opacities and thus determines in which layers the stellar irradiation is deposited. The circulation, in turn, modifies the composition of the atmosphere by mixing material from day to night and from deep layers to the upper layers. Because the composition of hot Jupiters atmospheres can be derived from observations (see introduction), we should be able to constrain the forcing term more efficiently in

the next years.

The damping term, however, is more difficult to quantify. As shown in Figure 3.6, the drag timescale have a strong influence on the mean wind speeds of the planet. In solar-system planets, the mechanism that damps the energy of the winds is unclear. In a hot Jupiter like HD 209458b, shear instabilities due to the interaction between the winds and the interior can dissipate winds that flow faster than $\approx$ 3km/s (Showman & Guillot 2002). Shocks are expected (Heng et al. 2012) and might play a significant role in the dissipation of the kinetic energy. Turbulence and breaking waves should ultimately dissipate the kinetic energy of the winds. Representing small scale turbulence and breaking waves in a global circulation model requires a parametrization of the dissipation, whose value is unknown for the moment (Li & Goodman 2010). Lastly magnetic drag could play a major role in ionized atmospheres. Until recently, the works involving magnetic interactions in the atmosphere of hot-Jupiters considered the magnetic effects as a simplified drag (Perna et al. 2010; Rauscher & Menou 2013). They show that the presence of a planetary magnetic field of $\approx$ 10G could decrease the mean wind speed by a factor of $\approx$ 3. Later, Batygin et al. (2013) showed that magnetic interactions could not only slow the mean winds, but could also affect qualitatively the atmospheric circulation by limiting the presence of a day-to-night flow. This is, however, an open question as hot Jupiters might not be ionized enough to have a magnetically controlled weather (Rogers & Showman 2014).

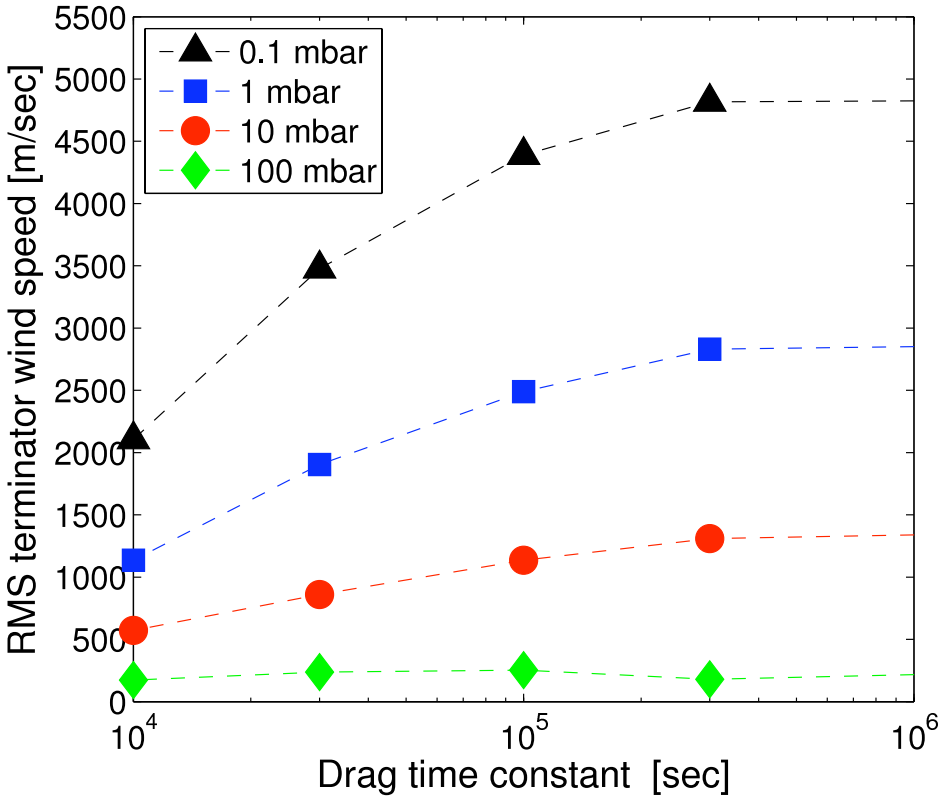

Figure 3.6. Steady-state root-mean-square wind speeds at the terminator for different pressures versus frictional drag time constant from a sequence of HD 209458b models including drag. Drag time constant of 10^4 are the lowest values obtained by Perna et al. (2010) for Ohmic drag. The wind speeds for $\tau_{\rm drag} = 10^6$ actually correspond to the no-drag case $\tau_{\rm drag} \to \infty$. Figure from Showman et al. (2013a)

Vertical velocities

Solving the primitive equations one can predict the vertical velocities in the planet's atmosphere, even though the primitive equations assume hydrostatic equilibrium. This apparent contradiction is actually not a problem. The hydrostatic equilibrium does not neglect the vertical motions, but

neglects their accelerations, what, for a typical hot Jupiter is a correct assumption (Showman et al. 2008). In stably-stratified atmospheres, such as the ones of hot-Jupiters, the vertical velocities are set by the thermodynamic energy equation and not the momentum equation. Adiabatic expansion (resp. contraction) in ascending (resp. descending) air causes the temperature of a parcel of gas to decrease (resp. increase) over time. In the absence of radiation, such steady flow patterns are unsustainable because they induce density perturbations that resist the motion (i.e., ascending air becomes denser and descending air becomes less dense than the surroundings at that altitude). Thus, steady vertical motion in a stable atmosphere can only occur as fast as radiation can remove the temperature perturbations caused by the adiabatic ascent/descent. A reliable non-grey radiative transfer scheme is therefore essential to model the vertical flows in hot Jupiters atmospheres. We note that this argument does not depend on the hydrostatic equilibrium assumption and remains valid if this assumption is removed. As shown by Mayne et al. (2014), the vertical velocities predicted by 3D models remain unaffected when the traditional approximation and the shallow-fluid approximation are released. The assumption of constant gravity, however, have larger consequences. For a typical hot Jupiter, gravity can vary by as much as 20% between the deep (≈ 100 bar) and the upper atmosphere (≈ 1 µbar). This changes the stratification of the atmosphere and leads to variations of up to a factor of 2 in the vertical velocities. In any cases, the exact value of the vertical velocities depends on the same forcing and damping mechanisms as the horizontal speeds. Thus, the values predicted by the circulation models are affected by large error bars that reflect our ignorance of the detailed physical processes that drive the dissipation on those planets.

3.3.3 Day/night temperature contrast

The day/night contrast in hot Jupiter atmospheres is a key observable that can be compared to models. The thermal phase curve of several planets show hint of a dependence of this day/night temperature contrast with the equilibrium temperature of the planet. Planets receiving higher flux might have a larger day/night temperature contrast. As shown by Perez-Becker & Showman (2013), this trend can be explained by the steep variation of the radiative timescale with the temperature: hotter planets cool faster. The exact trend, however, depends on the mechanism that transports heat from the dayside to the nightside of the planet. First studies such as Showman & Guillot (2002), proposed that direct advection of heat by the atmosphere was responsible for the redistribution of energy. Recent results from Perez-Becker & Showman (2013), however, show that gravity waves can do the job[1]. Gravity waves are the main way for the atmosphere to smooth atmospheric gradients. A heated parcel of gas adiabatically expands and pushes its neighbors. The stretching and expansion of atmospheric air parcels can efficiently transport energy without transporting material from the dayside to the nightside of the planet. In the isothermal case, the time for such a wave to cross one hemisphere is given by:

$$\tau_{\rm wave} \sim R_{\rm p}/\sqrt{gH}\,. \tag{3.35}$$

The propagation of gravity waves can be limited due to the Coriolis and drag forces. Thus, to smooth the day/night temperature contrast, gravity waves should propagate faster than the

[1]For strongly forced systems, the gravity wave timescale and the advection timescale become similar. Comparing the advection timescale and the radiative timescale can therefore provide a good estimate of the day/night temperature contrast. For less irradiated planets, this is no more true and the gravity wave timescale should be used.

cooling time of the fluid but also faster than they are damped by the Coriolis and drag forces. Large day/night contrast will thus persist if :

$$\tau_{\rm wave} < \sqrt{\tau_{\rm rad} \min(\tau_{\rm drag}, \Omega^{-1})}\,. \tag{3.36}$$

As shown in Fig. 3.7, this theory agrees well with the trend observed in current data. Planets with a ratio $\tau_{\rm wave}/\sqrt{\tau_{\rm rad}\Omega^{-1}}$ greater than ≈ 2 should have almost no day/night temperature contrast, whereas planets with a ratio lower than ≈ 1 should have a large day/night contrast.

In the drag-free case, the model of Perez-Becker & Showman (2013) predicts a thermal flux contrast between the day and the nightside of the planet equals to:

$$\frac{F_{\rm Day} - F_{\rm Night}}{F_{\rm Day}} = \left(1 + \frac{\tau_{\rm wave}^2}{f\tau_{\rm rad}}\right)^{-1} \tag{3.37}$$

$\tau_{\rm rad}$ can be estimated using equation (3.33) and $f \approx \Omega^{-1}$ in the mid-latitudes. We plotted in Figure 3.8 the expected day/night flux contrast for all planets with a known mass and radius assuming that the planet is tidally locked. This should be correct for planets with an orbital period smaller than 10 days but is uncertain for planets with larger orbital periods (see Figure 3.1). Planets with larger equilibrium temperatures cool more efficiently and should have a larger day/night contrast. Planets with a small rotation period have strong Coriolis forces that impede the gravity waves to smooth the temperature gradients, leading to a larger day/night flux contrast. Most hot Jupiters are believed to have a large day/night temperature contrast.

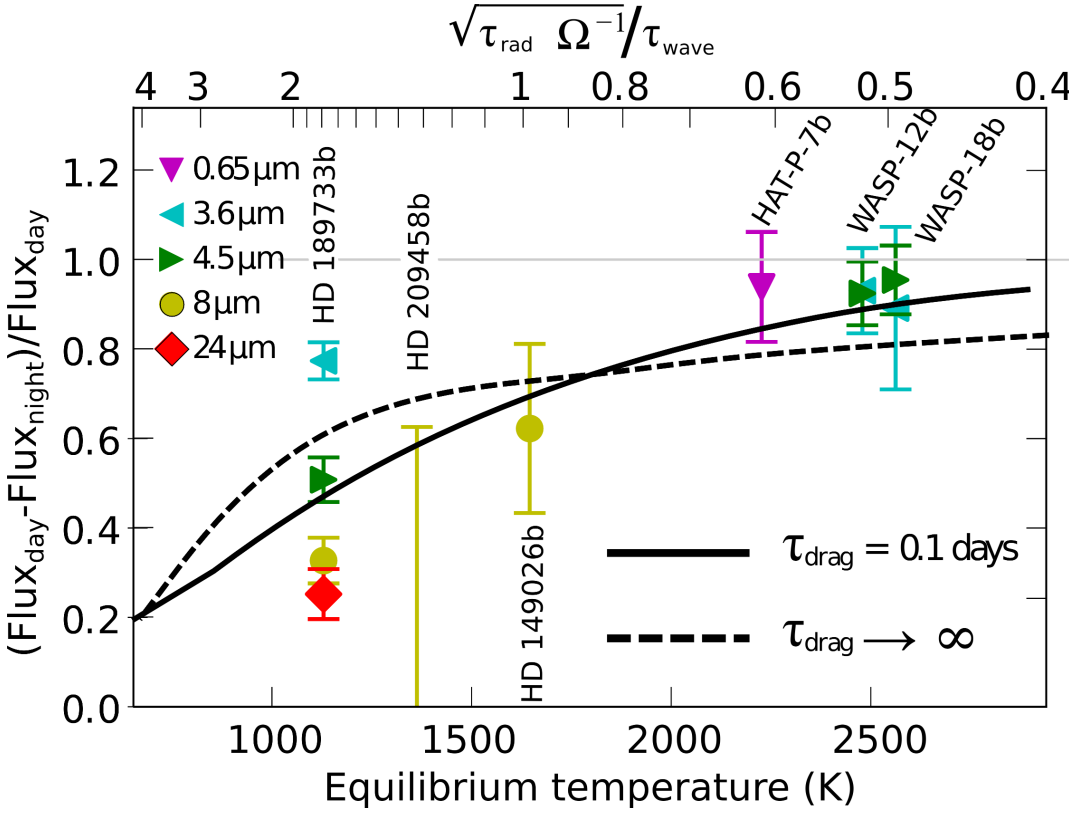

Figure 3.7. Comparison between the observed day/night in the thermal emission of a handful of hot Jupiters and the contrast predicted by the theory of Perez-Becker & Showman (2013). The observations are made in different spectral bands. I show two different theoretical profiles, drag-free (dotted line) or with a small drag (plain line). The radiative timescale was assumed to follow equation (3.33). The rotation period is $2\pi\Omega^{-1}$ is fixed at ≈ 2.3 days, a value that correspond to HD 189733b. The criteria $\sqrt{\tau_{\rm rad}\Omega^{-1}}/\tau_{\rm wave} < 1$ separates planets with a high day/night contrast from planets with a low day/night contrast (see upper x-axis), matching the possible trend observed in the data. Based on a figure from Perez-Becker & Showman (2013).

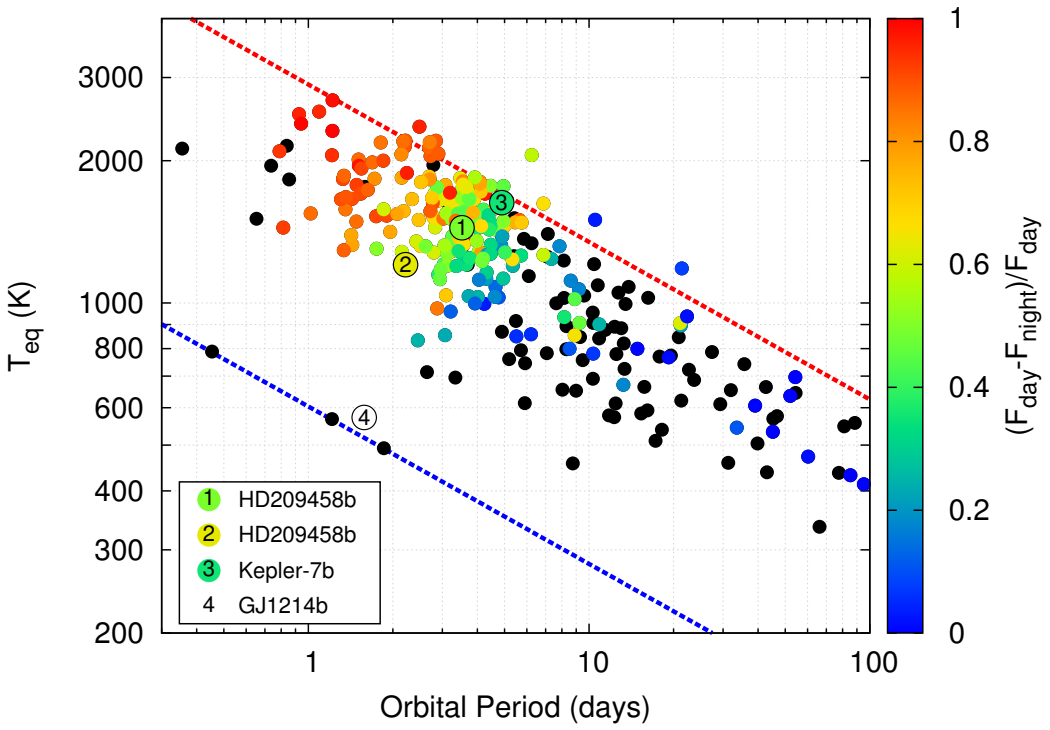

Figure 3.8. Expected day/night contrast for planets with a known mass and radius. The colors show the relative difference in thermal emission between the dayside hemisphere and the nightside hemisphere predicted by the model of Perez-Becker & Showman (2013) for drag-free atmospheres. We assumed that the planets are tidally locked, i.e. their rotation period is equal to their revolution period. This should be valid for planets with orbital period smaller than $\approx$ 10 days but is uncertain for planets with larger orbital periods. Planets are plotted in the equilibrium temperature/orbital period planet. Planets with higher equilibrium temperatures cool more efficiently and have larger day/night flux contrast. Planets with smaller orbital period have stronger Coriolis forces opposing to the redistribution of heat. They have therefore larger day/night flux contrast.

3.4 How does the day/night contrast affect the chemical composition of hot Jupiters atmospheres ?

The large day/night contrast predicted in most hot Jupiters atmospheres have strong implications for the chemical composition of their atmospheres. As shown in Figure 3.9 many chemical species that are stable in the dayside of the planet should condense in the nightside. Similarly, the chemical equilibrium of a reaction depends on the temperature and the pressure of the gas. Thus, the chemical equilibrium between different species, such as CO and CH_4 can be shifted toward different constituents at different locations on the planet. As the large-scale, powerful atmospheric circulation couples the dayside and the nightside atmospheres, the composition on the dayside and on the limb of the planet depends on the interactions between the condensation, chemical reactions, and atmospheric circulation.

In the following two papers we study the interactions between atmospheric circulation, con-

densation and chemical reactions in hot Jupiter atmospheres.

In the first paper, Parmentier et al. (2013), published in *Astronomy & Astrophysics*, we include a very simplified model of the condensation of chemical species in a complex, global circulation model. We use the planet HD 209458b as a proxy for hot Jupiters in general and study how the condensation on the nightside of the planet could deplete chemical species from the whole atmosphere. Chemical species condensing in the nightside should be incorporated into grains that settle down. Without vertical mixing of the material, all the chemical compound will eventually be lost in the deep layers of the atmosphere, affecting both the nightside and the dayside abundances. Using a global circulation model, we quantified the globally averaged vertical mixing rates and show that chemical species condensing in the nightside of the planet should remain aloft if they are incorporating in sub-micron grains. If the nightside condensates are larger than $\approx 1\mu$m, then their fast rain-out in the nightside cannot be overcome by vertical mixing and the condensable specie should disappear from both the nightside and the dayside of the planet. This model provides a good explanation for the lack of titanium oxide recently observed in several exoplanets (*e.g.* Sing et al. 2013; Huitson et al. 2013).

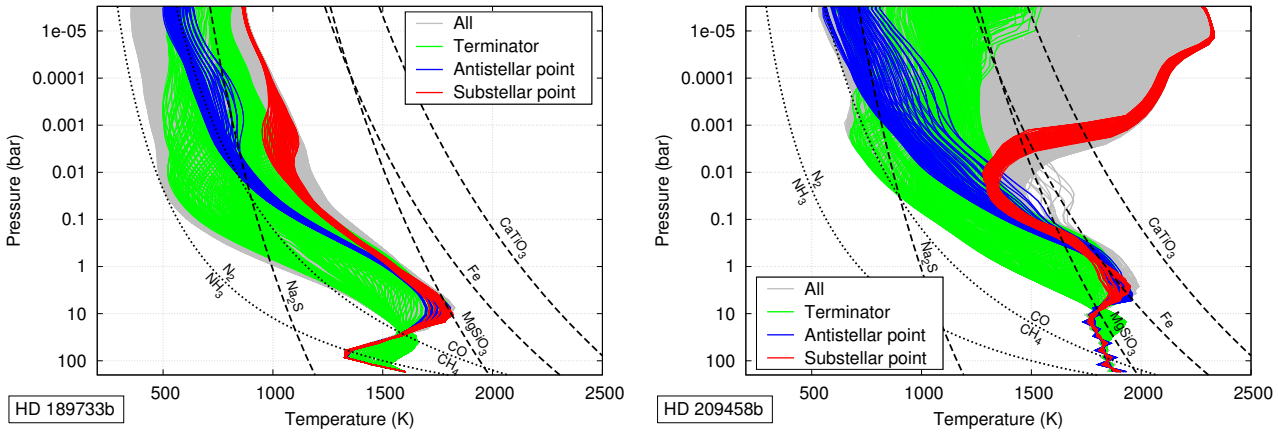

Figure 3.9. Pressure temperature profiles of HD 189733b (left) and HD 209458b (right) obtained with the SPARC/MITgcm. In grey are the profiles at all latitudes and longitudes. In red the profiles around the substellar point, in blue the ones around the antistellar point and in green around the limb of the planet. The condensation curves of the most important species are also shown (dashed lines). On the dotted lines, the chemical abundances of the mentioned species are equal.

In the second paper, Agúndez et al. (2014), also published in *Astronomy & Astrophysics*, we couple a simplified model of the atmospheric circulation to a complex chemical reaction network. The atmospheric circulation is modeled as a pseudo 2D circulation: a vertical column of gas is coherently advected from day-to-night by the super-rotating jet. In such a model the atmospheric circulation is parametrized by a vertical mixing coefficient and a mean eastward wind, both derived from global circulation models. The velocity of a chemical reaction depends strongly on the pressure and the temperature. Thus, a parcel of gas that is advected from the warm and high pressure deep atmosphere to the colder and low pressure upper atmosphere can have a composition that is quenched to the conditions that prevail in the deep atmosphere. Similarly, parcels of gas can be advected from the warm dayside to the cold nightside. If the time to reach the nightside chemical

equilibrium is longer than the time it spends on the nightside the composition of the nightside of the planet will be determined by the pressure and temperature of the dayside atmosphere. We show that horizontal and vertical quenching are efficient enough such that the composition of hot Jupiters atmospheres should be rather homogeneous with longitude. Variations in the thermal phase curves should therefore be due to longitudinal variations of the temperature and cloud coverage rather than variations in chemical composition

A&A 558, A91 (2013)
DOI: 10.1051/0004-6361/201321132

Astronomy & Astrophysics

3D mixing in hot Jupiters atmospheres

I. Application to the day/night cold trap in HD 209458b⋆

Vivien Parmentier[1], Adam P. Showman[2], and Yuan Lian[3]

[1] Université de Nice-Sophia Antipolis, Observatoire de la Côte d'Azur, CNRS UMR 6202, BP 4229, 06304 Nice Cedex 4, France
e-mail: vivien.parmentier@oca.eu
[2] Department of Planetary Sciences, Lunar and Planetary Laboratory, University of Arizona, Tucson AZ, USA
[3] Ashima Research, Suite 104, 600 South Lake Ave., Pasadena, CA 91106, USA

Received 18 January 2013 / Accepted 12 August 2013

ABSTRACT

Context. Hot Jupiters exhibit atmospheric temperatures ranging from hundreds to thousands of Kelvin. Because of their large day-night temperature differences, condensable species that are stable in the gas phase on the dayside – such as TiO and silicates – may condense and gravitationally settle on the nightside. Atmospheric circulation may counterbalance this tendency to gravitationally settle. This three-dimensional (3D) mixing of condensable species has not previously been studied for hot Jupiters, yet it is crucial to assess the existence and distribution of TiO and silicates in the atmospheres of these planets.

Aims. We investigate the strength of the nightside cold trap in hot Jupiters atmospheres by investigating the mechanisms and strength of the vertical mixing in these stably stratified atmospheres. We apply our model to the particular case of TiO to address the question of whether TiO can exist at low pressure in sufficient abundances to produce stratospheric thermal inversions despite the nightside cold trap.

Methods. We modeled the 3D circulation of HD 209458b including passive (i.e. radiatively inactive) tracers that advect with the 3D flow, with a source and sink term on the nightside to represent their condensation into haze particles and their gravitational settling.

Results. We show that global advection patterns produce strong vertical mixing that can keep condensable species aloft as long as they are trapped in particles of sizes of a few microns or less on the nightside. We show that vertical mixing results not from small-scale convection but from the large-scale circulation driven by the day-night heating contrast. Although this vertical mixing is not diffusive in any rigorous sense, a comparison of our results with idealized diffusion models allows a rough estimate of the effective vertical eddy diffusivities in these atmospheres. The parametrization $K_{zz} = \frac{5\times10^4}{\sqrt{P_{\rm bar}}}$ m^2 s^{-1}, valid from ∼1 bar to a few μbar, can be used in 1D models of HD 209458b. Moreover, our models exhibit strong spatial and temporal variability in the tracer concentration that could result in observable variations during either transit or secondary eclipse measurements. Finally, we apply our model to the case of TiO in HD 209458b and show that the day-night cold trap would deplete TiO if it condenses into particles bigger than a few microns on the planet's nightside, keeping it from creating the observed stratosphere of the planet.

Key words. planets and satellites: atmospheres – methods: numerical – diffusion

1. Introduction

The year 1988 was marked by the discovery of the first substellar object outside our solar system (Becklin & Zuckerman 1988). This discovery was followed by numerous other discoveries of cool brown dwarfs, whose spectra differ significantly from stars. This led to the definition of three new spectral classes beyond the stellar classes O to M: the L, T, and Y dwarfs, ranging from temperatures of 2300 K to 350 K (Cushing et al. 2011). To understand of these brown dwarfs and the mechanisms that cause the transition from one spectral class to another, it is fundamental to take condensation processes into account: in cold atmospheres molecules can form, condense, and rain out, affecting the observed spectral features of these objects. In particular, the M to L transition is marked by the disappearance of the titanium oxide (TiO) bands, which is understood by its transformation into titanium dioxide (TiO_2) and condensation into perovskite ($CaTiO_3$; Lodders 2002). The L to T transition is understood as the switch from a cloudy atmosphere to a cloud-free atmosphere as the cloud layer migrates into the deep, unobservable regions of the star (see Kirkpatrick 2005, for a review). Because brown dwarfs produce their own light, high-quality spectra of their atmosphere can be measured. Numerous atmospheric models have been built to fit the data, from simple models with a reduced set of free parameters (Ackerman & Marley 2001) to sophisticated models including the detailed physics of condensation, growth, and settling of particles (Woitke & Helling 2004).

The discovery and characterization of exoplanets followed close behind. The first detection of a planet around a main sequence star by Mayor & Queloz (1995) opened the trail for discovering hundreds of exoplanets. Some years later, atmospheric characterization of these objects became available, both from transit spectroscopy (Charbonneau et al. 2002) and from direct detection of the planet's thermal emission (Charbonneau et al. 2005). Although the global-mean effective temperatures of these planets are similar to those on brown dwarfs, a major difference is that hot Jupiters are strongly irradiated. Depending on the

⋆ Appendix A is available in electronic form at
http://www.aanda.org

incident stellar flux, planetary rotation rate, and other factors, atmospheric circulation models show that this day-night heating gradient can lead, at low pressures, to nightside temperatures that are at least ~1000 K colder than dayside temperatures (e.g., Showman et al. 2008, 2009; Dobbs-Dixon et al. 2010; Rauscher & Menou 2010, 2012a; Heng et al. 2011a,b; Perna et al. 2012). As a result, a wide variety of condensable species that are stable in the gas phase on the dayside may condense on the nightside, leading to the formation of particles there. In the absence of atmospheric vertical mixing, such particles would gravitationally settle, depleting the atmosphere of these species on both the dayside and the nightside. Sufficiently strong vertical mixing, anywhere on the planet, however, may keep these particles suspended in the atmosphere, allowing them to sublimate into the gas phase in any air transported from nightside to dayside. Thus, the existence of this nightside "cold trap" is crucial for understanding not only the existence of hazes on hot Jupiters (e.g., Pont et al. 2013) but also the gas-phase composition of the atmosphere on both the dayside and the nightside.

These arguments are relevant to a wide range of titanium and vanadium oxides, silicate oxides, and other species. In particular, chemical-equilibrium calculations show that, at temperatures of ~1000–2000 K, there exist a wealth of condensates including Ti_2O_3, Ti_3O_5, and Ti_4O_7 (among other titanium oxides), $MgAl_2O_4$, Mg_2SiO_4, $MgSiO_3$, $NaAlSi_3O_8$, $KAlSi_3O_8$, and several phosphorus oxides (Burrows & Sharp 1999; Lodders 2002). Understanding the possible existence of gas-phase TiO, Na, K, and other species on the dayside therefore requires an understanding of the nightside cold trap.

A particularly interesting problem in this regard is the existence of exoplanet stratospheres. For some transiting hot Jupiters, *Spitzer*/IRAC secondary-eclipse observations indicate the presence of thermal inversions (stratospheres) on these planets' daysides (Knutson et al. 2008). These stratospheres are generally thought to result from absorption of starlight by strong visible/ultraviolet absorbers, but debate exists about the specific chemical species that are responsible. Hubeny et al. (2003) and Fortney et al. (2008) showed that, because of their enormous opacities at visible wavelengths, the presence of gaseous titanium and vanadium oxides can lead to stratospheres analogous to those inferred on hot Jupiters. This hypothesis is supported by the possible detection of TiO by Désert et al. (2008) in the atmospheric limb of HD 209458b. Then, a crucial question is whether the nightside cold trap would deplete the atmosphere of TiO, preventing this species from serving as the necessary absorber (Showman et al. 2009; Spiegel et al. 2009).

As pointed out by several authors, there exists another possible cold trap. 1D radiative-transfer models suggest that, on some hot Jupiters, the global-mean temperature-pressure profile becomes sufficiently cold for condensation of gaseous TiO to occur at pressures of tens to hundreds of bars (e.g., Fortney et al. 2008). Even though a stratosphere on such a planet would be sufficiently hot for TiO – if present – to exist in the gas phase, the condensation of TiO and downward settling of the resulting grains at ~10–100 bars might prevent the existence of TiO in the atmosphere (Showman et al. 2009; Spiegel et al. 2009). The strength of these two cold traps is given by a competition between gravitational settling and upward mixing. The vertical mixing results from complex 3D flows and can be inhomogeneous over the planet (Cooper & Showman 2006; Heng et al. 2011a). When using a 1D-model, the vertical mixing is usually considered to be diffusive only, and parametrized by a diffusion coefficient K_{zz}. Several studies give an estimate for this vertical diffusion coefficient in hot Jupiters atmospheres. Heng et al. (2011a) uses the magnitude of the Eulerian mean streamfunction as a proxy for the strength of the vertical motions and derived a vertical mixing coefficient of the order of $K_{zz} \approx 10^6$ m^{2}s^{-1}. Other authors used an estimate based on the root mean squared vertical velocity either the local value (Cooper & Showman 2006) or the planet-averaged value (Moses et al. 2011). However these estimates are crude and there is a need for theoretical work to more rigorously characterize the vertical mixing rates in hot Jupiters atmospheres.

In this study we focus in the dynamical mixing of condensable species. We therefore neglect all the potential feedback of the condensable species on the atmospheric flow such as the radiative effects of the condensates (Heng et al. 2012; Dobbs-Dixon et al. 2012), non-equilibrium chemistry due to the depletion of a particular species, latent heat release during condensation among others. We present three-dimensional general circulation model (GCM) experiments of HD 209458b to model a chemical species that condenses and settles on the nightside of the planet. We show that mixing in hot Jupiters atmospheres is dominated by large-scale circulation flows resolved by the GCM. Finally, from the 3D model, we derive the values of an effective vertical mixing coefficient, representing the averaged vertical mixing in the planet atmosphere. We also compare these 3D models to an idealized 1D model parameterizing the mixing using an eddy diffusivity, with the goal of estimating an effective eddy diffusivity for the mixing rates in the 3D models. These are the first circulation models of hot Jupiters to include the influence of the dynamics on condensable species.

2. 3D model

Here, we use a state-of-the-art 3D circulation model, coupled to a passive tracer representing a condensable species, to determine how the interplay between dynamical mixing and vertical settling controls the spatial distribution of condensable species on hot Jupiters. Although the day/night cold trap should be present in most hot Jupiters, for concreteness, we must select a particular system to investigate. HD 209458b is among the best studied hot Jupiters. It is believed to harbor a stratosphere (Knutson et al. 2008) and a strong day-night temperature contrast (Showman et al. 2009). We decided to use it as our reference model in this study, keeping in mind that most of the mechanisms discussed here should apply to all hot Jupiters. To model the atmosphere of HD 209458b we use the 3D Substellar and Planetary Atmospheric Radiation and Circulation (SPARC/MITgcm) model of Showman et al. (2009), which couples the plane-parallel, multi-stream radiative transfer model of Marley & McKay (1999) to the MITgcm (Adcroft et al. 2004).

2.1. Dynamics

To model the dynamics of the planet we solve the global, three-dimensional primitive equations in spherical geometry using the MITgcm, a general circulation model for atmosphere and oceans developed and maintained at the Massachusetts Institute of Technology. The primitive equations are the standard equations used in stably stratified flows where the horizontal dimensions greatly exceed the vertical ones. In hot Jupiters, the horizontal scales are 10^7–10^8 m whereas the vertical scale height fall between 200 and 500 km leading to an aspect ration of 20 to 500. In order to minimize the constraints on the timestep by the CFL criterion, we solve the equations on the cubed-sphere grid as described in Adcroft et al. (2004). The simulations do

not contain any explicit viscosity nor diffusivity. However, in order to smooth the grid noise and ensure the stability of the code we use a horizontal fourth-order Shapiro filter (Shapiro 1970). In the vertical direction, no filtering process is applied. Kalnay (2003) provide a more detailed description of the equations (see Showman et al. 2009 for the numerical method used to solve them).

We use a gravity of 9.81 $\mathrm{m\,s^{-2}}$, a planetary radius of 9.44×10^7 m, and a rotation rate of 2.06×10^{-5} $\mathrm{s^{-1}}$ (implying a rotation period of 3.5 days). The average pressure ranges from 200 bars at the bottom of the atmosphere to p_{top} at the top of the second-highest level, with the uppermost level extending from a pressure of p_{top} to zero. In most models, p_{top} is 2 μbar with 53 vertical levels. In some models – particularly those with the largest cloud particle size – we adopt P_{top} of 20 µbar with 47 vertical levels. In either case, this leads to a resolution of almost three levels per scale height. We use a horizontal resolution of C32, equivalent to an approximate resolution of 128 cells in longitude and 64 in latitude and a timestep of 15 s. We reran some models at C64 resolution (equivalent to an approximate resolution of 256 × 128 in longitude and latitude) to check convergence.

It is worth mentioning that, although the primitive equations are hydrostatic in nature, it does not imply an absence of vertical motion (see Sect. 3.5 of Holton 1992). In the primitive equations, the horizontal divergence is generally non-zero, which requires the presence of vertical motions. Indeed, the dayside radiative heating and nightside radiative cooling are balanced by a combination of horizontal and vertical thermal advection. In many cases, including Earth's tropics, the vertical advection dominates; in such cases, vertical motions play a crucial, zeroth-order role in the thermodynamic energy balance. For conditions relevant to hot Jupiters, GCMs and order-of-magnitude calculations show that vertical motions of 10−100 $\mathrm{ms^{-1}}$ or more are expected, despite the fact that the atmosphere is stably stratified. Further discussion can be found in Showman & Guillot (2002) and in Sect. 6.2 of Showman et al. (2008).

2.2. Radiative transfer

The radiative transport of energy is calculated with the plane-parallel radiative transfer code of Marley & McKay (1999). The code was first developed for Titan's atmosphere (McKay et al. 1989) and since then has been extensively used for the study of giant planets (Marley et al. 1996), brown dwarfs (Marley et al. 2002; Burrows et al. 1997), and hot Jupiters (e.g., Fortney et al. 2005, 2008; Showman et al. 2009). We use the opacities developed by Freedman et al. (2008), including more recent updates, and the molecular abundances described by Lodders & Fegley (2002) and Visscher et al. (2006).

As in the models of HD 209458b presented by Showman et al. (2009), our opacity tables include gas-phase TiO and VO whenever temperatures are locally high enough for TiO to reside in gas phase. Note that, because of the assumption of local chemical equilibrium, we do not consider the effect of cold traps on the atmospheric composition, and thus on the opacities. TiO opacities are always taken into account where temperatures are high enough for TiO to exist in the gas phase. This causes a warm stratosphere on the dayside of our modeled planet, regardless of the 3D distribution of our tracers (to be described below).

Metallicities are solar, as given by Freedman et al. (2008). A metal enhanced atmosphere should modestly change the day-night temperature difference (at a given pressure) and the pressure of the photosphere itself, as shown in Showman et al. (2009). Cloud opacities are ignored in this study and might alter the flow more significantly (Dobbs-Dixon & Agol 2012).

Opacities are described using the correlated-k method (e.g., Goody 1961). We consider 11 frequency bins for the opacities ranging from 0.26 to 300 μm; within each bin, opacity information from typically 10 000 to 100 000 frequency intervals is represented statistically over 8 k-coefficients. This is radically different from other methods in the literature. In particular, Dobbs-Dixon & Agol (2012) uses a multi-bin approach for the opacity, but inside each of their 30 frequency bins they use a single average opacity. However, inside each bin of frequency, the line by line opacity varies by several orders of magnitudes and no mean, neither the Planck mean nor the Rosseland mean opacity (see Parmentier & Guillot 2013 and Parmentier et al., in prep., for more details) can take into account this large variability. Thus, as stated in Dobbs-Dixon & Agol (2012), our correlated-k radiative transfer is today's most sophisticated radiative transfer approach implemented in a hot Jupiters GCM. Showman et al. (2009) provide a detailed description of the radiative-transfer model and its implementation in the GCM.

2.3. Tracer fields

Our target species is represented by a passive tracer field. Tracer fields are often used in GCMs to follow the concentration of a chemical species such as water vapor or cloud amount in the atmosphere or salinity in the oceans. Cooper & Showman (2006) were the first to include a passive tracer in a circulation model of hot Jupiters, in their case to investigate the quenching of CO and CH_4 due to atmospheric mixing.

The tracer field is advected by the flow calculated in the GCM. Thus the tracer abundance χ is given by the continuity equation:

$$\frac{D\chi}{Dt} = S. \tag{1}$$

Here, χ represents the mole fraction of the tracer, i.e., the number of molecules of the species in a given volume, either in gaseous phase or trapped in condensed particles, with respect to the total number of atmospheric molecules in that volume. For simplicity the value of χ is normalized to its initial value in the deep layers of the planet. In the equation, S is a source term and the total derivative is defined by $D/Dt = \partial/\partial t + \boldsymbol{v} \cdot \nabla + \omega \frac{\partial}{\partial \mathrm{p}}$, where t is time, $\boldsymbol{v}$ is the horizontal velocity, ∇ is the horizontal gradient operator on the sphere, $\omega = DP/Dt$ is the vertical velocity in pressure coordinates, and P is pressure. We model the simplest possible horizontal cold trap in hot Jupiters atmospheres: a situation where the day/night temperature contrast is so strong that our target species is gaseous in the dayside of the planet but condenses and is incorporated in particles of size a in the nightside. Thus the source term S represents the gravitational settling of these particles and is given by

$$S = \begin{cases} 0 & \text{on the dayside} \\ \frac{1}{\rho} \frac{\partial (\rho \chi V_{\mathrm{f}})}{\partial z} & \text{on the nightside} \end{cases} \tag{2}$$

where z is the height, increasing upward, ρ is the density of the air and V_{f} is the settling velocity of the particles defined by Eq. (3). This velocity depends on the size of the particles, which is determined by the complex microphysics of condensation, out of the scope of this study (see Woitke & Helling 2003). Thus we treat a as a free parameter in our model. We model spherical particles of radii 0.1, 0.5, 1, 2.5, 5, and 10 μm. Equation (2)

describes a simple, bimodal mechanism for the condensation of chemical species on the nightside. Although this scheme is highly simplified (ignoring the detailed temperature and pressure dependence of the condensation curves of possible condensates in hot Jupiters atmospheres), it reflects the fact that a wide range of species will reside in gaseous form on the dayside yet condensed form at low pressures on the nightside.

We consider several independent passive tracers, representing species that condenses in different particle size. Thus, they do not influence either the dynamics or the radiative transfer of the simulation and does not interact with each others. This ignores a role for possible radiative feedback mechanisms – discussed in Sect. 6 – or particle growth but represents a necessary first step toward understanding how dynamics controls the 3D distribution of a condensable species.

2.4. Settling velocity

We assume that the target chemical species condenses, in the nightside only, into spherical particles of radius a that reach immediately their terminal fall speed, which is given by (Pruppacher & Klett 1978):

$$V_{\rm f} = \frac{2\beta a^2 g(\rho_{\rm p} - \rho)}{9\eta} \tag{3}$$

where η is the viscosity of the gas, g is the gravitational acceleration of the planet, $\rho_{\rm p}$ is the density of the particle, and ρ the density of the atmosphere. $V_{\rm f}$ is positive when the particles goes downward. The Cunningham slip factor, β, accounts for gas kinetic effects that become relevant when the mean free path of the atmospheric molecules is bigger than the size of the falling particle. This factor has been measured experimentally by numerous experiments. We adopt the expression from Li & Wang (2003) as done by Spiegel et al. (2009).

$$\beta = 1 + K_{\rm N}\left(1.256 + 0.4{\rm e}^{-1.1/K_{\rm N}}\right) \tag{4}$$

where the Knudsen number $K_{\rm N}$ is the ratio of the mean free path to the size of the particle:

$$K_{\rm N} = \frac{\lambda}{a}. \tag{5}$$

For a perfect gas, the mean free path can be expressed as (Chapman & Cowling 1970):

$$\lambda = \frac{k_{\rm B}T}{\sqrt{2}\pi d^2}\frac{1}{P} \tag{6}$$

with d the diameter of the gas molecules, P and T the pressure and temperature of the gas, and k_B the Boltzmann constant. In the limit of a high-density atmosphere, $\beta \rightarrow 1$ and the terminal speed $V_{\rm f}$ becomes the Stokes velocity $V_{\rm Stokes}$.

For low density gases, the dynamical viscosity is independent of pressure and can be expressed as a power law of the local temperature with an exponent varying between 1/2 in the hard-sphere model to near unity, depending on the strength of the interactions between the molecules. Following Ackerman & Marley (2001), we use the analytical formula given by Rosner (2000) for the viscosity of hydrogen:

$$\eta = \frac{5}{16}\frac{\sqrt{\pi m k_{\rm B}T}}{\pi d^2}\frac{(k_{\rm B}T/\epsilon)^{0.16}}{1.22} \tag{7}$$

with d the molecular diameter, m the molecular mass, and ϵ the depth of the Lennard-Jones potential well (for H_2 we use 2.827×10^{-10} m and $59.7k_{\rm B}$ K respectively). The power law behavior of the viscosity remains valid for temperatures ranging from 300 K to 3000 K and for pressures less than 100 bar (Stiel & Thodos 1963). At higher temperature, ionization of hydrogen becomes relevant and the viscosity reaches a plateau. However the temperatures of the model are everywhere less than 3000 K and so Eq. (7) remains valid.

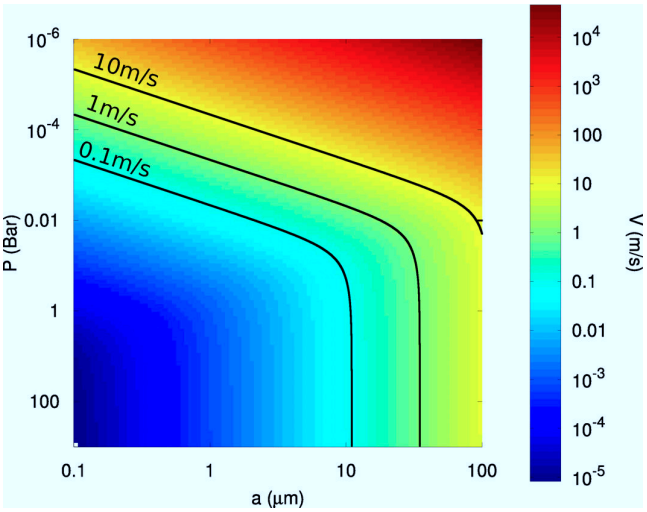

Fig. 1. Terminal velocity of a falling particle as a function of pressure and particle size for an H_2-atmosphere at 1000 K and a value of the gravitational acceleration of 15 m s^{-2}.

Figure 1 displays the resulting terminal velocity as a function of pressure and particle size. Two different regimes are observed. For Knudsen numbers smaller than unity, the terminal velocity is independent of pressure, whereas for Knudsen numbers exceeding unity, the terminal velocity is inversely proportional to the pressure. At low pressure and for particles bigger than a few tens of micrometers, the Reynolds number becomes higher than unity, and Eq. (3) is no longer valid. However, we show in Appendix A that these differences remain smaller than one order of magnitude and confined to a small parameter space thus we decided to neglect them for this work.

2.5. Integration time-limitation of the study

A challenge for any 3D numerical integrations of hot Jupiters dynamics is the wide range of timescales exhibited by these atmospheres. This is true for the radiative time constant, which varies significantly from low to high pressure (Iro et al. 2005; Showman et al. 2008). Nevertheless, Showman et al. (2009) showed that the computed light-curve of HD189733b changes little for integration time longer than hundreds of days, indicating that the dynamics in the millibar regime has stabilized. As we integrate ~1400 days, we consider the dynamics of the planet to be spun up at pressures less than ~100 mbar. For the settling of particles, another timescale must be taken into account. The particle settling timescale can be defined as the time for the particles to fall one atmospheric scale height. To obtain a correct picture of the problem at a given location of the planet, we need to integrate the simulation for at least several times longer than the settling timescale at this location. As we can see in Fig. 2 the settling timescale ranges from tens of seconds for big particles at low pressure to tens of years for small particles at high pressure.

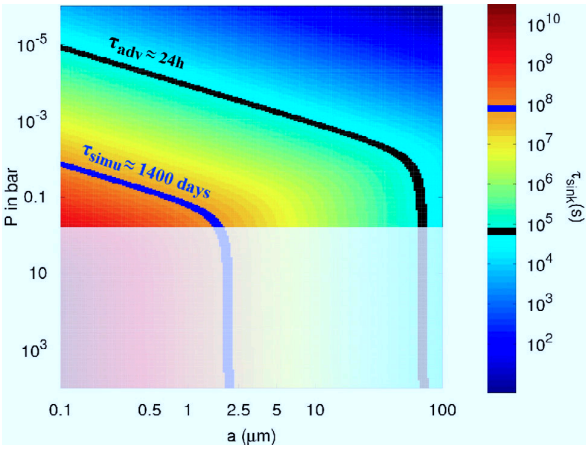

Fig. 2. Settling timescale as a function of pressure and particle size for the same conditions as in Fig. 1. Also shown are the advective timescale (black curve) and the simulation timescale (blue curve). In the shaded region (below 1 bar), the tracers are considered gaseous and the settling timescale is not relevant for our study.

Due to computational limitation it is not possible to run the simulation long enough to ensure that every considered tracer field has reached a statistical steady state for the full range of particle sizes we consider. The integration during 1400 days allows us to calculate the steady state for every particle size at pressure lower than 10 bar and at every pressure for nightside condensates bigger than 2 μm.

We define the advective timescale as the time for a parcel in the main jet stream (see Sect. 3.1) to cross one hemisphere of the planet. If the advective timescale exceeds the settling timescale at a given level, the particles at these levels will fall several scale heights while on the nightside. We thus expect that these levels will be depleted. Conversely when the advective timescale is shorter than the settling timescale, the coupling between the flow and the particle is essential and particles' behavior cannot be predicted easily. Typical advective times in our models are ~24 h; this is marked by the upper thick black curve in Fig. 2. We expect depletion to occur above this line.

Our initial conditions for the tracer field correspond to a tracer that is spatially constant everywhere at a normalized mole fraction of 1. The final tracer abundance in our models at low pressures (less than ≈0.1−1 bar) is qualitatively insensitive to the initial abundance at those low pressures. This results from the short vertical mixing and settling timescales at low pressures (e.g., Fig. 2).

3. Results

3.1. Dynamical regime

We run the simulations for 1400 days and calculate the time average for all the variables over the last 400 days only, once the simulation reaches a statistical steady state at upper levels. Understanding the flow structure is essential to understanding the Lagrangian advection of particles, thus we first present a brief description of the dynamics. A more complete description of the circulation in our simulations is presented in Showman et al. (2009). The temperature structure is shown in Fig. 3. A hot stratosphere is visible at altitudes above the 10-mbar level, due to the strong visible-wavelength absorption by titanium oxide present in solar abundances in the simulation. Titanium oxide abundances should be affected by the horizontal cold trap. However, as explained in Sect. 2.2, we consider its radiative effects as if it was in local chemical equilibrium, regardless of the behavior of our passive tracers. Temperatures reach ~2200 K at low pressures near the substellar point. By contrast, the temperatures deeper than 10 mbar in the dayside are relatively temperate. This could lead to the presence of a vertical cold trap, not considered in this study. The day-night temperature contrast becomes significant at pressures less than ~100 mbar, reaching 1600 K near the top of the model. This large temperature difference results from the short radiative timescale at low pressures in comparison to dynamical timescales (Iro et al. 2005; Cooper & Showman 2005; Showman et al. 2008).

The horizontal flow on isobars comprises an eastward (superrotating) jet close to the equator and a day-to-night flow pattern at higher latitude. As the pressure increases, the radiative time constant increases and the jet extends to higher latitudes. As seen in Fig. 3, the mean vertical velocities exhibit planet-wide variations. The highest velocities coincide with strong horizontal convergence of the flow and occur mostly at the equator. West of the anti-stellar point, the convergence of the day-to-night circulation forces strong downwelling motions. As described in Rauscher & Menou (2010), this convergence point appears in a range of hot Jupiters GCMs of varying complexity. It is usually associated with a shock-like feature (Heng 2012). Our simulations assume local hydrostatic equilibrium and thus can not treat properly the physics of shocks. To date, no global model of hot Jupiters atmospheric dynamics can handle shocks properly. Yet, a similar wind convergence pattern appears when considering the non-hydrostatic nature of the flow as can be seen in Dobbs-Dixon et al. (2010). Between the substellar point and the west terminator, there are additional convergence/divergence points associated with the jet, leading to a region of strong ascending motion ~40° of longitude west of the substellar point, and a broad region of descending motion west of that. These vertical flows remain coherent over several orders of magnitude in pressure, giving them the potential to transport vertically large quantities of material. Outside of these points of strong vertical motions, the vertical velocities are more than one order of magnitude smaller. They are mostly upward on the dayside and downward on the nightside.

3.2. Spatial distribution of condensable species

Our simulations show that, as expected, condensation and particle settling on the nightside deplete the tracer from upper levels relative to the abundances at depth-an effect that is stronger for larger particles. This is illustrated in Fig. 4 (solid curves), which shows the global-mean tracer abundance (averaged horizontally on isobars) versus pressure for simulations with nightside condensates sizes ranging from 0.1 μm to 10 μm. In all cases, the horizontally averaged tracer abundance decreases with altitude. The depletion is modest for the smallest particle size (0.1 μm), but for the largest particle sizes, tracer abundances at the top are almost two orders of magnitude smaller than abundances at the bottom. A useful metric is the "50% depletion pressure", that is, the pressure above which the global-mean tracer abundance is less than 50% of the deep abundance. This pressure is only 10 μbar for a particle size of 0.5 μm but is 0.1 bar for a particle size of 10 μm. We also note that, for all the models shown in Fig. 4, the particles settling times near the top of the model are much less than our integration times; at low pressures, the tracer abundances have reached a statistical equilibrium where

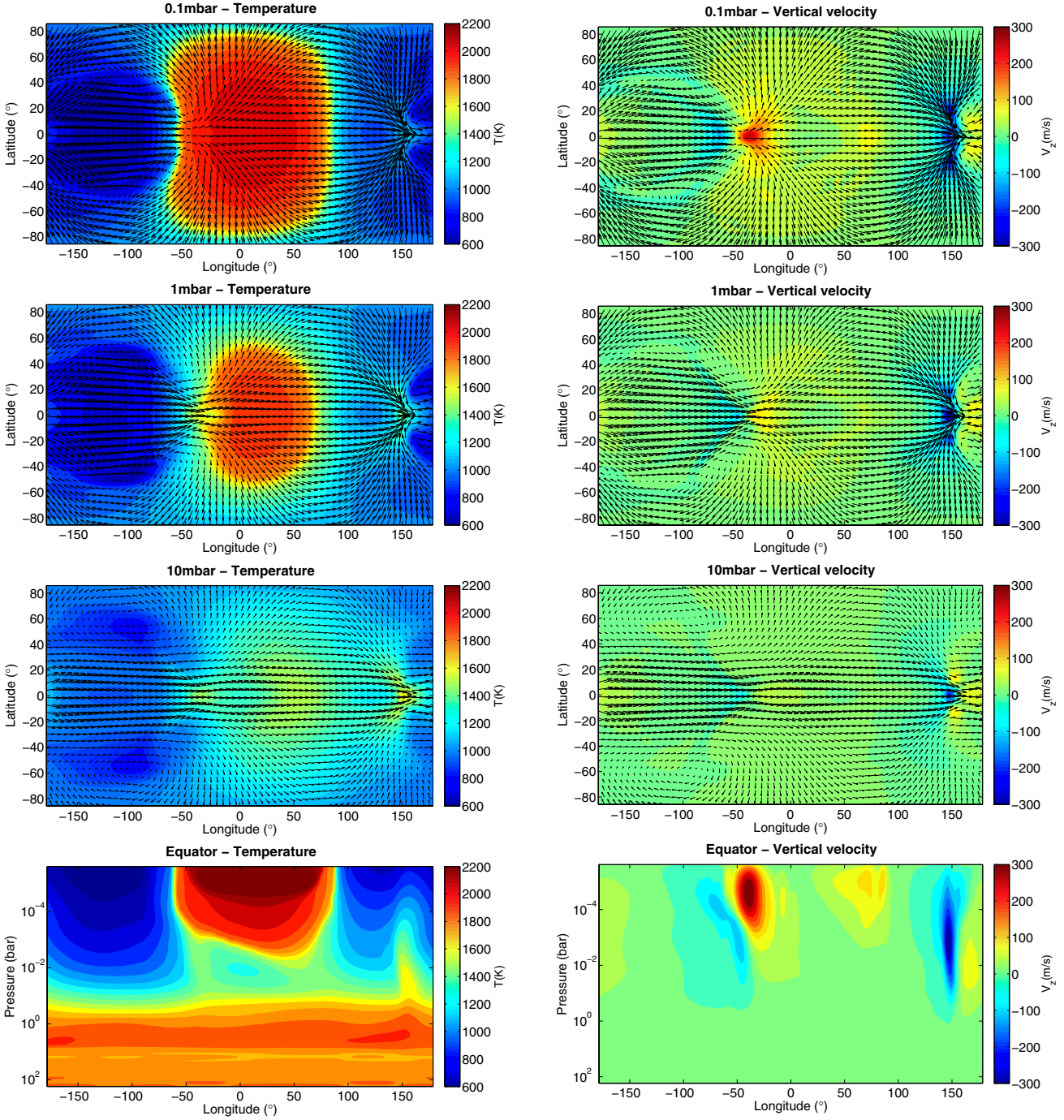

Fig. 3. Temperature (*left panel*, colorscale), vertical velocities (*right panel*, colorscale), and horizontal winds (arrows) in our model of HD 209458b. Positive velocities are upward. The *top three panels* show the flow at three different pressure (0.1 mbar, 1 mbar, and 10 mbar). The *bottom panel* shows the vertical velocities versus longitude and pressure along the equator. The substellar point is at longitude, latitude (0°, 0°), the dayside is between −90° and +90°. All the quantities are time averaged.

downward transport of tracer due to particle settling is balanced by upward mixing of tracer by the large-scale dynamics.

The tracer abundance on isobars exhibits a strong spatial variation as can be seen in Fig. 6. Although a day/night pattern is imposed in the tracer source/sink (with particle settling on the nightside but not the dayside), the three-dimensional advection of the tracer field by the atmospheric winds leads to a complex tracer distribution that does not exhibit an obvious day-night geometry. The main pattern appears to be an equator-to-pole gradient, with large zonal-mean abundances at the poles, and smaller zonal-mean abundances at the equator. This is particularly true around 0.1 mbar. Significant longitudinal tracer variations also occur; at ∼1 mbar (Fig. 6), these variations are particularly prominent at high latitudes. Interestingly, these variations

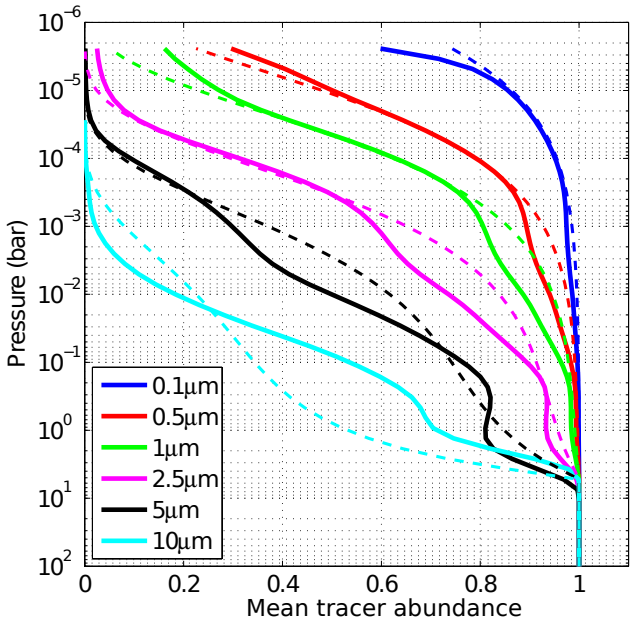

Fig. 4. Planet-wide, time averaged tracer abundances on isobars. The abundances are normalized to the abundance in the deepest layer. We compare the value of the 3D model (solid lines) and the fit using the 1D model (dashed lines).

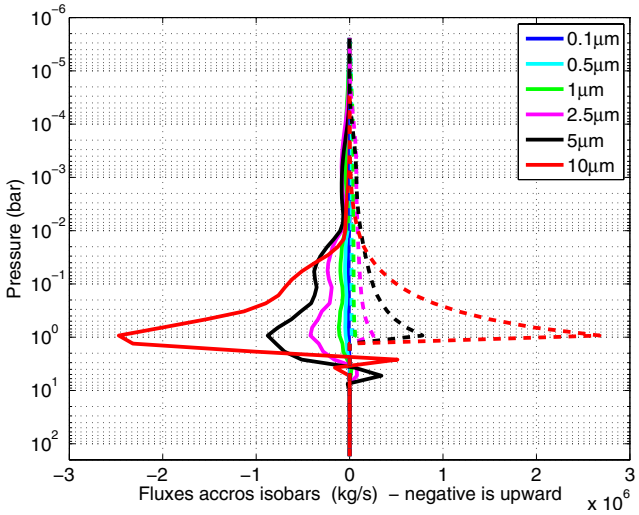

Fig. 5. Time averaged fluxes of tracers across isobars. Upwelling fluxes due to the dynamics (solid lines) balance the downwelling fluxes due to the gravitational settling of the tracers (dashed lines). Negative values are upward fluxes.

are phase shifted in longitude relative to the day-night pattern with maximum (minimum) peak tracer abundances occurring ~60–80° of longitude east of the substellar (antistellar) point.

On top of these main patterns, we clearly see two points depleted in tracers at the equator. These two points correspond to points of horizontal convergence of the flow and high downwelling motions as discussed in the previous section. This correlation between strong downwelling motions and low tracer abundances arises naturally in the presence of a background vertical gradient of tracer abundances. Due to their settling on the nightside, the local tracer abundance generally decreases with height and thus any downwelling motion would carry parcels of gas depleted in tracers whereas any upwelling motion should carry parcels of gas enhanced in tracers.

3.3. Geometry of the mixing

As discussed in the previous section, the tracer abundance is not null everywhere in the planet, which implies that tracers did not rain out during the simulation time. Yet the integration time greatly exceeds the fall times at low pressure for all particle sizes considered, and everywhere throughout the domain for particle sizes exceeding a few μm. Therefore vertical mixing must happen in order to keep these particles aloft. This vertical mixing is characterized by an upward dynamical flux of tracers that balances the downward flux due to the gravitational settling in the nightside. The upward dynamical flux of tracers across isobars can be calculated as $\left\langle \frac{-\omega\chi}{g} \right\rangle$ where ω is the vertical velocity in pressure coordinates, χ the tracer abundance, g the gravity of the planet and the brackets denote the average on isobars. As seen in Fig. 5, the upward flux of tracers due to the dynamics (solid lines) balances nicely the downward flux due to settling (dashed lines), showing that the simulation did reached a quasi steady-state.

Hot Jupiters atmospheres are heated from above and thus are believed to be stably stratified. Then, vertical mixing cannot be driven by small scale convection as it is the case in the deep atmosphere of brown dwarfs (Freytag et al. 2010) and the gas giants of the solar system. As explained in Sect. 2.1, our model does not use any parametrization of sub-grid scale mixing. Thus we do not account for mixing induced by small-scale turbulence and gravity wave breaking, two mechanisms that are believed to dominate the mixing in the radiative part of brown dwarfs atmospheres (Freytag et al. 2010). Rather, the upward flux of tracers in our model is due to the large-scale, resolved flow of the simulation.

Given that mass is conserved, any upward flux of gas is compensated by a downward flux of gas. Thus, if the tracers concentrations were horizontally homogeneous on isobars, there would be no net upward flux of tracer through that isobar. For a net upward flux of tracers across isobars to occur, there must be a correlation between the horizontal distribution of the tracers and the vertical velocities. Dynamics will produce an upward flux if – on an isobar – ascending regions exhibit greater tracer abundance than descending regions. In other words, an upward tracer flux due to dynamics will occur only if $(\chi - \langle\chi\rangle)\,\omega < 0$ where ω is the upward velocity in pressure coordinates, χ is the tracer abundance and the brackets are the mean over one isobar (note that negative ω implies upward motion). Given a vertical gradient of $\langle\chi\rangle$ such that the abundance of $\langle\chi\rangle$ decreases upward, an upward flux of gas will naturally bring enhanced material whereas a downward flux will naturally advect parcels of gas depleted in tracers, thereby creating the correlation between ω and χ favorable for upward tracer transport. Figure 7 shows the relative contribution to the upward mixing versus longitude and latitude at a given isobar, which can be estimated by the quantity:

$$F \equiv \frac{\omega(\chi - \langle\chi\rangle)}{\langle\omega\chi\rangle}\,. \tag{8}$$

Mass conservation in the primitive equations implies that $\langle\omega\langle\chi\rangle\rangle = 0$: the advection of $\langle\chi\rangle$ does not contribute to the net (horizontally averaged) upward flux of material and so we remove the contribution of this term when defining F in Eq. (8).

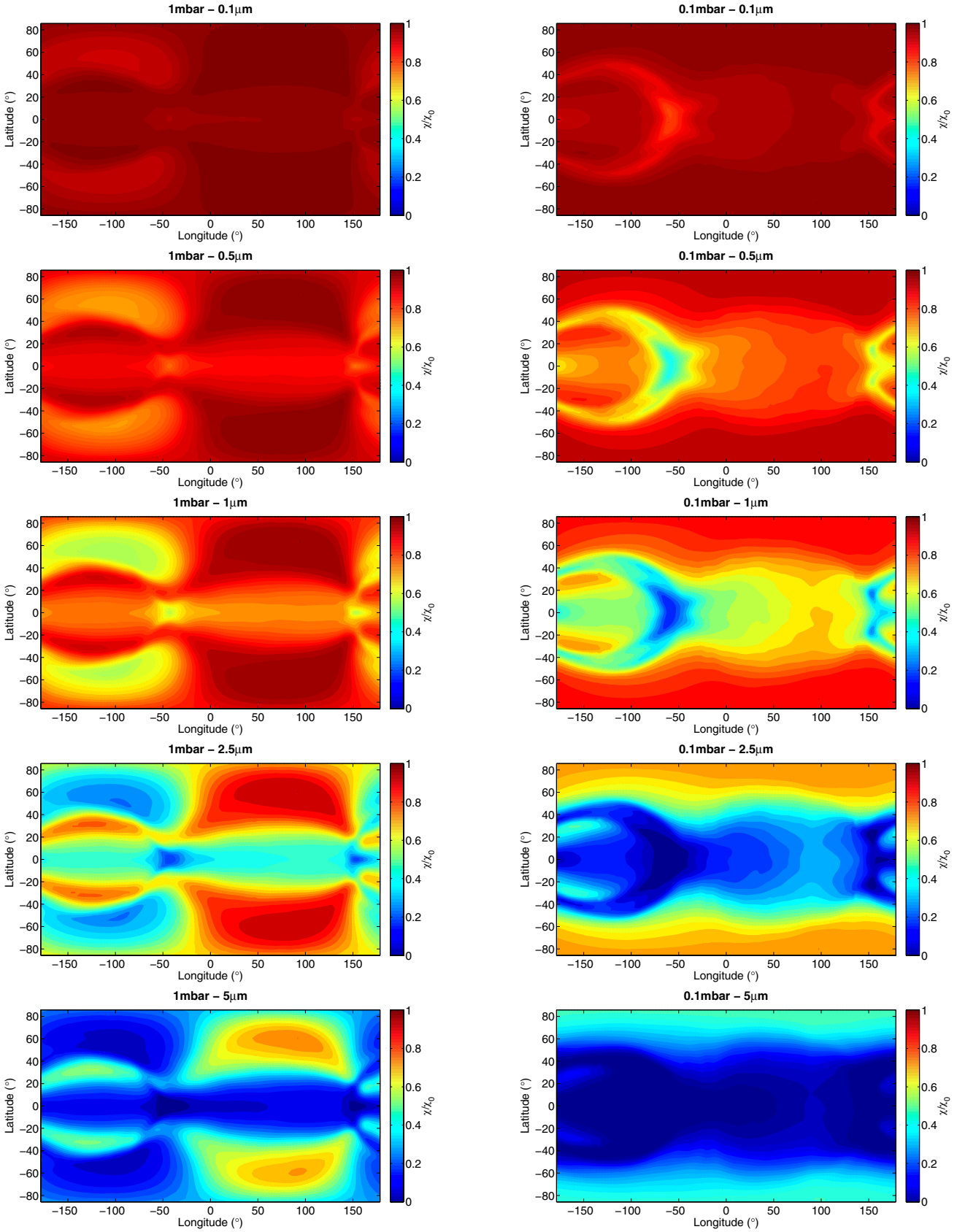

Fig. 6. Time averaged tracer abundance relative to the deep abundance (χ/χ_0) at two different pressures and for different particle sizes.

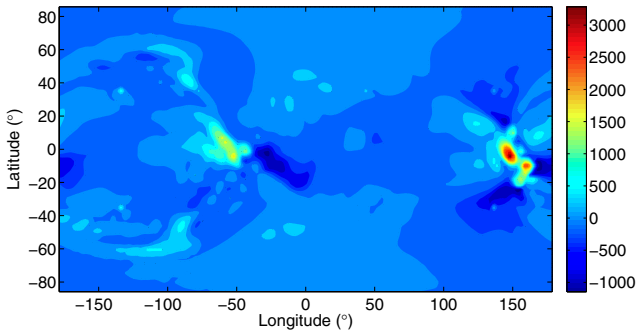

Fig. 7. 2D distribution of the mixing efficiency on the 1mbar isobar. We plot $F = \frac{\omega\chi - \omega\langle\chi\rangle}{\langle\omega\chi\rangle}$. Positive is either an upward flux of gas enhanced in tracers compared to the horizontal mean or a downward flux of gas depleted in tracer compared to the horizontal mean value. Negative is either a downward flux of gas enhanced in tracer or an upward flux of gas depleted in tracer. Thus a positive value enhances the (horizontally averaged) upward flux, whereas a negative value diminishes it. These fluxes are normalized to the mean upward flux of tracer and the global-mean on an isobar of the plotted quantity is 1.

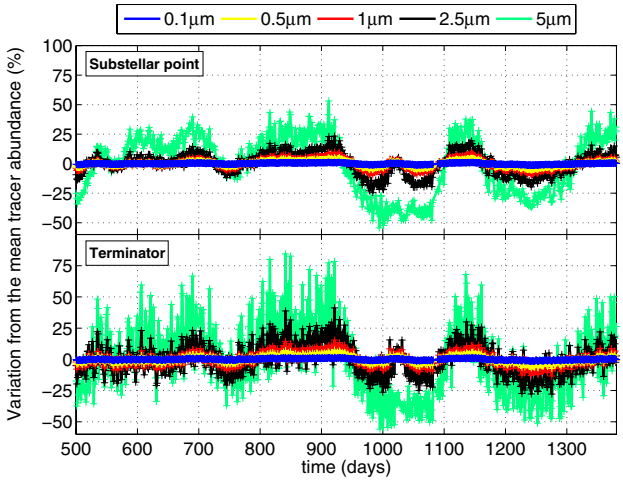

Fig. 8. Time dependence of the mean tracer abundance averaged between 1mbar and 0.1mbar. The abundances are averaged horizontally over a circular region of radius 45° centered on the substellar point (*top*) and averaged horizontally around the terminator, including all regions within ±5° of the terminator (*bottom*). The *top panel* is relevant for inferring the presence of a stratosphere (see Sect. 6.1), albedo variations (see Sect. 6.2) or secondary eclipse measurements (see Sect. 6.3). The *bottom panel* is relevant for transit spectroscopy measurements.

The quantity $-\frac{1}{g}\langle\omega\chi\rangle$ is the mean upward flux of material across isobars, thus the quantity F represents the local contribution to the total upward flux on isobars. It is normalized such that $\langle F\rangle = 1$.

The strength of the mixing varies significantly with longitude and latitude. Both upward and downward fluxes are one order of magnitude greater than typical values in a handful of specific small areas across the planet – particularly at the two points of horizontal convergence and strong vertical velocities described in Sect. 3.1. This vertical flow remains coherent over several order of magnitude in pressure (see Fig. 3), acting like a vertical "chimney" where efficient transport of material can be achieved.

In summary, the mechanism by which the large-scale, resolved atmospheric circulation transports tracers upward is extremely simple and straightforward. The settling of particles leads to a mean vertical gradient of tracer abundance, with, on average, small tracer mixing ratios aloft and large tracer mixing ratios at depth. Given this background gradient, advection by vertical atmospheric motions – whatever their geometry – *automatically* produces a correlation between ω and $(\chi - \langle\chi\rangle)$ on isobars, with ascending regions exhibiting larger values of $(\chi - \langle\chi\rangle)$ than descending regions. In turn, this correlation automatically causes an upward dynamical net flux of tracers when averaged globally over isobars. In statistical steady state, this upward dynamical flux balances the downward transport due to particle settling and allows the atmospheric tracer abundance to equilibrate at finite (non-zero) values despite the effect of particle settling. The mechanism does not require convection, and indeed, the vertical motions that cause the upward transport in our models are resolved, large-scale motions in the stably stratified atmosphere. These vertical motions are a key aspect of the global-scale atmospheric circulation driven by the day-night heating contrast.

3.4. Time variability

Besides the spatial variability at a given time, the model exhibits significant temporal variability, both in the 3D flow and especially in the tracer field. The equatorial jet exhibits an oscillation pattern at planetary scale as seen in Fig. 9. At the convergence point west of the substellar point, the jet orientation can be toward the north, the south or well centered on the equator. Whereas Dobbs-Dixon et al. (2010) described a variation in longitude with time of the convergence point of the flow in the nightside, we see a variation in latitude of this convergence point and interpret it as a result of the larger oscillation of the jet itself.

The tracers abundances at specific locations on the planet exhibit strong temporal variability. This is illustrated in Fig. 9, which shows the tracer abundance at 0.1 and 1 mbar over the globe at several snapshots in time for a model where the radius of particles on the nightside is 2.5 μm. Significant variations in tracer abundance are advected by the equatorial jet and, at high latitudes, by the day-to-night flow, leading to large local variations in time. In many cases, the strongest tracer variability seems to involve regional-scale structures with typical sizes of ~1–3 × 10^4 km but also includes hemispheric-scale fluctuations (e.g., in the abundance averaged over the day or night) and between the northern and southern hemispheres. Around the substellar point, the tracer abundance can vary by up to 50%, whereas along the terminator, this temporal variation can reach 75% relative to the mean value. Such variability – if it occurs in radiatively active species like TiO – has important implications for secondary-eclipse and transit observations, which probe the dayside and terminator, respectively.

Figure 8 sheds light on the different timescales at which this variability occurs. The top panel shows the tracer abundance averaged vertically between 0.1 and 1 mbar and horizontally over a circular patch of 45° centered on the substellar point; this gives a sense of how the tracer abundance would vary in secondary-eclipse measurements probing the dayside. The bottom panel shows the tracer abundance averaged vertically between 0.1–1 mbar and horizontally around the terminator, including all regions within 5° of the terminator itself; this gives a sense of how the tracer might vary in transit measurements. The variability exhibits two characteristic timescales: a short (fast) timescale of order of days and a long (slower) timescale of ~50 to 100 days. The bigger the particles on the nightside, the bigger the amplitude of the variations. This comes from the smaller settling timescale

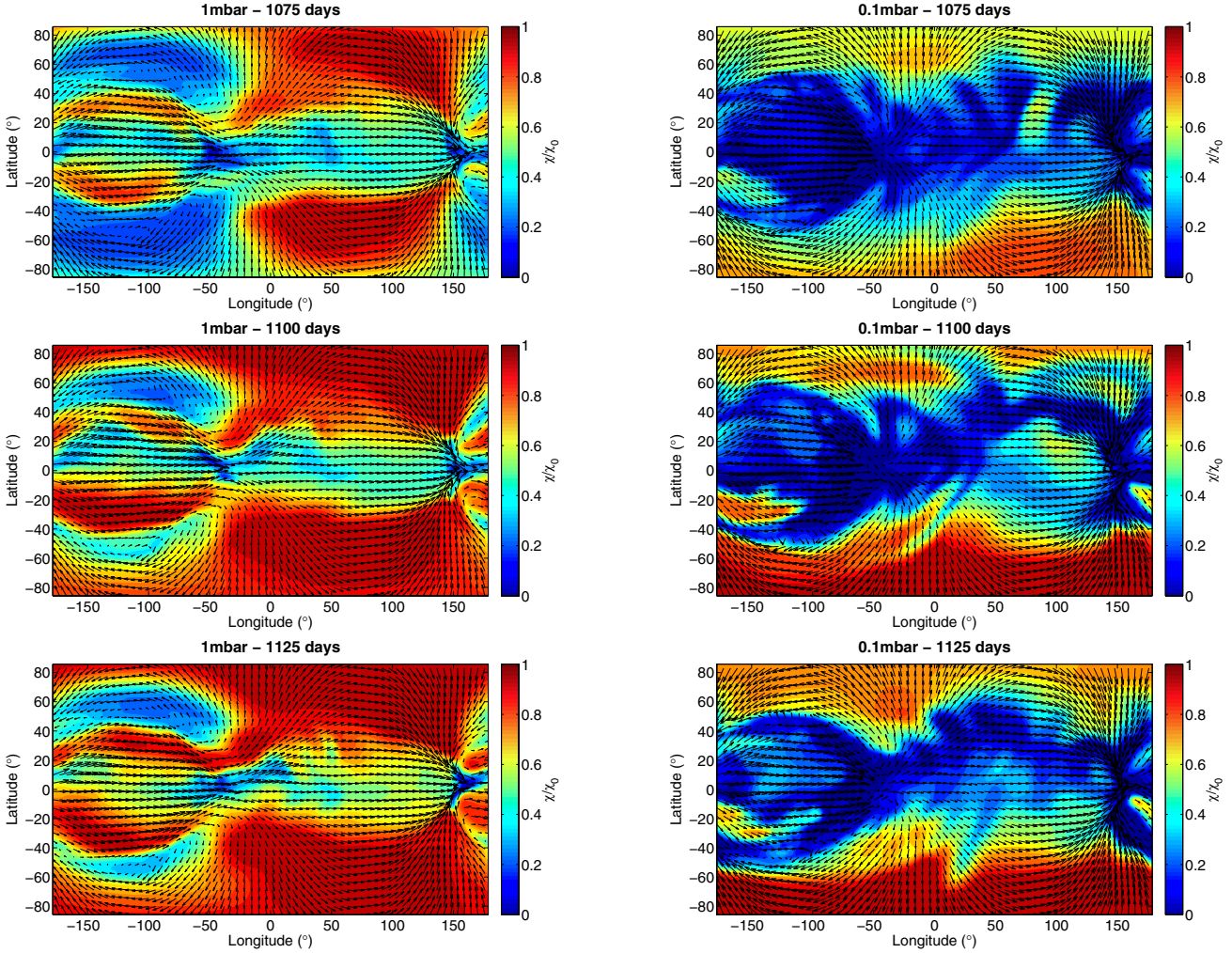

Fig. 9. Tracer abundance (colorscale) and winds (arrows) at two different pressure levels and three different times of the simulation for the case $a = 2.5\ \mu$m.

of bigger particles. In these models, the amplitude of the long-period variations exceeds those of the short-period variations by a factor of ∼2–3. The long-timescale variations exhibit similar amplitudes in the dayside and terminator time series. The short-period oscillations exhibit stronger amplitude at the terminator and seem related to variations of the flow itself, such as the oscillation of the jet described previously. Figure 8 suggests that radiatively active tracer species that can condense on the nightside, such as TiO or silicates, could lead to detectable time variations in transit or secondary eclipse spectra. The amplitude of this variability will depend on the type of tracer being considered (see Sect. 6) and may vary from planet to planet depending on the availability of the considered species. However we can predict the expected period of these variations: some days for the small amplitude ones and fifty to one hundred days for the biggest ones.

3.5. Limb profile

Transit observations are sensitive to atmospheric composition near the terminator, thus we want to characterize the distribution of our tracer species at the terminator. The possibility of variations in chemical composition between the leading and trailing limbs (as seen during transit) has been discussed in a variety of studies (e.g., Iro et al. 2005; Fortney et al. 2010). However, these studies did not investigate the particular depletion of species due to the interaction between their condensation and the atmospheric dynamics. Our model leads to the first quantitative estimate of how dynamics affects the spatial distribution of condensable species at the day-night terminators, relevant to the interpretation of transit observations. Figure 11 shows the tracer abundance at the terminator at a snapshot in time for our models with particle sizes of 0.1, 0.5, 1, 2.5, 5, and 10 μm. Angle represents angle around the terminator and the radial coordinate represents the logarithm of the pressure. In agreement with Fig. 4, the tracers tend to be depleted from upper levels, particularly in models where the particles on the nightside are larger. Moreover, Fig. 11 demonstrates that significant spatial variations occur along the terminator. Depletion occurs first at the equator along the leading limb, corresponding to the terminator 90° west of the substellar point. The superrotating jet carries air depleted in tracer from the nightside directly to this region of the terminator, explaining why abundances are particularly depleted there. In contrast, air along most of the remainder of the terminator has arrived from the dayside, where no particle settling occurs,

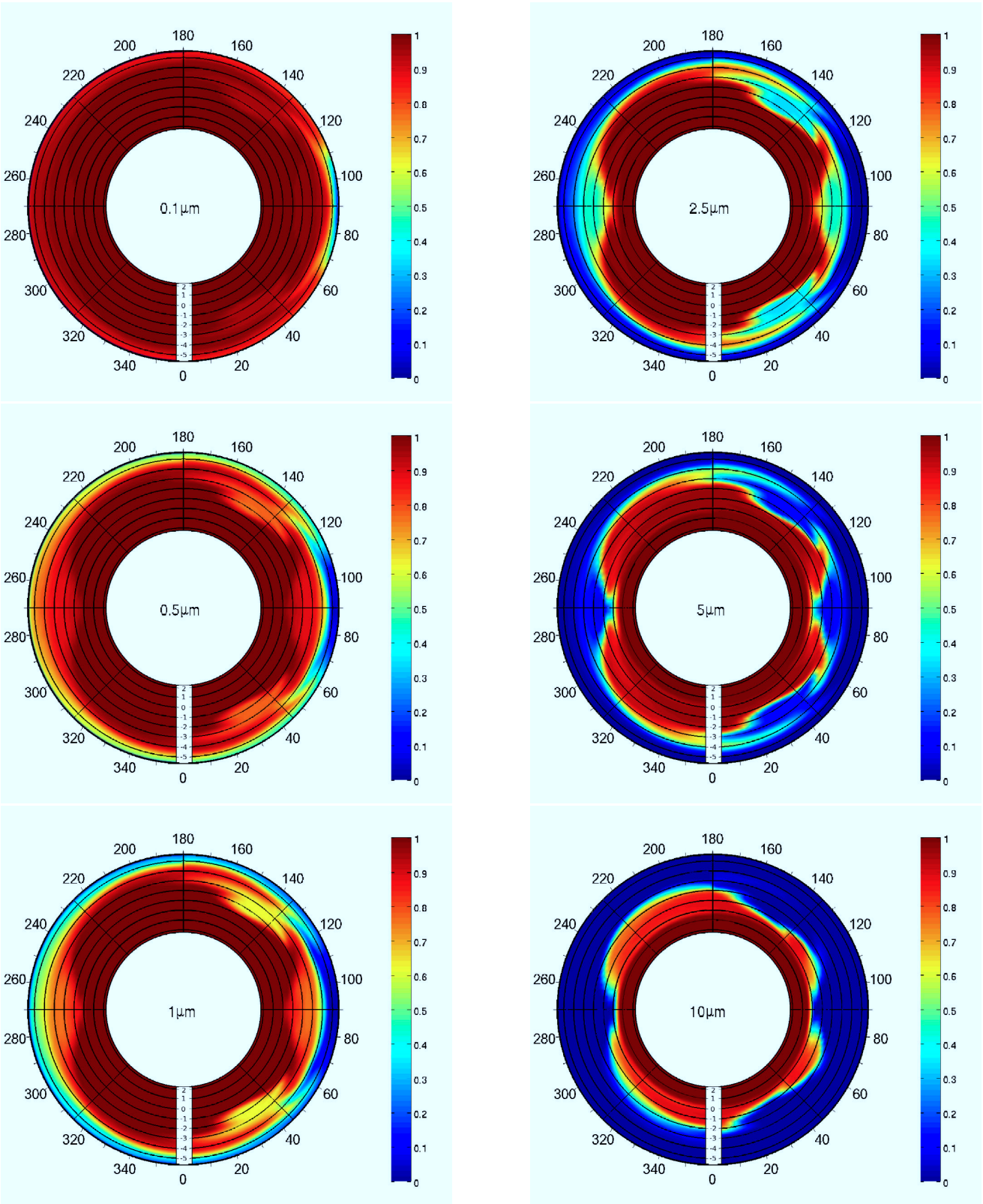

Fig. 10. Limb profiles of our tracer field from 200 bar to 1 μbar as seen during transit. Black circles are situated at 100 bar, 10 bar, 1 bar, 0.1 bar, 0.01 mbar, 1 mbar, 0.1 mbar, 0.01mbar, and 1 μbar. The north pole is on top and the leading limb on the right. The abundances are normalized to the abundance of the deepest level.

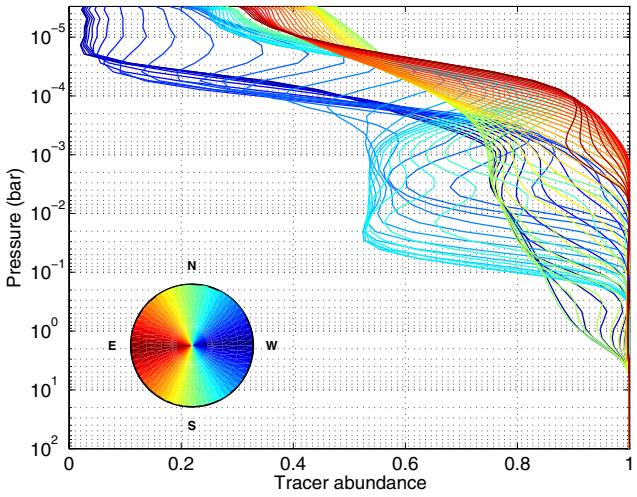

Fig. 11. Mean tracer abundance along the terminator for the case with nightside condensates of 1 μm. The different colors correspond to different latitudes along the terminator as shown in the legend. The colorwheel represents the terminator of the planet as seen during a transit, with the eastern hemisphere to the left. The mean profiles are almost symmetrical with respect to the equator, so only the profiles of the northern hemisphere are shown here.

so depletion is less strong-particularly for particle sizes $\lesssim 1\,\mu$m. Once the particle size becomes sufficiently large, however, depletion occurs everywhere along the terminator at upper levels regardless of whether the air arrived there from the dayside or nightside.

Considering now the depth dependence of the terminator abundances, our results suggest two different zones (see Figs. 10 and 11):

- At altitudes above the 1-mbar level, the tracer abundance is homogeneous over most of the limb except for the east (trailing) equatorial limb that is strongly depleted.
- At altitudes below the 1-mbar level, the east and west equatorial limb are rather homogeneous; however, the east/west dichotomy shifts to higher latitudes and the west limb above 45° is more depleted than the equivalent region of the east limb.

Moreover, it should be noted that due to the shift of the hot spot, the temperatures at the east limb are higher than at the west limb, thus a given species is more likely to be gaseous and detectable on the trailing limb than on the leading limb.

4. 1D model of the day-night cold trap

Although hot Jupiters atmospheres are inherently three-dimensional, 1D models continue to play a useful role for understanding the vertical thermal and chemical structure of these atmospheres. In particular, many groups have explored the chemistry of hot Jupiters using 1D models in which the vertical mixing caused by the large-scale dynamics is parameterized by a specified eddy diffusivity (e.g., Spiegel et al. 2009; Zahnle et al. 2009a,b; Youdin & Mitchell 2010; Line et al. 2010, 2011; Madhusudhan & Seager 2011). In these studies, the chosen eddy diffusivity is ad hoc, with no convincing theoretical support. Although the vertical mixing in our 3D models is not diffusive in any rigorous sense, there is merit in comparing the results of our 3D models with 1D models parameterized by eddy diffusivity. This allow us to make approximate estimates of the magnitudes of eddy diffusivity – in the context of a 1D model – that produce similar horizontal-mean behavior as our 3D models. Such estimates of eddy diffusivity should guide the parameter choices in 1D chemical models like those cited above. A comparison between our 3D models and 1D diffusive models also allow us to investigate how the horizontal-mean tracer depletion relates to the amplitudes of spatial tracer variation.

Therefore, in this section, we present a simple 1D model, including particle settling, with atmospheric mixing represented as an eddy diffusivity.

4.1. System studied

The presence of a superrotating, eastward equatorial jet is a dominant dynamical feature of many 3D circulation models of hot Jupiters. This superrotating jet was first predicted by Showman & Guillot (2002), and later emerges from almost all 3D simulations of hot Jupiters atmospheres (Cooper & Showman 2005; Showman et al. 2008, 2009, 2013; Dobbs-Dixon & Lin 2008; Rauscher & Menou 2010, 2012b,a; Perna et al. 2010, 2012; Heng et al. 2011a,b; Lewis et al. 2010; Kataria et al. 2013) including ours (see Sect. 3.1) and has been theoretically understood (Showman & Polvani 2011). A shift of the hottest point of the planet eastward from the substellar point has been directly observed in several exoplanets (Knutson et al. 2007, 2009, 2012; Crossfield et al. 2010) and interpreted as a direct consequence of this jet. Thus we believe that any study of the day/night cold trap in hot Jupiters atmospheres must account for this feature.

To include the presence of this jet in our model, we choose as a study system a vertical column of gas homogeneously advected around the equator by the superrotating jet. Such a column is transported from day to night and from night to day with a period $\tau_{\rm adv} = \frac{2\pi R_{\rm p}}{u_{\rm jet}}$ where $\tau_{\rm adv}$ is the advective timescale, $R_{\rm p}$ is the planetary radius and $u_{\rm jet}$ the equatorial jet velocity. $\tau_{\rm adv}$ is around 48h for HD 209458b.

As in the 3D case, we focus on a hypothetical chemical species which is gaseous on the dayside and trapped in condensates of size a on the nightside. This species freely diffuses with a vertical diffusion coefficient K_{zz} on both the dayside and the nightside. Because we envision the species as condensed on the nightside, we additionally include downward settling via Stokes-Cunningham drift on the nightside (Eq. (3)) but not on the dayside. The model includes no horizontal dimensions. Rather, we model a single column of gas that is advected from day to night. The horizontal variations therefore translate into a time-dependant settling term. We assume this chemical species to be a minor constituent of a H_2-atmosphere and neglect the latent heat released during the condensation.

4.2. 1D diffusion equation

As before, χ is the local mole fraction of the target chemical species i.e. the number of moles of tracer species (whether in gaseous or condensed form) to the total moles of air in a given volume. On the dayside, the molecules of the target chemical species can freely diffuse with a diffusion coefficient K_{zz}, according to the equation:

$$\frac{\partial \chi}{\partial t} - \frac{1}{\rho}\frac{\partial}{\partial z}\left(\rho K_{zz}\frac{\partial \chi}{\partial z}\right) = 0 \qquad (9)$$

with ρ the density of the atmosphere and z the vertical coordinate.

On the nightside, the molecules of the target species are trapped into particles that both diffuse and settle with the velocity V_f described in Sect. 2.4. Thus χ follows the same equation as Eq. (9), plus a source term describing the settling:

$$\frac{\partial \chi}{\partial t} - \frac{1}{\rho}\frac{\partial}{\partial z}\left(\rho K_{zz}\frac{\partial \chi}{\partial z}\right) = \frac{1}{\rho}\frac{\partial(\rho \chi V_f)}{\partial z}\cdot \quad (10)$$

We can define the diffusive time scale as $\tau_d = \frac{H^2}{K_{zz}}$ and a reference free fall time scale $\tau_s = H/V_s$ with $H = \frac{k_B T}{mg}$ the atmospheric scale height and V_s the Stokes velocity (see Sect. 2.4). We note that τ_d is a reference time scale and is not equal to the effective free fall time scale for high Knudsen numbers. Assuming hydrostatic balance, we can use the pressure P as the vertical coordinate and using the perfect gas law the system to solve become:

$$\begin{cases} \dfrac{\partial \chi}{\partial t} - \dfrac{\partial}{\partial P}\left(\dfrac{P^2}{\tau_d}\dfrac{\partial \chi}{\partial P}\right) = 0 & \text{on the dayside} \\ \dfrac{\partial \chi}{\partial t} - \dfrac{\partial}{\partial P}\left(\dfrac{P^2}{\tau_d}\dfrac{\partial \chi}{\partial P}\right) = -\dfrac{1}{\tau_s}\dfrac{\partial \beta P \chi}{\partial P} & \text{on the nightside.} \end{cases} \quad (11)$$

4.3. Time-dependent solution

In order to solve the system of Eq. (11) for $\chi(P,t)$, we need two boundary conditions. We assume the species to be well mixed below $P_1 = 1$ bar with a molecular abundance χ_0. At the top of the atmosphere, we assume that no molecule crosses the upper boundary (i.e. $\frac{\partial \chi}{\partial P}\Big|_{P=P_{top}} = 0$). Then we can solve the system with an implicit time stepping code using GNU OCTAVE[1], an open-source, free software equivalent to MATLAB. Assuming that the column of gas spends $\tau_{adv}/2 = 24$ h in each hemisphere, we can reach a periodic behavior where the initial condition is forgotten. While on the dayside, there is no settling and, at upper levels, the tracer diffuses upward. Thus at a given pressure the molecular abundance increases with time. This is shown by the red curves in Fig. 12. While on the nightside, the particles both diffuse vertically and settle downward at their terminal velocity and thus, at at given pressure level, the abundance decreases with time. This is shown by the blue curves in Fig. 12. In the upper atmosphere, the settling timescale and the diffusion timescale become smaller than the advective timescale. The particles have time to settle several scale heights during the time required for the air column to cross the dayside. Thus, at upper levels, the molecular abundance vary strongly throughout the diurnal cycle, and the vertical profiles vary widely around the mean value.

4.4. Steady-state solutions

Our system being forced periodically, there is no steady-state solution stricto sensu. However, the mean of the tracer abundance over one period should remain constant. We can thus integrate Eqs. (11) over one period and get an equation for $\bar{\chi}$, the mean molecular abundance over one period. Then, once the periodic state is reached, the mean over one period of the tracer abundance in our column of gas, $\bar{\chi}$, is the same as the mean over longitude at a given time, $\langle\chi\rangle$ and we obtain:

$$P^2\frac{\partial\langle\chi\rangle}{\partial P} - \frac{\beta}{2}\frac{\tau_d}{\tau_s}P\langle\chi\rangle = C \quad (12)$$

[1] http://www.octave.org

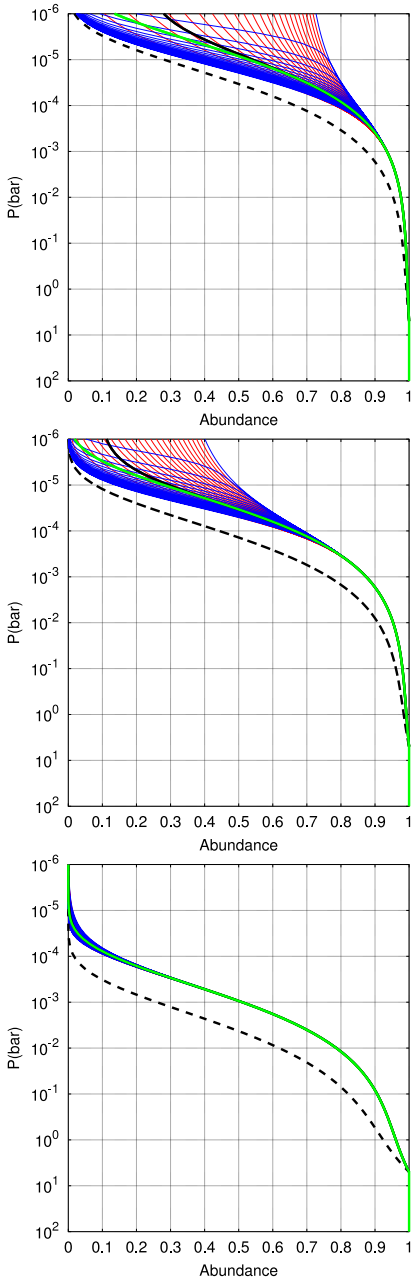

Fig. 12. Tracer abundance in the advected column of gas from the 1D model as a function of time. From *bottom to top* we used $K_{zz} = (10^4; 5\times10^4; 10^5)\sqrt{1\text{ bar}/P}$ m^{2}s^{-1} and a particle radius on the nightside of 1μm. We plot one profile every hour, corresponding to the profiles at equally spaced longitudes. The blue ones are on the nightside, the red ones on the dayside. The curve at the far left (right) of the envelope is the profile at the east (west) terminator. The black curve is the mean over one period. The green line is the analytical model (see Eq. (15) using $\alpha = 1/2$) and the dotted line is the solution for particles that would be constantly falling (both in the dayside and in the nightside).

where the factor $\frac{1}{2}$ appears because the source term is only integrated during the night. To derive Eq. (12) we assumed that the mean tracer abundance on the nightside is close to the global-mean tracer abundance. This is true given than $\beta\tau_s$ and τ_d are much bigger than τ_{adv}. This approximation breaks down at low

pressure and our analytical solution diverges from the real one as can be seen by comparing the black and the green curves in Fig. 12. However, the discrepancy is small such that the analytic solution is still a good representation of the time-mean of the full numerical solution of the 1D model everywhere deeper than the ~10 μbar level. C is a constant coming from the integration over pressure. When P goes to 0, χ goes to 0. Moreover we assume that $\frac{\partial \chi}{\partial P}$ does not go to infinity. Then the constant must be zero and we obtain:

$$\frac{\partial \langle \chi \rangle}{\partial P} = \frac{1}{2}\frac{\beta}{P}\frac{\tau_\mathrm{d}}{\tau_\mathrm{s}}\langle \chi \rangle. \tag{13}$$

To simplify the problem, we neglect the transitional regime for β from Eq. (4) and use the expression:

$$\beta = 1 + 1.656 K_N. \tag{14}$$

Then choosing a functional form $K_{zz} = K_{zz_0}(P_0/P)^\alpha$, where α is a constant, we can solve Eq. (13). For $\alpha \neq 0$ and $\alpha \neq 1$, we get:

$$\langle \chi \rangle = \chi_r \exp\left(\frac{1}{2\alpha}\frac{\tau_{\mathrm{d}_0}}{\tau_\mathrm{s}}\frac{P^\alpha - P_r^\alpha}{P_0^\alpha}\right) \times \exp\left(\frac{1}{2(\alpha-1)}\frac{\tau_{\mathrm{d}_0}}{\tau_\mathrm{s}}\frac{1.656 k_\mathrm{B} T}{\sqrt{2}\pi a d^2}\frac{P^{\alpha-1} - P_r^{\alpha-1}}{P_0^\alpha}\right). \tag{15}$$

For the particular case of a constant K_{zz} ($\alpha = 0$) the formula becomes:

$$\langle \chi \rangle = \chi_r \left(\frac{P}{P_r}\right)^{\tau_{\mathrm{d}_0}/2\tau_\mathrm{s}} \exp\left(-\frac{\tau_{\mathrm{d}_0}}{2\tau_s}\frac{1.656 k_\mathrm{B} T}{\sqrt{2}\pi a d^2}\left(\frac{1}{P} - \frac{1}{P_r}\right)\right). \tag{16}$$

In the case where K_{zz} is inversely proportional to P ($\alpha = 1$):

$$\langle \chi \rangle = \chi_r \exp\left(\frac{1}{2}\frac{\tau_{\mathrm{d}_0}}{\tau_\mathrm{s}}\frac{P - P_r}{P_0}\right)\left(\frac{P}{P_0}\right)^{\frac{1}{P_0}\frac{\tau_{\mathrm{d}_0}}{2\tau_\mathrm{s}}\frac{1.656 k_\mathrm{B} T}{\sqrt{2}\pi a d^2}}. \tag{17}$$

Where χ_r is the abundance of $\langle \chi \rangle$ at $P = P_r$ and $\tau_{\mathrm{d}_0} \equiv H/K_{zz_0}$.

4.5. Diffusivities needed to keep the tracers suspended

Because particle settling acts to transport condensates downward, the tracers only exhibit significant abundances in the upper regions of the atmosphere if the eddy diffusion coefficient exceeds some critical value, which depends on the particle size of the condensates. Here we solve for an approximate analytical expression for this critical magnitude as a function of particle size and other parameters.

Assuming a constant vertical diffusion coefficient, we can use Eq. (16) to derive an expression for the K_{zz} needed to achieve a given molecular abundance χ_lim at a given pressure P_lim. Like in Spiegel et al. (2009), we use $P_\mathrm{lim} = 1$ mbar and $\chi_\mathrm{lim} = 0.5$. We first note that Eq. (16) is composed of two terms. The first exponential is given by the Stokes regime ($\beta \approx 1$) whereas the second term is given by the Cuningham regime ($\beta \gg 1$). As can be seen in Fig. 1, particles smaller than 10 μm should be in the Cunhingham regime at $P = 1$ mbar. Thus the second term in Eq. (16) is dominant and we can use as a condition:

$$\frac{1}{2}\frac{\tau_\mathrm{d}}{\tau_\mathrm{s}}\frac{1.656 k_\mathrm{B} T}{\sqrt{2}\pi a d^2}\left(\frac{1}{P_\mathrm{lim}} - \frac{1}{P_r}\right) = -\ln(\chi_\mathrm{lim}/\chi_r). \tag{18}$$

As in the 3D model, we assume that below 1 bar the tracers are no more trapped into condensates and no more subject to settling. Thus we choose $\chi_r = 1$ at $P_r = 1$ bar. Then, for $P_r \gg P_\mathrm{lim}$, replacing τ_d and τ_s by their expressions, using Eq. (7) for the viscosity and Eq. (6) for the mean free path, we obtain a condition on the diffusion coefficient:

$$K_{zz_{\mathrm{lim}1}} \sim -\frac{HV_\mathrm{s}}{2}\frac{1.656 k_\mathrm{B} T}{\sqrt{2}\pi a d^2 \ln(\chi_\mathrm{lim}/\chi_r)}\frac{1}{P_\mathrm{lim}}. \tag{19}$$

For big particles, the Stokes regime become dominant thus we neglect the second term of Eq. (16) and the condition turns to be:

$$K_{zz_{\mathrm{lim}2}} \sim \frac{HV_\mathrm{s}\ln(P_\mathrm{lim}/P_1)}{2\ln(\chi_\mathrm{lim}/\chi_r)}. \tag{20}$$

As the relevant range of particle size span several order of magnitudes, a good approximation of K_{zz_lim} can be obtained by taking the sum of these two coefficient:

$$K_{zz_\mathrm{lim}} = K_{zz_{\mathrm{lim}1}} + K_{zz_{\mathrm{lim}2}}. \tag{21}$$

Again we note that these limits for the diffusion coefficient are independent of the planet considered. Spiegel et al. (2009) stated that an abundance of half the solar composition at 1mbar would be necessary to produce an observable stratosphere. Applying formula (21) with $\chi_\mathrm{lim} = 0.5$ and $P_\mathrm{lim} = 1$ mbar and assuming a well mixed layer below 1 bar (i.e. $P_r = 1$ bar and $\chi_r = 1$) we obtain $K_{zz_\mathrm{lim}} = 1.4 \times 10^4\,\mathrm{m^2\,s^{-1}}$ for $a = 0.1\,\mu$m, $K_{zz_\mathrm{lim}} = 1.4 \times 10^5\,\mathrm{m^2\,s^{-1}}$ for $a = 1\,\mu$m and $K_{zz_\mathrm{lim}} = 1.6 \times 10^6\,\mathrm{m^2\,s^{-1}}$ for $a = 10\,\mu$m. These results are of the same order of magnitude as the ones found by Spiegel et al. (2009) for the vertical cold trap. This is expected, since we compare two similar mechanisms: settling and diffusion of particles. However, this similarity of the results shows that the day-night cold trap is at least as important as the vertical one in hot Jupiters atmospheres. Moreover, the condition on K_{zz_lim} we derived is independent of the planet studied and holds for very hot Jupiters such as WASP-12b or WASP-33b where the vertical cold trap could be inefficient or nonexistent.

5. Effective vertical diffusion coefficient

As described previously, 1D models have been extensively used to investigate chemistry and vertical structure of hot Jupiter atmospheres, with the 3D dynamics parameterized as vertical eddy diffusion with a specified diffusivity (e.g Spiegel et al. 2009; Zahnle et al. 2009b,a; Youdin & Mitchell 2010; Line et al. 2010, 2011; Madhusudhan et al. 2011; Moses et al. 2011; Venot et al. 2012).

There is no theoretical reason for the mixing by the large scale flow patterns in hot Jupiters atmospheres to behave like a one-dimensional diffusion process. However, deriving an a posteriori effective diffusion coefficient that describes as closely as possible the averaged vertical mixing within the atmosphere can be a useful way to roughly characterize the strength of the vertical fluxes of material and guide 1D modelers in their choice of vertical mixing parameters.

A first way to define a vertical mixing coefficient from our simulation is to choose the K_{zz} that best reproduces the planet averaged tracer profiles. The 1D model developed in Sect. 4 describes the equilibrium between vertical diffusion of tracers with a specified height-dependent K_{zz} and their settling on the nightside. We tune the diffusivities to obtain a good match between the solutions of our 1D model and the horizontal-mean tracer abundance versus pressure from the 3D models. To use Eq. (15) we must specify the temperature of the atmosphere, constant in

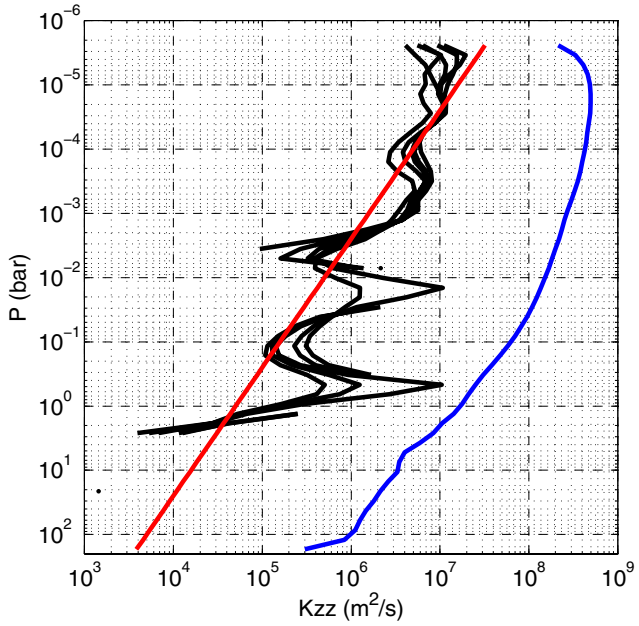

Fig. 13. Vertical diffusion coefficient from the 3D model estimated from the different tracer fields separately (black lines), from the 1D fit to the 3D model (red line) and the root mean square of the vertical velocity times the vertical scale height, a common estimate of K_{zz} in the literature (blue line) (see Lewis et al. 2010; Moses et al. 2011, for example).

the analytical model. The temperature appears in the expression for the Knudsen number and in the expression for the viscosity of hydrogen. Both quantities are related to the settling of the particles. Thus the temperature to consider is the nightside temperature. In our GCM nightside temperatures range from 600 to ≈1500 K and we decided to use a mean temperature of 1000 K. However, we note that the derived value of K_{zz} does not depend strongly on this choice. Then using a K_{zz} value proportional to the inverse square root of the pressure ($\alpha = 0.5$ in Eq. (15)), we obtain a remarkably good agreement between our 1D model (dotted lines in Fig. 4) and the horizontal average of the 3D model (solid lines of Fig. 4). The resulting value for the vertical mixing coefficient that best fits the different tracer field used in the simulation is:

$$K_{zz} = \frac{5 \times 10^4}{\sqrt{P_{\rm bar}}} \, {\rm m}^2 \, {\rm s}^{-1}, \tag{22}$$

which is valid over a pressure range from ∼1 bar to a few μbar (see Fig. 13). Fundamentally, this represents an ad-hoc fitting of our simulation results, although we find it a good match to the overall mixing properties of our 3D models over a wide range of particle sizes. Note that the upward-increasing mixing rates captured in Eq. (22) arise naturally from the fact that the radiative heating rates and vertical velocities tend to increase with decreasing pressure in our models, leading to greater mixing rates at lower pressure. The 3D models adopt the stellar insolation and other properties for HD 209458b, so the results are most germane to that planet; the mixing rates are likely to be higher for hotter planets and lower for cooler planets than implied by Eq. (22).

Another way to define a one dimensional vertical mixing coefficient from the three-dimensional simulation is to find the K_{zz} that leads to an upward diffusive flux of material that matches the averaged vertical flux produced by the dynamics. This can be written (e.g., Chamberlain & Hunten 1987, p. 90):

$$K_{zz} = \frac{\langle \rho \chi V_z \rangle}{\left\langle \rho \frac{\partial \chi}{\partial z} \right\rangle} \tag{23}$$

where the brackets represent the horizontal average along isobars over the whole planet. This expression does not necessitate any assumption on the functional form of K_{zz} nor on the nightside mean temperature. It also has the advantage that no comparisons or fits to a 1D diffusion model are necessary; the effective values of K_{zz} can be derived directly from the 3D GCM data via Eq. (23). As a trade-off, this expression depends on the vertical tracer gradients that are affected by long term temporal variability (see Sect. 3.4), which are not smoothed out completely given the limited integration time of the simulation. This leads to some strong vertical variation of K_{zz}. The profile of K_{zz} calculated from Eq. (23) are shown in the black curves of Fig. 13. Despite the vertical fluctuations, the overall shape of K_{zz} obtained with this method is close to the estimate using the planet averaged tracer profile (see the red curve in Fig. 13). Like before, we note that the derived value does not depend strongly on the particle size, consistent with the fact that Eq. (22) leads to a good fit between 1D models and our 3D model for a wide range of particle sizes.

Several previous studies have attempted to estimate the vertical diffusion coefficient in hot Jupiters atmospheres (Cooper & Showman 2006; Moses et al. 2011; Heng et al. 2011a; Lewis et al. 2010). Cooper & Showman (2006) adopted an estimate for K_{zz} based on the product of a root-mean-square vertical velocity from their 3D GCMs and an appropriately chosen vertical length scale following the formulation of Smith (1998). Moses et al. (2011) and Lewis et al. (2010) followed a similar procedure but adopted an atmospheric scale height for the vertical length scale. These estimates are crude, although Cooper & Showman (2006) showed that this formulation for K_{zz} allows 1D models to match the full tracer profiles from 3D GCMs reasonably well. More recently, Heng et al. (2011a) used the magnitude of the Eulerian mean streamfunction as a proxy for the strength of the vertical motions and derived a vertical mixing coefficient of $K_{zz} \sim 10^6 \, {\rm m}^2 \, {\rm s}^{-1}$. Note, however, that the Eulerian-mean velocities are known to be a poor descriptor of tracer advection rates in planetary atmospheres, since mixing by large scale eddies (potentially resolved by GCMs) often dominates over transport due to the Eulerian-mean circulation (see, e.g., Andrews et al. 1987, Chap. 9).

Although we confirm that mixing in hot Jupiters atmospheres is strong, we find a value that is significantly smaller than the previous ones. In particular, our value is two orders of magnitude smaller than what is obtained when multiplying the vertical scale height by the root mean square of the vertical velocity (blue curve in Fig. 13), a common estimate for K_{zz} in the literature (e.g., Lewis et al. 2010; Moses et al. 2011).

As stated in Sect. 2.1, the model does not include any sub-grid vertical diffusion coefficient. Yet, given the large values for K_{zz} that we derive from the resolved flow, it seems unlikely that sub-grid turbulent mixing would contribute significantly to the total mixing. However, the interaction between small-scale turbulence and the global flow might not be trivial and a more detailed study would be required to draw a firm conclusion.

We emphasize that vertical mixing by the global circulation appears to be planet-wide and differs from region to region. Although the globally averaged dynamics seem to be reasonably described by a vertical mixing coefficient, that is not the case for

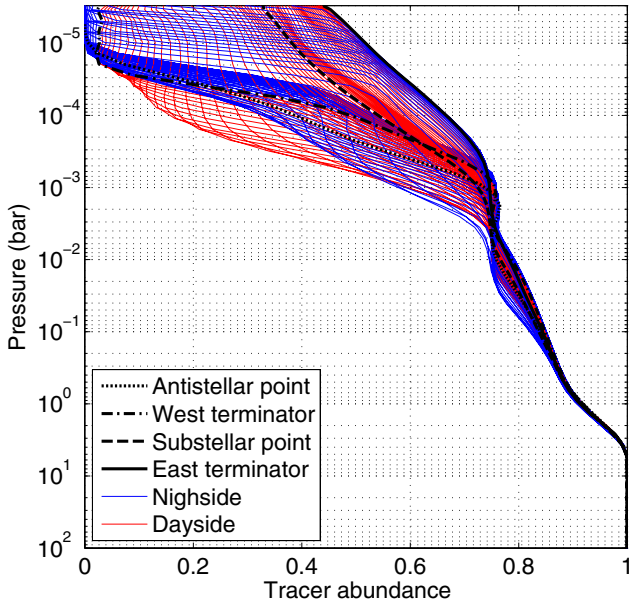

Fig. 14. Time averaged tracer abundance along the equator for nightside condensate of 1 μm. The profiles are equally spaced in longitude by 2.8°. The dayside profiles are in red whereas the nightside profiles are in blue. We highlight the profiles at the antistellar point (dotted line), the west terminator (dot-dashed line), the substellar point (dashed line) and the east terminator (plain line).

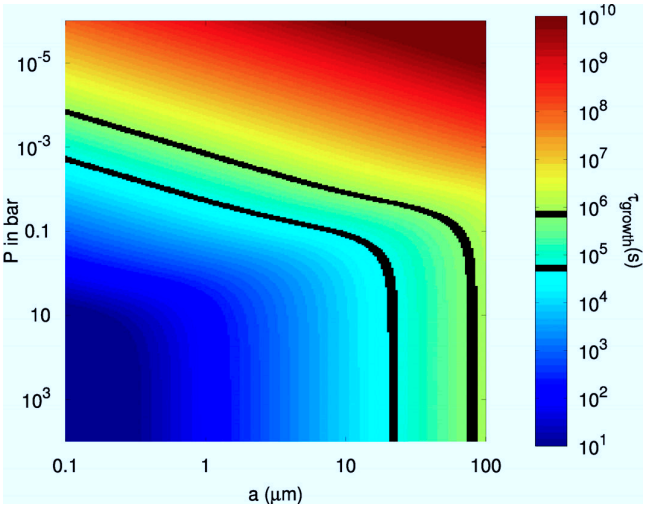

Fig. 15. Approximate growth time scale of TiO_2 grains in HD 209458b. The bottom black line shows the advective timescale and the top one is ten times the advective timescale.

the local flow in the simulation. It is therefore difficult to define mixing coefficient values for particular locations in the planet.

Along the equator, where the strong flow efficiently mixes the tracers longitudinally, we expect a good agreement of our 1D model to the 3D flow. Indeed, using the value of K_{zz} derived in Sect. 5 we realize that the spread of the tracer profiles along the equator (Fig. 14) is of the same order of magnitude as the spread predicted by the 1D model (middle panel of Fig. 12). However, in the 1D model, profiles from equally sampled longitude are equally spaced in abundances whereas the profiles obtained from the 3D model are sometimes packed together and sometimes widely spread, denoting an unequal strength of the vertical mixing longitudinally.

6. Applications

6.1. Presence of a stratosphere on hot Jupiters

TiO is a leading hypothesis for the absorber needed to create temperature inversions in hot Jupiters atmospheres (Hubeny et al. 2003; Fortney et al. 2008). However, TiO condenses at temperatures lower than ≈2000 K. On most hot Jupiters, while gaseous TiO can be stable on the dayside, it should condense on the nightside. Thus, our results allow us to address the question of whether TiO can remain suspended in the atmospheres of hot Jupiters, and hence whether TiO-induced stratospheres are indeed viable. Spiegel et al. (2009) predicted that for a solar abundance of TiO in the planet, an abundance of 0.5 times the deep abundance at 1 mbar is necessary to maintain a temperature inversion on the dayside. Our simulations suggest that if TiO condenses into particles bigger than several micrometers, the day-night cold trap will be sufficiently efficient to deplete it from the dayside. If, on the contrary, TiO cannot condense in particles bigger than several micrometers, it should remain present on the dayside and produce a stratosphere (see Figs. 4 and 6).

The size of the condensate, a free parameter in our study, results from complex microphysical processes. Once on the nightside, TiO is over-saturated, and thus Ti-bearing condensates are expected to appear. We used the formalism of Woitke & Helling (2003) to calculate the characteristic growth time scale of TiO_2 particles assuming that all the titanium is contained in $TiO_{2(g)}$ and that this last fully saturates the atmosphere. If the condensate growth time scale exceeds the advective time scale – the time for the jet to travel across one hemisphere – the condensate will be back in the dayside before reaching it's full size and will vaporize. Thus, all the particles above the black line in Fig. 15 are unlikely to form. The low elemental abundance of titanium – solar abundance is 10^{-7} compared to H (Lodders 2002) – kinetically inhibits the formation of micrometer size particles above 10 mbar.

However, titanium is not the only element that can form condensates on the nightside of hot Jupiters. Silicates are believed to condense and could incorporate titanium atoms into their grains. Sub-micron size TiO_2 particles could even be used as seeds for the formation of silicates grains. In that case the relevant time scale is not tied to the growth of TiO_2 grains but rather to the growth of SiO_2 based grains ($MgSiO_2$ for example). We calculated the growth time scale of SiO_2-based grains using the same formalism as for TiO_2 grains, assuming that $SiO_{2(g)}$ is fully saturated and that all the silica atoms are in $SiO_{2(g)}$ molecules. As can be seen in Fig. 16, particles as big as 10 μm can form at pressures as low as 10 mbar in that case.

The estimates in Fig. 16 show that the growth time of silicate particles is comparable to the time for the jet to cross an hemisphere in the pressure range where the stratosphere forms (∼0.01–1 mbar). This comparison suggests that more detailed calculations, coupling the 3D dynamics to microphysics that allow self-consistent prediction of particle growth, may be necessary to obtain a firm conclusion about whether particle growth timescales are sufficiently long to inhibit loss of TiO from the atmosphere.

Spiegel et al. (2009) studied the deep cold trap in the deep layer of the planet, at pressures exceeding tens of bars, where dynamical mixing rates are probably low. In planets that exhibit

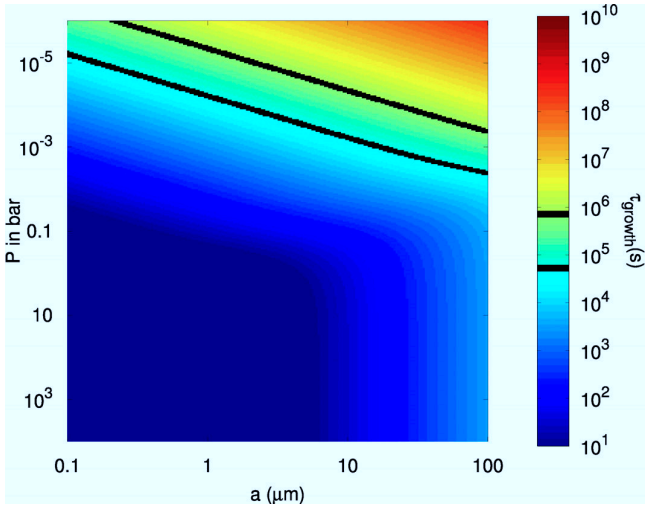

Fig. 16. Approximate growth time scale of SiO_2 grains in HD 209458b. The bottom black line shows the advective timescale and the top one is ten times the advective timescale.

such a cold trap, mixing TiO upward to altitudes where it could be affected by the day-night cold trap may be difficult. On the other hand, the opacities and therefore temperature structure in these deep regions are rather uncertain; moreover, hot Jupiters that are particularly highly irradiated would exhibit warmer temperatures and would therefore be less likely to exhibit such a vertical cold trap. On these planets, the day-night cold trap at low pressure ($P \lesssim 1$ bar) would then dominate.

The spatial variations in the gaseous tracer abundance in our 3D models (Fig. 6) suggest that the TiO abundance on the dayside, and hence the stratosphere itself, could be patchy, with some regions of the dayside exhibiting a stronger temperature inversion than others. This would have interesting consequences for the interpretation of dayside infrared spectra.

The time variability described in Sect. 3.4 could affect the presence of the stratosphere, leading to strong temporal variability in the upper atmospheric temperatures. In particular, the tracer abundance averaged over much of the dayside exhibits large-amplitude fluctuations (Fig. 8), particularly for larger particle sizes. This suggests that, at least for some planets, the TiO abundance could fluctuate between values large enough to generate a stratosphere and values too small for a stratosphere to form. The stratosphere itself might then fluctuate episodically in time, leading to variations of a factor two in the thermal flux emitted by the planet at some wavelength (see Fig. 12 of Fortney et al. 2008). Although not included in our current models, there is the possibility of feedbacks with the flow itself, since the presence (or absence) of a stratosphere exerts a significant impact on the flow structure and vertical mixing rates. If the feedback is positive, i.e. if the presence of high temperatures in the upper atmosphere enhances the mixing, then hot Jupiters could oscillate between a state with strong vertical mixing and stratospheric heating by TiO and a state with no stratospheric heating and less vertical mixing. This is a two-state atmosphere analogous to that described by Hubeny et al. (2003). However, this possibility remains speculative and further models that include the feedback of the tracer field on the flow are necessary to draw a firm conclusion.

TiO is thought to be the major Ti-bearing gas in hot Jupiters atmospheres (see Lodders 2002). However, other Ti-bearing gases, TiO_2 being the most abundant, are believed to be the condensable Ti-bearing species. Thus, a parcel of gas experiencing a sudden drop in temperature due to its advection to the nightside might not see all its titanium incorporated into condensates, but rather only the titanium atoms that already reside in other Ti-bearing molecules such as $TiO_{2(g)}$. The reaction between gaseous species $TiO + H_2O \rightleftharpoons TiO_2 + H_2$ is fast under the conditions relevant to the dayside of hot Jupiters (see Fortney et al. 2008). However, the reaction might be kinetically inhibited on the nightside of the planet where the temperature drops significantly, leading to a smaller depletion of Ti than in the hypothetical case where $TiO_{(g)}$ could condense by itself.

6.2. Clouds in hot Jupiters atmospheres

The huge day-night temperature difference and cold nightside temperatures predicted on many hot Jupiters at low pressure (e.g., Showman et al. 2009) suggest that, in addition to TiO, a wide range of other chemical species, including silicates and iron, will condense on the nightside. Some of them could also stay in a condensed state in part or all of the dayside hemisphere. The Rayleigh scattering slope in the transmission spectrum of HD189733b, first observed by Lecavelier Des Etangs et al. (2008) and later confirmed by numerous observations (see Pont et al. 2013, for a review of the different observations of this planet) is best fitted by models including sub-micron sized particles. Then the strong spatial and temporal variations observed in our model can also be interpreted as spatial variation of the cloud coverage in the atmospheres of hot Jupiters. This could lead to albedo variations along the dayside of the planet. As the hottest point of the planet is shifted to the east, the western part of the dayside is colder than the eastern one (see Fig. 3). Therefore, the western part of the dayside could be colder than the condensation temperature of some species whereas the eastern part could be at higher temperatures, leading to a more cloudy atmosphere west of the substellar point than east of it. Moreover, due to the eastward superrotating jet, material west of the substellar point arrives from the cold nightside – where condensation is thought to happen – whereas material east of the substellar point arrives from the hot substellar point – where the material is thought to have sublimated. Thus, clouds, if present on the dayside of the planet, should form more easily west of the substellar point than east of it, leading to a longitudinal variation of the albedo that contributes to the spatial variation described before. The large amount of data in the visible from the *Kepler* space telescope is ideal to search for such a spatial and temporal variability in albedo pattern of tidally locked planets.

6.3. Parameter retrieval

Atmospheric characteristics of hot Jupiters are usually derived from disk-integrated fluxes (for secondary eclipses measurements) or limb-integrated transmission (for transits spectroscopy). Therefore, interpretation of the data is usually done using one dimensional atmospheric models, assuming an homogenous atmosphere, both in term of temperature structure and composition (e.g., Madhusudhan & Seager 2009; Lee et al. 2012; Benneke & Seager 2012, among others). However, given the strong spatial variability in the tracer distribution both on the dayside hemisphere and in the limb profiles observed, some future exoplanet spectra – obtained with more and better data than nowadays – might be better understood by considering spatial variation in the atmospheric profiles and chemical composition along the planet (see also Agúndez et al. 2012, on the longitudinal variability in the chemical composition of

HD 209458b). For example, an inhomogeneous distribution of TiO would lead to strong brightness differences in the emitted flux from the different locations of the planet, which could affect features such as the apparent eastward offset of the brightest spot of the planet. Hazes could also show a similar behavior, leading to planetary spectra that might be better explained with the combination of two different (cloudy and cloudless) 1D models-as is the case in recent models of brown dwarfs (e.g., Marley et al. 2010; Burrows et al. 2011). The rising technique of secondary eclipse mapping (see Majeau et al. 2012; De Wit et al. 2012), combined with the accuracy of telescopes like EChO (Tinetti et al. 2012) or JWST might soon allow us to constrain better the spatial inhomogeneities in the disk of the planet.

Conclusion

We presented global, three-dimensional numerical simulations of the atmospheric circulation of HD 209458b including a passive tracer. This is the first circulation model of a hot Jupiter to include the dynamical mixing of condensable species. We applied our model to chemical species that are gaseous on the dayside but condense on the nightside of the planet and are trapped in particles of a given size. Given the strong day/night contrast present in hot Jupiters, our model applies to a wealth of different chemical species such as titanium, vanadium, and silicate oxides among others.

Prior studies of hot Jupiters circulation demonstrate the presence of 3D circulation patterns including both strong horizontal and vertical velocities that are necessary for mixing to happen (e.g., Showman & Guillot 2002; Cooper & Showman 2005, 2006; Showman et al. 2008, 2013; Rauscher & Menou 2012b,a, 2013; Heng et al. 2011a,b, 2012; Lewis et al. 2010; Dobbs-Dixon & Lin 2008; Dobbs-Dixon et al. 2010, 2012; Perna et al. 2010, 2012). While preliminary attempts have been made to quantify the mixing rates (Cooper & Showman 2006; Heng et al. 2011b), these methods are approximate and do not lead to a rigorous quantification of the mixing rate. Here we demonstrate that, although hot Jupiters atmospheres are believed to be stably stratified (i.e. locally non-convective), they are strongly mixed. In the presence of a background gradient of chemical species, large-scale circulation patterns naturally create upward mixing. This mixing, resolved by the GCM, is strong and likely dominates over molecular, convective or turbulent mixing. In HD 209458b, the mixing is strong enough to keep a condensable species aloft if it condenses into particles smaller than a few microns on the nightside of the planet.

The coupling between 3D flow and particle settling leads to strong spatial and temporal variations in the abundance of a given condensable species. Around 0.1 mbar, the tracer abundance is homogeneous in longitude but exhibits a large latitudinal variation, the equator being more depleted than the poles. Around 1 mbar, at high latitudes, the day/night contrast becomes important. According to our models, variability of up to ~50% in the dayside tracer abundance, and of up to ~75% in the tracer abundance along the limb, can occur for sufficiently large particle sizes (~5 μm). This variability characteristic periods ranging from days to ~50–100 days. The observability of such a variation depends on the radiative properties of the considered species and will be quantified in a future work.

These results can be applied to a wide range of molecules in hot Jupiters atmospheres. Titanium oxide, the best candidate for creating a temperature inversion in the dayside of hot Jupiters, should condense on the nightside of most planets. Our results imply that the day/night cold trap could impede the formation of a stratosphere in the dayside if TiO condenses into particles bigger than a few microns on the nightside. Growing particles to such a size seems difficult when TiO alone is considered due to its small abundance. However, TiO can be incorporated into condensates from more abundant gases such as silicate oxides. In that case the day/night cold trap could be strong enough to impede the formation of a hot stratosphere on the dayside. Spatial variability of TiO could significantly affect the dayside temperature structure and exert interesting effects on infrared spectra and lightcurves. For example, mid-to-high latitudes might keep enough TiO to create an inversion whereas the equator, more depleted, might not be able to sustain the inversion. Such a latitudinal contrast could be observed using the secondary eclipse mapping technique (e.g., Majeau et al. 2012; De Wit et al. 2012). The temporal variability observed in the model could lead to the appearance and disappearance of the stratosphere on timescales of ~10–100 earth days. Highly irradiated planets have significant thermal emission in the *Kepler* bandpass (e.g., Spiegel & Burrows 2010, for Hat-P-7b). Using the long photometric series from the *Kepler* Space Telescope, such a variability might be observable.

Our results also apply to silicate hazes. Temporal and spatial variability in the cloud coverage could strongly affect the albedo and the thermal emission of the planet. For moderately irradiated planets, the *Kepler* spacecraft observes the reflected light of the star by the planet (e.g., Demory et al. 2011, for Kepler-7b). Thus, the time series from *Kepler* could be used to build albedo, and therefore cloud maps of the planet.

Although there is no theoretical reason for the upward mixing driven by the global circulation to be diffusive, it is interesting to quantify the averaged vertical mixing with a diffusive model. The parameterization K_{zz} value of $K_{zz} = 5 \times 10^4 / \sqrt{P_{\rm bar}}\,{\rm m^2\,s^{-1}}$ or $K_{zz} = 5 \times 10^8 / \sqrt{P_{\rm bar}}\,{\rm cm^2 s^{-1}}$, between ~1 bar and ~1 μbar, can be used in 1D models of HD 209458b.

This study, the first one to include the influence of the dynamics on condensable species in a GCM of a hot Jupiter, confirms that hot Jupiters atmospheres are strongly mixed and that large scale spatial and temporal variability are expected in any condensable chemical constituents. Today, observers can already detect longitudinal variations in the emitted thermal flux of the planet. In the next decade, both longitudinal and latitudinal variations in thermal emission and albedo of the hot Jupiters will be observable, expanding the study of weather to extra-solar planets.

Acknowledgements. The authors wish to thank the ISIMA program (http://isima.ucsc.edu) where this project was initiated. This project was supported by NASA Planetary Atmospheres and Origins grants to APS. We thank Christiane Helling for discussions on dust formation, Franck Hersant for discussions on the K_{zz} calculations, Nikole Lewis for sharing her Matlab routines and Franck Selsis for useful input. We also acknowledge the anonymous referee whose numerous comments improved the clarity of this paper.

References

Ackerman, A. S., & Marley, M. S. 2001, ApJ, 556, 872
Adcroft, A., Campin, J.-M., Hill, C., & Marshall, J. 2004, Mon. Weather Rev., 132, 2845
Agúndez, M., Venot, O., Iro, N., et al. 2012, A&A, 548, A73
Andrews, D. G., Holton, J. R., & Leovy, C. B. 1987, Middle atmosphere dynamics (New York: Academic Press)
Becklin, E. E., & Zuckerman, B. 1988, Nature, 336, 656
Benneke, B., & Seager, S. 2012, ApJ, 753, 100
Burrows, A., & Sharp, C. M. 1999, ApJ, 512, 843
Burrows, A., Marley, M., Hubbard, W. B., et al. 1997, ApJ, 491, 856
Burrows, A., Heng, K., & Nampaisarn, T. 2011, ApJ, 736, 47

Chamberlain, J. W., & Hunten, D. M. 1987, Theory of planetary atmospheres. An introduction to their physics andchemistry (Orlando: Academic Press Inc)
Chapman, S., & Cowling, T. 1970, The mathematical theory of non-uniform gases, 3rd edn. (Cambridge mathematical library)
Charbonneau, D., Brown, T. M., Noyes, R. W., & Gilliland, R. L. 2002, ApJ, 568, 377
Charbonneau, D., Allen, L. E., Megeath, S. T., et al. 2005, ApJ, 626, 523
Cooper, C. S., & Showman, A. P. 2005, ApJ, 629, L45
Cooper, C. S., & Showman, A. P. 2006, ApJ, 649, 1048
Crossfield, I. J. M., Hansen, B. M. S., Harrington, J., et al. 2010, ApJ, 723, 1436
Cushing, M. C., Kirkpatrick, J. D., Gelino, C. R., et al. 2011, ApJ, 743, 50
De Wit, J., Gillon, M., Demory, B.-O., & Seager, S. 2012, A&A, 548, A128
Demory, B.-O., Seager, S., Madhusudhan, N., et al. 2011, ApJ, 735, L12
Désert, J.-M., Vidal-Madjar, A., Lecavelier Des Etangs, A., et al. 2008, A&A, 492, 585
Dobbs-Dixon, I., & Agol, E. 2012 [arXiv:1211.1709]
Dobbs-Dixon, I., & Lin, D. N. C. 2008, ApJ, 673, 513
Dobbs-Dixon, I., Cumming, A., & Lin, D. N. C. 2010, ApJ, 710, 1395
Dobbs-Dixon, I., Agol, E., & Burrows, A. 2012, ApJ, 751, 87
Fortney, J. J., Marley, M. S., Hubickyj, O., Bodenheimer, P., & Lissauer, J. J. 2005, Astron. Nachr., 326, 925
Fortney, J. J., Lodders, K., Marley, M. S., & Freedman, R. S. 2008, ApJ, 678, 1419
Fortney, J. J., Shabram, M., Showman, A. P., et al. 2010, ApJ, 709, 1396
Freedman, R. S., Marley, M. S., & Lodders, K. 2008, ApJS, 174, 504
Freytag, B., Allard, F., Ludwig, H.-G., Homeier, D., & Steffen, M. 2010, A&A, 513, A19
Goody, Y. 1961, Atmospheric Radiation Theoretical Basis (Oxford University Press)
Heng, K. 2012, ApJ, 761, L1
Heng, K., Frierson, D. M. W., & Phillipps, P. J. 2011a, MNRAS, 418, 2669
Heng, K., Menou, K., & Phillipps, P. J. 2011b, MNRAS, 413, 2380
Heng, K., Hayek, W., Pont, F., & Sing, D. K. 2012, MNRAS, 420, 20
Holton, J. R. 1992, An introduction to dynamic meteorology (New York: Academic Press)
Hubeny, I., Burrows, A., & Sudarsky, D. 2003, ApJ, 594, 1011
Iro, N., Bézard, B., & Guillot, T. 2005, A&A, 436, 719
Kalnay, E. 2003, Atmospheric modeling, data assimilation, and predictability (Cambridge, UK, New York: Cambridge University Press)
Kataria, T., Showman, A. P., Lewis, N. K., et al. 2013, ApJ, 767, 76
Kirkpatrick, J. D. 2005, ARA&A, 43, 195
Knutson, H. A., Charbonneau, D., Allen, L. E., et al. 2007, Nature, 447, 183
Knutson, H. A., Charbonneau, D., Allen, L. E., Burrows, A., & Megeath, S. T. 2008, ApJ, 673, 526
Knutson, H. A., Charbonneau, D., Cowan, N. B., et al. 2009, ApJ, 690, 822
Knutson, H. A., Lewis, N., Fortney, J. J., et al. 2012, ApJ, 754, 22
Lecavelier Des Etangs, A., Pont, F., Vidal-Madjar, A., & Sing, D. 2008, A&A, 481, L83
Lee, J.-M., Fletcher, L. N., & Irwin, P. G. J. 2012, MNRAS, 420, 170
Lewis, N. K., Showman, A. P., Fortney, J. J., et al. 2010, ApJ, 720, 344
Li, Z., & Wang, H. 2003, Phys. Rev. E, 68, 061206
Line, M. R., Liang, M. C., & Yung, Y. L. 2010, ApJ, 717, 496
Line, M. R., Vasisht, G., Chen, P., Angerhausen, D., & Yung, Y. L. 2011, ApJ, 738, 32
Lodders, K. 2002, ApJ, 577, 974
Lodders, K., & Fegley, B. 2002, Icarus, 155, 393
Madhusudhan, N., & Seager, S. 2009, ApJ, 707, 24
Madhusudhan, N., & Seager, S. 2011, ApJ, 729, 41
Madhusudhan, N., Mousis, O., Johnson, T. V., & Lunine, J. I. 2011, ApJ, 743, 191
Majeau, C., Agol, E., & Cowan, N. B. 2012, ApJ, 747, L20
Marley, M. S., & McKay, C. P. 1999, Icarus, 138, 268
Marley, M. S., Saumon, D., Guillot, T., et al. 1996, Science, 272, 1919
Marley, M. S., Seager, S., Saumon, D., et al. 2002, ApJ, 568, 335
Marley, M. S., Saumon, D., & Goldblatt, C. 2010, ApJ, 723, L117
Mayor, M., & Queloz, D. 1995, Nature, 378, 355
McKay, C. P., Pollack, J. B., & Courtin, R. 1989, Icarus, 80, 23
Moses, J. I., Visscher, C., Fortney, J. J., et al. 2011, ApJ, 737, 15
Parmentier, V., & Guillot, T. 2013, A&A, submitted
Perna, R., Menou, K., & Rauscher, E. 2010, ApJ, 719, 1421
Perna, R., Heng, K., & Pont, F. 2012, ApJ, 751, 59
Pont, F., Sing, D. K., Gibson, N. P., et al. 2013, MNRAS
Probstein, R. F. 1968, Problems of hydrodynamics and continuum mechanics (Society for industrial and applied mathematics)
Pruppacher, H., & Klett, J. 1978, Microphysics of clouds and precipitation (D. Reidel publishing compagny)
Rauscher, E., & Menou, K. 2010, ApJ, 714, 1334
Rauscher, E., & Menou, K. 2012a, ApJ, 750, 96
Rauscher, E., & Menou, K. 2012b, ApJ, 745, 78
Rauscher, E., & Menou, K. 2013, ApJ, 764, 103
Rosner, D. E. 2000, Transport processes in chemically reacting flow systems (Dover: Mineola)
Shapiro, R. 1970, Rev. Geophys., 8, 359
Showman, A. P., & Guillot, T. 2002, A&A, 385, 166
Showman, A. P., & Polvani, L. M. 2011, ApJ, 738, 71
Showman, A. P., Cooper, C. S., Fortney, J. J., & Marley, M. S. 2008, ApJ, 682, 559
Showman, A. P., Fortney, J. J., Lian, Y., et al. 2009, ApJ, 699, 564
Showman, A. P., Fortney, J. J., Lewis, N. K., & Shabram, M. 2013, ApJ, 762, 24
Smith, M. D. 1998, Icarus, 132, 176
Spiegel, D. S., & Burrows, A. 2010, ApJ, 722, 871
Spiegel, D. S., Silverio, K., & Burrows, A. 2009, ApJ, 699, 1487
Stiel, L., & Thodos, G. 1963, Indus. Eng. Chem. Fundamentals, 2, 233
Tinetti, G., Beaulieu, J. P., Henning, T., et al. 2012, Exp. Astron., 34, 311
Venot, O., Hébrard, E., Agúndez, M., et al. 2012, A&A, 546, A43
Visscher, C., Lodders, K., & Fegley, Jr., B. 2006, ApJ, 648, 1181
Woitke, P., & Helling, C. 2003, A&A, 399, 297
Woitke, P., & Helling, C. 2004, A&A, 414, 335
Youdin, A. N., & Mitchell, J. L. 2010, ApJ, 721, 1113
Zahnle, K., Marley, M. S., & Fortney, J. J. 2009a, ApJ, submitted [arXiv:0911.0728]
Zahnle, K., Marley, M. S., Freedman, R. S., Lodders, K., & Fortney, J. J. 2009b, ApJ, 701, L20

Pages 20 to 21 are available in the electronic edition of the journal at http://www.aanda.org

Appendix A: Departure from the Cunningham velocity

The Stokes-Cunningham velocity defined in Eq. (3) is derived under the assumption of low Reynolds number. Therefore it is not valid for turbulent flow and other expressions may be used when the Reynolds number increases. Here we derive better laws for intermediate and large Reynolds number.

A.1. Low Knudsen number

For small Reynolds number and small Knudsen number, the drag force exerted by a fluid on a sphere at rest is considered proportional to the kinetic energy of the fluid and the projected area of the sphere. The coefficient of proportionality, or drag coefficient, $C_{\rm D}$ is given by:

$$C_{\rm D} = \frac{F_{\rm drag}}{\rho V^2 \pi a^2/2}. \tag{A.1}$$

Then, equating gravity and drag forces leads to the settling velocity of a particle in an atmosphere:

$$V_{\rm f}^2 C_{\rm D} = \frac{8a}{3}\frac{\rho_{\rm p}-\rho}{\rho}. \tag{A.2}$$

Where $\rho_{\rm p}$ is the density of the particle. For small Reynolds numbers and high Knudsen number, $C_{\rm D} = 24$ is constant and the settling velocity is the Stokes velocity. When increasing the Reynolds number, the non linear terms of the Navier-Stokes equation become important and $C_{\rm D}$ is no longer constant. We used tabulated values of the drag coefficient as a function of the Reynolds number given by Pruppacher & Klett (1978). We assume that $C_{\rm D} = 24$ when the Reynolds number reaches 1 to stay consistent with Stokes flow and that $C_{\rm D}$ reaches its asymptotic value, $C_{\rm D} = 0.45$, when $N_{R_{\rm e}} \equiv 2R_{\rm e} = 1000$ and fit the relationship:

$$\log_{10}(N_{R_{\rm e}}) = -1.215047 + 0.923242\log_{10}\left(C_{\rm D}N_{R_{\rm e}}^2\right) - 0.031293\log_{10}\left(C_{\rm D}N_{R_{\rm e}}^2\right)^2. \tag{A.3}$$

Then we follow the same method as Ackerman & Marley (2001). Noting that:

$$C_{\rm D}N_{R_{\rm e}}^2 = \frac{32\rho g a^3(\rho_p-\rho)}{3\eta^2} \tag{A.4}$$

is independent of the velocity, we use the fit of Eq. (A.3) and extract the velocity:

$$V_{\rm f} = \frac{\eta}{2\rho a}10^{-1.21}\left(\frac{32\rho g a^3\Delta\rho}{3\eta^2}\right)^{0.92}\left(\frac{32\rho g a^3\Delta\rho}{3\eta^2}\right)^{-0.062}. \tag{A.5}$$

A.2. High Knudsen number

In the free-molecular regime, calculations have been made by Probstein (1968) leading to an expression for the drag coefficient:

$$C_{\rm D} = \frac{2}{3s_a}\sqrt{\pi} + \frac{2s_a^2+1}{s_a^3\sqrt{\pi}}\exp(-s_a^2) + \frac{4s_a^4+4s_a^2-1}{2s_a^4}erf(s_a) \tag{A.6}$$

where s_a is the ratio of the object velocity over the thermal speed of the gas ($V_T = \sqrt{\frac{2k_{\rm B}T}{m}} = \frac{\sqrt{\pi}}{2}\bar{c}$ where $\bar{c}$ is the sound speed) and erf is the error function.

For velocities much smaller than the sound speed, $s_a \to 0$ and we can use an equivalent of the error function in 0:

$$erf(s_a) = \frac{2}{\sqrt{(\pi)}}{\rm e}^{-s_a^2}\left(s_a + \frac{2}{3}s_a^3\right) + o\left(s_a^4\right). \tag{A.7}$$

Using this equation inside Eq. (A.6) and taking the limit $s_a \to 0$, the term ${\rm e}^{-s_a^2}$ goes to 1 and the terms proportional to $\frac{1}{s_a^3}$ cancels out leading to:

$$C_{\rm D} = \left(\frac{2\sqrt{\pi}}{3} + \frac{16}{3\sqrt{\pi}}\right)\frac{V_T}{V}. \tag{A.8}$$

For velocities much greater than the sound speed, the limit of Eq. (A.6) when $s_a \to \infty$ is:

$$C_{\rm D} \sim 2. \tag{A.9}$$

In order to simplify Eq. (A.6) we use the following expression for the drag coefficient at high Knudsen number:

$$C_{\rm D} = \left(\frac{2\sqrt{\pi}}{3} + \frac{16}{3\sqrt{\pi}}\right)\frac{V_T}{V} + 2. \tag{A.10}$$

Our approximation fits correctly the exact expression in the limit of low and high velocities. In between the difference to the exact expression is at most 30%. Replacing $C_{\rm D}$ by its value in Eq. (A.2) we obtain a second order equation for the velocity:

$$2\left(\frac{V}{V_T}\right)^2 + \left(\frac{2\sqrt{\pi}}{3} + \frac{16}{3\sqrt{\pi}}\right)\frac{V}{V_T} - \frac{8}{3}ag\frac{\Delta\rho}{\rho} = 0 \tag{A.11}$$

which leads to:

$$V_{\rm f} = \frac{A}{4}V_T\left(\sqrt{1 + \frac{96}{A^2\sqrt{\pi}}\frac{V_{\rm stokes}}{V_T}K_{\rm N}} - 1\right) \tag{A.12}$$

with $A = \left(\frac{2\sqrt{\pi}}{3} + \frac{16}{3\sqrt{\pi}}\right)$. When the speed becomes small compared to the sound speed ($V_{\rm stokes} \ll V_T$) we obtain:

$$V_{\rm f} = \frac{96}{8\sqrt{\pi}A}K_{\rm N}V_{\rm stokes} \approx 1.61K_{\rm N}V_{\rm stokes} \tag{A.13}$$

which is in good agreement with Eq. (3), derived for high Knudsen number and small Reynolds numbers.

A.3. Comparison with the Cunningham velocity

Figure A.1 shows the ratio of the Cunningham velocity (see Eq. (3)) to the ones we just derived. The difference is noticeable only for particles of the order of 100 μm at pressures less than the 10^{-4} bar level and exceeding the 10 bar level. This difference is always less than one order of magnitude and concern only a tiny portion of the parameter space which has little relevance to our study (the largest particle sizes considered in our 3D models is 10 μm). Thus we decided to neglect this discrepancy in the main study.

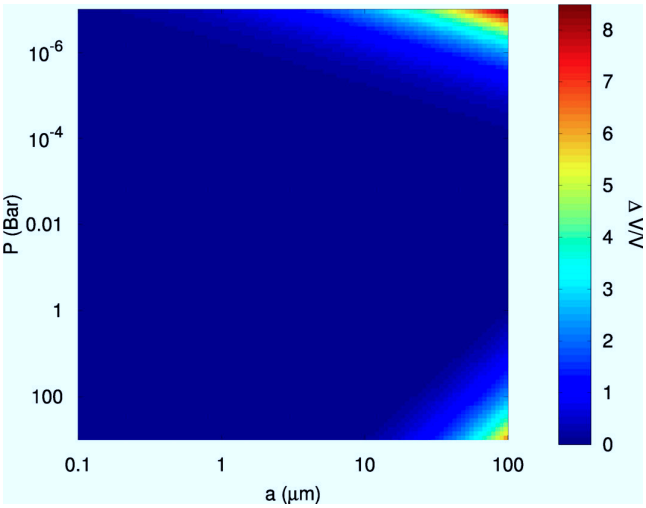

Fig. A.1. Ratio of the Cunningham velocity to the more sophisticated model of the particle settling velocity considered in the Appendix.

A&A 564, A73 (2014)
DOI: 10.1051/0004-6361/201322895

Astronomy & Astrophysics

Pseudo 2D chemical model of hot-Jupiter atmospheres: application to HD 209458b and HD 189733b

Marcelino Agúndez[1,2,⋆], Vivien Parmentier[3], Olivia Venot[4], Franck Hersant[1,2], and Franck Selsis[1,2]

[1] Univ. Bordeaux, LAB, UMR 5804, 33270 Floirac, France
e-mail: magundez@cab.inta-csic.es
[2] CNRS, LAB, UMR 5804, 33270, Floirac, France
[3] Université de Nice-Sophia Antipolis, Observatoire de la Côte d'Azur, CNRS UMR 6202, BP 4229, 06304 Nice Cedex 4, France
[4] Instituut voor Sterrenkunde, Katholieke Universiteit Leuven, Celestijnenlaan 200D, 3001 Leuven, Belgium

Received 22 October 2013 / Accepted 3 March 2014

ABSTRACT

The high temperature contrast between the day and night sides of hot-Jupiter atmospheres may result in strong variations of the chemical composition with longitude if the atmosphere were at chemical equilibrium. On the other hand, the vigorous dynamics predicted in these atmospheres, with a strong equatorial jet, would tend to supress such longitudinal variations. To address this subject we have developed a pseudo two-dimensional model of a planetary atmosphere, which takes into account thermochemical kinetics, photochemistry, vertical mixing, and horizontal transport, the latter being modeled as a uniform zonal wind. We have applied the model to the atmospheres of the hot Jupiters HD 209458b and HD 189733b. The adopted eddy diffusion coefficients were calculated by following the behavior of passive tracers in three-dimensional general circulation models, which results in much lower eddy values than in previous estimates. We find that the distribution of molecules with altitude and longitude in the atmospheres of these two hot Jupiters is complex because of the interplay of the various physical and chemical processes at work. Much of the distribution of molecules is driven by the strong zonal wind and the limited extent of vertical transport, resulting in an important homogenization of the chemical composition with longitude. The homogenization is more marked in planets lacking a thermal inversion such as HD 189733b than in planets with a strong stratosphere such as HD 209458b. In general, molecular abundances are quenched horizontally to values typical of the hottest dayside regions, and thus the composition in the cooler nightside regions is highly contaminated by that of warmer dayside regions. As a consequence, the abundance of methane remains low, even below the predictions of previous one-dimensional models, which probably is in conflict with the high CH_4 content inferred from observations of the dayside of HD 209458b. Another consequence of the important longitudinal homogenization of the abundances is that the variability of the chemical composition has little effect on the way the emission spectrum is modified with phase and on the changes in the transmission spectrum from the transit ingress to the egress. These variations in the spectra are mainly due to changes in the temperature, rather than in the composition, between the different sides of the planet.

Key words. planets and satellites: atmospheres – planets and satellites: individual: HD 189733b – planets and satellites: composition – planets and satellites: individual: HD 209458b

1. Introduction

Strongly irradiated by their close host star, hot Jupiters reside in extreme environments and represent a class of planets without analogue in our solar system. This type of exoplanets, the first to be discovered around main-sequence stars, remains the best available to study through observations and challenge a variety of models in the area of planetary science (see reviews on the subject by Baraffe et al. 2010; Seager & Deming 2010; Burrows & Orton 2011; Showman et al. 2011). In recent years, multiwavelength observations of transiting hot Jupiters have allowed scientists to put constraints on the physical and chemical state of their atmospheres. Among these hot Jupiters, the best characterized are probably HD 209458b and HD 189733b, which belong to some of the brightest and closest transiting systems, and for which primary transit, secondary eclipse, and phase curve measurements have been used to probe, though often with controversial interpretations, various characteristics of their atmospheres, such as the thermal structure (Deming et al. 2005, 2006; Knutson et al. 2008; Charbonneau et al. 2008), winds and day-night heat redistribution (Knutson et al. 2007, 2012; Cowan et al. 2007; Snellen et al. 2010), and mixing ratios of some of the main molecular constituents (Tinetti et al. 2007; Swain et al. 2008, 2009a, 2009b, 2010; Grillmair et al. 2008; Sing et al. 2009; Désert et al. 2009; Beaulieu et al. 2010; Gibson et al. 2011; Waldmann et al. 2012; Lee et al. 2012; Rodler et al. 2013; de Kok et al. 2013).

The ability of observations at infrared and visible wavelengths to characterize the physical and chemical state of exoplanet atmospheres has motivated the development of various types of theoretical models. On the one hand, there are those aiming at investigating the physical structure of hot-Jupiter atmospheres, either one-dimensional radiative models (Iro et al. 2005; Fortney et al. 2008; Parmentier et al. 2014) or three-dimensional general circulation models (Cho et al. 2008; Showman et al. 2009; Heng et al. 2011a,b; Dobbs-Dixon et al. 2012; Rauscher & Menou 2013; Parmentier et al. 2013). These models have shown how fascinating the climates of hot Jupiters are, with atmospheric temperatures usually in excess of 1000 K, and helped to understand some global observed trends. Some hot Jupiters are found to display a strong thermal inversion in the dayside while others do not (e.g. Fortney et al. 2008). Strong

⋆ Current address: Centro de Astrobiología INTA-CSIC, Carretera de Ajalvir, km.4, ES-28850 Madrid, Spain.

winds with velocities of a few km s^{-1} develop and transport the heat from the dayside to the nightside, reducing the temperature contrast between the two hemispheres. The circulation pattern in these planets is characterized by an equatorial superrotating eastward jet. On the other hand, the chemical composition of hot Jupiters has been investigated by one-dimensional models, which currently account for thermochemical kinetics, vertical mixing, and photochemistry (Zahnle et al. 2009; Line et al. 2010, 2011; Moses et al. 2011, 2013; Kopparapu et al. 2012; Venot et al. 2012, 2014; Agúndez et al. 2014). These models have revealed the existence of three different chemical regimes in the vertical direction. A first one at the bottom of the atmosphere, where the high temperatures and pressures ensure a chemical equilibrium composition. A second one located above this, where the transport of material between deep regions and higher layers occurs faster than chemical kinetics so that abundances are quenched at the chemical equilibrium values of the quench level. And a third one located in the upper atmosphere, where the exposure to ultraviolet (UV) stellar radiation drives photochemistry. The exact boundaries between these three zones depend on the physical conditions of the atmosphere and on each species.

In addition to the retrieval of average atmospheric quantities from observations, there is a growing interest in the physical and chemical differences that may exist between different longitudes and latitudes in hot-Jupiter atmospheres, and in the possibility of probing these gradients through observations. Indeed, important temperature contrasts between different planetary sides of hot Jupiters, noticeably between day and night sides, have been predicted (Showman & Guillot 2002), observed for a dozen hot Jupiters (see Knutson et al. 2007 for the first one), qualitatively understood (Cowan & Agol 2011; Perez-Becker & Showman 2013), and confirmed by three-dimensional general circulation models (e.g. Perna et al. 2012). These temperature gradients, together with the fact that photochemistry switches on and off in the day and night sides, are at the origin of a potential chemical differentiation in the atmosphere along the horizontal dimension, especially along longitude. On the other hand, strong eastward jets with speeds of a few km s^{-1} are believed to dominate the atmospheric circulation in the equatorial regions, as predicted by Showman & Guillot (2002), theorized in Showman & Polvani (2011), potentially observed by Snellen et al. (2010), and confirmed by almost all general circulation models of hot Jupiters. These strong horizontal winds are an important potential source of homogenization of the chemical composition between locations with different temperatures and UV illumination. The existence of winds and horizontal gradients in the temperature and chemical composition of hot-Jupiter atmospheres has mainly been considered from a theoretical point of view, although some of these effects can be studied through phase curve observations (Fortney et al. 2006; Cowan & Agol 2008; Majeau et al. 2012; de Wit et al. 2012), monitoring of the transit ingress and egress (Fortney et al. 2010), and Doppler shifts of spectral lines during the primary transit (Snellen et al. 2010; Miller-Ricci Kempton & Rauscher 2012; Showman et al. 2013).

The existence of horizontal chemical gradients has been addressed in the frame of a series of one-dimensional models in the vertical direction at different longitudes (e.g. Moses et al. 2011). An attempt to understand the interplay between circulation dynamics and chemistry was undertaken by Cooper & Showman (2006), who coupled a three-dimensional general circulation model of HD 209458b to a simple chemical kinetics scheme dealing with the interconversion between CO and CH_4. These authors found that, even in the presence of strong temperature gradients, the mixing ratios of CO and CH_4 are homogenized throughout the planet's atmosphere in the 1 bar to 1 mbar pressure regime. In our team, we have recently adopted a different approach in which we coupled a robust chemical kinetics scheme to a simplified dynamical model of HD 209458b's atmosphere (Agúndez et al. 2012). In this approach the atmosphere was assumed to rotate as a solid body, mimicking a uniform zonal wind, while vertical mixing and photochemistry were neglected. We found that the zonal wind acts as a powerful disequilibrium process that tends to homogenize the chemical composition, bringing molecular abundances at the limb and nightside regions close to chemical equilibrium values characteristic of the dayside. Here we present an improved model that simultaneously takes into account thermochemical kinetics, photochemistry, vertical mixing, and horizontal transport in the form of a uniform zonal wind. We apply our model to study the interplay between atmospheric dynamics and chemical processes, and the distribution of the main atmospheric constituents in the atmosphere of the hot Jupiters HD 209458b and HD 189733b.

2. Model

We modeled the atmospheres of HD 209458b and HD 189733b, for which we adopted the parameters derived by Southworth (2010). For the system of HD 209458 we took a stellar radius of 1.162 $R_\odot$, a planetary radius and mass of 1.38 R_J and 0.714 M_J (where R_J and M_J stand for Jupiter radius and mass), and an orbital distance of 0.04747 au. For the system of HD 189733 the adopted parameters are a stellar radius of 0.752 $R_\odot$, a planetary radius and mass of 1.151 R_J and 1.150 M_J, and a planet-to-star distance of 0.03142 au.

The atmosphere model is based on some of the outcomes of three-dimensional general circulation models (GCMs) developed for HD 209458b and HD 189733b (Showman et al. 2009; Parmentier et al. 2013, and in prep.), which indicate that circulation dynamics is dominated by a broad eastward equatorial jet. On the assumption that the eastward jet dominates the circulation pattern, it seems well justified to model the atmosphere as a vertical column that rotates along the equator, which mimicks a uniform zonal wind. The main shortcoming of this approach is that it reduces the whole circulation dynamics to a uniform zonal wind, although it has the clear advantage over more traditional one-dimensional models in the vertical direction of simultaneously taking into account the mixing and transport of material in the vertical and horizontal directions.

2.1. Pseudo two-dimensional chemical model

In one-dimensional models of planetary atmospheres, the distribution of each species in the vertical direction is governed by the coupled continuity-transport equation

$$\frac{\partial f_i}{\partial t} = \frac{P_i}{n} - f_i L_i - \frac{1}{nr^2}\frac{\partial (r^2 \phi_i)}{\partial r}, \quad (1)$$

where f_i is the mixing ratio of species i, t the time, n the total number density of particles, r the radial distance to the center of the planet, P_i and L_i the rates of production and loss, respectively, of species i, and ϕ_i the vertical transport flux of particles of species i (positive upward and negative downward). The first two terms on the right side of Eq. (1) account for the formation and destruction of species i by chemical and photochemical processes, while the third term accounts for the vertical transport in a spherical atmosphere. In this way, thermochemical kinetics,

photochemistry, and vertical mixing can be taken into account through Eq. (1). The transport flux can be described by eddy and molecular diffusion as

$$\phi_i = -K_{zz} n \frac{\partial f_i}{\partial z} - D_i n \left(\frac{\partial f_i}{\partial z} + \frac{f_i}{H_i} - \frac{f_i}{H_0} + \frac{\alpha_i}{T} \frac{\mathrm{d}T}{\mathrm{d}z} f_i \right), \quad (2)$$

where z is the altitude in the atmosphere with respect to some reference level (typically set at a pressure of 1 bar), T is the gas kinetic temperature, K_{zz} is the eddy diffusion coefficient, D_i is the coefficient of molecular diffusion of species i, H_i is the scale height of species i, H_0 is the mean scale height of the atmosphere, and α_i is the thermal diffusion factor of species i. More details on Eqs. (1) and (2) can be found, for instance, in Bauer (1973) and Yung & DeMore (1999). The coefficient of molecular diffusion D_i is estimated from the kinetic theory of gases (see Reid et al. 1988), while the factor of thermal diffusion α_i is set to −0.25 for the light species H, H_2, and He (Bauer 1973), and to 0 for the rest of species. The eddy diffusion coefficient K_{zz} is a rather empirical formalism to take into account advective and turbulent mixing processes in the vertical direction, and is discussed in more detail in Sect. 2.2.

To compute the abundances of the different species as a function of altitude, the atmosphere is divided into a certain number of layers and the continuous variables in Eqs. (1) and (2) are discretized as a function of altitude. After the discretization, Eq. (1) reads

$$\frac{\partial f_i^j}{\partial t} = \frac{P_i^j}{n^j} - f_i^j L_i^j - \frac{(r^{j+1/2})^2 \phi_i^{j+1/2} - (r^{j-1/2})^2 \phi_i^{j-1/2}}{n^j (r^j)^2 (z^{j+1/2} - z^{j-1/2})}, \quad (3)$$

where the superscript j refers to the jth layer, while $j + 1/2$ and $j - 1/2$ refer to its upper and lower boundaries, respectively, so that layers are ordered from bottom to top. The transport fluxes of species i at the upper and lower boundaries of layer j, $\phi_i^{j+1/2}$ and $\phi_i^{j-1/2}$, are then given by

$$\phi_i^{j\pm1/2} = -K_{zz}^{j\pm1/2} n^{j\pm1/2} \left. \frac{\partial f_i}{\partial z} \right|_{j\pm1/2} - D_i^{j\pm1/2} n^{j\pm1/2} \left[\left. \frac{\partial f_i}{\partial z} \right|_{j\pm1/2} + \left(\frac{f_i^{j\pm1/2}}{H_i^{j\pm1/2}} - \frac{f_i^{j\pm1/2}}{H_0^{j\pm1/2}} + \frac{\alpha_i}{T^{j\pm1/2}} \left. \frac{\mathrm{d}T}{\mathrm{d}z} \right|_{j\pm1/2} f_i^{j\pm1/2} \right) \right], \quad (4)$$

where the variables evaluated at $j + 1/2$ and $j - 1/2$ boundaries are approximated as the arithmetic mean of the values at layers j and $j + 1$ and at layers $j - 1$ and j, respectively. We assume that there is neither gain nor loss of material in the atmosphere, and thus the transport fluxes at the bottom and top boundaries of the atmosphere are set to zero.

The rates of production and loss of each species in Eqs. (1) and (3) are given by chemical and photochemical processes. Thermochemical kinetics is taken into account with a chemical network, which consists of 104 neutral species composed of C, H, N, and O linked by 1918 chemical reactions, that has been validated in the area of combustion chemistry by numerous experiments over the 300–2500 K temperature range and the 0.01–100 bar pressure regime, and has been found suitable to model the atmospheres of hot Jupiters. Most reactions are reversed with their rate constants fulfilling detailed balance to ensure that, in the absence of disequilibrium processes such as photochemistry or mixing, thermochemical equilibrium is achieved at sufficiently long times. The reaction scheme is described in Venot et al. (2012), with some minor modifications given in Agúndez et al. (2012). As photochemical processes we consider photodissociations, whose rates depend on the incident UV flux and the relevant cross sections. The incident UV flux is calculated by solving the radiative transfer in the vertical direction for a given zenith angle, where the spherical geometry of layers is taken into account when computing the path length along each of them. Absorption and Rayleigh scattering, the latter being treated through a two-ray iterative algorithm (Isaksen et al. 1977), both contribute to the attenuation of UV light throughout the atmosphere. Absorption and photodissociation cross-sections are described in detail in Venot et al. (2012). Rayleigh-scattering cross-sections are calculated for the most abundant species from their polarizability (see e.g. Tarafdar & Vardya 1969). As UV spectrum for the host star HD 209458, we adopt the spectrum of the Sun (mean between minimum and maximum activity from Thuillier et al. 2004) below 168 nm and a Kurucz synthetic spectrum[1] at longer wavelengths. For HD 189733b, below 335 nm we adopt a UV spectrum of ϵ Eridani based on the CAB X-exoplanets archive (Sanz-Forcada et al. 2011) and observations with FUSE and HST (see details in Venot et al. 2012), and a Kurucz synthetic spectrum[2] above 335 nm.

In one-dimensional vertical models of planetary atmospheres, the system of differential equations given by Eq. (3), with as many equations as the number of layers times the number of species, is integrated as a function of time, starting from some initial composition, usually given by thermochemical equilibrium, until a steady state is reached. During the evolution, the physical conditions of the vertical atmosphere column remain static. In the pseudo two-dimensional approach adopted here, we consider that the vertical atmosphere column rotates around the planet's equator, and thus the system of differential equations is integrated as a function of time with physical conditions varying with time, according to the periodic changes experienced during this travel. A vertical atmosphere column rotating around the equator mimics a uniform zonal wind, which is an idealization of the equatorial superrotating jet structure found by three-dimensional GCMs for hot-Jupiter atmospheres. This approach may be seen as a pseudo two-dimensional model in which the second dimension, which corresponds to the longitude (the first one being the altitude), is in fact treated as a time dependence in the frame of an atmosphere column rotating around the equator.

To build the pseudo two-dimensional chemical models of HD 209458b and HD 189733b the vertical atmosphere column is divided into 100–200 layers spanning the pressure range 500–10^{-8} bar. The evolution of the vertical atmosphere column starts at the substellar point with an initial composition given by either thermochemical equilibrium or a one-dimensional vertical model, the latter usually resulting in shorter integration times before a periodic state is reached. The convenience of starting with the composition of the hottest substellar regions is discussed in Agúndez et al. (2012). Thermochemical equilibrium calculations were carried out using a code that minimizes the Gibbs energy based on the algorithm of Gordon & McBride (1994) and the thermochemical data described in Venot et al. (2012) for the 102 species included. A solar elemental composition (Asplund et al. 2009) was adopted for the atmospheres of both HD 209458b and HD 189733b. The planetary sphere was then discretized into a certain number of longitudes (typically 100) and the system of differential equations given by Eq. (3) was integrated as the atmosphere column moves from one longitude to the next, at a constant angular

[1] See http://kurucz.harvard.edu/stars/hd209458
[2] See http://kurucz.harvard.edu/stars/hd189733

velocity. To speed up the numerical calculations, the physical variables that vary with longitude (in our case these are the vertical structures of temperature and incident UV flux) were discretized as a function of longitude, that is, they were assumed to remain constant within each discretized longitude interval. As long as there are important longitudinal temperature gradients, the atmospheric scale height also varies with longitude, so that the atmosphere expands or shrinks depending on whether it gets warmer or cooler. To incorporate this effect, which may have important consequences for transit spectra, the vertical atmosphere column was enlarged or compressed (the radius at the base of the atmosphere remaining fixed) to fulfill hydrostatic equilibrium at any longitude. The variation of the incident UV flux with longitude was taken into account through the zenith angle. At the limbs we considered a zenith angle slightly different from a right angle because of the finite apparent size of the star and because of atmospheric refraction, for which we adopted a refraction angle of half a degree as in the case of visible light at Earth.

The nonlinear system of first-order ordinary differential equations given by Eq. (3) was integrated as a function of time using a backward differentiation formula implicit method for stiff problems implemented in the Fortran solver DLSODES within the ODEPACK package[3] (Hindmarsh 1983; Radhakrishnan & Hindmarsh 1993). The evolution of the vertical atmosphere column was followed during several rotation cycles until the abundances of the main atmospheric constituents achieved a periodic behavior, which for HD 209458b and HD 189733b, occurs after some tens or hundreds of rotation periods.

2.2. Atmospheric dynamics and temperature (GCMs)

The pseudo two-dimensional chemical model needs some key input data related to the zonal wind speed, thermal structure, and strength of vertical mixing. These data are calculated with the three-dimensional general circulation model SPARC/MITgcm developed by Showman et al. (2009), in which dynamics and radiative transfer are coupled. The data used here for HD 209458b are based on the simulations by Parmentier et al. (2013), while those for HD 189733b are based on calculations by Parmentier et al. (in prep.), both of which cover a pressure range from about 200 bar to 2 μbar. These GCM simulations provide a wealth of detailed information regarding the physical structure of the atmosphere, although they remain limited with respect to the chemical structure as long as the composition is assumed to be given by local chemical equilibrium.

2.2.1. Wind structure

Circulation dynamics in the atmospheres of hot Jupiters is dominated by a fast eastward (or superrotating) jet stream at the equator. This superrotating jet was first predicted by Showman & Guillot (2002), has been found to emerge from almost all GCM simulations of hot Jupiters (Cooper & Showman 2005; Showman et al. 2008, 2009, 2013; Dobbs-Dixon & Lin 2008; Rauscher & Menou 2010, 2012a,b; Perna et al. 2010, 2012; Heng et al. 2011a,b; Lewis et al. 2010; Kataria et al. 2013; Parmentier et al. 2013), and is also understood theoretically (Showman & Polvani 2011). A shift of the hottest point of the planet eastward from the substellar point has been directly observed in several exoplanets (Knutson et al. 2007, 2009a, 2012; Crossfield et al. 2010) and interpreted as a direct consequence of this jet. The superrotating jet in HD 209458b and HD 189733b spans over all longitudes and has a well-defined location in latitude (around ±20°) and pressure (between 1–10 bar and 10^{-6}–10^{-3} bar), as illustrated in Figs. 1 and 2, where the zonally averaged zonal wind speed is depicted as a function of latitude and pressure for each planet. To derive a mean speed of the jet for our pseudo two-dimensional chemical model, we averaged the zonal wind speed longitudinally over the whole planet, latitudinally over ±20°, and vertically between 1 and 10^{-6} bar, the latter corresponding to the top of the atmosphere in the GCM simulations. We find mean zonal wind speeds of 3.85 km s^{-1} for HD 209458b and 2.43 km s^{-1} for HD 189733b, in both cases in the eastward direction. These values were adopted in the pseudo two-dimensional chemical model as the speed of the zonal wind at the equator and 1 bar pressure level, thus setting the angular velocity of the rotating vertical atmosphere column (i.e., its rotation period).

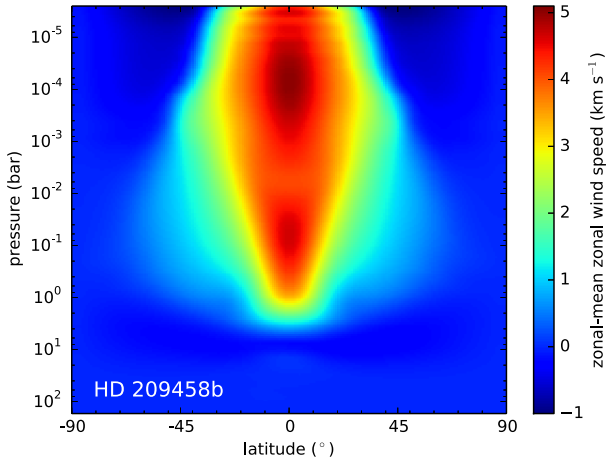

Fig. 1. Zonal-mean zonal wind speed (positive is eastward and negative westward) as a function of latitude and pressure, as calculated with a GCM simulation of HD 209458b (Parmentier et al. 2013). Note the superrotating wind above the 1 bar pressure level in the equatorial region (±20° in latitude).

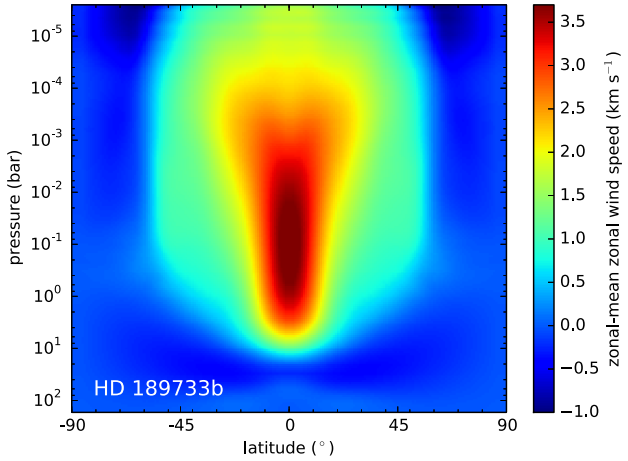

Fig. 2. Zonal-mean zonal wind speed as a function of latitude and pressure calculated with a GCM simulation of HD 189733b (Parmentier et al., in prep.). A strong superrotating equatorial jet is clearly present in the 10–10^{-3} bar pressure range.

[3] See http://computation.llnl.gov/casc/odepack

At high latitudes, above 50°, the circulation is no longer dominated by the superrotating jet; the zonal-mean zonal wind is westward and the flow exhibits a complex structure, with westward and eastward winds, and a substantial day-to-night flow over the poles (Showman et al. 2009). At low latitudes, the zonal-mean zonal wind is eastward over most of the vertical structure (above the 1–10 bar pressure level), although the shape of the superrotating jet changes gradually with altitude, from a well-defined banded flow with little longitudinal variability of the jet speed in the deep atmosphere to a less banded flow with important longitudinal variations of the wind speed in the upper levels (Showman et al. 2009). It is also worth noting that according to Showman et al. (2013), the circulation regime in the atmospheres of hot Jupiters changes from a superrotating one to a high-altitude day-to-night flow when the radiative or the frictional time scales become short, as occurs at low pressures under intense insolation or strong drag forces. In this regard, we note that the GCM simulations by Parmentier et al. (2013, and in prep.) used here are based on a drag-free case, and are thus the most favorable for the presence of a strong equatorial jet. That is, we would have found a somewhat slower equatorial jet if drag forces were included in the GCM simulations (Rauscher & Menou 2012a, 2013; Showman et al. 2013).

In view of the discussion above, our pseudo two-dimensional chemical model based on a uniform zonal wind probably is a good approximation for the equatorial region (±20°) in the 1 bar to 1 mbar pressure regime, and may still provide a reasonable description of upper equatorial layers, where an eastward jet is still present although with a less uniform structure. In the polar regions our formalism may not be adequate since the circulation regime is more complex, and thus the interplay between dynamics and chemistry may lead to a very different distribution of the chemical composition from that predicted by our model. It is interesting to note that low latitudes contribute more to the projected area of the planet's disk than polar regions, and thus planetary emission is to a large extent dominated by the equatorial regions modeled here. The same is not true for transmission spectra however, where low and high latitudes are both important.

2.2.2. Temperature structure

Among the dozen hot Jupiters for which we have good observational constraints on their atmospheric properties (Seager & Deming 2010), half of them are believed to have a strong thermal inversion at low pressure in the dayside, while the other half are thought to lack such an inversion. The presence of a stratosphere in hot Jupiters is commonly attributed to the survival in the gas phase of the strong absorbers at visible wavelengths TiO and VO (Fortney et al. 2008; Showman et al. 2009; Parmentier et al. 2013). In this theoretical framework, planets that are warm enough to have an appreciable opacity due to TiO and VO (pM class planets) host a stratosphere, while those that are cooler (pL class planets) do not develop a temperature inversion in their atmospheres (Fortney et al. 2008). This, not yet firmly established however because no unambigous detection of TiO has been obtained (Désert et al. 2008), the nature of the absorbers that cause temperature inversions in hot Jupiters is still debated. For example, photochemical products of some undetermined nature or arising from the photochemical destruction of H_2S have also been postulated as possible absorbers responsible for these stratospheres (Burrows et al. 2008; Zahnle et al. 2009). Moreover, not all planets fit into this pM/pL scheme, and other parameters such as the atmospheric

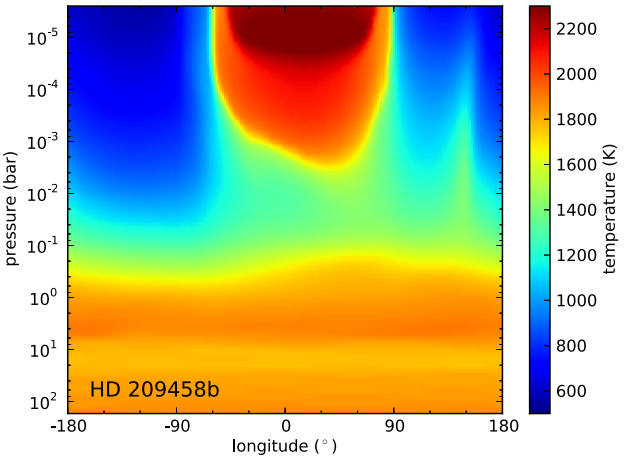

Fig. 3. Temperature structure averaged latitudinally over ±20° around the equator of HD 209458b, as calculated with a GCM simulation (Parmentier et al. 2013). Note the extremely hot dayside stratosphere above the 1 mbar pressure level.

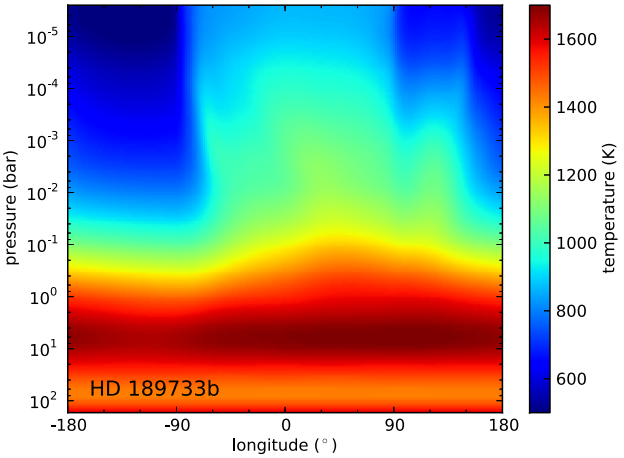

Fig. 4. Temperature structure averaged latitudinally over ±20° around the equator of HD 189733b, as calculated with a GCM simulation (Parmentier et al., in prep.).

elemental C/O abundance ratio (Madhusudhan 2012) or the stellar activity (Knutson et al. 2010) might control whether there are stratospheres in hot Jupiters.

HD 209458b and HD 189733b are good examples of these two types of hot Jupiters, the former hosting a strong thermal inversion in the dayside, while the latter does not. The temperature resulting from the GCM simulations and averaged latitudinally over an equatorial band ±20° in latitude is shown as a function of longitude and pressure in Fig. 3 for HD 209458b and in Fig. 4 for HD 189733b. This equatorial band of ±20° in latitude corresponds to the region where the equatorial jet is present in the GCM simulations (see Figs. 1 and 2). For the pseudo two-dimensional chemical model, which focuses on the equatorial region where the eastward jet develops, we adopted the temperature distribution shown in Figs. 3 and 4, assuming an isothermal atmosphere at pressures lower than 2 μbar.

In our previous study (Agúndez et al. 2012), the temperature structure of HD 209458b's atmosphere was calculated

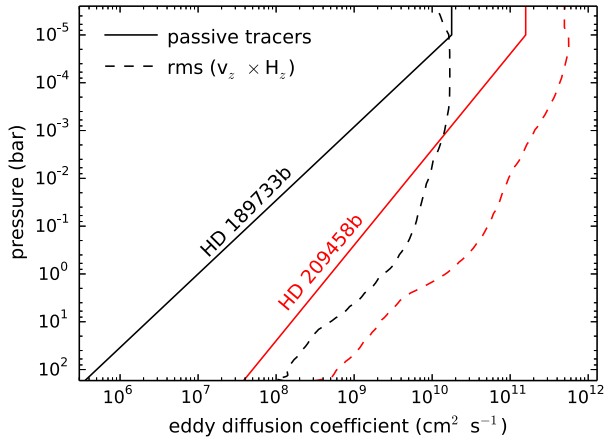

Fig. 5. Vertical eddy diffusion coefficient profiles for HD 209458b and HD 189733b, as calculated by following the behavior of passive tracers (solid lines; Parmentier et al. 2013, and in prep.), and as given by previous estimates based on the rms of the vertical velocity times the vertical scale height (dashed lines; Moses et al. 2011).

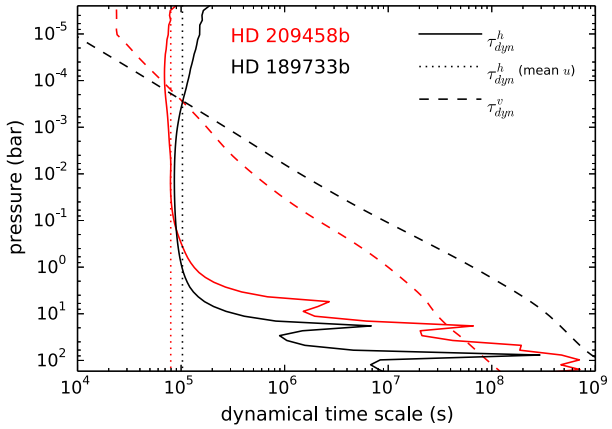

Fig. 6. Dynamical time scales of horizontal transport ($\tau^{\rm h}_{\rm dyn}$) and vertical mixing ($\tau^{\rm v}_{\rm dyn}$) as a function of pressure in HD 209458b and HD 189733b. $\tau^{\rm h}_{\rm dyn}$ is computed adopting as zonal wind speed either an average over an equatorial band of latitude ±20° (solid lines) or the mean values independent of height given in Sect. 2.2.1 (dotted lines).

with a one-dimensional time-dependent radiative model and resulted in an atmosphere without a strong temperature inversion. Here, the temperature structure calculated for the atmospheres of HD 209458b and HD 189733b comes from GCM simulations, which result in a strong temperature inversion for the former planet and an atmosphere without stratosphere for the latter one. This permits us to explore the chemistry of hot Jupiters with and without a stratosphere. It is also worth noting that in the case of HD 209458b, there is evidence of a dayside temperature inversion from observations of the planetary emission spectrum at infrared wavelengths (Knutson et al. 2008).

2.2.3. Vertical eddy diffusion coefficient

Another important outcome of GCM simulations is the quantification of the strength with which material is transported in the vertical direction in the atmosphere. Although this mixing is not diffusive in a rigorous sense, once averaged over the whole planet, it can be well represented by an effective eddy diffusion coefficient that varies with pressure (Parmentier et al. 2013). This variable enters directly as input into one-dimensional and pseudo two-dimensional chemical models of planetary atmospheres such as ours. The eddy diffusion coefficient is commonly estimated in the literature as the root mean square of the vertical velocity times the vertical scale height (Line et al. 2010; Moses et al. 2011). Recently, Parmentier et al. (2013) have used a more rigorous approach to estimate an effective eddy diffusion coefficient in HD 209458b by following the behavior of passive tracers in a GCM. These authors have shown that vertical mixing in hot-Jupiter atmospheres is driven by large-scale circulation patterns. There are large regions with ascending motions and large regions with descending motions, some of them contributing more to the global mixing than others. It has been also shown that a diffusion coefficient is a good representation of the vertical mixing that takes place in the three-dimensional model of the atmosphere. The resulting values for HD 209458b are 10–100 times lower than those obtained with the previous method (see Fig. 5), and are used here. The vertical profile of the eddy diffusion coefficient for HD 209458b can be approximated by the expression K_{zz} (cm^2 s^{-1}) = 5×10^8 $p^{-0.5}$, where the pressure p is expressed in bar (see Parmentier et al. 2013). In the case of HD 189733b we used the expression K_{zz} (cm^2 s^{-1}) = 10^7 $p^{-0.65}$, where the pressure p is again expressed in bar. This expression is based on preliminary results by Parmentier et al. (in prep.) using the method involving passive tracers, and results in values up to 1000 times lower than those obtained with the previous more crude method (see Fig. 5). In both HD 209458b and HD 189733b we considered a constant K_{zz} value at pressures lower than 10^{-5} bar.

2.2.4. Dynamical time scales

To assess the relative strengths of horizontal transport and vertical mixing in the atmospheres of HD 209458b and HD 189733b it is useful to argue in terms of dynamical time scales. The dynamical time scale of horizontal transport may be roughly estimated as $\tau^{\rm h}_{\rm dyn} = \pi R_{\rm p}/u$, where R_p is the planetary radius and u the zonal wind speed, while that related to vertical mixing can be approximated as $\tau^{\rm v}_{\rm dyn} = H^2/K_{zz}$, where H is the atmospheric scale height and K_{zz} the eddy diffusion coefficient. If we take a zonal wind speed uniform with altitude and equal to the mean value given in Sect. 2.2.1, we find that horizontal transport occurs faster than vertical mixing over most of the vertical structure of the atmospheres of HD 209458b and HD 189733b (see dotted and dashed lines in Fig. 6). Only in the upper layers, at pressures below 10^{-3}–10^{-4} bar, the high eddy diffusion coefficient makes vertical mixing faster than horizontal transport.

In the deep atmosphere, however, the equatorial superrotating jet vanishes and zonal winds become slower (see Figs. 1 and 2), although horizontal transport still remains faster than or at least similar to vertical mixing (see solid and dashed lines in Fig. 6). In these deep layers, below the 1–10 bar pressure level, our assumption of a zonal wind speed uniform with altitude and with values as high as a few km s^{-1} is not valid. This is clearly a limitation of the pseudo two-dimensional model, although the implications for the resulting two-dimensional distribution of atmospheric constituents are not strong because in these deep layers the temperature remains rather uniform with longitude, and molecular abundances are largely controlled by thermochemical

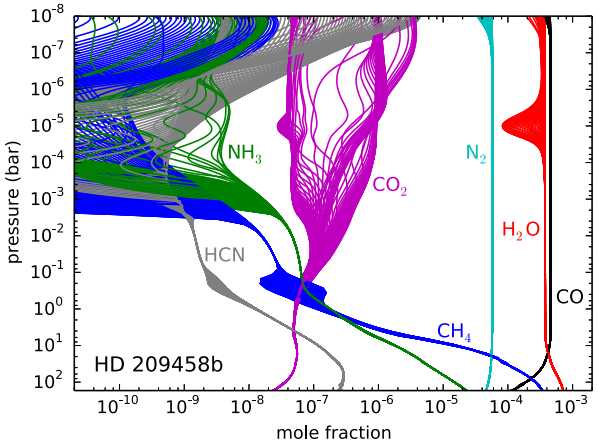

Fig. 7. Vertical cuts of the abundance distributions of some of the most abundant molecules at longitudes spanning the 0–360° range, as calculated with the pseudo two-dimensional chemical model for HD 209458b's atmosphere.

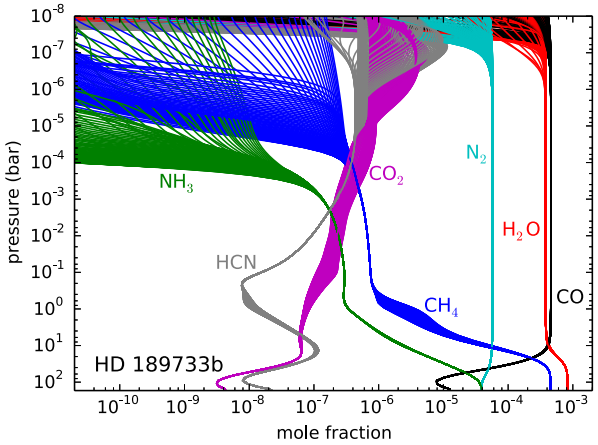

Fig. 8. Vertical cuts of the abundance distributions of some of the most abundant molecules at longitudes spanning the 0–360° range, as calculated with the pseudo two-dimensional chemical model for HD 189733b's atmosphere.

equilibrium, which makes them quite insensitive to the strength of horizontal transport. This has been verified by running models for HD 209458b and HD 189733b with zonal wind speeds down to 1000 times slower than the nominal mean values given in Sect. 2.2.1.

In the way the pseudo two-dimensional chemical model is conceived, it clearly deals with the equatorial region of hot Jupiter atmospheres. First, the formalism adopted, in which a vertical atmosphere column rotates around the equator at a constant angular velocity, is adequate for the equatorial region (±20° in latitude), where a strong eastward jet is found to dominate the circulation according to GCM simulations (see Figs. 1 and 2). Second, the temperature structure adopted (see Figs. 3 and 4) corresponds to the average over an equatorial band of width ±20° in latitude. Third, the rotation period of the atmosphere column is calculated from the wind speed retrieved from the GCM (which is also an average over an equatorial band ±20° in latitude) and the equatorial circumference. And fourth, the longitude-dependent zenith angle adopted to compute the penetration of stellar UV photons corresponds to the equatorial latitude. The adopted formalism is therefore adequate for the equatorial region as long as circulation is dominated by an eastward jet. With these limitations in mind, we now present and discuss the chemical composition distribution resulting from the pseudo two-dimensional chemical model for the atmospheres of HD 209458b and HD 189733b.

3. Distribution of atmospheric constituents

3.1. Overview

A first glance at the calculated distribution of the chemical composition with altitude and longitude in the atmospheres of HD 209458b and HD 189733b can be obtained by examining the ranges over which the vertical abundance profiles vary with longitude. This information is shown in Figs. 7 and 8 for some of the most abundant species, after H_2 and He. We can see that some molecules such as CO, H_2O, and N_2 show little abundance variation with longitude, while some others such as CH_4, CO_2, NH_3, and HCN experience important changes in their abundances as longitude varies. Abundance variations are usually restricted to the upper regions of the atmosphere (above the 10^{-1}–10^{-3} bar pressure level, depending on the molecule) but not to the lower atmosphere, where molecules maintain rather uniform abundances with longitude. On the one hand, longitudinal gradients in the temperature and incident stellar UV flux drive the abundance variations with longitude, while on the other, the zonal wind tends to homogenize the chemical composition in the longitudinal direction, resulting in the complex abundance distributions shown in Figs. 7 and 8. These results agree with the predictions of Cooper & Showman (2006) concerning the CO distribution in HD 209458b's atmosphere. These authors coupled a GCM to a simple chemical kinetics scheme dealing with the interconversion between CO and CH_4 and found that CO shows a rather homogeneous distribution with longitude and latitude in spite of the strong variations predicted by chemical equilibrium. We also find a rather homogeneous distribution of CO with longitude, although the same is not true for other molecules that display important longitudinal abundance gradients.

In Figs. 9 and 10 we show the atmospheric distribution of selected molecules that may influence planetary spectra as a function of longitude and pressure. Water vapor illustrates the case of a molecule with a rather uniform distribution throughout the atmosphere of both planets, except for a slight enhancement at high pressures (>10 bar) and a small depletion, which in HD 209458b occurs at about 10^{-5} bar eastward of the substellar point and is induced by the warm stratosphere, and in HD 189733b takes place in the upper dayside layers (above the 10^{-7} bar pressure level) through photochemical destruction. Carbon monoxide also has a quite uniform distribution and is not shown in Figs. 9 and 10. Carbon dioxide is perhaps the most abundant molecule showing important longitudinal abundance variations, with a marked day-to-night contrast. In HD 209458b this molecule is enhanced in the cooler nightside, where it is thermodynamically favored. In HD 189733b the nightside enhancement is only barely apparent in the 10^{-5}–10^{-1} bar pressure range, while in upper layers the situation is reversed and CO_2 becomes depleted in the nightside regions because of a complex interplay between chemistry and dynamics. In the atmospheres of both planets, CO_2 maintains a mixing ratio between a few 10^{-8} and a few 10^{-5}. The hydrides CH_4 and NH_3 show important abundance variations in the vertical direction, their abundance decrease when moving toward upper low-pressure layers,

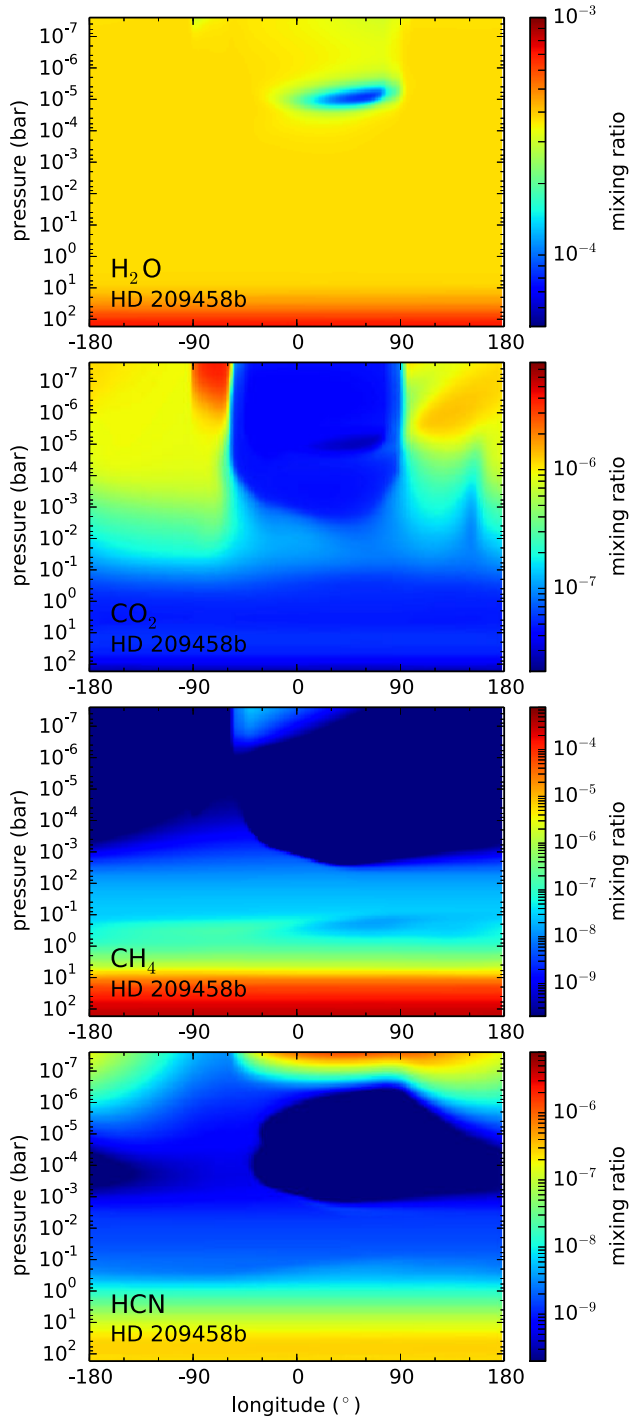

Fig. 9. Distribution of H_2O, CO_2, CH_4, and HCN as a function of longitude and pressure in the equatorial band of HD 209458b's atmosphere, as calculated with the pseudo two-dimensional chemical model.

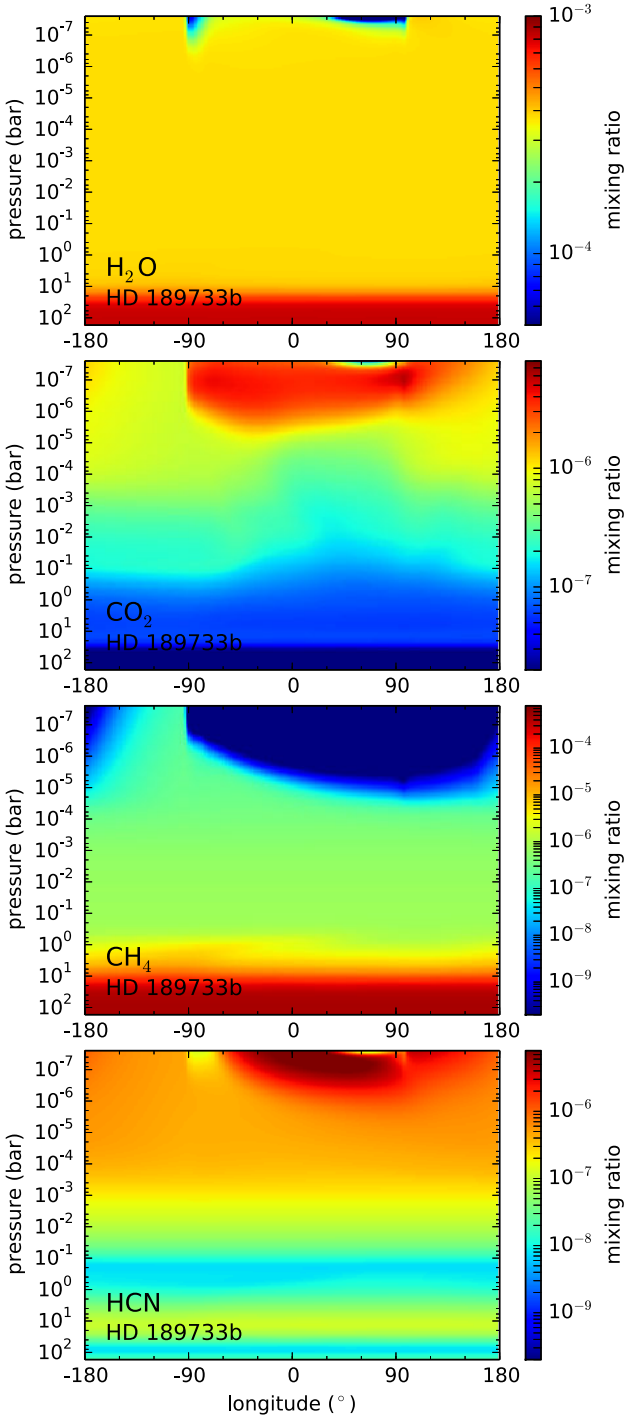

Fig. 10. Same as Fig. 9, but for HD 189733b.

and also some longitudinal variability, which is only important at low abundance levels, however. In HD 209458b, methane is largely suppressed above the 1 mbar pressure level because of the stratosphere. In HD 189733b it is present at a more important level, except in the very upper layers where its depletion in the warmer dayside regions is propagated by the jet to the east, contaminating the nightside regions to a large extent. Hydrogen cyanide also shows important abundance variations with both longitude and altitude. This molecule is greatly enhanced by the action of photochemistry, and thus becomes quite abundant in the upper dayside regions of HD 189733b and to a lower extent in the upper dayside layers of HD 209458b, where photochemistry is largely supressed by the presence of the stratosphere (Moses et al. 2011; Venot et al. 2012). The distribution of HCN

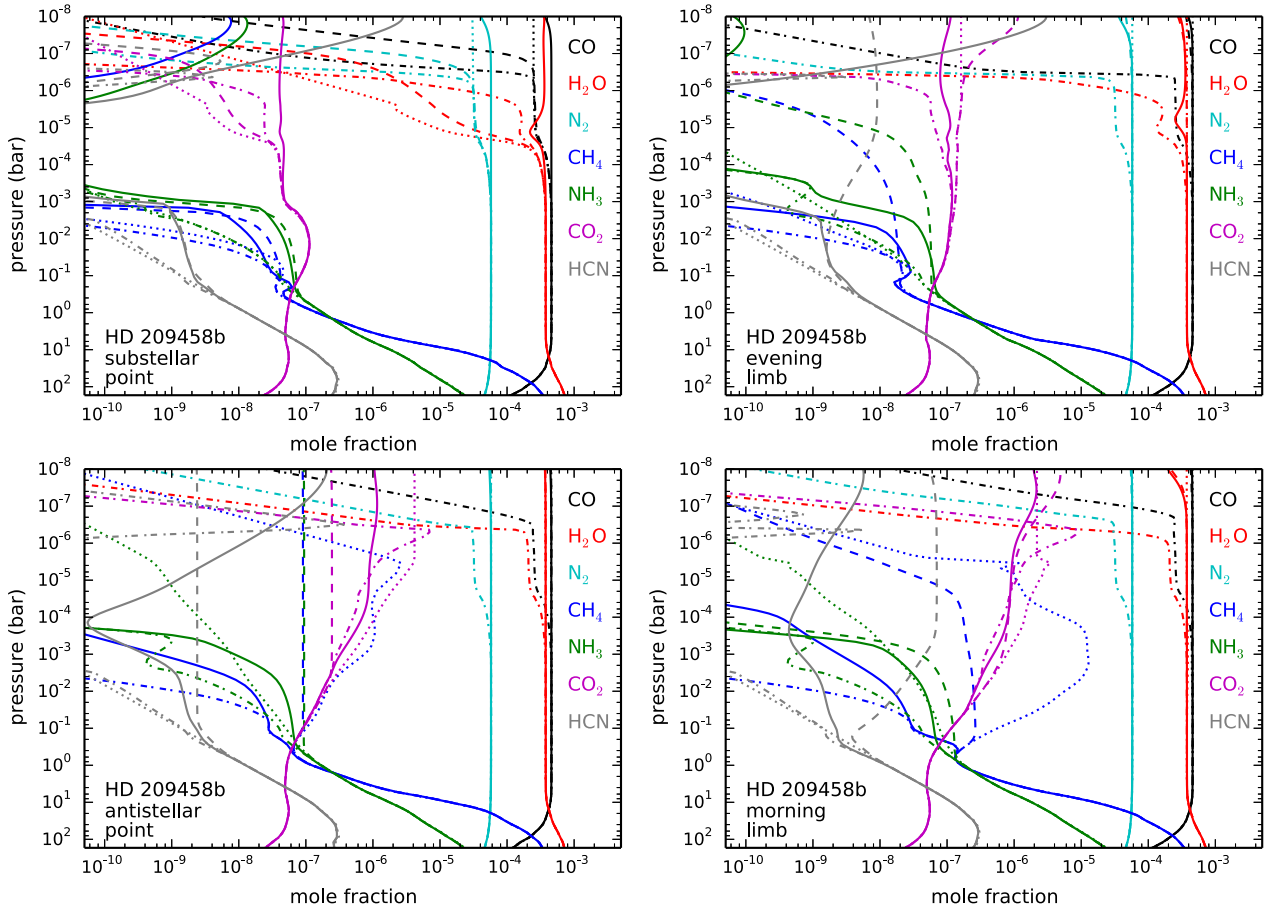

Fig. 11. Vertical distributions of the most abundant atmospheric constituents, after H_2 and He, at four longitudes: substellar point (0°), evening limb (+90°), antistellar point (±180°), and morning limb (−90°) in the atmosphere of HD 209458b. We show the mole fractions calculated by the pseudo two-dimensional chemical model (solid lines), by a model that neglects vertical mixing (horizontal transport case; dashed-dotted lines), by a one-dimensional vertical model that neglects horizontal transport (vertical mixing case; dashed lines), and by local thermochemical equilibrium (dotted lines). Photochemistry is taken into account in all cases but the last.

in the upper atmosphere shows that the eastward jet results in a contamination of nightside regions with HCN formed in the dayside.

As long as there is an important departure from chemical equilibrium in the atmospheric composition of both planets, the assumption of local chemical equilibrium in the GCM simulations may be an issue and one potential source of inconsistency between the GCM and the chemical model. Much of the thermal budget of these atmospheres, however, is controlled by water vapor, whose abundance is rather uniform and close to chemical equilibrium. This fact may justify to some extent the assumption of local chemical equilibrium in GCMs. We note however that other atmospheric constituents such as CO and CO_2 can also play an important role in the thermal balance of hot-Jupiter atmospheres, especially for elemental compositions far from solar, in which case the hypothesis of chemical equilibrium usually adopted in GCMs may not be adequate. Obviously, a more accurate and self-consistent approach would be to couple a robust chemical kinetics network to a GCM, although this is a very challenging computational task.

3.2. Comparison with limiting cases

To obtain insight into the predicted distribution of molecules in the atmospheres of HD 209458b and HD 189733b, a useful and pedagogical exercise is to compare the abundance distributions calculated by the pseudo two-dimensional chemical model with those predicted in various limiting cases. A first one in which vertical mixing is neglected and therefore the only disequilibrium processes are horizontal advection and photochemistry (horizontal transport case), a second one consisting of a one-dimensional vertical model including vertical mixing and photochemistry, which neglects horizontal transport (vertical mixing case), and a third one which is given by local thermochemical equilibrium. Figures 11 and 12 show the vertical distributions of some of the most abundant species, after H_2 and He, in the atmospheres of HD 209458b and HD 189733b, respectively, at four longitudes (substellar and antistellar points, and evening and morning limbs[4]), as calculated by the pseudo two-dimensional model and the three aforementioned limiting cases. We may summarize the effects of horizontal transport (modeled as a uniform zonal wind) and vertical mixing (modeled as an eddy diffusion process) by saying that horizontal transport tends to homogenize abundances in the horizontal direction, bringing

[4] We use the terms morning and evening limb to refer to the situation encountered by the traveling wind when crossing each of the two meridians of the planet's terminator. Morning, also called west or leading, and evening, also called east or trailing, limbs are probed by transmission spectra at the ingress and egress, respectively, during primary transit.

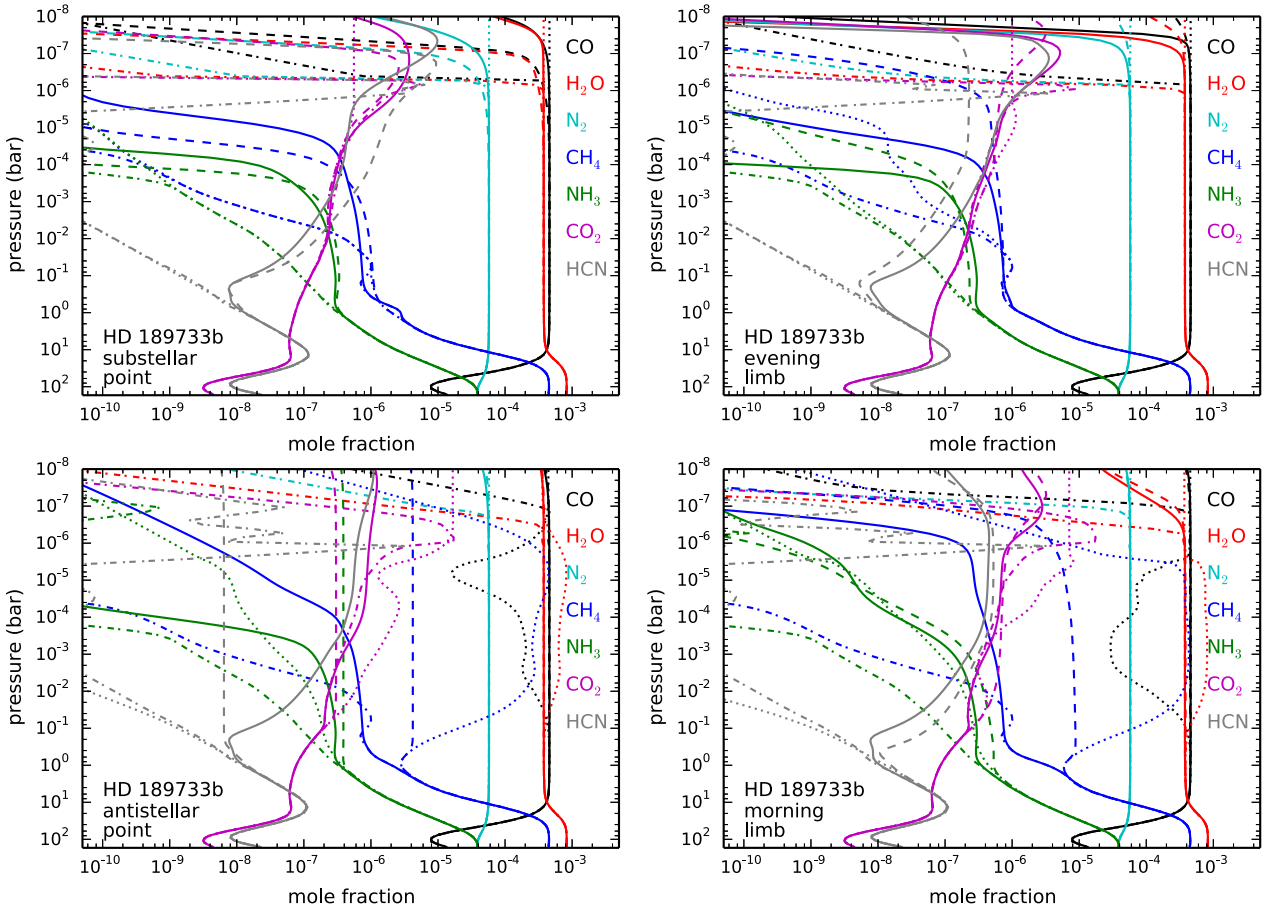

Fig. 12. Same as Fig. 11, but for HD 189733b.

them close to chemical equilibrium values of the hottest dayside regions, while vertical mixing tends to homogenize abundances in the vertical direction, bringing them close to chemical equilibrium values of hot bottom regions.

The effect of horizontal transport is perfectly illustrated in the case of methane. In both HD 209458b and HD 189733b, the abundance profile of CH_4 given by the horizontal transport case (blue dashed-dotted lines in Figs. 11 and 12) almost perfectly resembles the chemical equilibrium profile at the substellar point (blue dotted lines in upper left panel of Figs. 11 and 12), and remains almost invariant with longitude in spite of the important abundance enhancement predicted by chemical equilibrium in the cooler nightside and morning limb regions. The existence of a strong stratosphere in HD 209458b introduces important differences with respect to HD 189733b. The hot temperatures in the upper dayside layers of HD 209458b result in short chemical time scales and therefore allows chemical kinetics to mitigate to some extent the horizontal quenching induced by the zonal wind. This is clearly seen for CO_2 (magenta dashed-dotted lines in Figs. 11 and 12), whose abundance varies longitudinally within 2–3 orders of magnitude in HD 209458b, while in HD 189733b it shows an almost uniform distribution with longitude. The abundance distributions obtained in the horizontal transport case are qualitatively similar to those presented by Agúndez et al. (2012), although there are some quantitative differences due to the lack of photochemistry and a temperature inversion for HD 209458b in that previous study. Photochemistry plays in fact an important role in the horizontal transport case (dashed-dotted lines in Figs. 11 and 12), as it causes molecular abundances to vary with longitude in the upper layers due to the switch on/off of photochemistry in the day and night sides, as the wind surrounds the planet. Note also that the lack of vertical mixing in this case causes the photochemically active region to shift down to the level where, in the absence of vertical transport, chemical kinetics is able to counterbalance photodissociations, that is, to synthesize during the night the molecules that have been photodissociated during the day. Another interesting consequence of photochemistry in the horizontal transport case is that molecules such as HCN (gray dashed-dotted lines in Figs. 11 and 12), which are formed by photochemistry in the upper dayside regions, remain present in the upper nightside regions as a consequence of the continuous horizontal transport, and can in fact increase their abundances through the molecular synthesis ocurring during the night.

In the extreme case where vertical transport completely dominates over any kind of horizontal transport, the homogenization is produced in the vertical, and not longitudinal, direction. The value at which a given molecular abundance is quenched vertically corresponds to the chemical equilibrium abundance at the altitude where the rates of chemical reactions and vertical transport become similar, the so-called quench region. This quench region may be located at a different altitude for each species, although in hot Jupiters such as HD 209458b and HD 189733b it is usually located in the 10–10^{-2} bar pressure range (Moses et al. 2011; Venot et al. 2012; also this study). Assuming the strength of vertical mixing does not vary with longitude (as done in this

study), the vertical mixing case would yield uniform abundances with longitude if temperatures do not vary much with longitude in the range of altitudes where abundances are usually quenched vertically. In this case, the quench region for a given species would be the same at all longitudes, and so would the vertically quenched abundance. According to the GCM simulations of HD 209458b and HD 189733b, the temperature varies significantly with longitude above the 1 bar pressure level, and thus the exact values at which the abundances of the different species are quenched vertically vary with longitude. The temperature constrast between day and nightside regions is therefore one of the main causes of abundance variations with longitude, as illustrated by CH_4 in both planets (blue dashed lines in Figs. 11 and 12). Another factor that drives longitudinal abundance gradients in the vertical mixing case is photochemistry, which switches on and off in the day and nightsides, respectively. Without horizontal transport that connects the day and nightsides, abundances become rather flat in the vertical direction in the nightside, where photochemistry is suppressed, and display more complicated vertical abundance profiles in the dayside, where photochemistry causes molecules such as NH_3 to be depleted while some others such as HCN are enhanced. Note that because we used eddy diffusion coefficients significantly below those adopted in previous studies (e.g. Moses et al. 2011; Venot et al. 2012), the vertical quench of abundances in the dayside is not as apparent because it is strongly counterbalanced by photochemistry.

In the pseudo two-dimensional model, in which both horizontal transport and vertical mixing are simultaneously taken into account, the distribution of atmospheric constituents (solid lines in Figs. 11 and 12) results from the combined effect of various processes that tend to drive the chemical composition to a variety of distributions. On the one hand, chemical kinetics proceeds to drive the composition close to local chemical equilibrium. On the other hand, horizontal transport tends to homogenize abundances longitudinally, while vertical mixing does the same in the vertical direction. Finally, stellar UV photons tend to photodissociate molecules in the upper dayside layers, and new molecules are formed through chemical reactions involving the radicals produced in the photodissociations. Among these processes, horizontal transport and vertical mixing compete in homogenizing the chemical composition in the longitudinal and vertical directions, respectively. In the atmospheres of HD 209458b and HD 189733b horizontal transport occurs faster than vertical mixing below the ∼1 mbar pressure level (see Sect. 2.2.4), and therefore molecular abundances are strongly homogenized in the longitudinal direction in this region. In upper layers the competition of mixing and photochemical processes results in a more complex distribution of atmospheric constituents.

Molecular abundances show a wide variety of behaviors when both horizontal transport and vertical mixing are considered simultaneously. The abundances of molecules such as CH_4, NH_3, and HCN tend to follow those given by the vertical mixing case at the substellar region, but at other longitudes the situation is quite different depending on the molecule (blue, green, and gray solid lines in Figs. 11 and 12). At the antistellar point, for example, the abundance profiles of CH_4 and NH_3 are closer to those predicted by the pure horizontal transport case than by the vertical mixing one, but HCN does follow a behavior completely different from each of these two limiting cases. The abundances of CO, H_2O, and N_2 show little variation with longitude or altitude and are therefore not affected by whether horizontal transport or vertical mixing dominates. Nevertheless, the coupling of horizontal transport and vertical mixing results in some curious behaviors, such as that of water vapor at the substellar point of HD 209458b (red lines in Fig. 11). The two limiting cases of pure horizontal transport and pure vertical mixing predict a decline in its abundance in the upper layers because of photodissociation and because of a low chemical equilibrium abundance at these low pressures. However, horizontal and vertical dynamics working simultaneously bring water from more humid regions so that there is no decline in its abundance up to the top of the atmosphere (at 10^{-8} bar in our model). In summary, taking into account both horizontal transport and vertical mixing produces complex abundance distributions that in many cases cannot be predicted a priori.

We may have a different view of the situation by looking at the ranges over which the vertical abundance profiles vary with longitude in the various limiting cases (see Figs. 13 and 14). Our attention first focuses on the fact that local chemical equilibrium predicts strong variations of the chemical composition with longitude in the atmospheres of both HD 209458b and HD 189733b. This is especially true for CH_4 and CO in the latter planet, where methane becomes more abundant than carbon monoxide in the cooler nightside regions. Disequilibrium processes, however, in particular horizontal transport and vertical mixing, reduce to a large extent the longitudinal variability of molecular abundances. As already stated, although perhaps more clearly seen in Figs. 13 and 14, horizontal transport tends to homogenize abundances with longitude. The effect of a purely horizontal transport is perfectly illustrated in HD 189733b's atmosphere, where, except for the photochemically active region in the upper layers, the distribution of molecules is remarkably homogeneous with longitude (see horizontal transport panel in Fig. 14). In the atmosphere of HD 209458b, on the other hand, a pure horizontal transport allows for some longitudinal variability in the abundances of CO_2 and NH_3 above the 10^{-3} bar pressure level (see horizontal transport panel in Fig. 13), mainly because of the activation of chemical kinetics in the dayside stratosphere and its ability to counterbalance the homogenization driven by horizontal transport. In the vertical mixing case (i.e., no horizontal transport), abundances are more uniform in the vertical direction but show important longitudinal variations, with a marked day/night asymmetry characterized by rather flat vertical abundance profiles in the nightside and abundances varying with altitude in the dayside because of the influence of photochemistry (see e.g. CH_4, NH_3, and HCN in vertical mixing panels of Figs. 13 and 14). When horizontal transport and vertical mixing are considered simultaneously (top panels of Figs. 13 and 14), the distribution of molecules in the lower atmosphere of both HD 209458b and HD 189733b, below the 10^{-3} bar pressure level, remains remarkably homogeneous with longitude and close to that given by the pure vertical mixing case at the substellar regions. That is, the chemical composition of the hottest dayside regions propagates to the remaining longitudes, which indicates that the zonal wind transports material faster than vertical mixing processes do. In the upper atmosphere the abundance profiles become more complicated because of the combined effect of the photochemistry that takes place in the dayside and the mixing of material ocurring in both the vertical and horizontal directions.

3.3. Comparison with previous one-dimensional models

It is interesting to compare the results obtained with the pseudo two-dimensional model with previous results from

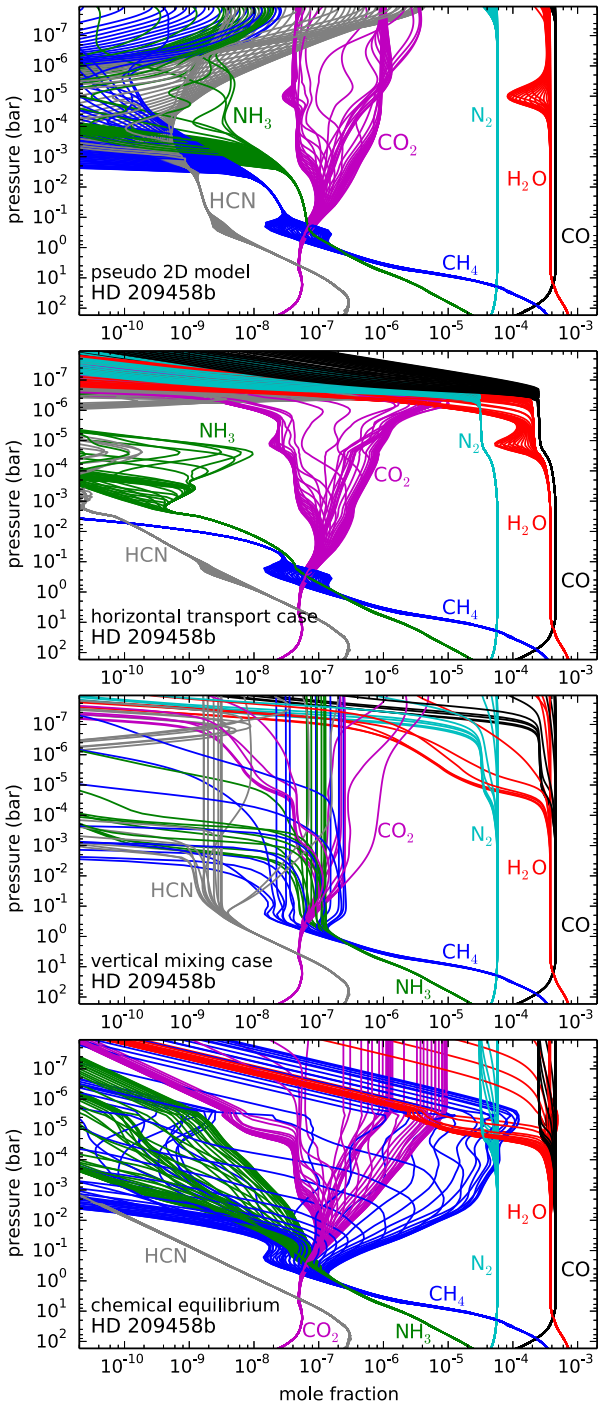

Fig. 13. Vertical cuts of the abundance distributions of some of the most abundant molecules in HD 209458b's atmosphere at longitudes spanning the 0–360° range, as calculated (*from top to bottom*) with the pseudo two-dimensional model, in the horizontal transport and vertical mixing cases, and under local chemical equilibrium.

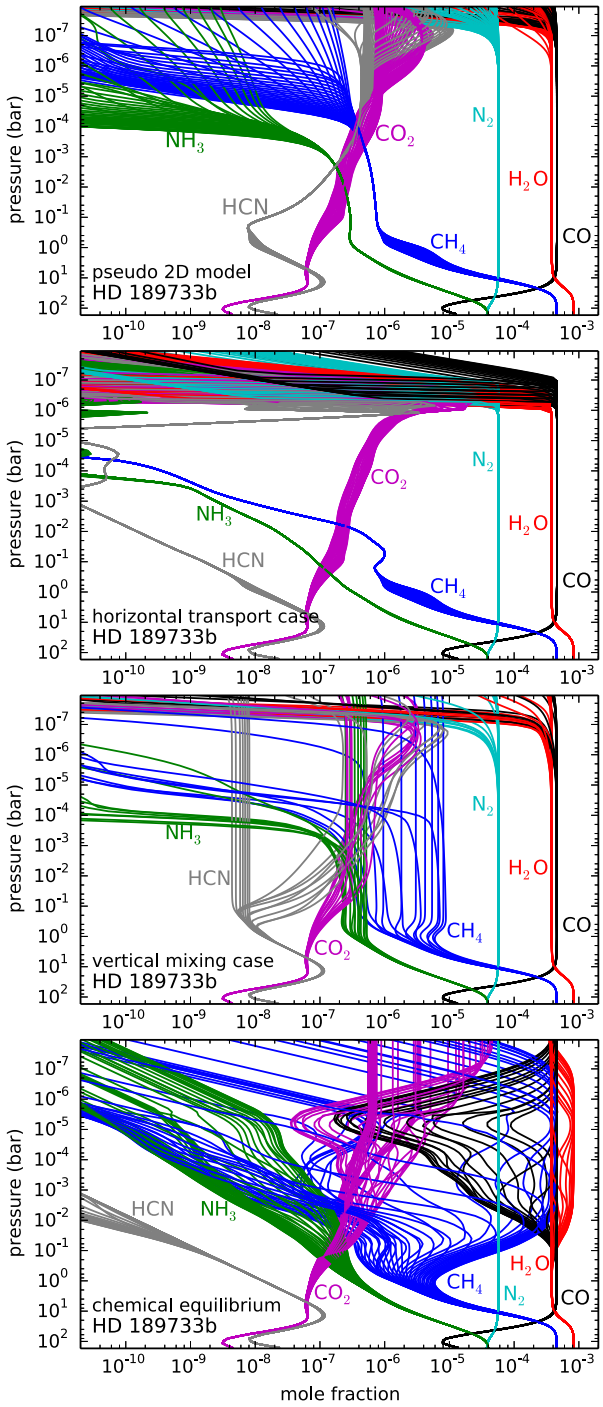

Fig. 14. Same as Fig. 13, but for HD 189733b.

one-dimensional vertical models (Moses et al. 2011; Venot et al. 2012). There are two main differences between our model and these previous ones. The first is related to the eddy diffusion coefficients adopted, which are noticeably lower in this study because they are calculated by following the behavior of passive tracers in GCM simulations, while those used previously were also estimated from GCM simulations but as the root mean square of the vertical velocity times the vertical scale height. The second is related to the very nature of the model, which in our case is a pseudo two-dimensional model that simultaneously takes into account horizontal transport and vertical mixing, while in these previous studies horizontal transport is neglected. To isolate the differences caused by each of these factors we compare in Figs. 15 and 16 the vertical abundance

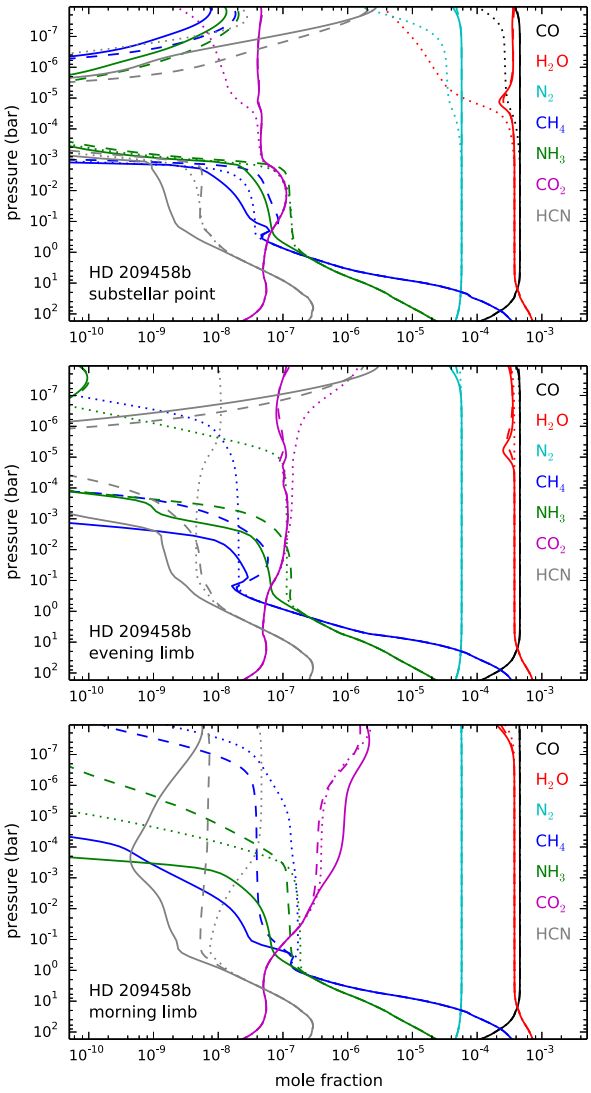

Fig. 15. Effect of eddy coefficient profile and 1D/2D character of the model on the vertical abundance profiles of some of the most abundant molecules in HD 209458b. We show abundances at the substellar point and at the evening and morning limbs, as given by the pseudo 2D model using the nominal eddy coefficient profile (solid lines), by the pseudo 2D model using the Moses et al. 2011's eddy profile (dashed lines), and by a one-dimensional vertical model using the Moses et al. 2011's eddy profile (dotted lines).

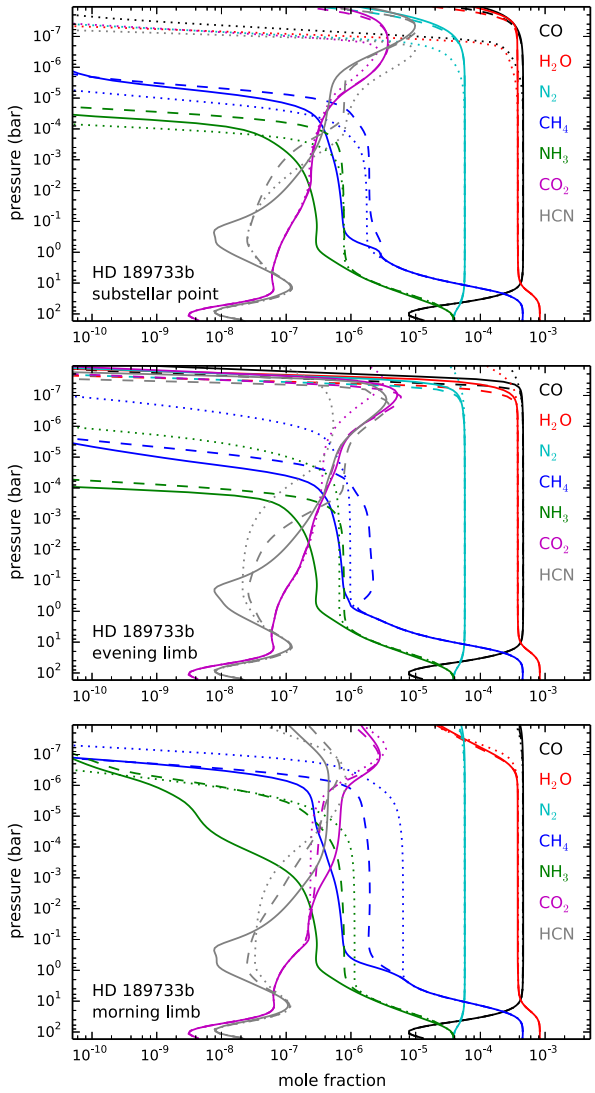

Fig. 16. Same as Fig. 15, but for HD 189733b.

distributions of some of the most abundant molecules at the substellar point and at the two limbs, as calculated with our pseudo two-dimensional model using the nominal vertical profile of the eddy diffusion coefficient (see Sect. 2.2.3), as given by the same pseudo two-dimensional model but using the high eddy diffusion coefficient profiles derived by Moses et al. (2011), which are about 10–100 times higher than ours for HD 209458b and about 10–1000 times higher than ours for HD 189733b, and as computed with a one-dimensional vertical model using the high eddy diffusivity values of Moses et al. (2011).

The main effect of increasing the strength of vertical mixing in the frame of a pseudo two-dimensional model is that the quench region shifts down to lower altitudes. For molecules such as CH_4, NH_3, and HCN, this implies that their vertically quenched abundances increase (compare solid and dashed lines in Figs. 15 and 16). If horizontal transport is completely supressed, that is, moving from a pseudo two-dimensional model to a one-dimensional vertical model (from dashed to dotted lines in Figs. 15 and 16), the horizontal homogenization of abundances is completely lost and thus the abundances of species such as CH_4 experience more important variations with longitude. Another interesting consequence of suppressing horizontal transport concerns water vapor, carbon monoxide, and molecular nitrogen, whose abundances decrease in the upper layers of the dayside regions (see upper panel in Figs. 15 and 16). In HD 209458b the depletion of these molecules is caused by the hot stratosphere, where neutral O and C atoms are favored over molecules, while in HD 189733b it is caused by photodissociation by UV photons. This loss of H_2O, CO, and N_2 molecules in the upper dayside layers is shifted to higher altitudes when horizontal transport, which brings molecules from other longitudes, is taken into account.

The vertical abundance profiles calculated with the one-dimensional vertical model at the substellar point and at the two

limbs (dotted lines in Figs. 15 and 16) can be compared with the one-dimensional results of Moses et al. (2011) using averaged thermal profiles for the dayside and terminator regions (see also Venot et al. 2012). There is a good overall agreement between our substellar point results and their dayside results, on the one hand and on the other, between our results at the two limbs and their results at the terminator region, except for CH_4, NH_3, and HCN, for which we find vertically quenched abundances lower by about one order of magnitude. Although there are some differences in the adopted elemental abundances, stellar UV spectra, and zenith angles, the main source of the discrepancies is attributed to the different temperature profiles adopted. On the one hand there are slight differences between the GCM results of Showman et al. (2009), adopted by Moses et al. (2011) and Venot et al. (2012), and those of Parmentier et al. (2013, and in prep.), which are adopted here. On the other, and more importantly, the temperature profiles have a different nature. They are averages over the dayside and terminator regions in their case, while in ours they correspond to specific longitudes. The dayside average temperature profile of Moses et al. (2011) is cooler than our substellar temperature profile by about 100 K around the 1 bar pressure level in both planets, which results in vertically quenched abundances of CH_4 and NH_3 higher than ours by about one order of magnitude (part of the abundance differences are also due to the different chemical network adopted; see Fig. 7 of Venot et al. 2012). This serves to illustrate how relatively small changes of temperature in the 0.1−10 bar pressure regime – the quench region for most molecules – may induce important variations in the vertically quenched abundance of certain molecules. This also raises the question of whether it is convenient to use a temperature profile averaged over the dayside in one-dimensional chemical models that aim at obtaining a vertical distribution of molecules representative of the dayside. Although it may be a reasonable choice if one is limited by the one-dimensional character of the model, averaging the temperature over the whole dayside masks the temperatures of the hottest regions, near the substellar point, which are in fact the most important as they control much of the chemical composition at other longitudes if horizontal transport becomes important.

In summary, the main implications of using a pseudo two-dimensional approach and of the downward revision of the eddy values in the atmospheres of HD 209458b and HD 189733b are that, on the one hand, the longitudinal variability of the chemical composition is greatly reduced compared with the expectations of pure chemical equilibrium or one-dimensional vertical models and, on the other hand, the mixing ratios of CH_4, NH_3, and HCN are significantly reduced compared with results of previous one-dimensional models (by one order of magnitude or more with respect to the results of Moses et al. 2011), down to levels at which their influence on the planetary spectra are probably minor.

4. Calculated vs. observed molecular abundances

We now proceed to a discussion in which we compare the molecular abundances calculated with the pseudo two-dimensional chemical model and those derived from observations. Our main aim here is to evaluate whether or not the calculated composition, which is based on plausible physical and chemical grounds, is compatible with the mixing ratios derived by retrieval methods used to interpret the observations. The molecules H_2O, CO, CO_2, and CH_4 have all been claimed to be detected in the atmospheres of HD 209458b and HD 189733b either in the terminator region of the planet from primary transit observations, in the dayside from secondary eclipse observations, or in both regions using the two methods. Although we are not in a position to cast doubt on any of these detections, given the controversial results often found by different authors in the interpretation of spectra of exoplanets it is advisable to be cautious when using the derived mixing ratios to argue in any direction. Having this in mind, hereafter we use the term detection instead of claim of detection.

Water vapor and carbon monoxide are calculated with nearly their maximum possible abundances in both planets and show a rather homogeneous distribution as a function of both altitude and longitude (see Figs. 7 and 8). Adopting a solar elemental composition, as done here, the calculated mixing ratios of both H_2O and CO are around 5×10^{-4}. Water vapor being the species that provides most of the atmospheric opacity at infrared wavelengths, it was the first molecule to be detected in the atmosphere of an extrasolar planet, concretely in the transmission spectrum of HD 189733b (Tinetti et al. 2007), and H_2O mixing ratios derived from observations for both HD 189733b and HD 209458b are usually in the range of the calculated value of 5×10^{-4} (Tinetti et al. 2007; Grillmair et al. 2008; Swain et al. 2008, 2009a,b; Madhusudhan & Seager 2009; Beaulieu et al. 2010; Lee et al. 2012; Line et al. 2013; Deming et al. 2013). Carbon monoxide, although less evident than water vapor, has also been detected in both planets and the mixing ratios derived are in the range of the values inferred for H_2O and expected from the chemical model (Swain et al. 2009a; Désert et al. 2009; Madhusudhan & Seager 2009; Lee et al. 2012; Line et al. 2013).

The calculated mixing ratio of carbon dioxide in the two hot Jupiters is in the range 10^{-7}–10^{-6} depending on the pressure level, with a more important longitudinal variation in the atmosphere of HD 209458b than in that of HD 189733b (see Figs. 7 and 8). This molecule has been also detected through secondary-eclipse observations in the dayside of HD 189733b, with mixing ratios spanning a wide range from 10^{-7} up to more than 10^{-3} (Swain et al. 2009a; Madhusudhan & Seager 2009; Lee et al. 2012; Line et al. 2013), and in the dayside of HD 209458b, with a mixing ratio in the range 10^{-6}–10^{-5} (Swain et al. 2009b). Taking into account the uncertainties associated with the values retrieved from observations, the agreement with the calculated abundance is reasonably good for CO_2.

The most important discrepancies between calculated and observed abundances are probably found for methane. This molecule is predicted to be very abundant in the cooler nightside regions of both planets, especially in HD 189733b, according to chemical equilibrium (see lower panels in Figs. 13 and 14), but reaches quite low abundances everywhere in the atmosphere according to the pseudo two-dimensional non-equilibrium model (see upper panels in Figs. 13 and 14). In both hot Jupiters, the calculated mixing ratio of CH_4 is in fact significantly lower than the predictions of previous one-dimensional models (Moses et al. 2011; Venot et al. 2012), a finding that strengthens the conflict with observations. We find that the mixing ratio of CH_4 above the 1 bar pressure level is below 10^{-7} in HD 209458b and below 10^{-6} in HD 189733b, whatever the side of the planet.

In HD 209458b, secondary-eclipse observations have been interpreted as evidence of methane being present in the dayside with a mixing ratio between 2×10^{-5} and 2×10^{-4} (Swain et al. 2009b), or within the less constraining range 4×10^{-8}–3×10^{-2} (Madhusudhan & Seager 2009). In fact, the abundance of CH_4 retrieved in these studies is similar or even higher than that retrieved for H_2O, which is clearly not the case according to our predictions. It seems difficult to reconcile the low abundance of CH_4 calculated by the pseudo two-dimensional chemical model

with the high methane content inferred from observations, which points to some fundamental problem in either of the two sides. As concerns the chemical model, an enhancement of the vertical transport to the levels adopted by Moses et al. (2011) or the supression of horizontal transport would increase the abundance of CH_4 only slightly (see Fig. 15). Photochemistry, which might potentially enhance the abundance of CH_4, is largely supressed by the stratosphere in the dayside atmosphere of HD 209458b. An elemental composition of the planetary atmosphere far from the solar one with, for example, an elemental C/O abundance ratio higher than 1, or some unidentified disequilibrium process, which might be related to, for instance, clouds or hazes, might lead to a high methane content in the warm atmospheric layers of HD 209458b's dayside. Some problems on the observational side cannot be ruled out, taking into account the difficulties associated to the acquisition of photometric fluxes of exoplanets and the possibility of incomplete spectroscopic line lists of some molecules relevant to the interpretation of spectra of exoplanets (see e.g. the recently published line list for hot methane by Hargreaves et al. 2012).

In HD 189733b, contradictory results exist on the detection of methane in both the terminator and dayside regions. Swain et al. (2008) reported the detection of CH_4 through primary-transit observations, with a derived mixing ratio of about 5×10^{-5}, although Sing et al. (2009) did not find evidence of its presence in the transmission spectrum. These contradictory results obtained using NICMOS data could point to non-negligible systematics in the data (e.g., Gibson et al. 2012). Controversial results also exist on the detection of CH_4 in the dayside emission spectrum of HD 189733b (Swain et al. 2009a, 2010; Madhusudhan & Seager 2009; Waldmann et al. 2012; Lee et al. 2012; Line et al. 2013; Birkby et al. 2013). Until observations can draw more reliable conclusions it is difficult to decide whether or not observations and models are in conflict regarding the abundance of CH_4 in HD 189733b.

5. Variations in the planetary spectra

The calculated distribution of molecules in the atmospheres of HD 209458b and HD 189733b may be probed by observations. Instead of comparing synthetic spectra and available observations of these two planets, we are here mainly interested in evaluating whether the longitudinal variability of the chemical composition may be probed by observations. For example, the monitoring of the emission spectrum of the planet at different phases during an orbital period would probe the composition in the different sides of the planet. In addition, the observation of the transmission spectrum at the ingress and egress during primary transit conditions would allow one to probe possible chemical differentiation between the morning and evening limbs of the planet's terminator. Planetary emission and transmission spectra were computed using the line-by-line radiative transfer code described in Appendix A. Since the code is currently limited because it is one-dimensional in the vertical direction, we adopted mean vertical profiles by averaging the temperature structure in longitude and latitude given by the GCM simulations of Parmentier et al. (2013, and in prep.) and the longitudinal distribution of abundances obtained with the pseudo two-dimensional chemical model. In the case of emission spectra, we adopted a weighted average profile of temperature and of mixing ratios over the hemisphere facing the observer (weighted by the projected area on the planetary disk to better represent the situation encountered by an observer), where mixing ratios were assumed to be uniform with latitude. In transmission spectra, vertical profiles are simply obtained by averaging over the whole terminator, or over the morning or evening limb. After adopting an average pressure-temperature profile, the planetary radius (see values in Sect. 2) is assigned to the 1 bar pressure level and the altitude of each layer in the atmosphere is computed according to hydrostatic equilibrium. We note that similarly to the case of one-dimensional chemical models, the use of average vertical profiles in calculating planetary spectra is an approximation that masks the longitudinal and latitudinal structure of temperature and chemical composition and may result in non-negligible inaccuracies in the appearance of the spectra, which we plan to investigate in the future.

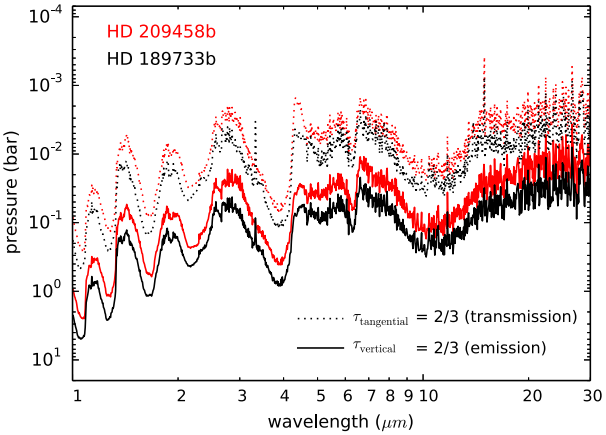

Fig. 17. Pressure level probed by transmission and emission spectra as a function of wavelength for HD 209458b and HD 189733b. Dashed lines correspond to a model with a mean vertical profile averaged over the terminator and show the pressure level at which the tangential optical depth equals 2/3, which is in fact a transmission spectrum expressed in terms of atmospheric pressure instead of planetary radius. Solid lines correspond to a model with a mean vertical profile averaged over the dayside and indicate the pressure level at which the optical depth in the vertical outward direction equals 2/3, which is an approximate location of the region from where most of the planetary emission arises, the regions below being opaque and those above being translucent.

Is is useful to begin our discussion on planetary spectra with a pedagogical plot that shows the pressure level probed by transmission and emission spectra for HD 209458b and HD 189733b (see Fig. 17). We first note that transmission and emission spectra probe different pressure levels, with transmission spectra being sensitive to upper atmospheric layers than emission spectra. At infrared wavelengths (1–30 μm), and for the thermal and chemical composition profiles adopted by us for these two hot Jupiters, emission spectra probe pressures between 10 and 10^{-2} bar, while transmission spectra probes the 1–10^{-3} bar pressure regime. A second aspect worth noting is that there are strong variations with wavelength in both types of spectra, which implies that observations at different wavelengths are sensitive to the physical and chemical conditions of different pressure levels. It is always useful to keep these ideas in mind when analyzing the vertical distribution of molecules calculated with a chemical model, because only a very specific region of the atmosphere becomes relevant to planetary spectra.

5.1. Variation of emission spectra with phase

A modulation of the planetary emission with the orbital phase has been observed for HD 189733b by monitoring the photometric flux in the 8 μm band of *Spitzer* IRAC during

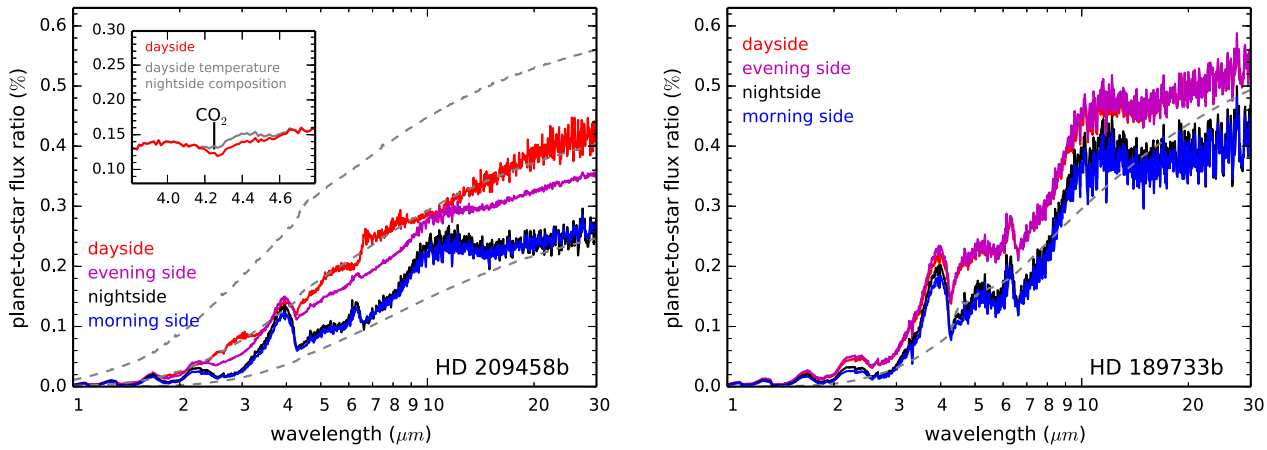

Fig. 18. Calculated emission spectra for HD 209458b (*left panel*) and HD 189733b (*right panel*) at 4 different phases in which the planet faces the observer the day and night sides, and the two sides in between, centered on the evening and morning limbs. Spectra have been smoothed to a resolving power $R = 300$. The adopted vertical profiles of temperature and mixing ratios are projected area-weighted averages over the corresponding emitting hemisphere, with the distribution of molecules given by our nominal pseudo two-dimensional chemical model. The planetary flux is shown relative to that of the star, for which the Kurucz synthetic spectrum and stellar radius given in Sect. 2 are adopted. Gray dashed lines correspond to planetary blackbody temperatures of 2000, 1500, and 1000 K (from top to bottom in HD 209458b's panel) and of 1000 K (in HD 189733b's panel). The *inset* in HD 209458b's panel compares the emission spectrum around 4.3 μm as calculated for the dayside and as computed using the mean dayside temperature profile and the mean chemical composition of the nightside. The two spectra are nearly identical except for a slight difference at 4.3 μm due to CO_2.

a good part of the orbit of the planet (Knutson et al. 2007). This has served to evidence the important temperature contrast between the different sides of the planet, noticeably between day and night, and indirectly the presence of strong winds that can redistribute the energy from the day to the night side, due to an observed shift between the hot spot and the substellar point. Various theoretical studies have also been interested in predicting the variation of the planetary flux with the orbital phase in HD 209458b and HD 189733b using the temperature structure calculated with GCM simulations (Fortney et al. 2006; Showman et al. 2008, 2009; Rauscher et al. 2008; Burrows et al. 2010; Rauscher & Menou 2013). Most previous studies have focused on the link between light curves and variations of temperature between the different planetary sides, and on the comparison between predicted and observed photometric fluxes. Here we are instead interested in discussing the influence of the temperature but also that of the chemical composition (assumed to be given by chemical equilibrium in previous studies) on the variation of the planetary emission with phase.

We show in Fig. 18 how the calculated emission spectra of HD 209458b and HD 189733b vary with the phase of the planet. Important variations with phase are apparent in HD 209458b, whose strong dayside stratosphere causes the dayside emission spectrum to be significantly brighter and to have a noticeably different spectral shape than at other phases. In HD 189733b, the modulation of the flux and the variation of the spectral shape with phase are also important although less pronounced. Emission spectra are controlled on the one hand, by the vertical temperature structure, and on the other, by the abundances of the main atmospheric constituents providing opacity. The sensitivity of emission spectra to the thermal structure is illustrated in HD 209458b, whose dayside (facing a temperature inversion to the observer) shows some spectral features that appear in emission and not in absorption, as occurs for the other planetary sides of HD 209458b and for HD 189733b. These differences in the spectra can be used to infer whether there is a stratosphere in the atmosphere of a hot Jupiter from observations of its dayside emission spectrum (Knutson et al. 2008, 2009b; Burrows et al. 2008; Machalek et al. 2008, 2010; Todorov et al. 2010; Madhusudhan & Seager 2010). It is also interesting to note how similar the emission spectra of night and morning sides are in the two planets, as are the day and evening sides in the case of HD 189733b. This is a consequence of the eastward transport of energy by the superrotating jet, which shifts the hottest and coldest regions to the east of the substellar and antistellar points, respectively. In the calculated emission spectra of both HD 209458b and HD 189733b, most of the atmospheric opacity along the 1–30 μm wavelength range is provided by water vapor, with carbon monoxide contributing at 2.3 and 4.6 μm, CO_2 at 4.3 and 15 μm, and collision-induced absorption by H_2-H_2 in certain wavelength ranges below 4 μm. No other species leaves appreciable signatures in the calculated emission spectra of HD 209458b, although in that of HD 189733b CH_4 contributes around 3.3 and 7.7 μm, NH_3 around 10.6 μm, and HCN at 14 μm.

An interesting question that arises from the change in the emission spectrum with phase is whether it is entirely caused by the variation of temperature in the different sides of the planet or whether the longitudinal variation of the chemical composition contributes to an important extent. To illustrate this point we compare in the inset of HD 209458b's panel in Fig. 18 the dayside emission spectrum with a synthetic spectrum calculated using the mean vertical temperature structure of the dayside and the mean chemical composition of the nightside. The two spectra are nearly identical except for a slight difference around 4.3 μm, a spectral region where atmospheric opacity is to a large extent dominated by CO_2. Similar models in which the temperature structure and the chemical composition are adopted from different planetary sides indicate that variations of HD 209458b's emission spectrum with phase are almost entirely caused by changes of temperature, with the only effect that can be purely adscribed to variations in the chemical composition being restricted to the tiny variation (less than 0.02% in the planet-to-star flux ratio) at 4.3 μm, which is caused by

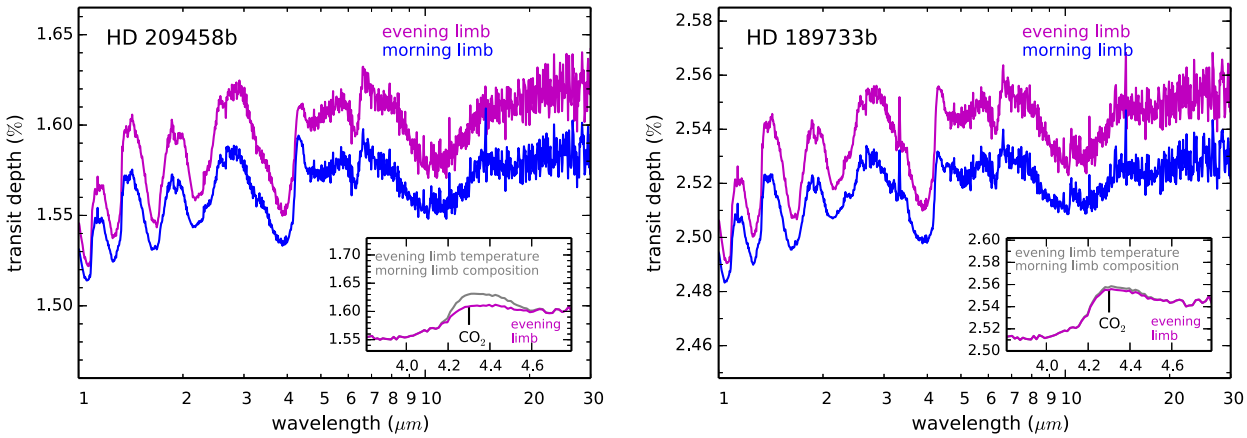

Fig. 19. Calculated transmission spectra for the evening and morning limbs of HD 209458b (*left panel*) and HD 189733b (*right panel*), where the vertical structure is obtained by averaging the temperature over each limb and adopting the abundance profiles at each limb from the nominal pseudo two-dimensional chemical model. Spectra have been smoothed to a resolving power $R = 300$. The transit depth is simply calculated as $(R_p(\lambda)/R_*)^2$, where $R_p(\lambda)$ is the calculated radius of the planet as a function of wavelength and R_* is the stellar radius (see values in Sect. 2). The absolute scale of the transmission spectrum is set by our choice of assigning the value of the planetary radius given in Sect. 2 to the 1 bar pressure level. Since no attempt has been made to reproduce the absolute scale indicated by primary transit observations, calculated transit depths are somewhat higher than given by observations. The insets in both panels compare the transmission spectrum around 4.3 μm as calculated for the evening limb and as computed using the mean temperature profile of the evening limb and the chemical composition corresponding to the morning limb. The most important differences between both spectra occur around 4.3 and 15 μm, due to CO_2.

the longitudinal variation of about one order of magnitude in the abundance of CO_2 (see Fig. 7). The reasons of the small impact of the chemical composition on the variation of emission spectra with phase are related to the important longitudinal homogenization of the abundances driven by the zonal wind in HD 209458b (see Fig. 7). In fact, most of the atmospheric opacity affecting the emission spectrum comes from H_2O, CO, and CO_2, in order of decreasing importance, and the two former molecules show remarkably uniform abundances with longitude, while only the abundance of the latter molecule experiences some longitudinal variation, leading to a slight variation of the planetary flux with phase around 4.3 μm. In HD 189733b, the homogenization of the chemical composition with longitude is even more marked than in HD 209458b because of the lack of a stratosphere and the rather low eddy coefficient values (compare Figs. 7 and 8). Because the abundances of H_2O, CO, CO_2, CH_4, NH_3, and HCN (the main molecules providing opacity, in order of decreasing importance) vary little between the different sides of HD 189733b at the pressures probed by emission spectra ($>10^{-2}$ bar), the impact of the chemical composition on the change of the emission spectrum with phase becomes almost negligible, even around 4.3 μm because of the reduced longitudinal variation of the abundance of CO_2.

5.2. Transmission spectra of evening and morning limbs

Variations in the composition of the atmosphere between the different sides of the planet may also be probed by transmission spectroscopy. Indeed, it is a priori possible to probe differences in the thermal and chemical structure of the two limbs if observations are able to obtain the transmission spectrum during the first half of the primary transit ingress, which would probe the leading or morning limb, and during the second half of the transit egress, which would probe the trailing or evening limb. Although a non-zero impact parameter during the transit would complicate the situation somewhat and such observations are very challenging today, they may be feasible in the near future. The subject has been addressed theoretically for hot Jupiters such as HD 189733b and HD 209458b in some studies in which the differences between the transmission spectra of leading and trailing limbs are evaluated under different assumptions for the chemical composition of each of the two limbs, either chemical equilibrium or some disequilibrium estimation (Fortney et al. 2010; Burrows et al. 2010). Here we revisit the subject in the light of the molecular abundances calculated in this study with the pseudo two-dimensional chemical model.

To illustrate the possibility that transmission spectroscopy might be able to distinguish between the two limbs of HD 209458b and HD 189733b we show in Fig. 19 the transmission spectrum calculated by adopting the chemical composition and mean temperature of the evening and morning limbs of these two exoplanets. Since we are mainly interested in comparing the spectra at the two limbs and not in comparing with observations, we set the absolute scale of transmission spectra by simply assigning the value of the planetary radius given in Sect. 2 to the 1 bar pressure level and made no attempt to reproduce the absolute scale of the photometric transit depths derived from observations. In HD 209458b and HD 189733b, the transmission spectrum of the evening limb shows a higher degree of absorption and also the variations of the transit depth with wavelength have a larger amplitude than at the morning limb, whose transmission spectrum is flatter. These differences are mainly due to the different temperature profile of the two limbs. Because the atmosphere at the morning limb is cooler and thus has a smaller scale height than at the evening limb, it becomes more compact, resulting in smaller apparent radii at all wavelengths and a flatter transmission spectrum. In addition to this dependence of the transmission spectrum on temperature, which causes it to shift up or down and to have a more elongated or flattened overall shape, the spectral structure is controlled by the relative abundances of the main species that provide opacity in the atmosphere. Figure 20 shows the relative contributions of the different sources of opacity taken into account in calculating the transmission spectra. Similarly to the emission spectra, in the calculated transmission spectra of

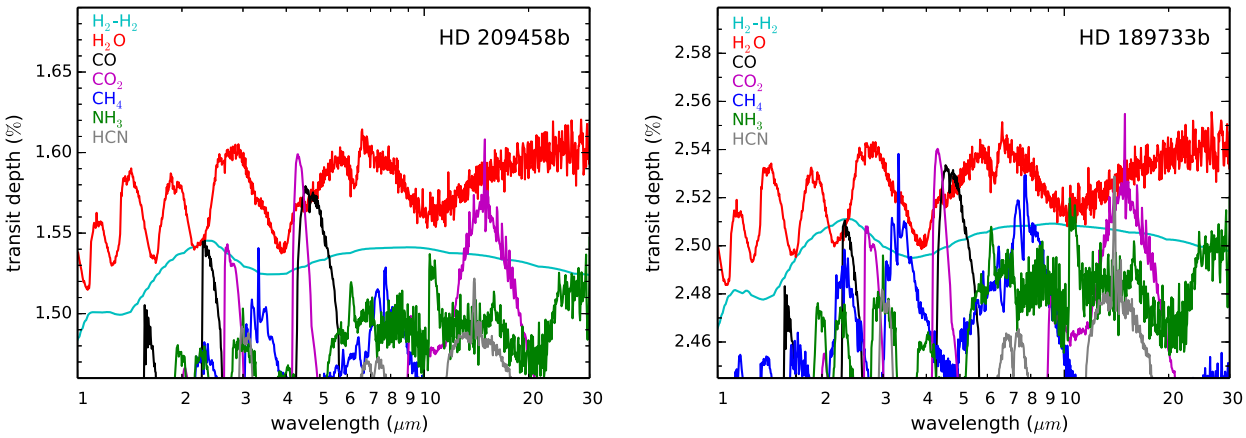

Fig. 20. Contributions of the different sources of opacity to the transmission spectra of HD 209458b (*left panel*) and HD 189733b (*right panel*) smoothed to a resolving power $R = 300$. The H_2-He continuum, whose contribution is similar in shape to the H_2-H_2 continuum but lower because of the lower abundance of He with respect to H_2, is not shown. The spectra have been calculated using the temperature from GCM simulations and the chemical composition from the nominal pseudo two-dimensional chemical model averaged over the whole terminator. Each line represents the transmission spectrum that results from a model in which only the opacity provided by each source is taken into account.

HD 209458b and HD 189733b most of the atmospheric opacity at infrared wavelengths is provided by H_2O, with CO being important at 2.3 and 4.6 μm, CO_2 at 4.3 and 15 μm, the H_2-H_2 continuum at certain wavelengths below 3 μm, and, in the case of HD 189733b, CH_4 having some contribution around 3.3 and 7.7 μm, NH_3 around 10.6 μm, and HCN at 14 μm.

Similarly to emission spectra, we evaluated to which extent differences in the chemical composition of evening and morning limbs contribute to the change of the transmission spectrum from one limb to the other. To this purpose, we computed transmission spectra in which we switched the temperature and chemical profiles between the two different limbs. As an example we compare in the insets of left and right panels in Fig. 19 the transmission spectrum of the evening limb with a synthetic spectrum calculated using the temperature structure of the evening limb and the chemical composition of the morning limb. In HD 209458b the two spectra are very similar, except for a different degree of absorption around 4.3 and 15 μm, which is due to the difference of nearly one order of magnitude in the abundance of CO_2 between the two limbs (see Fig. 11). Similarly to emission spectra, the longitudinal homogenization driven by horizontal transport is at the origin of the weak impact of other molecules on the variation of transmission spectra between both limbs. Because the abundances of CO and H_2O are very similar in both limbs, and other molecules such as CH_4, NH_3, and HCN contribute little to the atmospheric opacity at infrared wavelengths because of their rather low abundances, the only chemical effect contributing to the change of the transmission spectrum from one limb to the other of HD 209458b is restricted to carbon dioxide. In HD 189733b, the even stronger longitudinal homogenization of abundances (compare Figs. 7 and 8) diminishes the extent of chemical effects, which are now restricted to a very weak change of the absorption around 4.3 and 15 μm (see inset in HD 189733b's panel of Fig. 19), again due to a slight increase in the abundance of CO_2 when moving from the evening limb to the morning one (see Fig. 12).

6. Summary

We have developed a pseudo two-dimensional model of a planetary atmosphere that takes into account thermochemical kinetics, photochemistry, vertical mixing, and horizontal transport, and allows one to calculate the distribution with altitude and longitude of the main atmospheric constituents. Horizontal transport was modeled through a uniform zonal wind and thus the model is best suited for studying the atmosphere of planets whose circulation dynamics is dominated by an equatorial superrotating jet, as is expected to be the case of hot Jupiters. We therefore applied the model to study the atmospheres of the well-known exoplanets HD 209458b and HD 189733b. We used the temperature structure from GCM simulations and parameterized the turbulent mixing in the vertical direction using an eddy coefficient profile, which was calculated by following the behavior of passive tracers in GCM simulations, a method that results in substantially lower eddy values, by a factor of 10–100 in HD 209458b and of 10–1000 in HD 189733b, than previous estimates based on cruder methods.

Molecular abundances homogenized with longitude to values typical of the hottest dayside regions. – We found that the distribution of molecules in the atmospheres of HD 209458b and HD 189733b is quite complex because of the interplay of the various (photo)chemical and dynamical processes at work, which form, destroy, and transport molecules throughout the atmosphere. Much of the distribution of the atmospheric constituents is driven by the strong zonal wind, which reaches speeds of a few km s^{-1}, and the limited extent of vertical transport, with relatively low eddy diffusion coefficients below 10^9 cm^2 s^{-1} around the 1 bar pressure level, resulting in an important homogenization of molecular abundances with longitude, in particular in the atmosphere of HD 189733b, which lacks a stratosphere and has quite low eddy diffusion coefficients. Moreover, molecular abundances are quenched horizontally to values typical of the hottest dayside regions, and therefore the composition of the cooler nightside regions is highly contaminated by that of warmer dayside regions. In hot Jupiters with a temperature inversion, such as HD 209458b, the longitudinal homogenization of molecular abundances is not as marked as in planets lacking a stratosphere, such as HD 189733b. In general, the cooler the planet, the stronger the homogenization of the chemical composition with longitude. Furthermore, in cooler planets such as hot Neptunes orbiting M dwarfs (e.g., GJ 436b) the temperature contrast between day and nightsides decreases because the cooling rate scales with the cube of temperature (e.g.,

Lewis et al. 2010), and therefore the composition is expected to be even more homogeneous with longitude than in warmer planets such as HD 209458b and HD 189733b. However, unlike hot Jupiters, hot Neptunes may have an atmospheric metallicity much higher than solar (Line et al. 2011; Moses et al. 2013; Agúndez et al. 2014; Venot et al. 2014), which makes it interesting to investigate the extent of the spatial variation of molecular abundances in their atmospheres.

Low methane content. – A major consequence of our pseudo two-dimensional chemical model is that methane reaches quite low abundances in the atmospheres of HD 209458b and HD 189733b, lower than the values calculated by previous one-dimensional models. The main reason for the low CH_4 abundance is that most of the atmosphere is contaminated by the hottest dayside regions, where the chemical equilibrium abundance of CH_4 is the lowest. The calculated mixing ratio of CH_4 in the dayside of HD 209458b is significantly below the values inferred from observations, which points to some fundamental problem in either the chemical model or the observational side. If the strength of vertical transport is substantially higher than in our nominal model, the calculated abundance of some molecules such as CH_4 and NH_3 would experience significant enhancement, especially in HD 189733b, although a conflict with observations would still exist regarding CH_4 in the dayside of HD 209458b.

Variability of planetary spectra driven by thermal, rather than chemical, gradients. – An important consequence of the strong longitudinal homogenization of molecular abundances in the atmospheres of HD 209458b and HD 189733b is that the variability of the chemical composition has little effect on the way the emission spectrum is modified with phase and on the changes of the transmission spectrum from the transit ingress to the egress. Temperature variations and not chemical gradients are therefore at the origin of these types of variations in the planetary spectra. Only the longitudinal variation of the abundance of CO_2, of nearly one order of magnitude, in the atmosphere of HD 209458b, is predicted to induce variations in the planetary spectra around 4.3 and 15 μm. We note, however, that an inhomogenous distribution of clouds and/or hazes (none of them included in our model) may induce important variations in the emission spectra with phase and in the transmission spectra from one limb to the other. These variations are best characterized at short wavelengths. Indeed, there is evidence of the presence of hazes in the atmosphere of HD 189733b (Lecavelier des Etangs et al. 2008; Sing et al. 2009), and an inhomogeneous distribution of clouds has recently been inferred for the hot Jupiter Kepler 7b (Demory et al. 2013).

The main drawback of our pseudo two-dimensional chemical model is the oversimplification of atmospheric dynamics, which is probably adequate for equatorial regions, but not at high latitudes. Ideally, GCM simulations coupled to a robust chemical network would provide an even more realistic view of the distribution of molecules in the atmospheres of HD 209458b and HD 189733b, but such calculations are very challenging from a computational point of view. Telescope facilities planned for the near or more distant future, such as the *James Webb* Space Telescope, Spica, and EChO, will be able to test some of the predictions of our pseudo two-dimensional model, in particular the low abundance of methane in the two planets and the important longitudinal homogenization of the chemical composition.

Acknowledgements. We thank our anonymous referee for insightful comments which helped to improve this article. We acknowledge Adam P. Showman and Jonathan J. Fortney for the use of the SPARC/MITgcm code, Vincent Hue for useful discussions on photochemical models, Sergio Blanco-Cuaresma and Christophe Cossou for their help with Python and Fortran, and Vincent Eymet and Philip von Paris for kindly helping to validate the line–by–line radiative transfer code. M.A. and F.S. acknowledge support from the European Research Council (ERC Grant 209622: E_3ARTHs). O.V. acknowledges support from the KU Leuven IDO project IDO/10/2013 and from the FWO Postdoctoral Fellowship Program. Computer time for this study was provided by the computing facilities MCIA (Mésocentre de Calcul Intensif Aquitain) of the Université de Bordeaux and of the Université de Pau et des Pays de l'Adour.

Appendix A: Calculation of planetary spectra

To investigate the influence of the physical and chemical structure of the atmospheres of HD 209458b and HD 189733b on their transmission and emission spectra, we developed a line-by-line radiative transfer code that is independent of the pseudo two-dimensional chemical code. Currently, the code is limited because it is one-dimensional in the sense that the atmosphere is divided into various layers in the vertical direction (typically 60 spanning the 10–10^{-6} bar pressure range) and each layer is assumed to be homogeneous with longitude and latitude. Therefore, each layer is characterized by a given pressure, temperature, and chemical composition, and longitudinal and latitudinal gradients are neglected. For transmission spectra, the physical and chemical profile in the vertical direction at either the east or west limb, or a mean of the profiles at both limbs, can be used. For emission spectra, the limitations caused by the one-dimensional character of the code can be partially alleviated by adopting thermal and chemical vertical profiles averaged in some manner over the hemisphere facing the observer.

It is common in infrared spectroscopy to use the wavenumber with units of cm^{-1}, instead of frequency or wavelength, and we therefore adopt this choice hereafter as well. At this stage, there are various sources of opacity included in the code. On the one hand, we consider collision induced absorption (CIA) by H_2-H_2, for which available absorption coefficients cover the wavelength range 10–25 000 cm^{-1} and temperatures between 60 and 7000 K (Borysow et al. 2001; Borysow 2002), and by H_2-He, in which case absorption coefficients in the wavelength range 10–25 000 cm^{-1} and for temperatures in the range 100–7000 K are available (Borysow et al. 1989, 1997; Borysow & Frommhold 1989). CIA absorption coefficients scale with the square of pressure and thus become the dominant source of opacity at high pressures, usually above 1 bar. On the other hand, we consider spectroscopic transitions (mostly ro-vibrational transitions lying at infrared wavelengths) of H_2O, CO, and CO_2, whose data are taken from HITEMP (Rothman et al. 2010), and of CH_4, NH_3, and HCN, for which data from HITRAN (Rothman et al. 2009) are adopted.

The spectral region of interest is divided into a certain number of spectral bins, whose widths are determined by the spectral resolution imposed. In each layer of the atmosphere, the contribution of a spectroscopic transition j (centered on a wavenumber $\tilde{\nu}_j$ and which belongs to a species i) to the absorption coefficient $k(\tilde{\nu}_l)$ in a spectral bin l (centered on a wavenumber $\tilde{\nu}_l$ and having a width $\Delta\tilde{\nu}_l$), which we may label as $k^S_{ij}(\tilde{\nu}_l)$, can be expressed as

$$k^S_{ij}(\tilde{\nu}_l) = S_j(T) n_i \int_{\tilde{\nu}_l - \Delta\tilde{\nu}_l/2}^{\tilde{\nu}_l + \Delta\tilde{\nu}_l/2} \phi_j(\tilde{\nu}' - \tilde{\nu}_j) \mathrm{d}\tilde{\nu}' \frac{1}{\Delta\tilde{\nu}_l}, \quad \text{(A.1)}$$

where $S_j(T)$ is the line intensity of the spectroscopic transition j, which depends on the temperature T and is usually given with units of cm^{-1}/(molecule cm^{-2}) in the HITRAN and HITEMP databases, n_i is the number density of species i in the atmospheric layer where the absorption coefficient is to be evaluated,

and ϕ_j is the line profile function of transition j, which has units of inverse of wavenumber (i.e., cm) and must be normalized such that the integral of $\phi_j(\tilde{\nu}' - \tilde{\nu}_j)$ from $\tilde{\nu}' - \tilde{\nu}_j = -\infty$ to $\tilde{\nu}' - \tilde{\nu}_j = +\infty$ yields unity. The absorption coefficient $k(\tilde{\nu}_l)$ has units of cm^{-1}. The integral in Eq. (A.1) extends between the lower and upper wavenumber edges of the spectral bin l. The line profile function $\phi_j(\tilde{\nu}' - \tilde{\nu}_j)$ is taken as a Voigt profile, which results from the convolution of a Gaussian and a Lorentzian profile, and thus accounts for the Doppler and pressure broadening of spectral lines in each layer of the atmosphere due to thermal motions and collisions, respectively. The Voigt profile function is calculated numerically with a routine based on an implementation of Humlicek's algorithm by Kuntz (1997).

Ideally, extremely high spectral resolution would be desirable to properly resolve the narrowest line profiles, although in practice this is too expensive in terms of computing time. For the calculations carried out here we adopted a spectral resolution of 0.03 cm^{-1}, which is on the order of the line widths in the layers that provide most atmospheric opacity and has been found to be high enough to yield relative errors below 1% in the computed spectra. Spectroscopic transitions lying farther away than 50 cm^{-1} of a given spectral bin l have not been taken into account when computing the absorption coefficient $k(\tilde{\nu}_l)$. In addition, a cutoff in the line intensity S_j(296 K) of 10^{-40} cm^{-1}/(molecule cm^{-2}) was adopted to neglect weak lines and speed up the calculations. This is perhaps the most delicate aspect because weak lines are numerous, especially in the HITEMP line lists, and at high temperatures the sum of all them results in non-negligible opacity enhancements in certain spectral regions. Calculations carried out with different line intensity cutoffs in selected spectral regions indicate that the relative error in the calculated spectra is at most 10% in the hottest case studied here (the dayside emission spectrum of HD 209458b), and lower than 5% in the remaining computed spectra. Currently, the code does not take into account light scattering, which becomes important at wavelengths shorter than $\sim$1 μm, and therefore calculated spectra are reliable at infrared wavelengths, but not in the visible region of the electromagnetic spectrum. The code does not take into account the Doppler shift of spectral lines due to atmospheric winds either, an effect that may be observable in high-resolution spectra of hot Jupiters, where winds are strong (Snellen et al. 2010; Miller-Ricci Kempton & Rauscher 2012; Showman et al. 2013).

At each atmospheric layer, the absorption coefficient $k(\tilde{\nu}_l)$ in each wavenumber bin l is calculated as the sum of the contributions from all the spectroscopic transitions of the various absorbing species included, together with the contributions of the CIA couples, that is,

$$k(\tilde{\nu}_l) = \sum_i \sum_j k_{ij}^S(\tilde{\nu}_l) + \sum_m k_m^{CIA}(\tilde{\nu}_l), \tag{A.2}$$

where the sum in m extends to the H_2-H_2 and H_2-He couples.

After calculating the absorption coefficient in each wavenumber bin and at each atmospheric layer, computing the transmission and emission planetary spectra becomes straightforward, provided scattering is not considered. To calculate the transmission spectrum, the optical depth $\tau(\tilde{\nu}_l, b)$ along a tangential line of sight intersecting the planet's atmosphere is computed as a function of the impact parameter b in each spectral interval l as

$$\tau(\tilde{\nu}_l, b) = \sum_{h=1}^{N(b)} k_h(\tilde{\nu}_l) \Delta\ell_h(b), \tag{A.3}$$

where $\Delta\ell_h(b)$ is the path length (in cm) intersected by layer h along the tangential line of sight at impact parameter b, and the sum in h extends to all atmospheric layers $N(b)$ intersected by the tangential line of sight. The apparent radius of the planet in each wavenumber interval is then retrieved as the impact parameter for which the optical depth along the tangential line of sight becomes 2/3. This latter value is rather arbitrary and is mainly chosen for similarity with the definition of a stellar photosphere, although it is very close to the value of 0.56 inferred by Lecavelier des Etangs et al. (2008) and is not critical to derive the apparent radius of the planet. To obtain the emission spectrum, the emergent specific intensity along the observer's line of sight is computed as a function of impact parameter in each wavenumber bin. We thus need to solve the equation of radiative transfer along the various paths pointing toward the observer that pass through the planetary atmosphere at different impact parameters. As long as the different atmospheric layers are homogeneous, the equation of radiative transfer can be solved sequentially from the back to the front for each of the atmospheric layers intersected by the path. For each intersected layer, the equation of radiative transfer reads (see e.g. Rybicki & Lightman 2004)

$$I_{\tilde{\nu}} = \mathrm{e}^{-\tau_{\tilde{\nu}}}[I_{\tilde{\nu}}^0 + B_{\tilde{\nu}}(T)(\mathrm{e}^{\tau_{\tilde{\nu}}} - 1)], \tag{A.4}$$

where the subscript $\tilde{\nu}$ indicates wavenumber dependence, $I_{\tilde{\nu}}^0$ and $I_{\tilde{\nu}}$ are the incoming and outgoing specific intensities that enter and emerge, respectively, from the current layer along a given path, $\tau_{\tilde{\nu}}$ is the optical depth along the path within the current layer, and $B_{\tilde{\nu}}(T)$ is Planck's function. The final emission spectrum is then computed by averaging the wavenumber-dependent specific intensity, calculated as a function of the impact parameter, over the projected area of the emitting hemisphere.

The line-by-line radiative transfer code was checked against the suite of radiative transfer tools "kspectrum"[5], which has been widely used to model the atmosphere of solar system planets such as Venus (Eymet et al. 2009).

References

Agúndez, M., Venot, O., Iro, N., et al. 2012, A&A, 548, A73
Agúndez, M., Venot, O., Selsis, F., & Iro, N. 2014, ApJ, 781, 68
Asplund, M., Grevesse, N., Sauval, A. J., & Scott, P. 2009, ARA&A, 47, 481
Baraffe, I., Chabrier, G., & Barman, T. 2010, Rep. Prog. Phys., 73, 016901
Bauer, S. J. 1973, Physics of Planetary Ionospheres (Berlin: Springer-Verlag)
Beaulieu, J.-P., Kipping, D. M., Batista, V., et al. 2010, MNRAS, 409, 963
Birkby, J. L., de Kok, R. J., Brogi, M., et al. 2013, MNRAS, 436, 35
Borysow, A. 2002, A&A, 390, 779
Borysow, A., & Frommhold, L. 1989, ApJ, 341, 549
Borysow, A., Frommhold, L., & Moraldi, M. 1989, ApJ, 336, 495
Borysow, A., Jørgensen, U. G., & Zheng, C. 1997, A&A, 324, 185
Borysow, A., Jørgensen, U. G., & Fu, Y. 2001, J. Quant. Spectr. Rad. Transf., 68, 235
Burrows, A., & Orton, G. 2011, in Exoplanets, ed. S. Seager (Tucson, AZ: Univ. Arizona Press), 419
Burrows, A., Budaj, J., & Hubeny, I. 2008, ApJ, 678, 1436
Burrows, A., Rauscher, E., Spiegel, D. S., & Menou, K. 2010, ApJ, 719, 341
Charbonneau, D., Knutson, H. A., Barman, T., et al. 2008, ApJ, 686, 1341
Cho, J. Y.-K., Menou, K., Hansen, B. M. S., & Seager, S. 2008, ApJ, 675, 817
Cooper, C. S., & Showman, A. P. 2005, ApJ, 629, L45
Cooper, C. S., & Showman, A. P. 2006, ApJ, 649, 1048
Cowan, N. B., & Agol, E. 2008, ApJ, 678, L129
Cowan, N. B., & Agol, E. 2011, ApJ, 726, 82
Cowan, N. B., Agol, E., & Charbonneau, D. 2007, MNRAS, 379, 641
Crossfield, I. J. M., Hansen, B. M. S., Harrington, J., et al. 2010, ApJ, 723, 1436
de Kok, R. J., Brogi, M., Snellen, I. A. G., et al. 2013, A&A, 554, A82
de Wit, J., Gillon, M., Demory, B.-O., & Seager, S. 2012, A&A, 548, A128

[5] See http://code.google.com/p/kspectrum/

Deming, D., Seager, S., Richardson, L. J., & Harrington, J. 2005, Nature, 434, 740
Deming, D., Harrington, J., Seager, S., & Richardson, L. J. 2006, ApJ, 644, 560
Deming, D., Wilkins, A., McCullough, P., et al. 2013, ApJ, 774, 95
Demory, B.-O., de Wit, J., Lewis, N., et al. 2013, ApJ, 776, 25
Désert, J.-M., Vidal-Madjar, A., Lecavelier des Etangs, A., et al. 2008, A&A, 492, 585
Désert, J.-M., Lecavelier des Etangs, A., Hébrard, G., et al. 2009, ApJ, 699, 478
Dobbs-Dixon, I., & Lin, D. N. C. 2008, ApJ, 673, 513
Dobbs-Dixon, I., Agol, E., & Burrows, A. 2012, ApJ, 751, 87
Eymet, V., Fournier, R., Dufresne, J.-L., et al. 2009, J. Geophys. Res. Planets, 114, 11008
Fortney, J. J.,Cooper, C. S., Showman, A. P., et al. 2006, ApJ, 652, 746
Fortney, J. J., Lodders, K., Marley, M. S., & Freedman, R. S. 2008, ApJ, 678, 1419
Fortney, J. J., Shabram, M., Showman, A. P., et al. 2010, ApJ, 709, 1396
Gibson, N. P., Pont, F., & Aigrain, S. 2011, MNRAS, 411, 2199
Gibson, N. P., Aigrain, S., Pont, F., et al. 2012, MNRAS, 422, 753
Gordon, S., & McBride, B. J. 1994, NASA Reference Publication, 1311, I
Grillmair, C. J., Burrows, A., Charbonneau, D., et al. 2008, Nature, 456, 767
Hargreaves, R. J., Beale, C. A., Michaux, L., et al. 2012, ApJ, 757, 46
Heng, K., Menou, K., & Phillipps, P. J. 2011a, MNRAS, 413, 2380
Heng, K., Frierson, D. M. W., & Phillipps, P. J. 2011b, MNRAS, 418, 2669
Hindmarsh, A. C. 1983, in Scientific Computing, eds. R. S. Stepleman et al. (Amsterdam: North-Holland), vol. 1 of IMACS Transactions on Scientific Computation, 55
Humlicek, J. 1982, J. Quant. Spectr. Rad. Transf., 27, 437
Iro, N., Bézard, B., & Guillot, T. 2005, A&A, 436, 719
Isaksen, I. S. A., Midtbø, K. H., Sunde, J., & Crutzen, P. J. 1977, Geophys. Norveg., 31, 11
Kataria, T., Showman, A. P., Lewis, N. K., et al. 2013, ApJ, 767, 76
Knutson, H. A., Charbonneau, D., Allen, L. E., et al. 2007, Nature, 447, 183
Knutson, H. A., Charbonneau, D., Allen, L. E., et al. 2008, ApJ, 673, 526
Knutson, H. A., Charbonneau, D., Cowan, N. B., et al. 2009a, ApJ, 703, 769
Knutson, H. A., Charbonneau, D., Burrows, A., et al. 2009b, ApJ, 691, 866
Knutson, H. A., Howard, A. W., Isaacson, H., et al. 2010, ApJ, 720, 1569
Knutson, H. A., Lewis, N., Fortney, J. J., et al. 2012, ApJ, 754, 22
Kopparapu, R. K., Kasting, J. F., & Zahnle, K. J. 2012, ApJ, 745, 77
Kuntz, M. 1997, J. Quant. Spectr. Rad. Transf., 57, 819
Lecavelier des Etangs, A., Pont, F., Vidal-Madjar, A., & Sing, D. 2008, A&A, 481, L83
Lee, J.-M., Fletcher, L. N., & Irwin, P. G. J. 2012, MNRAS, 420, 170
Lewis, N. K., Showman, A. P., Fortney, J. J., et al. 2010, ApJ, 720, 344
Line, M. R., Liang, M. C., & Yung, Y. L. 2010, ApJ, 717, 496
Line, M. R., Vasisht, G., Chen, P., et al. 2011, ApJ, 738, 32
Line, M. R., Knutson, H., Wolf, A. S., & Yung, Y. L. 2013, ApJ, 783, 70
Machalek, P., McCullough, P. R., Burke, C. J., et al. 2008, ApJ, 684, 1427
Machalek, P., Greene, T., McCullough, P. R., et al. 2010, ApJ, 711, 111
Madhusudhan, N. 2012, ApJ, 758, 36
Madhusudhan, N., & Seager, S. 2009, ApJ, 707, 24
Madhusudhan, N., & Seager, S. 2010, ApJ, 725, 261
Majeau, C., Agol, E., & Cowan, N. B. 2012, ApJ, 747, L20
Miller-Ricci Kempton, E., & Rauscher, E. 2012, ApJ, 751, 117
Moses, J. I., Visscher, C., Fortney, J. J., et al. 2011, ApJ, 737, 15
Moses, J. I., Madhusudhan, N., Visscher, C., & Freedman, R. S. 2013, ApJ, 763, 25
Parmentier, V., Showman, A. P., & Lian, Y. 2013, A&A, 558, A91
Parmentier, V., Guillot, T., Fortney, J. F., & Marley, M. S. 2014, A&A, submitted [arXiv:1311.6322]
Perez-Becker, D., & Showman, A. P. 2013, ApJ, 776, 134
Perna, R., Menou, K., Rauscher, E. 2010, ApJ, 719, 1421
Perna, R., Heng, K., & Pont, F. 2012, ApJ, 751, 59
Radhakrishnan, K., & Hindmarsh, A. C. 1993, NASA Reference Publication 1327, LLNL Report UCRL-ID-113855
Rauscher, E., & Menou, K. 2010, ApJ, 714, 1334
Rauscher, E., & Menou, K. 2012a, ApJ, 745, 78
Rauscher, E., & Menou, K. 2012b, ApJ, 750, 96
Rauscher, E., & Menou, K. 2013, ApJ, 764, 103
Rauscher, E., Menou, K., Cho, J. Y-K., et al. 2008, ApJ, 681, 1646
Reid, R. C., Prausnitz, J. M., & Poling, B. E. 1988, The Properties of Gases and Liquids (McGraw-Hill Book Company)
Rothman, L. S., Gordon, I. E., Barbe, A., et al. 2009, J. Quant. Spectr. Rad. Transf., 110, 533
Rothman, L. S., Gordon, I. E., Barber, R. J., et al. 2010, J. Quant. Spectr. Rad. Transf., 111, 2139
Rodler, F., Kürster, M., & Barnes, J. R. 2013, MNRAS, 432, 1980
Rybicki, G. B., & Lightman, A. P. 2004, Radiative Processes in Astrophysics (Wiley-VCH)
Sanz-Forcada, J., Micela, G., Ribas, I., et al. 2011, A&A, 532, A6
Seager, S., & Deming, D. 2010, ARA&A, 48, 631
Showman, A. P., & Guillot, T. 2002, A&A, 385, 166
Showman, A. P., & Polvani, L. M. 2011, ApJ, 738, 71
Showman, A. P., Cooper, C. S., Fortney, J. J., & Marley, M. S. 2008, ApJ, 682, 559
Showman, A. P., Fortney, J. J., Lian, Y., et al. 2009, ApJ, 699, 564
Showman, A. P., Cho, J. Y.-K., & Menou, K. 2011, in Exoplanets, ed. S. Seager (Tucson: Univ. Arizona Press), 471
Showman, A. P., Fortney, J. J., Lewis, N. K., & Shabram, M. 2013, ApJ, 762, 24
Sing, D. K., Désert, J.-M., Lecavelier des Etangs, A., et al. 2009, A&A, 505, 891
Snellen, I. A. G., de Kok, R. J., de Mooij, E. J. W., & Albrecht, S. 2010, Nature, 465, 1049
Southworth, J. 2010, MNRAS, 408, 1689
Swain, M. R., Vasisht, G., Tinetti, G., et al. 2008, Nature, 452, 329b
Swain, M. R., Vasisht, G., Tinetti, G., et al. 2009a, ApJ, 690, L114
Swain, M. R., Tinetti, G., Vasisht, G., et al. 2009b, ApJ, 704, 1616
Swain, M. R., Deroo, P., Griffith, C. A., et al. 2010, Nature, 463, 637
Tarafdar, S. P., & Vardya, M. S. 1969, MNRAS, 145, 171
Todorov, K., Deming, D., Harrington, J., et al. 2010, ApJ, 708, 498
Thuillier, G., Floyd, L., Woods, T. N., et al. 2004, Adv. Space Res., 34, 256
Tinetti, G., Vidal-Madjar, A., Liang, M.-C., et al. 2007, Nature, 448, 169
Venot, O., Hébrard, E., Agúndez, M., et al. 2012, A&A, 546, A43
Venot, O., Agúndez, M., Selsis, F., et al. 2014, A&A, 562, A51
Waldmann, I. P., Tinetti, G., Drossart, P., et al. 2012, ApJ, 744, 35
Yung, Y. L., & DeMore, W. B. 1999, Photochemistry of Planetary Atmospheres (Oxford University Press)
Zahnle, K., Marley, M. S., Freedman, R. S., et al. 2009, ApJ, 701, L20

3.5 Clouds, albedos and atmospheric circulation

3.5.1 Inhomogeneous clouds in hot Jupiters: the case of Kepler-7b

Cloud formation in close-in, irradiated planets atmospheres are still uncertain and no model correctly account for all the interactions between the flow and the clouds. Whereas Parmentier et al. (2013) focused on the effect of the flow on possible condensates without considering radiative feedback of cloud particles, Dobbs-Dixon & Agol (2013) used a crude representation of the cloud opacities without taking into account the spatial variations of the clouds induced by the advection. For hot Jupiter both interactions are be important. Particularly, cloud formation might be different from what has been studied so far. In Solar-system planets, cloud formation is thought vertically: the cloud deck is located where the temperature profile crosses the saturation curve and the vertical extent of the cloud depends on the competition between the vertical mixing and the settling of cloud particles. The parcel of gas that contain cloud particles are usually slightly oversaturated. In hot Jupiters, horizontal advection can transport parcels of gas from hot to cold regions. While the gas might be undersaturated in the hot regions, it can be oversaturated by several orders of magnitudes in other locations[2]. Horizontal advection and horizontal temperature gradients should therefore be at least as important as the combined effects of vertical mixing and vertical temperature gradients for cloud formation.

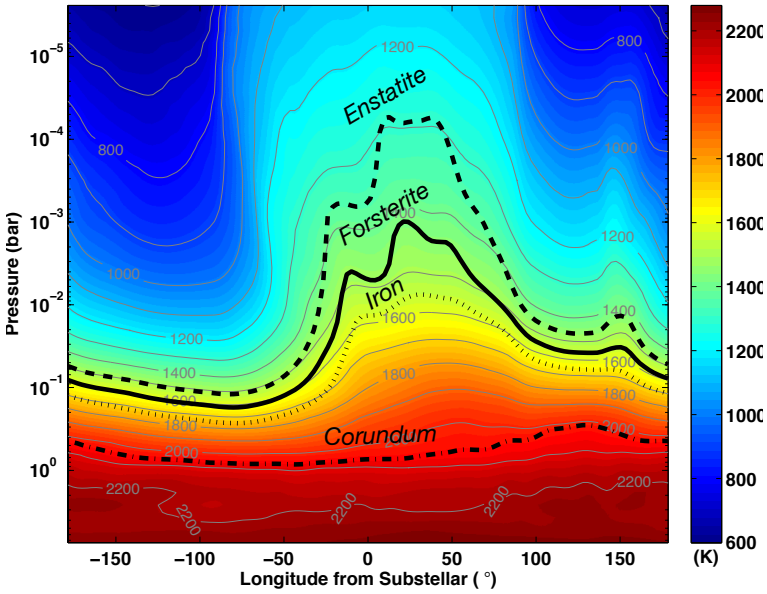

Figure 3.10. Temperatures at the equator of Kepler-7b obtained with the MITgcm by Lewis et al. (in prep.). The condensation curves of several compound are over-plotted. Because the hottest point of the planet is shifted to the east of the substellar point, we expect more clouds west of the substellar point than east of it. Courtesy of Nikole Lewis.

A first, naive guess for the location of clouds in a hot Jupiter atmosphere can be obtained by determining which part of the atmosphere lays below the condensation line. Particularly, the presence of hot spot west of the substellar point could lead to longitudinal variations in the cloud coverage of some planets, as shown in Figure 3.10 for the case of Kepler-7b. Such an inhomogeneous cloud coverage in the dayside atmosphere of an exoplanet could have a strong signature in the visible phase curve of the planet. Indeed, an inhomogeneous cloud coverage would translate into spatial variations of the albedo.

[2]The saturation is proportional to the exponential of the temperature.

The following letter, published in *The Astrophysical Journal* (Demory et al. 2013) described observational evidences of inhomogeneous clouds in the planet Kepler-7b as observed by the Kepler spacecraft.

The Astrophysical Journal Letters, 776:L25 (7pp), 2013 October 20 doi:10.1088/2041-8205/776/2/L25

INFERENCE OF INHOMOGENEOUS CLOUDS IN AN EXOPLANET ATMOSPHERE

Brice-Olivier Demory[1], Julien de Wit[1], Nikole Lewis[1,10], Jonathan Fortney[2], Andras Zsom[1], Sara Seager[1], Heather Knutson[3], Kevin Heng[4], Nikku Madhusudhan[5], Michael Gillon[6], Thomas Barclay[7], Jean-Michel Desert[3], Vivien Parmentier[8], and Nicolas B. Cowan[9]
[1] Department of Earth, Atmospheric and Planetary Sciences, Massachusetts Institute of Technology, 77 Massachusetts Avenue, Cambridge, MA 02139, USA; demory@mit.edu
[2] Department of Astronomy and Astrophysics, University of California, Santa Cruz, CA 95064, USA
[3] Division of Geological and Planetary Sciences, California Institute of Technology, Pasadena, CA 91125, USA
[4] Center for Space and Habitability, University of Bern, Sidlerstrasse 5, CH-3012, Bern, Switzerland
[5] Department of Physics and Department of Astronomy, Yale University, New Haven, CT 06520, USA
[6] Institut d'Astrophysique et de Géophysique, Université de Liège, Allée du 6 Août, 17, Bat. B5C, B-4000 Liège 1, Belgium
[7] NASA Ames Research Center, M/S 244-30, Moffett Field, CA 94035, USA
[8] Laboratoire J.-L. Lagrange, UMR 7293, Université de Nice-Sophia Antipolis, CNRS, Observatoire de la Côte d'Azur B.P. 4229, F-06304 Nice Cedex 4, France
[9] Department of Physics and Astronomy, Northwestern University, 2145 Sheridan Road, F165, Evanston, IL 60208, USA
Received 2013 June 25; accepted 2013 August 20; published 2013 October 3

ABSTRACT

We present new visible and infrared observations of the hot Jupiter Kepler-7b to determine its atmospheric properties. Our analysis allows us to (1) refine Kepler-7b's relatively large geometric albedo of $Ag = 0.35 \pm 0.02$, (2) place upper limits on Kepler-7b thermal emission that remains undetected in both *Spitzer* bandpasses and (3) report a westward shift in the *Kepler* optical phase curve. We argue that Kepler-7b's visible flux cannot be due to thermal emission or Rayleigh scattering from H_2 molecules. We therefore conclude that high altitude, optically reflective clouds located west from the substellar point are present in its atmosphere. We find that a silicate-based cloud composition is a possible candidate. Kepler-7b exhibits several properties that may make it particularly amenable to cloud formation in its upper atmosphere. These include a hot deep atmosphere that avoids a cloud cold trap, very low surface gravity to suppress cloud sedimentation, and a planetary equilibrium temperature in a range that allows for silicate clouds to potentially form in the visible atmosphere probed by *Kepler*. Our analysis does not only present evidence of optically thick clouds on Kepler-7b but also yields the first map of clouds in an exoplanet atmosphere.

Key words: planetary systems – stars: individual (Kepler-7) – techniques: photometric

Online-only material: color figures

1. INTRODUCTION

Clouds and hazes are ubiquitous in the solar system's giant-planet and brown-dwarf atmospheres. In cloudy L-type brown dwarf atmospheres, the role of clouds has long been appreciated (e.g., Ackerman & Marley 2001; Burrows et al. 2001; Tsuji 2002; Kirkpatrick 2005; Witte et al. 2009) and the observed spectra of such objects cannot be modeled correctly without clouds (Cushing et al. 2008). It has been long suggested that clouds would also play a strong role in shaping the spectra of exoplanets in general (Barman et al. 2001; Marley et al. 2013), and hot Jupiters in particular (Marley et al. 1999; Seager et al. 2000; Sudarsky et al. 2000) before having been actually reported (Evans et al. 2013).

Most hot Jupiters are "dark" at visible wavelengths (e.g., Rowe et al. 2008; Coughlin & López-Morales 2012; Barclay et al. 2012) and only a handful exhibit appreciable geometric albedos. Caution is needed when interpreting hot-Jupiter geometric albedos, as for the most irradiated objects, a significant part of the planetary spectral energy distribution leaks into visible wavelengths, complicating the distinction between reflected light and thermal emission.

Kepler-7b (Latham et al. 2010) is a hot Jupiter orbiting a subgiant G star in 4.89 days. Its relatively low mass $M_p = 0.44 \pm 0.04\,M_{\rm Jup}$ and large radius $R_p = 1.61 \pm 0.02\,R_{\rm Jup}$ result in a very low density $\rho_p = 0.14$ g cm^{-3} (Demory et al. 2011b, hereafter D11). Remarkably, Kepler-7b has a significant geometric albedo $A_g \sim 0.35$ and exhibits a clear phase-curve modulation in the *Kepler* bandpass (D11; Kipping & Bakos 2011; Coughlin & López-Morales 2012). Kepler-7b's effective temperature places this hot Jupiter in an exceptionally rich region of condensation phase space. Because of the extreme difference between its equilibrium temperature and the brightness temperature as derived from its occultation in the *Kepler* bandpass, the origin of Kepler-7b's albedo has been attributed to the presence of a cloud or haze layer in its atmosphere or to Rayleigh scattering (D11).

In this Letter, we use both optical phase-curve and infrared occultation data to determine the origin of Kepler-7b's visible flux. Section 2 presents the *Spitzer* observations and data analysis. Section 3 describes our analysis of *Kepler* data employing three times more data than in D11. Section 4 presents our discussion about the origin of flux observed in the *Kepler* bandpass.

2. *SPITZER* 3.6 AND 4.5 μm PHOTOMETRY

2.1. Observations and Data Analysis

We observed two occultations of Kepler-7b with *Spitzer* (Werner et al. 2004) in IRAC (Fazio et al. 2004) 3.6 μm channel as well as two other in IRAC 4.5 μm channel between 2011 August and November. All Astronomical Observation Requests (AORs) were obtained as part of program 80219 (PI:

[10] Sagan Fellow.

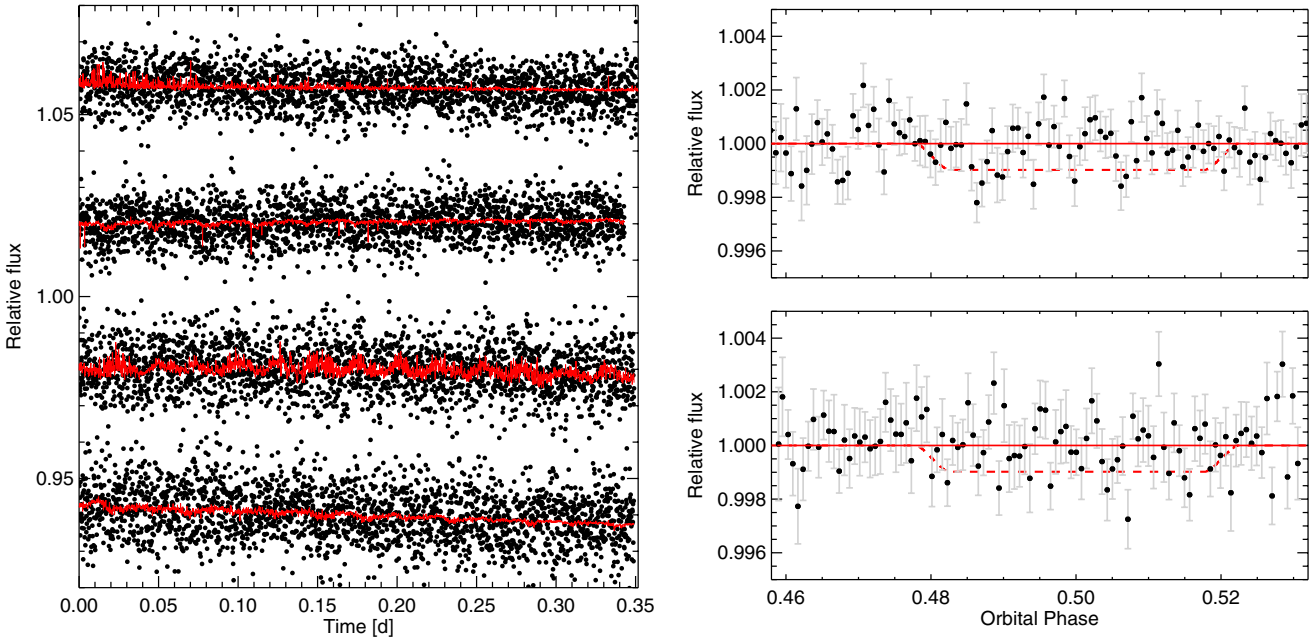

Figure 1. *Spitzer* 3.6 and 4.5 μm occultation photometry of Kepler-7b. Left: raw photometry of the four AORs with the best-fit model superimposed (see Section 2). The lightcurves are shifted on the vertical axis for clarity. The two IRAC 3.6 μm lightcurves are at the top and the two 4.5 μm lightcurves at the bottom. Right: phase-folded occultations divided by the best-fit model. The IRAC 3.6 μm lightcurve is shown at the top and the 4.5 μm at the bottom. Data are binned per 5 minutes. For illustration purposes we depict a 1 mmag occultation in red dash-line, the best-fit model for the two channels being a null occultation.

(A color version of this figure is available in the online journal.)

H. Knutson). Datasets are ~9 hr long and were obtained in full-array mode with an individual exposure time of 10.4 s. A total of 2440 frames was collected for each AOR. We perform a data reduction of all AORs similar to Demory et al. (2011a), using as input the Basic Calibrated Data files produced by the *Spitzer* pipeline version 18.18.0. In a first step, we test 12 apertures ranging from 1.8 to 4.5 pixels and find the lowest rms using 2.6 and 2.8 pixel apertures at 3.6 and 4.5 μm respectively. We obtain an rms of 6380 and 6710 ppm for the two 4.5 μm AORs with a moderate contribution from correlated noise of less than 20%. Our analysis of the 3.6 μm data resulted in significant correlated noise in both time-series (>40%). Because of the long occultation duration of Kepler-7b (5.3 hr), the remaining out-of-transit photometry is small on each side of the eclipse, making the occultation parameters retrieval delicate in the presence of correlated noise. In a second step, we apply the noise-pixel variable aperture technique (Lewis et al. 2013) to all AORs. We find this method mitigates systematics found at 3.6 μm. We report corresponding rms of 4900 and 4750 ppm for both AORs in this channel using this technique, with a reduced correlated noise contribution of ~15%. We do not notice any improvement using noise-pixel aperture over the classical fixed-aperture photometry reduction at 4.5 μm.

In order to model these data, we use the Markov Chain Monte Carlo (MCMC) implementation presented in Gillon et al. (2012). We assume a circular orbit (D11), set the occultation depth as a jump parameter and impose priors on the orbital period P, transit duration W, time of minimum light T_0 and impact parameter $b = a\cos i/R_\star$ based on D11. For each MCMC fit (at 3.6 and 4.5 μm), we run two chains of 10^5 steps and assess their convergence using the statistical test from Gelman & Rubin (1992).

We use the Bayesian Information Criterion (BIC) to select the optimal baseline model for our 4.5 μm observations. We find the most adequate model based on a classical second order x–y polynomial (Demory et al. 2011a; Equation (1)) to correct the "pixel-phase" effect, added to a time-dependent linear trend. The baseline model for our 3.6 μm data consists of the noise-pixel parameter alone. We discard the first ~25–35 minutes of all AORs that are affected by a noticeable detector ramp and/or increased noise, already noticed in warm-*Spitzer* photometry (e.g., Deming et al. 2011). Our *Spitzer*/IRAC raw lightcurves are shown on Figure 1 (left).

2.2. The Thermal Emission of Kepler-7b

We repeat the same MCMC fits for both channels setting the occultation depth to zero, to compare the BIC between a model that includes the occultation and a model that does not. The MCMC fits including the occultation model yield an occultation depth of 164 ± 150 ppm at 3.6 μm and 367 ± 221 ppm at 4.5 μm. We compare the BIC of these runs to the MCMC fits that do not include the occultation model. The odds ratio between both models is ~180 and ~100 in favor of the model without occultation at 3.6 and 4.5 μm respectively. Based on our dataset, the occultation is detected in none of the channels. We derive corresponding 3σ upper limits of 615 and 1010 ppm at 3.6 and 4.5 μm. We employ a PHOENIX (Hauschildt et al. 1999) model of Kepler-7 using the D11 stellar parameters to convert these occultation depth upper-limits into brightness temperatures. We find these 3σ upper-limits to be 1700 and 1840 K at 3.6 and 4.5 μm. Our final phase-folded occultation lightcurves are shown on Figure 1 (right).

3. *KEPLER* OBSERVATIONS AND DATA ANALYSIS

3.1. Data Reduction

We base our analysis on *Kepler* (Batalha et al. 2013) quarters 1–14 long-cadence simple aperture photometry (Jenkins et al. 2010) that span more than 1200 days of quasi-continuous

observations, which is three times more data than in D11. We mitigate instrumental systematics by fitting the first four cotrending basis vectors (CBVs) to each quarter using the PyKE software (Still & Barclay 2012). We find that outliers represent less than ∼0.5% of the dataset. We then normalize each quarter to the median. In total, 56,000 datapoints are collected. We employ our MCMC framework presented in Section 2 to account for photometric trends longer than twice the planetary orbital period by fitting a second-order polynomial to the out-of-eclipse data.

We then evaluate the contribution from correlated noise on timescales corresponding to the orbital period. We cut the whole data into 5 day duration segments and compute a scaling factor β based on the standard deviation of the binned residuals for each light curve using different time-bins (Gillon et al. 2010). We keep the largest β value as a criterion to discard data segments affected by significant correlated noise. We obtain a mean $\beta = 1.19$ over the whole data set and discard those with threshold $\beta > 2.1$, which account for ∼5% of the complete dataset. All data discarded affect predominantly quarters 12–14, when increased solar activity and coronal mass ejections resulted in a decrease of *Kepler*'s pointing accuracy and thus an increase in systematic noise. We finally note that in contrary to pre-whitening techniques (as employed in D11), the data-reduction method presented here preserves all phase-curve properties.

3.2. Robustness of the Planetary Phase-curve Signal

To assess the robustness of the phase-curve properties, we repeat the analysis presented above several times, by increasing the number of CBV components up to 8, by decreasing the threshold β values and by using linear or third-order polynomials to account for the long-term trends. We find the phase amplitude, peak-offset and occultation depth values to remain consistent within 1σ uncertainties (see Section 3.3). The phase-curve signal is therefore not due to (nor affected by) the detrending. Two of us (B.O.D., T.B.) performed independent analyses of the dataset and obtained results in excellent agreement.

Figures 2 and 3 demonstrate the stability of the phase-curve signal across Q1–Q14. This would not be the case if the phase curve was of instrumental origin as while *Kepler* systematics can be consistent in amplitude across quarters, they are definitely not consistent in phase (e.g., Kinemuchi et al. 2012). Any signal due to *Kepler* systematics would thus average out across quarters. This strongly favors the phase-curve being of astrophysical origin.

We search for all frequencies in the dataset to assess any risk of contamination of the planetary phase curve. To quantify how frequencies and amplitudes evolve with time, we perform a wavelet transform analysis using the weighted wavelet Z-transform algorithm developed by Foster (1996). We do not detect any clear signature, apart from the planet orbital signal. Kepler-7 is intrinsically quiet and any stellar activity remains nominal over Q1–Q14 observations, with no quarter-dependent fluctuations. We notice a barely detectable periodicity at ∼16.7 days that could correspond to the rotational period of the star, which translates to an equatorial velocity of $V_{\rm eq} \sim 6$ km s^{-1} assuming $R_\star = 2.02\,R_\odot$ (D11). This is broadly consistent with Kepler-7's stellar projected rotation $v \sin i = 4.2$ km s^{-1} (Latham et al. 2010).

The host star is unlikely to contaminate our phase-curve for several reasons. As we phase-fold data over more 3.5 yr, only stellar variability exactly phased on the planetary orbital period (or a multiple) and consistent over the duration of the observations could affect the phase-curve shape. First, the stellar rotational velocity suggests that the star is not tidally locked to the planet, as the planetary orbital period is only ∼4.89 days. The stellar rotation and planetary orbital periods are different by a non-integer factor of ∼3.4. Second, stellar pulsations with a period of ∼5 days are unlikely for a sub-giant star and would have been visible in the data. Third, as we do not clearly detect stellar variability in the photometry, only small starspots could be present, but those starspots would have a short lifetime (e.g., Strassmeier 2009). Even in the case of starspots that are stable over more than 3 yr, differential rotation would cause distortions in the lightcurve across quarters that are not observed (Figure 2). Furthermore, spots or group of spots do not usually produce sinusoidal lightcurves but rather sequences of flat and V-shaped lightcurves (e.g., Harrison et al. 2012). Finally, we do not detect interactions between the star and the planet in the form of ellipsoidal or beaming components in the phase curve.

We finally take into account a faint stellar companion located 1.″9 east of Kepler-7 with a Δmag = 4.0 both in J and Ks bands (Adams et al. 2012). These flux ratios suggest a similar spectral type and discard the possibility of a cool star. In order to detect a significant contamination from the companion star with a period commensurate with Kepler-7b's orbital period, we split the full dataset in segments of duration equal to a quarter. Each quarter has a specific aperture with a different contribution from the fainter companion star. The reported consistency at the 1σ level of the phase curve properties (amplitude, phase-peak offset) across quarters suggest a negligible contamination from the stellar neighbor.

We therefore conclude that the phase curve is of planetary origin.

3.3. Phase Curve Analysis

Kepler-7b's phase curve deviates from a pure Lambert-law phase-dependent behavior (e.g., Sobolev 1975) expected for isotropic scattering alone (Figure 3, green). The main feature of Kepler-7b's phase curve is a delay of 13 ± 3.5 hr of the phase-curve's peak from the occultation center. This delay implies that the hemisphere-integrated flux is maximum to the west of Kepler-7b's substellar point. We further measure a phase-curve amplitude of 50 ± 2 ppm and an occultation depth of 48 ± 3 ppm, corresponding to a geometric albedo $A_g = 0.35 \pm 0.02$. This occultation depth translates to a brightness temperature of 2645^{+20}_{-30} K in the *Kepler* bandpass, which is 1000 K and 800 K larger than the infrared brightness temperatures upper limits measured at 3.6 and 4.5 μm respectively (see Section 2). We found our phase-curve amplitude and occultation depth to be in agreement with previous analyses (D11; Kipping & Bakos 2011; Coughlin & López-Morales 2012).

The key features of Kepler-7b's phase-curve translate directly into constraints on maps (Cowan & Agol 2008) assuming a tidally locked planet on a circular orbit. A planetary phase-curve $F_p/F_\star$ measures the planetary hemisphere-averaged relative brightness $\langle I_p \rangle / \langle I_\star \rangle$ as follows:

$$\frac{F_p}{F_\star}(\alpha) = \frac{\langle I_p \rangle(\alpha)}{\langle I_\star \rangle} \left(\frac{R_p}{R_\star} \right)^2, \quad (1)$$

where α is the orbital phase.

We first notice that Kepler-7b's planetary flux contribution starts from phase 0.18 ± 0.03, when the meridian centered

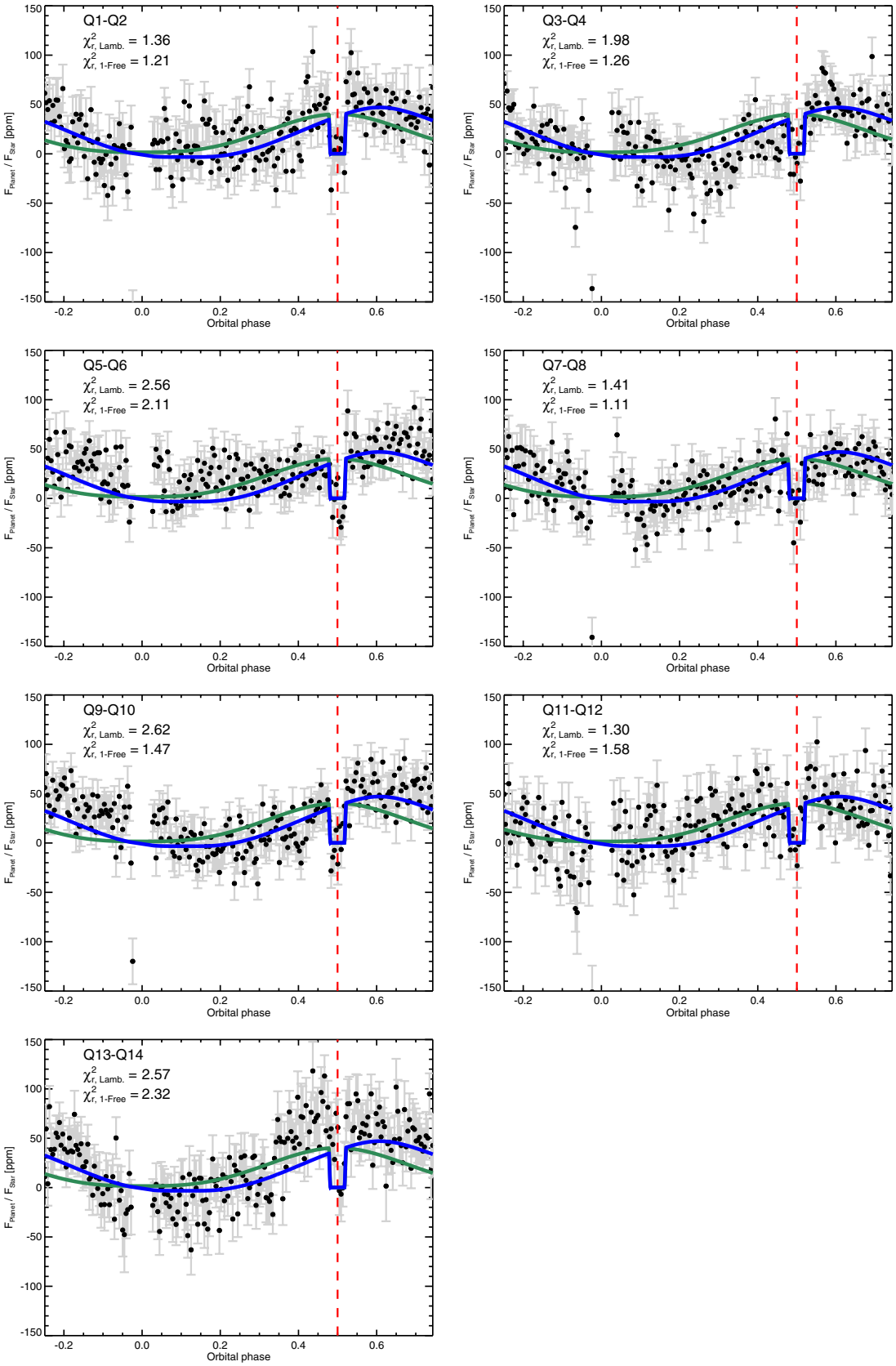

Figure 2. Matrix of Kepler-7b phase curves based on pairs of *Kepler* quarters. Data are binned per 5 minutes. The symmetric Lambertian sphere (green) and asymmetric 1-free-band model (blue) are superimposed, along with the corresponding χ^2_r values (See Section 3.3). The occultation's phase is indicated in red. The asymmetric model is preferred for all quarter pairs, excepted Q11–Q12.

(A color version of this figure is available in the online journal.)

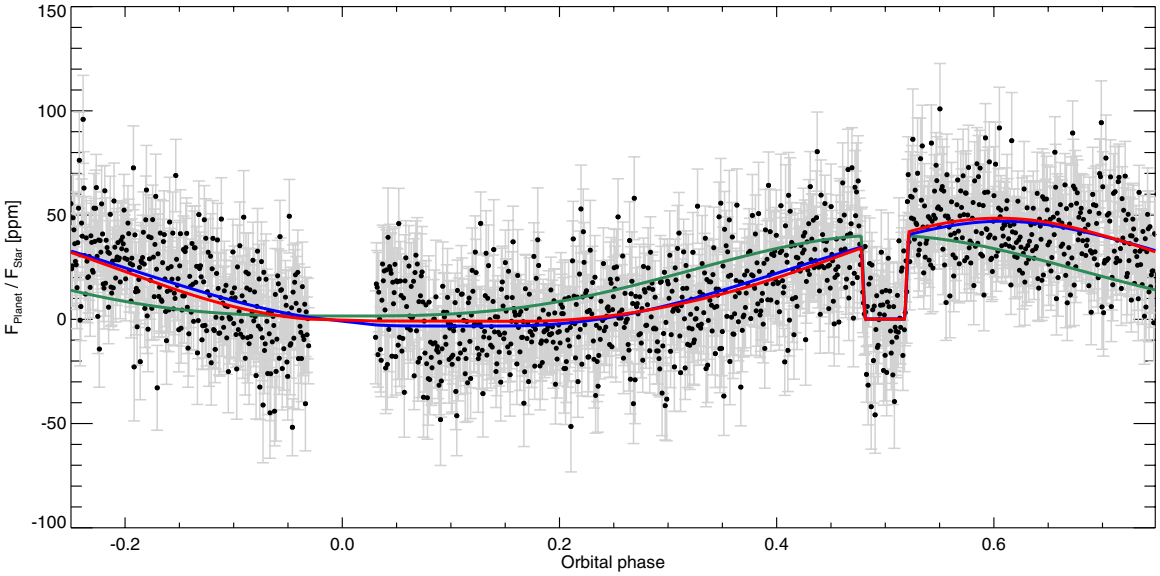

Figure 3. Phase curve of Kepler-7b based on *Kepler* Q1–Q14 data. Data are binned per 5 minutes. The Lambertian sphere (green), 1-free-band (blue) and 3-fixed-band (red) best-fit models (see Section 3.3) are superimposed.

(A color version of this figure is available in the online journal.)

$25 \pm 12^{\circ}$ east of the substellar point appears. Second, the phase-curve's maximum is located at phase 0.61 ± 0.03, implying that the brightest hemisphere is centered on the meridian located $41 \pm 12^{\circ}$ west of the substellar point. Third, the planetary flux contribution vanishes around the transit, implying that the "bright" area extends up to the western terminator, while its extension to the east of the substellar point is nominal. We finally note that the phase-curve's amplitude of 50 ± 2 ppm converts into an hemisphere-averaged relative brightness $74 \pm 2 \times 10^{-4}$ (Equation (1)).

We longitudinally map Kepler-7b using the MCMC implementation presented in de Wit et al. (2012). This method has been developed to map exoplanets and to mitigate the degeneracy between the planetary brightness distribution and the system parameters. We use two model families similar to the "beach-ball models" introduced by Cowan et al. (2009): one using n longitudinal bands with fixed positions on the dayside and another using longitudinal bands whose positions and widths are jump parameters in the MCMC fit. We choose the two simplest models from these families: a 3-fixed-band model and 1-free-band model so as to extract Kepler-7b's longitudinal dependence of the dayside brightness as well as the extent of the "bright" area. For both models, we compute each band's amplitude from their simulated lightcurve by using a perturbed singular value decomposition method. The corresponding median brightness maps are shown on Figure 4. The 1-free-band model (Figure 3, blue) finds a uniformly bright longitudinal area extending from $105 \pm 12^{\circ}$ west to $30 \pm 12^{\circ}$ east with a relative brightness $78 \pm 4 \times 10^{-4}$ (Figure 4, left). The 3-fixed-band model (Figure 3, red) finds bands of relative brightness decreasing from the west to the east with the following values: 100 to 68 and $3 \pm 6 \times 10^{-4}$ (Figure 4, right). We finally note that the 1-free-band model finds a bright sector extending to the night side, due to the sharp flux increase observed around transit (Figure 3).

4. THE ORIGIN OF KEPLER-7B'S VISIBLE FLUX

The combined information from the *Spitzer* and *Kepler* observations of Kepler-7b strongly favor the conclusion that the planetary phase-dependent flux variations seen in the *Kepler* light curve are the result of scattered light from optically thick clouds, whose properties change as a function of longitude.

The lack of significant thermal emission from Kepler-7b in the *Spitzer* 3.6 and 4.5 μm bandpasses supports the fact that Kepler-7b's visible light curve is driven by reflected light. Kepler-7b's phase curve exhibits a westward asymmetry suggesting, if of thermal origin, a temperature structure that does not follow the expected temperature structure for tidally locked hot Jupiters, which would yield an eastward shift. This eastward shift is consistently produced from a range of general circulation models for tidally locked hot-Jupiters forced using various methods, including Newtonian cooling (e.g., Cooper & Showman 2005; Showman et al. 2008; Dobbs-Dixon et al. 2010; Rauscher & Menou 2010; Heng et al. 2011a), dual-band radiative transfer (e.g., Heng et al. 2011b; Rauscher & Menou 2012) or multi-wavelength radiative transfer (e.g., Showman et al. 2009). Combining these results with the analytical theory of Showman & Polvani (2011) suggests that thermal phase-curve eastward shifts are robust outcomes of the hot-Jupiter circulation regime. As we do not detect thermal flux from Kepler-7b with *Spitzer*, the most likely conclusion is that the westward shift in the visible phase-curve is indicative of a variation in the cloud properties (cloud coverage, optical depth, particle size distribution, vertical extent, composition, etc.) as a function of longitude, governed by the planet's wind and thermal patterns.

We use the methods of Fortney et al. (2005, 2008) to compute Kepler-7b's one-dimensional temperature structure and emission spectrum (Figure 5). The orange model is cloud-free. The blue model uses the cloud model of Ackerman & Marley (2001) to calculate the vertical distribution and optical depths of Mg_2SiO_4 clouds. Both models assume modest redistribution of energy, with the assumption that 1/4 of the incident energy is lost to the un-modeled night side. The particle size distribution in the cloud is assumed to be log-normal with a mode of 0.5 μm at all heights. A low sedimentation efficiency free parameter ($f_{\rm sed}$) of 0.1 is used, which suppresses sedimentation.

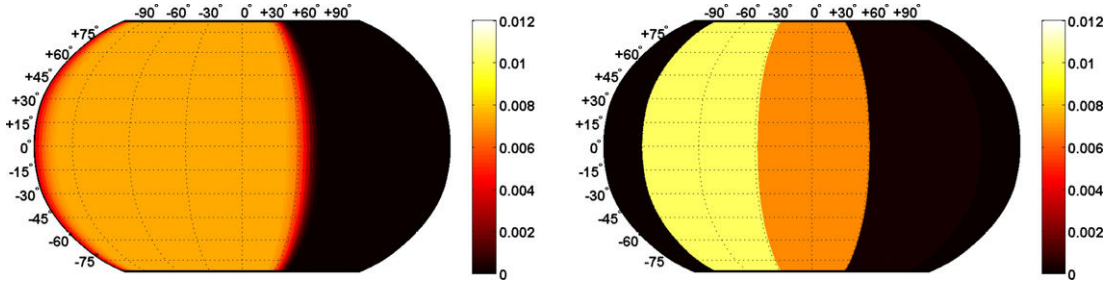

Figure 4. Longitudinal brightness maps of Kepler-7b. Kepler-7b's longitudinal brightness distributions $I_p/I_\star$ as retrieved in *Kepler*'s bandpass using the 1-free-band model (left) and the 3-fixed-band model (right) detailed in Section 3.3.

(A color version of this figure is available in the online journal.)

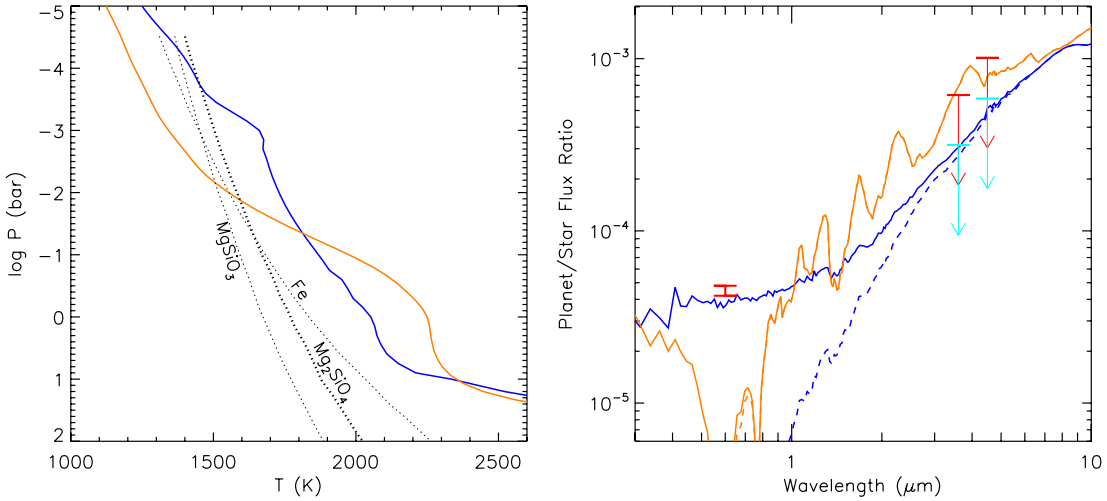

Figure 5. One-dimensional models of the dayside temperature structure and flux ratios of Kepler-7b. Left: condensation curves for several species are also shown, although only Mg_2SiO_4 is used in the calculations. The model in orange is cloud-free, while the model in blue includes cloud opacity. Right: the cloud-free model is dark in the optical and emits more flux in the mid-infrared IRAC bands. Dashed curves are the thermal emission component and solid curves are the total flux. The cloudy model is brighter in the optical, owing to scattered light, with suppression of mid-infrared flux. The optical detection in the *Kepler* band is shown in red, along with the *Spitzer* 1σ (cyan) and 3σ (red) upper limits.

(A color version of this figure is available in the online journal.)

It is clear that the cloudy model (blue) provides a much better fit to the combined occultation measurements from *Spitzer* and *Kepler*. The clouds dramatically enhance the flux in the optical, increase the model Bond albedo, and suppress emission in the infrared (Figure 5, right). We note that many other combinations of cloud and thermal properties might also provide an adequate match to the data. However, we exclude Rayleigh scattering from H_2 molecules and homogeneous cloud structures as possible sources of visible phase-curve signatures, which would both result in a symmetric phase curve.

Kepler-7b may be relatively more likely to show the effects of cloud opacity than other hot Jupiters. The planet's incident flux level is such that model profiles cross silicate condensation curves in the upper, observable atmosphere, making these clouds a possible explanation. The same would not be true for warmer planets (where temperatures would be too hot for dayside clouds) or for cooler planets (where silicates would only be present in the deep unobservable atmosphere). Furthermore, the planet's very low surface gravity may play an important role in hampering sedimentation of particles out the atmosphere. Finally, the planet's large radius implies a relatively high specific entropy adiabatic in the interior, and a correspondingly warm adiabat in the deep atmosphere at tens of bars. This removes the possibility of silicate clouds condensing at pressures of 100–1000 bars, as may happen in other hot Jupiters.

Our results suggest that one broad-band visible phase curve is probably insufficient to constrain the cloud properties. The problem might remain degenerate until more observations (such as narrow-band optical phase curves and polarimetry) become available. In the near future it is likely that similar brightness maps of other *Kepler* planets will emerge, thereby providing an invaluable means to improve our understanding of cloud formation in exoplanet atmospheres.

We thank G. Basri and both anonymous referees for helpful comments that improved the Letter. This work is based in part on observations made with the *Spitzer Space Telescope*, which is operated by the JPL, Caltech under a contract with NASA. A. Zsom was supported by the German Science Foundation (DFG) under grant ZS107/2-1. This work was performed in part under contract with the California Institute of Technology funded by NASA through the Sagan Fellowship Program executed by the NASA Exoplanet Science Institute. J. de Wit acknowledges support from the Belgian American Educational Foundation and Wallonie-Bruxelles International.

Facilities: Kepler, *Spitzer*

REFERENCES

Ackerman, A. S., & Marley, M. S. 2001, ApJ, 556, 872
Adams, E. R., Ciardi, D. R., Dupree, A. K., et al. 2012, AJ, 144, 42
Barclay, T., Huber, D., Rowe, J. F., et al. 2012, ApJ, 761, 53
Barman, T. S., Hauschildt, P. H., & Allard, F. 2001, ApJ, 556, 885
Batalha, N. M., Rowe, J. F., Bryson, S. T., et al. 2013, ApJS, 204, 24
Burrows, A., Hubbard, W. B., Lunine, J. I., & Liebert, J. 2001, RvMP, 73, 719

Cooper, C. S., & Showman, A. P. 2005, ApJL, 629, L45
Coughlin, J. L., & López-Morales, M. 2012, AJ, 143, 39
Cowan, N. B., & Agol, E. 2008, ApJL, 678, L129
Cowan, N. B., Agol, E., Meadows, V. S., et al. 2009, ApJ, 700, 915
Cushing, M. C., Marley, M. S., Saumon, D., et al. 2008, ApJ, 678, 1372
Deming, D., Knutson, H., Agol, E., et al. 2011, ApJ, 726, 95
Demory, B.-O., Gillon, M., Deming, D., et al. 2011a, A&A, 533, 114
Demory, B.-O., Seager, S., Madhusudhan, N., et al. 2011b, ApJL, 735, L12
de Wit, J., Gillon, M., Demory, B.-O., & Seager, S. 2012, A&A, 548, A128
Dobbs-Dixon, I., Cumming, A., & Lin, D. N. C. 2010, ApJ, 710, 1395
Evans, T. M., Pont, F., Sing, D. K., et al. 2013, ApJL, 772, L16
Fazio, G. G., Hora, J. L., Allen, L. E., et al. 2004, ApJS, 154, 10
Fortney, J. J., Lodders, K., Marley, M. S., & Freedman, R. S. 2008, ApJ, 678, 1419
Fortney, J. J., Marley, M. S., Lodders, K., Saumon, D., & Freedman, R. 2005, ApJL, 627, L69
Foster, G. 1996, AJ, 112, 1709
Gelman, A., & Rubin, D. 1992, StaSc, 7, 457
Gillon, M., Lanotte, A. A., Barman, T., et al. 2010, A&A, 511, 3
Gillon, M., Triaud, A. H. M. J., Fortney, J. J., et al. 2012, A&A, 542, A4
Harrison, T. E., Coughlin, J. L., Ule, N. M., & López-Morales, M. 2012, AJ, 143, 4
Hauschildt, P. H., Allard, F., & Baron, E. 1999, ApJ, 512, 377
Heng, K., Frierson, D. M. W., & Phillipps, P. J. 2011a, MNRAS, 418, 2669
Heng, K., Menou, K., & Phillipps, P. J. 2011b, MNRAS, 413, 2380
Jenkins, J. M., Caldwell, D. A., Chandrasekaran, H., et al. 2010, ApJL, 713, L120
Kinemuchi, K., Barclay, T., Fanelli, M., et al. 2012, PASP, 124, 963
Kipping, D., & Bakos, G. 2011, ApJ, 730, 50
Kirkpatrick, J. D. 2005, ARA&A, 43, 195
Latham, D. W., Borucki, W. J., Koch, D. G., et al. 2010, ApJL, 713, L140
Lewis, N. K., Knutson, H. A., Showman, A. P., et al. 2013, ApJ, 766, 95
Marley, M. S., Ackerman, A. S., Cuzzi, J. N., & Kitzmann, D. 2013, arXiv:1301.5627v1
Marley, M. S., Gelino, C., Stephens, D., Lunine, J. I., & Freedman, R. 1999, ApJ, 513, 879
Rauscher, E., & Menou, K. 2010, ApJ, 714, 1334
Rauscher, E., & Menou, K. 2012, ApJ, 750, 96
Rowe, J. F., Matthews, J. M., Seager, S., et al. 2008, ApJ, 689, 1345
Seager, S., Whitney, B. A., & Sasselov, D. D. 2000, ApJ, 540, 504
Showman, A., Fortney, J., Lian, Y., et al. 2009, ApJ, 699, 564
Showman, A. P., Cooper, C. S., Fortney, J. J., & Marley, M. S. 2008, ApJ, 682, 559
Showman, A. P., & Polvani, L. M. 2011, ApJ, 738, 71
Sobolev, V. V. 1975, Light Scattering in Planetary Atmospheres (International Series of Monographs in Natural Philosophy, Vol. 76; Oxford: Pergamon), 6213
Still, M., & Barclay, T. 2012, PyKE: Reduction and Analysis of Kepler Simple Aperture Photometry Data (Astrophysics Source Code Library)
Strassmeier, K. G. 2009, A&ARv, 17, 251
Sudarsky, D., Burrows, A., & Pinto, P. 2000, ApJ, 538, 885
Tsuji, T. 2002, ApJ, 575, 264
Werner, M. W., Roellig, T. L., Low, F. J., et al. 2004, ApJS, 154, 1
Witte, S., Helling, C., & Hauschildt, P. H. 2009, A&A, 506, 1367

3.5.2 Analytical model for planets optical phase curves with spatial variations of the albedo

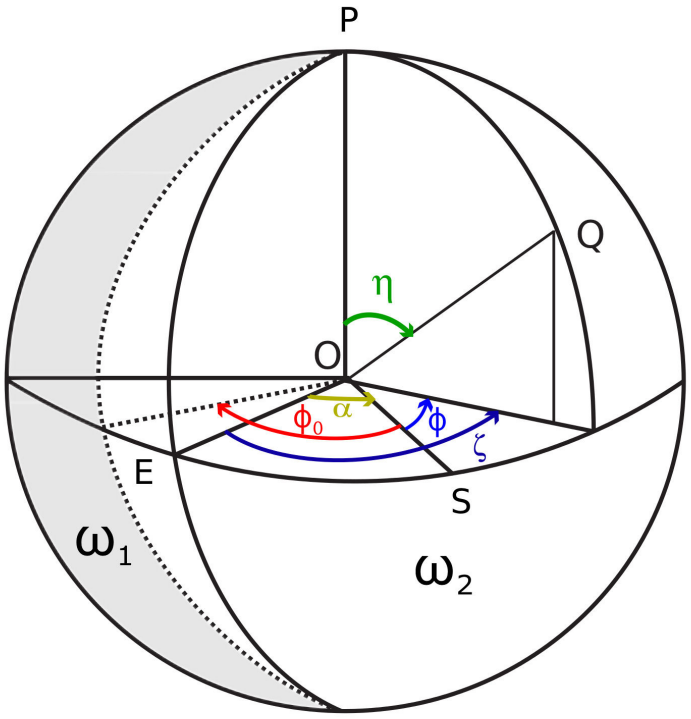

Figure 3.11. Main notations used in this section. Based on a figure from Madhusudhan & Burrows (2012).

The presence of clouds in hot Jupiters seems now ubiquitous. Their signatures appear both in the transit spectrum and the the albedo of numerous planets (see Section 1.2.4 and 1.3.3). Atmospheric circulation of highly irradiated giant planets shapes the horizontal variations of clouds. In particular, the displacement of the hottest point of the planet east of the substellar point should lead to a displacement of the most cloudy part of the dayside hemisphere west of the planet. In Section 3.5.1 we saw observational evidence for this pattern in the phase curve of Kepler-7b. We now derive an analytical model for the optical phase curve of a tidally locked planet with a longitudinal variation of the cloud coverage. Our model is based on more physical grounds than the homogeneously bright bands model used in 3.5.1. It can therefore immediately be linked to physical characteristics of the atmosphere, such as the variations of the single-scattering albedo with longitude.

We consider a planet that is tidally-locked in a 1:1 resonance with its parent star. The coordinate system used afterwards is defined in Figure 3.11. The substellar point is our reference for longitude ϕ and latitude η and is noted S in Figure 3.11. The direction of the Earth is our reference for the angle ζ and is noted E. The angle between the direction of the Earth and the substellar point is the *phase angle* and is noted α. $\alpha \in [-\pi, \pi]$ and during the secondary eclipse of the planet, $\alpha = 0$. The north pole is noted P. Q is a point on the planet, the angle between the earth direction and Q is $\zeta = \alpha + \phi$. The angle between Q and the substellar point is θ_0 such that $\mu_0 = \cos\theta_0 = \sin\eta\cos(\zeta - \alpha)$. The angle between Q and the Earth direction is θ such that $\mu = \cos\theta = \sin\eta\cos\zeta$.

We now assume that the planet's dayside is divided into two zones: west of a point of longitude ϕ_c the planet has a single-scattering albedo ω_1, east of this point it has a single-scattering albedo ω_2. We further suppose that the clouds reflect the stellar light as a Lambertian surface, i.e. that the reflected specific intensity is the same in all directions. A surface $\mathrm{d}S$ of single-scattering albedo ω receives a flux $\mu_* F$ from its star and reflects an intensity (Kattawar & Adams 1971):

$$I = \omega F \mu_0 \tag{3.38}$$

More sophisticated scattering models, such as Rayleigh scattering could be taken into account. Lambert scattering, however, can capture the main features of the planet lightcurve and is easy to handle analytically. The total intensity observed from earth can be calculated by integrating the intensity over the visible planetary crescent (Madhusudhan & Burrows 2012):

$$j(\alpha) = \int_0^{\pi} \sin^2\eta \,\mathrm{d}\eta \int_{\alpha-\pi/2}^{\pi/2} I(\eta,\zeta)\cos(\zeta)\,\mathrm{d}\zeta\,. \tag{3.39}$$

Using expression (3.38), the above expression becomes:

$$j(\alpha) = F\int_0^{\pi} \sin^3\eta \,\mathrm{d}\eta \int_{\alpha-\pi/2}^{\pi/2} \omega(\zeta)\cos(\zeta-\alpha)\,\mathrm{d}\zeta\,.\cos(\zeta) \tag{3.40}$$

The integral on η is trivial and equal to $4/3$. The integral on ζ depends on the phase angle. The intensity then become:

$$\begin{aligned}
j_1(\alpha) &= \frac{4F}{3}\left(\int_{\alpha-\pi/2}^{\phi_c+\alpha} \omega_1\cos(\zeta-\alpha)\cos(\zeta)\,\mathrm{d}\zeta + \int_{\phi_c+\alpha}^{\pi/2} \omega_2\cos(\zeta-\alpha)\cos(\zeta)\,\mathrm{d}\zeta\right) \text{for } \alpha\in[0,\pi/2-\phi_c]\\
j_2(\alpha) &= \frac{4F}{3}\int_{\alpha-\pi/2}^{\pi/2} \omega_2\cos(\zeta-\alpha)\cos(\zeta)\,\mathrm{d}\zeta \text{for } \alpha\in[\pi/2-\phi_c,\pi]\\
j_{-1}(\alpha) &= \frac{4F}{3}\left(\int_{-\pi/2}^{\phi_c+\alpha} \omega_1\cos(\zeta-\alpha)\cos(\zeta)\,\mathrm{d}\zeta + \int_{\phi_c+\alpha}^{\pi/2+\alpha} \omega_2\cos(\zeta-\alpha)\cos(\zeta)\,\mathrm{d}\zeta\right) \text{for } \alpha\in[-\pi/2-\phi_c,0]\\
j_{-2}(\alpha) &= \frac{4F}{3}\int_{-\pi/2}^{\pi/2+\alpha} \omega_2\cos(\zeta-\alpha)\cos(\zeta)\,\mathrm{d}\zeta \text{for } \alpha\in[-\pi,-\pi/2-\phi_c]
\end{aligned} \tag{3.41}$$

The expression can be simplified defining:

$$f(x,y) = \int_x^y \cos(\zeta)\cos(\zeta-\alpha)\,\mathrm{d}\zeta\,, \tag{3.42}$$

that can be expressed as:

$$f(x,y) = \frac{1}{4}\left(-2(x-y)\cos(\alpha) + \sin(\alpha-2x) - \sin(\alpha-2y)\right)\,, \tag{3.43}$$

Using the Heaviside function ($\mathcal{H}(x) = 0$ for $x<0$ and 1 for $x>0$), we can merge the different

expressions in (3.41) and obtain one expression for the mean intensity valid for $\alpha \in [-\pi, \pi]$:

$$\begin{aligned} j(\alpha, \phi_c) =& \frac{4F}{3} \times \\ & \{ \left[\omega_1 f(\alpha - \pi/2, \alpha + \phi_c) + \omega_2 f(\alpha + \phi_c, \pi/2)\right] \mathcal{H}(\alpha)\mathcal{H}(-\phi_c - \alpha + \pi/2) \\ & + \omega_1 f(\alpha - \pi/2, \pi/2)\mathcal{H}(a)\mathcal{H}(\phi_c + \alpha - \pi/2) \\ & + \left[\omega_1 f(-\pi/2, \alpha + \phi_c) + \omega_2 f(\alpha + \phi_c, \pi/2 + \alpha)\right] \mathcal{H}(-a)\mathcal{H}(\phi_c + \alpha + \pi/2) \\ & + \omega_2 f(-\pi/2, \pi/2 + \alpha)\mathcal{H}(-a)\mathcal{H}(-\phi_c - \alpha - \pi/2) \} \ , \end{aligned} \tag{3.44}$$

The phase curve is obtained by :

$$\psi_{\phi_c}(\alpha) = \frac{j(\alpha, \phi_c)}{j(0, \phi_c)} \, , \tag{3.45}$$

where $j(0, \phi_c)$ is given by:

$$j(0, \phi_c) = \frac{2F}{3} \left[\pi \frac{\omega_1 + \omega_2}{2} + (2\phi_c + \sin 2\phi_c) \frac{\omega_1 - \omega_2}{2} \right] . \tag{3.46}$$

The geometric albedo of the planet can be calculated as:

$$A_g = \frac{j(0, \phi_c)}{\pi F} \, . \tag{3.47}$$

For $\phi_c = \pi/2$ we obtain a geometrical albedo $A_g = 4\omega_1/3$ and for $\phi_c = -\pi/2$ we obtain $A_g = 4\omega_2/3$, which are the expected values. The planet-star flux ratio observed at Earth as a function of the phase angle is given by:

$$\frac{F_p}{F_*} = A_g \left(\frac{R_p}{a} \right)^2 \psi_{\phi_c}(\alpha) \tag{3.48}$$

The model was used to fit the Kepler-7b lightcurve described in Section 3.5.1. As shown in Figure 3.12 it provides a fit almost as good as with the model used in Section 3.5.1. This model assumes Lambertian scattering of the clouds whereas the model of Section 3.5.1 assumes constant brightness surfaces. This model is therefore built on more physical ground and allows the retrieval of physical characteristics of the atmosphere. For a model with two bands of different albedos, we retrieve $\omega_1 \approx 1$, $\omega_2 \approx 0.1$ and $\phi_c \approx -14°$, leading to a geometrical albedo for the dayside of the planet of $A_g \approx 0.27$, a value slightly smaller than derived by Demory et al. (2011). Our model can directly be related to the single scattering albedo, a fundamental parameters to understand exoplanets' atmospheres. We find a high albedo $\omega_1 = 1$ on the west of the dayside and a small albedo $\omega_2 \approx 0.1$ on the east of the substellar point. The value $\omega_1 = 1$ corresponds to an atmosphere dominated by the scattering by cloud particles. The value $\omega_2 = 0.1$ is compatible with the expected value for clear-sky hot Jupiters atmospheres (*e.g.* Sudarsky et al. 2000).

Although the best fit phase curves from our model and from Demory et al. (2013) are similar (compare the plain and the dotted lines of Figure 3.12), the retrieved clouds longitude is different ($-14°$ compared to $+30°$). This difference is due to the different physical parametrization of the planet flux. Whereas Demory et al. (2013) assume different bands of constant brightness, we assume different bands that reflect the stellar irradiation as a Lambertian surface. Thus, the difference in ϕ_c between the two models must be considered as part of the total uncertainty on ϕ_c.

Our model does not fit correctly the beginning of the phase curve. In order to represent the sharp decrease observed, our model would need a single scattering albedo higher than 1. At those planet phases, near transit, forward scattering might become significant and a more sophisticated scattering model, such as Rayleigh scattering might provide a better fit.

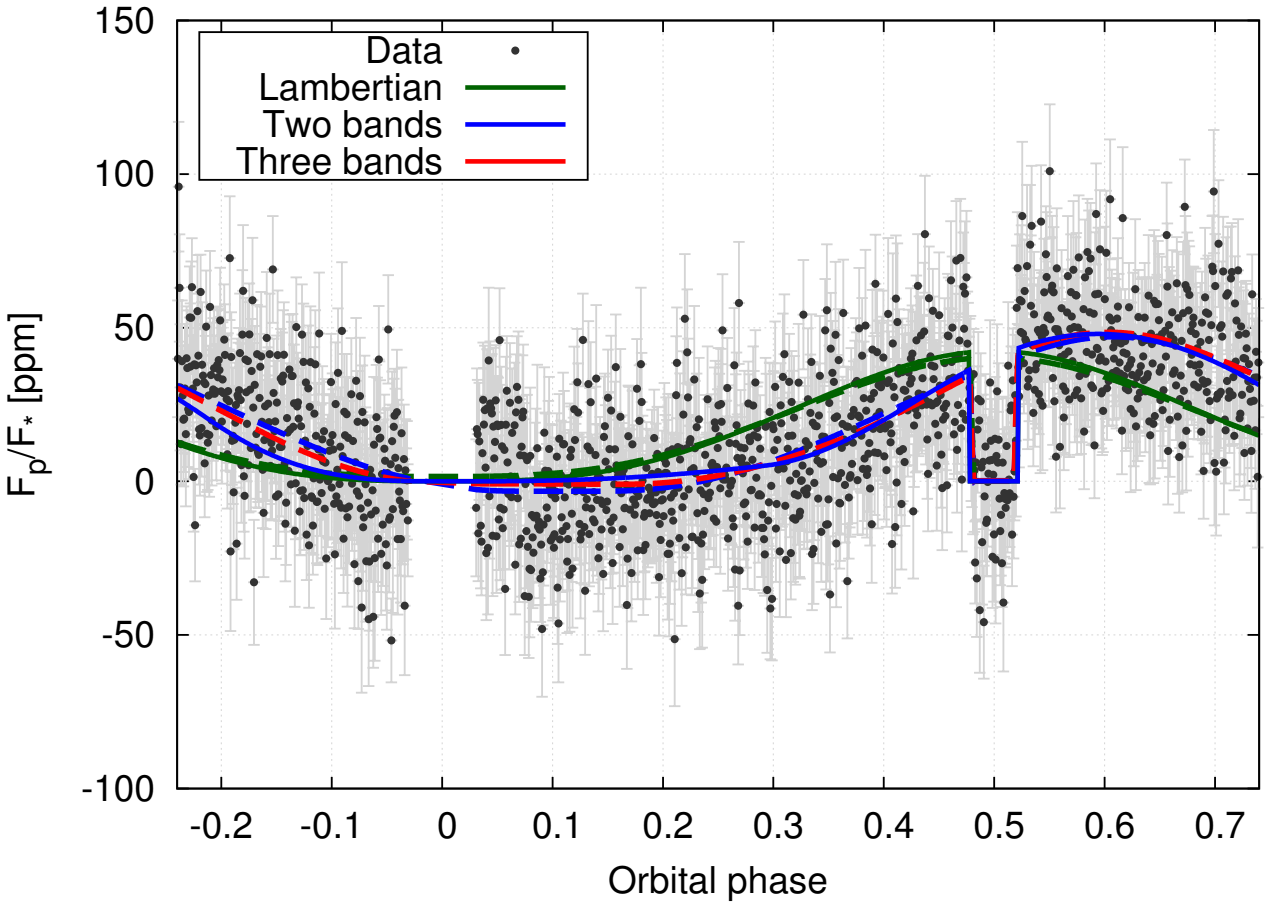

Figure 3.12. Phase curve of Kepler-7b as modeled with the multi-band Lambertian model (plain lines) or with multi-bands of constant brightness (dotted lines) such as in Demory et al. (2013).

Conclusion

Atmospheric dynamics is the main physical process that drives the atmosphere out of radiative equilibrium. The atmospheric motions can transport heat and material over the whole planet. Particularly, a fast equatorial superrotating jet transports heat and material between the hot dayside and the cold nightside.

In the dayside, the atmospheric circulation lead to an eastward shift of the hottest point of the planets that is observed in the thermal phase curves. The amplitude of the day/night temperature contrast is also set by the circulation: the hotter the planet, the greater the day/night contrast.

In the nightside a wealth of species can condense and form clouds. The consecutive advection of the clouds toward the dayside of the planet leads to longitudinal variations of the clouds. In particular, a westward displacement of the most reflective point of the planet have been observed in Kepler-7b and interpreted as a dayside with a cloudy western part.

The chemical composition should also be affected by the circulation. Species that condense on the nightside of the planet can rain out and disappear from the whole atmosphere. Moreover,

species that does not condense have slower chemical reactions in the cold nightside and might be unable to reach chemical equilibrium.

Thermal structure and atmospheric composition are therefore strongly affected by the atmospheric dynamics. In the following chapter, we see how they both affect the long term evolution and thus the observed radius of planets.

L'homme n'a point de port, le temps n'a point de rive ;
Il coule, et nous passons !

Alphonse de Lamartine - Le lac

Chapter 4

Structure and evolution of exoplanets

Contents

Introduction

In the last decade, we discovered planets of all possible radii ranging from Mercury's to twice the one of Jupiter. By measuring their masses, we realized that, for a given planetary mass, the radius of a planet can vary by a factor two or more (see Figure 4.1). This large radius range directly translates into a range of bulk densities: planets with similar masses can have widely different internal structures.

The ingredients to build planets are usually separated into four components: iron, silicates (so-called "rocks"), water and hydrogen/helium. Given the large density ratio between those main components, the radius of a planets is mainly determined by the relative abundances of iron, rocks, ices and hydrogen/helium. Different compositions can, however, lead to planets with similar radius. Determining the composition of a planet based on its mass and radius only is therefore a difficult task.

Planets form hot and cool down with time. The current state of a planet therefore depends on its age and its ability to transport its energy from the deep layers to the outer space. By regulating the exchanges between the planet and its surroundings, the atmosphere plays an important role in the planet history. This is of particular importance for planets dominated by a large H/He envelope as their radius is very sensitive to their entropy content.

In this chapter we first discuss the main equations that determine the internal structure and evolution of planets. Then we focus on the physical mechanisms that determine the radius of gas giant planets. Finally, we discuss the possibility to determine the composition of smaller planets for which iron, rocks and water form a significant part of the mass.

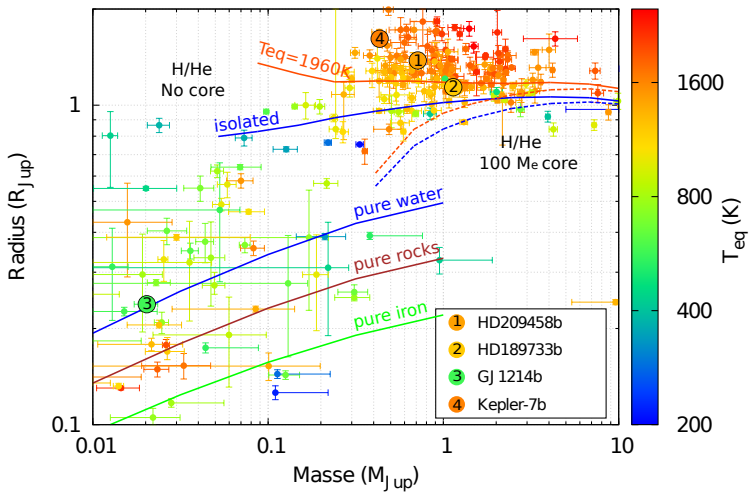

Figure 4.1. Mass-radius relationship for planets with different compositions. Pure H/He planets of 4.5 Gyr are plotted as plain lines (isolated planet in blue and $T_{\rm eq}$ = 1960K in red). Giant planets with a $100 M_{\rm Earth}$ core are plotted as dotted lines. The relationships for an hypothetical pure iron, pure rocks or pure water planets are also shown. All the exoplanets with a known mass and radius are overplotted and color coded by their equilibrium temperature assuming zero albedo.

4.1 Structure and evolution

4.1.1 Basic equations

Conversely to stars, planets are too small to trigger nuclear reactions in their deep interior. Gravitational and radioactive energy, however, still need to be evacuated from the interior of the planet

to the outer space. At any given time, the planet is in hydrostatic equilibrium: the pressure gradient balances the self-gravity of the planet. As the planet radiates energy out, it cools down.

The interior of a planet can be indexed by the mass M that lays below a given layer. The structure is described by the variations with mass of the radius, the pressure, the temperature, the luminosity and the density.

The pressure balances the gravity and maintains a quasi-static equilibrium. The gravity force acting on a spherical shell of mass $\mathrm{d}M$ with a mass M below it is $GM\mathrm{d}M/R^2$ whereas the pressure gradient force is given by $4\pi R^2 \mathrm{d}P$. Hydrostatic equilibrium can therefore be written:

$$\frac{\partial P}{\partial M} = -\frac{GM}{4\pi R^4}\,. \tag{4.1}$$

The mass conservation equation links the radius and the mass: the mass of a spherical shell of radius $\mathrm{d}R$ situated at a radius R from the center of the planet is $\mathrm{d}M = 4\pi R^2 \rho \mathrm{d}R$ where ρ is the local density. Thus, the mass conservation can be written:

$$\frac{\partial R}{\partial M} = \frac{1}{4\pi R^2 \rho}\,. \tag{4.2}$$

The variation of the temperature with mass is usually expressed as a function of the temperature gradient $\nabla_\mathrm{T} = \frac{\partial \log T}{\partial \log P}$:

$$\frac{\partial T}{\partial M} = \left(\frac{\partial P}{\partial M}\right)\frac{T}{P}\nabla_\mathrm{T}\,. \tag{4.3}$$

This equation does not actually contain physical information until the temperature gradient is specified. ∇_T depends on the exact mechanism transporting the energy through the planet. This is further discussed in Section 4.1.2

The luminosity is the energy radiated away by the planet. This energy either originates from the surroundings of the planet, such as the stellar irradiation absorbed and re-emitted by the atmosphere, or from the planet itself (so-called *intrinsic luminosity*. The intrinsic luminosity originates from the planet interior and is transported to the surface where it is radiated to space. In the following, we call *luminosity* L the *total* energy that crosses a spherical surface of radius R in a time $\mathrm{d}\,t$. This energy can be transported by radiation, conduction, convection or any other way. Local energy sources can originate, for example, from nuclear reactions (for large objects), latent heat release or chemical reactions. The internal energy of the material can also be converted into luminosity. We write the conservation of energy:

$$\frac{\partial L}{\partial M} = \dot{\epsilon} - T\frac{\partial S}{\partial t}\,, \tag{4.4}$$

where $T\frac{\partial S}{\partial t}$ is the contribution of the internal energy of the material and $\dot{\epsilon}$ stands for any other source of energy.

Finally, the equation of state links the values of P and T to the values of S and ρ. It is an intrinsic property of the medium that can be calculated *a-priori* from *ab-initio* calculation or can be measured in laboratory experiments. For example, from the Helmholtz free energy per unit mass of the system (denoted F) we can retrieve the entropy and the density via the relationships :

$$S = -\frac{\partial F}{\partial T}\,,\; P = \frac{\partial F}{\partial \rho} \tag{4.5}$$

Equations 4.1 to 4.5 are five equations that allow to solved our five variables (pressure, temperature, radius, density and luminosity) provided an initial condition (i.e. the whole structure at $t = 0$) and a boundary condition (i.e. the values of the variable at some points in the model). The boundary condition for L and R can be taken at the bottom of the model: at $M = 0$, $R = 0$ and $L = 0$. The boundary conditions for P, T and ρ are usually taken at the top of the model and necessitate an accurate atmospheric model, such as the one derived in Chapter 2.

At a time t, the internal structure is characterized by $T(M)$, $P(M)$, $R(M)$, $L(M)$ and $\rho(M)$. During the interval $\mathrm{d}t$, the planet looses $4\pi R_\mathrm{p} L(M_\mathrm{p})\mathrm{d}t$ of energy to space via atmospheric radiation. The top boundary condition is therefore modified and the internal structure can be recalculated. Planets interior are initially hot and usually cool down with time. Their physical properties at a given time depend on their history, particularly on their capacity to transport their internal heat outward. For example, for solid planets, the energy transport is the main driver of the plaque tectonics. Because plaque tectonics enhances the interactions between the planet interior and its atmosphere, the thermal evolution of solid planets is important to understand their current atmospheric composition. For planets with a significant amount of hydrogen and helium, the thermal history have a strong influence on the observed radius of the planet itself: as the planet cools down, the hydrogen/helium envelop contracts leading to a smaller radius.

4.1.2 Energy transport

The internal structure and evolution of a planet is determined by its ability to transport energy from the deep interior to the outer space. The energy present in the planet interior results mainly from the accretion phase. For solid planets, some of the energy originates from radioactive heating. The energy is mainly transported by convection, radiation and conduction.

Radiative transport

We derived in Chapter 2 the equations for the temperature structure when the energy is transported by radiation. The radiative transfer inside the deep interior of the planet is best modeled by the so-called *diffusion approximation*: the opacities are considered grey and equal to the Rosseland mean opacity. The temperature gradient is then (Guillot & Morel 1995):

$$\nabla_\mathrm{rad} = \frac{\partial \log T}{\partial \log P} = \frac{3}{64\pi G\sigma}\frac{\chi_\mathrm{R} L P}{M T^4} \,. \tag{4.6}$$

The temperature gradient is directly proportional to the luminosity: a large gradient transports more flux than a small one. The gradient is inversely proportional to the temperature to the fourth power: the hotter the gas and the easier the transport. It is also proportional to the Rosseland mean extinction opacity χ_R. The larger the opacity, the more difficult is it to transport the luminosity by radiation. In gas giant planets, the opacities increase rapidly with pressure, inhibiting the radiative transport of energy in the deep interior.

In the atmosphere, the diffusion approximation does not hold and a more sophisticated radiative transfer model, such as the model developed in Chapter 2 is needed.

Conductive transport

When conduction is the main transport of energy, the transported flux can be directly related to the temperature gradient via the standard diffusion equation:

$$\vec{F} = -K_{\rm c} \nabla T \,, \tag{4.7}$$

Where $K_{\rm c}$ is the thermometric conductivity. An equivalent conductive opacity can be defined:

$$\kappa_{\rm c} = \frac{16}{3} \frac{\sigma T^4}{\rho K_{\rm c}} \,. \tag{4.8}$$

Both the radiation and the conduction can be represented by a diffusion law. We can thus define a conductive+radiative opacity:

$$\frac{1}{\kappa} = \frac{1}{\kappa_{\rm R}} + \frac{1}{\kappa_{\rm c}} \,. \tag{4.9}$$

Conduction becomes important in opaque and viscous medium such as the interior of solid planets. It is also important in the deep layers of giant planets, where degenerate electrons efficiently conduct the heat.

Convective transport

When the temperature gradient needed to transport the luminosity by either radiation or conduction is too large, the medium becomes unstable to convection. The threshold is given by the Schwarzschild criterion:

$$\nabla_{\rm T} > \nabla_{\rm ad} \,, \tag{4.10}$$

where the adiabatic gradient is an intrinsic property of the material and is given by its equation of state:

$$\nabla_{\rm ad} = \left. \frac{\partial \log T}{\partial \log P} \right|_S \,. \tag{4.11}$$

When convection dominates the transport of energy, the temperature gradient is equal to the adiabatic temperature gradient and is independent of the transported flux: a higher flux is transported by faster convective movements. When viscosity, rotation or radiative losses become important, this is no more true and the gradient can become higher than the adiabatic one.

4.1.3 Equation of state

The equation of state is an intrinsic property of the mixture of material considered. It links the density and the entropy of a material to its pressure and temperature. For planets, the temperature and pressure vary by several orders of magnitude between the atmosphere and the core. Pressure varies from $\approx$ 1 bar or less in the atmosphere to $\approx$ 300 GPa and $\approx$ 10TPa at the center of an Earth-like and a Jupiter-Like planet respectively. Temperature ranges from $\approx$ 100 to $\approx$ 1000 K in the atmosphere (depending on the stellar irradiation) to 6000 K in the center of the Earth and 20000 K in the center of Jupiter.

Determining the equation of state for materials at these high temperatures and pressures is challenging. In the last decade, the increase of the experimental capacities and the development of first principle calculations led to major advances in our knowledge of the state of matter in conditions relevant for planetary interiors.

Mainly two types of experiments have been carried. The first way to reach large pressure is to apply directly a strong force on a material: the sample is placed in between two diamonds and a strong pressure is applied. The sample can be characterized through the diamond and characterize via its interactions with an electromagnetic radiation (absorption of light, diffraction of X-rays etc..). The sample is heated by a laser so large temperatures can be obtained. The pressure and the temperature can therefore be set independently and a good coverage of the pressure/temperature space can be obtained. Pressures up to ≈ 300 GPa and temperatures up to 5000 K have been reached with this mechanism (Anzellini et al. 2013). This is relevant for the study of the core of the Earth, but far from the conditions in the central parts of Jupiter.

Higher pressures, usually of the order of 100 GPa and up to 2 TPa can be reached by shock compression experiments (see for example Mochalov et al. 2012). The sample is placed in the middle of numerous powerful lasers. The ignition of all the lasers at the same time produces a shock wave that crushes the sample. The rapid compression heats the sample and the pressure and temperature of the sample follows an isentropic curve. The main drawback is that shock compression experiments can probe the pressure/temperature plane along isentropic curves only and the equation of state has to be extrapolated beyond.

The numerical calculation of the equation of state has become feasible with the recent advances in computer technology. Today, it is possible to solve the Schrödinger equations for a set of ≈ 100 interacting molecules. Those *ab-initio* calculations can be performed for all the pressure and temperature range relevant for planetary interiors. As an example, French et al. (2009) calculated the equation of state of water up to 10 GPa to 10 TPa and from 3000 to 24000 K (see also Militzer & Hubbard 2013, for an equivalent work on a hydrogen/helium mixture). Several limits remain in these calculations. For example, the number of molecules considered is usually less than 100 and, in the case of mixtures, only one molecule of a given compound is considered (see Wilson & Militzer 2012a,b, for the solubility of water and rocks in metallic hydrogen). Such calculations should thus always be validated by a comparison with direct compression and shock wave experiments.

For most compounds, the equation of state is determined experimentally at a limited number of points. At low pressure $P < 100$ GPa, parametrized equations of state are used and calibrated to match the direct compression experiments. The Vinet and Birch-Murnhagan formulations, based on a series expansion of the inter-atomic binding energy are commonly used for isothermal bodies. When the temperature dependence becomes important, the Mie-Gruneisen-Deby formulation is usually preferred. At very high pressures ($P > 10$ TPa), the electrons become degenerate and dominate the pressure. The equation of state becomes independent of the exact structure of the solid atoms and the Thomas-Fermi-Dirac equation, based on quantum mechanics calculations is used. In the intermediate range (100 GPa $< P <$ 10 TPa), our knowledge of the equation of state rely on a few, extrapolated, shock compression experiments. Different techniques can be used to extrapolate the equation of state in this region. Seager et al. (2007) interpolated between the Birch-Murnhagan and the Thomas-Fermi-Dirac equations. Grasset et al. (2009) preferred to use ANEOS, a code initially set up set up for shock physics studies and providing analytic equation of state for many materials. Although the extrapolations used in ANEOS are not explicitly stated, it has the advantage to provide an homogeneous model for all necessary species. For some compounds, mainly water, hydrogen and hydrogen/helium mixture, *ab-initio* calculations have been performed. Recent results on shock compression of water show that these *ab-initio* calculations were in good agreement with the experiments (Knudson et al. 2012). When possible, they should therefore be used in this intermediate pressure range.

4.2 Gas giant planets

We now focus more specifically on the internal structure of gas giant planets. Those were the first exoplanets to be discovered and the ones with the better determination of the radius and the mass. We first describe the standard model for the internal structure and evolution of those planets. Then, we focus on a major mystery of this last decade: the radius anomaly of hot Jupiters. Finally, we discuss some unpublished work on the influence of the atmosphere in the evolution of giant planets.

4.2.1 Standard model

Initial condition

Gas giant planets are believed to form either by core-accretion or by gravitational instability. In the first scenario, a rocky core forms inside the protoplanetary disk and slowly accretes the surrounding gas. Once it reaches a critical mass, a runaway accretion process occurs where the accretion rate is mostly limited by the density of the protoplanetary disk. During this runaway accretion phase, a one Jupiter mass planet can accrete its envelope in ≈ 30000 years (Marley et al. 2007). Infalling materials form a shock that can efficiently radiate away the initial energy of the gas. Thus the resulting planet has a low entropy content. Gravitational instability is a much more violent process. Once a sufficiently large clump of density appears in the protoplanetary disk, it collapses from a size of hundreds of Jupiter radii down to some Jupiter radii in less than a year (Bodenheimer et al. 1980). In that case, the gas cannot radiate away its initial energy (Vaytet et al. 2013) leading to a high entropy planet.

Once this formation phase is over, the planet is in quasi-static equilibrium and its radius slowly shrinks while it releases its internal energy. The two different scenarios described above lead to two different possible initial conditions for the following evolution of the planet. If the gas forming the planet efficiently releases its gravitational energy during the planet formation, the planet history begins in a low entropy state, referred as a *cold start*. Conversely, if the gas forming the planet kept its gravitational energy during the formation process, the initial internal structure has a larger entropy, a situation referred as a *hot start*.

Recent calculations by Mordasini (2013) showed that the size of the initial core influences the energy release during the runaway accretion. Planets with a very high core mass could therefore begin their life as *hot* even if they formed via the core-accretion scenario. Thus, *cold* and *hot* starts might not reflect the complex reality of the planetary formation process. They should be considered as two extreme cases for the initial state of a giant planet, with all intermediate states being possible (Spiegel & Madhusudhan 2012).

As shown in Figure 4.2, hotter planets cool faster than colder planets and the radius after gigayears of cooling is not affected by the initial condition. When modeling young planets, the initial condition is thus primordial but can be approximate when modeling old planets.

Heavy element content

The total heavy element mass of a giant planet influences directly its evolution by increasing its ability to contract. At a given time, a planet with a larger heavy element mass should be smaller than a pure hydrogen/helium planet. This sensitivity is used to determine the heavy

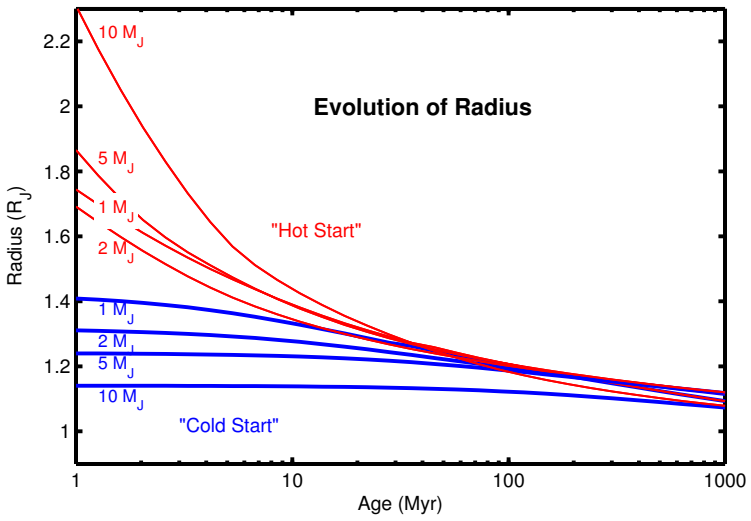

Figure 4.2. Radius as a function of time for planets with different masses for a *cool* (blue lines) or a *hot* initial conditions. Figure from Spiegel & Burrows (2012).

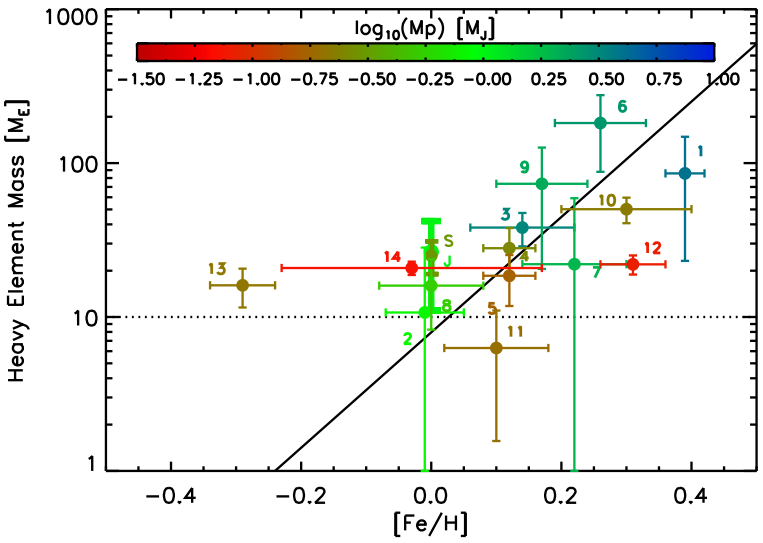

Figure 4.3. Stellar metallicity and inferred planet heavy element mass for gas giant exoplanets with an equilibrium temperature lower than 1000K, assuming zero albedo. The mass of the planet is color-coded. Only few gas giants have been observed around metal-poor stars (Fischer & Valenti 2005), and only HAT-P-12b (planet 13) is shown here. The large error bars are due to the poor constrains on other parameters, such as the atmospheric opacities, the equation of state or the age of the system. Figure from Miller & Fortney (2011)

element content of exoplanets for which we know the radius, the mass and the age. As shown by Guillot (2008), the mass fraction of heavy elements present in giant exoplanets is correlated with the metallicity of the host star. Metal-rich stars harbor planets with a larger fraction of heavy elements than metal-poor stars. The radius anomaly (see section 4.2.2 hereafter) of hot Jupiters, however, perturbs the determination of the heavy element mass for those planets. Miller & Fortney (2011) performed the same analysis on a sub-sample of planets that are further away from their host star, removing the uncertainty due to the planet-star interactions. As shown in Figure 4.3, the correlation between the planet heavy element content and stellar metallicity is still present and no planet seems to possess less than $\approx 10 M_{\rm Earth}$ of heavy elements, which gives an important constraint for planet formation models.

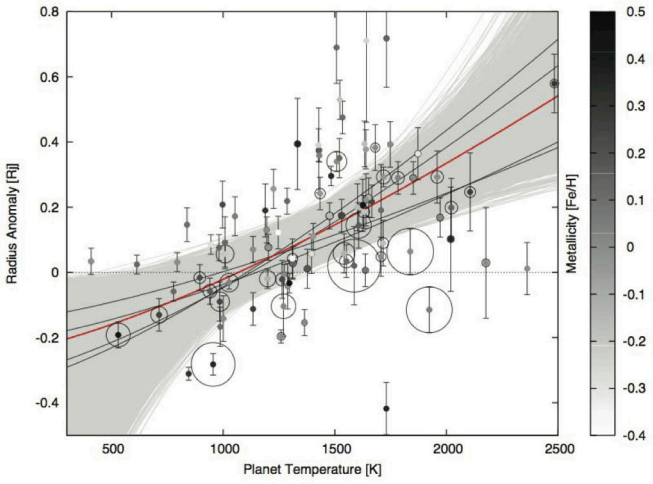

Figure 4.4. Radius anomaly of giant exoplanets *vs.* the planet equilibrium temperature for zero albedo. The circles are proportional to the mass of the planet. The red line is the best power-law fit of the data. The grey lines show analogous best-fit power laws to bootstrapped data sets. The black lines show the 5^{th}, 15^{th}, 85^{th} and 95^{th} percentile bootstrap. The 1σ confidence is roughly given by the 15^{th} and 85^{th} percentile fits. The resulting best fit power law is $\mathcal{R} \propto T^{1.4\pm0.6}$. Clearly, planets with equilibrium temperatures greater than 1000K are inflated. Figure from Laughlin et al. (2011)

4.2.2 Radius anomaly

Observations

Figure 4.1 shows that the majority of hot Jupiters have larger radii than the expected radius for pure H/He planet irradiated by its parent star. The difference between the observed radius of a giant exoplanet and the expected radius of a pure H/He irradiated planet, known as the *radius anomali* is presented in Figure 4.4. The radius anomaly is clearly correlated with the equilibrium temperature of the planet: the hotter the planet, the larger the radius anomaly. Proposed mechanisms to explain this trend consist in slowing down the planet's contraction, either by inhibiting the energy transport from the interior to the outer space or by injecting an extra source of energy in the deep layers of the planet. In the later case, an extra energy source of $\approx 1\%$ of the received stellar irradiation deposited close or below the radiative/convective boundary is sufficient to explain most, but not all, radius anomalies (*e.g.* Guillot & Showman 2002; Baraffe et al. 2003; Guillot 2005; Burrows et al. 2007; Guillot & Havel 2011). However, none of the proposed theories to transport this $\approx 1\%$ extra energy in the deep layers of the planet was confirmed neither ruled out by the observations, mainly because of the large range in the calculated radius anomaly and the lack of self-consistent models of the atmosphere and the interior of those planets.

Direct deposition of the stellar flux

A first natural hypothesis to slow down the contraction of the planet is that the stellar irradiation directly penetrates in the optically thick layers of the planet. As shown by Guillot (2010) (see also Burrows et al. (2007)), dividing the visible to thermal opacity ratio by a factor of ten allows the deposition of enough stellar flux in the optically thick part of the atmosphere to explain the inflated radius of the planet HD 209458b. Such a variation in the opacities would lead to an increase of 1000K compared to what is expected for a Solar-metallicity atmosphere. A metal-free atmosphere, for example, would provide low enough opacities. However, the detection of sodium and water in hot Jupiters atmospheres rule out such an unexpected composition. The hypothesis

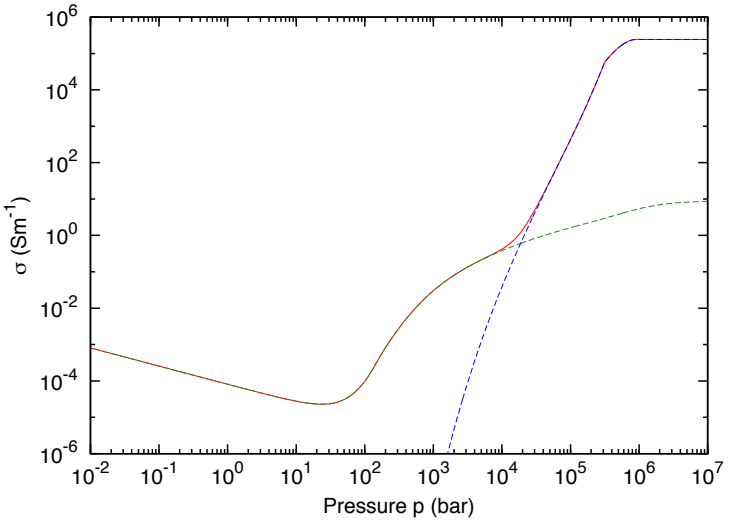

Figure 4.5. Conductivity inside the interior of a hot Jupiter model with an isothermal atmosphere at 1500K down to a pressure of 10bar. The contributions from alkali metals (dashed green curve) and hydrogen (dashed blue curve) are shown. From Huang & Cumming (2012)

of a direct deposition of the stellar flux seems therefore unlikely.

Kinetic energy transport

The second natural idea to transport some of the energy from the stellar irradiation to the deep layers of the planet is via the atmospheric circulation. The strong day/night contrast in the received irradiation produces a large scale atmospheric circulation. The kinetic energy present in the circulation could be transported and deposited in the deep atmospheric layers, either via direct advection or via gravity waves (Guillot & Showman 2002; Showman & Guillot 2002). Cooper & Showman (2005) found that kinetic energy was indeed still propagating downward after 5000 days of simulations. However, no current atmospheric models are able to reach an equilibrium at pressures larger than $\approx$ 3bar due to the large physical timescales at those pressures and the total kinetic energy transport may depend on the set of equations solved (*e.g.* primitive *vs.* Navier-Stokes) (Mayne et al. 2014). Several mechanisms to dissipate this energy at those pressures of been proposed (viscous damping, turbulent mixing (Youdin & Mitchell 2010), thermal tide (Arras & Socrates 2010), shocks (Heng 2012), breaking waves...) but have not been self-consistently studied yet. Thus, the kinetic energy transport hypothesis remain to be tested.

Ohmic dissipation

Ohmic dissipation is another way to transport and dissipate the kinetic energy of the atmospheric winds into the deep layers of the planet. Hot Jupiters atmospheres can reach temperatures of 1000K or more. These temperatures are not high enough to ionize H or He significantly; however, alkali metals, mainly potassium and sodium (Huang & Cumming 2012) should be partially ionized. The electrical conductivity of hot Jupiter should therefore be high both in the interior, where it is dominated by the ionized hydrogen, and in the atmosphere, where it is dominated by the ionization of alkali metals (see Figure 4.5).

An electric current is naturally produced by the large scale circulation of hot Jupiters atmospheres, especially by the equatorial superrotating jet (see Chapter 3). Interactions between this current and the planetary magnetic field produce an induced current that plunges into the deep interior of the planet where it can be dissipated by Ohmic dissipation. Whether Ohmic dissipation

can deposit enough energy in the convective zone to explain the inflated radii of hot Jupiters is unclear. First pioneering studies by Batygin & Stevenson (2010) showed that inflating hot Jupiters with Ohmic dissipation was so easy that it could even lead to the evaporation of some planets Batygin et al. (2011). Self-consistently solving for the internal structure of the planet and the Ohmic dissipation simultaneously is a difficult task. First of all, as the conductivity is a strong function of pressure, most of the Ohmic dissipation that contributes to the inflation of the planet occurs in the uppermost layers of the convective zone (Wu & Lithwick 2013). Thus, a small change in the depth of the radiative/convective boundary can affect the efficacy of the process. Particularly, Ohmic dissipation itself pushes the radiative/convective boundary at deeper pressures, adding to the aforementioned uncertainties concerning the depth of the radiative/convective boundary in giant exoplanets. More importantly, the efficiency of the Ohmic dissipation (the fraction of the irradiation that is converted to Ohmic power) is crucial to understand the strength of the process. Typically an efficiency smaller than $\approx 1\%$ cannot explain the radius anomalies of hot Jupiters. This efficiency, however, depends strongly on the details of the atmospheric temperature structure, composition and dynamics. The large atmospheric temperature contrast expected in hot Jupiters atmospheres should influence this efficiency as the ionization rate is an exponential function of the temperature. The wind pattern is also fundamental to understand Ohmic dissipation. As shown by Perna et al. (2010), Ohmic drag could limit the wind speed of ionized atmospheres. In the hottest hot Jupiters, magnetic interactions could change the nature of the circulation (Batygin et al. 2013). Eventually, wind speed one order of magnitude larger than predicted by full MHD simulations at $P > 10$bar (Rogers & Showman 2014) or very large (up to 1000G) induced magnetic fields (Huang & Cumming 2012) seem necessary to raise the efficiency of the Ohmic dissipation mechanism and explain the inflated radii of hot Jupiters.

Layered convection

Most giant planets interior models assume an homogeneous envelope. However, heavy elements in the envelope could have an inhomogeneous distribution. The presence of compositional gradients through the planet could lead to layered convection, a state where numerous convective zones are separated by zones where the transport of heat and material is done by diffusion (see Figure 4.6 and also Chabrier & Baraffe 2007; Leconte & Chabrier 2012). The bottleneck for the heat transport toward the outer space becomes those numerous diffusive layers. Convection is then much less efficient and the evolution of the planet is slowed down. Although layered convection is a possible state for the interior of giant planets, its presence and magnitude cannot be measured easily. The Juno mission arriving at Jupiter should constrain the deep interior density profile and might shed light on the possibility of layered convection. For exoplanets, even if layered convection plays a significant role, it is not correlated with the distance to the star and thus cannot explain by itself the radius anomaly of hot Jupiters.

4.2.3 The role of the atmosphere

Irradiation from the parent star

Because hot Jupiters orbit very close to their parent star, the atmospheric thermal structure is strongly affected by the intense stellar flux. As proposed by Guillot & Showman (2002) and as shown in Figure 4.7, the stellar irradiation stabilizes the atmosphere against convection and a

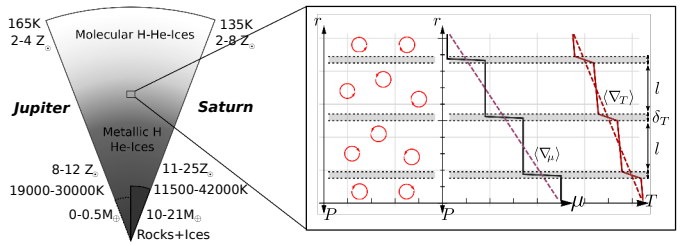

Figure 4.6. Schematic representation of the interior of Jupiter and Saturn with an interior dominated by layered convection (left), with the resulting compositional and thermal radial profiles (right). The abundance of metals is constant within the well mixed convective cells and undergoes a steep variation within the diffusive interfaces of thermal size δT (grey regions). Thanks to this steep gradient, these interfaces are stable against convection and energy and matter are transported therein by diffusive processes. Because the size of these layers is very small compared with the size of the planet the mean thermal and compositional gradients can be used in good approximation to infer the global planet and structure. From Leconte & Chabrier (2012).

radiative zone that extends to hundreds of bars can develop. In optically thick regions of gas giant planets, radiation is much less efficient than convection to transport the energy[1]. Thus, the presence of a forced deep radiative zone acts as a bottleneck that slows down the energy transport inside the planet. As an example, Figure 4.1 shows the mass-radius relationship for gas giant planets isolated and with an equilibrium temperature of 1960K. At a given mass, the irradiated planet is larger than the isolated one. Although this increase of radius is important, it is not sufficient to explain the large radius of most hot Jupiters. Moreover, the effect could be significantly smaller depending on the redistribution of heat in the planet : if the convective zone can reach lower pressures at the poles (Rauscher & Showman 2014) or in the night side (Budaj et al. 2012) than predicted by the averaged temperature profile, the cooling might be much more efficient (see also Spiegel & Burrows 2013).

Atmospheric composition

The chemical composition of the atmosphere has a major role in setting the opacities. A key question regarding the atmospheric composition of irradiated planets is the presence of titanium oxide in their atmospheres. In solar composition atmospheres, titanium oxide should dominate the opacities at visible wavelengths (Hubeny et al. 2003; Fortney et al. 2005). As shown in Chapter 2, such a broadband absorber affects the temperature profile in two different ways. First, it increases the absorption of the stellar light, reducing the amount of energy deposited by the star in the deep atmospheric layers. Second, it flattens the spectral variations of the opacities and reduces the efficiency of the non-grey blanketing effect. Those two mechanisms contribute equally to set

[1] As seen in equation (4.6), radiative transport becomes much more efficient in optically thin layers (small κ_R) such as planetary atmospheres or if temperatures are very large, such as in the deep interior of stars

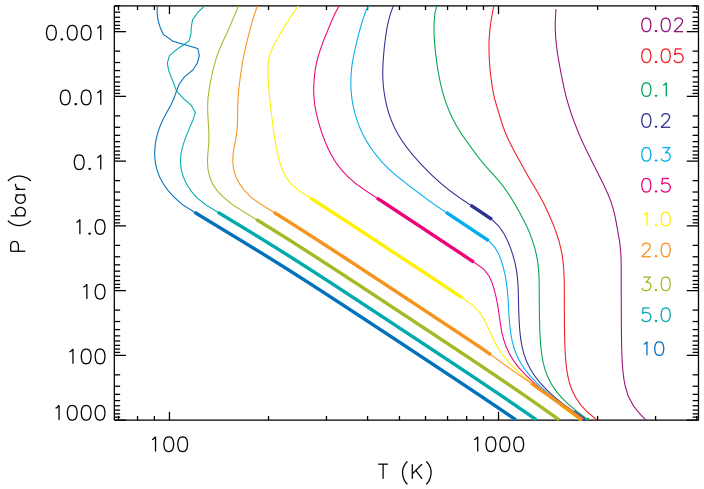

Figure 4.7. Atmospheric pressure-temperature profile of exoplanets from Fortney et al. (2007) as a function of orbital distance. The thick line is the convective zone. The closer the planet to its star, the deeper is the radiative/convective boundary. Figure from Fortney et al. (2007)

the deep atmospheric temperature of irradiated exoplanets. Due to its importance, titanium oxide have been looked for in the transit spectrum of several hot Jupiters but have not been found yet (see Section 1.2.4 for a review of the observations). As proposed by Spiegel & Burrows (2010) and Parmentier et al. (2013) and detailed in Chapter 3, several mechanisms could deplete the atmosphere of hot Jupiters in titanium oxide. Atmospheres without TiO should have higher deep atmospheric temperatures and thus a more extended radiative zone than atmospheres with TiO. This can be studied with the evolution code CEPAM (Code d'Evolution Planetaire Adaptatif et Modulable) developed by Guillot & Morel (1995) solves the equations for the internal structure of the planet using realistic equations of states. I implemented the analytical atmospheric model described in Chapter 2 as a top boundary condition for CEPAM. This allows us to compute the thermal evolution of a gas giant planet with or without TiO. As shown in Figure 4.8, the presence or absence of TiO in the atmosphere of irradiated planets can change the final radius by more than 5%. The importance of TiO for the planet evolution is maximum for equilibrium temperatures of $\approx$ 2000K. At smaller temperatures, TiO condenses and does not contribute to the opacities anymore. At higher temperatures, the collision-induced absorption of hydrogen becomes significant, even in the upper atmosphere, leading to similar opacities in the case with and without TiO.

Plan-parallel approximation

In most atmospheric models, the curvature of the planet is neglected, this is valid as long as the size of the modeled atmosphere is small compared to the size of the planet. Another approximation is the one of constant gravity. As shown previously in table 3.1, both approximations are barely valid for hot Jupiters' atmospheres.

To test how these two approximations may influence the planetary radius, I first developed a 1D, spherical, semi-grey atmospheric model with a varying gravity. To do so I modified the interior model CEPAM to include semi-grey opacities. As explained in Chapter 2, the stellar irradiation can be considered as a source term in the radiative transfer equations. Thus, instead of effectively adding a radiative transfer scheme for the incoming stellar light, we model the absorption of the stellar flux as an ad-hoc input of energy in each layer of the planet, corresponding to the $\dot{\epsilon}$ parameter of the equation (4.4). To determine how much energy is deposited in the atmospheric

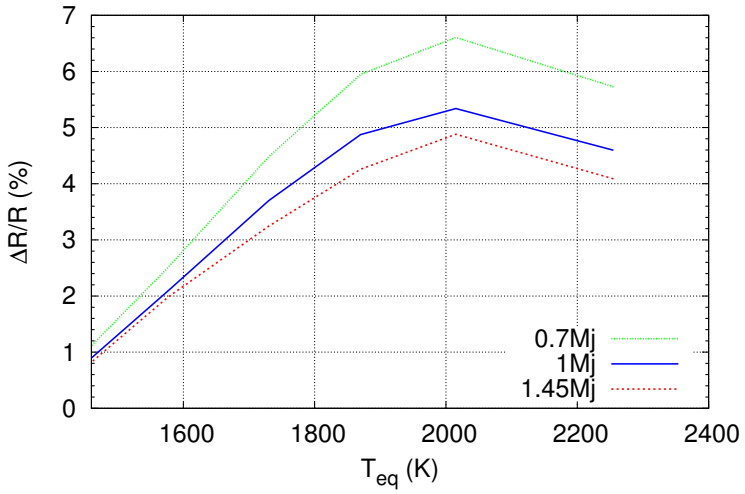

Figure 4.8. Radius increase of a planet due to the absence of titanium oxide in function of the equilibrium temperature of the planet. More massive planets are less sensitive to the presence of titanium oxide in their atmospheres.

layers, we use the atmospheric, plan-parallel semi-grey model of Guillot (2010):

$$T(\tau) = \frac{3T_{\rm int}^4}{4}\left\{\frac{2}{3}+\tau\right\} + \frac{3T_{\rm eq}^4}{4}\left\{\frac{2}{3}+\frac{2}{3\gamma}\left[1+\left(\frac{\gamma\tau}{2}-1\right)e^{-\gamma\tau}\right]+\frac{2\gamma}{3}\left(1-\frac{\tau^2}{2}\right)E_2(\gamma\tau)\right\}, \quad (4.12)$$

where γ is the ratio of the visible to the thermal opacities, $\sigma T_{\rm int}^4$ is the internal flux, $T_{\rm eq}$ is the equilibrium temperature and E_2 is the second exponential integral. The flux transported by the semi-grey atmosphere can be easily calculated :

$$F(\tau) = \frac{{\rm d}\sigma T^4}{{\rm d}\tau} = \frac{3}{4}\sigma T_{\rm int}^4 + \frac{3}{4}\sigma T_{\rm eq}^4\left(2E_3(\gamma\tau) - \frac{2}{3}\gamma^2 E_1(\gamma\tau)\right) \quad (4.13)$$

The first term is the the contribution of the internal luminosity to the flux, which is already taken into account in the CEPAM code. The second term is the contribution of the visible flux. It exhibits a stepper decrease than an exponential because of the greater absorption of the grazing rays (Guillot 2010). The third term comes from the stimulated emission : an incident visible photon can provoke the decay of an excited atom without being absorbed, producing a new photon at the same wavelength in the same direction. The net effect is a smaller absorption of the visible flux. The total energy crossing a layer of radius r in the planet is $4\pi r^2 F$. Thus the energy per mass unit deposited by the stellar irradiation in the semi-grey case is given by:

$$\dot{\epsilon} = \frac{d(4\pi r_2^2 F)}{dm} \quad (4.14)$$

We now have a spherical, semi-grey interior model with varying gravity. This model can be stopped at any given optical depth $\tau_{\rm lim}$ with the analytical expression (4.12) as a top boundary condition. The CEPAM model uses the diffusion approximation to determine the temperature gradient in the atmosphere, which is similar to the Eddington approximation. Thus, the CEPAM model and the (4.12) model are now equivalent formulations of the semi-grey radiative transfer solution, the remaining difference being the varying gravity and the spherical formulation included into CEPAM and not in (4.12) . We test the influence of those approximation by varying the depth of the limit between the two models. As shown in Fig. 4.9, the combined plan-parallel and constant gravity approximations lead to a larger error on the radius of hotter planets. This is

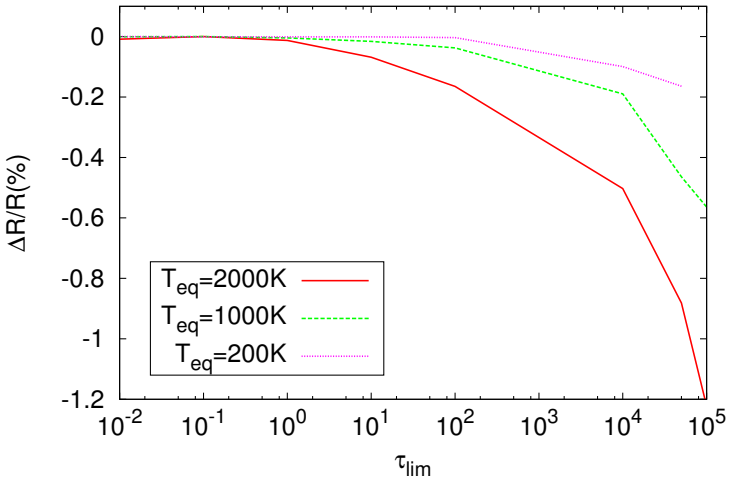

Figure 4.9. Relative variation of the radius of a $1M_J$ planet in function of the infrared optical depth of the boundary atmosphere/interior. The opacities are constant in the whole planet $\kappa_{\rm R} = 10^{-2}\,{\rm cm^2\,g^{-1}}$, $\kappa_{\rm v} = 5{\times}10^{-3}\,{\rm cm^2\,g^{-1}}$. The different curves are for different equilibrium temperatures. All the models assume an internal luminosity of $L_{int} = 5 \times 10^{25}\,{\rm erg\,s^{-1}}$.

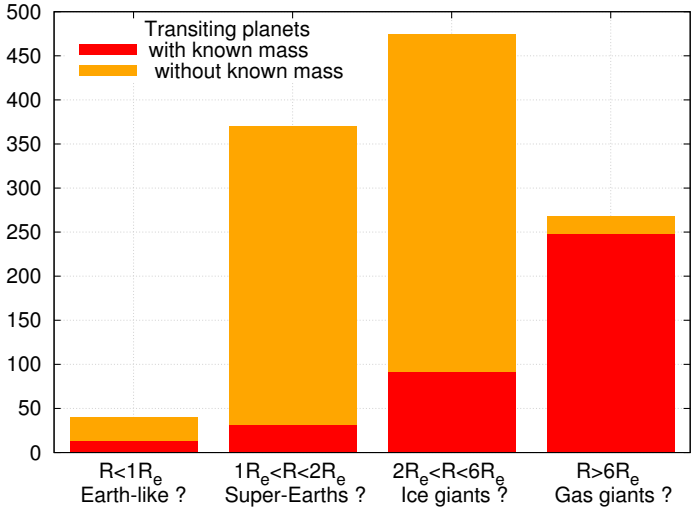

Figure 4.10. Number of known transiting planets as a function of radius. Planets for which the mass is known are in red.

expected, as hotter atmospheres are more extended. The error on the radius increases with $\tau_{\rm lim}$ and reach 1% for $\tau_{\rm lim} \approx 10^5$. This is small compared to other sources of uncertainties (the age, the opacities etc).

4.3 The case of small planets

One of the most striking result learned from the Kepler mission is the prevalence of planets with a size between Earth and Neptune (see Fig. 4.10). We expect the smallest of these planets to be rocky whereas the largest ones should contain a significant amount of hydrogen and helium. In between, the presence of planets with a large amount of water but no hydrogen/helium envelope, known as Ocean-planets have been postulated (Leger et al. 2004). Given the large spread in radius shown in Figure. 4.1, planets with the same mass could have very different compositions. Here, we first focus on planets composed of iron, rock and water (hereafter called *solid planets*) and then study the case of planets with a thick hydrogen/helium envelop.

4.3.1 Compositions of solid planets

Our own planet have been studied for centuries. We have a direct access to rocks that formed in its deep interior, we determined accurately its gravitational potential, we drill kilometer-deep hole to measure the temperature structure of the upper layers and we measure continuously the propagation of seismic waves.

The bulk composition of the Earth is dominated by oxygen, magnesium, silica and iron. The Earth is differentiated: heavier elements lay at the center whereas lighter ones are at the surface. The planet is mainly composed of an iron core below a mantle of silicates (*e.g.* $MgSiO_2$, Mg_2SiO_4). Planets that form in cooler environments than the Earth can accrete large amount of ices (principally water ice, but also ammonia and methane). For example, 50% of the mass of Ganymede and Callisto is composed of ices. It thus appear that the internal structure of a solid body can be approximated as a superposition of an iron core, a silicate mantle and an icy crust. Some mixing can happen between the layers. For example, part of the iron can be contained in the silicate mantle. However, as shown by Grasset et al. (2009), for a given mass, the radius of the planet is almost insensitive to this mixing. Because of the large differences in density between the three components (roughly, iron is $2-3$ times denser than silicates and silicates are $2-3$ times denser than ices), the mass of the planet is determined by its bulk composition.

The numerous mass-radius relationships proposed by different authors for solid planets differ mainly by the chosen equation of state. Whereas the pioneering work of Zapolsky & Salpeter (1969) relied on equation of states derived from quantum calculations, valid only in the high pressure range, most recent developments are based on experimental determinations of the equation of state. Fortney et al. (2007) choose to use ANEOS, a very practical numerical routine that provides approximated values for the equation of state of many materials. ANEOS was first developed to study shock physics experiments and its behavior at low pressure remains unvalidated. Careful checks are necessary when using it. Valencia et al. (2006), Sotin et al. (2007) and Seager et al. (2007) base their work on the experience gathered from the study of Earth and the other bodies of the solar-system. They use low pressures ($P < 200\,\mathrm{GPa}$) equations of state calibrated on direct compression experimental data and high pressure ($P > 20\mathrm{TPa}$) equations of state based on the Thomas-Fermi-Dirac formulation. Between the low and the high pressure ranges, Seager et al. (2007) performed a direct interpolation whereas Sotin et al. (2007) decided to use the ANEOS routine. More recently, the equation of state of water has been calculated *ab-initio* by French et al. (2009) and integrated into the latest interior models (*e.g.* Valencia et al. 2010; Nettelmann et al. 2011; Lopez et al. 2012; Zeng & Sasselov 2013; Valencia et al. 2013; Yunsheng Tian & Stanley 2013).

From the mass and radius measurements alone, it is not possible to derive the respective amounts of water, rocks and iron. For a given planetary mass, a planet with less silicate but more iron and more water can have the same radius as a planet with more silicates but less water and less iron. Clearly, with only two measurements, three different properties of the planet cannot be retrieved. Atmospheric observations might provide clues toward the internal composition. Indeed, atmospheric composition of rocky bodies are highly influenced by their long-term interactions with the internal layers of the planet. On Earth, for example, the carbon-silicate cycle is known to regulate the long-term atmospheric abundances carbon (Kasting & Catling 2003). In a planet with a significant mass of water, the thick layer of ice between the atmosphere and the silicate core could impede the carbon-silicate cycle as we know it. Another cycle, based on the transport of methane clathrates trapped in the icy mantle could equivalently regulate the carbon abundance of planets

with a thick icy mantle (Fu et al. 2010; Levi et al. 2013). Further study, however, are necessary to understand the complex interactions between the interior and atmosphere of planets with a large fraction of water and, up to date, no conclusions concerning their atmospheric composition can be drawn.

4.3.2 Mini-Neptune *vs.* solid planets

The degeneracies in the bulk composition of solid planets become even more important when they possess a thick hydrogen/helium envelope. A hydrogen dominated envelope adds two kinds of degeneracies. First, even a small amount of hydrogen dramatically changes the radius of the planet, increasing significantly the error bars on the retrieved abundances of other materials. Second, the thermal evolution the planet becomes important and affects the observed radius to a first order. Conversely to the case of solid planets, a time-evolution model is needed to investigate the mass-radius relationships of mini-Neptunes. This implies both an accurate equation of state and an accurate representation of the opacities.

In the following paper published in *The Astrophysical Journal* (Valencia et al. 2013) we construct such a model and investigate the degeneracies that limit our possibilities to retrieve the composition of those planets. The model is consist of a semi-grey analytical model for the atmosphere, the CEPAM code for the envelope and the model of Valencia et al. (2010) for the planet core. Whereas iron and silicates are considered to be part of the solid core, water and hydrogen/helium are modeled as an homogeneous mixture that forms the envelope and the atmosphere of the planet. The equation of state of the envelope is obtained as a mix between the H/He equation of state of Saumon et al. (1995) and the *ab-initio* water equation of state of French et al. (2009). The opacities are obtained from a fit to the Freedman et al. (2008) opacity database valid for different pressure, temperature and metallicities. The water/H/He envelope being considered as a metal-rich H/He envelope for the opacities.

The Astrophysical Journal, 775:10 (12pp), 2013 September 20 doi:10.1088/0004-637X/775/1/10

BULK COMPOSITION OF GJ 1214b AND OTHER SUB-NEPTUNE EXOPLANETS

Diana Valencia[1], Tristan Guillot[2], Vivien Parmentier[2], and Richard S. Freedman[3,4]
[1] Earth, Atmosphere and Planetary Sciences Department, Massachusetts Institute of Technology,
77 Massachusetts Avenue, Cambridge, MA 02139, USA; dianav@mit.edu
[2] Observatoire de la Côte d'Azur, Université de Nice-Sophie Antipolis, CNRS UMR 7293, BP 4229, F-06300 Nice Cedex 4, France
[3] Nasa Ames Research Center, MS 245-3, P.O. Box 1, Moffett Field, CA 94035-0001, USA
[4] Seti Institute, 189 Bernardo Avenue, 100 Mountain View, CA 94043, USA
Received 2012 September 10; accepted 2013 May 2; published 2013 August 29

ABSTRACT

GJ 1214b stands out among the detected low-mass exoplanets, because it is, so far, the only one amenable to transmission spectroscopy. Up to date there is no consensus about the composition of its envelope although most studies suggest a high molecular weight atmosphere. In particular, it is unclear if hydrogen and helium are present or if the atmosphere is water dominated. Here, we present results on the composition of the envelope obtained by using an internal structure and evolutionary model to fit the mass and radius data. By examining all possible mixtures of water and H/He, with the corresponding opacities, we find that the bulk amount of H/He of GJ 1214b is at most 7% by mass. In general, we find the radius of warm sub-Neptunes to be most sensitive to the amount of H/He. We note that all (Kepler-11b,c,d,f, Kepler-18b, Kepler-20b, 55Cnc-e, Kepler-36c, and Kepler-68b) but two (Kepler-11e and Kepler-30b) of the discovered low-mass planets so far have less than 10% H/He. In fact, Kepler-11e and Kepler-30b have 10%–18% and 5%–15% bulk H/He. Conversely, little can be determined about the H_2O or rocky content of sub-Neptune planets. We find that although a 100% water composition fits the data for GJ 1214b, based on formation constraints the presence of heavier refractory material on this planet is expected, and hence, so is a component lighter than water required. The same is true for Kepler-11f. A robust determination by transmission spectroscopy of the composition of the upper atmosphere of GJ 1214b will help determine the extent of compositional segregation between the atmosphere and the envelope.

Key words: opacity – planets and satellites: composition – planets and satellites: individual (GJ 1214b, Kepler-11e) – planets and satellites: interiors

Online-only material: color figure

1. INTRODUCTION

The first step toward characterizing a planet is to infer its composition, which can only be done if at least its mass and radius are known. Within the realm of low-mass exoplanets, or super-Earths ($M < 10\,M_E$), there are now a handful of them with measured radii and masses. From internal structure models, the interpretation of the data shows two types of discovered planets: the rocky planets, including the high-density ones CoRoT-7b and Kepler-10b, with a composition similar to that of Mercury (Valencia et al. 2010; Wagner et al. 2012), and Kepler-36b with an Earth-like composition, and the "volatile" planets GJ 1214b, the Kepler-11 system, 55 Cnc-e, Kepler-18b, Kepler-36c, Kepler-68b, and Kepler-30b that are too big to be made of rocks, as well as Kepler-20b, which sits at the boundary between necessarily volatile rich and possibly rocky. These last assessments come from comparing their size to the radius of planets made of the lightest rocky composition, one devoid of iron (i.e., a planet made of magnesium silicate oxides, $MgO+SiO_2$). In addition, all these planets have effective temperatures that would preclude an icy composition ($T_{\rm eq} >$ 300 K). Thus, it is clear that the volatile planets have gaseous envelopes. What remains to be determined is the nature of this envelope. In particular, it is important to assess if there is hydrogen and helium as this would mean that these planets formed while the protoplanetary nebula was still around.

Several studies have looked at the problem of inferring the bulk composition of these planets, including their envelopes, through internal structure models. However, the implementation of the opacities so far has been too simple to carry out a consistent and systematic comparison between volatile compositions. These studies have taken into account the effect of composition in density (and entropy) via the equation of state (EOS), but not in the values for the opacities. The main reason for this shortcoming is that available opacity tables exist only at discrete metallicity values. Because the evolution of gaseous planets toward contraction depends on how opaque or transparent the atmosphere is, deconvolving composition and opacity values may cause an over- or underestimation of the final radius of the planet, skewing the interpretation of the data. In view of this problem, we focus on obtaining an analytical fit to the discrete Rosseland opacity tables that would allow us to interpolate to any composition spanning a hydrogen/helium + water/ices composition for the envelope.

In this study, we focus our attention on GJ 1214b, and compare its bulk composition to the other volatile planets, because it is the first low-mass planet with a measured spectrum and hence with an estimate of the composition of the upper atmosphere. Due to its size relative to its host star and the fact that the system is close enough to be bright, this planet is amenable to transmission spectroscopy. So far, several groups have obtained data at different wavelengths leading to a rough spectrum of GJ 1214b. Bean et al. (2010, 2011), Désert et al. (2011), Crossfield et al. (2011), Berta et al. (2011), and Fraine et al. (2013) have all suggested a water-dominated atmosphere or hazes to explain the featureless spectra they obtain, while Croll et al. (2011) and de Mooij et al. (2012) suggested a low-molecular weight atmosphere. One caveat of these studies is that the inferences depend on small differences between the data and the 1σ level uncertainty of the atmospheric compositional models. Increasing the uncertainty twofold would greatly impair the inference of atmospheric composition.

On the other hand, internal structure models can help constrain the bulk composition of a planet and thus complement the results from transmission spectroscopy. Two previous studies have investigated the composition of GJ 1214b. Rogers & Seager (2010b) proposed three different compositions and their respective origin for the envelope of GJ 1214b: a primordial hydrogen and helium envelope acquired while the protosolar nebula was still around, a water envelope acquired in ice form with subsequent evaporation, or a hydrogen envelope which was outgassed from the rocky interior. They used the opacity values by Freedman et al. (2008) and a static model (no contraction from the envelope) based on the parameterized gray atmospheric model by Guillot (2010). Nettelmann et al. (2011) considered the composition of GJ 1214b to be a mixture of H/He and water, with varying proportions of the two. They have an evolution model that considers cooling and contraction of the envelope, a non-gray atmospheric model, and opacities that are 50 times solar. We add to the discussion by using an internal structure model that improves on the implementation of the opacities and a comprehensive study of the possibilities for the composition of the planet.

In Section 2, we describe the structure model used and the implementation of the opacities. In Section 3, we show the results for GJ 1214b and compare them to the other volatile transiting low-mass planets. Finally, we present our summary and conclusions in Section 4.

2. MODEL

2.1. Structure and Equation of State

We treat planets as differentiated objects with an Earth-like nucleus below an envelope composed of hydrogen and helium (H/He) as well as water (H_2O). We use the combined internal structure model of Valencia et al. (2006) for the Earth-like nucleus (with composition 33% by mass iron core + 67% magnesium silicate mantle with 10% iron by mol − [$(Mg_{0.9}, Fe_{0.1})SiO_3$ + $(Mg_{0.9}, Fe_{0.1})O$]) and CEPAM numerical model (Guillot & Morel 1995) for the gaseous envelope. The two are tied at the solid surface by ensuring continuity in mass and pressure. At this point, we have not imposed continuity in the temperature justified in part by the small effect of temperature in the density of rocks.

The EOS used is the Vinet EOS (Vinet et al. 1989) for the rocky interior by combining the EOS of the end members with the additive density rule to obtain an EOS of the mixture that is then used in the integration of the structure equations. For the envelope we use the EOS of Saumon et al. (1995) for hydrogen and helium, considering always a fixed proportion of helium by mass of 0.27 to the total amount of H_2 + He. For the water, we combine the EOS of French et al. (2009) that is relevant for temperatures above 1000 K with the NIST EOS (Saul & Wagner 1989), which is well suited for low temperatures, to span the temperature range between the critical point of water and 10,000 K.

2.2. Opacities

Owing to the fact that we are interested in constraining the composition of the envelope by spanning all possible combinations between the end members H/He and H_2O, we need corresponding opacities. Unfortunately, the data available for opacities are limited to a few discrete compositions. It is also limited in its maximal pressure, implying that interior models must rely (often implicitly) on extrapolations. We use the data from Freedman et al. (2008) updated to include revised collisional induced absorption by H_2 molecules for a solar composition, 2 and 1/2 times solar composition, plus an additional two data sets at 30 and 50 times solar (hereafter F08). We obtain an analytical fit to the Rosseland opacities by using a nonlinear least-squares minimization approach useful within the temperature and pressure ranges relevant for planetary interiors. The data sets span temperatures between 75 and 4000 K, and pressures between 10^{-6} and 300 bar, and the fit extrapolates smoothly in pressure, temperature (see Figure 1), and metallicity.

Table 1
Coefficients for Opacity Fit

	All T		$T < 800$ K	$T > 800$ K
c_1	−37.50	c_6	−14.051	82.241
c_2	0.00105	c_7	3.055	−55.456
c_3	3.2610	c_8	0.024	8.754
c_4	0.84315	c_9	1.877	0.7048
c_5	−2.339	c_{10}	−0.445	−0.0414
		c_{11}	0.8321	0.8321

The analytical fit has the form for the opacity $\kappa_{\rm gas}$ (in g cm^{-2})

$$\kappa_{\rm gas} = \kappa_{\rm lowP} + \kappa_{\rm highP} \quad (1)$$

$$\log_{10}\kappa_{\rm lowP} = c_1(\log_{10} T - c_2 \log_{10} P - c_3)^2 + (c_4\,{\rm met} + c_5) \quad (2)$$

$$\log_{10}\kappa_{\rm highP} = (c_6 + c_7 \log_{10} T + c_8 \log_{10} T^2) + \log_{10} P\,\left(c_9 + c_{10}\log_{10} T\right) + {\rm met}\, c_{11}\left(\frac{1}{2} + \frac{1}{\pi}\arctan\left(\frac{\log_{10} T - 2.5}{0.2}\right)\right), \quad (3)$$

where T is the temperature in kelvin, P is the pressure in dyn cm^{-2}, and met is the metallicity with respect to solar in the logarithmic scale (i.e., met = [M/H]). This fit effectively transitions smoothly between two different functions that are relevant at low ($\kappa_{\rm lowP}$) and high pressures ($\kappa_{\rm highP}$), respectively. The values for the coefficients are shown in Table 1. Figure 1 shows a comparison between the data from F08 for a solar composition and a metallicity 30 times higher ([M/H] = 1.5) and the results from our proposed analytical fit.

The calculations by F08 consider a grain-free atmosphere with a composition that evolves depending on the condensates that form and get removed from the gaseous phase. We are interested in assessing whether or not grains have an impact on the inference in envelope composition. We focus on the end-member case of refractory grains not settling into clouds, but remaining mixed within the background gas. To model this type of grains we turn to the calculations by Alexander & Ferguson (1994, hereafter AF94) to come up with a simple prescription that includes the opacity contribution from mixed grains. Alexander & Ferguson (1994) examined opacities at warm to high temperatures (between 700 and 12,500 K), and low-density values captured in $\log_{10}\bar{R} = -7$ to +1 where $\bar{R} = \rho/T_6^3$, ρ is the density in g cm^{-3}, and T_6 is the temperature expressed in millions of degrees (corresponding densities are 10^{-15} to 10^{-8} g cm^{-3} at 1000 K and 10^{-13} to 10^{-5} g cm^{-3} at 10,000 K) most relevant to the conditions of the protoplanetary

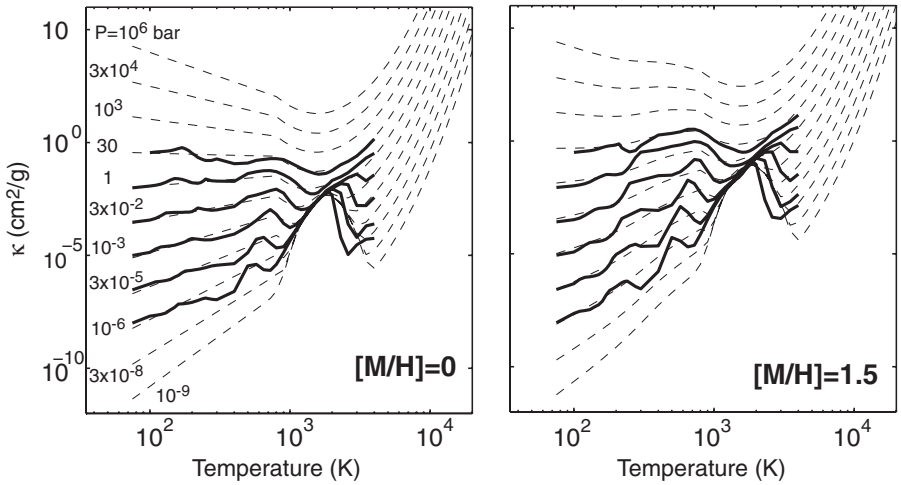

Figure 1. Opacity fit. The comparison between the Rosseland opacity data by Freedman et al. (2008) (solid lines) and our analytical fit (dashed lines) is shown for solar metallicity (left) and a metallicity 30 times higher than solar (right). The extrapolation to low and high pressures as well as large temperatures is smooth.

nebula. In contrast, planetary interiors have larger density/pressure so that typical values are $+6 < \log_{10} \bar{R} < +7$. Their results show that grains are only present below a certain temperature, which depends on the value of $\bar{R}$. Despite the fact that AF94's data are calculated at very low values of $\bar{R}$, there is a clear trend on the effect of grains that we extrapolate to larger values of $\bar{R}$ (see Figure 6 in Alexander & Ferguson 1994). We fit a simple linear trend within the regions where grains are present and add this to the gas opacity:

$$\kappa = \begin{cases} \kappa_{\rm gas} + \kappa_{\rm grains} & \text{if } T < T_1^*, \text{ and} \\ \quad \log_{10} \kappa_{\rm grains} = 0.430 & \\ \quad +1.3143(\log_{10} T - 2.85) & \\ \kappa_{\rm gas} & \text{if } T > T_2^*, \end{cases} \tag{4}$$

where $\log_{10} T_1^* = 0.0245 \log \bar{R} + 1.971$ and $\log_{10} T_2^* = 0.0245 \log \bar{R} + 3.221$. The region between these two critical points is just a linear interpolation between $\kappa_{\rm gas}(T_1^*) + \kappa_{\rm grains}(T_1^*)$ and $\kappa_{\rm gas}(T_2^*)$.

We show the comparison between the two data sets (from AF94 and F08) and our fit to the data with a prescription for grains at low temperatures (dashed lines) and without grains (dotted lines) in Figure 2. On the left, we compare the data (thin lines for AF94, thick lines for F08) and our fit (dashed) for low densities ($\log_{10} \bar{R} = -1$ (black) and $\log_{10} \bar{R} = +1$ (blue)) and a solar composition. According to AF94, the majority of the opacities for temperatures lower than T_2^* (or ~1800 K for $\log_{10} \bar{R} = +1$) are due to grains, which we account for. The second feature of AF94 is a modest increase (a "bump") in the opacities due to the presence of water vapor at temperatures right above T_2^* (between 1800 K and 3000 K for $\log_{10} R = -1$), which becomes less prominent with increasing value of $\bar{R}$ (Alexander & Ferguson 1994). We note that this feature is missing in our fit to the data by F08 yielding differences in the opacities of almost an order of magnitude around the 10^{-2} cm^2 g^{-1} level within this high-temperature and low-pressure (e.g., low $\bar{R}$) range. However, this mismatch we think may be less of an issue at pressure–temperature values pertinent to planetary interiors given that the trend is for this feature to be less prominent with increasing $\bar{R}$ values, and that the opacities relevant for planetary atmospheres are in the $1–10^6$ mag range.

We compare the effect of envelope composition by showing in Figure 2 (right) the opacities for a solar ($Z_{\rm ices} = 0.01$, where $Z_{\rm ices}$ is the ratio of water/ices to envelope mass, pink), a 50% H/He + 50% H_2O/ices mixture ($Z_{\rm ices} = 0.5$, purple), and a 100% H_2O/ices envelope ($Z_{\rm ices} = 1$, blue) at a constant, more relevant value of $\log_{10} \bar{R} = +6.5$. It can be seen that the opacities increase smoothly and monotonically without grains (solid lines). In the presence of grains there is a considerable (almost step-like) increase in opacities for temperatures below ~2000 K that depends on how much water there is, from more than 1 order of magnitude for solar composition to just a few tens of dex for envelopes rich in water/ices. The small effect of grains on water-rich atmospheres is due to the fact that the opacities are already quite high for such compositions.

We find that very quickly the opacities become high as soon as the envelopes have non-negligible amounts of water/ices so that the difference between opacities for a 50× solar envelope (or $Z_{\rm ices} = 0.25$) and a pure water/ices is only of the order of ~50 g cm^{-2} over a range that covers several orders of magnitude (see Figure 2).

Extrapolation. The pressure–temperature regime of super-Earths is between millibars to a few megabars, and between a few hundred to ~10,000 K. The opacity database from which the fit is derived covers this regime partially, and extrapolation is needed beyond 300 bar and 4000 K (Figure 1). In fact, no current database covers the planetary regime fully. Therefore, internal structure studies of planets use some sort of extrapolation. We used the work by AF94 to serve as a guide for the extrapolation to high temperatures, and note that the opacities become increasingly more uncertain as the pressures and temperatures increase much beyond the database of AF08. This may not be too much of a problem as the high PT regime corresponds to the deep interior of the planet (which is fully convective), and most of the cooling is controlled by the radiative upper part of the envelope/atmosphere ($P <$ kbar, $T < 2000$ K), where the opacities are either not too far from or within the database range. However, it is important to keep in mind the limitations of the extrapolation.

In general, the construction of high-temperature databases requires that transitions that originate in energy levels above the ground state be included in the calculations. If this is not done, then there will be missing opacity that will increase in magnitude as the temperature increases. In the case of the opacity tables provided for this study, wherever possible opacity data using "hot" line lists have been used. These lists include

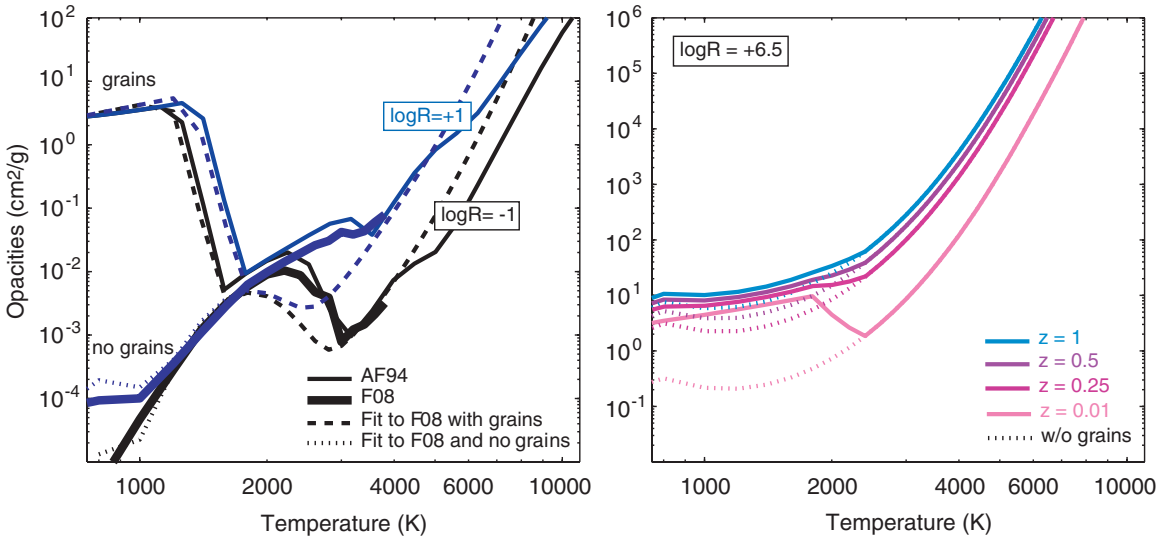

Figure 2. Comparison opacities. Left: for a solar composition, opacities according to Alexander & Ferguson (1994) are shown in thin solid lines, according to Freedman et al. (2008) in thick solid lines, our fit with grains in dashed lines and without grains in dotted lines at $\log_{10} \bar{R} = -1$ in black and $\log_{10} \bar{R} = +1$ in blue. Right: comparison for three different envelope compositions: solar, $Z_{\rm ices} = 0.01$, pink; 50% ices + 50% H/He, $Z_{\rm ices} = 0.5$, purple; and pure ices, $Z_{\rm ices} = 1$, blue for $\log_{10} \bar{R} = +6.5$ (relevant to planetary interiors) and grainy (solid) and grain-free (dotted) cases. Our fit is an extrapolation of the data beyond 4000 K, 300 bar, and $Z_{\rm ices} = 0.25$.

line transitions from levels that are not populated at room temperature so that the opacity is more accurately represented at higher temperatures, but these lists still may not include all the opacity at the highest temperatures. It is difficult to include in a quantum-mechanical model all the levels that may contribute opacity at the highest temperatures.

By considering the species individually and assessing how they contribute to the total opacity, it is reasonable to assume that the opacity will continue to increase with T but only up to the point where the population of the upper states reaches a limit where the effects of additional increases in T are slight (due to the exponential dependence of the Boltzmann factor). Since for most polyatomics the first excited electronic state is far above the ground state, it is only the vibrational/rotational levels in the ground electronic state that need to be considered. This is especially true in the case of a main source of opacity, water, where the first bound, excited state is ~7.5 eV above the ground state. On the other hand, an important source of absorption at high T is the presence of free electrons and the associated free–free and bound–free opacities, which may have a more significant effect than the filling of the band gaps, counteracting the saturation effect previously discussed.

In addition, the effect of very high pressure may also have a leveling-off component. For moderate pressures, the line width will increase with pressure, but eventually a limit is reached when the density approaches a value where the gas starts to behave more like a liquid and the line width no longer increases linearly with pressure. Unfortunately, the actual line width at these high pressures is not at all well known and the simple theories for line shape are no longer valid, making extrapolation rather uncertain.

To test how sensitive the extrapolation is to high temperatures we use a synthetic opacity fit with a much lower dependence on temperature (parameter $c_8 = 5$). We consider two planets with a mass of 0.020 $M_{\rm Jup}$, $T_{\rm eq} = 500$ K, and a core mass fraction of 50%: one with a 100% water/ices envelope and one with a mixture of 90% H/He and 10% water/ices. We find that the radiative–convective boundary moves shallower by 10% and 20% in pressure at 10 Gyr, respectively, and that the opacity values increase by 12% and 17%, respectively—not enough to change the PT structure or total radius significantly (by 0.2% and 5%, respectively, at 2.5 Gyr and by less than 1 part in 1000 for both cases at 10 Gyr). This confirms that the PT regime for the opacities is most important up to the pressures and temperatures that include the radiative–convective transition, which for these warm sub-Neptunes is <5 kbar and <2000 K.

In addition, the database used (AF08) only spans a limited range of envelope compositions: solar, 1/2× solar, 2× solar, 30× solar, and 50× solar in gaseous form (no solids). Thus, extrapolation is needed to cover the whole space from solar to water-rich envelopes. From this set we observe that the dominant dependence of the logarithm of the opacity with metallicity is a linear dependence beyond some estimated temperature (~3000 K). This simple fit (see Equation (3)) captures the intuitive behavior that opacity increases with the number of molecules present, while fitting the database well. It is, of course, too simple of an extrapolation to capture the details. We await actual data at larger metallicity values to compare to our fit, especially as more sub-Neptune planets are found.

We hope that in the future there will be no need for extrapolation, and we encourage the expansion of opacity databases to higher PT and water-rich compositions, as they are important for modeling the structure of low-mass exoplanets; in the meantime our proposed fit may serve as a starting point.

2.3. Metallicity and Composition

To use the opacity fit, we relate the composition of the envelope to metallicity. We consider the envelope to be composed of H_2–He and "ices," where the ices are composed of water, ammonia, and methane ($H_2O + NH_3 + CH_4$), in the same proportions as in the solar nebula. We implicitly assume that there are no rock-forming minerals that could bind to oxygen, so that the amount of water in the envelope is reflected in the amount of oxygen atoms ($N_{\rm O}$), and that the other ices are fixed by the solar ratios of carbon and nitrogen to oxygen.

This means that $Z_{\rm ices}$, the amount of "ices" by mass, is

$$Z_{\rm ices} = \frac{N_{\rm O}\mu_{\rm H_2O} + N_{\rm C}\mu_{\rm CH_4} + N_{\rm N}\mu_{\rm NH_3}}{N_{\rm H}\mu_{\rm H} + N_{\rm He}\mu_{\rm He} + N_{\rm O}\mu_{\rm O} + N_{\rm C}\mu_{\rm C} + N_{\rm N}\mu_{\rm N}},$$

where N_i and μ_i are the number of atoms and the molecular weight of species i, respectively. We take constant the proportion of He to the total amount of mass in the non-metallic portion (H_2+He) and equal to $c = 0.27$ (i.e., using the conventional notation: $Y/(X+Y) = 0.27$). Therefore, the metallicity can be expressed as

$$\left(\frac{N_{\rm O}}{N_{\rm H}}\right) = \left(\frac{1}{1-c}\right)\frac{\mu_{\rm H}\, Z_{\rm ices}}{a - b\, Z_{\rm ices}}$$

$$10^{\rm met} = \left(\frac{N_{\rm O}}{N_{\rm H}}\right) \Big/ \left(\frac{N_{\rm O}}{N_{\rm H}}\right)_{\rm solar},$$

where $a = \mu_{\rm H_2O} + (N_{\rm C}/N_{\rm O})\,\mu_{\rm CH_4} + (N_{\rm N}/N_{\rm O})\,\mu_{\rm NH_3}$, and $b = (\mu_{\rm O} - 2c(\mu_{\rm H}/1-c)) + (N_{\rm C}/N_{\rm O})(\mu_C - 3c(\mu_{\rm H}/1-c)) + (N_{\rm N}/N_{\rm O})(\mu_{\rm N} - 4c(\mu_{\rm H}/1-c))$. We used the values of $N_{\rm C}/N_{\rm O} = 0.501$, $N_{\rm N}/N_{\rm O} = 0.138$, and $(N_{\rm O}/N_{\rm H})_{\rm solar} = 4.898\times10^{-4}$ from Lodders (2003). This means that our opacity fit spans values for the metallicity from solar to 457 times solar (met = 2.66), corresponding to $Z_{\rm ices} = 1$.

2.4. Atmospheric Model

The upper boundary condition of our interior model is given by the atmospheric model of Guillot (2010). This analytical model is valid for a plane–parallel atmosphere which transports both a thermal intrinsic flux and a visible flux from the star. The visible flux propagates downward from the top of the atmosphere and is absorbed with an opacity $\kappa_{\rm v}$. The ratio of the visible to the infrared opacities $\gamma \equiv \kappa_{\rm v}/\kappa_{\rm IR}$ is considered constant. Its value determines at which depth the radiative energy from the star is deposited. For high values of γ, the energy is deposited in the upper layers of the atmosphere and can be lost toward space very easily. For values of γ lower than unity, the energy is deposited in deeper layers, where the atmosphere is optically thick in the infrared. There, the energy cannot escape the planet, and contributes to its global energy, slowing its contraction. Theoretically, γ could be calculated from the opacity tables. However, we note that the temperature of the isothermal zone around the 1 bar level is very sensitive to its value. Thus, we use the value of γ that better reproduces the more sophisticated radiative transfer models of Miller-Ricci & Fortney (2010). We choose $\gamma = 0.032$, which gives a temperature of 1000 K around 1 bar for GJ 1214b, as can be seen in Figure 3. Miller-Ricci & Fortney (2010) show that, in the case of GJ 1214b, the temperature around 1 bar does not depend strongly on the composition of the planet. Thus, we use the same γ for the different compositions considered. For GJ 1214b, we find that the interior temperature is 62 K at 0.1 Gyr, 40 K at 1 Gyr, 35 K at 2.5 Gyr, and 24 K at 10 Gyr for a solar atmosphere, and 80 K at 0.1 Gyr, 50 K at 1 Gyr, 42 K at 2.5 Gyr, and 35 K at 10 Gyr for a water-rich envelope.

Note that γ will change with orbital distance. It is expected to be higher for planets that are close-in. The Rosseland opacities are calculated from the line-by-line opacities weighted by the Planck function. Thus, planets with different equilibrium temperatures have different values of the Rosseland thermal opacities. Changing the equilibrium temperature by a small amount ($\sim O(100\,{\rm K})$) will not change the position of the peak of the Planck function very much. However, for hotter planets, not considered in this study, the value of gamma could change significantly.

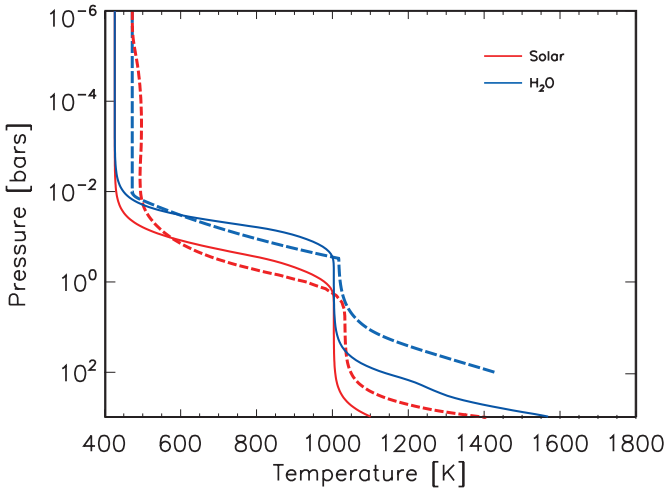

Figure 3. Upper atmosphere of GJ 1214b. Temperature pressure profiles from Miller-Ricci & Fortney (2010) (thin lines) and from our model at 10 Gyr (thick lines) for a solar composition atmosphere (red) and for a water atmosphere (blue).

(A color version of this figure is available in the online journal.)

3. RESULTS

3.1. GJ 1214b

We obtain the structure and total radius for planets with a mass of 5.09, 6.36, 7.63, 8.90, and 10.2 $M_{\rm Earth}$ (or 0.016, 0.020, 0.024, 0.028, and 0.032 $M_{\rm Jup}$) to span the mass of GJ 1214b, for different proportions of Earth-like nucleus to envelope, while spanning all combinations of the end members H/He and H_2O for the envelope. In other words, we find a relationship between mass (M), radius (R), Earth-like nucleus fraction to total mass (nf), and proportion of water to total envelope mass (wf), in the form $R = R(M, {\rm nf}, {\rm wf})$, and spline interpolate in the three dimensions (mass, nf, wt). Since we are interested in inferring the composition of a planet from its transit radius, we consider the radius of the planet to be the height at which the path traveled by the starlight would be equal to an optical depth of unity. We examined three cases: (1) a grain-free envelope, (2) a grainy envelope at an equilibrium temperature of $T_{\rm eq} = 500$ K, and (3) a grain-free envelope at $T_{\rm eq} = 600$ K.

Figure 4 shows typical calculations for the planets considered. In this case, the planets have an Earth-like nucleus that makes up half of the planet's mass below envelopes of different compositions: (1) 100% H_2O (blue), (2) 50% H_2O+ 50% H/He (purple), and (3) 100% H/He (pink). Starting from a high entropy state (corresponding to $S = S(\chi_{\rm env}, T_{10}, P_{10})$, where $\chi_{\rm env}$ is the envelope's composition, T_{10} and P_{10} are the temperature and pressure at 10 bar), the planets cool and contract according to how much energy is being transported out (bottom left panel). The solid and dashed lines correspond to equilibrium temperatures of 500 and 600 K. As can be seen, this small difference in equilibrium temperature has little effect on the interior structure or evolution of the planets.

Not surprisingly, the envelopes that have lower molecular weight yield the largest radii, while at the same time suffer the most contraction. We find this trend to be true for most planets except for the ones that have less than 10% content of water in the envelope. That is to say, we find that planets that have envelopes of 100% H/He are slightly smaller than

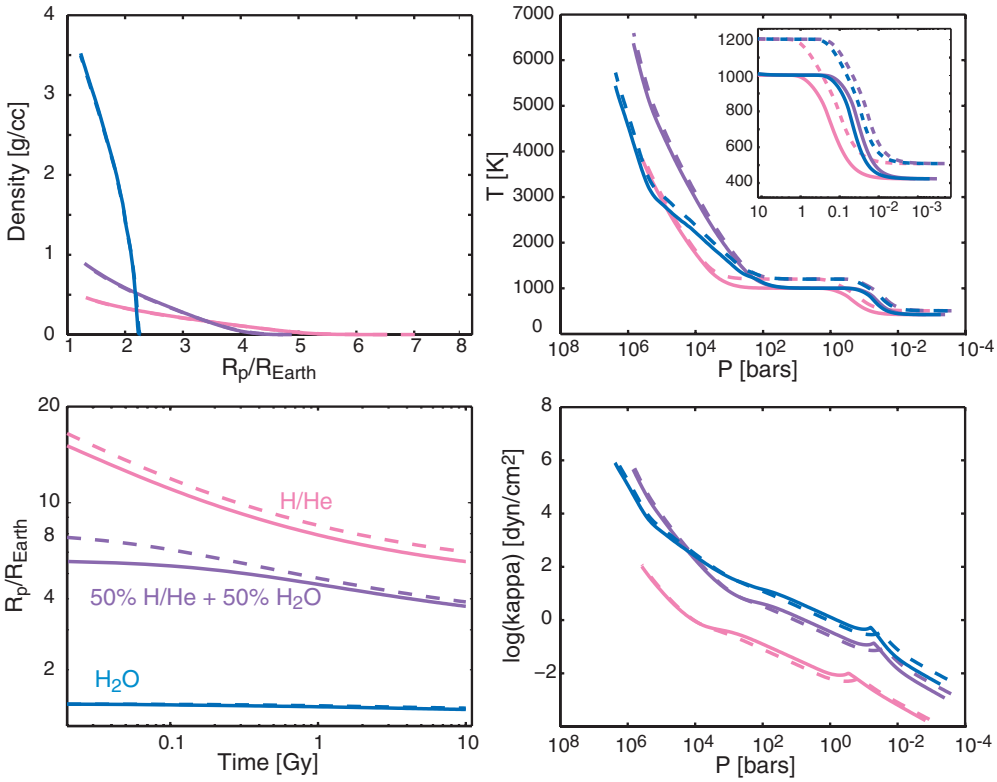

Figure 4. Envelope structure of a sub-Neptune. Top left: density structure; top-right: pressure–temperature structure; bottom left: evolution (contraction) tracks; and bottom right: opacity values for planets that are made of 50% by mass Earth-like core below envelopes of different compositions. Blue: 100% H_2O envelopes; purple: 50% H_2O + 50% H/He; pink: 100% H/He envelope. Solid and dashed lines correspond to equilibrium temperatures of 500 and 600 K, respectively. The envelopes are grain-free in this case. The total mass of the planet is 0.020 M_{Jup}.

those that have 90% H/He+10% water/ices envelopes. We attribute this to a competing effect between larger envelope density that would make planets smaller for a given mass and higher opacities that slow down the cooling. At larger fractions of water content in the atmosphere, the density effect dominates. Interestingly, this effect gives rise to a new kind of degeneracy. For the same value of envelope mass, two different combinations of H/He + water/ices with two different evolutionary tracks yield the same radius at some given age (see Figure 5). This illustrates the importance of using evolutionary models, as static ones could miss these possibilities. By implementing the physics behind contraction and evolution, the internal structure model is able to resolve time-dependent possibilities. This degeneracy stands in contrast to the one that arises from trade-offs between three or more compositional end members with different molecular weights—iron cores, silicate mantles, water/icy envelopes or oceans, H/He envelopes—which has been readily identified (Valencia et al. 2007; Adams et al. 2008; Rogers & Seager 2010a). The new degeneracy arises from differences in molecular weight and thermo-physical properties (opacities) between water and H/He that determine the cooling histories of the envelopes.

For the specific example shown in Figure 5, a planet with a mass of 0.020 M_{Jup} and an envelope that makes up 3% of the total mass, two different envelope compositions yield the same radius of 6.55 R_E at 3 Gyr: an envelope that is mostly H/He (99.9% H/He and only 0.1% water in the envelope) that starts very expanded and contracts rapidly initially, and an envelope that is made of 3/4 of H/He and 1/4 of water that contracts initially more slowly. To resolve this kind of degeneracy one would need a radius measurement at two different ages, which

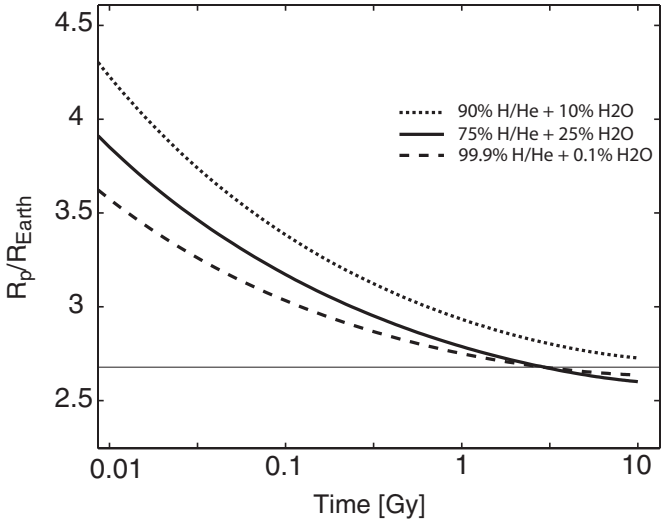

Figure 5. Degeneracy in envelope composition. Evolutionary tracks are shown for a planet of mass 0.020 M_{Jup} and T_{eq} =500 K, with an envelope that is 3% by mass and different compositions: 75% H/He + 25% H_2O (solid line), 99.9% H/He + 0.1% H_2O (dashed line), and 90% H/He + 10% H_2O (dotted lines). The latter is shown for reference. The radius of 6.55 R_E is met by the first two compositions at an age of ∼3 Gyr (fine horizontal line).

is impossible to obtain. Therefore, we find that for low-mass planets with a non-negligible envelope or sub-Neptunes, there is an intrinsic and persistent degeneracy that stems from the contraction history of the planet.

The age of GJ 1214b is estimated to be between 3 and 10 Gyr (Charbonneau et al. 2009), which means the planet may contract

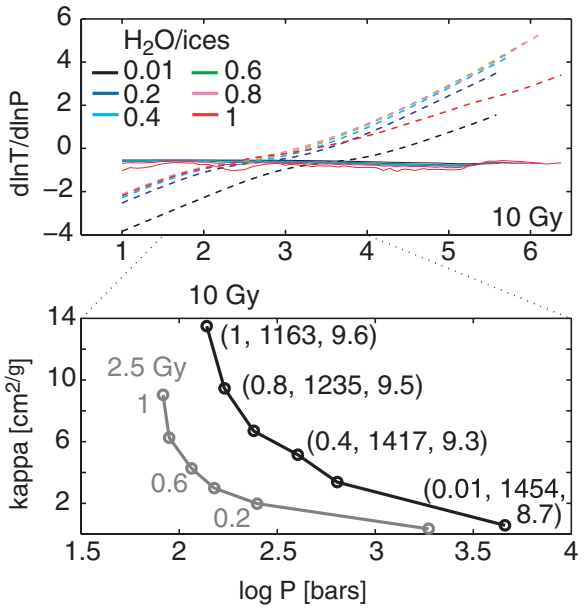

Figure 6. Adiabatic–radiative boundary of a sub-Neptune with mass 0.020 $M_{\rm Jup}$ and $T_{\rm eq}$ =500 K. Top: adiabatic (solid lines) and radiative (dashed) gradients at 10 Gyr of envelopes with compositions: solar (black), 80% H/He + 20% H_2O/ices (blue), 60% H/He + 40% H_2O/ices (cyan), 40% H/He + 60% H_2O/ices (green), 20% H/He + 80% H_2O/ices (pink), 100% H_2O/ices (red), over an Earth-like nucleus that makes 50% of the planet by mass. In the region where the radiative gradient is lower than the adiabatic one, the planet loses heat via radiation. Bottom: the pressure (depth) and corresponding opacity of the radiative–convective boundary for planets of 2.5 Gyr (gray) and at 10 Gyr (black). The labels correspond to the proportion of H_2O/ices in the envelope, and the temperature and entropy (in log) of the radiative–convective boundary. For 2.5 Gyr these values are (0.01, 1478, 8.7), (0.2, 1438, 9.1), (0.4, 1391, 9.3), (0.6, 1357, 9.4), (0.8, 1278, 9.5), (1, 1211, 9.6); and for 10 Gyr: (0.01, 1454, 8.7), (0.2, 1452, 9.1), (0.4, 1417, 9.3), (0.6, 1307, 9.4), (0.8, 1235, 9.5), (1, 1163, 9.6).

considerably within this age range, adding another source of uncertainty when inferring the composition of the envelope. The effect of contraction is most significant in the early stages of evolution (<1 Gyr) and for H/He dominated envelopes, and less important as the age of the planet increases or its envelope is H_2O dominated. These two effects are shown in the bottom left panel of Figure 4. To infer the composition of GJ 1214b, we use a nominal age of 4.6 Gyr and then explore the effects of the uncertainty in the age.

Heat is normally transferred out of the planet's envelope by convection in the interior where the adiabatic gradient is lower than the radiative one, and by radiation in the upper layers where the opacity is lower and the converse is true. We find that this radiative–convective boundary happens at deeper levels, larger temperatures, and lower local entropies, as the amount of water+ices in the envelope decreases (see Figure 6). The variation in opacity and pressure of this boundary is at least an order of magnitude and decreases with increasing water+ice content (from 4600 bar for a solar composition to 138 bar for a water/ice envelope). In addition, with increasing age this boundary happens at a similar local entropy, which means it moves deeper (higher pressures) as the planet cools in time. Below the boundary, the envelope is fully adiabatic and the values for opacities are less important, as long as they do not preclude the envelope from being convective. This means that the extrapolation of the opacities is most important up to several kilobars (∼5000 bar) and a few thousand kelvin (∼2000 K) for these warm sub-Neptune planets.

The effect of grain opacity is shown in Figure 7, where we present the results for the transit radius corresponding to two different envelope compositions: (1) 100% H_2O, (2) 50% H_2O+ 50% H/He, while also changing the proportion of envelope to Earth-like nucleus. The effect of grains (dash-dotted lines) is most noticeable for low molecular weight atmospheres and is negligible for water-dominated envelopes. This is because for water-dominated atmospheres the gas opacities are already high (∼10 g cm^{-2}) and comparable to the grain opacities (within a factor of ∼0.5 dex), while for H/He dominated atmospheres the gas opacity is 0.1–1 g cm^{-2}, one order of magnitude smaller than with grains (compare solid and dotted pink lines in Figure 2).

It is important to note that the mass and radius data for GJ 1214b are consistent with a pure H_2O/ices composition (see Figure 7(left)), regardless of the uncertainty in age, as contraction is negligible for water-dominated atmospheres. However, this composition is unlikely to exist. The condensation temperature of water and ices is much lower than that of rocks, so that during condensation some refractory material should have condensed out of the solar nebula before the bulk of the water and ices did, entailing the existence of some amount of rocky material in this planet. This, in turn, implies the presence of a material lighter than water as well, so as to offset the high-density character of the refractory material and fit the radius of the planet. The most obvious component is H/He because of its abundance in astrophysical objects, although another possibility is outgassed hydrogen (Rogers & Seager 2010b).

The effect of temperature is very small for super-Earths but modest for sub-Earths (see Figure 7). It is in fact comparable to the effect of grains, which is more important for low molecular-weight envelopes. Relevant to GJ 1214b we can quantify the effect of equilibrium temperature by noting that a 100 K increase in equilibrium temperature (that translates to an increase of ∼200 K at 10 bar) increases the radius of the planet by only ∼2%. The temperature effect is small as long as the species in the envelope do not change phase with different equilibrium temperatures.

More systematically, we ran the internal structure model to span all possible compositions for the envelope between the two extremes of solar ($Z_{\rm ices}$ = 0.01) to 100% H_2O/ices ($Z_{\rm ices}$ = 1), and varying amounts of rocky cores to envelope ratios. We show the results at a nominal age of 4.6 Gyr for GJ 1214b and at 8 Gyr for Kepler-11e in the ternary diagrams that relate Earth-like nucleus, water/ices, and H/He by mass (see Figure 8). Each ternary diagram corresponds to a specific planetary mass, and every point in the ternary diagram depicts one unique composition. These ternary diagrams are equivalent to the (x, y, z)-plane where $x + y + z = 1$, and $x, y, z > 0$. The values for the transit radius are shown in color in terms of Earth radii and the lines of constant radii are labeled. There are a few important aspects to note from the results contained in these ternary diagrams.

1. The presence of H/He considerably increases the transit radius. We find that all detected low-mass planets with a measured mass, that have an envelope, and that happen to have an equilibrium temperature warmer than 500 K (Kepler-11b,c,d,e,f, Kepler-18b, Kepler-20b, 55Cnc-e, Kepler-68b, Kepler-36c, and Kepler-30b) have a radius no larger than five times that of the Earth. This suggests (see isoradius lines in Figure 8) that the H/He content is limited to less than ∼20% by mass for hot sub-Neptunes (less than 10 $M_\oplus$). In fact, if we remove Kepler-11e and Kepler-30b from the list of planets, we find that the rest of the low-mass transiting

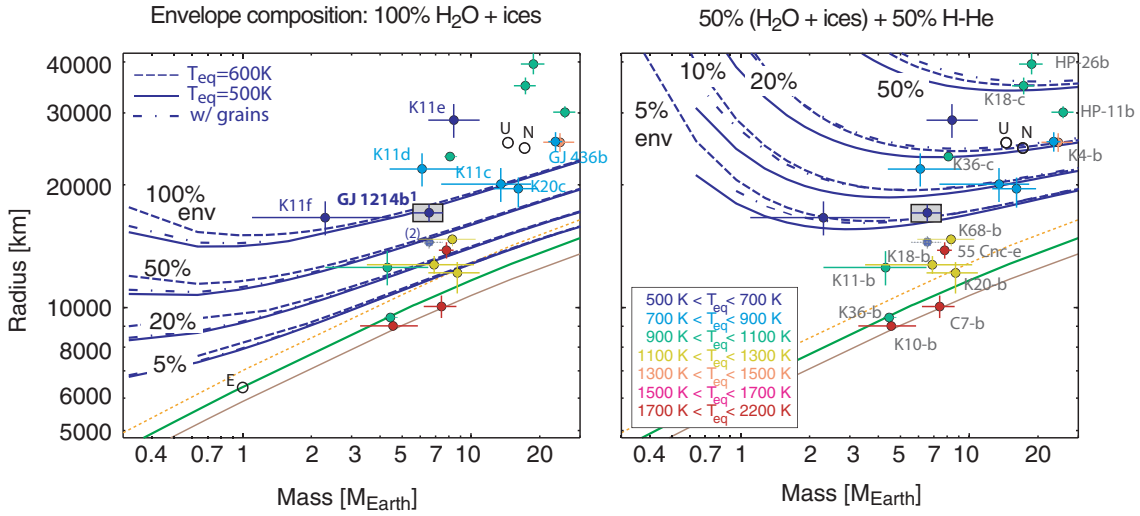

Figure 7. Mass–radius relationships for sub-Neptunes. The relationships between mass and radius for planets with an Earth-like nucleus below envelopes of varying mass fraction (100%, 50%, 20%, 10%, and 5%) are shown for a grain-free atmosphere at $T_{eq} = 500$ K (solid blue), and $T_{eq} = 600$ K (dashed blue), and a grainy atmosphere at $T_{eq} = 500$ K (dash-dotted blue). Two envelope compositions are shown: 100% H_2O/ices (left) and with 50% (H_2O/ices)+50% H/He (right). These MR relationships apply only to the planets GJ 1214b, Kepler-11e, Kepler-11f, Kepler-30b, and GJ 3470b as their equilibrium temperatures are ∼560 K, ∼650 K, ∼575 K, ∼600 K, and almost 700 K, respectively. The MR relationships shown correspond to an age of 4.6 Gyr. Planets are color coded by their equilibrium temperatures (calculated for an albedo of zero and an atmospheric redistribution factor of 1/4). Uranus and Neptune are shown for reference. The mass–radius relationships for three rocky compositions are shown: an Earth-like composition (green), a Mercury-like—enriched in iron with respect to Earth with an iron to silicate ratio six times that of Earth—(brown), and one voided of iron completely (pure magnesium-silicate oxides, orange). The latter shows the limit above which a planet has to have volatiles and cannot be completely rocky.

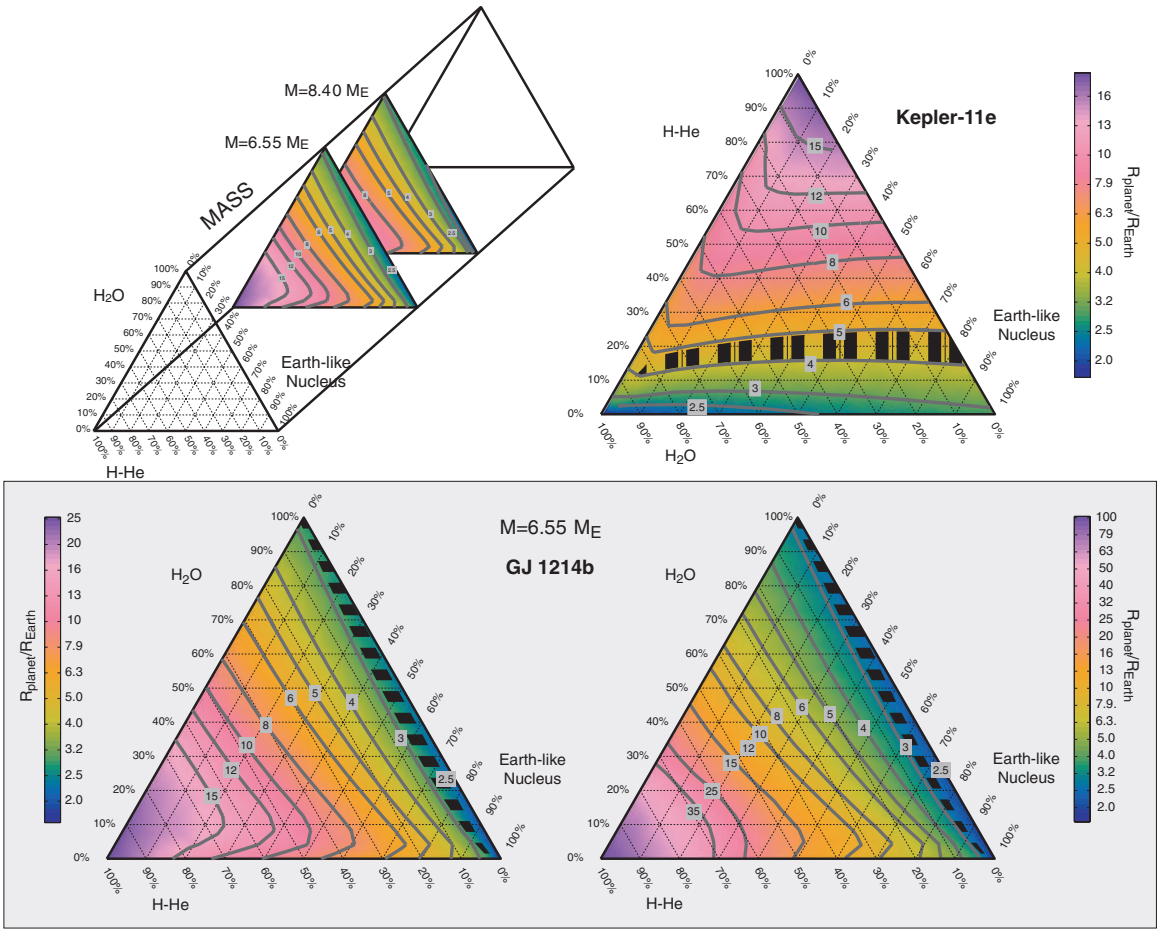

Figure 8. Ternary diagrams for GJ 1214b and Kepler-11e. These triangular diagrams relate the composition χ in terms of Earth-like nucleus fraction, water+ices fraction, and H/He fraction to total mass, to the radius for a specific planetary mass. Each vertex corresponds to 100%, and the opposite side to 0% of a particular component. The color bar shows the radius in terms of Earth radii, and the gray lines are the isoradius curves labeled in terms of Earth radii. The collection of ternary diagrams for a range of planetary masses forms a triangular prism (top left). The black band shows the compositions constrained by data for GJ 1214b for a grain-free envelope (bottom left), and a grainy envelope (bottom right), and Kepler-11e for a grain free envelope (top right) as projected onto the planetary mass M from the ternary diagrams at $M + \Delta M$ and $M - \Delta M$ (where ΔM are the uncertainty values taken from the observational data).

planets so far, with a measured mass, have a maximum of 10% by mass of H/He. Given the bias toward measuring bigger masses, it remains to be determined if there is a population of planets hidden in the *Kepler* candidates with radius 4–5 R_E that have more H/He content.

2. The radius is most sensitive to the amount of H/He and much less to the amount of H_2O/ices and rocky nucleus. This is seen from how parallel the lines of constant radius are to increasing amounts of H/He content. This means that with a radius measurement and just some knowledge that the planetary mass ranges between 5 and 10 $M_\oplus$, it is possible to estimate the H/He content of the planet. Conversely, even with perfect data for mass and radius, it is not possible to estimate the amount of water/ices or refractory material, as they trade off quite efficiently.
3. The effect of the presence of grains is nonlinear and most noticeable for planets with large contents of H/He.

The possible compositions for GJ 1214b that take into account the uncertainty in mass and radius are shown with a black band in the bottom panel of Figure 8. It is clear that this planet has less than 10% by mass of H/He, but that it can have a wide range of compositions because of the trade-off between water/ices and rocky nucleus. Another way to show the results is depicted in Figure 9, where the trade-off between bulk H/He and rocky nucleus (middle figure) or bulk H/He and H_2O/ices (bottom figure) is shown. This can be translated to the content of H/He and H_2O/ices in the atmosphere (top of Figure 9). As the amount of the solid core increases, the percentage of H/He in the envelope increases while that of water decreases. This translates to a bulk H/He content that increases as the solid core increases up to a point where it decreases again. The maximum amount of bulk H/He the planet may have happens in conjunction with some water in the envelope.

We show the range in compositions of the envelope admitted by the data at the two limiting ages of 3 Gyr (dash-dotted lines) and 10 Gyr (solid lines) to examine the effect of age. In general, an older planet would admit more H/He than a younger planet for a given radius. For GJ 1214b, the fact that the age is not well constrained does not constitute a problem when inferring the composition of its envelope, as the effect is small. For planets older than ~1 Gyr with water-dominated envelopes, age has an effect of less than 1% in the inference of envelope composition. We conclude that while the total amount of H/He in GJ 1214b can be robustly constrained to be less than 7% by mass, the data admit almost all possible compositions for the envelope at any given age. In the scenario of a solar metallicity envelope (H/He + $z = 0.01$), we find that the data constraints the content to be ~3% by mass.

According to their transmission spectra, Bean et al. (2010, 2011) suggest an atmosphere of more than 70% water. If we assume that the upper atmosphere has the same composition as the envelope below, this range would slightly narrow the composition of the planet to have a rocky component of less than 90% by mass (see the top panel of Figure 9). In summary, because of the large trade-offs between refractory material and water/ices, even with spectroscopic measurements and the assumption that the atmosphere is well mixed, it is not possible to sufficiently narrow the refractory or water/ices composition of the planet.

Previous studies. Our maximum content for H/He agrees with both Rogers & Seager (2010b) and Nettelmann et al. (2011) despite having different treatments. Rogers & Seager (2010b) considered three compositions: a four-layer model with

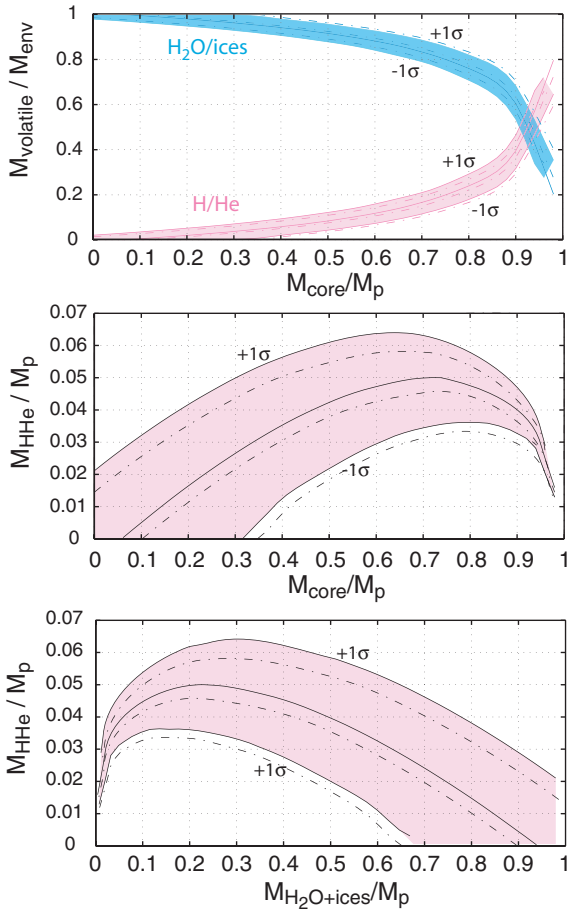

Figure 9. Composition of GJ 1214b. We fit the mass and radius of GJ 1214b including the 1σ uncertainty to estimate the content of H/He, H_2O+ices, and rocky nucleus. Each of the three sets of lines corresponds to the combinations $M+\Delta M$, $R-\Delta R$, M, R, and $M-\Delta M$, $R+\Delta R$, for an old age of the system of 10 Gyr (solid lines, and shaded region) and a younger age of 3 Gyr (dash-dotted lines). Bottom: trade-off between the bulk amount of H/He and water+ices by mass; middle: trade-off between the bulk amount of H/He and rocky nucleus by mass; top: proportion of H–He and water+ices in the envelope as a function of rocky nucleus.

H/He above an ice layer, above an Earth-like nucleus of silicate mantle above an iron core, or a three-layer model with vapor or outgassed H_2 above an Earth-like nucleus. In their four-layer model they find a range of 10^{-4} to 0.068 for H/He is admitted by the data at the 1σ level, in their three-layer model with vapor they find a range of 47%–100%, and with outgassed H_2 a small value of only 5×10^{-4}. While we agree on the maximum amount of H/He and water (for obvious reasons), we find a different value for the minimum amount of water if there is no H/He. Our calculations show a minimum value of 65% (see the bottom panel of Figure 9). A possible explanation for this discrepancy is that the opacity treatment from Rogers & Seager (2010b), which uses the Planck means from molecular line data from F08, does not extend to very water-rich atmospheres. On the other hand, Nettelmann et al. (2011) considered a similar structure to ours with a homogeneous gas envelope. A minor difference that should not influence the results is that they model a homogeneous rocky interior, while we consider a layered Earth-like one below the envelope. In their models of H/He envelope above a rocky core they claim a range of 1.3%–3.4% of H/He. They suggest that the upper limit of H/He can rise up to 5%–6% if the envelope contains 60%–90% water in mass. In comparison, we obtain a value of 3% of H/He envelope at

3 Gyr, and also obtain a maximum amount of H/He by adding 80%–90% by mass of water to the envelope (corresponding to 25% of water by total planetary mass). We suggest that this small difference may come from different opacity values as well.

In addition, we find that our results are robust to reasonable variations of thermal inertia of the planet including different radioactive heat production or heat capacity of the Earth-like nucleus. The lower boundary heat flux entering the envelope is $\dot{L}_{\rm sol} = \dot{\epsilon}_{\rm rad} + C_v dT/dt$, where $\dot{\epsilon}_{\rm rad}$ is the radioactive heat production, and C_v is the heat capacity. We used a chondritic value for the heat generation (2×10^{20} J s^{-1} g^{-1}) which is a factor of ~2 lower than Earth's bulk silicate value, and a heat capacity of 7×10^7 J K^{-1} g^{-1} which is appropriate for the Earth (Stacey 1981). By increasing $\dot{\epsilon}_{\rm rad}$ by a factor of five we find a discrepancy at 3 Gyr of ~2%, and by increasing C_v by a factor of 10 we find a discrepancy of ~6% for a planet with an H/He envelope that makes 3% and 20% of the planet. Being that H/He envelopes are the ones more susceptible to changes in temperature, we conclude that the radius of a sub-Neptune planet is not very sensitive to the thermal evolution of its rocky nucleus. This stands in contrast to the findings by Nettelmann et al. (2011) and Lopez et al. (2012).

3.2. Mass Loss

It is well recognized that atmospheric escape may play an important role in highly irradiated exoplanets (Valencia et al. 2010), and GJ 1214b is no exception. Although a detailed study is beyond the scope of this paper, we can estimate the order-of-magnitude effect of atmospheric escape on GJ 1214b. Starting from the commonly used energy-limited escape formulation (Watson et al. 1981), the mass lost per unit time of a planet of mass M is

$$\dot{M} = \pi \epsilon R_{\rm XUV}^2 R\, F_{\rm XUV}/GMK_{\rm tide}, \quad (5)$$

where $R_{\rm XUV}$ is the radius at which the bulk of the X-ray and extreme-UV (XUV) flux is absorbed, R is the radius below which molecules are bound to the planet, $F_{\rm XUV}$ is the XUV flux at the planet's location, G is the gravitational constant, $K_{\rm tide}$ is a correction factor that takes into account that the molecules only need to reach the Roche lobe before they escape (Erkaev et al. 2007), and ϵ is the heating efficiency defined as the ratio of the net heating rate to the rate of stellar energy absorption. One conservative, simple, and commonly used approach is to assume $R_{\rm XUV} \sim R$. In reality the height at which the planet absorbs X-rays and the XUV are different and also larger than the planetary radius (Lammer et al. 2003). By adopting the assumption, we can simplify Equation (5) to $\dot{M} = 3\epsilon F_{\rm XUV}/4G\rho K_{\rm tide}$ where ρ is the density of the planet, which increases with time as the planet loses mass. Mass loss progresses from fast early on, to slow as time increases, due to two facts: (1) the lighter outer regions get stripped away, leaving a denser planet from which molecules have a harder time escaping, and (2) the XUV flux from the star decreases with time.

The most unconstrained parameter, and where most of the physics is hidden in the mass-loss equation, is the heating efficiency, although common values range between 0.1 and 0.4. Finally, it is important to know how the XUV flux of the star has varied over time, and while GJ 1214 is considered to be a quiet star currently (Charbonneau et al. 2009), being a low-mass M star, it most likely had an active period early on. We implement the model of XUV flux proposed by Ribas (2010). The XUV luminosity starts in a saturated phase after which it drops off as a power-law function of age. The saturation phase duration (t^*) depends on the type of star, as seen by its bolometric luminosity. If we focus on a conservative estimate we can further simplify the mass-loss equation by assuming that the planet loses mass at the present density held constant. This is obviously an idealization and a lower bound for estimating the amount of mass lost, since at a young age planets are lighter and less capable of binding their upper atmospheres. We also set $K_{\rm tide} = 1$. The expression for the XUV flux (Ribas 2010) is

$$F_{\rm XUV} = \begin{cases} 4.04 \times 10^{-24}\, L_{\rm bol}^{0.79}\, a^{-2}\ ({\rm erg^{-1}\ s^{-1} cm^{-2}}) & \text{if } t_9 < t_9^*, \text{ and} \\ 29.7\, t_9^{-1.72} a^{-2}\ ({\rm erg^{-1}\ s^{-1} cm^{-2}}) & \text{if } t_9 > t_9^* \end{cases} \quad (6)$$

where $t_9^* = 1.66 \times 10^{20}\, L_{\rm bol}^{-0.64}$ in Gyr. We use a value of $L_{\rm bol} = 0.00328\, L_{\rm Sun}$ (Charbonneau et al. 2009) and obtain a saturation phase duration of 2 Gyr for GJ 1214b. We calculate a mass loss between 100 Myr and 3 Gyr of 0.6 $M_{\rm E}$ and 2.5 $M_{\rm E}$ for a heating efficiency of 0.1 and 0.4, respectively. This corresponds to a planet losing 9% or 27% of its mass, respectively. This will affect the composition and structure of the planet. This is most important when trying to assess the origin of the planet and the stability of an envelope. Charbonneau et al. (2009) estimated through a hydrodynamic calculation that it would take 700 Myr to lose an envelope of H/He that makes 5% of the planet's mass. According to our simple calculation, the current flux at the planet's semi-major axis is 39 W m^{-2}, and the present mass-loss rate is $2.4 \times 10^8 \epsilon$ kg s^{-1} or $\sim 1.25\epsilon$ Earth-masses per billion years. If the heating efficiency is close to 1, then a modest envelope ($\gtrsim 0.2\, M_p$) may be stable for a billion year timescale. Without a detailed calculation of atmospheric escape that includes the effects of a mixed atmosphere, it is unclear how stable or vulnerable a thin envelope may be. On the other hand, our simple calculation more robustly suggests that the compositional cases, where GJ 1214b has a modest envelope, seem to be stable. Therefore, while atmospheric escape might have been significant in the past, it appears to be moderate at present for GJ 1214b.

3.3. Comparison to Kepler-11

A good starting point to compare low-mass planets is GJ 1214b, because it is the coolest volatile planet and lies right at the threshold of a pure water mass–radius relationship. This means that any volatile planet over 1 Gyr old, as cool as or colder than GJ 1214b with a radius comparable to or larger than GJ 1214b necessarily has H/He. Even though the planets shown in Figure 7 have different ages, they are all older than 1 Gyr, with CoRoT-7b being the youngest (1.2–2.3 Gyr; Léger et al. 2009), so that the MR relationships apply. In fact, most of the transiting planets with known mass are older than the solar system, so the inferred amount of H–He from a younger age (of 4.6 Gyr) would be a minimum.

From Figure 7 we infer that Kepler-11f also has some H/He in its envelope, despite its very low mass of $(2.0–0.9) \pm 0.8\, M_\oplus$ (Lissauer et al. 2011) as its radius stands above the pure-water relationship adequate for its equilibrium temperature. In fact, because of the behavior of the mass–radius relationships for volatile compositions that flare out toward low masses, both planets Kepler-11f and GJ 1214b could have the same composition. This flaring effect is due to the fact that low-mass planets have low gravities that do not bind efficiently their volatile envelopes.

Furthermore, we focus on Kepler-11e as this planet is as cool as GJ 1214b but its radius is 1.6 times larger. We obtain all possible compositions for Kepler-11e (top left, Figure 8) with the new reported data in Lissauer et al. (2013) and find that the minimum amount of bulk H/He is 10% and the maximum is 18% by mass (an improvement from the old reported radius (Lissauer et al. 2011) that yielded 10%–25% content). Being that this planet is the largest and coolest of the transiting super-Earths, it means that all other detected volatile planets have less than 20% bulk H/He. In fact, we find that all volatile super-Earths discovered so far have less than 10% H/He by mass, comparable to Uranus and Neptune (Hubbard & MacFarlane 1980), except for Kepler-11e and Kepler-30b. We find the latter to have between 5% and 15% H/He. This also brings into light that the solar system trend of decreasing H/He with heliocentric distance for the gaseous planets (Hubbard & MacFarlane 1980) does not apply to the Kepler-11 system.

A study by Lopez et al. (2012) investigated the possible compositions for each planet of the Kepler-11 system with an evolutionary model and connected it to atmospheric escape histories. For the structure part, they considered the envelope to be made of an outer layer of H/He above an interior water layer. They use a non-gray model for their atmosphere and opacities at 50 times solar for all their models. For water-less worlds they report that present-day (at 8 Gyr) inventories of H/He are 17.2% for Kepler-11e, and less than ∼8% for all other planets. This stands in excellent agreement with our results considering that the amount of H/He would increase somewhat once they take into account the 1σ uncertainty in masses and radii.

Placing constraints on the amount of H/He helps validate formation models. According to our model, GJ 1214b must have formed rather early, when there was still enough H/He in the solar nebula. In addition, multi-planet systems pose an additional constraint, which is to explain either the trend or lack thereof of H/He content with heliocentric distance. The latter is the case of Kepler-11, with planet e having to have at least 10% of H/He and up to 18% at 42 $R_{\rm Sun}$, and neighboring planets d at 34 $R_{\rm Sun}$ and low-mass planet f at 44 $R_{\rm Sun}$ with at most 10% H/He. A study by Ikoma & Hori (2012) investigates the formation of single low-mass planets with H/He envelopes by invoking in situ accretion that they then apply to Kepler-11. While they do not consider H/He+H_2O mixtures for envelopes which would have an effect on the rate of cooling and accretion due to higher opacities, they explain the H/He content of most of the planets in the system. It remains to be shown how accretion of low-mass multiple planets can acquire envelopes that also have water/ices.

4. SUMMARY AND CONCLUSIONS

To assess the bulk composition of low-mass, low-density exoplanets and specifically GJ 1214b, we ran a comprehensive suite of internal structure and evolutionary models with a proposed prescription for opacity values that span from solar to about 450 times solar—corresponding to a composition of 100% H_2O/ices.

Given that the opacity tables that are commonly used by internal structure models are only known at discrete metallicity values that do not cover all the possible envelope compositions that the sub-Neptune planets may have, we focused our efforts in fitting these opacity tables to an analytical function that describes the global behavior of opacities in the pressure–temperature (P–T) and metallicity regime (from water/ices) in which they are derived, as well as extrapolate smoothly into higher P–T and water content space. The most important regimes for opacities for warm sub-Neptune planets (with an equilibrium temperature ∼500 K) are up to ∼5 kbar and ∼2000 K, which covers the radiative–convective boundary in the envelope. Opacities at larger pressures (with corresponding larger temperatures) fall within the fully convective interior.

Interestingly, we find that the differences in opacity values of a pure water/ices envelope and a 50× solar envelope, which is one of the most metal-rich opacity tables available and corresponds to 1/3 water/ices + 2/3 H/He, are not too large, on the order of a few dex. This means that while using it for envelopes with much larger water contents is not consistent, it probably does not introduce a big source of error in the results.

We find that there is another type of degeneracy pertinent to sub-Neptune planets that arises from the evolutionary history of the planet. Two different envelope compositions of the same mass around the same rocky nucleus may yield the same radius at a given age while differing in the rest of their evolutionary tracks. This degeneracy is different in character to the one that arises from the trade-offs between the different compositional end members.

We obtain the bulk composition of GJ 1214b and find that no more than 7% of H/He is needed to explain the radius of this planet given its mass. In addition, based on formation arguments we expect to have some H/He present in the envelope. This is due to the fact that some refractory material is expected to compose this planet (from the condensation sequence). Our result is consistent with two previous studies focused on GJ 1214b, which use different treatments for the opacities.

More generally, we find that the radius of low-density planets with a mass between 5 and 10 $M_\oplus$ is most sensitive to the amount of H/He, and much less on the amount of water and rocks. On the upside, this means that it is possible to place good constraints on the amount of H/He in these planets, which can be used to further constrain formation models. On the down side, it means that little can be said about the amount of water or rocks in these planets because these two compositional end members trade off very efficiently.

For GJ 1214b and similar planets, the implication is that the inference of a water-rich upper atmosphere from transmission spectroscopy studies does not help constrain the bulk composition of the envelope and planet, whereas an H/He dominated atmosphere would restrict the bulk composition much more, only if we assume a homogeneous composition between the upper atmosphere and deeper envelope.

Furthermore, we find that almost all discovered low-mass planets—Kepler 11b,c,d,f, Kepler-18b, Kepler-20b, 55Cnc-e, Kepler-68b, Kepler-36c—have a maximum H/He component of less than 10% by mass. While it could be that some of them have no H/He whatsoever, it seems that, despite having much hotter equilibrium temperatures, the low-density, low-mass exoplanets share a similar trait to Neptune and Uranus of having a few percent of H/He. The exceptions are Kepler-11e and Kepler-30b with a range of 10%–18% and 5%–15% of bulk H/He, respectively. Being that there is a bias toward detecting larger planets, the fact that the majority of the low-mass planets have less than 10% H/He indicates that larger contents are probably not common. The tightly packed Kepler-11 system seems to have a range of H/He that does not vary monotonically with heliocentric distance, with planets d and f having less H/He than planet e, which may point to more local/planet-specific conditions determining the compositional outcome. In

other words, it remains to be explained why Kepler-11e acquired 10%–18% by mass of H/He while simultaneously its inner and outer neighbors acquired less. Multiplanet sub-Neptune systems with known H/He contents may prove to be key in understanding planet formation.

Inferring the bulk composition of low-mass planets helps us clarify the differences in nature between the solid super-Earths and the sub-Neptune planets that share the same mass range, and also provide useful constraints to formation and migration scenarios for this new class of planets.

This work was performed (in part) under contract with the California Institute of Technology (Caltech) funded by NASA through the Sagan Fellowship Program executed by the NASA Exoplanet Science Institute. We thank Ignasi Ribas for his comments on the XUV fluxes of stars. We thank Jonathan Fortney for his careful and insightful review that has significantly increased the quality of the manuscript.

REFERENCES

Adams, E., Seager, S., & Elkins-Tanton, L. 2008, ApJ, 673, 1160
Alexander, D. R., & Ferguson, J. W. 1994, ApJ, 437, 879
Bean, J. L., Désert, J.-M., Kabath, P., et al. 2011, ApJ, 743, 92
Bean, J. L., Kempton, E., & Homeier, D. 2010, Natur, 468, 669
Berta, Z. K., Charbonneau, D., Bean, J., et al. 2011, ApJ, 736, 12
Charbonneau, D., Berta, Z. K., Irwin, J., et al. 2009, Natur, 462, 891
Croll, B., Albert, L., Jayawardhana, R., et al. 2011, ApJ, 736, 78
Crossfield, I. J. M., Barman, T., & Hansen, B. M. S. 2011, ApJ, 736, 132
de Mooij, E. J. W., Brogi, M., de Kok, R. J., et al. 2012, A&A, 538, A46
Désert, J.-M., Bean, J., Miller-Ricci Kempton, E., et al. 2011, ApJL, 731, L40
Erkaev, N. V., Kulikov, Y. N., Lammer, H., et al. 2007, A&A, 472, 329
Freedman, R. S., Marley, M. S., & Lodders, K. 2008, ApJS, 174, 504
Fraine, J. D., Deming, D., Gillon, M., et al. 2013, ApJ, 765, 127
French, M., Mattsson, T. R., Nettelmann, N., & Redmer, R. 2009, PhRvB, 79, 054107
Guillot, T. 2010, A&A, 520, A27
Guillot, T., & Morel, P. 1995, A&A, 109, 109
Hubbard, W. B., & MacFarlane, J. J. 1980, JGR, 85, 225
Ikoma, M., & Hori, Y. 2012, ApJ, 753, 66
Lammer, H., Selsis, F., Ribas, I., et al. 2003, ApJL, 598, L121
Léger, A., Rouan, D., Schneider, J., et al. 2009, A&A, 506, 287
Lissauer, J. J., Fabrycky, D. C., Ford, E. B., et al. 2011, Natur, 470, 53
Lissauer, J. J., Jontof-Hutter, D., Rowe, J. F., et al. 2013, ApJ, 770, 131
Lodders, K. 2003, ApJ, 591, 1220
Lopez, E. D., Fortney, J. J., & Miller, N. 2012, ApJ, 761, 59
Miller-Ricci, E., & Fortney, J. J. 2010, ApJL, 716, L74
Nettelmann, N., Fortney, J. J., Kramm, U., & Redmer, R. 2011, ApJ, 733, 2
Ribas, I. 2010, in IAU Symp. 264, Solar and Stellar Variability: Impact on Earth and Planets, ed. A. G. Kosovichev, A. H. Andrei, & J.-P. Rozelot (Cambridge: Cambridge Univ. Press), 3
Rogers, L. A., & Seager, S. 2010a, ApJ, 712, 974
Rogers, L. A., & Seager, S. 2010b, ApJ, 716, 1208
Saul, A., & Wagner, W. 1989, JPCRD, 18, 1537
Saumon, D., Chabrier, G., & van Horn, H. M. 1995, ApJS, 99, 713
Stacey, F. D. 1981, in Evolution of the Earth, ed. R. J. O'Connell & W. S. Fyfe (Washington, DC: AGU), 272
Valencia, D., Ikoma, M., Guillot, T., & Nettelmann, N. 2010, A&A, 516, A20
Valencia, D., O'Connell, R. J., & Sasselov, D. D. 2006, Icar, 181, 545
Valencia, D., Sasselov, D. D., & O'Connell, R. J. 2007, ApJ, 665, 1413
Vinet, P., Rose, J., Ferrante, J., & Smith, J. 1989, JPCM, 1, 1941
Wagner, F. W., Tosi, N., Sohl, F., Rauer, H., & Spohn, T. 2012, A&A, 541, A103
Watson, A. J., Donahue, T. M., & Walker, J. C. G. 1981, Icar, 48, 150

Conclusion

Gaseous planets slowly cool and contract by releasing their initial accretion heat and gravitational energy. The composition of the planet, the equation of state of its elements, the opacities of its interior and atmosphere determine the time-evolution of the planet. Recent advances in experimental devices increased our knowledge of the equation of state of hydrogen, helium and water. The composition of hot Jupiters, however, cannot be determined accurately: most of them are larger than allowed by our current understanding of giant planet's internal structure and evolution. Many physical mechanisms have been proposed to explain the radius of these inflated planets but none of these theories was confirmed neither ruled out by the observations because of the large spread in the calculated radius anomaly. To constrain the physical mechanism responsible for the inflation, it is necessary to understand better our models and the physics they already incorporate. Here, we focused on the effect of the atmosphere on the radius of gas giant planets. We showed that the plan-parallel approximation leads up to 1% errors in the calculation of the final planetary radius. We also showed that the composition of the planet, especially the presence of titanium oxide, influences the planet's evolution. As an example, planets without titanium oxide in their atmospheres have a hotter deep atmosphere that leads to a less efficient convective transport and thus a slower evolution than planets with a solar-composition, the resulting difference in radius being of the order of a few percents.

For smaller planets made principally of ices and rocks it is difficult to determine the bulk composition of the planet from a measurement of its mass and its radius only. When a small amount of hydrogen/helium is present, it becomes even more difficult. Here we used the CEPAM evolutionary code coupled with the analytical model for the atmosphere described in Chapter 2 to infer the possible bulk compositions for GJ1214b. Taking into account the thermal evolution of the planet led to a new source of degeneracies. A planet with a larger quantity of water has larger opacities and thus a slower evolution. At a given time it may have the same radius as a planet with a larger hydrogen/helium content, which is initially larger but contracts faster.

Future instruments such as GAIA, CHEOPS, TESS, PLATO, and others will discover even more planets, derive their radius with a better precision and provide a much better knowledge of their host star. A better characterization of exoplanets atmospheres coupled with better measurements of their mass and radius will unveil the relationships between atmospheric properties and bulk composition of the planet, an essential step to understand planetary formation.

Quand tu regarderas le ciel, la nuit, puisque j'habiterai dans l'une d'elles, puisque je rirai dans l'une d'elles, alors ce sera pour toi comme si riaient toutes les étoiles. Tu auras, toi, des étoiles qui savent rire !

Antoine de Saint-Exupéry - Le Petit Prince

Conclusion

More than a thousand of exoplanets have been discovered in the last decade and numerous techniques are now available to probe their atmospheres. The thermal structure, the composition and the dynamics of the atmosphere of exoplanets can be retrieved from the observations. During this PhD I have built a variety of tools to study the interactions between dynamics, thermal structure, and composition of irradiated planetary atmospheres and their contribution to the planet's internal structure and evolution. Thanks to my implication in the EChO science team, I realized that observations by future ground-based and space-based instruments will provide much better constraints on exoplanets atmospheres. Models such as the ones developed in this PhD will be essential to interpret these observations.

Numerous observations...

With the improvement of observational techniques and the development of dedicated instruments, atmospheric characterization is entering a new era where the diversity of exoplanets will challenge our current understanding of planetary atmospheres. Numerous techniques have been used to probe the characteristics of these atmospheres. Their insights are necessary to constrain the models and understand the physics of these extreme atmospheres.

- During the transit of a planet in front of its host star, the stellar light is filtered through the planet atmosphere. Absorption features due to specific atmospheric compounds are observed. Their amplitude reveals the molecular abundances whereas their shape is determined by the thermal structure.

- During a secondary eclipse, i.e. when the planet is occulted by its host star, the light emitted by the planet atmosphere is measured. The chemical composition and the thermal structure of the atmosphere together shape the spectral variations of the thermal emission. However, current observations remained inconclusive because of their low signal-to-noise ratio and their poor spectral resolution. Yet, they raised numerous questions that should be answered by future instruments.

- The stellar light reflected by the planet is also measured during a secondary eclipse. Measuring the planet albedo is a key point to understand the thermal budget of the planet. It reveals the presence and the properties of clouds.

- With very high resolution the single spectral lines of a given molecule are observed both during transit and secondary eclipse. The atmospheric thermal profile determines the line shape whereas the atmospheric winds are responsible for the Doppler shift of the lines.

- The combined light coming from both the planet and the star is observed as a function of the orbital phase for favorable targets. These phase curves provide a longitudinal resolution of the light emitted and reflected by the planet.

- During the ingress and the egress of the planet's secondary eclipse, the latitudinal variation of the planet's luminosity is observed.

To date, dozens of exoplanets have been observed to search for specific chemical species, both from space and ground based observatories. In the hottest planets, sodium, potassium, magnesium, calcium, hydrogen, carbon monoxide, and water have been detected and, in some cases, their mean abundances have been quantified on the dayside and on the atmospheric limb. These signatures become weaker in cooler planets, where clouds unambiguously shape the transit spectra, thermal emission and albedo. The dayside mean temperature, the day/night temperature contrast and the longitudinal variations of the temperature have been observed in a handful of hot planets. By interpreting these observations with atmospheric models, the main physical mechanisms that shape exoplanets atmospheres can be determined.

... and plenty of models

During this PhD, I built a large variety of tools to understand the main physical mechanisms that shape the thermal structure, the composition, the dynamics and the thermal evolution of irradiated planets.

Thermal Structure

I first focused on the thermal structure of irradiated planets atmospheres at radiative equilibrium. The atmosphere of irradiated planet is globally in radiative equilibrium: all the absorbed stellar irradiation is reemitted back to space. The opacities, which are set by the chemical composition, determine at which depth the energy is absorbed and reemitted by the atmosphere. Their spectral variations are determinant to understand the thermal structure of planets' atmospheres at radiative equilibrium. I built a simple yet reliable analytical model for the thermal structure of planetary atmospheres. The gaseous opacities of the model consist of an array of lines for the thermal and for the optical ranges. Inside each spectral range, they are represented by three parameters: the width of the lines and their maximal and minimal values. I quantified the effect of non-grey thermal opacities in shaping the thermal structure of planetary atmospheres. Non-grey effects lead to an efficient cooling of the upper atmosphere and a warming of the deep atmosphere.

I further used a state-of-the-art numerical model based on the correlated-k distribution method that properly takes into account the line-by-line opacities. The calculated temperature profiles were used to calibrate the coefficients of our analytical model. As a result, I obtained a fast and accurate analytical solution for the thermal structure of irradiated planets that is valid for a wide range of irradiation temperatures and planet gravities. I showed that the condensation of chemical species affects both the optical and the thermal opacities. For example, titanium oxide is a major contributor to the optical opacities of hot, solar-composition atmospheres. I showed that its broad-band opacity flattens the total atmospheric opacities and reduces the non-grey thermal effects. As a consequence, planets without titanium oxide in their dayside atmosphere should have a hotter deep atmosphere than planets with a solar-composition atmosphere.

Atmospheric dynamics and composition

The strong stellar irradiation of planets in thigh orbits lead to a powerful atmospheric circulation. In the third chapter of this PhD I showed how the transport of heat and material by the atmospheric circulation drives the planet out of local radiative and chemical equilibrium and studied the observational consequences.

Planets that orbit in less than 10 days around their host star are believed to be tidally-locked: they have a dayside hemisphere always facing the star and a nightside hemisphere that receives no irradiation. Atmospheric circulation transports heat and material from the dayside to the nightside. By doing so, it determines the magnitude of the day/night temperature contrast and more broadly the longitudinal variations of the temperature.

I showed that the transport of *material* by the atmospheric circulation plays a major role in determining the mean chemical composition of the planets' atmosphere. Numerous gaseous species in the planets' dayside should condense and rain out in the nightside. Vertical mixing is necessary to bring this material back in the upper atmosphere where it is observed from Earth. Irradiated planets atmospheres are stably-stratified by the intense irradiation from their host star. Mixing in such stably-stratified atmospheres differs from the mixing by convection that occurs in most solar-system examples. Using a three-dimensional global circulation model of HD 209458b, I showed that dynamical mixing in hot Jupiters' atmospheres is clearly not diffusive. Planetary-scale atmospheric motions dominate the mixing processes. I showed that chemical species that are trapped inside particles larger than a micron in the nightside of the planet should settle down and disappear from the whole atmosphere. In particular, this day/night cold trap could explain why TiO has not been detected in hot Jupiter' atmospheres yet.

Although vertical mixing is clearly not diffusive at small scales, I provided an equivalent globally-averaged vertical mixing coefficient. Such a coefficient correctly represents the globally averaged distribution of chemical species and is a much more robust measure of the vertical mixing than coefficients derived by former authors.

Many chemical reactions are likely to occur in planetary atmospheres. Coupling a full chemical network to a global circulation atmospheric model is a difficult task. I therefore contributed to the construction of a pseudo-2D chemical model of irradiated atmospheres. The system consists of a column of gas that is advected from day to night at the equator of the planet. The horizontal advection is calculated based on the mean equatorial wind speeds at the equator and the vertical mixing is described with a vertical diffusion coefficient. Both are calculated from my global circulation models. We showed that both horizontal and vertical quenchings are important in hot Jupiters' atmospheres. In the dayside, the abundances are vertically quenched to the deep abundances whereas in the nightside they are horizontally quenched to the dayside abundances. As a result, we predicted a rather homogeneous chemical composition of hot Jupiters' atmospheres.Thus, any variation in the thermal phase curve must be interpreted in terms of longitudinal variations of the temperature and cloud coverage but not of chemical composition.

Given the large temperature contrasts that prevail in hot Jupiters' atmospheres, clouds should form preferentially in the cold areas of the planet, such as the nightside. The atmospheric circulation of these planets is dominated by a strong, equatorial superrotating jet. The advection of heat by the jet leads to a colder western dayside hemisphere. The advection of material brings clouds from the cold nightside to the western dayside hemisphere. Combined, those effects lead to a cloudier western dayside hemisphere than the eastern dayside hemisphere. I derived an analytical model of the phase curve of a partially cloudy atmosphere. This model allows to retrieve the

properties of the clouds, such as their longitudinal distribution and their single-scattering albedo. I applied this model to the optical phase curve of Kepler-7b, which peaks after the secondary eclipse of the planet. I showed that this phase curve is can be explained by a partially cloudy atmosphere, with a western dayside hemisphere (from $-14°$ to the western limb) having an albedo of 1, compatible with the presence of thick clouds, and a eastern hemisphere having an albedo of 0.1, compatible with a clear-sky atmosphere.

Long-term evolution

The atmosphere of giant planets regulates the exchange of energy between the interior of the planet and the outer space. During this PhD I coupled the internal structure model CEPAM to my analytical atmospheric model. This allowed me to study how the atmospheric properties influence the long-term evolution of the planet and specifically its present radius.

Gaseous planets slowly cool and contract by releasing their initial accretion heat and gravitational energy. Most known hot Jupiters are tens of percents larger than allowed by our current understanding of giant planets' internal structure and evolution, the discrepancy being larger for planets with stronger irradiation. Many ideas have been proposed to explain this discrepancy but none of these theories was confirmed neither ruled out by the observations because of the large spread in the calculated radius anomaly. A thick atmosphere is a valve that determines how much energy can escape from the planet, influencing how the planetary radius changes over time. I discussed our estimate of the planet radius in regards to the current knowledge of the atmospheric properties and to their modeling. I showed that the plan-parallel approximation leads up to 1% errors in the final planetary radius. I also showed that the composition of the planet, especially the presence of titanium oxide, influences the planet evolution. Planets without TiO in their atmospheres have a hotter deep atmosphere that leads to a less efficient convective transport and thus a slower evolution than planets with a solar-composition. The resulting difference in radius, of the order of a few percents, is too small to explain the radius anomaly but is surely part of the puzzle.

One of the great surprises from the Kepler data is the abundant and continuous planet population that lies between the sizes of Earth and Neptune, and for which no analogue exists in our solar-system. Some of these planets have a density smaller than a pure rocky planet. Thus they might have a large hydrogen / helium envelope or a large ice content like the icy satellites of the solar system. Even with less than a percent of hydrogen/helium in the planet's atmosphere, its thermal evolution is important to understand its present radius. My co-authors and I provided an analytical representation of the Rosseland mean opacities of atmospheres that are composed partly of water and of hydrogen/helium. We used the evolutionary code CEPAM coupled with my analytical model for irradiated atmospheres to infer the bulk composition of GJ1214b. We confirmed that the radius of mini-Neptunes is very sensitive to the bulk abundance of hydrogen/helium. The relative amount of rocks and ices is therefore difficult to estimate. A planet with a larger quantity of water has larger opacities and thus a slower evolution. At a given time it can have the same radius as a planet with a larger hydrogen/helium content, which is initially larger but contracts faster.

The best is yet to come

In the next decade, the number of known exoplanets will increase significantly. Missions like TESS and PLATO will look for exoplanets in the whole sky and discover the best targets for atmospheric characterization.

In the future, an optimization of current ground-based instruments will provide observations of higher quality in spectral ranges that are not accessible from current space-based instruments. The next generation of telescopes like the Giant Magellan Telescope (25 m, planned for 2018), the Thirty Meter Telescope (30 m, planned for 2022), the European Extremely Large Telescope (40 m, planned for 2022), and the space-based James Web Space Telescope (6.5 m, planned for 2018), will revolutionize astronomy and especially the study of exoplanets' atmospheres. Molecular signatures in giant planets' atmospheres that are barely resolved with current instruments will be accessible in one observation. Unambiguous molecular detections in the atmospheres of smaller, Neptune-like planets will be accessible with a small number ($\approx$ 10) of transits, whereas characterizing the atmospheres of Earth-like planets will remain challenging. The three-dimensional thermal structure, composition and dynamics of numerous exoplanets' atmospheres will be characterized in details.

Proper models of those extreme planetary atmospheres will be challenging: cloud formation, magnetic interactions, interior/atmosphere exchanges, small-scale atmospheric waves, shock waves are some of the important physical mechanisms that will have to be taken into account. Only then the diversity of exoplanets' atmospheres will be unveiled and a statistical understanding of atmospheric physics will become possible.

Résumé long

Plus d'une centaine d'exoplanètes ont été découvertes ces dix dernières années. De nombreuses techniques permettent maintenant de sonder leur atmosphère. Les observations permettent de déterminer la structure thermique, la composition et la dynamique de l'atmosphère de ces exoplanètes. Pendant cette thèse j'ai construit des outils variés pour étudier les interactions entre la dynamique, la structure thermique et la composition des atmosphères d'exoplanètes ainsi que leur influence sur l'évolution de la structure interne de la planète. Des observations de meilleure qualité sont nécessaires pour aller plus loin. Cela sera possible avec les futurs télescopes au sol et spatiaux tels que le projet EChO dans lequel j'ai été impliqué. Les modèles tels que ceux développés dans cette thèse seront essentiels pour interpréter ces futures observations.

De nombreuses observations...

Grâce à l'amélioration des techniques d'observation et l'arrivée d'instruments dédiés, la caractérisation des atmosphères de planètes extrasolaires est en passe d'entrer dans une nouvelle ère. La diversité des exoplanètes viendra bientôt questionner notre compréhension de la physique des atmosphères planétaires. De nombreuses techniques ont été utilisées pour sonder l'atmosphère de ces mondes lointains. Leurs contributions sont nécessaires pour contraindre les modèles et comprendre la physique de ces planètes sans équivalents dans le système-solaire.

- Pendant le transit de la planète devant son étoile hôte, la lumière de l'étoile est filtrée par l'atmosphère de la planète. Le spectre obtenu pendant le transit porte la signature de nombreux composés. L'amplitude des signatures dépend directement de l'abondance des espèces tandis que leur forme est déterminée par la structure thermique de l'atmosphère.

- En comparant la lumière reçue avant et pendant l'éclipse de la planète par son étoile, le spectre d'émission du côté jour de la planète peut être mesuré. Ce spectre dépend à la fois de la composition chimique mais aussi de la structure thermique de l'atmosphère. Les observations actuelles sont malheureusement trop bruitées pour que des conclusions fermes aient pu être tirées de l'analyse des spectres d'éclipses secondaires. Néanmoins, leur observation a soulevé de nombreuses questions dont la réponse sera donnée par la prochaine génération de télescopes.

- La lumière de l'étoile réfléchie par la planète est aussi observée pendant l'éclipse secondaire. La mesure de l'albédo de la planète est fondamentale pour comprendre son equilibre thermique. De plus, l'albédo et ses variations spectrales permettent de détecter et de caractériser la présence de nuages dans ces atmosphères.

- Lorsqu'une très haute résolution angulaire est disponible, les lignes spectrales caractéristiques d'une molécule donnée peuvent être observées, à la fois dans la lumière transmise et dans la lumière émise par la planète. Le profil de température détermine la forme des lignes tandis que les vents sont responsables de leur décalage Doppler.

- La lumière combinée de l'étoile et de la planète peut être observée en fonction de la phase de l'orbite. Ces courbes de phase permettent de mesurer la variation en longitude de la lumière émise et réfléchie par la planète.

- Pendant les phases d'entrée et de sortie de l'éclipse secondaire, la variation en latitude de la luminosité de la planète est observable.

Jusqu'à présent, des dizaines d'atmosphère d'exoplanètes ont été observées depuis le sol et l'espace. Dans les plus chaudes d'entre elles, de nombreuses molécules ont été détectées: sodium, potassium, magnésium, calcium, hydrogène, monoxyde de carbone, eau. Dans certains cas, l'abondance de ces molécules a pu être mesurée. Dans les planètes plus froides, la présence de nuages domine le spectre en transit, le spectre d'émission et l'albédo. La température moyenne du côté jour, le contraste de température entre le jour et la nuit et la variation longitudinale de la température d'une poignée de planètes ont aussi été mesurés. En modélisant ces observations, nous pouvons déterminer les principaux mécanismes physique qui régissent la structure des atmosphères d'exoplanètes.

... et de nombreux modèles

Pendant cette thèse j'ai construit une variété d'outils pour comprendre les principaux mécanismes physique qui déterminent la structure thermique, la composition, la dynamique de l'atmosphère et l'évolution thermique des planètes irradiées.

Structure thermique

J'ai tout d'abord concentré mon attention sur la structure thermique des planètes irradiées. Ces planètes sont globalement à l'équilibre radiatif: l'atmosphère réémet toute l'énergie qu'elle reçoit de l'étoile. Les opacités dépendent de la composition chimique, elles déterminent à quelle profondeur de l'atmosphère la lumière de l'étoile est absorbée et depuis quelle profondeur elle est réémise. Les variations spectrales des opacités sont cruciales pour comprendre la structure thermique de l'atmosphère d'une planète. J'ai construit un modèle analytique de la structure thermique de l'atmosphère d'une planète à l'équilibre radiatif. Dans ce modèle, les opacités sont représentées par deux peignes de fréquence: un pour les opacités optiques et un pour les opacités thermiques. Dans chaque plage de fréquences les opacités sont représentées par trois paramètres: la largeur des lignes, leur valeur maximale et leur valeur minimale. J'ai estimé l'importance des effets non-gris dus aux opacités thermiques: ils provoquent un refroidissement efficace de la haute atmosphère et un réchauffement significatif de la basse atmosphère.

J'ai ensuite utilisé un modèle numérique basé sur la méthode des k-coefficients pour calculer la structure thermique de planètes irradiées de composition solaire. J'ai utilisé les profils de température calculés par le modèle numérique pour calibrer mon modèle analytique. J'ai obtenu une solution analytique pour la structure thermique de l'atmosphère qui est valide pour des planètes de différentes gravités et recevant différentes quantités de lumière de leur étoile. J'ai montré que la condensation des espèce chimiques affectait à la fois les opacités optiques et thermiques. Par exemple, l'oxyde de titane contribue de manière très importante à l'opacité des atmosphères de composition solaire à haute température. J'ai montré que l'opacité relativement constante de l'oxyde de titane efface les effets non-gris. En conséquence, des planètes sans oxyde de titane dans leur atmosphère devraient avoir une atmosphère profonde plus chaude que des planètes de composition solaire.

Dynamique et composition de l'atmosphère

Les planètes orbitant proche de leur étoile reçoivent une intense irradiation de leur côté jour qui est la source d'une puissante circulation atmosphérique. Dans le troisième chapitre de cette thèse, je montre comment le transport de chaleur et de matière par cette circulation atmosphérique conduit l'atmosphère à être en déséquilibre radiatif et chimique, ce qui a d'importantes conséquences observationelles.

Les planètes qui orbitent en moins de dix jours autour de leur étoile devraient être en rotation synchrone: elles ont un côté jour qui est toujours face à l'étoile et un côté nuit qui ne reçoit jamais d'irradiation. La circulation atmosphérique transporte de l'énergie et de la matière du côté jour au côté nuit de la planète. Ce faisant, elle détermine le contraste de température entre le jour et la nuit et, plus généralement, les variations longitudinales de températures.

Durant cette thèse, j'ai montré que le transport de matière par la circulation atmosphérique détermine en partie la composition chimique de l'atmosphère. De nombreuses espèces, gazeuses du côté jour, devraient condenser du côté nuit, pleuvoir et disparaitre. Le mélange vertical permet de transporter ces espèces dans la haute atmosphère où elles peuvent être observées depuis la Terre. Les planètes irradiées sont stabilisées verticalement par l'intense irradiation de leur étoile. Le mélange se fait donc de manière très différente dans ces atmosphères que dans celles du système-solaire, dominées par la convection. J'ai ajouter des traceurs passifs dans un modèle de circulation générale de HD 209458b afin de représentant les nuages formés côté nuit. J'ai montré que les espèces chimiques qui condensent en particules de plus de un micron côté nuit devraient sédimenter et disparaitre complètement de l'atmosphère. En particulier, ce piège froid côté nuit pourrait expliquer pourquoi l'oxyde de titane n'a pas encore été détecté dans l'atmosphère des Jupiters Chauds.

Bien que le mélange vertical dans les atmosphères de Jupiters Chauds ne soit pas diffusif à petite échelles, l'effet de la circulation moyenné sur toute la planète peut être représenté par un coefficient de diffusion vertical. J'ai suivi la trajectoire moyenne de traceurs passifs incorporés dans le modèle de circulation générale afin de calculer le coefficient de diffusion vertical moyen de la simulation, une méthode bien meilleure que les méthodes utilisées précédemment. L'estimation que je propose est inférieure d'un facteur cent aux estimations précédentes, ce qui a une influence directe sur l'abondance de molécules dans l'atmosphère observable de ces planètes.

De nombreuses réactions chimiques peuvent se produire dans les atmosphères. Combiner un réseau chimique complet avec un modèle de circulation global de l'atmosphère est difficile. Nous avons donc construit un modèle simplifié de la circulation atmosphérique. Le modèle consiste en une colonne de gaz transportée à vitesse constante le long de l'équateur de la planète. Le transport horizontal est déterminé par la vitesse moyenne des vents tandis que le transport vertical est déterminé par le coefficient de diffusion vertical. Ces deux paramètres sont calculés à partir de mes modèles de circulation générale. Au final, nous avons prédit que la composition chimique des Jupiters Chauds devrait être assez homogène. La composition du côté jour est déterminée par les couches profondes tandis que la composition du côté nuit est déterminée par celle du côté jour. Nous pensons donc que toute modulation de la courbe de phase de la planète peut s'interpréter comme une variation longitudinale de la température ou de la couverture nuageuse mais pas de la composition chimique.

Etant donné les grands contrastes de température qui existent sur les Jupiters Chauds, les nuages devraient se former préférentiellement dans les parties froides de la planète, telles que le côté nuit. La circulation atmosphérique de ces planètes est dominée par un vent violent soufflant

d'ouest en est dans les régions équatoriales transportant chaleur et matière. L'ouest du côté jour est donc plus froid que la partie est. De plus les nuages formés du côté nuit sont transportés à l'ouest du côté jour. Combinés, ces deux effets produisent un hémisphère jour plus nuageux à l'ouest qu'à l'est. J'ai construit un modèle analytique de la courbe de phase d'une planète partiellement couverte de nuages. Ce modèle permet de contraindre les propriétés des nuages, comme leur répartition en longitude ou leur albédo. J'ai appliqué ce modèle à la courbe de phase de Kepler-7b qui atteint son maximum *après* l'éclipse secondaire de la planète. J'ai montré que cette courbe de phase pouvait être expliquée par une atmosphère partiellement couverte de nuages, avec un côté ouest d'albédo compatible avec la présence d'une épaisse couche nuageuse et un côté est d'albédo compatible avec une atmosphère sans nuages.

Evolution

L'atmosphère des planètes géantes régule les échanges d'énergie entre l'intérieur et l'extérieur de la planète. Pendant cette thèse j'ai combiné le modèle de structure interne CEPAM avec mon modèle analytique d'atmosphère. Cela m'a permis d'étudier comment les propriétés de l'atmosphère influencent l'évolution à long terme de la planète et plus particulièrement son rayon.

Les planètes géantes refroidissent et se contractent au fur et à mesure qu'elles libèrent leur énergie d'accrétion et leur énergie gravitationnelle. La plupart des Jupiters Chauds sont plus de dix pour-cents plus larges que les prédictions actuelles. Plus la planète reçoit d'irradiation, plus l'anomalie de rayon est grande. Beaucoup d'idées ont été proposées pour expliquer cette différence mais aucune de ces théories n'a été confirmée ou infirmée par les observations, principalement à cause de la grande dispersion dans les valeurs d'anomalie de rayon calculées.

Une atmosphère épaisse est une valve qui détermine combien d'énergie peut s'échapper de la planète, ce qui influence l'évolution de la planète et donc son rayon à un âge donné. J'ai étudié comment les propriétés de l'atmosphère et leur modélisation influencent le calcul du rayon de planètes géantes. J'ai montré que l'approximation plan-parallèle souvent utilisée par les modèles d'atmosphères peut provoquer des erreurs de 1% au maximum sur le rayon de la planète. J'ai aussi montré que la composition de la planète, en particulier la présence d'oxyde de titane, influe sur l'évolution de la planète. Une planète dont le TiO a disparu de l'atmosphère a une atmosphère profonde plus chaude, une convection moins efficace et donc une évolution plus lente qu'une planète de composition solaire. La différence de rayon est de l'ordre de quelques pour-cents, trop petite pour expliquer l'anomalie de rayon, mais suffisamment grande pour y contribuer.

Une des grandes surprises des découvertes du télescope spatial Kepler est l'abondante population d'exoplanètes d'une taille comprise entre celle de la Terre et celle de Neptune, et pour lesquels aucun exemple n'existe dans le système solaire. Certaines de ces planètes ont une densité plus petite que celle d'une planète rocheuse. Elle doivent donc posséder une enveloppe riche en hydrogène et en hélium ou bien être composées en grande partie de glaces, à l'image des satellites glacés du système solaire. Les planètes solides ont un rayon presque constant avec le temps, ce qui n'est plus le cas dès qu'une faible quantité d'hydrogène et d'hélium est présente. Dans ce dernier cas, l'évolution thermique de la planète devient importante pour comprendre son rayon actuel. Nous avons proposé une représentation analytique des opacités de Rosseland pour des atmosphères composées d'un mélange d'eau, d'hydrogène et d'hélium. Nous avons utilisé le code CEPAM combiné avec mon modèle d'atmosphère pour déterminer la composition globale de GJ1214b. Nous avons confirmé que le rayon des mini-Neptunes est très sensible à l'abondance d'hydrogène/hélium. L'abondance relative des roches et des glaces est donc difficile à estimer pour

ces petites planètes. De plus nous avons montré qu'une planète avec une grande quantité d'eau a des opacités grandes et donc une évolution lente. A un instant donné, elle peut donc avoir la même taille qu'une planète avec moins d'eau, initialement plus grande mais se contractant plus vite.

Le meilleur est à venir

Dans la prochaine décennie le nombre d'exoplanètes connues va encore augmenter. Les missions spatiales telles que CHEOPS, TESS et PLATO vont scruter l'intégralité du ciel à la recherche des planètes les plus faciles à caractériser.

Dans le futur, en optimisant les instruments actuels, de meilleures observations seront disponibles. La prochaine génération de télescopes, tels que le "Giant Magellan Telescope" (25 m, prévu pour 2018), le "Thirty Meter Telescope" (30 m, prévu en 2022), le "European Extremely Large Telesope" (40 m, prévu en 2022) et le "James Web Space Telescope" (6.5 m, prévu en 2018) vont révolutionner l'astronomie et en particulier la caractérisation des atmosphères d'exoplanètes. Les signatures moléculaires dans les spectres d'atmosphère des planètes géante sont aujourd'hui à peine visibles. Avec ces futurs télescopes elles seront clairement apparentes avec une seule observation. La détection de molécules dans l'atmosphère des planètes de la taille de Neptune sera possible en sommant une dizaine d'observations. La caractérisation des atmosphères de planètes terrestres sera par contre toujours difficile. Nous aurons une vision tridimensionelle de la structure thermique, la composition et la dynamique de l'atmosphère de nombreuses planètes.

Des modèles réalistes de ces atmosphères extrêmes seront difficiles à obtenir. La formation des nuages, les interactions magnétiques, les échanges entre l'intérieur et l'atmosphère, les structures à petites échelles de la circulation et les ondes de chocs sont quelques-uns des mécanismes physiques que les futurs modèles devront prendre en compte. La diversité des atmosphères d'exoplanètes sera alors mise à jour et une compréhension statistique de la physique des atmosphères deviendra possible.

Bibliography

Agúndez, M., Parmentier, V., Venot, O., Hersant, F., & Selsis, F. 2014, A&A, 564, A73

Agúndez, M., Venot, O., Iro, N., et al. 2012, A&A, 548, A73

Anzellini, S., Dewaele, A., Mezouar, M., Loubeyre, P., & Morard, G. 2013, Science, 340, 464

Arras, P. & Socrates, A. 2010, The Astrophysical Journal, 714, 1

Astudillo-Defru, N. & Rojo, P. 2013, A&A, 557, A56

Ballester, G. E., Sing, D. K., & Herbert, F. 2007, Nature, 445, 511

Baraffe, I., Chabrier, G., Barman, T. S., Allard, F., & Hauschildt, P. H. 2003, A&A, 402, 701

Barclay, T., Huber, D., Rowe, J. F., et al. 2012, The Astrophysical Journal, 761, 53

Barman, T. 2007, ApJ, 661, L191

Barman, T. S., Hauschildt, P. H., Schweitzer, A., et al. 2002, ApJ, 569, L51

Barstow, J. K., Aigrain, S., Irwin, P. G. J., et al. 2013, MNRAS, 430, 1188

Batygin, K., Stanley, S., & Stevenson, D. J. 2013, The Astrophysical Journal, 776, 53

Batygin, K. & Stevenson, D. J. 2010, ApJ, 714, L238

Batygin, K., Stevenson, D. J., & Bodenheimer, P. H. 2011, The Astrophysical Journal, 738, 1

Beaulieu, J. P., Carey, S., Ribas, I., & Tinetti, G. 2008, The Astrophysical Journal, 677, 1343

Beaulieu, J. P., Kipping, D. M., Batista, V., et al. 2010, MNRAS, 409, 963

Ben-Jaffel, L. 2007, ApJ, 671, L61

Ben-Jaffel, L. & Ballester, G. E. 2013, A&A, 553, A52

Berdyugina, S. V., Berdyugin, A. V., Fluri, D. M., & Piirola, V. 2008, ApJ, 673, L83

Berdyugina, S. V., Berdyugin, A. V., Fluri, D. M., & Piirola, V. 2011, ApJ, 728, L6

Birkby, J. L., de Kok, R. J., Brogi, M., et al. 2013, MNRAS, 436, L35

Bloemen, S., Marsh, T. R., Østensen, R. H., et al. 2011, MNRAS, 410, 1787

Bodenheimer, P., Grossman, A. S., Decampli, W. M., Marcy, G., & Pollack, J. B. 1980, Icarus, 41, 293

Borucki, W. J., Koch, D., Jenkins, J., et al. 2009, Science, 325, 709

Brogi, M., de Kok, R. J., Birkby, J. L., Schwarz, H., & Snellen, I. A. G. 2014, ArXiv e-prints

Brogi, M., Snellen, I. A. G., de Kok, R. J., et al. 2012, Nature, 486, 502

Brogi, M., Snellen, I. A. G., de Kok, R. J., et al. 2013, The Astrophysical Journal, 767, 27

Budaj, J. 2013, A&A, 557, A72

Budaj, J., Hubeny, I., & Burrows, A. 2012, A&A, 537, A115

Burrows, A., Hubeny, I., Budaj, J., & Hubbard, W. B. 2007, The Astrophysical Journal, 661, 502

Chabrier, G. & Baraffe, I. 2007, ApJ, 661, L81

Chamberlain, J. W. & Hunten, D. M. 1987, Theory of planetary atmospheres. An introduction to their physics andchemistry.

Chandrasekhar, S. 1960, Radiative transfer

Charbonneau, D., Brown, T. M., Noyes, R. W., & Gilliland, R. L. 2002, The Astrophysical Journal, 568, 377

Cho, J. Y.-K. & Polvani, L. M. 1996, Science, 273, 335

Claret, A. & Bloemen, S. 2011, A&A, 529, A75

Colón, K. D., Ford, E. B., Redfield, S., et al. 2012, MNRAS, 419, 2233

Cooper, C. S. & Showman, A. P. 2005, ApJ, 629, L45

Cooper, C. S. & Showman, A. P. 2006, The Astrophysical Journal, 649, 1048

Cowan, N. B., Agol, E., & Charbonneau, D. 2007, MNRAS, 379, 641

Cowan, N. B., Machalek, P., Croll, B., et al. 2012, The Astrophysical Journal, 747, 82

Croll, B., Rappaport, S., DeVore, J., et al. 2014, ArXiv e-prints

Crossfield, I. J. M., Barman, T., Hansen, B. M. S., & Howard, A. W. 2013, A&A, 559, A33

Crossfield, I. J. M., Barman, T., Hansen, B. M. S., Tanaka, I., & Kodama, T. 2012a, The Astrophysical Journal, 760, 140

Crossfield, I. J. M., Hansen, B. M. S., & Barman, T. 2012b, The Astrophysical Journal, 746, 46

Crossfield, I. J. M., Hansen, B. M. S., Harrington, J., et al. 2010, The Astrophysical Journal, 723, 1436

Crouzet, N., McCullough, P. R., Burke, C., & Long, D. 2012, The Astrophysical Journal, 761, 7

de Kok, R. J., Brogi, M., Snellen, I. A. G., et al. 2013, A&A, 554, A82

de Kok, R. J. & Stam, D. M. 2012, Icarus, 221, 517

de Wit, J., Gillon, M., Demory, B.-O., & Seager, S. 2012, A&A, 548, A128

de Wit, J. & Seager, S. 2013, Science, 342, 1473

Deming, D., Wilkins, A., McCullough, P., et al. 2013, The Astrophysical Journal, 774, 95

Demory, B.-O., de Wit, J., Lewis, N., et al. 2013, ApJ, 776, L25

Demory, B.-O., Seager, S., Madhusudhan, N., et al. 2011, ApJ, 735, L12

Désert, J.-M., Lecavelier des Etangs, A., Hébrard, G., et al. 2009, The Astrophysical Journal, 699, 478

Désert, J.-M., Sing, D., Vidal-Madjar, A., et al. 2011, A&A, 526, A12

Désert, J.-M., Vidal-Madjar, A., Lecavelier Des Etangs, A., et al. 2008, A&A, 492, 585

Dobbs-Dixon, I. & Agol, E. 2013, MNRAS, 435, 3159

Durran, D. R. 1988, Journal of the Atmospheric Sciences, 45, 4020

Ehrenreich, D., Hébrard, G., Lecavelier des Etangs, A., et al. 2007, ApJ, 668, L179

Ehrenreich, D., Lecavelier Des Etangs, A., Hébrard, G., et al. 2008, A&A, 483, 933

Esteves, L. J., De Mooij, E. J. W., & Jayawardhana, R. 2013, The Astrophysical Journal, 772, 51

Evans, T. M., Pont, F., Sing, D. K., et al. 2013, ApJ, 772, L16

Ferraz-Mello, S. 2013, Celestial Mechanics and Dynamical Astronomy, 116, 109

Fischer, D. A. & Valenti, J. 2005, The Astrophysical Journal, 622, 1102

Fortney, J. J., Lodders, K., Marley, M. S., & Freedman, R. S. 2008, The Astrophysical Journal, 678, 1419

Fortney, J. J., Marley, M. S., & Barnes, J. W. 2007, The Astrophysical Journal, 659, 1661

Fortney, J. J., Marley, M. S., Hubickyj, O., Bodenheimer, P., & Lissauer, J. J. 2005, Astronomische Nachrichten, 326, 925

Fortney, J. J., Shabram, M., Showman, A. P., et al. 2010, The Astrophysical Journal, 709, 1396

Fossati, L., Haswell, C. A., Froning, C. S., et al. 2010, ApJ, 714, L222

Freedman, R. S., Marley, M. S., & Lodders, K. 2008, ApJS, 174, 504

French, M., Mattsson, T. R., Nettelmann, N., & Redmer, R. 2009, Phys. Rev. B, 79, 054107

Fu, Q. & Liou, K. N. 1992, Journal of Atmospheric Sciences, 49, 2139

Fu, R., O'Connell, R. J., & Sasselov, D. D. 2010, The Astrophysical Journal, 708, 1326

Fukui, A., Narita, N., Kurosaki, K., et al. 2013, The Astrophysical Journal, 770, 95

Gaulme, P., Vannier, M., Guillot, T., et al. 2010, A&A, 518, L153

Gibson, N. P., Aigrain, S., Barstow, J. K., et al. 2013, MNRAS

Gibson, N. P., Aigrain, S., Pont, F., et al. 2012, MNRAS, 422, 753

Goldreich, P. & Soter, S. 1966, Icarus, 5, 375

Grasset, O., Schneider, J., & Sotin, C. 2009, The Astrophysical Journal, 693, 722

Grillmair, C. J., Burrows, A., Charbonneau, D., et al. 2008, Nature, 456, 767

Guillot, T. 2005, Annual Review of Earth and Planetary Sciences, 33, 493

Guillot, T. 2008, Physica Scripta Volume T, 130, 014023

Guillot, T. 2010, A&A, 520, A27+

Guillot, T., Burrows, A., Hubbard, W. B., Lunine, J. I., & Saumon, D. 1996, ApJ, 459, L35

Guillot, T. & Havel, M. 2011, A&A, 527, A20

Guillot, T. & Morel, P. 1995, A&AS, 109, 109

Guillot, T. & Showman, A. P. 2002, A&A, 385, 156

Hansen, B. M. S. 2008, ApJS, 179, 484

Hansen, C. J., Schwartz, J. C., & Cowan, N. B. 2014, ArXiv e-prints

Harrington, J., Hansen, B. M., Luszcz, S. H., et al. 2006, Science, 314, 623

Harrington, J., Luszcz, S., Seager, S., Deming, D., & Richardson, L. J. 2007, Nature, 447, 691

Haswell, C. A., Fossati, L., Ayres, T., et al. 2012, The Astrophysical Journal, 760, 79

Heng, K. 2012, ApJ, 761, L1

Heng, K. & Demory, B.-O. 2013, The Astrophysical Journal, 777, 100

Heng, K., Hayek, W., Pont, F., & Sing, D. K. 2012, MNRAS, 420, 20

Huang, X. & Cumming, A. 2012, The Astrophysical Journal, 757, 47

Hubeny, I., Burrows, A., & Sudarsky, D. 2003, The Astrophysical Journal, 594, 1011

Huitson, C. M., Sing, D. K., Pont, F., et al. 2013, MNRAS, 434, 3252

Huitson, C. M., Sing, D. K., Vidal-Madjar, A., et al. 2012, MNRAS, 422, 2477

Hut, P. 1981, A&A, 99, 126

Iro, N., Bézard, B., & Guillot, T. 2005, A&A, 436, 719

Jensen, A. G., Redfield, S., Endl, M., et al. 2012, The Astrophysical Journal, 751, 86

Jensen, A. G., Redfield, S., Endl, M., et al. 2011, The Astrophysical Journal, 743, 203

Kalnay, E. 2003, Atmospheric modeling, data assimilation, and predictability (Cambridge, U.K., New York: Cambridge University Press)

Kasting, J. F. & Catling, D. 2003, ARA&A, 41, 429

Kattawar, G. W. & Adams, C. N. 1971, The Astrophysical Journal, 167, 183

Knudson, M. D., Desjarlais, M. P., Lemke, R. W., et al. 2012, Physical Review Letters, 108, 091102

Knutson, H. A., Benneke, B., Deming, D., & Homeier, D. 2014, Nature, 505, 66

Knutson, H. A., Charbonneau, D., Allen, L. E., Burrows, A., & Megeath, S. T. 2008, The Astrophysical Journal, 673, 526

Knutson, H. A., Charbonneau, D., Allen, L. E., et al. 2007a, Nature, 447, 183

Knutson, H. A., Charbonneau, D., Cowan, N. B., et al. 2009a, The Astrophysical Journal, 703, 769

Knutson, H. A., Charbonneau, D., Cowan, N. B., et al. 2009b, The Astrophysical Journal, 690, 822

Knutson, H. A., Charbonneau, D., Noyes, R. W., Brown, T. M., & Gilliland, R. L. 2007b, The Astrophysical Journal, 655, 564

Knutson, H. A., Howard, A. W., & Isaacson, H. 2010, The Astrophysical Journal, 720, 1569

Knutson, H. A., Lewis, N., Fortney, J. J., et al. 2012, The Astrophysical Journal, 754, 22

Kreidberg, L., Bean, J. L., Désert, J.-M., et al. 2014, Nature, 505, 69

Kurokawa, H. & Nakamoto, T. 2014, ArXiv e-prints

Laughlin, G., Crismani, M., & Adams, F. C. 2011, ApJ, 729, L7+

Laughlin, G., Deming, D., Langton, J., et al. 2009, Nature, 457, 562

Lecavelier Des Etangs, A. 2007, A&A, 461, 1185

Lecavelier Des Etangs, A., Ehrenreich, D., Vidal-Madjar, A., et al. 2010, A&A, 514, A72

Lecavelier Des Etangs, A., Pont, F., Vidal-Madjar, A., & Sing, D. 2008a, A&A, 481, L83

Lecavelier Des Etangs, A., Vidal-Madjar, A., Désert, J.-M., & Sing, D. 2008b, A&A, 485, 865

Leconte, J. & Chabrier, G. 2012, A&A, 540, A20

Lee, J.-M., Heng, K., & Irwin, P. G. J. 2013, The Astrophysical Journal, 778, 97

Leger, A., Selsis, F., Sotin, C., et al. 2004, Icarus, 169, 499

Levi, A., Sasselov, D., & Podolak, M. 2013, The Astrophysical Journal, 769, 29

Levrard, B., Winisdoerffer, C., & Chabrier, G. 2009, ApJ, 692, L9

Lewis, N. K., Knutson, H. A., Showman, A. P., et al. 2013, The Astrophysical Journal, 766, 95

Li, J. & Goodman, J. 2010, The Astrophysical Journal, 725, 1146

Lian, Y. & Showman, A. P. 2010, Icarus, 207, 373

Line, M. R., Wolf, A. S., Zhang, X., et al. 2013, The Astrophysical Journal, 775, 137

Line, M. R. & Yung, Y. L. 2013, The Astrophysical Journal, 779, 3

Linsky, J. L., Yang, H., France, K., et al. 2010, The Astrophysical Journal, 717, 1291

Lockwood, A. C., Johnson, J. A., Bender, C. F., et al. 2014, The Astrophysical Journal Letters, 783, L29

Lopez, E. D. & Fortney, J. J. 2013, The Astrophysical Journal, 776, 2

Lopez, E. D., Fortney, J. J., & Miller, N. 2012, The Astrophysical Journal, 761, 59

Madhusudhan, N. 2012, The Astrophysical Journal, 758, 36

Madhusudhan, N. & Burrows, A. 2012, The Astrophysical Journal, 747, 25

Madhusudhan, N., Harrington, J., Stevenson, K. B., et al. 2011a, Nature, 469, 64

Madhusudhan, N., Lee, K. K. M., & Mousis, O. 2012, ApJ, 759, L40

Madhusudhan, N., Mousis, O., Johnson, T. V., & Lunine, J. I. 2011b, The Astrophysical Journal, 743, 191

Madhusudhan, N. & Seager, S. 2010, The Astrophysical Journal, 725, 261

Madhusudhan, N. & Seager, S. 2011, The Astrophysical Journal, 729, 41

Majeau, C., Agol, E., & Cowan, N. B. 2012, ApJ, 747, L20

Mandell, A. M., Haynes, K., Sinukoff, E., et al. 2013, The Astrophysical Journal, 779, 128

Marley, M. S., Fortney, J. J., Hubickyj, O., Bodenheimer, P., & Lissauer, J. J. 2007, The Astrophysical Journal, 655, 541

Mayne, N. J., Baraffe, I., Acreman, D. M., et al. 2014, A&A, 561, A1

Mazeh, T. & Faigler, S. 2010, A&A, 521, L59

Menou, K. 2012, ApJ, 754, L9

Miguel, Y. & Kaltenegger, L. 2014, The Astrophysical Journal, 780, 166

Mihalas, D. & Mihalas, B. W. 1984, Foundations of radiation hydrodynamics

Militzer, B. & Hubbard, W. B. 2013, The Astrophysical Journal, 774, 148

Miller, N. & Fortney, J. J. 2011, ApJ, 736, L29

Mochalov, M. A., Il'kaev, R. I., Fortov, V. E., et al. 2012, Soviet Journal of Experimental and Theoretical Physics, 115, 614

Mordasini, C. 2013, A&A, 558, A113

Moses, J. I., Madhusudhan, N., Visscher, C., & Freedman, R. S. 2013, The Astrophysical Journal, 763, 25

Mousis, O., Lunine, J. I., Madhusudhan, N., & Johnson, T. V. 2012, ApJ, 751, L7

Murgas, F., Palle, E., Zapatero Osorio, M. R., et al. 2014, ArXiv e-prints

Murray-Clay, R. A., Chiang, E. I., & Murray, N. 2009, The Astrophysical Journal, 693, 23

Narita, N., Suto, Y., Winn, J. N., et al. 2005, PASJ, 57, 471

Nascimbeni, V., Piotto, G., Pagano, I., et al. 2013, A&A, 559, A32

Nettelmann, N., Fortney, J. J., Kramm, U., & Redmer, R. 2011, The Astrophysical Journal, 733, 2

Nikolov, N., Sing, D. K., Pont, F., et al. 2014, MNRAS, 437, 46

Parmentier, V. & Guillot, T. 2014, A&A, 562, A133

Parmentier, V., Guillot, T., Fortney, J. J., & Marley, M. S. 2014a, ArXiv:1311.6322

Parmentier, V., Showman, A. P., & de Wit, J. 2014b, ArXiv e-prints

Parmentier, V., Showman, A. P., & Lian, Y. 2013, A&A, 558, A91

Perez-Becker, D. & Chiang, E. 2013, MNRAS, 433, 2294

Perez-Becker, D. & Showman, A. P. 2013, The Astrophysical Journal, 776, 134

Perna, R., Menou, K., & Rauscher, E. 2010, The Astrophysical Journal, 719, 1421

Phillips, N. A. 1966, Journal of Atmospheric Sciences, 23, 626

Phillips, N. A. 1968, Journal of Atmospheric Sciences, 25, 1155

Pierrehumbert, R. T. 2010, Principles of Planetary Climate

Pont, F., Sing, D. K., Gibson, N. P., et al. 2013, MNRAS

Poppenhaeger, K., Schmitt, J. H. M. M., & Wolk, S. J. 2013, The Astrophysical Journal, 773, 62

Prinn, R. G. & Barshay, S. S. 1977, Science, 198, 1031

Rappaport, S., Levine, A., Chiang, E., et al. 2012, The Astrophysical Journal, 752, 1

Rasio, F. A., Tout, C. A., Lubow, S. H., & Livio, M. 1996, The Astrophysical Journal, 470, 1187

Rauer, H., Catala, C., Aerts, C., et al. 2013, ArXiv e-prints

Rauscher, E. & Menou, K. 2013, The Astrophysical Journal, 764, 103

Rauscher, E. & Showman, A. P. 2014, The Astrophysical Journal, 784, 160

Redfield, S., Endl, M., Cochran, W. D., & Koesterke, L. 2008, ApJ, 673, L87

Richardson, L. J., Deming, D., Horning, K., Seager, S., & Harrington, J. 2007, Nature, 445, 892

Robinson, T. D. & Catling, D. C. 2012, The Astrophysical Journal, 757, 104

Rodler, F., Kürster, M., & Barnes, J. R. 2013, MNRAS, 432, 1980

Rodler, F., Lopez-Morales, M., & Ribas, I. 2012, ApJ, 753, L25

Rogers, T. M. & Showman, A. P. 2014, ApJ, 782, L4

Saumon, D., Chabrier, G., & van Horn, H. M. 1995, ApJS, 99, 713

Seager, S., Kuchner, M., Hier-Majumder, C. A., & Militzer, B. 2007, The Astrophysical Journal, 669, 1279

Shapiro, R. 1970, Rev. Geophys., 8, 359

Showman, A. P., Cooper, C. S., Fortney, J. J., & Marley, M. S. 2008, The Astrophysical Journal, 682, 559

Showman, A. P., Fortney, J. J., Lewis, N. K., & Shabram, M. 2013a, The Astrophysical Journal, 762, 24

Showman, A. P., Fortney, J. J., Lian, Y., et al. 2009, The Astrophysical Journal, 699, 564

Showman, A. P. & Guillot, T. 2002, A&A, 385, 166

Showman, A. P. & Polvani, L. M. 2011, The Astrophysical Journal, 738, 71

Showman, A. P., Wordsworth, R. D., Merlis, T. M., & Kaspi, Y. 2013b, Atmospheric Circulation of Terrestrial Exoplanets, ed. S. J. Mackwell, A. A. Simon-Miller, J. W. Harder, & M. A. Bullock, 277–326

Sing, D. K., Désert, J.-M., Fortney, J. J., et al. 2011a, A&A, 527, A73

Sing, D. K., Désert, J.-M., Lecavelier Des Etangs, A., et al. 2009, A&A, 505, 891

Sing, D. K., Huitson, C. M., Lopez-Morales, M., et al. 2012, MNRAS, 426, 1663

Sing, D. K., Lecavelier des Etangs, A., Fortney, J. J., et al. 2013, MNRAS

Sing, D. K., Pont, F., Aigrain, S., et al. 2011b, MNRAS, 416, 1443

Sing, D. K., Vidal-Madjar, A., Désert, J.-M., Lecavelier des Etangs, A., & Ballester, G. 2008a, The Astrophysical Journal, 686, 658

Sing, D. K., Vidal-Madjar, A., Lecavelier des Etangs, A., et al. 2008b, The Astrophysical Journal, 686, 667

Skålid Amundsen, D., Baraffe, I., Tremblin, P., et al. 2014, ArXiv e-prints

Snellen, I., de Kok, R., de Mooij, E., et al. 2011, in IAU Symposium, Vol. 276, IAU Symposium, ed. A. Sozzetti, M. G. Lattanzi, & A. P. Boss, 208–211

Snellen, I. A. G., Albrecht, S., de Mooij, E. J. W., & Le Poole, R. S. 2008, A&A, 487, 357

Snellen, I. A. G., de Kok, R. J., de Mooij, E. J. W., & Albrecht, S. 2010, Nature, 465, 1049

Snellen, I. A. G., de Mooij, E. J. W., & Albrecht, S. 2009, Nature, 459, 543

Sotin, C., Grasset, O., & Mocquet, A. 2007, Icarus, 191, 337

Spiegel, D. S. & Burrows, A. 2010, The Astrophysical Journal, 722, 871

Spiegel, D. S. & Burrows, A. 2012, The Astrophysical Journal, 745, 174

Spiegel, D. S. & Burrows, A. 2013, The Astrophysical Journal, 772, 76

Spiegel, D. S. & Madhusudhan, N. 2012, The Astrophysical Journal, 756, 132

Spiegel, D. S., Silverio, K., & Burrows, A. 2009, The Astrophysical Journal, 699, 1487

Stevenson, K. B., Bean, J. L., Seifahrt, A., et al. 2013, ArXiv e-prints

Sudarsky, D., Burrows, A., & Pinto, P. 2000, The Astrophysical Journal, 538, 885

Swain, M., Deroo, P., Tinetti, G., et al. 2013, Icarus, 225, 432

Swain, M. R., Bouwman, J., Akeson, R. L., Lawler, S., & Beichman, C. A. 2008a, The Astrophysical Journal, 674, 482

Swain, M. R., Deroo, P., Griffith, C. A., et al. 2010, Nature, 463, 637

Swain, M. R., Vasisht, G., & Tinetti, G. 2008b, Nature, 452, 329

Tennyson, J. & Yurchenko, S. N. 2012, MNRAS, 425, 21

Tinetti, G., Deroo, P., Swain, M. R., et al. 2010, ApJ, 712, L139

Tinetti, G., Vidal-Madjar, A., Liang, M.-C., et al. 2007, Nature, 448, 169

Valencia, D., Guillot, T., Parmentier, V., & Freedman, R. S. 2013, The Astrophysical Journal, 775, 10

Valencia, D., Ikoma, M., Guillot, T., & Nettelmann, N. 2010, A&A, 516, A20

Valencia, D., O'Connell, R. J., & Sasselov, D. 2006, Icarus, 181, 545

Van Werkhoven, T. I. M., Brogi, M., Snellen, I. A. G., & Keller, C. U. 2014, A&A, 561, A3

Vaytet, N., Chabrier, G., Audit, E., et al. 2013, A&A, 557, A90

Vidal-Madjar, A., Désert, J.-M., Lecavelier des Etangs, A., et al. 2004, ApJ, 604, L69

Vidal-Madjar, A., Huitson, C. M., Bourrier, V., et al. 2013, A&A, 560, A54

Vidal-Madjar, A., Huitson, C. M., Lecavelier Des Etangs, A., et al. 2011a, A&A, 533, C4

Vidal-Madjar, A., Lecavelier des Etangs, A., Désert, J.-M., et al. 2003, Nature, 422, 143

Vidal-Madjar, A., Sing, D. K., Lecavelier Des Etangs, A., et al. 2011b, A&A, 527, A110

Visscher, C. & Moses, J. I. 2011, The Astrophysical Journal, 738, 72

Waldmann, I. P. 2012, The Astrophysical Journal, 747, 12

Welsh, W. F., Orosz, J. A., Seager, S., et al. 2010, ApJ, 713, L145

White, A. A. & Bromley, R. A. 1995, Quarterly Journal of the Royal Meteorological Society, 121, 399

Wilson, H. F. & Militzer, B. 2012a, Physical Review Letters, 108, 111101

Wilson, H. F. & Militzer, B. 2012b, The Astrophysical Journal, 745, 54

Wood, P. L., Maxted, P. F. L., Smalley, B., & Iro, N. 2011, MNRAS, 412, 2376

Woodgate, B. E., Kimble, R. A., Bowers, C. W., et al. 1998, PASP, 110, 1183

Wu, Y. & Lithwick, Y. 2013, The Astrophysical Journal, 763, 13

Youdin, A. N. & Mitchell, J. L. 2010, The Astrophysical Journal, 721, 1113

Yunsheng Tian, B. & Stanley, S. 2013, The Astrophysical Journal, 768, 156

Yurchenko, S. N. & Tennyson, J. 2014, MNRAS

Zapolsky, H. S. & Salpeter, E. E. 1969, The Astrophysical Journal, 158, 809

Zeng, L. & Sasselov, D. 2013, PASP, 125, 227

Zhou, G. & Bayliss, D. D. R. 2012, MNRAS, 426, 2483